ADVANCED MATERIALS FOR THE RESTORATION AND RECONSTRUCTION OF DENTAL FUNCTIONS

EDITED BY: Jianxun Ding, Junchao Wei, Bing Han and Chider Chen
PUBLISHED IN: Frontiers in Bioengineering and Biotechnology and
Frontiers in Materials

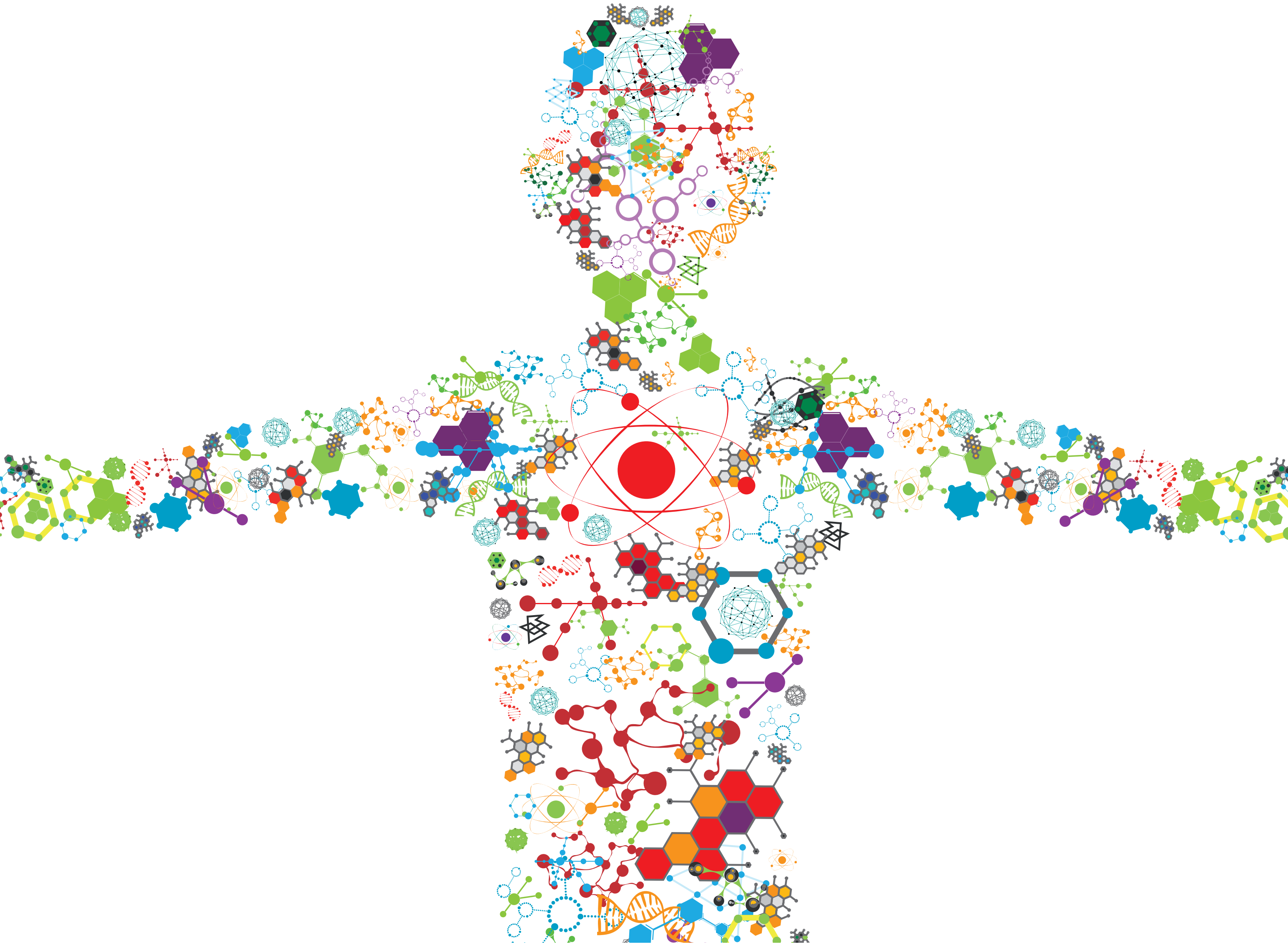

frontiers Research Topics

Frontiers eBook Copyright Statement

The copyright in the text of individual articles in this eBook is the property of their respective authors or their respective institutions or funders. The copyright in graphics and images within each article may be subject to copyright of other parties. In both cases this is subject to a license granted to Frontiers.

The compilation of articles constituting this eBook is the property of Frontiers.

Each article within this eBook, and the eBook itself, are published under the most recent version of the Creative Commons CC-BY licence. The version current at the date of publication of this eBook is CC-BY 4.0. If the CC-BY licence is updated, the licence granted by Frontiers is automatically updated to the new version.

When exercising any right under the CC-BY licence, Frontiers must be attributed as the original publisher of the article or eBook, as applicable.

Authors have the responsibility of ensuring that any graphics or other materials which are the property of others may be included in the CC-BY licence, but this should be checked before relying on the CC-BY licence to reproduce those materials. Any copyright notices relating to those materials must be complied with.

Copyright and source acknowledgement notices may not be removed and must be displayed in any copy, derivative work or partial copy which includes the elements in question.

All copyright, and all rights therein, are protected by national and international copyright laws. The above represents a summary only. For further information please read Frontiers' Conditions for Website Use and Copyright Statement, and the applicable CC-BY licence.

ISSN 1664-8714
ISBN 978-2-88971-517-6
DOI 10.3389/978-2-88971-517-6

About Frontiers

Frontiers is more than just an open-access publisher of scholarly articles: it is a pioneering approach to the world of academia, radically improving the way scholarly research is managed. The grand vision of Frontiers is a world where all people have an equal opportunity to seek, share and generate knowledge. Frontiers provides immediate and permanent online open access to all its publications, but this alone is not enough to realize our grand goals.

Frontiers Journal Series

The Frontiers Journal Series is a multi-tier and interdisciplinary set of open-access, online journals, promising a paradigm shift from the current review, selection and dissemination processes in academic publishing. All Frontiers journals are driven by researchers for researchers; therefore, they constitute a service to the scholarly community. At the same time, the Frontiers Journal Series operates on a revolutionary invention, the tiered publishing system, initially addressing specific communities of scholars, and gradually climbing up to broader public understanding, thus serving the interests of the lay society, too.

Dedication to Quality

Each Frontiers article is a landmark of the highest quality, thanks to genuinely collaborative interactions between authors and review editors, who include some of the world's best academicians. Research must be certified by peers before entering a stream of knowledge that may eventually reach the public - and shape society; therefore, Frontiers only applies the most rigorous and unbiased reviews.
Frontiers revolutionizes research publishing by freely delivering the most outstanding research, evaluated with no bias from both the academic and social point of view. By applying the most advanced information technologies, Frontiers is catapulting scholarly publishing into a new generation.

What are Frontiers Research Topics?

Frontiers Research Topics are very popular trademarks of the Frontiers Journals Series: they are collections of at least ten articles, all centered on a particular subject. With their unique mix of varied contributions from Original Research to Review Articles, Frontiers Research Topics unify the most influential researchers, the latest key findings and historical advances in a hot research area! Find out more on how to host your own Frontiers Research Topic or contribute to one as an author by contacting the Frontiers Editorial Office: frontiersin.org/about/contact

ADVANCED MATERIALS FOR THE RESTORATION AND RECONSTRUCTION OF DENTAL FUNCTIONS

Topic Editors:
Jianxun Ding, Chinese Academy of Sciences, China
Junchao Wei, Nanchang University, China
Bing Han, Peking University School and Hospital of Stomatology, China
Chider Chen, University of Pennsylvania, United States

Citation: Ding, J., Wei, J., Han, B., Chen, C., eds. (2021). Advanced Materials for the Restoration and Reconstruction of Dental Functions. Lausanne: Frontiers Media SA. doi: 10.3389/978-2-88971-517-6

Table of Contents

_05_ ***Editorial: Advanced Materials for the Restoration and Reconstruction of Dental Functions***
Junchao Wei, Jianxun Ding, Bing Han and Chider Chen

_08_ ***Hierarchical Micro-Nano Topography Promotes Cell Adhesion and Osteogenic Differentiation via Integrin α2-PI3K-AKT Signaling Axis***
Huimin Zheng, Yujuan Tian, Qian Gao, Yingjie Yu, Xianyou Xia, Zhipeng Feng, Feng Dong, Xudong Wu and Lei Sui

_24_ ***Microporous Frameworks as Promising Platforms for Antibacterial Strategies Against Oral Diseases***
Yao Wan, Wenzhou Xu, Xuan Ren, Yu Wang, Biao Dong and Lin Wang

_44_ ***An Evaluation of Norspermidine on Anti-fungal Effect on Mature* Candida albicans *Biofilms and Angiogenesis Potential of Dental Pulp Stem Cells***
Yan He, Yanfan Cao, Yangfan Xiang, Fengting Hu, Fengyu Tang, Yanni Zhang, Abdullkhaleg Ali Albashari, Zhenjie Xing, Lihua Luo, Yan Sun, Qiang Huang, Qingsong Ye and Keke Zhang

_56_ ***Recent Advances on Synthetic and Polysaccharide Adhesives for Biological Hemostatic Applications***
Dawei Li, Jing Chen, Xing Wang, Mingming Zhang, Chunlin Li and Jin Zhou

_72_ ***E-quality Control in Dental Metal Additive Manufacturing Inspection Using 3D Scanning and 3D Measurement***
Liang Du, Yiwen Lai, Chunwang Luo, Yong Zhang, Jun Zheng, Xiaohong Ge and Yuangang Liu

_81_ ***Recent Advances of Chitosan-Based Injectable Hydrogels for Bone and Dental Tissue Regeneration***
Guoke Tang, Zhihong Tan, Wusi Zeng, Xing Wang, Changgui Shi, Yi Liu, Hailong He, Rui Chen and Xiaojian Ye

_96_ ***Electrospinning With Lyophilized Platelet-Rich Fibrin Has the Potential to Enhance the Proliferation and Osteogenesis of MC3T3-E1 Cells***
Jing Nie, Shumei Zhang, Peng Wu, Yuangang Liu and Yanjun Su

_106_ ***Current Trends of Targeted Drug Delivery for Oral Cancer Therapy***
Mingming Zhang, Jianqin Liang, Yanyu Yang, Huize Liang, Huaping Jia and Dawei Li

_117_ ***Biologically Modified Polyether Ether Ketone as Dental Implant Material***
Zhangyu Ma, Xingyu Zhao, Jing Zhao, Zhilong Zhao, Qihui Wang and Congxiao Zhang

_134_ ***Customized Borosilicate Bioglass Scaffolds With Excellent Biodegradation and Osteogenesis for Mandible Reconstruction***
Peng Zhang, Kang Yang, Ziyu Zhou, Xingrong Zhu, Wenchao Li, Chuanliang Cao, Kui Zhou, Lan Liao and Fanrong Ai

_143_ ***Enhanced Osseointegration by the Hierarchical Micro-Nano Topography on Selective Laser Melting Ti-6Al-4V Dental Implants***
Tianyu Shu, Yuchen Zhang, Guo Sun, Yang Pan, Gang He, Yilong Cheng, Ang Li and Dandan Pei

156 ***Adhesion of Teeth***
Zhilong Zhao, Qihui Wang, Jing Zhao, Bo Zhao, Zhangyu Ma and Congxiao Zhang

167 ***Graphene-Modified Titanium Surface Enhances Local Growth Factor Adsorption and Promotes Osteogenic Differentiation of Bone Marrow Stromal Cells***
Jiayu Lu, Jiayue Sun, Derong Zou, Jinlin Song and Sheng Yang

177 ***Bioinspired Modifications of PEEK Implants for Bone Tissue Engineering***
Xinming Gu, Xiaolin Sun, Yue Sun, Jia Wang, Yiping Liu, Kaixuan Yu, Yao Wang and Yanmin Zhou

192 ***Nanostructured Zirconia Surfaces Regulate Human Gingival Fibroblasts Behavior Through Differential Modulation of Macrophage Polarization***
Jincheng Wu, Pei Yu, Huling Lv, Shuang Yang and Zhe Wu

206 ***Combination of Polydopamine Coating and Plasma Pretreatment to Improve Bond Ability Between PEEK and Primary Teeth***
Rui Teng, Yuchen Meng, Xiaodan Zhao, Jie Liu, Rui Ding, Yilong Cheng, Yunhe Zhang, Yanfeng Zhang, Dandan Pei and Ang Li

215 ***Composite System of 3D-Printed Polymer and Acellular Matrix Hydrogel to Repair Temporomandibular Joint Disc***
Ping Yi, Jiadi Liang, Futing Huang, Zuodong Zhao, Xiaohui Zhou, Qianya Gao, Min Huang, Baoyi Chen, Zhenzhao Guo and Chang Liu

227 ***The Optimization of Ti Gradient Porous Structure Involves the Finite Element Simulation Analysis***
Bowen Liu, Wei Xu, Xin Lu, Maryam Tamaddon, Mingying Chen, Jiaqi Dong, Yitong Liu, Lijia Guo, Jiazhen Zhang, Xuanhui Qu, Xinbo He and Chaozong Liu

frontiers
in Bioengineering and Biotechnology

EDITORIAL
published: 03 September 2021
doi: 10.3389/fbioe.2021.756860

Editorial: Advanced Materials for the Restoration and Reconstruction of Dental Functions

Junchao Wei[1,2], Jianxun Ding[3]*, Bing Han[4]* and Chider Chen[5]**

[1]School of Stomatology, Nanchang University, Nanchang, China, [2]Key Laboratory of Oral Biomedicine, Nanchang, China, [3]Key Laboratory of Polymer Ecomaterials, Changchun Institute of Applied Chemistry, Chinese Academy of Sciences, Changchun, China, [4]Department of Orthodontics, School and Hospital of Stomatology, Peking University, Beijing, China, [5]Department of Oral and Maxillofacial Surgery and Pharmacology, School of Dental Medicine, University of Pennsylvania, Philadelphia, PA, United States

Keywords: biomaterial, dental material, antibacterial material, implant, drug delivery, bone regeneration, tissue engineering

OPEN ACCESS

Edited and reviewed by:
Hasan Uludag,
University of Alberta, Canada

****Correspondence:***
Junchao Wei
weijunchao@ncu.edu.cn
Jianxun Ding
jxding@ciac.ac.cn
Bing Han
kqbinghan@bjmu.edu.cn
Chider Chen
chenc10@upenn.edu

Specialty section:
This article was submitted to Biomaterials, a section of the journal Frontiers in Bioengineering and Biotechnology

Received: *11 August 2021*
Accepted: *18 August 2021*
Published: *03 September 2021*

Citation:
Wei J, Ding J, Han B and Chen C (2021) Editorial: Advanced Materials for the Restoration and Reconstruction of Dental Functions. Front. Bioeng. Biotechnol. 9:756860. doi: 10.3389/fbioe.2021.756860

Editorial on the Research Topic

Advanced Materials for the Restoration and Reconstruction of Dental Functions

Various dental diseases, such as periodontal infection, endodontic diseases, dentition and tooth defects, malocclusion, maxillofacial trauma, and oral squamous cell carcinoma, have caused severe suffering to patients. To solve these problems, many effective treatments, such as periodontal scaling, root canal therapy, orthodontic treatment, and tooth implantation, have been used in clinic. During most of these treatments, it must be noted that dental materials have played a critical role in realizing the restoration or reconstruction of dental functions.

Dental materials have brought many advanced choices for clinicians to treat various oral diseases and orthopedic aesthetics, thus significantly improving the oral health of human beings. Up until now, different types of materials, including polymers, inorganic materials, and metal materials, have been widely used for dental restoration, dental implantation, fracture fixation, orthodontic appliances and retainers, removable denture, and so forth. To fulfill the clinical requirements, materials with unique properties, such as antibacterial, osteoinductive, bioactive, adhesive, and mechanical properties, are well investigated. Furthermore, some innovative materials, which can be used for controlled drug delivery, are also helpful to treat oral and dental diseases. Besides, biocompatible scaffolds have gained more attention in the dental tissue engineering fields.

In the current Research Topic, the preparation and applications of advanced materials for the restoration and reconstruction of dental functions were contributed by 134 authors, containing seven review articles and 11 research articles (total views 36,348; as of August 25, 2021). These studies developed advanced polymers, inorganic materials, and metal materials for antibacterial, drug delivery, tissue regeneration, and so forth.

The formation of biofilm after the bacterial infection has been a significant headache for patients and physicians, and thus it is essential to investigate the antibacterial dental materials. Norspermidine (NSPD), a kind of polyamine, was a potential anti-biofilm agent, and its effect on mature biofilm of *Candida albicans* and human dental pulp stem cells was investigated (He et al.), demonstrating that the anti-biofilm effect of NSPD was dose-dependent. Microporous materials, such as zeolite, metal-organic frameworks, and covalent organic frameworks, have potential antibacterial properties and their application to treat oral infection diseases, including dental caries, periodontitis, peri-implantitis, endodontic infections, and so forth, were reviewed (Wan et al.). Moreover, the microporous materials could be used as carriers to deliver antibacterial agents, which were widely used as dental materials. Except for antibacterial agents, the delivery of other bioactive agents by various materials, such as polymer/inorganic nanoparticles, liposomes, nanolipids, and hydrogels, is also essential for treating oral cancers. Typically, the state of the art of targeting drug delivery systems for oral delivery of different therapeutics was summarized, and the improvement of clinical efficiency, well-control of drug release, and reduction of side effects of drugs are still significant challenges (Zhang M. et al.).

Materials-mediated bone and dental tissue regeneration is also a hot topic. Tissue engineering has been a promising approach to regenerating the defect tissues and reconstructing the functions, while scaffolds are critical in practical tissue engineering. The injectable chitosan-based hydrogels with various stimuli-responsiveness and payloads have been widely investigated as tissue engineering scaffolds in dental repairs, such as periodontal and dental-pulp regeneration (Tang et al.). Bioactive glass has shown great potential in bone regeneration. Herein, a kind of borosilicate bioglass scaffolds was prepared, and their biodegradation and osteogenesis for mandible reconstruction were well investigated (Zhang P. et al.). Besides, platelet-rich fibrin (PRF) has become an attractive candidate in instrument implantation and regenerative medicine and was used to prepare scaffold blended with poly(vinyl alcohol) and sodium alginate through electrospinning (Nie et al.). PRF could enhance the proliferation and osteogenesis of osteogenic precursor cells, and thus the composite scaffolds can be a promising candidate for bone tissue engineering. Although tissue engineering has aroused much attention, great efforts are still required to expand the clinical applications.

Tissue engineering is a promising approach to attenuate symptoms of temporomandibular disorder (TMD), even repair or potentially replace the injured temporomandibular joint (TMJ) discs. Poly(ε-caprolactone)/polyurethane (PCL/PU) scaffolds were prepared *via* three-dimensional (3D) printing technology to imitate the region-specific biomechanical properties of TMJ discs (Yi et al.). Generally, 3D printing technology has been well used to process dental materials. For example, a metal crown for dental restoration could be prepared through 3D printing, while quality control is a challenge for dental metal. Herein, a combination of 3D scanning and 3D measurement for 3D inspection of the metal crown was proposed, which may archive 3D model and achieve rapid and high-quality control (Du et al.).

The surface performances of materials always determine their bioproperties and affect their functions. In this Research Topic, several studies focused on the surface management of dental materials and investigated their osteogenic properties. Titanium is one of the essential metal materials and widely used as a dental implant, and the surface morphology properties along with compositions may significantly affect its application. The osteointegration and osteogenic properties of titanium implants with hierarchical micro-nano topographies were investigated (Zheng et al.; Shu et al.). Furthermore, graphene-coated titanium was also prepared and used to adsorb local growth factors and promote osteogenic differentiation of bone marrow stromal cells (Lu et al.).

Polyetheretherketone (PEEK) was approved by the United States Food and Drug Administration (FDA) as an implantable biomaterial and has excellent potential for fixed-definition dental bridge brackets, implant abutments, and implants. However, PEEK has insufficient biological activity when used as an implant and cannot form good osseointegration with the surrounding bone tissue. For that, various techniques, such as plasma treatment and polydopamine coatings, have been developed to modify PEEK to improve the bondability between PEEK and teeth (Teng et al.). Besides, Zhang and coworkers summarized the current modification methods for PEEK, including surface modification and blending modification (Ma et al.). Furthermore, inspired by the component, structure, and function of bone tissue, biocompatible and multifunctional PEEK implants could be fabricated (Gu et al.).

There are also other kinds of materials, such as hemostatic and adhesion materials, which are also very essential as dental materials. Both synthetic polymer- and natural polysaccharide-based multifunctional adhesives could be used for hemostasis (Li et al.). Besides, there are also many other requirements for dental adhesives to restore the function of teeth, and the basic adhesion theory and application of adhesion in dental bonding materials were presented (Zhao et al.).

The immune response toward nanomaterials has been an essential factor affecting the reconstruction of functional tissue. Furthermore, the surface morphology, structure, and composition may significantly affect the immune response. Wu and colleagues prepared nanoscale zirconia nanoparticles with various surface performances and investigated their effect on macrophage phenotypes and gingival fibroblasts, and the macrophage modulation could provide a favorable immune microenvironment for soft tissue cell integration (Wu et al.).

The biomechanical properties of dental implants are another essential factor for the restoration and reconstruction of dental functions. Finite element simulation was used to simulate the mechanical behaviors of implants and surrounding bone tissue, which showed that the bone could achieve optimal ingrowth into the gradient porous structure (Liu et al.).

Overall, this Research Topic covered several cutting edge fields in materials used for restoration and reconstruction of dental functions, such as antibacterial materials, bone tissue engineering scaffolds, implants, and so forth, which may help readers get more about the development of dental materials. Furthermore, the works may connect the material scientists and physicians and promote the studies from theoretical investigation to clinical transformation.

AUTHOR CONTRIBUTIONS

All authors listed have made a substantial, direct, and intellectual contribution to the work, and approved it for publication.

FUNDING

JW also appreciates the support of the Key Research and Development Program of Jiangxi Province (Grant No. 20202BBG73012).

ACKNOWLEDGMENTS

The editors appreciate the contributions of all the authors to this Research Topic, the constructive comments of all the reviewers, and the editorial support from Frontiers throughout the publication process.

Conflict of Interest: The authors declare that the research was conducted in the absence of any commercial or financial relationships that could be construed as a potential conflict of interest.

frontiers
in Bioengineering and Biotechnology

ORIGINAL RESEARCH
published: 19 May 2020
doi: 10.3389/fbioe.2020.00463

Hierarchical Micro-Nano Topography Promotes Cell Adhesion and Osteogenic Differentiation via Integrin α2-PI3K-AKT Signaling Axis

Huimin Zheng[1,2†], Yujuan Tian[1,2†], Qian Gao[1,2], Yingjie Yu[3], Xianyou Xia[2], Zhipeng Feng[1], Feng Dong[2], Xudong Wu[2‡] and Lei Sui[1*‡]*

[1] Department of Prosthodontics, School and Hospital of Stomatology, Tianjin Medical University, Tianjin, China, [2] Department of Cell Biology, 2011 Collaborative Innovation Center of Tianjin for Medical Epigenetics, Tianjin Key Laboratory of Medical Epigenetics, Tianjin Medical University, Tianjin, China, [3] Health Science Center, Institute of Translational Medicine, The First Affiliated Hospital of Shenzhen University, Shenzhen, China

Edited by:
Jianxun Ding,
Changchun Institute of Applied Chemistry, CAS, China

Reviewed by:
Shengbin Huang,
Wenzhou Medical University, China
Sheng Yang,
Chongqing Medical University, China
Zhaoyang Li,
Tianjin University, China

***Correspondence:**
Xudong Wu
wuxudong@tmu.edu.cn
Lei Sui
suilei@tmu.edu.cn

‡ORCID:
Xudong Wu
orcid.org/0000-0001-9594-479X
Lei Sui
orcid.org/0000-0003-3586-9999

† These authors have contributed equally to this work

Specialty section:
This article was submitted to Biomaterials, a section of the journal Frontiers in Bioengineering and Biotechnology

Received: *20 March 2020*
Accepted: *21 April 2020*
Published: *19 May 2020*

Citation:
Zheng H, Tian Y, Gao Q, Yu Y, Xia X, Feng Z, Dong F, Wu X and Sui L (2020) Hierarchical Micro-Nano Topography Promotes Cell Adhesion and Osteogenic Differentiation via Integrin α2-PI3K-AKT Signaling Axis. Front. Bioeng. Biotechnol. 8:463. doi: 10.3389/fbioe.2020.00463

Surface topography dictates important aspects of cell biological behaviors. In our study, hierarchical micro-nano topography (SLM-AHT) with micro-scale grooves and nano-scale pores was fabricated and compared with smooth topography (S) and irregular micro-scale topography (SLA) surfaces to investigate mechanism involved in cell-surface interactions. Integrin α2 had a higher expression level on SLM-AHT surface compared with S and SLA surfaces, and the expression levels of osteogenic markers icluding Runx2, Col1a1, and Ocn were concomitantly upregulated on SLM-AHT surface. Moreover, formation of mature focal adhesions were significantly enhanced in SLM-AHT group. Noticablely, silencing integrin α2 could wipe out the difference of osteogenic gene expression among surfaces with different topography, indicating a crucial role of integrin α2 in topography induced osteogenic differentiation. In addition, PI3K-AKT signaling was proved to be regulated by integrin α2 and consequently participate in this process. Taken together, our findings illustrated that integrin α2-PI3K-AKT signaling axis plays a key role in hierarchical micro-nano topography promoting cell adhesion and osteogenic differentiation.

Keywords: topography, adhesion, osteogenic differentiation, integrin α2, PI3K-AKT

INTRODUCTION

Surface topography is a key determinant of the cellular response to foreign materials (Chen et al., 2014; Dalby et al., 2014; Gautrot et al., 2014; Denchai et al., 2018), which is extremely important for intraosseous implants to achieve osseointegration. In the past few years, there has been growing interest in the effects of different surface features at various scales on cell adhesion, proliferation, and osteogenic differentiation (Anselme et al., 2010; Chen et al., 2014; Li et al., 2016; Skoog et al., 2018; Zhang et al., 2019). It is well recognized that micro-scale structures ensure the initial stability of the implant and promote the bone locking (Saruta et al., 2019), while nano-scale structures have more significant effects on the adhesion and differentiation of cells (Kim et al., 2013; Gorelik and Gautreau, 2014; Cimmino et al., 2018). Furthermore, it has been illustrated that the regulatory effect of nano-scale structures is precisely based on the mechanical retention provided by the micro-scale structures, i.e., the initial stability of intraosseous implants (Deng et al., 2019). Accordingly, hierarchical micro-nano topography is a better choice for intraosseous implants in mediating cell-surface interactions compared to single-scale topography. It is noteworthy that natural bone is a loose porous multi-ordered structure composed of nano-scale collagen and hydroxyapatite and micro-scale bone plates and pores (Robling et al., 2006; Karsenty et al., 2009; Zhu et al., 2020). To mimic this environment, it is also of great significance to manufacture intraosseous implants with hierarchical micro-nano surface topography (Shah et al., 2018; Cui et al., 2019; Zhang et al., 2019). In our previous work, we fabricated titanium surfaces with hierarchical microprotrusion-nanonotch topography using direct metal laser sintering technique together with acid etching treatment, which could promote osteogenic differentiation of stem cells (Zheng et al., 2018). To enable further performance improvements, hierarchical microgroove-nanopore topography was fabricated by selective laser melting (SLM) technique combined with alkali heat treatment (AHT) because of higher fabricating efficiency and less consumption of raw materials. And our preliminary results indicated that this topography could better promote cell adhesion and osteogenic differentiation. However, the mechanisms implicated in the cell-surface interactions remain unclear.

In the early stages of the cell-surface interactions, cells sense the environment through lamellipodia and filopodia composed of integrins (Mattila and Lappalainen, 2008; You et al., 2014; Sun et al., 2016; Michael and Parsons, 2020). During spreading on the surface, cells initially form nascent adhesions (NAs) at their periphery (Bachir et al., 2014). Some of NAs mature into focal complexes (FCs) (Sun et al., 2014). Both NAs and FCs are not stable. They either disappear in minutes or transform into focal adhesions (FAs) (Valdembri and Serini, 2012), which consist of several proteins including integrin, vinculin, talin, paxillin, tensin, zyxin, focal adhesion kinase (FAK), and α-actinin (Wozniak et al., 2004), and anchor cells to the substrate (Li et al., 2017). It was reported that by simply controlling the topography of surfaces, one can modulate the formation of FAs, and consequently alter cell-surface interactions (Geiger et al., 2009; Nasrollahi et al., 2016; Lou et al., 2019; Janssen et al., 2020). Integrin, one of the indispensable component of FAs, is likely to be involved in this process (Ginsberg, 2014; De Franceschi et al., 2015; Karimi et al., 2018). Various integrins consisting of different α and β subunits are recruited on different surface topography (De Franceschi et al., 2015). Among them, integrin α2 is considered playing an important role in regulating cell adhesion and osteogenic differentiation (Olivares-Navarrete et al., 2015). Knockdown of α2 integrin subunits inhibited the formation of osteogenic microenvironment (Raines et al., 2019). And it was also reported that integrin α2 is required for activation of Runx2, the following expression of Ocn, and ECM mineralization procedure (Siebers et al., 2005; Hui-Min, Hu et al., 2013). Accordingly, we hypothesize that integrin α2 expression could be regulated by surface structures and subsequently influence osteoblast differentiation.

The osteogenic promoting effect of integrin α2 is possibly related to PI3K-AKT signaling which is involved in multiple cell behaviors including proliferation, apoptosis, glucose metabolism, differentiation and migration (Gu et al., 2013; Edlind and Hsieh, 2014; Feng et al., 2018). PI3Ks are composed of a regulatory subunit (p85) and a catalytic subunit (p110), and can be activated via tyrosine kinase and cytosolic tyrosine kinases (Xu et al., 2015; Arienti et al., 2019). Recent study showed that integrin α2 could active PI3K by enhancing phosphorylation of FAK (p397 FAK) (Yoon et al., 2017), and upregulation of PIP2 would result in loss of FAs (Izard and Brown, 2016). In addition, PI3K-AKT signaling and Runx2 were demonstrated mutually dependent on each other in the regulation of cell differentiation (Chuang et al., 2013; Choi et al., 2014). Taken all aspects above, we suppose that hierarchical micro-nano topography upregulates integrin α2 expression, which in turn activates PI3K-AKT signaling and thereby promotes osteogenic differentiation.

This study aims to investigate the role of integrin α2-PI3K-AKT signaling axis in hierarchical micro-nano topography induced cell adhesion and osteogenic differentiation. SLM-AHT titanium surfaces were fabricated and characterized, machined (S) and conventional sand-blasted, large grit and acid etching (SLA) titanium surfaces were used as control. To understand the effect of micro-nano topography on FAs, we stained the cells for vinculin, performed image analysis, and measured the numbers and size of the FAs on three surfaces. Meanwhile, in order to elucidate the role of integrin α2, we knockdown and overexpress integrin α2 in MC3T3-E1 cell line. Our results indicate that hierarchical micro-nano topography could promote cell adhesion by enhancing assembling of mature FAs through increased expression of integrin α2. Furthermore, PI3K-AKT signaling is also influenced by the expression of integrin α2 while consequently regulates osteogenic differentiation, therefore, integrin α2-PI3K-AKT signaling axis plays a key role in hierarchical micro-nano topography promoting cell adhesion and osteogenic differentiation.

MATERIALS AND METHODS

Specimen Preparation

Three groups of titanium specimens (disk-shaped, 6-mm in diameter and 2-mm in thickness, Ti-6Al-4V; Institute of Aeronautical Materials, Beijing, China) were prepared, including SLM-AHT group, SLA group and smooth titanium (S) group. SLM-AHT disks were fabricated in an argon atmosphere with Yb fiber laser system (EOS M280, EOS GmbH, Krailling, Germany) using a wave length of 1054 nm, continuous power of 200 W, scanning speed of 7 m-s and a laser spot size of 0.1 mm. The resultant disks were then etched with 1.5% HF for 30 min. After that, titanium specimens were treated in 5 mol/L NaOH at 100°C for 2 h and then heated in Muffle furnace (200°C for 20 min, 400°C for 20 min, 600°C for 20 min) to generate surfaces with hierarchical microgroove-nanopore topography. The SLA disks were prepared by sandblasting and acid-etching technology. Smooth Ti disks were polished with silicon carbide sandpaper of No. 240, 360, 400, 600, 800, 1000, and 2000 grits in series. All the specimens were washed with acetone, absolute alcohol and MilliQ water sequentially. Finally, specimens were cleaned with double-distilled water (ddH2O) in an ultrasonic cleaner for 30 min, dried at room temperature for 1 h and sterilized in an autoclave at 120°C for 20 min before use.

Surface Topography Observation

Surface topography of S, SLA, and SLM-AHT surfaces were observed by scanning electron microscopy (SEM, Carl Zeiss SMT Ltd., Cambridge, United Kingdom). High-magnification images were used to qualitatively evaluate the surface nano-scale features. In addition, the average pore diameter was calculated by ImageJ software.

Cell Culture

Mouse calvaria-derived osteogenic cells MC3T3-E1 from American Type Culture Collection (ATCC) were cultured in fresh DMEM (HyClone, Logan, UT, United States) with 10% FBS (Gibco, New York, NY, United States) and 1% penicillin-streptomycin at 37°C in a humidified atmosphere with 5% CO_2. Cells were seeded at a density of 1×10^4 cells-well and incubated on specimens. Culture medium was replaced the next day with osteo-induction (OI) medium containing 10% FBS, 1% penicillin-streptomycin, 50 μg-mL ascorbic acid, 10 nmol-L dexamethasone and 5 mmol-L β-glycerophosphate. The medium was changed every 2 days. Samples were cultured for desired times in the following experiments.

Cell Morphology and Cell Spreading Assay

For cell morphological and spreading analysis, cells were fixed for 30 min at 4°C in 4% paraformaldehyde, subsequently permeabilized with 0.05% Triton X-100 (Sigma-Aldrich) for 10 min. After rinsed with PBS three times, cells were dehydrated through an ethanol series (30%, 50%, 70%, 90%, 95%, and two times 100%), followed by drying in a Critical Point Drier (Balzers CPD 030, Hudson, NH, United States). Characterization of the cell morphology on S, SLA, and SLM-AHT surfaces were carried out by SEM and confocal laser scanning microscope (CLSM, Olympus, Japan).

Cell Proliferation Assay

For cell proliferation assay, cells were seeded on S, SLA, and SLM-AHT surfaces in culture medium with DAPI (0.5 mg-mL) at a density of 1×10^4 cells-well. After culturing for 6 and 24 h, entire substrates were surveyed photographically at 10× magnification and the DAPI stained nucleus were automatically detected and counted using ImageJ software.

Scratch Assay

Scratch assay was performed as a model for wounding on S, SLA, and SLM-AHT surfaces. In a confluent monolayer of cells that had been serum-starved in DMEM for 8 h, a scratch was made with a cell scraper. The width of the scratch was measured at the beginning and after 6 or 24 h of culturing in DMEM with 0.5% serum. Cells at the edge of the wound were observed by DAPI staining for cell visualization. Relative closure was calculated by dividing the different group wound closures by that of the blank group.

Immunofluorescence Staining

MC3T3-E1 were seeded on titanium specimens in 12-well plates at a density of 2×10^4 cells-well. After 3 days of culture, the samples were fixed in 4% paraformaldehyde for 10 min before being permeabilized with 0.05% Triton X-100 (Sigma-Aldrich) for 5 min. The samples were blocked in BSA (5 mg/mL) solution for 1 h. The primary antibody was rabbit anti-Runx2 antibody (1:1000 dilution, Cell Signaling Technology), and cells were incubated overnight at 4°C with it. After incubation, the secondary antibody, a fluorescein isothiocyanate (FITC)-conjugated anti-rabbit antibody (1:2000 dilution, Invitrogen) was applied for 1 h at room temperature. After removing the secondary antibody solution, a FITC-conjugated anti-F-actin antibody (1:200 dilution, Solarbio) was used to stained cytoskeleton for 2 h and then the nucleus were stained with DAPI (5 mg-mL) for 5 min and stored in 1X PBS at 4°C until visualizing with CLSM. All steps of the incubations were performed in a humidified environment at room temperature in the dark. Between each incubation step, the samples were rinsed three times (3 min each) in PBS.

Immunofluorescence Visualization of FAs

To visualize the FAs, two samples of cells grown on S, SLA, and SLM-AHT surfaces were stained with rabbit anti-Vinculin antibody (1:1000 dilution, Sigma), FITC-conjugated anti-F-actin antibody (1:200 dilution, Solarbio) and DAPI according to manufacture protocols as above described. The samples were analyzed with a Zeiss Axio Imager M2 Optical Microscope (Carl Zeiss, Jena, Germany). High-magnification immunofluorescence imaging was used to study the FAs of the cells.

Image Analysis

To estimate the number and size of the FAs, the area occupied by vinculin staining was measured and quantified. For each substrate, three individual cells were evaluated after 6 and 24 h from two independent experiments. Immunofluorescence images were taken at 60× to obtain an optimal quality for processing. The captured color images were separated into single-channel greyscale images using the ImageJ split-channel command. To quantify the distribution and size of FAs throughout the cells, punctate vinculin sites were manually traced and the size of each FA was obtained using the Analyze Particle tool in ImageJ. And the FA whose area is larger than 3.14 μm^2 was defined as mature FA (Parsons et al., 2010; Hanein and Horwitz, 2012). The Shape Descriptors tool in ImageJ was used to measure cell area.

Western Blot Analysis

The proteins of 6 h, 24 h, 3 days, and 7 days cultured cells on S, SLA, and SLM-AHT surfaces were collected, sonicated and then centrifuged. The proteins in the supernatant were transferred to polyvinylidene difluoride (PVDF) membranes with a semidry transfer apparatus (Bio-Rad, Hercules, CA, United States).

The membranes were blocked with 5% dehydrated milk for 2 h and then incubated with following primary antibodies overnight at 4°C. Integrin α2 (Abclonal), Vinculin (Sigma), FAK (Cell Signaling Technology), P-FAK (Cell Signaling Technology), Runx2 (Cell Signaling Technology), Col1a1 (Solarbio), Ocn (Solarbio), PI3K (Cell Signaling Technology), PIP2 (Abcam), PIP3 (Novus), AKT (Cell Signaling Technology), P-AKT (Cell Signaling Technology), and housekeeping protein, glyceraldehyde 3-phosphate dehydrogenase (GAPDH) were used. Membranes were then incubated with a secondary antibody (1:1000 dilution) for 1 h at room temperature, and the antibody-bound proteins were detected using an ECL Western Blotting Analysis System (CWBIO, Beijing, China). The integrated optical density (IOD) was quantified using ImageJ software.

qRT-PCR Analysis

Quantitative real-time PCR was carried out at 6 h, 24 h, on 3 days and 7 days after cell seeding to evaluate the gene expression levels in cells grown on three titanium surfaces. The oligonucleotide primers for the adhesion and osteogenic related genes integrin α2, Vinculin, Runx2, Col1a1, and Ocn are listed in **Table 1**. RPO was used as the reference gene. Following incubation, the samples were washed in PBS, and the total RNA was extracted using Trizol reagent (Invitrogen-Life Technologies), according to the manufacturer's protocols. The amount of total RNA from each sample was quantified using a BioDrop DUO micro-volume spectrophotometer (Montreal Biotech Inc., Canada). qRT-PCR reactions were performed in 10 μl of PCR mixture containing 1 μg of each cDNA sample and specific primers using the QuantiTect SYBR Green PCR Kit (Qiagen, Hilden, Germany). The following conditions were used: 50°C for 10 min, followed by 95°C for 2 min, then 60 cycles of 95°C for 5 s, and 60°C for 10 min.

Construction of Integrin α2 Knockdown Plasmid

To knockdown the integrin α2 (ITGA2) gene, we designed three short hairpin RNAs (shRNA) from https://portals.broadinstitute.org/gpp/public/. The forward and reverse oligonucleotides were synthesized corresponding to the selected shRNA. The shRNA oligonucleotides sequences are listed in **Table 2**. Mix 1 μl of 10 μM of forward and reverse oligonucleotides in 10 μl of 1X T4 ligase buffer. Incubate at 95°C for 5 min and then ramp down to 25°C at 5°C/min. Prepare a 10 μl ligation reaction mix by adding 50 ng of pLKO.1 digestion product, 1 μl annealed shRNA oligonucleotides, 0.5 μl T4 ligase, 1 μl of 10X T4 ligase buffer. Incubate for 16°C overnight. Transform the ligation product into DH5α cells for 30 min on ice. Heat shock at 42°C for 90 s and return to the ice for 2 min. Add 500 μl of LB medium and incubate at 37°C with shaking for 1 h. Plate the transformation mixture on LB agar plates containing 100 μg-mL ampicillin. Incubate the plates overnight at 37°C in a microbiological incubator. After incubation, pick 3–5 colonies to identify a correct clone for proper insert identification by Sanger sequencing.

Construction of Integrin α2 Overexpression Plasmid

To overexpress integrin α2, we divided ITGA2 into A and B two segments and designed 4 clone primers: ITGA2-A-F, ITGA2-A-R, ITGA2-B-F, ITGA2-B-R (**Table 3**) because of the long sequence. Mix 1 μl of 10 μM forward and reverse oligonucleotides with 1 μl template (MC3T3-E1 cDNA as the template) in 50 μl 1X DNA Polymerase mix. PCR Program are as follows: step1: 95°C Pre-denaturation 3 min; step2: Denaturation 95°C 30 s; step3: Annealing 58°C 30 s; step4: Extension 72°C 90 s; step5: Cycle step2 to step4 35 cycles; step6: Final Extension 72°C 5 min. ITGA2-A and ITGA2-B were amplified. Then the homologous recombination primers oligonucleotides (ITGA2-OE-A-F, ITGA2-OE-B-R) were designed (**Table 3**). The forward and reverse oligonucleotides were added in the 5′ of ITGA2-A and 3′ of ITGA2-B using the same PCR program, respectively. ITGA2-OE-A and ITGA2-OE-B were amplified. Digest 1 μg

TABLE 1 | Primer sequences used for qRT-PCR analysis of gene expression.

Gene	Primer sequence	
Integrin α2	F	AAGTGCCCTGTGGACCTACCCA
	R	TGGTGAGGGTCAATCCCAGGCT
Vinculin	F	ACCTGCAGACCAAAACCAAC
	R	CTTACCGACTCCACGGTCAT
Runx2	F	ATCACTGACGTGCCCAGGCGTA
	R	AGGGCCCAGTTCTGAAGCACCT
Col1a1	F	CTCCTGACGCATGGCCAAGAA
	R	TCAAGCATACCTCGGGTTTCCA
Ocn	F	AGTCTGACAAAGCCTTCA
	R	AAGCAGGGTTAAGCTCACA
RPO	F	TTCATTGTGGGAGCAGAC
	R	CAGCAGTTTCTCCAGAGC

TABLE 2 | Oligonucleotides sequence used for integrin α2 knockdown.

Primer		Oligonucleotides sequence
shITGA2 1	F	CCGGTCGCAAGAGACTACGCTTATTCTCGAGAATAAGCGTAGTCTCTTGCGATTTTTG
	R	AATTCAAAAATCGCAAGAGACTACGCTTATTCTCGAGAATAAGCGTAGTCTCTTGCGA
shITGA2 2	F	CCGGATAGCAGTTCTTGGGTATTTACTCGAGTAAATACCCAAGAACTGCTATTTTTTG
	R	AATTCAAAAAATAGCAGTTCTTGGGTATTTACTCGAGTAAATACCCAAGAACTGCTAT
shITGA2 3	F	CCGGGACTGGCTAGTCCAGCGTTTACTCGAGTAAACGCTGGACTAGCCAGTCTTTTTG
	R	AATTCAAAAAGACTGGCTAGTCCAGCGTTTACTCGAGTAAACGCTGGACTAGCCAGTC

TABLE 3 | Oligonucleotides sequence used for integrin α2 overexpression.

Primer		Oligonucleotides sequence
ITGA2-A	F	ATGGGACCGGGACAGGCAGG
	R	ACCATAGCCATCCAGGGACCTTC
ITGA2-B	F	ACCATAGCCATCCAGGGACCTTC
	R	TTAGCTGTTGAGTTCTGTGGTCTC
ITGA2-OE-A	F	GATGACGATGACAAGGAATTCATGGGACCGGGACAGGCAGG
ITGA2-OE-B	R	GATCCTTCGCGGCCGCGGATCCTTAGCTGTTGAGTTCTGTGGTCTC

pCDH plasmid backbone with 1 μl of EcoRI and 1 μl of BamHI in a final volume of 20 μl of 1 FastDigest Green Buffer. Vazyme Clon Express MultiS One Step Cloning Kit was recombined these 3 fragments. Transformation and identification steps are the same as shRNA cloning.

Virus Infection

To produce recombinant lentivirus, HEK293-T packaging cells were prepared in 10 cm dishes at a density of 70–80%. Then the cells were transfected with the packaging plasmids pVSVG and psPAX8 encoding lentiviral proteins (Gag, Pol, and Env) and the transfer pLKO.1-shRNA or pCDH-ITGA2 plasmid. The medium was changed after 8–12 h. After 24 h, viral supernatants were harvested, and the new medium was added. Viral supernatants were collected the next day. Virus of scramble was a kind of gift from Wu lab. MC3T3-E1 cells with a density of 70% were infected with viral supernatants in the presence of a serum-inactivated medium supplemented. The viral-containing medium was removed after 24 h and cells were grown in serum-containing medium for another day. Cells were then treated with puromycin (2 μg-ml) for selection. The knockdown and overexpression efficiency were confirmed by qRT-PCR and western blot.

Statistical Analysis

All experiments were repeated at least 3 times to ensure the validity of observations, and all values are expressed as the mean ± standard deviation (SD). The data were tested for homogeneity and then assessed using one-way ANOVA. Error bars represent SD ($n = 3$). $P < 0.05$ was considered significant ($^{*}P < 0.05$, $^{**}P < 0.01$, $^{***}P < 0.005$, $^{****}P < 0.001$).

RESULTS

Topography of S, SLA, and SLM-AHT Titanium Surfaces

Topographies of S, SLA and SLM-AHT titanium disks were shown in **Figure 1A**. As observed by SEM, there exhibited a hierarchical topography combining micro-scale grooves (30–40 um in width) and nano-scale pores (10–100 nm in diameter) on SLM-AHT surface. And irregular micro-scale features with seldom-scattered nano-scale defects could be seen on SLA surface. By contrast, S titanium has a smooth surface without recognizable topographical features. In addition, as shown in **Figure 1B**, the nanopores on SLM-AHT titanium surface distributed uniformly, most of which were about 40 nm in diameter (**Figure 1C**).

Hierarchical Micro-Nano Topography Promoted Cell Adhesion, Proliferation, and Migration

To observe cell behaviors on different topography, we seeded MC3T3-E1 cells on S, SLA and SLM-AHT titanium disks,

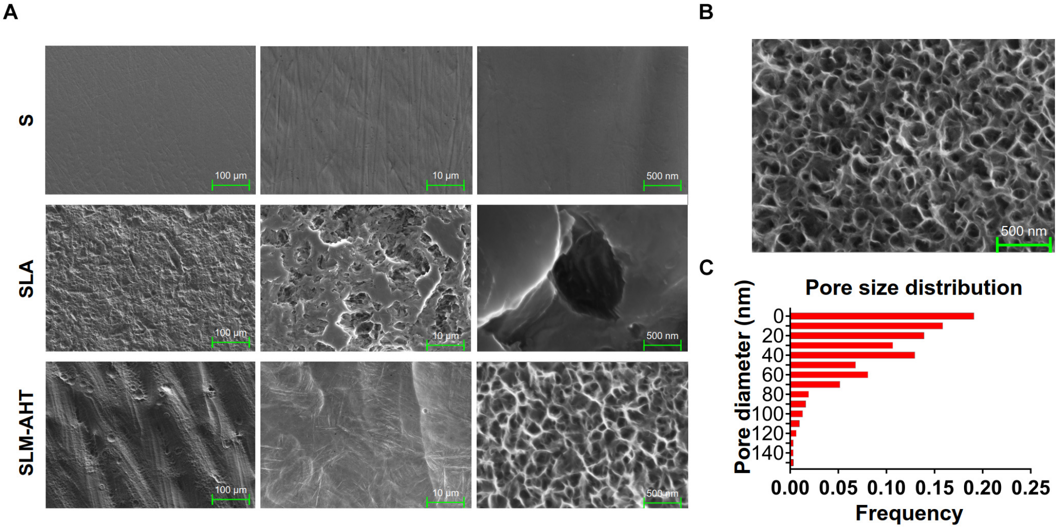

FIGURE 1 | Surface observation of S, SLA and SLM-AHT titanium disks. **(A)** SEM images of the S, SLA and SLM-AHT titanium surfaces. **(B)** SEM images of the hierarchical micro-nano topography titanium surface and the size distribution **(C)** of the nanopores on it.

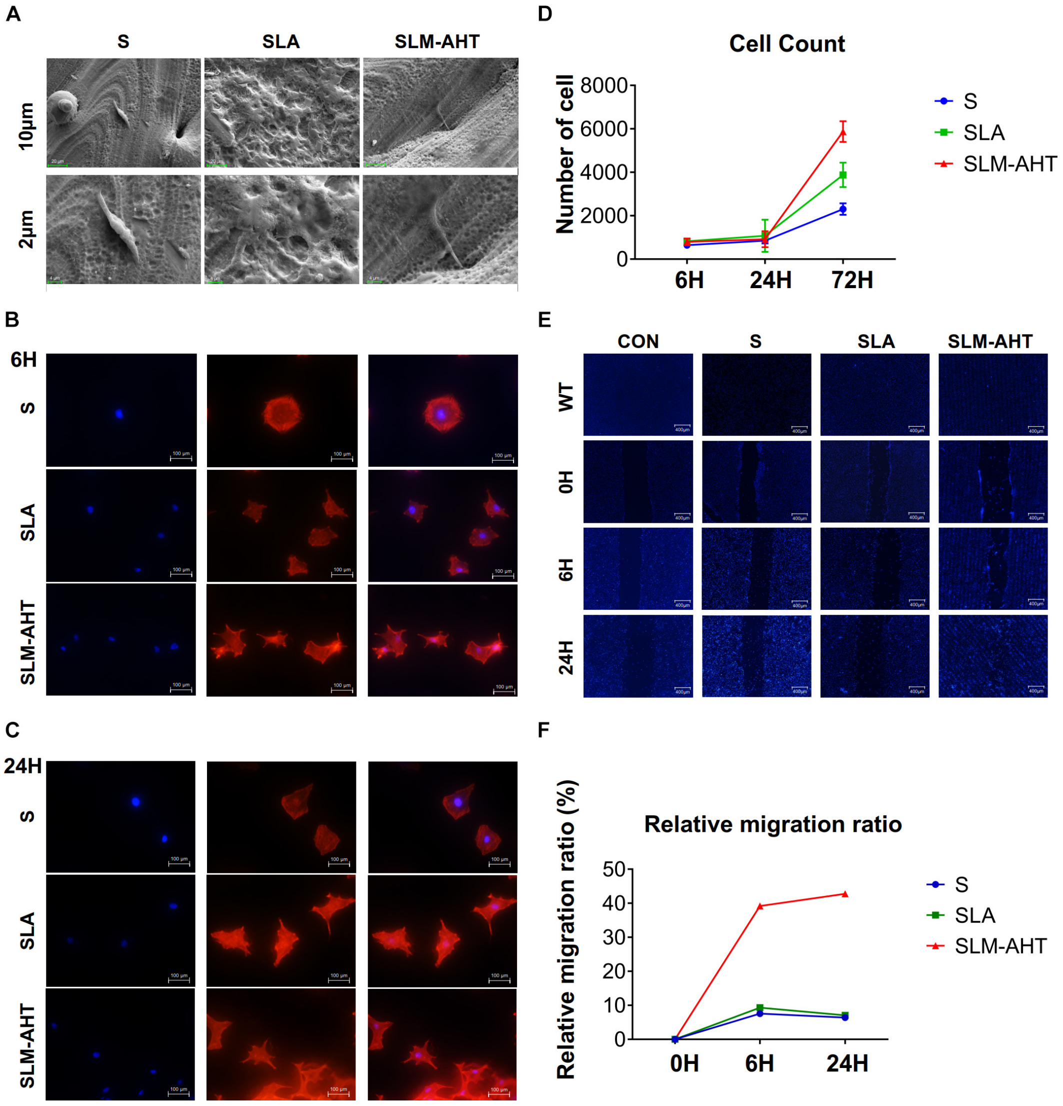

FIGURE 2 | Surface topography influences cell adhesion, proliferation and migration. **(A)** SEM observation of pseudopodia of cell extending on S, SLA, and SLM-AHT titanium surfaces after 6 h of seeding. **(B,C)** Immunofluorescence images of cell (red, F-actin; blue, DAPI) on S, SLA and SLM-AHT titanium surfaces after 6 and 24 h of seeding. **(D)** Cell count on S, SLA and SLM-AHT titanium surfaces for 6, 24, and 72 h. **(E)** Scratch assay of cell on different groups culturing for 0, 6, and 24 h visualized via DAPI (blue) staining. **(F)** Relative closure determined by measuring wound widths from images **(E)** in the upper panel.

and observed morphology and cell numbers by SEM and CLSM at 6 and 24 h after seeding. As shown in **Figure 2A**, longer pseudopodia were observed on the SLM-AHT surface (hierarchical micro-nano topography) than S (smooth topography) and SLA (irregular micro-scale topography) surfaces. Immunofluorescence imaging revealed that cells appeared with a round shape and barely any polarity on S surface, while cells exhibited multipolarity on SLA and SLM-AHT surfaces, especially the latter (**Figures 2B,C**). Significantly increased cell numbers were observed on the hierarchical micro-nano topography compared with the other two surfaces. As shown in **Figure 2D**, cell numbers on three different surfaces were comparable at 6 and 24 h, but progressive increase in cell number was observed on SLM-AHT surface at 72 h. In the wound healing assay, all the scratches became narrowed somewhat 6 h after scratching, but few cells migrated across the edges of scratches, and there was no obvious difference among the three groups. However, 24 h later, the scratches in SLM-AHT group were completely healed, while those in S and SLA groups were still not (**Figures 2E,F**), suggesting that SLM-AHT surface could promote cell migration. The rapid migration can establish a cohesive layer of cells on SLM-AHT surface, which is indispensable for cell adhesion and subsequent osteogenic differentiation.

To further understand the impact of hierarchical micro-nano topography on cell adhesion, vinculin staining was performed, cells were round on S surface, while appeared polygon in shape on SLA and SLM-AHT surfaces (**Figures 3A,B**). The size and

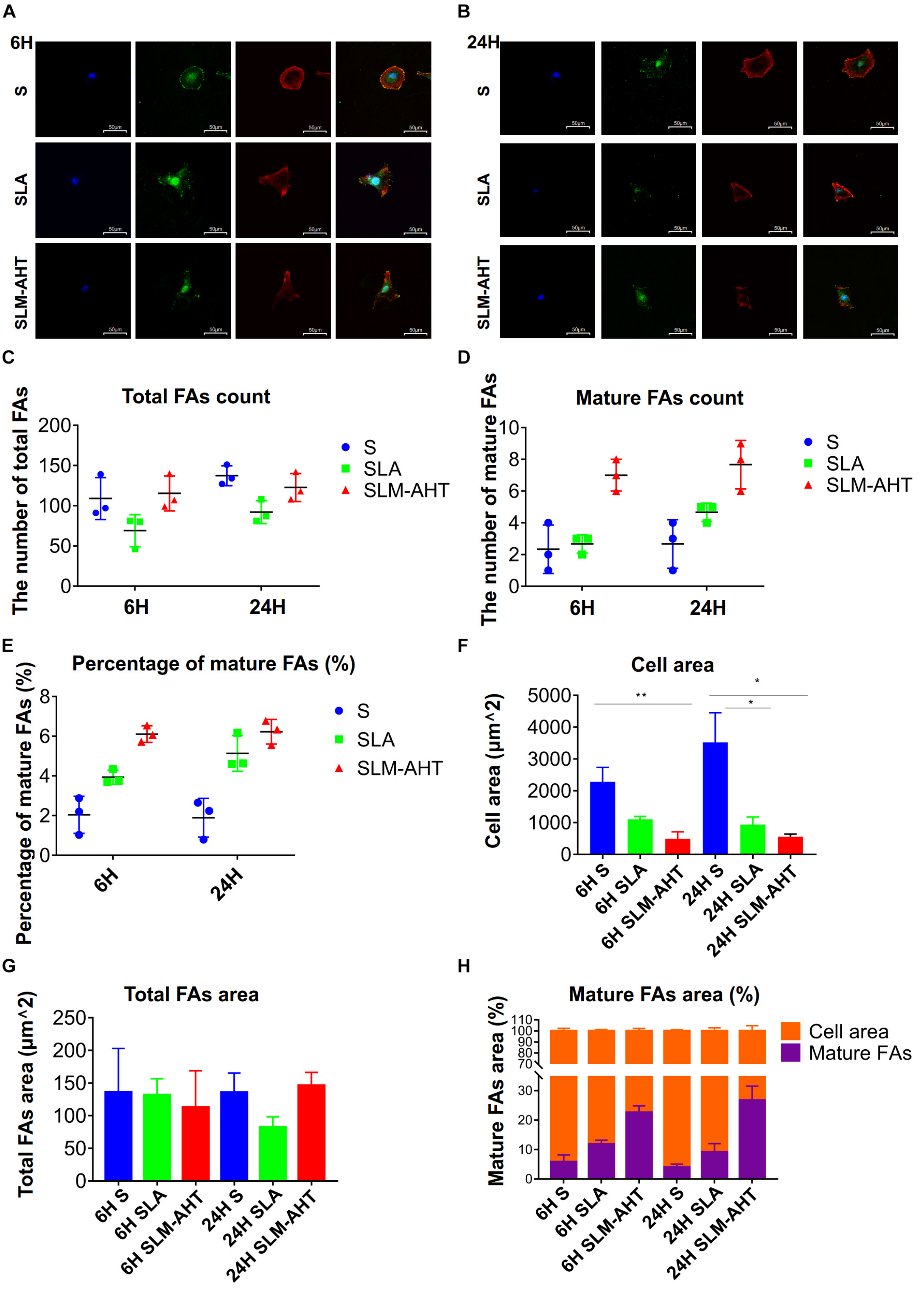

FIGURE 3 | Surface topography influences formation of FAs. **(A,B)** Confocal fluorescence micrographs of cell on three surfaces cultured for 6 **(A)** and 24 h **(B)**. Stained with DAPI (blue) for nuclei, F-actin (red) for actin, and anti-vinculin (green) for vinculin. **(C,D)** The number of total **(C)** and mature **(D)** FAs of MC3T3-E1 cells on three surfaces cultured for 6 and 24 h. **(E)** Percentage of mature FAs number. **(F)** Measurements of the cell area. **(G)** Measurements of the total FAs area. **(H)** Percentage of the cell area occupied by the mature FAs. Statistical significance was determined by one-way ANOVA. Error bars represent SD (*n* = 3). $^{*}P < 0.05$, $^{**}P < 0.01$.

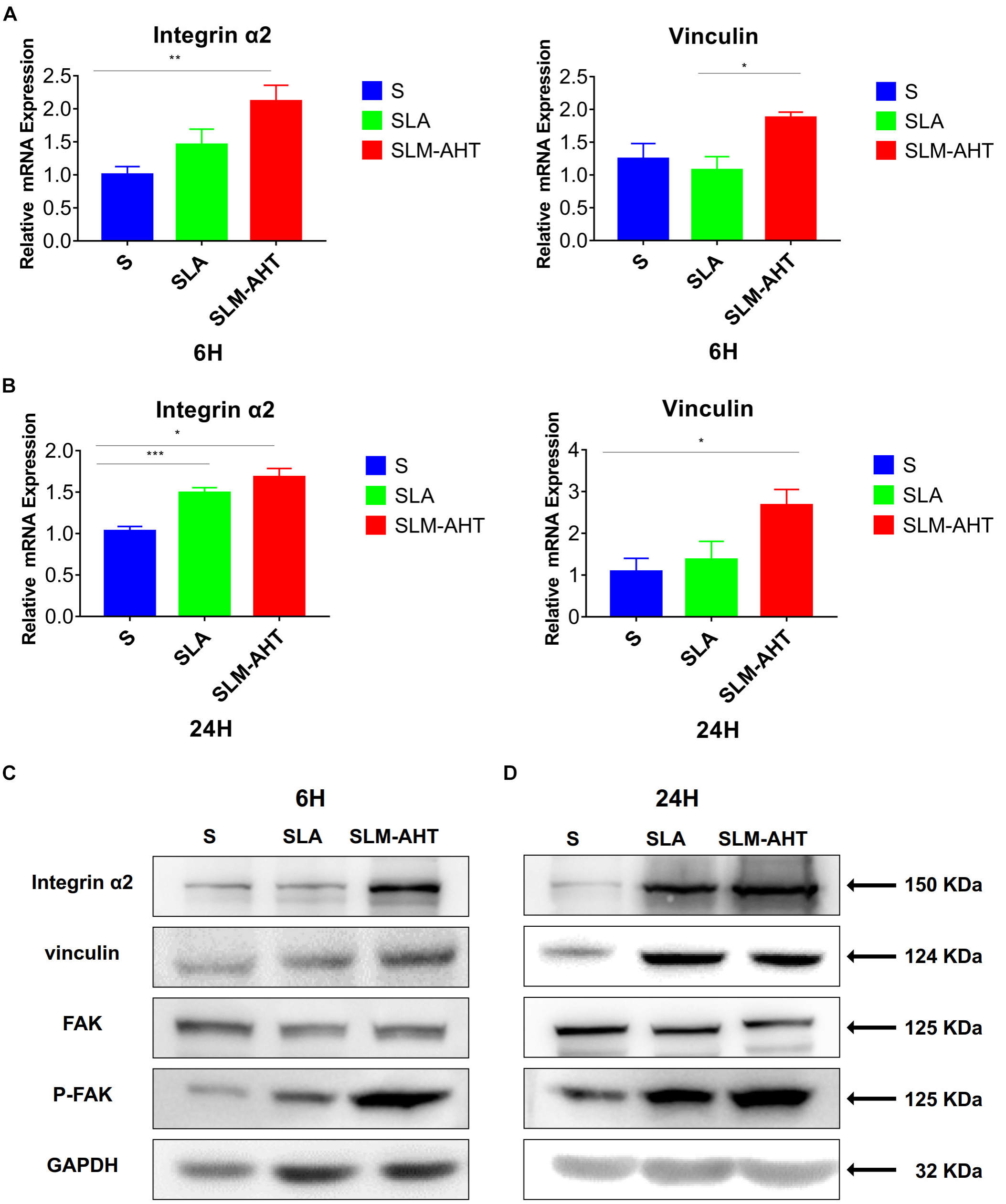

FIGURE 4 | Surface topography influences cell adhesion. **(A,B)** The relative mRNA levels of integrin α2 and vinculin in cell cultured on different titanium surfaces for 6 and 24 h. Statistical significance was determined by one-way ANOVA. Error bars represent SD (*n* = 3). **P* < 0.05. ***P* < 0.01. ****P* < 0.005. **(C,D)** Western blot analysis of integrin α2, vinculin, FAK and p-FAK in cell cultured on different titanium surfaces for 6 **(C)** and 24 h **(D)**. Cells were cultured on different materials as indicated above.

number of FAs in cells on three surfaces were measured. On average, cells formed more FAs on smooth surface (**Figure 3C**). However, more mature FAs were found on hierarchical micro-nano topography (**Figure 3D**), and the percentage of mature FAs on SLM-AHT surface was much higher compared with S and SLA surfaces (**Figure 3E**). Interestingly, since the quantitative analysis of images revealed that the average cell area on S surface was larger than that of SLA and SLM-AHT surfaces (**Figure 3F**), while no statistical difference was detected among total FA areas of the 3 groups (**Figure 3G**), there was a significantly higher proportion of mature FA areas on SLM-AHT surface (**Figure 3H**).

Next, we examined the effect of hierarchical micro-nano topography on cell adhesion at molecular level. The expression levels of integrin α2 and vinculin were examined by qRT-PCR and western blot (WB) analysis (**Figure 4** and **Supplementary Figure 1**). Compared with the other two surfaces, SLM-AHT group exhibited a significantly higher mRNA and protein expression level of integrin α2 and vinculin at both 6 and

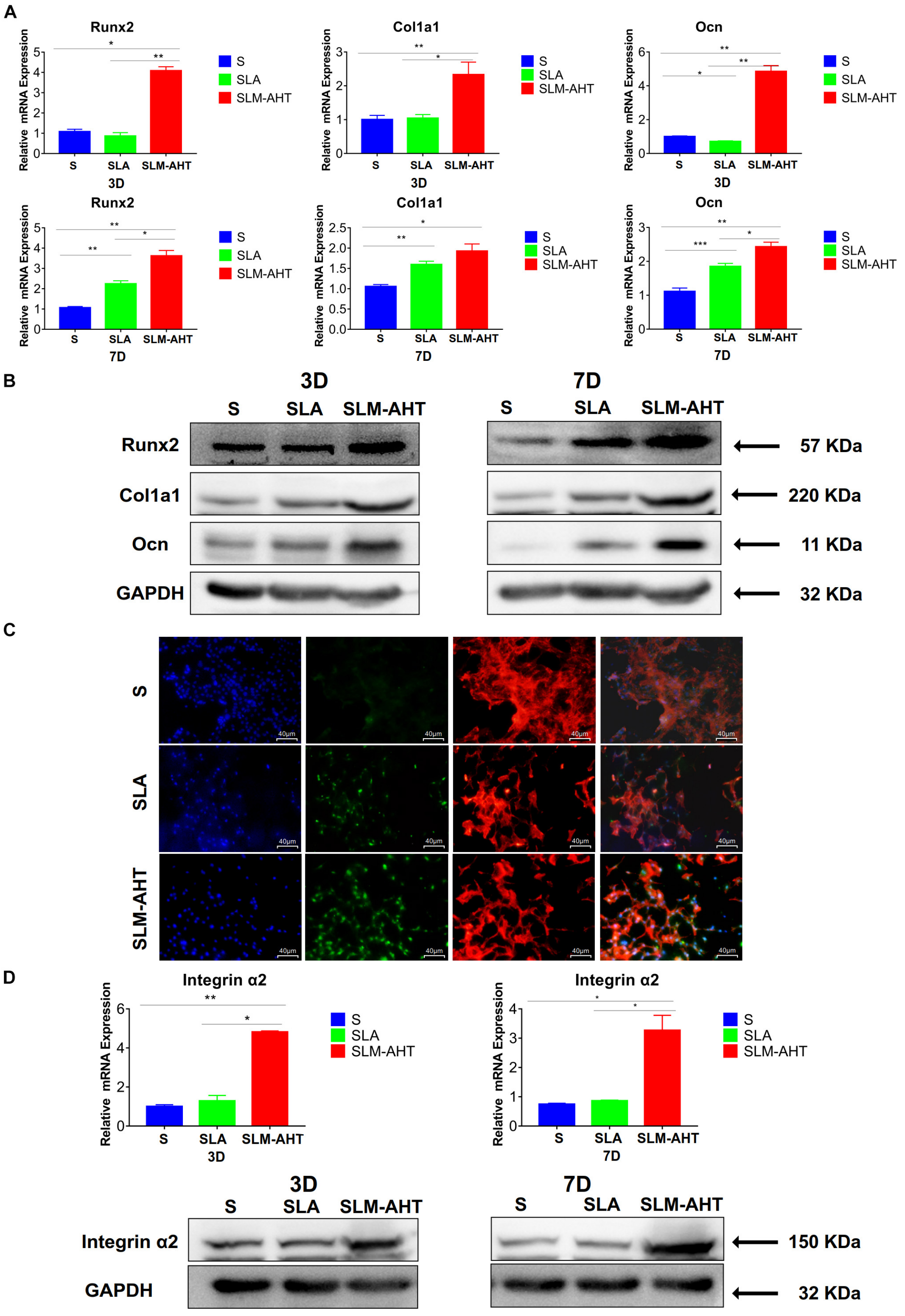

FIGURE 5 | Surface topography influences cell osteogenic differentiation. **(A)** The relative mRNA levels of Runx2, Col1a1 and Ocn in cell cultured on different materials for 3 and 7 days. **(B)** Western blot analysis of Runx2, Col1a1, and Ocn in cell cultured on different materials for 3 and 7 days. **(C)** Immunofluorescence staining showing surface topography dependent diverse expression of Runx2 in cell cultured on different materials for 3 days. (red, F-actin; blue, DAPI; green, Runx2). **(D)** The relative mRNA and protein levels of integrin α2 in cell cultured on different materials for 3 and 7 days. Statistical significance was determined by one-way ANOVA. Error bars represent SD (*n* = 3). *$P < 0.05$, **$P < 0.01$, ***$P < 0.005$.

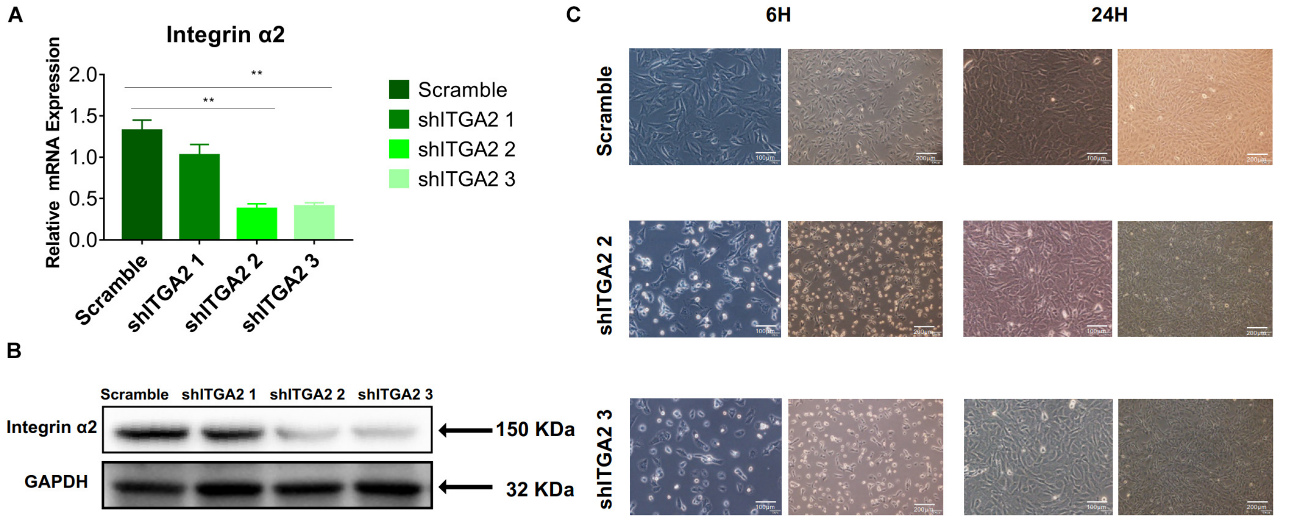

FIGURE 6 | Efficiency of integrin α2 knockdown. **(A)** The relative mRNA expression levels of integrin α2 in scramble and integrin α2 silenced cell for 3 days. Statistical significance was determined by one-way ANOVA. Error bars represent SD ($n = 3$). $^{**}P < 0.01$. **(B)** Western blot analysis of integrin α2 in scramble and integrin α2 silenced cell for 3 days. **(C)** Microscope images of morphology of scramble and integrin α2 silenced cell for 6 and 24 h.

24 h. Phosphorylated and total FAK protein levels were also evaluated by WB assay (**Supplementary Figure 1**). Although no significant difference in the total FAK protein expression among three groups was revealed, substantially upregulated FAK phosphorylation level was observed on SLM-AHT surface, suggesting that hierarchical micro-nano topography could promote integrin α2 expression and FAK activation.

Hierarchical Micro-Nano Topography Promoted Osteogenic Differentiation

As shown in **Figures 5A,B** and **Supplementary Figure 2A**, the expression levels of Runx2, Col1a1, and Ocn in cells cultured on SLM-AHT surface were significantly higher than those of S and SLA groups on both day 3 and day 7. In addition, immunofluorescence staining further confirmed that Runx2 expression levels were significantly increased in cells cultured on SLM-AHT surface (**Figure 5C**), indicating an obvious osteogenic promoting effect of the hierarchical micro-nano topography. Furthermore, the expression levels of integrin α2 in cells cultured on SLM-AHT surface were also found significantly upregulated compared to S and SLA groups, while there was no significant difference between the latter two groups (**Figure 5D** and **Supplementary Figure 2B**), suggesting integrin α2 was involved in hierarchical micro-nano topography regulating osteogenic differentiation.

The Role of α2 -PI3K-AKT Signaling Axis

To further investigate the role of integrin α2 and its relationship with PI3K-AKT signaling, we designed three shRNAs. Two of them (shITGA2 2 and shITGA2 3) were proved effective and with no adverse effect on cell morphology as well as cell proliferation (**Figures 6A–C** and **Supplementary Figure 3**). Accordingly, scramble, shITGA2 2 and shITGA2 3 cells were seeded on both cell-culture dishes and three titanium specimens to study the role of integrin α2 in osteogenic differentiation. qRT-PCR and WB analysis revealed that knockdown of integrin α2 dramatically decreased expression of osteogenic markers including Runx2, Col1a1 and Ocn (**Figures 7A,B** and **Supplementary Figure 4**). And the significantly downregulated expression of Runx2 was further confirmed by immunofluorescence staining (**Figure 7C**). Noticeably, scramble cells cultured on SLM-AHT surface exhibited significantly increased expression of Runx2, Col1a1 and Ocn compared to S and SLA surface, while integrin α2 silenced cells showed no difference of osteogenic gene expression on three surfaces (**Figure 7D**), indicating that integrin α2 played a key role in hierarchical micro-nano topography directing osteogenic differentiation.

The activity of PI3K-AKT signaling was then investigated on different surfaces. The related factors including PI3K, PIP2, PIP3, total AKT and phosphorylated AKT (P-AKT) were detected by WB. As shown in **Figure 8** and **Supplementary Figure 5**, the protein expression of PI3K and PIP3 was higher on SLM-AHT surface than S and SLA surfaces on both day 3 and 7, while PIP2 had a lower expression on SLM-AHT surface compared to the other two groups. Interestingly, although no marked alteration in total AKT expression on all three surfaces was found, significantly increased AKT phosphorylation level was revealed on SLM-AHT surface, confirming the activation of PI3K-AKT signaling on the hierarchical micro-nano topography. We then examined the interaction of integrin α2 and PI3K-AKT signaling. Integrin α2 was stably overexpressed in MC3T3-E1 cells (ITGA2-OE) (**Figures 9A,B** and **Supplementary Figure 6A**). WB analysis showed that integrin α2 overexpression significantly promoted expression levels of PI3K and PIP3, while strongly decreased PIP2 expression (**Figure 9C** and **Supplementary Figure 6B**). Furthermore, while total AKT expression did not change significantly, increased P-AKT was

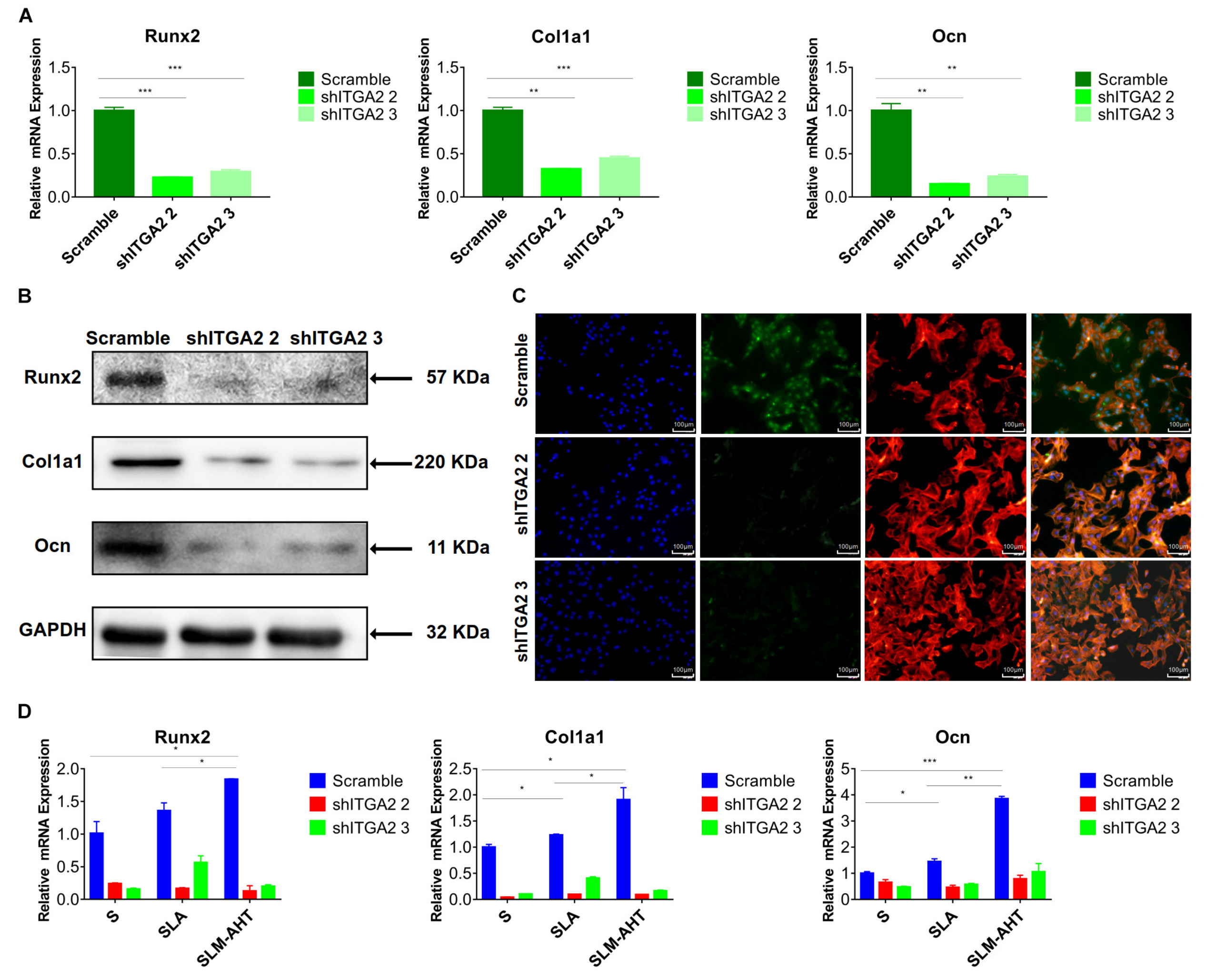

FIGURE 7 | Integrin α2 influences cell osteogenic differentiation. **(A)** The relative mRNA levels of Runx2, Col1a1, and Ocn in scramble and integrin α2 silenced cell. **(B)** Western blot analysis of Runx2, Col1a1, and Ocn proteins in scramble and integrin α2 silenced cell. **(C)** Immunofluorescence staining showing integrin α2 dependent diverse expression of Runx2 (red, F-actin; blue, DAPI: green, Runx2). **(D)** The relative mRNA levels of Runx2, Col1a1, and Ocn in scramble and integrin α2 silenced cell culturing on S, SLA, and SLM-AHT surfaces for 3 days. Statistical significance was determined by one-way ANOVA. Error bars represent SD (*n* = 3). *$P < 0.05$, **$P < 0.01$, ***$P < 0.005$.

observed after integrin α2 overexpression. The above results suggested that PI3K-AKT signaling was highly influenced by integrin α2. That was to say, there exists an integrin α2-PI3K-AKT signaling axis which was possibly involved in the regulation of cell behaviors including osteogenic differentiation. In addition, scramble and forced integrin α2 cells were seeded on both cell-culture dishes and three titanium specimens. And it was found that the mRNA and protein expression levels of osteogenic markers were increased after integrin α2 overexpression (**Figures 10A,B** and **Supplementary Figure 7**). Furthermore, the significantly upregulated expression of Runx2 was observed by immunofluorescence staining after integrin α2 overexpression (**Figure 10C**). Noticeably, both integrin α2 overexpressed cells and scramble cells cultured on SLM-AHT surface exhibited significantly increased mRNA expression of Runx2, Col1a1 and Ocn compared to S and SLA groups (**Figure 10D**), once again proving the key role of integrin α2 in surface topography regulating cell fate.

DISCUSSION

In the human body, cells are exposed to complex microenvironments consisting of varying micro-scale and nano-scale structural features which convey different topographical cues to regulate cell behaviors (Fu et al., 2020). It is believed that the development of appropriate hierarchical micro-nano topographies mimicking the structure of natural bone helps to improve the osseointegration ability of intraosseous implants (Gongadze et al., 2011; Khang et al., 2012; Xu et al., 2016; Shah et al., 2018). And recent studies revealed that surface with nano-scale features was effective at improving osteoblasts

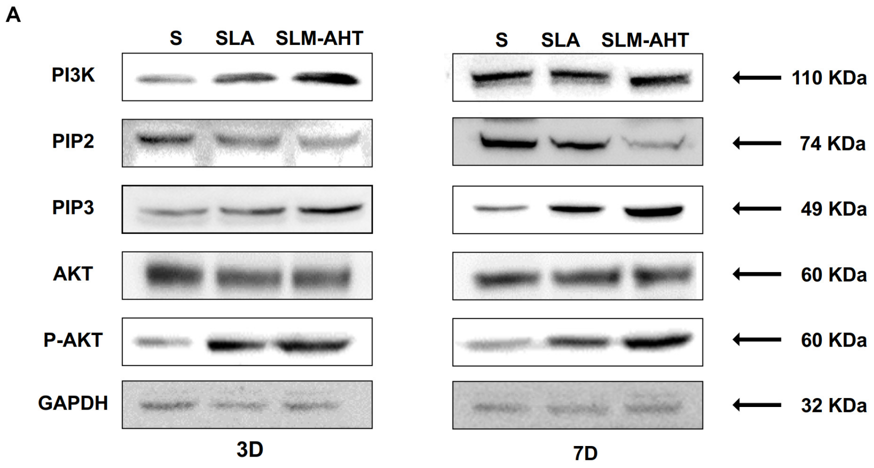

FIGURE 8 | Surface topography influences PI3K-AKT signaling pathway. **(A,B)** Western blot analysis of PI3K, PIP2, PIP3, AKT, and p-AKT in cell cultured on S, SLA and SLM-AHT surfaces for 3 and 7 days. Cells were cultured on different materials as indicated above.

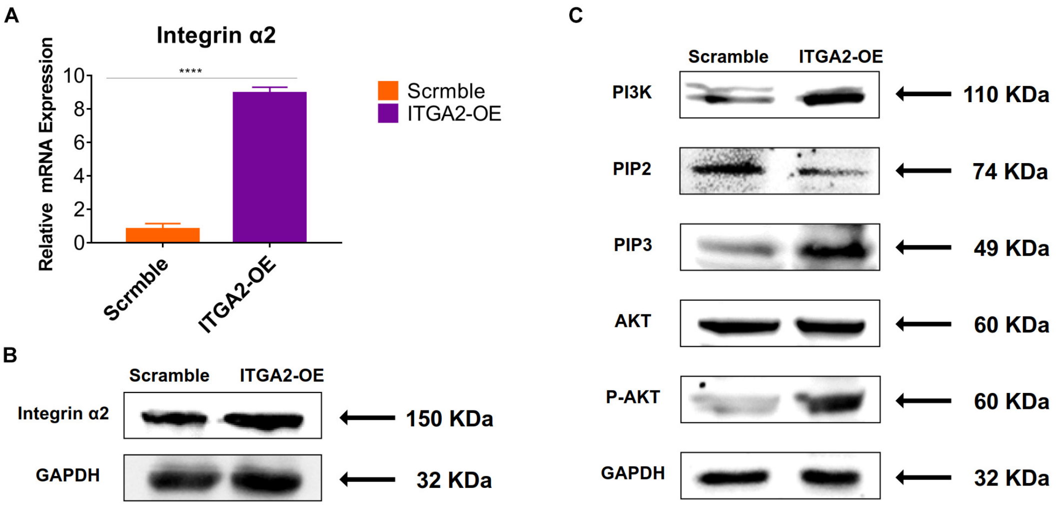

FIGURE 9 | Integrin α2 overexpression activates PI3K-AKT signal pathway. **(A)** The relative mRNA levels of integrin α2 in scramble and integrin α2 overexpressed cell for 3 days. Statistical significance was determined by one-way ANOVA. Error bars represent SD (*n* = 3). $^{****}P < 0.001$. **(B)** Western blot analysis of integrin α2 in scramble and integrin α2 overexpressed cell. **(C)** Western blot analysis of PI3K, PIP2, PIP3, AKT, and p-AKT in scramble and integrin α2 overexpressed cell.

adhesion and differentiation (Gautrot et al., 2014; Rosa et al., 2014; Huang et al., 2016; Guadarrama Bello et al., 2017; Lopes et al., 2019). However, the mechanism by which surface topography manipulates cell fate remains controversial. In this study, hierarchical micro-nano topography (SLM-AHT) with micro-scale grooves and nano-scale pores was fabricated and compared with smooth topography (S) as well as irregular micro-scale topography (SLA) surfaces to investigate the mechanism involved in cell-surface interactions.

Topography-induced changes in cell morphology could be conveniently observed at the initial stage of cell-surface contact (Dupont, 2016) and would greatly influence subsequent cell behaviors (Nasrollahi et al., 2016). In this study, cells showed multipolarity on SLM-AHT surface while showed round on the other surfaces, which could be attributed to the large amount of sharp convex or spikes of hierarchical micro-nano topography. These features have the highest negative surface charge density (Gongadze et al., 2011), and could, therefore, recruit more positively charged anchor proteins to improve cell adhesion (Smeets et al., 2009), as observed in the following FA visualization and detection of integrin α2, vinculin and p-FAK expression.

Focal adhesions were intensively studied because they are regarded as important transducers of mechanical cues including topography (You et al., 2014). In this study, more FAs were found in cells cultured on S surface. However, most of them are dot-like nascent adhesions (NAs) or premature round focal complexes (FCs), which are not stable and usually disappear within several minutes (Valdembri and Serini, 2012). Since total

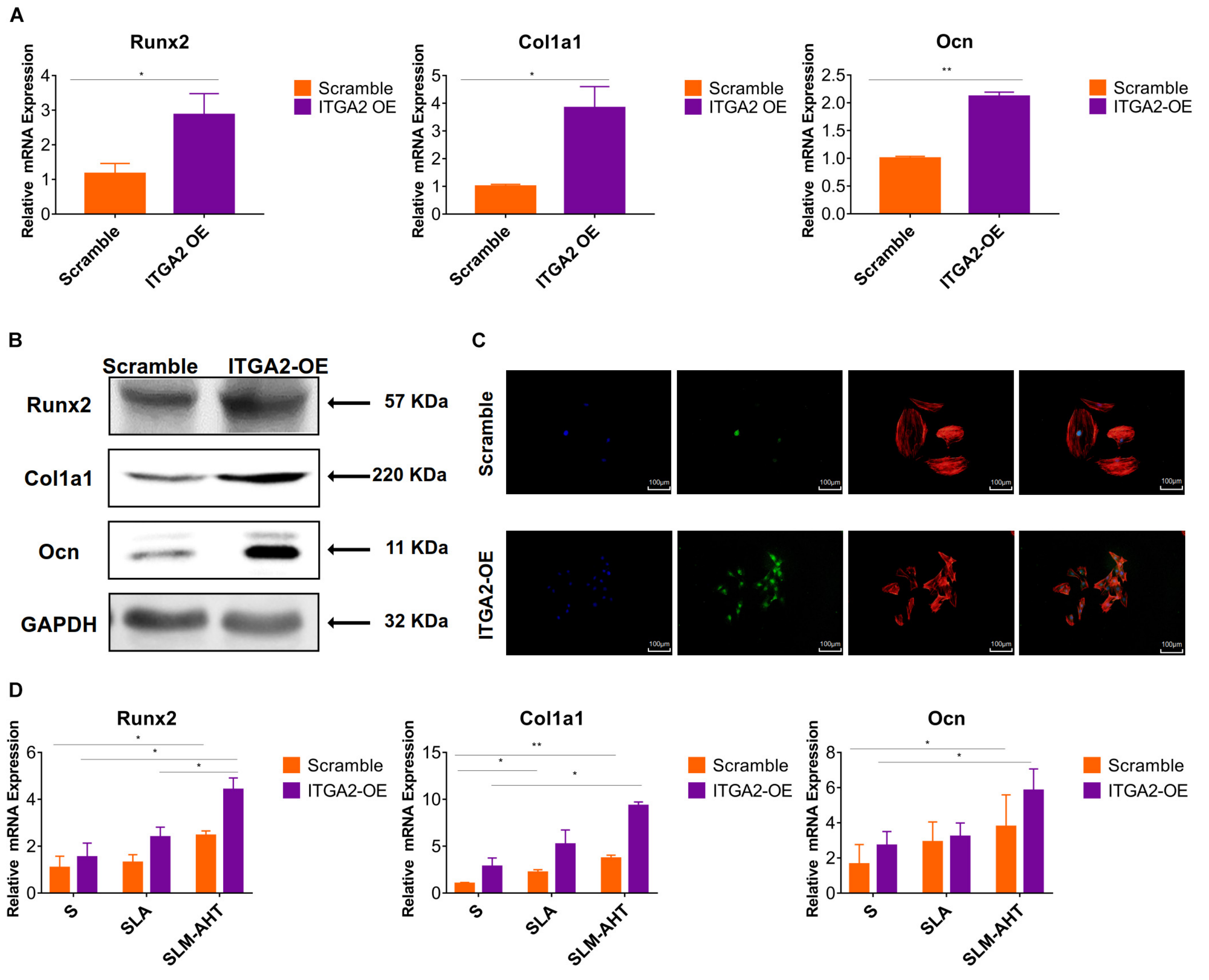

FIGURE 10 | Integrin α2 overexpression enhances cell osteogenic differentiation. **(A)** The relative mRNA levels of Runx2, Col1a1, and Ocn in scramble and integrin α2 overexpressed cell for 3 days. **(B)** Western blot analysis of Runx2, Col1a1, and Ocn proteins in scramble and integrin α2 overexpressed cell for 3 days. **(C)** Immunofluorescence staining showing integrin α2 dependent diverse expression of Runx2 (red, F-actin; blue, DAPI: green, Runx2). **(D)** The relative mRNA levels of Runx2, Col1a1, and Ocn in scramble and integrin α2 overexpressed cell cultured on S, SLA and SLM-AHT surfaces for 3 days. Statistical significance was determined by one-way ANOVA. Error bars represent SD (*n* = 3). **P* < 0.05, ***P* < 0.01.

FAs cannot present the real adhesion status of cells, mature FAs were measured. And cells cultured on SLM-AHT surface exhibited much more mature FAs, indicating hierarchical micro-nano topography may contribute to cell adhesion via enhancing the maturation of FAs. The possible reason may be that FAs are favorably constructed with an average integrin interspacing of about 45 nm (Dalby et al., 2014), while the diameter of nanopores on SLM-AHT surface is about 40 nm. The evenly distributed nano-scale features on the surface substantially match the preferable interspacing of integrins to form mature FAs, and therefore improve cell adhesion (Cavalcanti-Adam et al., 2007).

In consistence with previous studies, our results showed that the titanium surface with hierarchical microgroove-nanopore topography would favor osteogenic differentiation. More importantly, the role of integrin α2, an important component of FAs, in the observed topography induced osteogenic differentiation was thoroughly investigated in this study. Compared to S and SLA surfaces, protein expression level of integrin α2 was found significantly increased at early stage of cell cultured on SLM-AHT surface, and concomitantly, cells on SLM-AHT surface also exhibited an early increase in mRNA expression levels of osteogenic markers. Moreover, we established the causal-effect relationship through gain and loss of function of integrin α2 in cells cultured on SLM-AHT. Although the osteogenic marker expression was higher on SLA surface than on the S surface on day 7, the protein expression level of integrin α2 showed no significant difference between the two groups, indicating that less prominent osteogenic promoting effect of irregular micro-scale topography was not integrin α2 dependent (Huang et al., 2019). Therefore, integrin α2 mediated osteogenic differentiation could be considered topography specific, and in the existing three surfaces, only hierarchical micro-nano topography (SLM-AHT) could activate this process. And our finding helps to endorse the recently proposed possible function of integrin α2 in bone formation (Leem et al., 2016; Raines et al., 2019).

Moreover, the downstream signaling of integrin α2 in promoting osteogenic differentiation was further investigated in this study. Our outcomes showed that PI3K-AKT signaling pathway was activated on SLM-AHT surface, combing with high expression of integrin α2. Since PI3K-AKT signaling had been proved involved in multiple cell functions including cell proliferation, apoptosis, growth, glucose metabolism, migration and differentiation (Gu et al., 2013; Choi et al., 2014; Xu et al., 2015; Fan et al., 2018), we supposed that there might be cross-talk between integrin α2 and PI3K-AKT signaling pathway, and hierarchical micro-nano topography by itself could affect this integrin α2-PI3K-AKT signaling axis. However, whether integrin α2 could activate PI3K-AKT signaling pathway was still unknown. Thus, we stably upregulated endogenous integrin α2 expression to investigate the effect of integrin α2 on PI3K-AKT signaling pathway. To our delight, the high expression level of integrin α2 was indeed accompanied by an activated PI3K-AKT signaling. Furthermore, following by PI3K-AKT signaling pathway activation, osteogenic markers were also upregulated in integrin α2 overexpressed cells. Altogether, it could be inferred that forced expression of integrin α2 could activate PI3K-AKT signaling pathway and thereby promote osteogenic differentiation.

To our knowledge, this is the very first report illustrating that osteogenic differentiation induced by hierarchical micro-nano topography is mediated by activation of integrin α2-PI3K-AKT signaling axis, as well as is the first study demonstrating overexpression of integrin α2 is sufficient to activate PI3K-AKT signaling pathway on titanium surfaces. Our research contributes to surface modification targeting the enhancement of osteogenic capacity. And for cells with compromised osteogenic capacity, it provides a possibility of overexpressing integrin α2 to promote the osteogenic differentiation. However, integrin α2 is also involved in metabolism of tumor cells (Adorno-Cruz and Liu, 2019). Thus, the safety of long-time high expression of integrin α2 is worrisome which needs rigorous evaluation. Despite a helpful step in uncovering a novel signaling axis involved in cell-surface interactions, our understanding of it remains incomplete and there are some shortcomings in this study. Whether the same mechanism can play its role in vivo, and whether integrin α2 can activate other signaling pathways to promote osteogenic differentiation of cell cultured on surface with hierarchical micro-nano topography, are still unknown. Collectively, we proposed α2-PI3K-AKT signaling axis plays a crucial role in hierarchical micro-nano topography induced osteogenic differentiation. More mechanistic insights still require further studies.

DATA AVAILABILITY STATEMENT

The original contributions presented in the study are included in the article/**Supplementary Material**, further inquiries can be directed to the corresponding authors.

AUTHOR CONTRIBUTIONS

All the authors were involved in this work. XW and LS conceived the idea of the study. YT fabricated and characterized the materials. HZ and XX designed and performed the experiments. QG and FD helped with the experiments and provided constructive discussions. YY provided the financially supporting for this work. ZF analyzed the data. HZ, XW, and LS interpreted the data and wrote the manuscript.

FUNDING

We acknowledge support provided by the National Natural Science Foundation of China (Grant No. 81970958), the National Key Research and Development Program (Grant No. 2017YFA0504102), and the China Postdoctoral Science Foundation (Grant No. 2019TQ0213).

ACKNOWLEDGMENTS

We shall extend our thanks to Lei Cao, Yu Kong, Guoying Zheng, Penghui Hu, Rui Li, Yingying Zhao, Yuying Hou, Yaxin Lin, and Xiaoyu Yao for all their kindness and help.

SUPPLEMENTARY MATERIAL

The Supplementary Material for this article can be found online at: https://www.frontiersin.org/articles/10.3389/fbioe.2020.00463/full#supplementary-material

REFERENCES

Adorno-Cruz, V., and Liu, H. (2019). Regulation and functions of integrin alpha2 in cell adhesion and disease. *Genes Dis.* 6, 16–24. doi: 10.1016/j.gendis.2018.12.003

Anselme, K., Davidson, P., Popa, A. M., Giazzon, M., Liley, M., and Ploux, L. (2010). The interaction of cells and bacteria with surfaces structured at the nanometre scale. *Acta Biomater.* 6, 3824–3846. doi: 10.1016/j.actbio.2010.04.001

Arienti, C., Pignatta, S., and Tesei, A. (2019). Epidermal growth factor receptor family and its role in gastric cancer. *Front. Oncol.* 9:1308. doi: 10.3389/fonc.2019.01308

Bachir, A. I., Zareno, J., Moissoglu, K., Plow, E. F., Gratton, E., and Horwitz, A. R. (2014). Integrin-associated complexes form hierarchically with variable stoichiometry in nascent adhesions. *Curr. Biol.* 24, 1845–1853. doi: 10.1016/j.cub.2014.07.011

Cavalcanti-Adam, E. A., Volberg, T., Micoulet, A., Kessler, H., Geiger, B., and Spatz, J. P. (2007). Cell spreading and focal adhesion dynamics are regulated by spacing of integrin ligands. *Biophys. J.* 92, 2964–2974. doi: 10.1529/biophysj.106.089730

Chen, W., Shao, Y., Li, X., Zhao, G., and Fu, J. (2014). Nanotopographical surfaces for stem cell fate control: engineering mechanobiology from the bottom. *Nano Today* 9, 759–784. doi: 10.1016/j.nantod.2014.12.002

Choi, Y. H., Kim, Y. J., Jeong, H. M., Jin, Y. H., Yeo, C. Y., and Lee, K. Y. (2014). Akt enhances Runx2 protein stability by regulating Smurf2 function during osteoblast differentiation. *FEBS J.* 281, 3656–3666. doi: 10.1111/febs.12887

Chuang, L. S. H., Ito, K., and Ito, Y. (2013). RUNX family: regulation and diversification of roles through interacting proteins. *Int. J. Cancer* 132, 1260–1271. doi: 10.1002/ijc.27964

Cimmino, C., Rossano, L., Netti, P. A., and Ventre, M. (2018). Spatio-temporal control of cell adhesion: toward programmable platforms to manipulate cell functions and fate. *Front. Bioeng. Biotechnol.* 6:190. doi: 10.3389/fbioe.2018.00190

Cui, Y., Zhu, T., Li, D., Li, Z., Leng, Y., Ji, X., et al. (2019). Bisphosphonate-functionalized scaffolds for enhanced bone regeneration. *Adv. Healthc. Mater.* 8:e1901073.

Dalby, M. J., Gadegaard, N., and Oreffo, R. O. (2014). Harnessing nanotopography and integrin-matrix interactions to influence stem cell fate. *Nat. Mater.* 13, 558–569. doi: 10.1038/nmat3980

De Franceschi, N., Hamidi, H., Alanko, J., Sahgal, P., and Ivaska, J. (2015). Integrin traffic – The update. *J. Cell Sci.* 128, 839–852. doi: 10.1242/jcs.161653

Denchai, A., Tartarini, D., and Mele, E. (2018). Cellular response to surface morphology: electrospinning and computational modeling. *Front. Bioeng. Biotechnol.* 6:155. doi: 10.3389/fbioe.2018.00155

Deng, C., Lin, R., Zhang, M., Qin, C., Yao, Q., Wang, L., et al. (2019). Micro/nanometer-structured scaffolds for regeneration of both cartilage and subchondral bone. *Adv. Funct. Mater.* 29:1806068.

Dupont, S. (2016). Role of YAP/TAZ in cell-matrix adhesion-mediated signalling and mechanotransduction. *Exp. Cell Res.* 343, 42–53. doi: 10.1016/j.yexcr.2015.10.034

Edlind, M. P., and Hsieh, A. C. (2014). PI3K-AKT-mTOR signaling in prostate cancer progression and androgen deprivation therapy resistance. *Asian J. Androl.* 16, 378–386.

Fan, Y. S., Li, Q., Hamdan, N., Bian, Y. F., Zhuang, S., Fan, K., et al. (2018). Tetrahydroxystilbene glucoside regulates proliferation, differentiation, and OPG/RANKL/M-CSF expression in MC3T3-E1 cells via the PI3K/Akt pathway. *Molecules* 23:E2306.

Feng, S., Zhou, L., Zhang, Y., Lu, S., and Long, M. (2018). Mechanochemical modeling of neutrophil migration based on four signaling layers, integrin dynamics, and substrate stiffness. *Biomech. Model. Mechanobiol.* 17, 1611–1630. doi: 10.1007/s10237-018-1047-2

Fu, J., Liu, X., Tan, L., Cui, Z., Liang, Y., Li, Z., et al. (2020). Modulation of the mechanosensing of mesenchymal stem cells by laser-induced patterning for the acceleration of tissue reconstruction through the Wnt/beta-catenin signaling pathway activation. *Acta Biomater.* 101, 152–167. doi: 10.1016/j.actbio.2019.10.041

Gautrot, J. E., Malmstrom, J., Sundh, M., Margadant, C., Sonnenberg, A., and Sutherland, D. S. (2014). The nanoscale geometrical maturation of focal adhesions controls stem cell differentiation and mechanotransduction. *Nano Lett.* 14, 3945–3952. doi: 10.1021/nl501248y

Geiger, B., Spatz, J. P., and Bershadsky, A. D. (2009). Environmental sensing through focal adhesions. *Nat. Rev. Mol. Cell Biol.* 10, 21–33. doi: 10.1038/nrm2593

Ginsberg, M. H. (2014). Integrin activation. *BMB Rep.* 47, 655–659.

Gongadze, E., Kabaso, D., Bauer, S., Slivnik, T., Schmuki, P., van Rienen, U., et al. (2011). Adhesion of osteoblasts to a nanorough titanium implant surface. *Int. J. Nanom.* 6, 1801–1816.

Gorelik, R., and Gautreau, A. (2014). Quantitative and unbiased analysis of directional persistence in cell migration. *Nat. Protoc.* 9, 1931–1943. doi: 10.1038/nprot.2014.131

Gu, Y. X., Du, J., Si, M. S., Mo, J. J., Qiao, S. C., and Lai, H. C. (2013). The roles of PI3K/Akt signaling pathway in regulating MC3T3-E1 preosteoblast proliferation and differentiation on SLA and SLActive titanium surfaces. *J. Biomed. Mater. Res. A* 101, 748–754. doi: 10.1002/jbm.a.34377

Guadarrama Bello, D., Fouillen, A., Badia, A., and Nanci, A. (2017). A nanoporous titanium surface promotes the maturation of focal adhesions and formation of filopodia with distinctive nanoscale protrusions by osteogenic cells. *Acta Biomater.* 60, 339–349. doi: 10.1016/j.actbio.2017.07.022

Hanein, D., and Horwitz, A. R. (2012). The structure of cell-matrix adhesions: the new frontier. *Curr. Opin. Cell Biol.* 24, 134–140. doi: 10.1016/j.ceb.2011.12.001

Huang, Q., Elkhooly, T. A., Liu, X., Zhang, R., Yang, X., Shen, Z., et al. (2016). Effects of hierarchical micro/nano-topographies on the morphology, proliferation and differentiation of osteoblast-like cells. *Colloids Surf. B Biointerfaces* 145, 37–45. doi: 10.1016/j.colsurfb.2016.04.031

Huang, T. B., Li, Y. Z., Yu, K., Yu, Z., Wang, Y., Jiang, Z. W., et al. (2019). Effect of the Wnt signal-RANKL/OPG axis on the enhanced osteogenic integration of a lithium incorporated surface. *Biomater. Sci.* 7, 1101–1116. doi: 10.1039/c8bm01411f

Hui-Min, Hu, L. Y., Wang, Z., Liu, Y.-W., Fan, J.-Z., Fan, J., et al. (2013). Overexpression of integrin a2 promotes osteogenic differentiation of hBMSCs from senile osteoporosis through the ERK pathway. *Int. J. Clin. Exp. Pathol.* 5, 841–852.

Izard, T., and Brown, D. T. (2016). Mechanisms and functions of vinculin interactions with phospholipids at cell adhesion sites. *J. Biol. Chem.* 291, 2548–2555. doi: 10.1074/jbc.r115.686493

Janssen, S., Gach, S., Kant, S., Aveic, S., Rutten, S., Olschok, S., et al. (2020). Enhanced osteogenic differentiation of human mesenchymal stromal cells as response to periodical microstructured Ti6Al4V surfaces. *J. Biomed. Mater. Res. B Appl. Biomater.* 108, 2218–2226.

Karimi, F., O'Connor, A. J., Qiao, G. G., and Heath, D. E. (2018). Integrin clustering matters: a review of biomaterials functionalized with multivalent integrin-binding ligands to improve cell adhesion, migration, differentiation, angiogenesis, and biomedical device integration. *Adv. Healthc. Mater.* 7:e1701324.

Karsenty, G., Kronenberg, H. M., and Settembre, C. (2009). Genetic control of bone formation. *Annu. Rev. Cell Dev. Biol.* 25, 629–648. doi: 10.1146/annurev.cellbio.042308.113308

Khang, D., Choi, J., Im, Y. M., Kim, Y. J., Jang, J. H., Kang, S. S., et al. (2012). Role of subnano-, nano- and submicron-surface features on osteoblast differentiation of bone marrow mesenchymal stem cells. *Biomaterials* 33, 5997–6007. doi: 10.1016/j.biomaterials.2012.05.005

Kim, J., Kim, H. N., Lim, K. T., Kim, Y., Seonwoo, H., and Park, S. H. (2013). Designing nanotopographical density of extracellular matrix for controlled morphology and function of human mesenchymal stem cells. *Sci. Rep.* 3:3552.

Leem, Y. H., Lee, K. S., Kim, J. H., Seok, H. K., Chang, J. S., and Lee, D. H. (2016). Magnesium ions facilitate integrin alpha 2- and alpha 3-mediated proliferation and enhance alkaline phosphatase expression and activity in hBMSCs. *J. Tissue Eng. Regen. Med.* 10, E527–E536.

Li, J., Yu, Y., Myungwoong, K., Li, K., Mikhail, J., Zhang, L., et al. (2017). Manipulation of cell adhesion and dynamics using RGD functionalized polymers. *J. Mater. Chem. B* 5, 6307–6316. doi: 10.1039/c7tb01209h

Li, N.-B., Xiao, G.-Y., Liu, B., Wang, Z., Zhu, R.-F., and Lu, Y.-P. (2016). Rapid deposition of spherical apatite on alkali–heat treated titanium in modified simulated body fluid at high temperature. *Surf. Coat. Technol.* 301, 121–125. doi: 10.1016/j.surfcoat.2015.12.067

Lopes, H. B., Freitas, G. P., Fantacini, D. M. C., Picanco-Castro, V., Covas, D. T., Rosa, A. L., et al. (2019). Titanium with nanotopography induces osteoblast differentiation through regulation of integrin alphaV. *J. Cell. Biochem.* 120, 16723–16732. doi: 10.1002/jcb.28930

Lou, H. Y., Zhao, W., Li, X., Duan, L., Powers, A., Akamatsu, M., et al. (2019). Membrane curvature underlies actin reorganization in response to nanoscale surface topography. *Proc. Natl. Acad. Sci. U.S.A.* 116, 23143–23151. doi: 10.1073/pnas.1910166116

Mattila, P. K., and Lappalainen, P. (2008). Filopodia: molecular architecture and cellular functions. *Nat. Rev. Mol. Cell Biol.* 9, 446–454. doi: 10.1038/nrm2406

Michael, M., and Parsons, M. (2020). New perspectives on integrin-dependent adhesions. *Curr. Opin. Cell Biol.* 63, 31–37. doi: 10.1016/j.ceb.2019.12.008

Nasrollahi, S., Banerjee, S., Qayum, B., Banerjee, P., and Pathak, A. (2016). Nanoscale matrix topography influences microscale cell motility through adhesions, actin organization, and cell shape. *ACS Biomater. Sci. Eng.* 3, 2980–2986. doi: 10.1021/acsbiomaterials.6b00554

Olivares-Navarrete, R., Rodil, S. E., Hyzy, S. L., Dunn, G. R., Almaguer-Flores, A., Schwartz, Z., et al. (2015). Role of integrin subunits in mesenchymal stem cell differentiation and osteoblast maturation on graphitic carbon-coated microstructured surfaces. *Biomaterials* 51, 69–79. doi: 10.1016/j.biomaterials.2015.01.035

Parsons, J. T., Horwitz, A. R., and Schwartz, M. A. (2010). Cell adhesion: integrating cytoskeletal dynamics and cellular tension. *Nat. Rev. Mol. Cell Biol.* 11, 633–643. doi: 10.1038/nrm2957

Raines, A. L., Berger, M. B., Schwartz, Z., and Boyan, B. D. (2019). Osteoblasts grown on microroughened titanium surfaces regulate angiogenic growth factor production through specific integrin receptors. *Acta Biomater.* 97, 578–586. doi: 10.1016/j.actbio.2019.07.036

Robling, A. G., Castillo, A. B., and Turner, C. H. (2006). Biomechanical and molecular regulation of bone remodeling. *Annu. Rev. Biomed. Eng.* 8, 455–498. doi: 10.1146/annurev.bioeng.8.061505.095721

Rosa, A. L., Kato, R. B., Castro Raucci, L. M., Teixeira, L. N., de Oliveira, F. S., Bellesini, L. S., et al. (2014). Nanotopography drives stem cell fate toward osteoblast differentiation through alpha1beta1 integrin signaling pathway. *J. Cell. Biochem.* 115, 540–548. doi: 10.1002/jcb.24688

Saruta, J., Sato, N., Ishijima, M., Okubo, T., Hirota, M., and Ogawa, T. (2019). Disproportionate effect of sub-micron topography on osteoconductive capability of titanium. *Int. J. Mol. Sci.* 20:E4027.

Shah, F. A., Thomsen, P., and Palmquist, A. (2018). A review of the impact of implant biomaterials on osteocytes. *J. Dent. Res.* 97, 977–986. doi: 10.1177/0022034518778033

Siebers, M. C., ter Brugge, P. J., Walboomers, X. F., and Jansen, J. A. (2005). Integrins as linker proteins between osteoblasts and bone replacing materials. A critical review. *Biomaterials* 26, 137–146. doi: 10.1016/j.biomaterials.2004.02.021

Skoog, S. A., Kumar, G., Narayan, R. J., and Goering, P. L. (2018). Biological responses to immobilized microscale and nanoscale surface topographies. *Pharmacol. Ther.* 182, 33–55. doi: 10.1016/j.pharmthera.2017.07.009

Smeets, R., Kolk, A., Gerressen, M., Driemel, O., Maciejewski, O., Hermanns-Sachweh, B., et al. (2009). A new biphasic osteoinductive calcium composite material with a negative Zeta potential for bone augmentation. *Head Face Med.* 5:13.

Sun, Z., Guo, S. S., and Fassler, R. (2016). Integrin-mediated mechanotransduction. *J. Cell Biol.* 215, 445–456. doi: 10.1083/jcb.201609037

Sun, Z., Lambacher, A., and Fässler, R. (2014). Nascent adhesions: from fluctuations to a hierarchical organization. *Curr. Biol.* 24, R801–R803.

Valdembri, D., and Serini, G. (2012). Regulation of adhesion site dynamics by integrin traffic. *Curr. Opin. Cell Biol.* 24, 582–591. doi: 10.1016/j.ceb.2012.08.004

Wozniak, M. A., Modzelewska, K., Kwong, L., and Keely, P. J. (2004). Focal adhesion regulation of cell behavior. *Biochim. Biophys. Acta* 1692, 103–119.

Xu, J. Y., Chen, X. S., Zhang, C. Y., Liu, Y., Wang, J., and Deng, F. L. (2016). Improved bioactivity of selective laser melting titanium: surface modification with micro-/nano-textured hierarchical topography and bone regeneration performance evaluation. *Mater. Sci. Eng. C Mater. Biol. Appl.* 68, 229–240. doi: 10.1016/j.msec.2016.05.096

Xu, W., Yang, Z., and Lu, N. (2015). A new role for the PI3K/Akt signaling pathway in the epithelial-mesenchymal transition. *Cell Adhes. Migr.* 9, 317–324. doi: 10.1080/19336918.2015.1016686

Yoon, S. O., Shin, S., Karreth, F. A., Buel, G. R., Jedrychowski, M. P., Plas, D. R., et al. (2017). Focal adhesion- and IGF1R-dependent survival and migratory pathways mediate tumor resistance to mTORC1/2 inhibition. *Mol. Cell.* 67, 51–527.e514.

You, R., Li, X., Liu, Y., Liu, G., Lu, S., and Li, M. (2014). Response of filopodia and lamellipodia to surface topography on micropatterned silk fibroin films. *J. Biomed. Mater. Res. A* 102, 4206–4212.

Zhang, Y., Liu, X., Zeng, L., Zhang, J., Zuo, J., Zou, J., et al. (2019). Polymer fiber scaffolds for bone and cartilage tissue engineering. *Adv. Funct. Mater.* 29:1903279.

Zheng, G., Guan, B., Hu, P., Qi, X., Wang, P., and Kong, Y. (2018). Topographical cues of direct metal laser sintering titanium surfaces facilitate osteogenic differentiation of bone marrow mesenchymal stem cells through epigenetic regulation. *Cell Prolif.* 51:e12460. doi: 10.1111/cpr.12460

Zhu, L., Luo, D., and Liu, Y. (2020). Effect of the nano/microscale structure of biomaterial scaffolds on bone regeneration. *Int. J. Oral Sci.* 12:6.

Conflict of Interest: The authors declare that the research was conducted in the absence of any commercial or financial relationships that could be construed as a potential conflict of interest.

frontiers
in Bioengineering and Biotechnology

REVIEW
published: 12 June 2020
doi: 10.3389/fbioe.2020.00628

Microporous Frameworks as Promising Platforms for Antibacterial Strategies Against Oral Diseases

Yao Wan[1,2†], *Wenzhou Xu*[2,3†], *Xuan Ren*[1,2], *Yu Wang*[2,4], *Biao Dong*[5*] and *Lin Wang*[1,2*]

[1] Department of Oral Implantology, School and Hospital of Stomatology, Jilin University, Changchun, China, [2] Jilin Provincial Key Laboratory of Sciences and Technology for Stomatology Nanoengineering, Changchun, China, [3] Department of Periodontology, School and Hospital of Stomatology, Jilin University, Changchun, China, [4] Department of Prosthodontics, School and Hospital of Stomatology, Jilin University, Changchun, China, [5] State Key Laboratory on Integrated Optoelectronics, College of Electronic Science and Engineering, Jilin University, Changchun, China

Edited by:
Jianxun Ding,
Changchun Institute of Applied Chemistry (CAS), China

Reviewed by:
Huakun Xu,
University of Maryland, Baltimore, United States
Lei Cheng,
Sichuan University, China
Ana Palcic,
Rudjer Boskovic Institute, Croatia
Kok Giap Haw,
National University of Singapore, Singapore

***Correspondence:**
Biao Dong
dongb@jlu.edu.cn
Lin Wang
wanglin1982@jlu.edu.cn

†These authors have contributed equally to this work and share first authorship

Specialty section:
This article was submitted to Biomaterials, a section of the journal Frontiers in Bioengineering and Biotechnology

Received: 03 May 2020
Accepted: 22 May 2020
Published: 12 June 2020

Citation:
Wan Y, Xu W, Ren X, Wang Y, Dong B and Wang L (2020) Microporous Frameworks as Promising Platforms for Antibacterial Strategies Against Oral Diseases. Front. Bioeng. Biotechnol. 8:628. doi: 10.3389/fbioe.2020.00628

Nowadays, the heavy burden of oral diseases such as dental caries, periodontitis, endodontic infections, etc., and their consequences on the patients' quality of life indicate a strong need for developing effective therapies. Bacterial infections played an important role in the field of oral diseases, in-depth insight of such oral diseases have given rise to the demand for antibacterial therapeutic strategies. Recently, microporous frameworks have attracted tremendous interest in antibacterial application due to their well-defined porous structures for drug delivery. In addition, intensive efforts have been made to enhance the antibacterial performance of microporous frameworks, such as ion doping, photosensitizer incorporation as building blocks, and surface modifications. This review article aims on the major recent developments of microporous frameworks for antibacterial applications against oral diseases. The first part of this paper puts concentration on the cutting-edge researches on the versatile antibacterial strategies of microporous materials via drug delivery, inherent activity, and structural modification. The second part discusses the antibacterial applications of microporous frameworks against oral diseases. The applications of microporous frameworks not only have promising therapeutic potential to inhibit bacterial plaque-initiated oral infectious diseases, but also have a wide applicability to other biomedical applications.

Keywords: microporous frameworks, nanomaterials, drug delivery, antibacterial, oral infections

INTRODUCTION

Oral diseases such as caries, periodontitis, and endodontic infections, attracted tremendous attentions all over the world since such diseases account for a vast burden of morbidity and healthcare spending. For example, an authoritative report claimed that dental caries and periodontitis were the first and 11th most prevalent causes of disease worldwide in 2016 (Vos et al., 2017), which was 5.4 million as a result of severe periodontitis, 4.6 million as a result of untreated caries in permanent teeth (Papapanou and Susin, 2017). The estimated costs of totaling worldwide in dental infectious diseases amounted to more than $540 billion dollars in 2015 (Righolt et al., 2018). Besides local destruction of teeth and supporting tissues, these bacterial-related oral diseases were closely related with pulmonary disease (Manger et al., 2017), cardiovascular disease (Sanz et al., 2020), and gastrointestinal cancer (Chen et al., 2019). Antibiotics are usually applied as major or auxiliary approach in treatment of such oral infectious diseases. Currently, the growing resistance of microorganisms to conventional antibiotics has become a public health problem and raises highly demand to look for more effective solutions (Wyszogrodzka et al., 2016). Amounts of antibacterial agents such as metallic ions and natural extracts were alternatively applied in the antibacterial field (Li et al., 2018). However, the inferior biocompatibility, short half-time period, and unexpected cytotoxicity limit the potential applications for these materials.

Nowadays, there has been a continuous and fast-paced emergence of new synthetic porous nanomaterials developed to meet pharmacological and biological requirements for antibacterial application over the past several decades. Thereinto, microporous solid is a category of nanomaterial with pore < 2 nm in diameter. On the basis of framework composition, there are three types of crystalline porous solids: hybrid inorganic–organic hybrids [for example, metal-organic frameworks (MOFs)], inorganic (for example, zeolites), and organic frameworks [for example, covalent organic frameworks (COFs)] (Xue et al., 2016). The well-ordered microporous structure of these frameworks was taken advantage in many applications in different fields, such as catalysts, sensors, purification, etc. (Wang et al., 2011; Beale et al., 2015; Zhang et al., 2018; Cui et al., 2019). With respect to antibacterial application, the porous feature also gives rise to the ability to serve as a carrier for drug and biological molecule delivery, since well-defined pores can provide the opportunity to store active antibacterial agents and then release them at the appropriate time and at the correct rate (Rimoli et al., 2008). Besides drug delivery, these microporous frameworks could also exert antibacterial effects via their own degradation along with the release of metal ions, ligands into saliva, gingival crevicular fluid, and other body liquid (Li X. et al., 2019). Furthermore, several promising molecules have potential as functional building blocks in COFs due to their planar geometry and rigidity coupled with inherent functionalities, such as photosensitizing and redox-active properties (Liu et al., 2017; Hynek et al., 2018). Upon external light radiation, the COFs with these active organic building blocks would be activated to generate reactive oxygen species (ROS) to exert photodynamic inactivation against microorganisms. The microporous structure could carry more oxygen to amplify the photodynamic inactivation efficacy (Restrepo et al., 2017).

Currently, several valuable reviews on microporous frameworks have described on their materials design (Mori et al., 2004; Zhao et al., 2018), processing approaches (Valtchev et al., 2013; Xue et al., 2016), catalysis (Beale et al., 2015), and purification (Krishna, 2018; Prasetya et al., 2019), which will not be repeated here. As shown in **Figure 1**, this article reviews the major new developments on microporous frameworks as promising platforms for antibacterial strategies including inherent property, drug delivery, and different modifications, particularly focusing on potential application against oral diseases.

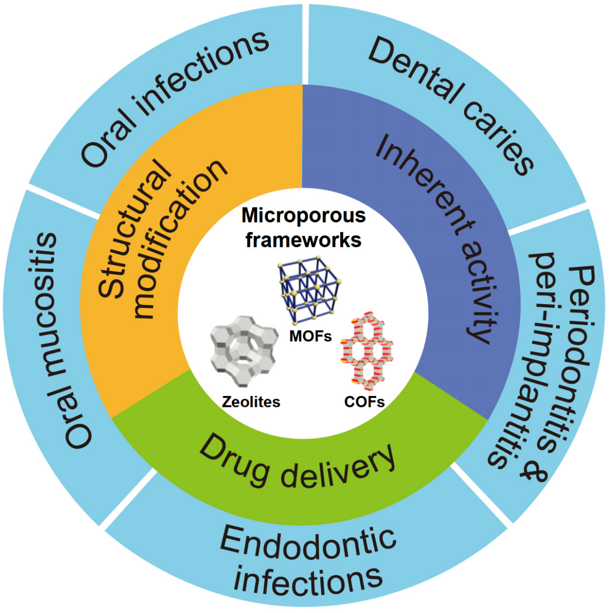

FIGURE 1 | Schematic diagram of the application of microporous frameworks in dentistry. Notes: The microporous frameworks had potential to treat many oral diseases including dental caries, periodontitis, peri-implantitis, oral mucositis, and other oral infections. Abbreviations: COFs, covalent organic frameworks; MOFs, metal organic frameworks.

MICROPOROUS MATERIALS WITH DIFFERENT ANTIBACTERIAL STRATEGIES

The growing resistance of pathogens to antibiotic therapy has become a matter of concern. Because of the widespread use of antibiotics, major pathogens of infections such as *Staphylococcus aureus* are gradually developing drug resistance, leading to "super" infections. Hence, it is an urgent need to develop new and effective bactericidal agents to combat these drug-resistant microbes (Hughes, 2003). Therefore, developing antimicrobial nanomaterials is one of the most attractive approaches for eliminating the major perniciousness of pathogenic bacteria (Zhang Y. et al., 2019). Recently, the microporous materials have shown a promising perspective as an alternative method to combat the drug-resistant microbes by the following methods: (1) serving as drug reservoirs (Horcajada et al., 2010; Amorim et al., 2012); (2) acting as antimicrobial agents by degrading and releasing metal ions (Wyszogrodzka et al., 2016); and (3) turning into antibacterial drugs through different modifications (e.g., metal ions doping for bactericidal performance enhancement) (Li X. et al., 2019).

Nanomaterials With Inherent Antibacterial Activity

Metal-organic frameworks, also known as porous coordination polymers, are a category of hybrid materials comprising metal ions/clusters linked by polydentate bridging ligands typically under mild conditions, bonding types of which include metal coordination, hydrogen bonding, electrostatic interactions, and p–p stacking (Carné et al., 2011; Della Rocca et al., 2011). Compared to conventional nanomedicines, nanoscale MOFs have greater advantages in the aspect of structural and chemical diversity, high loading capacity, and biodegradability (Wyszogrodzka et al., 2016). It was reported that the most probable mechanism of the inherent antibacterial effect for MOFs was the structural degradation, along with the release of metal ions and ligands (Berchel et al., 2011; Tamames-Tabar et al., 2015). A previous study demonstrated that Ag-based MOF, acting as a reservoir of bactericidal metal ions, was able to release Ag^+ into solution steadily and subsequently and had the bactericidal effect against *S. aureus*, *Escherichia coli*, and *Pseudomonas aeruginosa* (Berchel et al., 2011). When contacting with Ag^+, the bacterial envelopes were seriously destroyed, following by the loss of the cellular cohesion, ultimately leading to the bacterial cytoplasm drained and the bacteria dead (Lu et al., 2014). Besides Ag^+-based MOFs, copper ion is also well—known as its antibacterial effect since it could induce damage to the outer membranes of bacteria (Santo et al., 2012). A copper-based MOF $Cu_3(BTC)_2$ (BTC = 1,3,5-benzenetricarboxylate), also known as CuBTC and HKUST-1 could be synthesized via an ultrasonic method at ambient temperature and atmospheric pressure (Li et al., 2009). The deposition of CuBTC on silk fibers by layer-by-layer technique exhibited a strong inhibitory activity against Gram-negative bacteria *E. coli* and Gram-positive bacteria *S. aureus* (Abbasi et al., 2012). It was also reported that CuBTC exerted a favorable antifungal capability against *Saccharomyces cerevisiae* (completely inhibition) and *Geotrichum candidum* (reduction from 6.16 to 1.29 CFU/mL) (Chiericatti et al., 2012). A recent study also indicated an acceptable antibacterial activity of manganese-based MOF (UoB-4) against both Gram-positive and Gram-negative bacteria (Aryanejad et al., 2020). Moreover, zeolitic imidazolate frameworks (ZIFs), a sub-family of MOFs, are constructed from transition metal ions (Zn^{2+}, Co^{2+}, etc.) and imidazolate linkers, the structures of which are similar to zeolite topologies (Aguado et al., 2014). ZIF-8 nanocomposite coatings showed excellent antibacterial activity against Gram—negative *E. coli* (Miao et al., 2018). Unlike silver-based and copper-based MOFs, the antibacterial mechanism of zinc-based ZIF-8 is the generation of ROS speeding up the inflammatory response (Li X. et al., 2019). In addition, MIL-100(Fe), MIL-88B, and MOF-53(Fe) are the representative iron-based MOFs nanoparticles. MOF-53(Fe) nanoparticles were composed with ferric ion clusters and ligands of the terephthalic acid. Lin S. et al. (2017) discovered the bactericidal viability of the group MOF-53(Fe) with concentrations in the range of 20–160 μg/mL was increasing against *S. aureus* comparing with that of the control group. Comparably, two cobalt-based MOF (ZIF-67 and Co-SIM-1) also exhibited bactericidal effects against *Pseudomonas putida* and *E. coli* with over 50% growth inhibition at the concentrations in the 5–10 mg/mL range (Aguado et al., 2014). Similarly, Zhuang et al. (2012) synthesized a novel cobalt-based MOF (Co-TDM) showing the strong killing effect on *E. coli* with minimal bactericidal concentration ranging from 10 to 15 mg/L. Although membrane damage was stated as the major reason, the following mechanism is comprehensively applicable for bacterial inactivation: (1) diffusion-directed lipid-oxidation, (2) cation transport interruption, (3) direct interaction, (4) ROS generation, (5) chelation effects, and (6) membrane depolarization (Zhuang et al., 2012). Several organic chemicals also possess antibacterial activity and could serve as ligands for MOF synthesis. Tamames-Tabar et al. (2015) formulated a bioactive BioMIL—5, synthesized from a Zn^{2+} salt and azelaic acid, both with interesting biocide properties. Afterward, Restrepo et al. (2017) also developed a zinc-based MOF with hydrazinebenzoate linkers. This novel MOF inhibited bacterial growth with a minimal bactericidal concentration of 20 μg/mL, which was mainly attributed to the release of 4-hydrazinebenzoate linker (Restrepo et al., 2017).

Zeolites, consisting of TO_4 (T = Si and Al) tetrahedra linked to each other by oxygen atoms, are crystalline aluminosilicate materials with a three-dimensional microporous structure containing uniformly distributed channels (Fakin et al., 2015). According to the number of T-atoms in the ring, zeolites are conventionally classified into small pore opening (eight-membered ring), medium (10-membered ring), and large one (12-membered ring), the pore diameters of which range from 0.5 to 2.0 nm (McCusker and Baerlocher, 2005). In addition to natural sources, zeolites can be synthesized by sol–gel (Zhang et al., 2015), hydrothermal (Abdullahi et al., 2017), and microwave methods (Boosari et al., 2018). At present, zeolites are widely used in the field of biomedicine, which are able to act as antibacterial materials and drug carriers (Amorim et al., 2012; Ferreira et al., 2012). Zeolite exerts antibacterial effect mainly via an antibacterial ion-exchanging process, while zeolite *per se* does not possess any antibacterial activity. However, antibacterial and anti-adhesive zeolite coating was developed on titanium alloy surface by 2% Ag^+ exchange. Interestingly, the bacteria adhered on zeolite-Ti was also remarkably reduced compared with the Ti surface without zeolites, indicating that non-silver containing zeolite coating possessed high hydrophilicity to donate Ti surface with certain antibacterial and antifouling properties (Wang et al., 2011).

Covalent organic frameworks, as novel crystalline porous organic compounds, consist of light atoms, like H, B, C, N, and O, through dynamic covalent bonds with periodic skeletons and ordered nanopores (Xue et al., 2016; Zhao et al., 2018). Furthermore, inherent properties, such as large accessible pore size, specific surface area, channel type-ordered structure, low density, crystallinity, and high thermal stability, can provide a unique advantage over MOFs (Bhanja et al., 2017). The feature of structural variability is beneficial to wide application in different fields through the design of holes and skeletons, such as semiconduction, photoconductor, gas adsorption and storage, diagnoses, and treatment (Wan et al., 2008, 2009; Fang et al., 2015; Huang et al., 2016; Mitra et al., 2017; Zhu and Zhang, 2017). Recently, nanomaterial-based antibacterial photodynamic therapy gradually gained increasing attention (Qi et al., 2019). The antibacterial photodynamic therapy bases on the interaction of harmless nanosized-photosensitizers, tissue oxygen, and visible light to yield high level of ROS, which has a strong oxidation and high reactivity, thus causing rapid lipid oxidation of the bacteria. COFs are promising for serving asnanosized-photosensitizers for antibacterial photodynamic therapy since traditional photosensitizers such as porphyrins are potential functional building blocks in COF structures. Before the year of 2017, the COF-based antibacterial photodynamic therapy function was well-reviewed in a previous paper by Li and Yang (2017), which were not repeated in the present article. In later 2017, Liu et al. (2017) fabricated two COFs (COF-SDU1 and COFs-Trif-Benz) by covalent linking benzidine or p-phenylenediamine in the structure. Both COF frameworks showed excellent photocatalytic antibacterial activity against *S. aureus* and *E. coli* via singlet oxygen ($^1O_2$) generation by visible light irradiation. A pioneering work by Hynek et al. (2018) designed and synthesized porphyrin-based COFs by Schiff-base chemistry. These porphyrinic COFs with high photostability and broad spectral efficiency exerted strong antibacterial effects toward *P. aeruginosa* and *Enterococcus faecalis* biofilms upon visible light radiation (460 or 525 nm).

Microporous Frameworks for Antimicrobial Drug Delivery

Besides inherent antimicrobial functions, the porous feature of microporous frameworks also gives rise to the ability to serve as carriers for drug and biological molecule delivery. To meet pharmacological and biological requirements, microporous materials serving as nanocarriers for antibacterial application need to possess following important properties: (1) well-control and release behavior without avoid initial burst, (2) high drug loading capability, (3) modifiable surface for targeted therapy, and (5) no cytotoxicity.

Metal-Organic Frameworks

In addition to their inherent antibacterial effects, MOFs have been broadly applied in the field of drug delivery due to their adjustable aperture, large surface area, large pore capacity, and easy modification (Horcajada et al., 2010; Simon-Yarza et al., 2018). MOFs were able to encapsulate antibacterial substances (such as antibiotics, metals and metal oxides, plant natural products, and nitric oxide) in their constructions, via the non-covalent connection between metal open sites in their structures and antibacterial agents (Guerra et al., 2016). Subsequently, the release of drug can be effectively controlled through fine-tuning of MOFs porosity, biodegradability, and external stimulus conditions, such as light, pH, etc. (Li et al., 1999; Cai et al., 2019; Liu Y. et al., 2019). In addition, the degradation of MOFs also leads to the release of metal ions, which exerts a synergistic antibacterial effect.

Since pure antibiotics are difficult to cross cell membranes and maintain effective antibacterial concentrations for long periods of time (Brown and Wright, 2016), MOFs have attracted much more attentions as antibiotic carriers. In a previous study, the antibiotics such as tetracycline hydrochloride and doxycycline monohydrate were encapsulated in iron-based MOF (nano-MIL-100), showing excellent controlled release behavior (Taherzade et al., 2017). Furthermore, a new method of using photo-responsive ZIF-8 as drug carriers for rifampicin has been reported (Song et al., 2018). A pH-jump reagent (2−nitrobenzaldehyde) was modified into the porous structure of ZIF-8 as a gatekeeper, allowing the UV-light (365 nm) responsive *in situ* production of acid, which subsequently induced pH-dependent degradation of ZIF-8 and promoted the release of the antibiotic loaded in the pores in a controlled manner (Song et al., 2018). The combination of the UV-light, the pH-triggered precise antibiotic release, and the zinc ions enabled the light-activated nanocomposite to significantly inhibit bacteria-induced wound infection and accelerate wound healing (Song et al., 2018). Based on the above researches, Zhang Y. et al. (2019) synthesized a novel tetracycline@ZIF-8@hyaluronic acid nanocomposite by wrapping tetracycline in ZIF-8 and hyaluronic acid and proved that the tetracycline@ZIF-8@hyaluronic acid nanocomposite was promising for eradication of pathogenic bacteria *in vitro* and *in vivo* experiments (**Figure 2**). The antibacterial activity *in vitro* of the tetracycline@ZIF-8@hyaluronic acid nanocomposite against *S. aureus* and *Salmonella* was evaluated by minimum inhibitory concentration. The result showed that fractional inhibitory concentration index calculated to be less than 0.5 verified the synergistic effect of the ZIF-8 and tetracycline components in the tetracycline@ZIF-8@hyaluronic acid nanocomposite (Zhang X. et al., 2019). In another research, incorporation of ciprofloxacin into zirconium-based MOF (UiO-66) had larger inhibitory ring range against *S. aureus* and *E. coli* in contrast to ciprofloxacin alone (Nasrabadi et al., 2019). Currently, different kinds of MOFs encapsulated varieties of antibacterial agents with dissimilar antibacterial efficient, which detailedly displayed in **Table 1**.

Moreover, the multifunctional combination of MOFs with metal/metal oxides nanoparticles further improves their bactericidal capacities. Ximing et al. (2017) successfully synthesized copper-based MOF (CuTCPP MOF) to encapsulate silver nanoparticles and prepared a new composite material Ag-CuTCPP MOF. The inhibition rates on *E. coli*, *Bacillus subtilis*, *S. aureus*, and their mixed strains were 82.18, 72.8, 89.1, and 80.4%, respectively, which were significantly higher than positive control penicillin (Ximing et al., 2017). The bactericidal principle was that the silver nanoparticles encapsulated in MOFs contacted with oxygen to form Ag^+, which destroyed cell membrane permeability and caused bacterial death (Ximing et al., 2017). Similar results about Ag nanoparticles-MOF as antibacterial hybrid could also be found in recent studies (Zhu et al., 2015; Thakare and Ramteke, 2017; Abd El Salam et al., 2018). Beyond that, zinc oxide (ZnO) showed excellent antibacterial properties, and could be combined with other materials (such as gelatin, hydrogels) to further develop its antibacterial ability (Lin J. et al., 2017; Li et al., 2018). Recently, Redfern et al. successfully synthesized ZnO@ZIF-8 composite by spontaneously forming ZnO nanorods on the surface of ZIF-8 nanocrystals exposed to an aqueous solution of silver nitrate at room temperature. The authors drew a conclusion that catheter-associated urinary tract infection pathogens could be eliminated by ZnO@ZIF-8 composite (Redfern et al., 2018). The strong bactericidal effect was not only attributed to the action of ZnO, but also related to the direct attack and killing of pathogenic

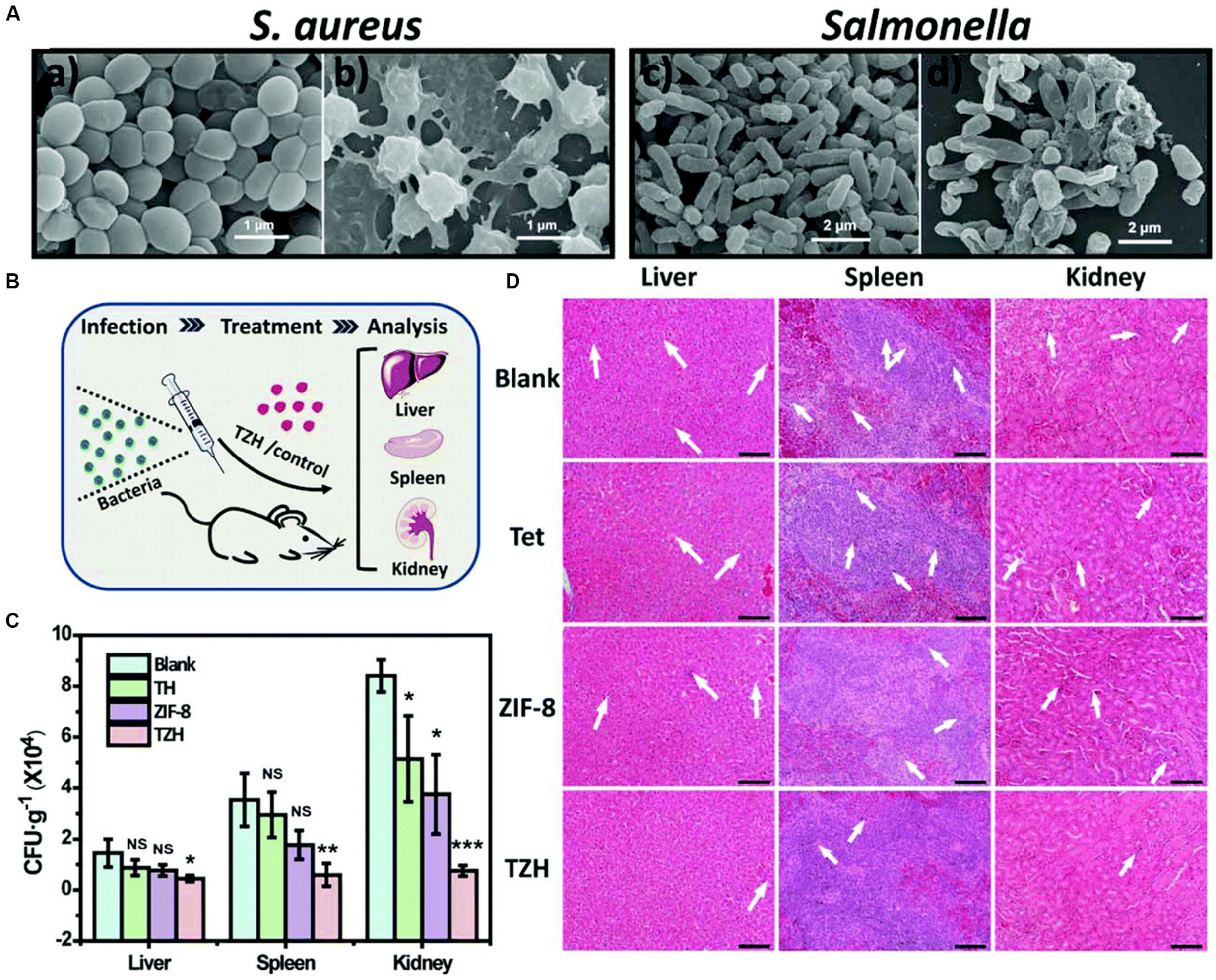

FIGURE 2 | The sterilization situation of TZH *in vitro* and *in vivo*. Notes: **(A)** SEM images of untreated **(a,c)** and TZH-treated (50 μg/mL) **(b,d)** *S. aureus* and *Salmonella*. **(B)** The scheme for constructing *in vivo* animal experimental model. **(C)** CFU of bacteria in liver, spleen, and kidney after the treatment by TZH or other control groups (blank, Tet, ZIF-8). (*$P < 0.05$; **$P < 0.01$; ***$P < 0.001$; NS, not significant.) **(D)** Pictures of histological sections with H&E stain in TZH and other control groups. The abnormal areas were shown by the white arrows. Scale bar = 50 μm. [Reprinted with permission from Zhang X. et al., 2019; Copyright (2019) Royal Society of Chemistry]. Abbreviations: CFU, colony forming unit; SEM, scanning electron microscopy; *S. aureus*, *Staphylococcus aureus*; Tet, tetracycline; TZH, tetracycline@ZIF-8@hyaluronic acid.

microorganisms by zinc ions and imidazole ligands of ZIF-8 (Redfern et al., 2018).

Furthermore, some plant natural products showed satisfactory antibacterial properties. Liu X. et al. (2019) developed the ultrathin two-dimensional MOF nanosheet [two-dimensional Cu-TCPP(Fe)] as a physical adsorption model of glucose oxidase for peroxidase simulators (enzyme catalyst). The designed system could self-activate the peroxidase-like activity of two-dimensional MOF nanosheets owing to the formation of gluconic acid, which significantly improved the generation rate of toxic •OH and enhanced the antibacterial effects. Besides, Naseri et al. (2018) have described the antibacterial effect of Cu-H_2bpdc-cy MOF by mixing cytosine with copper-based MOF (Cu-H_2bpdc) on *Proteus strangis*. When Cu-H_2bpdc-cy MOF contacted with bacteria, the released copper ions were combined with negatively charged lipoproteins in bacterial cell wall, then entered the cell, and finally damaged the cell wall.

In addition, the antibacterial properties of nitric oxide were widely reported since it played a pivotal role in the body's immune response to pathogens. The antibacterial mechanism of nitric oxide was due to the nitrosative and oxidative stress imposed by its reactive byproducts (e.g., nitrous oxide and pernitrite), which eventually led to the rupture of the bacterial membrane (Fang, 1997). Actually, nitrogen atoms are able to interact with the exoskeleton cations in MOFs to realize nitric oxide loading. The small molecule of nitric oxide would be released by exchanging with cations in the interstitial fluid. Consequently, the high concentrations of nitric oxide could promote the bactericidal effect of macrophages toward the pathogens (Horcajada et al., 2012). Therefore, nano-MOF materials make use of their gas storage capacity to carry

TABLE 1 | Metal organic frameworks as drug delivery systems for antibacterial application.

Name	Framework metal	Antibacterial agents	Pathogenic bacteria	Antibacterial activity	References
CuTTP	Cu	Ag NPs	*E. coli S. aureus B. subtilis mixed strains*	*E. coli*: Antibacterial efficiency = 82.18% *S. aureus*: Antibacterial efficiency = 72.8% *B. subtilis*: Antibacterial efficiency = 89.1% *mixed strains*: Antibacterial efficiency = 80.4%	Ximing et al., 2017
CuTCPP(Fe)	Cu/Fe	Glucose oxidase	*E. coli S. aureus*	*E. coli*: Antibacterial efficiency = 88% *S. aureus*: Antibacterial efficiency = 90%	Liu X. et al., 2019
ZIF-8	Zn	Ag nanowires	*B. subtilis E. coli*	*B. subtilis*: MIC = 200 μg/mL *E. coli*: MIC = 300 μg/mL	Guo et al., 2018
		Ciprofloxacin	*E. coli S. aureus*	*E. coli*: ZOI = 46 mm *S. aureus*: ZOI = 49 mm	Nabipour et al., 2017
		Rifampicin	*E. coli* AREC *MRSA*	N/A	Song et al., 2018
		ZnO	*E. coli K. pneumoniae P. mirabilis S. aureus*	MBC = 0.25 mg/mL	Redfern et al., 2018
		Iodine	*E. coli S. aureus S. epidermidis*	*E. coli*: Sterilizing time = 3 min *S. aureus*: Sterilizing time = 2 min *S. epidermidis*: Sterilizing time = 2 min	Au-Duong and Lee, 2017
Ni−MOF	Ni	Ag NPs	*B. subtilis E. coli P. aeruginosa C. albicans*	MIC = 0.025 μg/mL MBC = 2.5 μg/mL	Abd El Salam et al., 2018
NH_2−MOP(Ti)	Ti	Ag NPs	N/A	Sterilization activity is high under Xenon lamp	Zhu et al., 2015
MOF-5	Zn	Ag NPs	*E. coli*	Under visible light irradiation, less than 91% bacteria were rapidly inactivated within 70 min	Thakare and Ramteke, 2017
MIL−100(Fe)	Fe	Gentamicin	*S. aureus S. epidermidis P. aeruginosa*	*S. aureus*: MIC = 0.5–1 μg/mL; MBC = 1 μg/mL *S. epidermidis*: MIC = 0.125 μg/mL; MBC = 0.125–0.25 μg/mL *P. aeruginosa*: MIC = 1–2 μg/mL; MBC = 4–8 μg/mL	Unamuno et al., 2018
UIO-66	Zr	Gentamicin	N/A	N/A	Unamuno et al., 2018
		Ciprofloxacin	*E. coli S. aureus*	The inhibitory ring was larger in diameter than ciprofloxacin alone	Nasrabadi et al., 2019
Cu-H_2bpdc	Cu	Cytosine	*P. mirabilis*	MIC = 1.6–1.8 mg/mL MBC = 1.8–2.0 mg/mL	Naseri et al., 2018

Abbreviations: Ag NPs, silver nanoparticles; AREC, ampicillin-resistant Escherichia coli; B. subtilis, Bacillus subtilis; C. albicans, Candida albicans; E. coli, Escherichia coli; K. pneumoniae, Klebsiella pneumonia; MBC, minimal bactericidal concentration; MIC, minimal inhibition concentration; MRSA, multidrug−resistant Staphylococcus aureus; P. aeruginosa, Pseudomonas aeruginosa; P. mirabilis, Proteus mirabilis; S. aureus, Staphylococcus aureus; S. epidermidis, Staphylococcus epidermidis; ZnO, zinc oxide; ZOI, zone of inhibition.

nitric oxide, which can play an antibacterial role (Zhu et al., 2015). Another study reported that *Staphylococcus epidermidis*, *S. aureus*, *and E. coli* of 1 × 10^{10} CFU/mL in PBS solution (pH = 6) were totally killed at ZIF-8@I (iodine loaded ZIF-8) dosage of 0.2 g/L within 3 min (Au-Duong and Lee, 2017). Its bactericidal activity probably depended on the irreversible damage to bacterial cells caused by the release of iodine and zinc in the framework.

Yet some MOF nanomaterials are able to biodegrade and release metal ions making it possible for biological toxicity to occur. In addition, recent toxicological studies have shown that their toxicity is closely related to organic ligands in their structures (Tamames-Tabar et al., 2014; Shearier et al., 2016). The hydrophobic–hydrophilic balance of the constituent organic ligands may be responsible for cytotoxicity. To solve these problems, the cytotoxicity of MOF nanoparticles can be minimized by using biocompatible cations to construct MOFs and improving the hydrophilicity of organic ligands.

Zeolites

Zeolites have also appeared in drug controlled release systems in recent years due to their orderly and uniform pore shape and highly ion-exchanging capability (Rimoli et al., 2008). The basic chemical composition of zeolites is based on a silica framework (SiO_2) where a proportion of the silicon atoms are be substituted by aluminum. Then replacing Si^{4+} with Al^{3+} produces a negatively charged aluminosilicate skeleton, requiring the exchange of additional skeleton cations (such as Na^+) to keep the overall skeleton neutral (Torres-Giner et al., 2017). Those cations are not part of the frame but are located in the pores of the structure and they are exchanged out of the material since replaced by other cations (such as Ag^+) (Hedström, 2001). A large number of studies have reported on the antibacterial properties of metal ions-loaded zeolites. Ag^+ is one of the most antimicrobial metal ions exchanging in zeolites, because of its good stability and broad-spectrum antibacterial properties (Abe et al., 2004). Fortunately, zeolites have strong affinity for Ag^+, which can be electrostatically combined to make the ratio of Ag^+ to the weight of the frame up to 40% (Uchida, 1995). Afterward, Ag^+ could be released from the zeolites by exchanging with the cations in external environment. Thereafter, it enters into the bacterial cell by penetrating through the cell wall and consequently changes the DNA into condensed form, finally causing the cell death (Rai et al., 2009). A previous study recently developed a new method for the green synthesis of highly stable zeolites such as green β-zeolite based on the seed—assisted synthesis, without the use of any organic structure—directing agent. After exchanging with Ag^+, the green β-zeolite had the ability to inhibit the activity of *E. coli* (Saint-Cricq et al., 2012). After adding 20 mg of silver-loaded green β-zeolite into culture medium (10 mL, 10^8 CFU/mL) for 1 h, no colonies of *E. coli* were found by agar plate counting. Besides, other types of zeolites, such as zeolite X and EMT zeolite, were also reported to exchange with Ag^+ for antibacterial application (Dong et al., 2014; Chen S. et al., 2017; Tosheva et al., 2017). In addition to Ag^+, other metal ions including zinc ions, copper ions, etc., were also exchanged into different types of zeolites to exert antibacterial properties. All exchanging zeolites exhibited favorable bacterial killing efficacy against different pathogens. The details could be found in **Table 2**.

In addition, metal and metal oxides nanoparticles supported into zeolites are widely used in antibacterial field. Recently, ZnO and titanium dioxide (TiO_2) nanoparticles have attracted considerable attentions due to the characteristic that they can produce ROS to exert their bactericidal capacity (Dizaj et al., 2014). Azizi-Lalabadi et al. (2019) assessed the antimicrobial activity of 4A zeolite loading with TiO_2, ZnO, and TiO_2/ZnO nanoparticles and concluded that TiO_2/ZnO nanoparticles loaded with 4A zeolite had the superior antibacterial effects on

TABLE 2 | Microporous zeolites as drug delivery systems for antibacterial application.

Name	Antibacterial drug	Pathogenic bacteria	Antibacterial activity	References
Zeolite X	Ag^+	*S. aureus*	ZOI: 11–12 mm	Chen S. et al., 2017
	Ag^+	*E. coli C. albicans*	N/A	Tosheva et al., 2017
Zeolite Y	Au NPs	*E. coli S. typhi*	Antibacterial efficiency = 90–95%	Lima et al., 2013
	(0.05 M)Ag^+/(0.025 M)Zn^{2+}	*E. coli B. subtilis C. albicans S. cerevisiae*	*E. coli*: MIC = 0.10 mg/mL *B. subtilis*: MIC = 0.10 mg/mL *C. albicans*: MIC = 0.30 mg/mL *S. cerevisiae*: MIC = 0.30 mg/mL	Ferreira et al., 2016
EMT	Ag^+/Ag NPs	*E. coli*	Sterilizing time < 6 min	Dong et al., 2014
	Ag^+	*S. mutans S. gordonii S. sanguinis*	The biofilm CFU count were reduced by two orders of magnitude at most	Li W. et al., 2020
ZSM-5	Gentamicin	*S. epidermidis*	Antibacterial efficiency = 94.32%	Guo et al., 2014
Zeolite β	Ag^+	*E. coli C. albicans*	*E. coli*: Sterilizing time < 7 min N/A	Tosheva et al., 2017
	Ag^+	*E. coli*	Sterilizing time = 1 h	Saint-Cricq et al., 2012
Zeolite A	Cu^{2+}/Cu_2O	*E. coli*	Cu^{2+}: antibacterial efficiency = 98.15% Cu_2O: antibacterial efficiency = 96.19%	Du et al., 2017
	TiO_2/ZnO	*E. coli S. aureus P. fluorescens L. monocytogenes*	*E. coli*: MIC = 1 ± 0.01 mg/mL; MBC = 2 ± 0.01 mg/mL *S. aureus*: MIC = 2 ± 0.01 mg/mL; MBC = 3 ± 0.01 mg/mL *P. fluorescens*: MIC = 1 ± 0.01 mg/mL; MBC = 2 ± 0.01 mg/mL *L. monocytogenes*: MIC = 2 ± 0.01 mg/mL; MBC = 3 ± 0.01 mg/mL	Azizi-Lalabadi et al., 2019
	Ag^+	*S. milleri E. faecalis S. aureus*	The bactericidal effect is dose dependent	Çınar et al., 2009
	Ag^+	*E. faecalis S. aureus C. albicans E. coli P. aeruginosa P. gingivalis A. israelii P. intermedia*	*E. faecalis*: ZOI: 7.06 ± 0.36 mm *S. aureus*: ZOI: 7.54 ± 0.36 mm *C. albican*: ZOI: 10.73 ± 0.54 mm *E. coli*: ZOI: 9.44 ± 0.18 mm *P. aeruginosa*: ZOI: 11.00 ± 0.34 mm *P. gingivalis*: ZOI: 8.84 ± 0.88 mm *A. israelii*: ZOI: 0.00 ± 0.00 mm *P. intermedia*: ZOI: 0.00 ± 0.00 mm	Odabaş et al., 2011

Abbreviations: Ag NPs, silver nanoparticles; Ag^+, silver ion; A. israelii, Actinomyces israelii; Au NPs, gold nanoparticles; B. subtilis, Bacillus subtilis; C. albicans, Candida albicans; CFU, colony forming unit; Cu^{2+}, copper ions; Cu_2O, cuprous oxide; E. coli, Escherichia coli; E. faecalis, Enterococcus faecalis; L. monocytogenes, Listeria monocytogenes; MBC, minimal bactericidal concentration; MIC, minimal inhibition concentration; P. aeruginosa, Pseudomonas aeruginosa; P. fluorescens, Pseudomonas fluorescens; P. intermedia, Prevotella intermedia; P. gingivalis, Porphyromonas gingivalis; S. aureus, Staphylococcus aureus; S. cerevisiae, Saccharomyces cerevisiae; S. epidermidis, Staphylococcus epidermidis; S. gordonii, Streptococcus gordonii; S. milleri, Streptococcus milleri; S. mutans, Streptococcus mutans; S. sanguinis, Streptococcus sanguinis; S. typhi, Salmonella typhi; TiO_2, cerium dioxide; Zn^{2+}, zinc ion; ZnO, zinc oxide; ZOI, zone of inhibition.

S. aureus, *Pseudomonas fluorescens*, *Listeria monocytogenes*, and *E. coli*. Although 4A zeolite *per se* has no antibacterial ability, it can be used as a carrier for ZnO and TiO_2 nanoparticles and control the release of them to improve the bactericidal ability. After ZnO and TiO_2 nanoparticles were released, they could produce metal ions and ROS together, and then destroyed the bacterial cells structure and inhibited their growth, thus playing a synergistic bactericidal effect (Azizi-Lalabadi et al., 2019). Moreover, another study reported that zeolite A loading with cuprous oxide possessed the antibacterial efficiency of more than 96% against *E. coli* (Du et al., 2017). The antibacterial mechanisms of zeolites with metal/metal oxides nanoparticles were attributed to the connection with microbial DNA and proteins, following by prevention of bacterial replication and inactivation of the bacterial electron transport chain, finally leading to the death of bacteria (Dizaj et al., 2014).

Besides, zeolites can also act as vehicles for other antimicrobial agents, such as gentamicin (GM). GM has broad spectrum antibacterial function, but high dose of which might lead to serious side-effects such as nephrotoxicity. Therefore, a study synthesized ZSM-5 zeolites loaded with GM with the hydrogen bond interaction between the functional group of GM and ZSM-5 zeolites, the purpose of which was to avoid the side effects of high doses of GM (Guo et al., 2014). For ZSM-5 zeolites containing GM, continuous release of drug minimized bacterial adhesion and prevented biofilm formation of *S. epidermidis*.

Despite of the promising perspective of zeolites in antibacterial application, some of the zeolites have certain biotoxicity to limit their adhibition in biomedical field. One study showed that the non-functionalized nanoscale zeolite L possessed higher cytotoxic with increasing concentrations, which might be due to the presence of a large number of surface acid sites on pure zeolites that catalyzed certain chemical reactions on cells (Li et al., 2013). Moreover, Kihara et al. (2011) also proved that the cytotoxicity of zeolites might be related to its surface morphology. Therefore, more studies are urgently needed on how to reduce the toxicity of zeolites so as to make safe utilization of zeolites in the field of drug delivery.

Covalent Organic Frameworks

Recently, COFs have become a hot topic because of their high load capacity and biocompatibility as the drug delivery vehicles, which can be connected to guest molecules by non-covalent action (Vyas et al., 2016). However, they are not yet widely used for antimicrobial delivery. Hence, COFs as antibacterial agent delivery carriers are a very promising research direction.

The Modified Nanomaterials Possessing Excellent Antibacterial Effects

Modifiability is one of the most remarkable properties of microporous nanomaterials, which can improve their stability, adjust their structural characters, and feature them with antimicrobial functions. Hence, modification is an effective way to broaden the application range of microporous nanomaterials and adapts them to biomedical applications, which can be achieved by doping metal ions, surface functionalization and incorporating with other organic or inorganic substances by functionalized skeleton or added substituents to form new antibacterial nanocomposites.

On the basis of a large number of reports, researchers attempted to understand the role of metal-doped microporous nanomaterials in antimicrobial applications. Studies have shown that when MOF materials were doped with a certain proportion of metal ions that were close to the metal ion radius in the structure of MOFs, the structure of could be kept stable. At the same time, MOF materials doped with other metal ions could be endowed with new functions (e.g., anti-inflammatory effect, osteogenesis) or enhanced certain abilities (e.g., antibacterial ability) to some extent (Horike et al., 2015; Schejn et al., 2015; Shen et al., 2019). Recently, zinc-based MOFs have received more attention due to the favorable bactericidal performance. Li P. et al. (2019) doped cerium ions into antibacterial ZIF-8 to endow with new anti-inflammatory properties. For the past few years, intensive studies tried to incorporate metal ions such as Co, Ag, Mn, into the vacant T-atom sites (T = Al) of the BEA zeolite (zeolite-β) (Dzwigaj and Che, 2006; Baran et al., 2016; Popovych et al., 2016). However, the corresponding antibacterial evaluations were not carried out.

As the therapeutic agents for infectious diseases, microporous nanomaterials could play their roles relying on surface modification with biocompatible parts. It has been reported that amino modified zeolite L can increase its ability of targeted binding to the surface of non-pathogenic *E. coli* (Popović et al., 2007). Butthis property had not been applied for therapeutic purposes. Whereafter, Strassert et al. (2009) synthesized a novel multifunctional nano-hybrid for targeting, labeling, and inactivating the antibiotic resistance bacteria (including *E. coli* and *Neisseria gonorrhoeae*). DXP [*N,N'*-bis(2,6-dimethylphenyl)perylene-3,4,9,10-tetracarbodiimide] was encapsulated in zeolite L, which was functionalized with photosensitizer phthalocyanine dihydroxide. Finally, multifunctional zeolites were coated with amino groups on their surface to promote adhesion to bacteria. The sterilized function mainly was attributed to the production of singlet oxygen on the surface of the photosensitizer under light. The result showed that the inactivation efficiency of *E. coli* and *N. gonorrhoeae* reached to 95% after 2 h of exposure to light radiation.

The latest study found a surprising improvement in the bactericidal activity of ZIF-8 functionalized with graphene oxide (GO) (Ahmad et al., 2020). When the ratio of GO to ZIF-8 was 1–100, ZIF-8/GO composites exhibited fivefolds of the antibacterial properties of the original ZIF-8 at the same concentration against *S. aureus* and *E. coli*. Moreover, a recent pioneer study attempted to introduce the GO to the silver-based MOF to form a new nanocomposite (GO-Ag-MOF) (Firouzjaei et al., 2018). The result showed that antibacterial effect of GO-Ag-MOF was more prominent than that of silver-based MOF on *B. subtilis* and *E. coli* (**Figure 3**). Furthermore, Hatamie et al. (2019) prepared a novel microporous hybrid material (GO/cobalt-based MOF) by modifying cobalt-based MOF with GO, and demonstrated that the antimicrobial activity of cobalt-based MOF was significantly enhanced by modified with GO. The result showed that the growth inhibition of the GO/cobalt-based MOF against *E. coli* and *S. aureus* could exceed

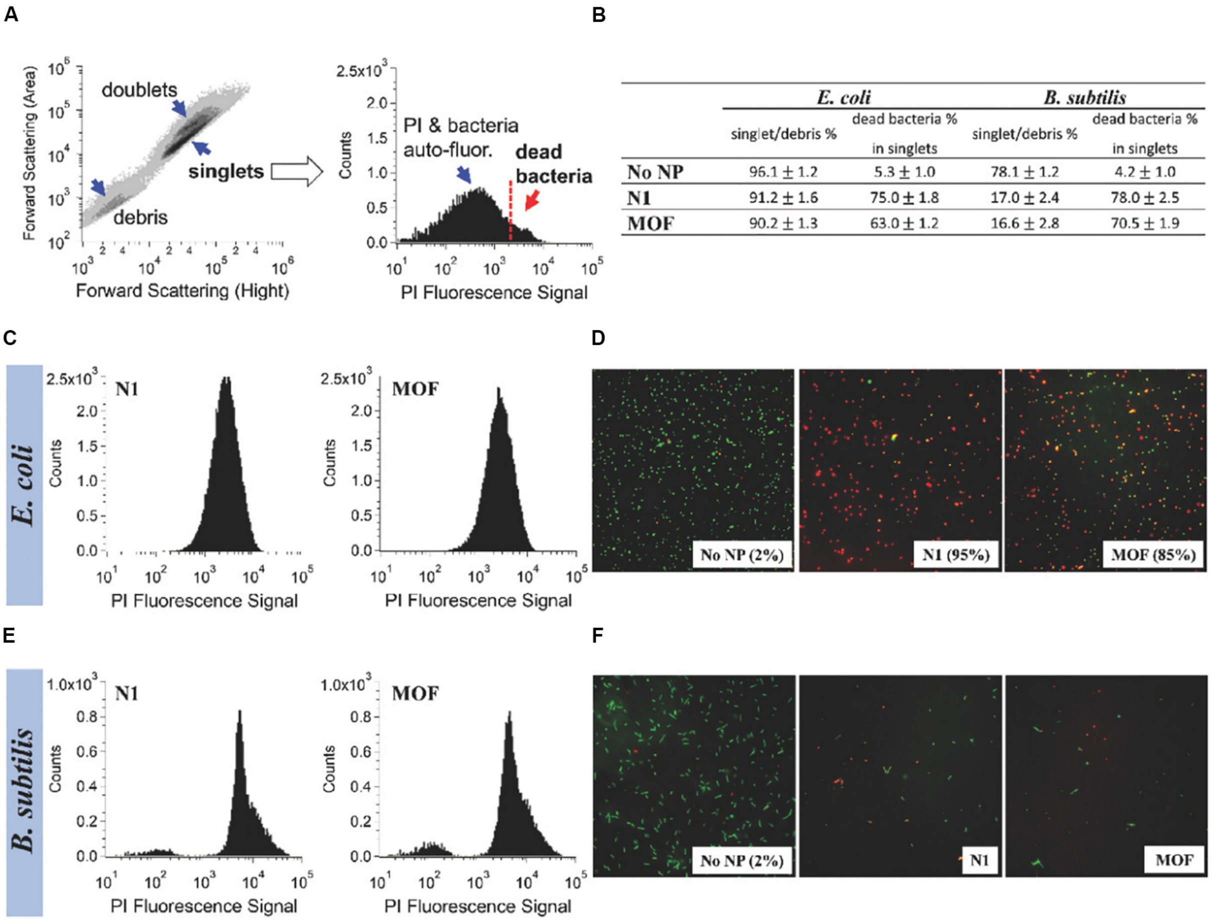

	E. coli singlet/debris %	E. coli dead bacteria % in singlets	B. subtilis singlet/debris %	B. subtilis dead bacteria % in singlets
No NP	96.1 ± 1.2	5.3 ± 1.0	78.1 ± 1.2	4.2 ± 1.0
N1	91.2 ± 1.6	75.0 ± 1.8	17.0 ± 2.4	78.0 ± 2.5
MOF	90.2 ± 1.3	63.0 ± 1.2	16.6 ± 2.8	70.5 ± 1.9

FIGURE 3 | Comparison of the antibacterial activity of Ag-MOF and N1. Notes: The information shown in **(B)**, **(C)**, and **(E)** was obtained by taking the contour map and the PI fluorescence histogram of the untreated *E. coli* sample **(A)** as example. The flow cytometry of *E. coli* and *B. subtilis* after about 3 h of treatment with 100 μg/mL of complex and MOF were shown in **(C)** and **(E)**. **(D,F)** The fluorescence images of the blank control group and the experimental groups. [Reprinted with permission from Firouzjaei et al., 2018; Copyright (2018) Wiley-Blackwell.] Abbreviations: Ag-MOF, silver-based metal organic framework; *B. subtilis*, *Bacillus subtilis*; *E. coli*, *Escherichia coli*; N1, the nanocomposite consisting of Ag-MOF and graphene oxide; PI, propidium iodide.

99% at the concentration of 100 μg/mL. The major antibacterial mechanisms of the nanocomposites synthesized from MOFs and GO are summarized as follows: (1) interactions between metal ions released by MOFs and bacterial cells are described in Section "Nanomaterials With Inherent Antibacterial Activity," (2) the sharp edges of GO nanosheets scratch the cell walls of bacteria and then initiate to destroy their membranes (Akhavan and Ghaderi, 2010), and (3) GO produces superoxide anions that damage bacterial cell membranes (Kotchey et al., 2011). Moreover, using photocatalyst to synergistically fight bacteria to antibacterial application is a novel and important approach. Li J. et al. (2020) prepared a novel bactericidal nanocomposite by using (3-aminopropyl) triethoxysilane mounted on the surface of ZIF-8 as an intermediate junction to realize the connection between ZIF-8 and the photosensitizer chloroethane. It has been proved that ZIF-8 nanomaterial conjugated with chloroethane had synergistically antibacterial effect on *S. aureus* and methicillin-resistant *S. aureus* upon light triggering. The sterilization mechanisms include (1) the production of ROS stimulated by light, (2) zinc ions released out of ZIF-8 framework as a toxin to inhibit bacterial growth, and (3) the fact that nanocomposites with a rough surface could greatly influence the interactions between bacterial cells and thus play a bactericidal role. Besides, MOFs also had the ability to combine with other materials, such as activated carbon (Azad et al., 2016), polyvinylidene fluoride/perfluorooctyltriethoxysilane (Miao et al., 2018), sodium alginate/niflumic acid (Luo et al., 2020), and humic acid (Liu et al., 2020), to form hybrids to improve their antibacterial performance. All of them have greatly expanded the application potential and efficiency of MOF materials as antimicrobial agents. These hybrids have showed excellent bactericidal effect on common wound infection pathogenic bacteria *S. aureus* or *E. coli*, which can be used for the treatment of wound infection. Especially in the study of the Miao et al. (2018) the compound of polyvinylidene fluoride/perfluorooctyltriethoxysilane and ZIF-8 also possessed a good self-cleaning function, to some extent inhibiting bacterial adhesion.

With respect to the modification of zeolites, Nosrati et al. (2015) immobilized TiO_2 nanoparticles onto the surface of Ag-exchanged-zeolite-A to form a novel hybrid with enhanced antibacterial and photocatalytic properties. This nanoscale hybrid was used as additive in the matrix of polyacrylic latex to construct a promising nanocomposite coating, which exhibited outstanding advantage in the aspects of anti-microorganism, self-cleaning, and stability in water (Nosrati et al., 2015). The authors applied the novel coating to the sterile glass and placed it in a bacterial plate, and then found that the Gram-positive bacteria (*S. aureus*, *L. monocytogenes*, *Salmonella thyphimurium*) had no growth zone around it, while the Gram-negative bacteria (*E. coli*, *Bacillus anthraci*) had the opposite result. Recently, a new study hinted that NaA zeolites exchanged with silver and copper ions could combine with epoxy to form the high flux thin-film zeolite AgA/epoxy and zeolite CuA/epoxy nanocomposite membranes (Khademi et al., 2020). According to the inhibition experiment, zeolite AgA/epoxy nanocomposite membrane had better antibacterial capacity against *E. coli* and *S. aureus* compared with zeolite CuA/epoxy nanocomposite membrane. Similar results have been published by Ruparelia et al. (2008) where weaker biocidal effect of Cu nanoparticles in comparison with Ag nanoparticles was found. The antibacterial difference was due to the higher sensitivity of *E. coli and S. aureus* to Ag nanoparticles compared with the same concentration of Cu nanoparticles (Ruparelia et al., 2008).

In addition to aforementioned MOFs and zeolites, there are also increasing researches on antibacterial compounds based on COFs. Ionic covalent organic nanosheets (iCONs) are belonging to a kind of COFs with the morphology of nanofilm. By using three self-exfoliate guanidinium halide based porous iCONs ($TpTG_{Cl}$, $TpTG_{Br}$, and $TpTG_{I}$) and polysulfone, Mitra et al. (2016) produced iCONs@polysulfone mixed matrix membrane with excellent antimicrobial performance on porous non-woven support fabrics. It was reported that the interaction of positively charged guanidine units on the surface of the iCONs@polysulfone mixed matrix membrane with negatively charged phospholipid bilayer of Gram-positive (*S. aureus*) and Gram-negative (*E. coli*) bacteria was the main cause of sterilization. As shown in **Figure 4**, the iCONs@polysulfone mixed matrix membrane had destroyed the membranes of *E. coli* and *S. aureus*, resulting in bacterial cell death (Mitra et al., 2016).

ANTIBACTERIAL MICROPOROUS NANOMATERIALS AGAINST ORAL DISEASES

This section describes a variety of oral infections and related pathogens. Moreover, it also reviews the frontier researches on the application of microporous nanomaterials in oral infectious diseases and the progress in the treatment of related pathogens.

Dental Caries

Dental caries is one of the most common diseases in the world (Cagetti et al., 2013). In a study in 2015 about Global Burden of Disease, the age-standardized prevalence rates of untreated caries in deciduous teeth and permanent teeth were estimated up to 7.8 and 34.1%, respectively (Kassebaum et al., 2017). Untreated caries in permanent teeth affect 2.5 billion people worldwide (Kassebaum et al., 2017) and accounts for 12% of global productivity losses due to dental diseases (Righolt et al., 2018). Dental caries is regarded to be caused by bacterial biofilms on the surfaces of the teeth, the formation of which is regulated by a complex interaction between pathogenic bacteria and their hosts, including teeth and saliva (Selwitz et al., 2007). The main pathogenic bacteria of dental caries, represented by *Streptococcus mutans*, tend to adhere to the teeth surfaces and produce organic acids to dissolve the mineralized tissues of the teeth, thus leading to the development of dental caries from the teeth surfaces to the insides (Rainey et al., 2018). The conventional treatment for dental caries is to remove the infectious tooth tissue and to restore with filling material such as polymeric resin (BaniHani et al., 2017). However, the traditional approach is apt to lead to the microleakage of the interface of dental tissue and restorations, which was consequent in the occurrence of secondary caries (Jokstad, 2016).

Secondary caries was reported as one of the main causes of restoration failures (Nedeljkovic et al., 2015). The formation of the biofilm between restoration or backfill and dental tissue is considered as a risk factor for secondary caries (Jokstad, 2016). It is generally believed that the pathogenic biofilm of secondary caries is similar to that of primary caries, mainly composed of bacteria represented by *S. mutans* (González-Cabezas et al., 1999). It has been reported that silver-containing EMT zeolite can be used to prevent the occurrence of secondary caries (Li W. et al., 2020). EMT type zeolite crystal with ultra-small nanoscale size is an ideal carrier for efficient and high volume silver ion exchange. Previous study showed that EMT zeolite containing Ag had good antibacterial activity against *E. coli* (Dong et al., 2014). Recently, based on the previous study, Li W. et al. (2020) added large amounts of nanoscale Ag-EMT zeolites into dental adhesive to prevent the development of secondary dental caries, as well as to avoid the color change caused by direct addition of silver ions. It could be further concluded that the antibacterial efficient was enhanced with the increasing exchange time of Ag^+ (**Figure 5**). The sample with the longest exchange time reduced CFU counts of the biofilms of *S. mutans*, *Streptococcus gordonii*, and *Streptococcus sanguinis* bacteria by nearly two orders of magnitude.

In the research by Cao et al. (2020), three types of MOFs, $[AgL]_n \cdot nH_2O$ (p-MOF), MOF-5, and ZIF-8, were synthesized to fight *S. mutans*, *Fusobacterium nucleatum*, and *Porphyromonas gingivalis* bacteria, which possessed the slow-release sterilization abilities. The result indicated that MOFs were promising candidates in the field of the treatment of dental caries and periodontitis. Massoudinejad et al. (2018) also discovered that the UIO-66 could be applied to efficiently load fluoride. It is well known that fluoride ion can effectively prevent the occurrence of dental caries. Hence, it is a promising research direction to use MOFs to load fluoride to prevent dental caries.

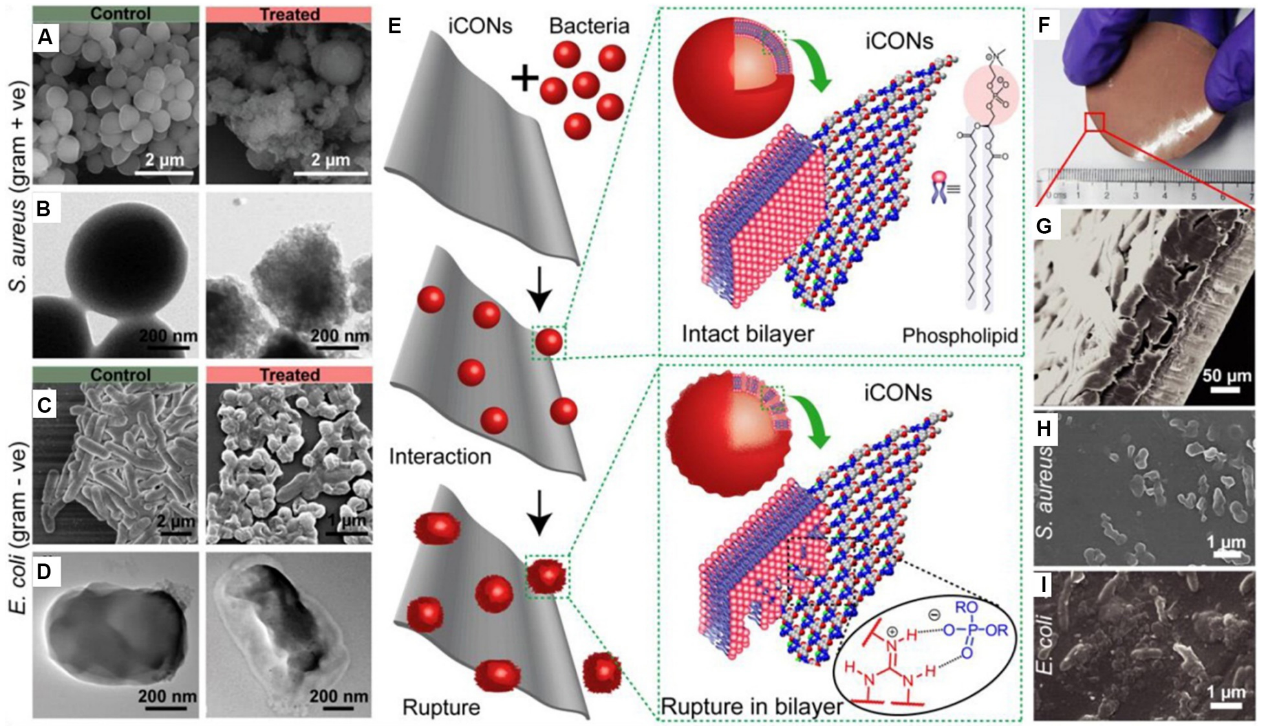

FIGURE 4 | The antibacterial activity of iCONs@PSF mixed matrix membrane. Notes: **(A,C)** SEM images and **(B,D)** TEM images of control and $TpTG_{Cl}$ treated *S. aureus* and *E. coli*. **(E)** The schematic illustration of the interaction between the bacteria and the iCONs. **(F)** Digital image and **(G)** SEM image of $TpTG_{Cl}$@PSF mixed matrix membrane. Growth inhibition of **(H)** *S. aureus* and **(I)** *E. coli* on the surface of $TpTG_{Cl}$@PSF mixed matrix membrane. [Reprinted with permission from Mitra et al., 2016; Copyright (2016) American Chemical Society.] Abbreviations: *E. coli*, *Escherichia coli*; iCONs, ionic covalent organic nanosheets; iCONs@PSF, the composite of ionic covalent organic nanosheets and polysulfone; SEM, scanning electron microscopy; *S. aureus*, *Staphylococcus aureus*; TEM, transmission electron microscopy; $TpTG_{Cl}$, self-exfoliate guanidinium halide-based ionic covalent organic nanosheets; $TpTG_{Cl}$@PSF, the composite of $TpTG_{Cl}$ and polysulfone.

Periodontitis and Peri-Implantitis

Periodontitis becomes a major global health care problem, with increasing costs to individuals and society (Tonetti et al., 2017), since it is regarded as one of the leading causes of tooth loss and ranks as the sixth most common disease in the world (Papapanou, 1996; Kassebaum et al., 2017). Periodontitis is caused by pathogenic microorganisms in biofilms or plaque that eventually destroy the periodontal tissue that supports the teeth (Pihlstrom et al., 2005). It is closely related to a defined microbial composition (the "red-complex" bacteria: *P. gingivalis*, *Tannerella forsythia*, and *Treponema denticola*) found on the surface and root of teeth (Darveau, 2010). They have significant virulence and can interfere with host's defense ability through a variety of mechanisms, thus causing the destruction of periodontal tissues. Mechanical debridement is often used in conjunction with systemic or topical antibiotic therapy to treat periodontitis (Herrera et al., 2012). However, long-term use of antibiotics will lead to the rampant growth of drug-resistant strains, reducing the effectiveness of periodontitis treatment (Wyszogrodzka et al., 2016). Therefore, the development of microporous frame structure is particularly important in the treatment of periodontitis.

Kawahara et al. (2000) proposed that under the anaerobic conditions, silver-zeolite had prominent antibacterial effect on major periodontal pathogens such as *P. gingivalis*, *Prevotella intermedia*, and *Actinobacillus actinomycetemcomitans*. Therefore, silver zeolite could be applied to the anaerobic area of the mouth (periodontal pocket), and acts as an effective drug for periodontitis treatment. In addition, a recent study described ZIF-8 nanoparticles containing different proportions of cerium (Ce) for treating periodontitis (Li X. et al., 2019). The result showed that as the proportions of Ce increased, the antibacterial effect of nanoparticles slightly decreased against *P. gingivalis* and *F. nucleatum*. Even that, the antibacterial efficacy of 10% Ce doped ZIF-8 against these two pathogens was still beyond two orders of magnitude. Moreover, the addition of Ce could provide ZIF-8 nanoparticles with excellent anti-inflammatory properties. The anti-inflammatory effect is mainly achieved by the presence of a large number of oxygen vacancies in Ce-based nanomaterials and the reversible conversion between $Ce^{(III)}$ and $Ce^{(IV)}$ ions to eliminate excess ROS (Huang et al., 2018).

Peri-implantitis is an important cause of dental implant failure. The prevalence of peri—implantitis on implant level ranged from 1.1 to 85.0% and the incidence from 0.4% within 3 years, to 43.9% within 5 years, respectively (Dreyer et al., 2018). Similar to periodontitis, dental plaque was considered as the initiator of peri-implantitis. Treatment of mild and moderate

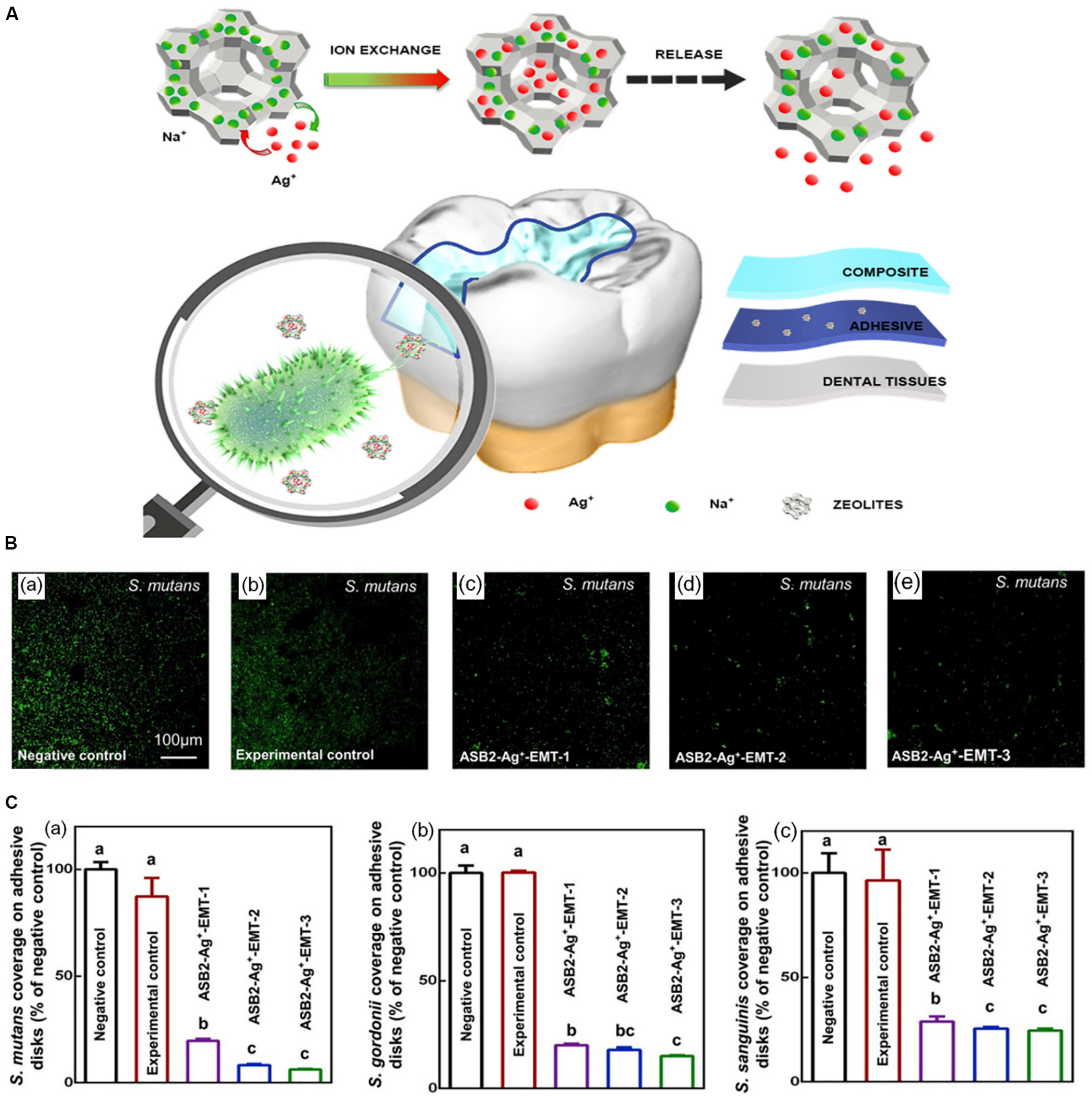

FIGURE 5 | The schematic diagram of the synthesis and antimicrobial activity of ASB2 containing 5% Ag^+-EMT. Notes: **(A)** The diagram of Ag^+-EMT and their antibacteria performance in dental restoration. **(B)** Fluorescent images of *S. mutans* in the groups of **(a)** negative control (pure ASB2), **(b)** experimental control (ASB2 + 5% EMT zeolites), and **(c–e)** ASB2-Ag + -EMT (ASB2 + 5% EMT zeolites with silver ion exchange for 10, 20, and 40 min). **(C)** The histogram of early bacterial coverage for 4 h of **(a)** *S. mutans*, **(b)** *S. gordonii*, and **(c)** *S. sanguinis*. Different letters indicate that the difference between them is statistically significant. [Reprinted with permission from Li W. et al., 2020. Copyright (2020) Elsevier.] Abbreviations: Ag^+-EMT, silver-exchanged EMT zeolites; ASB2, the dental adhesive; *S. gordonii*, *Streptococcus gordonii*; *S. mutans*, *Streptococcus mutans*; *S. sanguinis*, *Streptococcus sanguinis*.

forms of peri-implantitis is similar to that of periodontitis. The therapeutic methods included a variety of manual ablation, laser-supported systems, and photodynamic therapies, which can be extended with topical or systemic antibiotics (Smeets et al., 2014). However, severe peri—implantitis often requires surgical treatment (Smeets et al., 2014). As the treatment method for peri—implantitis, the microporous frameworks can not only reduce the use of antibiotics but also prevent the pain of patients caused by surgical treatment.

A paper published by Wuttke et al. (2017) assessed the safety of different MOFs [MIL-100(Fe), MIL-101(Cr), and Zr-fum MOF of different sizes] for dental applications, for instance, multifunctional surface coatings of implants (Wuttke et al., 2017). Notably, primary gingival fibroblasts had no significant toxic response to all MOF nanoparticles tested. In addition, there was no significant change in the morphology and metabolic activity of fibroblasts, suggesting that the MOF nanoparticles tested had good biocompatibility (Wuttke et al., 2017). The above experimental results demonstrated the feasibility of using MOF nanoparticles as dental implant coatings because of their excellent biosecurity and biocompatibility to human gingival fibroblasts. Recently, Chen J. et al. (2017) made the first attempt to prepare ZIF-8 nanofilm on the surface of titanium. It was found that the number of *S. mutans* was significantly reduced on the titanium surface with ZIF-8 nanofilm compared with the control group. Interestingly, in addition to the favorable antibacterial properties, ZIF-8 nanofilm could also play an osteogenic role by up-regulating the genes for alkaline phosphatase and the key osteogenic transcription factor Runx2 through the release of zinc ions after degradation (Yang et al., 2012; Yuan et al., 2016).

Endodontic Infections

In case of dental caries, when the enamel or cementum of the tooth is destroyed by bacteria, the bacteria can invade pulp through the dentin tubules and progress into infections of dental pulp, leading to endodontic infections. Endodontic infections are a common type of oral diseases. In the Brazilian adult population, the majority of endodontically treated teeth were found in 46–60 years of age (47.6%), and the prevalence increased with age (Hollanda et al., 2008). The most common biological cause of endodontic disease is the root canal biofilm, which is significantly formed by *E. faecalis* and other microorganisms (Mohammadi et al., 2014). Hence, the most important purpose for effective treatment of endodontic infections is to eliminate suspected pathogens from the root canal (Siqueira, 2002). Root canal therapy is the usual clinical treatment strategy for endodontic infections (Li and Wang, 2015). However, the failures of root canal therapy are often caused by the incomplete removal of infectious pathogens in the root canal (Siqueira and Rôças, 2004). In order to increase the cure rate of endodontic infections, the application of microporous frameworks was studied in root canal treatment including the endodontic cavity flushing and endodontic filling (Odabaş et al., 2011; Ghivari et al., 2017).

One study showed that the antibacterial ability of the root canal filling material glass ionomer cement was significantly enhanced due to the addition of silver-zeolite (Çınar et al., 2009). The experiment suggested that the inhibition diameters of *Streptococcus milleri*, *S. aureus*, and *E. faecalis* by glass ionomer cement with 2 and 0.2% mass fraction silver-zeolite, was nearly one to two times greater than that by glass ionomer cement without any additives. After that, Odabaş et al. (2011) attempted to incorporate silver-zeolite to the mineral trioxide aggregate as a root-end filling material with high antimicrobial activity in order to achieve a good effect of endodontic therapy. It was proved that compared with pure mineral trioxide aggregate, mineral trioxide aggregate with 0.2 and 2% silver-zeolite had increased inhibition of bacteria, especially *S. aureus* and *E. faecalis*, and also remarkably strengthened the sterilization effects of fungi (Odabaş et al., 2011). Moreover, Ghivari et al. (2017) first investigated the antibacterial effects of silver-zeolite as a root canal irrigant. The result showed that the silver-zeolite (2%) showed the lowest antibacterial activity against *E. faecalis*, *S. aureus*, and *Candida albicans* biofilm, compared with the commonly used root canal irrigants, sodium hypochlorite (5.25%), chlorhexidine (2%), and otinidine hydrochloride (0.10%). It was demonstrated that silver-zeolite needed to come into contact with bacterial cells to perform its bactericidal action (Matsumura et al., 2003). The reason for the decreased antibacterial activity of silver-zeolite may be due to the presence of biofilm reducing the interaction between silver-zeolite and bacteria.

In addition, the MIL family of MOF nanomaterials is crafted from trivalent metal centers and carboxylic acid bridging ligands, which has attracted much attention due to its considerable loading capacity (Huxford et al., 2010). On basis of this, Golmohamadpour et al. (2018) had synthesized three types of MOF nanomaterials including Al-MIL-101-NH_2, Fe-MIL-88B-NH_2, and Fe-MIL-101-NH_2 loaded with indocyanine green, which showed obvious antibacterial activity on *E. faecalis*. Under the laser irradiation at wavelength of 810 nm, MOF nanomaterials loaded with indocyanine green significantly reduced the survival rate of *E. faecalis* compared with pure MOF nanomaterials. The enhancement of antibacterial and anti-biofilm capability of indocyanine green loaded MOF nanomaterials was due to the fact that indocyanine green could enhance the generation capacity of ROS after laser irradiation (Omar et al., 2008).

Oral Mucositis

Denture stomatitis is a common oral mucous membrane infection. The prevalence of denture stomatitis in the elderly population has been concluded to be between 15 and 71% (Gendreau and Loewy, 2011). It is generally believed to be caused by a number of factors (such as lack of clean dentures, dietary factors, continued use of dentures without removal, etc.) (Schneid, 1992). One of the causes of denture stomatitis is the presence of biofilm on the denture surface. This biofilm matrix created a physical barrier for oral microbes like *C. albicans*, which were thought to be the main pathogen in the pathogenesis of denture stomatitis, to protect them from the outside world (Ramage et al., 2004). Broad-spectrum antifungal agents are commonly used to treat denture stomatitis (Mima et al., 2012). Although the drugs can be used topically, however, they are difficult to be effective because of the large amount of saliva flowing and the protection of biofilm matrix. Therefore, Casemiro et al. (2008) added zeolites exchanged with silver and zinc ions at varying percentages into the denture base material acrylic resin to increase the antibacterial activity against *C. albicans*. As the percentage of silver-zinc zeolite increased from 2.5 to 10%, the diameters of the inhibitory zones for *C. albicans* and *S. mutans* increased linearly. Moreover, Nikawa et al. (1997) added silver zeolite to the tissue conditioner (soft lining material) for the first time, which could effectively control dental plaque and inhibit the growth of *C. albicans*. The inhibitory effect of *C. albicans* was studied by monitoring the change of pH in the growth medium. It was concluded that the soft lining materials had more obvious bacteriostatic efficacy after the addition of silver zeolites. In a previous study, Nikawa et al. (1993) also proposed that the presence of saliva promoted the colonization of multiple layers of *C. albicans* and the formation of biofilms, thereby reducing the antibacterial effect of soft lining materials on *C. albicans*. However, the effect of saliva on antibacterial efficacy of silver-zeolite doped soft lining materials had not been systematically addressed in this study (Nikawa et al., 1993). Subsequently, Abe et al. (2004) further studied the effect of saliva on the antibacterial efficiency of silver-zeolite doped tissue conditioner. It could be concluded that, after 28 days of treatment with water or saliva, there was no significant difference in the bactericidal efficacy of silver-zeolite doped tissue conditioner against *C. albicans*. Currently, intensive studies have been made on the resistance of MOFs to *C. albicans* (Wojciechowska et al., 2015; Emam et al., 2018). However, there have been no reports on the application of MOFs in the treatment of denture stomatitis.

In addition, oral ulcerative disease is one of the most common complaints of oral mucosa (Leão et al., 2007). The pathogenesis is complex, with local and systemic conditions as well as genetic, immune, and microbial factors that may play a role. The combination of Chinese and western medicine is often used to treat oral ulcerative disease. But it is difficult to achieve the desired results. It is still difficult to achieve a favorable and satisfied effect on oral mucosal ulcer by current available treatments. Salehi et al. (2017) prepared a starch-based nanocomposite hydrogel scaffold enhanced by zeolite nanoparticles. In addition, herbs (chamomile extract) were added into the matrix to promote wound healing (Salehi et al., 2017). Animal experiments and clinical trials both showed that the combination of starch/zeolite nanocomposites and extracts could preferably improve wound healing, which washighly expected to be applied to the treatment of intractable ulcers in the mouth.

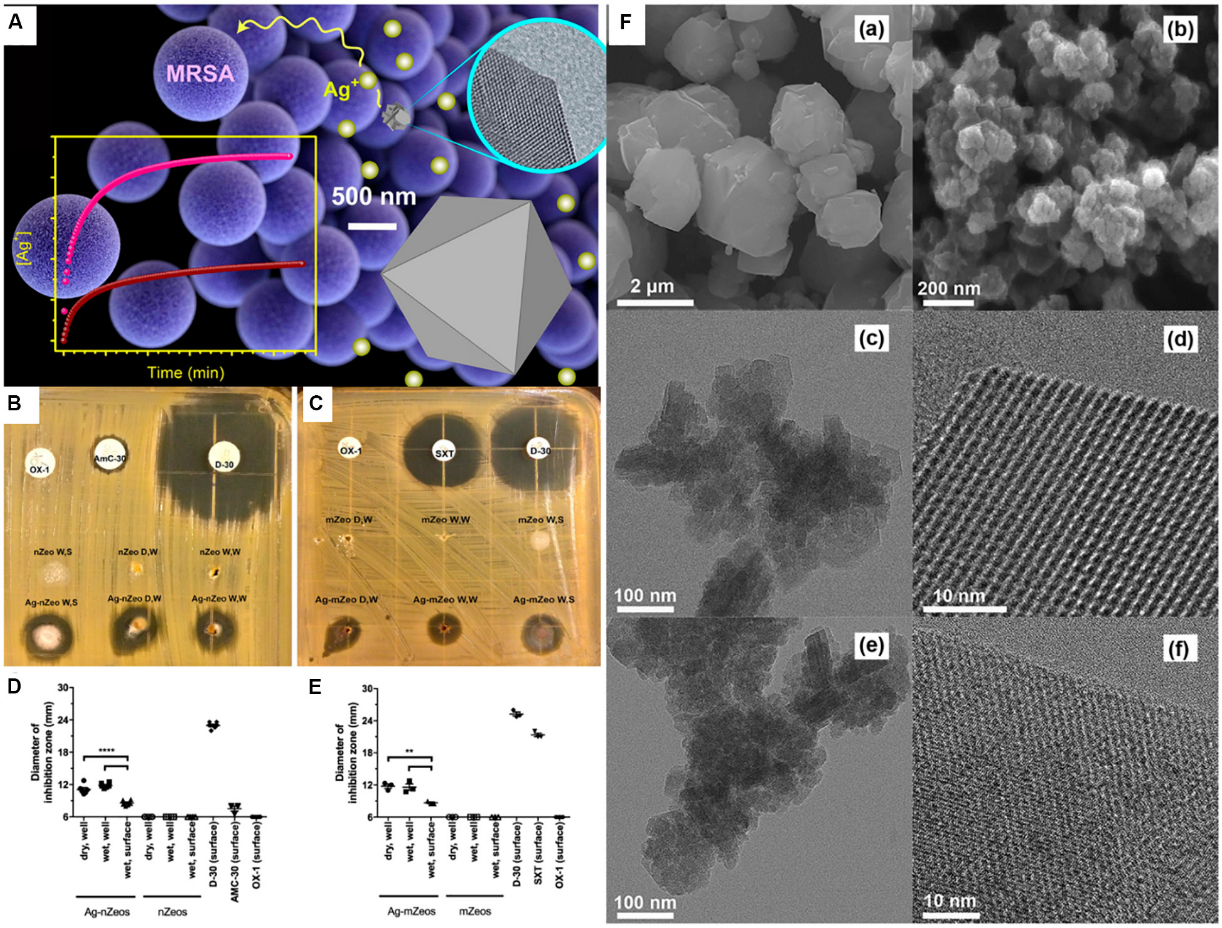

FIGURE 6 | Comparison of Ag-nZeo and Ag-mZeo on growth inhibition of MRSA. Notes: **(A)** Schematic diagram of the bactericidal action of mZeo and nZeo on MRSA and their silver ion release rate. **(B)** Ag-nZeo and **(C)** Ag-mZeo ion diffusion and MRSA inhibition demonstrated by agar diffusion test. The bacteriostatic diameter of **(D)** Ag-nZeo and nZeo or **(E)** Ag-mZeo and mZeo compared with AmC-30, D-30, OX-1, and SXT ($^{**}P < 0.01$; $^{****}P < 0.0001$). **(F)** SEM images of **(a)** mZeo and **(b)** nZeo; TEM and HRTEM images of **(c,e)** Ag–mZeo and **(d,f)** Ag–nZeo. [Reprinted with permission from Chen S. et al., 2017; Copyright (2017) American Chemical Society.] Abbreviations: Ag–mZeo, Ag-ion-exchanged microsized zeolites; Ag–nZeo, Ag-ion-exchanged nanostructured zeolites; AmC-30, amoxicillin with clavulanic acid; D-30, doxycycline; HRTEM, high resolution transmission electron microscopy; MRSA, methicillin-resistant *Staphylococcus aureus*; mZeo, microsized zeolites; nZeo, nanostructured zeolites; OX-1, oxacillin; SEM, scanning electron microscopy; SXT, trimethoprim/sulfamethoxazole; TEM, transmission electron microscopy.

Oral Infections

In addition to the treatment of the above diseases, microporous nanomaterials can also be used for the treatment of oral infections such as jaws osteomyelitis and oral multi-space infection. Conventional treatment for oral infections is the use of antibiotics (Levi and Eusterman, 2011). However, due to the emergence of drug-resistant strains, the satisfied therapeutic effect is difficult to achieve. Therefore, it is necessary to study novel antibacterial agents for oral infection treatments.

Jaws osteomyelitis is a devastating infection of bone and bone marrow, of which Gram-positive *Staphylococcus* is one of the most common pathogens (Kavanagh et al., 2018). In recent study, ZIF-8 nanocrystals loaded with vancomycin were embedded into chitosan scaffolds to obtain three-dimensional scaffolds with antibacterial properties and excellent osteogenesis, which could be used to treat severe bone tissue infections such as osteomyelitis (Karakeçili et al., 2019). The result showed that under the simulated inflammation acidic condition (pH = 5.4), the chitosan scaffold containing 5% vancomycin loaded ZIF-8 crystals had the superior antibacterial performance against *S. aureus*. The reason for its excellent antibacterial efficacy was to promote the degradation of ZIF-8 and the release of vancomycin under acidic condition. Furthermore, it could simultaneously promote the bone regeneration to restore the surrounding bone damage.

Similar to jaws osteomyelitis, *S. aureus* is also the prevalent pathogenic bacteria of oral multi-space infection. Methicillin-resistant *S. aureus* is an increasingly dangerous and antibiotic-resistant bacterium, which is able to lead to oral soft-tissue infections, such as cellulitis and multigap infections. Chen S. et al. (2017) quantified the inhibition and bactericidal activity of the silver-exchange nanostructured zeolite X on methicillin-resistant *S. aureus*, and compared it with the micro-sized zeolite. It was found that the antimicrobial diameter of the nanostructured zeolite was larger than that of the micro-sized zeolite, suggesting that nanostructured zeolite had superior antibacterial effect (**Figure 6**). The difference in the antibacterial effect between different sized zeolites was probably due to the fact that nanoscale silver-exchange zeolite X could release more silver ions. Due to the short diffusion lengths and higher external surface area of the nanostructured zeolites, compared with the traditional micro-scale zeolites, they have higher ion release efficiency (Izumi and Nakazawa, 1986).

CONCLUSION AND PERSPECTIVE

This article reviewed recent research progress of antibacterial microporous nanomaterials with respect to oral diseases. With the development of drug resistance, it is necessary to find a drug delivery system compatible with a variety of antimicrobial agents and new antimicrobial agents. Novel microporous nanomaterials and their composites offer a valuable opportunity and are compatible with a wide range of antibiotics for oral infectious diseases. In this paper, three types of microporous frameworks were summarized, including zeolites, metal organic frameworks, covalent organic frameworks, particularly on their potential of antibacterial effects via inherent properties, drug delivery, and modification. Importantly, their application in the treatment of oral infection diseases was detailedly reviewed. However, it is considered that most of these microporous frameworks and their nanocomposites are uncommercialized and their acquisition procedures are complex, which limits their wide range of clinical applications. Therefore, the faster and more efficient production of these nanomaterials remains to be further investigated. In addition, more and more studies should be focus on the biocompatibility improvement and evaluate the therapeutic efficiency against oral diseases in animal studies and clinical trials.

AUTHOR CONTRIBUTIONS

YaW and WX wrote the manuscript. XR and YuW participated and helped with the final revision of the manuscript. LW and BD designed and critically revised the review manuscript. All the authors read and approved the final version of the manuscript prior to submission.

FUNDING

This study was supported by the Natural Science Foundation of China NSFC 81400487 (LW); China Postdoctoral Science Foundation 2015M581405 and 2017T100213 (LW); General program of Natural Science Foundation of Jilin Province 20200201356JC (LW) and 20200201317JC (CL); and seed grant from Jilin University School of Dentistry (LW).

REFERENCES

Abbasi, A. R., Akhbari, K., and Morsali, A. (2012). Dense coating of surface mounted CuBTC metal–organic framework nanostructures on silk fibers, prepared by layer-by-layer method under ultrasound irradiation with antibacterial activity. *Ultrason. Sonochem.* 19, 846–852. doi: 10.1016/j.ultsonch.2011.11.016

Abd El Salam, H. M., Nassar, H. N., Khidr, A. S. A., and Zaki, T. (2018). Antimicrobial activities of green synthesized Ag nanoparticles @ Ni-MOF nanosheets. *J. Inorg. Organomet. Polym.* 28, 2791–2798. doi: 10.1007/s10904-018-0950-4

Abdullahi, T., Harun, Z., and Othman, M. H. D. (2017). A review on sustainable synthesis of zeolite from kaolinite resources via hydrothermal process. *Adv. Powder Technol.* 28, 1827–1840. doi: 10.1016/j.apt.2017.04.028

Abe, Y., Ishii, M., Takeuchi, M., Ueshige, M., Tanaka, S., and Akagawa, Y. (2004). Effect of saliva on an antimicrobial tissue conditioner containing silver–zeolite. *J. Oral Rehabil.* 31, 568–573. doi: 10.1111/j.1365-2842.2004.01267.x

Aguado, S., Quirós, J., Canivet, J., Farrusseng, D., Boltes, K., and Rosal, R. (2014). Antimicrobial activity of cobalt imidazolate metal–organic frameworks. *Chemosphere* 113, 188–192. doi: 10.1016/j.chemosphere.2014.05.029

Ahmad, N., Md Nordin, N. A. H., Jaafar, J., Nik Malek, N. A. N., Ismail, A. F., Yahya, M. N. F., et al. (2020). Eco-friendly method for synthesis of zeolitic imidazolate framework 8 decorated graphene oxide for antibacterial activity enhancement. *Particuology* 49, 24–32. doi: 10.1016/j.partic.2019.04.007

Akhavan, O., and Ghaderi, E. (2010). Toxicity of graphene and graphene oxide nanowalls against bacteria. *ACS Nano* 4, 5731–5736. doi: 10.1021/nn101390x

Amorim, R., Vilaça, N. L., Martinho, O., Reis, R. M., Sardo, M., Rocha, J., et al. (2012). Zeolite structures loading with an anticancer compound as drug delivery systems. *J. Phys. Chem. C* 116, 25642–25650. doi: 10.1021/jp3093868

Aryanejad, S., Bagherzade, G., and Moudi, M. (2020). Green synthesis and characterization of novel Mn-MOFs with catalytic and antibacterial potentials. *New J. Chem.* 44, 1508–1516. doi: 10.1039/c9nj04977k

Au-Duong, A.-N., and Lee, C.-K. (2017). Iodine-loaded metal organic framework as growth-triggered antimicrobial agent. *Mater. Sci. Eng. C Mater. Biol. Appl.* 76, 477–482. doi: 10.1016/j.msec.2017.03.114

Azad, F. N., Ghaedi, M., Dashtian, K., Hajati, S., and Pezeshkpour, V. (2016). Ultrasonically assisted hydrothermal synthesis of activated carbon–HKUST-1-MOF hybrid for efficient simultaneous ultrasound-assisted removal of ternary organic dyes and antibacterial investigation: taguchi optimization. *Ultrason. Sonochem.* 31, 383–393. doi: 10.1016/j.ultsonch.2016.01.024

Azizi-Lalabadi, M., Ehsani, A., Divband, B., and Alizadeh-Sani, M. (2019). Antimicrobial activity of titanium dioxide and zinc oxide nanoparticles supported in 4A zeolite and evaluation the morphological characteristic. *Sci. Rep.* 9:17439. doi: 10.1038/s41598-019-54025-0

BaniHani, A., Deery, C., Toumba, J., Munyombwe, T., and Duggal, M. (2017). The impact of dental caries and its treatment by conventional or biological approaches on the oral health-related quality of life of children and carers. *Int. J. Paediatr. Dent.* 28, 266–276. doi: 10.1111/ipd.12350

Baran, R., Valentin, L., and Dzwigaj, S. (2016). Incorporation of Mn into the vacant T-atom sites of a BEA zeolite as isolated, mononuclear Mn: FTIR, XPS, EPR and DR UV-Vis studies. *Phys. Chem. Chem. Phys.* 18, 12050–12057. doi: 10.1039/c6cp01713d

Beale, A. M., Gao, F., Lezcano-Gonzalez, I., Peden, C. H., and Szanyi, J. (2015). Recent advances in automotive catalysis for NOx emission control by small-pore microporous materials. *Chem. Soc. Rev.* 44, 7371–7405. doi: 10.1039/c5cs00108k

Berchel, M., Le Gall, T., Denis, C., Le Hir, S., Quentel, F., Elléouet, C., et al. (2011). A silver-based metal–organic framework material as a 'reservoir'of bactericidal metal ions. *New J. Chem.* 35, 1000–1003. doi: 10.1039/c1nj20202b

Bhanja, P., Mishra, S., Manna, K., Mallick, A., Das Saha, K., and Bhaumik, A. (2017). Covalent organic framework material bearing phloroglucinol building units as a potent anticancer agent. *ACS Appl. Mater. Interfaces* 9, 31411–31423. doi: 10.1021/acsami.7b07343

Boosari, S., Eskandari, S., Shakouri, A., and Fathizadeh, M. (2018). Effect of heating period and temperature on the synthesis of nano-beta zeolite assisted by microwaves. *J. Membr. Sci. Technol.* 8:180. doi: 10.4172/2155-9589.1000180

Brown, E. D., and Wright, G. D. (2016). Antibacterial drug discovery in the resistance era. *Nature* 529, 336–343. doi: 10.1038/nature17042

Cagetti, M., Mastroberardino, S., Milia, E., Cocco, F., Lingström, P., and Campus, G. (2013). The use of probiotic strains in caries prevention: a systematic review. *Nutrients* 5, 2530–2550. doi: 10.3390/nu5072530

Cai, W., Wang, J., Chu, C., Chen, W., Wu, C., and Liu, G. (2019). Metal–organic framework-based stimuli-responsive systems for drug delivery. *Adv. Sci.* 6:1801526. doi: 10.1002/advs.201801526

Cao, P., Wu, X., Zhang, W., Zhao, L., Sun, W., and Tang, Z. (2020). Killing oral bacteria using metal–organic frameworks. *Ind. Eng. Chem. Res.* 59, 1559–1567. doi: 10.1021/acs.iecr.9b05659

Carné, A., Carbonell, C., Imaz, I., and Maspoch, D. (2011). Nanoscale metal–organic materials. *Chem. Soc. Rev.* 40, 291–305. doi: 10.1039/c0cs00042f

Casemiro, L. A., Martins, C. H. G., Pires-de-Souza, F., de, C. P., and Panzeri, H. (2008). Antimicrobial and mechanical properties of acrylic resins with incorporated silver–zinc zeolite – part I. *Gerodontology* 25, 187–194. doi: 10.1111/j.1741-2358.2007.00198.x

Chen, J., Zhang, X., Huang, C., Cai, H., Hu, S., Wan, Q., et al. (2017). Osteogenic activity and antibacterial effect of porous titanium modified with metal-organic framework films. *J. Biomed. Mater. Res. A* 105, 834–846. doi: 10.1002/jbm.a.35960

Chen, S., Popovich, J., Iannuzo, N., Haydel, S. E., and Seo, D.-K. (2017). Silver-ion-exchanged nanostructured zeolite X as antibacterial agent with superior ion release kinetics and efficacy against methicillin-resistant *Staphylococcus aureus*. *ACS Appl. Mater. Interfaces* 9, 39271–39282. doi: 10.1021/acsami.7b15001

Chen, Y., Chen, X., Yu, H., Zhou, H., and Xu, S. (2019). Oral microbiota as promising diagnostic biomarkers for gastrointestinal cancer: a systematic review. *Onco Targets Ther.* 12, 11131–11144. doi: 10.2147/ott.s230262

Chiericatti, C., Basilico, J. C., Basilico, M. L. Z., and Zamaro, J. M. (2012). Novel application of HKUST-1 metal–organic framework as antifungal: biological tests and physicochemical characterizations. *Microporous Mesoporous Mater.* 162, 60–63. doi: 10.1016/j.micromeso.2012.06.012

Çınar, Ç., Ulusu, T., Özçelik, B., Karamüftüoğlu, N., and Yücel, H. (2009). Antibacterial effect of silver-zeolite containing root-canal filling material. *J. Biomed. Mater. Res. B Appl. Biomater.* 90, 592–595. doi: 10.1002/jbm.b.31321

Cui, W. G., Hu, T. L., and Bu, X. H. (2019). Metal–organic framework materials for the separation and purification of light hydrocarbons. *Adv. Mater.* 32:e1806445. doi: 10.1002/adma.201806445

Darveau, R. P. (2010). Periodontitis: a polymicrobial disruption of host homeostasis. *Nat. Rev. Microbiol.* 8, 481–490. doi: 10.1038/nrmicro2337

Della Rocca, J., Liu, D., and Lin, W. (2011). Nanoscale metal–organic frameworks for biomedical imaging and drug delivery. *Acc. Chem. Res.* 44, 957–968. doi: 10.1021/ar200028a

Dizaj, S. M., Lotfipour, F., Barzegar-Jalali, M., Zarrintan, M. H., and Adibkia, K. (2014). Antimicrobial activity of the metals and metal oxide nanoparticles. *Mater. Sci. Eng. C Mater. Biol. Appl.* 44, 278–284. doi: 10.1016/j.msec.2014.08.031

Dong, B., Belkhair, S., Zaarour, M., Fisher, L., Verran, J., Tosheva, L., et al. (2014). Silver confined within zeolite EMT nanoparticles: preparation and antibacterial properties. *Nanoscale* 6, 10859–10864. doi: 10.1039/c4nr03169e

Dreyer, H., Grischke, J., Tiede, C., Eberhard, J., Schweitzer, A., Toikkanen, S. E., et al. (2018). Epidemiology and risk factors of peri-implantitis: a systematic review. *J. Periodontal Res.* 53, 657–681. doi: 10.1111/jre.12562

Du, B. D., Phu, D. V., Quoc, L. A., and Hien, N. Q. (2017). Synthesis and investigation of antimicrobial activity of Cu2O nanoparticles/zeolite. *J. Nanopart.* 138, 2823–2828. doi: 10.1155/2017/7056864

Dzwigaj, S., and Che, M. (2006). Incorporation of Co (II) in dealuminated BEA zeolite at lattice tetrahedral sites evidenced by XRD, FTIR, diffuse reflectance UV- Vis, EPR, and TPR. *J. Phys. Chem. B* 110, 12490–12493. doi: 10.1021/jp0623387

Emam, H. E., Darwesh, O. M., and Abdelhameed, R. M. (2018). In-growth metal organic framework/synthetic hybrids as antimicrobial fabrics and its toxicity. *Colloids Surf. B Biointerfaces* 165, 219–228. doi: 10.1016/j.colsurfb.2018.02.028

Fakin, T., Ristić, A., Mavrodinova, V., and Zabukovec Logar, N. (2015). Highly crystalline binder-free ZSM-5 granules preparation. *Microporous Mesoporous Mater.* 213, 108–117. doi: 10.1016/j.micromeso.2015.04.010

Fang, F. C. (1997). Perspectives series: host/pathogen interactions. Mechanisms of nitric oxide-related antimicrobial activity. *J. Clin. Invest.* 99, 2818–2825. doi: 10.1172/jci119473

Fang, Q., Wang, J., Gu, S., Kaspar, R. B., Zhuang, Z., Zheng, J., et al. (2015). 3D porous crystalline polyimide covalent organic frameworks for drug delivery. *J. Am. Chem. Soc.* 137, 8352–8355. doi: 10.1021/jacs.5b04147

Ferreira, L., Fonseca, A. M., Botelho, G., Almeida-Aguiar, C., and Neves, I. C. (2012). Antimicrobial activity of faujasite zeolites doped with silver. *Microporous Mesoporous Mater.* 160, 126–132. doi: 10.1016/j.micromeso.2012.05.006

Ferreira, L., Guedes, J. F., Almeida-Aguiar, C., Fonseca, A. M., and Neves, I. C. (2016). Microbial growth inhibition caused by Zn/Ag-Y zeolite materials with different amounts of silver. *Colloids Surf. B Biointerfaces* 142, 141–147. doi: 10.1016/j.colsurfb.2016.02.042

Firouzjaei, M. D., Shamsabadi, A. A., Sharifian, G. M., Rahimpour, A., and Soroush, M. (2018). A novel nanocomposite with superior antibacterial activity: a silver-based metal organic framework embellished with graphene oxide. *Adv. Mater. Interfaces* 5:1701365. doi: 10.1002/admi.201701365

Gendreau, L., and Loewy, Z. G. (2011). Epidemiology and etiology of denture stomatitis. *J. Prosthodont.* 20, 251–260. doi: 10.1111/j.1532-849x.2011.00698.x

Ghivari, S. B., Bhattacharya, H., Bhat, K. G., and Pujar, M. A. (2017). Antimicrobial activity of root canal irrigants against biofilm forming pathogens-An *in vitro* study. *J. Conserv. Dent.* 20, 147–151. doi: 10.4103/jcd.jcd_38_16

Golmohamadpour, A., Bahramian, B., Khoobi, M., Pourhajibagher, M., Barikani, H. R., and Bahador, A. (2018). Antimicrobial photodynamic therapy assessment of three indocyanine green-loaded metal-organic frameworks against *Enterococcus faecalis*. *Photodiagnosis Photodyn. Ther.* 23, 331–338. doi: 10.1016/j.pdpdt.2018.08.004

González-Cabezas, C., Li, Y., Gregory, R. L., and Stookey, G. K. (1999). Distribution of three cariogenic bacteria in secondary carious lesions around amalgam restorations. *Caries Res.* 33, 357–365. doi: 10.1159/000016534

Guerra, W., Silva-Caldeira, P. P., Terenzi, H., and Pereira-Maia, E. C. (2016). Impact of metal coordination on the antibiotic and non-antibiotic activities of tetracycline-based drugs. *Coord. Chem. Rev.* 327, 188–199. doi: 10.1016/j.ccr.2016.04.009

Guo, Y.-F., Fang, W.-J., Fu, J.-R., Wu, Y., Zheng, J., Gao, G.-Q., et al. (2018). Facile synthesis of Ag@ZIF-8 core-shell heterostructure nanowires for improved antibacterial activities. *Appl. Surf. Sci.* 435, 149–155. doi: 10.1016/j.apsusc.2017.11.096

Guo, Y.-P., Long, T., Song, Z.-F., and Zhu, Z.-A. (2014). Hydrothermal fabrication of ZSM-5 zeolites: biocompatibility, drug delivery property, and bactericidal property. *J. Biomed. Mater. Res. B Appl. Biomater.* 102, 583–591. doi: 10.1002/jbm.b.33037

Hatamie, S., Ahadian, M. M., Soufi Zomorod, M., Torabi, S., Babaie, A., Hosseinzadeh, S., et al. (2019). Antibacterial properties of nanoporous graphene oxide/cobalt metal organic framework. *Mater. Sci. Eng. C Mater. Biol. Appl.* 104:109862. doi: 10.1016/j.msec.2019.109862

Hedström, A. (2001). Ion exchange of ammonium in zeolites: a literature review. *J. Environ. Eng.* 127, 673–681. doi: 10.1061/(asce)0733-93722001127:8(673)

Herrera, D., Matesanz, P., Bascones-Martínez, A., and Sanz, M. (2012). Local and systemic antimicrobial therapy in periodontics. *J. Evid. Based Dent. Pract.* 12, 50–60. doi: 10.1016/s1532-3382(12)70013-1

Hollanda, A. C. B., de Alencar, A. H. G., de Araújo Estrela, C. R., Bueno, M. R., and Estrela, C. (2008). Prevalence of endodontically treated teeth in a Brazilian adult population. *Braz. Dent. J.* 19, 313–317. doi: 10.1590/s0103-64402008000400005

Horcajada, P., Chalati, T., Serre, C., Gillet, B., Sebrie, C., Baati, T., et al. (2010). Porous metal–organic-framework nanoscale carriers as a potential platform for drug delivery and imaging. *Nat. Mater.* 9, 172–178. doi: 10.1038/nmat2608

Horcajada, P., Gref, R., Baati, T., Allan, P. K., Maurin, G., Couvreur, P., et al. (2012). Metal–organic frameworks in biomedicine. *Chem. Rev.* 112, 1232–1268. doi: 10.1021/cr200256v

Horike, S., Kadota, K., Itakura, T., Inukai, M., and Kitagawa, S. (2015). Synthesis of magnesium ZIF-8 from Mg (BH4)2. *Dalton Trans.* 44, 15107–15110. doi: 10.1039/c5dt01183c

Huang, N., Wang, P., and Jiang, D. (2016). Covalent organic frameworks: a materials platform for structural and functional designs. *Nat. Rev. Mater.* 1:16068. doi: 10.1038/natrevmats.2016.68

Huang, X., Li, L.-D., Lyu, G.-M., Shen, B.-Y., Han, Y.-F., Shi, J.-L., et al. (2018). Chitosan-coated cerium oxide nanocubes accelerate cutaneous wound healing by curtailing persistent inflammation. *Inorg. Chem. Front.* 5, 386–393. doi: 10.1039/c7qi00707h

Hughes, D. (2003). Exploiting genomics, genetics and chemistry to combat antibiotic resistance. *Nat. Rev. Genet.* 4, 432–441. doi: 10.1038/nrg1084

Huxford, R. C., Rocca, J. D., and Lin, W. (2010). Metal-organic frameworks as potential drug carriers. *Curr. Opin. Chem. Biol.* 14, 262–268. doi: 10.1016/j.cbpa.2009.12.012

Hynek, J., Zelenka, J., Rathouskyì, J., Kubaìt, P., Ruml, T., Demel, J., et al. (2018). Designing porphyrinic covalent organic frameworks for the photodynamic inactivation of bacteria. *ACS Appl. Mater. Interfaces* 10, 8527–8535. doi: 10.1021/acsami.7b19835

Izumi, Y., and Nakazawa, T. (1986). Development of zeolite for non-phosphated detergents in Japan. *Pure Appl. Chem.* 58, 1397–1404. doi: 10.1351/pac198658101397

Jokstad, A. (2016). Secondary caries and microleakage. *Dent. Mater.* 32, 11–25. doi: 10.1016/j.dental.2015.09.006

Karakeçili, A., Topuz, B., Korpayev, S., and Erdek, M. (2019). Metal-organic frameworks for on-demand pH controlled delivery of vancomycin from chitosan scaffolds. *Mater. Sci. Eng. C Mater. Biol. Appl.* 105:110098. doi: 10.1016/j.msec.2019.110098

Kassebaum, N. J., Smith, A. G. C., Bernabé, E., Fleming, T. D., Reynolds, A. E., Vos, T., et al. (2017). Global, regional, and national prevalence, incidence, and disability-adjusted life years for oral conditions for 195 countries, 1990–2015: a systematic analysis for the global burden of diseases, injuries, and risk factors. *J. Dent. Res.* 96, 380–387. doi: 10.1177/0022034517693566

Kavanagh, N., Ryan, E. J., Widaa, A., Sexton, G., Fennell, J., O'Rourke, S., et al. (2018). Staphylococcal osteomyelitis: disease progression, treatment challenges, and future directions. *Clin. Microbiol. Rev.* 31:e00084-17. doi: 10.1128/cmr.00084-17

Kawahara, K., Tsuruda, K., Morishita, M., and Uchida, M. (2000). Antibacterial effect of silver-zeolite on oral bacteria under anaerobic conditions. *Dent. Mater.* 16, 452–455. doi: 10.1016/S0109-5641(00)00050-6

Khademi, S., Roozbehani, B., Hamadanian, M., and Khademi, N. (2020). Synthesis and characterization of high flux and antibacterial film nanocomposite based on epoxy-zeolite NaA. *J. Nanostruct.* 10, 177–184. doi: 10.22052/jns.2020.01.019

Kihara, T., Zhang, Y., Hu, Y., Mao, Q., Tang, Y., and Miyake, J. (2011). Effect of composition, morphology and size of nanozeolite on its *in vitro* cytotoxicity. *J. Biosci. Bioeng.* 111, 725–730. doi: 10.1016/j.jbiosc.2011.01.017

Kotchey, G. P., Allen, B. L., Vedala, H., Yanamala, N., Kapralov, A. A., Tyurina, Y. Y., et al. (2011). The enzymatic oxidation of graphene oxide. *ACS Nano* 5, 2098–2108. doi: 10.1021/nn103265h

Krishna, R. (2018). Methodologies for screening and selection of crystalline microporous materials in mixture separations. *Sep. Purif. Technol.* 194, 281–300. doi: 10.1016/j.seppur.2017.11.056

Leão, J. C., Gomes, V. B., and Porter, S. (2007). Ulcerative lesions of the mouth: an update for the general medical practitioner. *Clinics* 62, 769–780. doi: 10.1590/S1807-59322007000600018

Levi, M. E., and Eusterman, V. D. (2011). Oral infections and antibiotic therapy. *Otolaryngol. Clin. North Am.* 44, 57–78. doi: 10.1016/j.otc.2010.10.003

Li, H., Eddaoudi, M., O'Keeffe, M., and Yaghi, O. M. (1999). Design and synthesis of an exceptionally stable and highly porous metal-organic framework. *Nature* 402, 276–279. doi: 10.1038/46248

Li, J., Gopal, A., Karaosmanoglu, S., Lin, J., Munshi, T., Zhang, W., et al. (2020). Photosensitizer doped zeolitic imidazolate framework-8 nanocomposites for combined antibacterial therapy to overcome methicillin-resistant *Staphylococcus aureus* (MRSA). *Colloids Surf. B Biointerfaces* 190:110900. doi: 10.1016/j.colsurfb.2020.110900

Li, P., Li, J., Feng, X., Li, J., Hao, Y., Zhang, J., et al. (2019). Metal-organic frameworks with photocatalytic bactericidal activity for integrated air cleaning. *Nat. Commun.* 10:2177. doi: 10.1038/s41467-019-10218-9

Li, W., Qi, M., Sun, X., Chi, M., Wan, Y., Zheng, X., et al. (2020). Novel dental adhesive containing silver exchanged EMT zeolites against cariogenic biofilms to combat dental caries. *Microporous Mesoporous Mater.* 299:110113. doi: 10.1016/j.micromeso.2020.110113

Li, S., Dong, S., Xu, W., Tu, S., Yan, L., Zhao, C., et al. (2018). Antibacterial hydrogels. *Adv. Sci.* 5:1700527. doi: 10.1002/advs.201700527

Li, X., Qi, M., Li, C., Dong, B., Wang, J., Weir, M. D., et al. (2019). Novel nanoparticles of cerium-doped zeolitic imidazolate frameworks with dual benefits of antibacterial and anti-inflammatory functions against periodontitis. *J. Mater. Chem. B* 7, 6955–6971. doi: 10.1039/c9tb01743g

Li, X., and Wang, Q. (2015). Effects of different root canal preparation methods on root fracture resistance: a systematic review of the literature. *World J. Stomatol.* 4, 108–114. doi: 10.5321/wjs.v4.i2.108

Li, Z., Hüve, J., Krampe, C., Luppi, G., Tsotsalas, M., Klingauf, J., et al. (2013). Internalization pathways of anisotropic disc-shaped Zeolite L Nanocrystals with different surface properties in HeLa cancer cells. *Small* 9, 1809–1820. doi: 10.1002/smll.201201702

Li, Z., and Yang, Y.-W. (2017). Creation and bioapplications of porous organic polymer materials. *J. Mater. Chem. B* 5, 9278–9290. doi: 10.1039/c7tb02647a

Li, Z.-Q., Qiu, L.-G., Xu, T., Wu, Y., Wang, W., Wu, Z.-Y., et al. (2009). Ultrasonic synthesis of the microporous metal–organic framework Cu3(BTC)2 at ambient temperature and pressure: an efficient and environmentally friendly method. *Mater. Lett.* 63, 78–80. doi: 10.1016/j.matlet.2008.09.010

Lima, E., Guerra, R., Lara, V., and Guzmán, A. (2013). Gold nanoparticles as efficient antimicrobial agents for *Escherichia coli* and *Salmonella typhi*. *Chem. Cent. J.* 7:11. doi: 10.1186/1752-153x-7-11

Lin, J., Ding, J., Dai, Y., Wang, X., Wei, J., and Chen, Y. (2017). Antibacterial zinc oxide hybrid with gelatin coating. *Mater. Sci. Eng. C Mater. Biol. Appl.* 81, 321–326. doi: 10.1016/j.msec.2017.08.009

Lin, S., Liu, X., Tan, L., Cui, Z., Yang, X., Yeung, K. W., et al. (2017). Porous iron-carboxylate metal–organic framework: a novel bioplatform with sustained antibacterial efficacy and nontoxicity. *ACS Appl. Mater. Interfaces* 9, 19248–19257. doi: 10.1021/acsami.7b04810

Liu, T., Hu, X., Wang, Y., Meng, L., Zhou, Y., Zhang, J., et al. (2017). Triazine-based covalent organic frameworks for photodynamic inactivation of bacteria as type-II photosensitizers. *J. Photochem. Photobiol. B* 175, 156–162. doi: 10.1016/j.jphotobiol.2017.07.013

Liu, X., Yan, Z., Zhang, Y., Liu, Z., Sun, Y., Ren, J., et al. (2019). Two-dimensional metal–organic framework/enzyme hybrid nanocatalyst as a benign and self-activated cascade reagent for *in vivo* wound healing. *ACS Nano* 13, 5222–5230. doi: 10.1021/acsnano.8b09501

Liu, Y., Gong, C. S., Dai, Y., Yang, Z., Yu, G., Liu, Y., et al. (2019). *In situ* polymerization on nanoscale metal-organic frameworks for enhanced physiological stability and stimulus-responsive intracellular drug delivery. *Biomaterials* 218:119365. doi: 10.1016/j.biomaterials.2019.119365

Liu, Z., Tan, L., Liu, X., Liang, Y., Zheng, Y., Yeung, K. W. K., et al. (2020). Zn2+-assisted photothermal therapy for rapid bacteria-killing using biodegradable humic acid encapsulated MOFs. *Colloids Surf. B Biointerfaces* 188:110781. doi: 10.1016/j.colsurfb.2020.110781

Lu, X., Ye, J., Zhang, D., Xie, R., Bogale, R. F., Sun, Y., et al. (2014). Silver carboxylate metal–organic frameworks with highly antibacterial activity and biocompatibility. *J. Inorg. Biochem.* 138, 114–121. doi: 10.1016/j.jinorgbio.2014.05.005

Luo, D., Wang, C., Tong, Y., Liu, C., Xiao, Y., Zhu, Z., et al. (2020). An NIF-doped ZIF-8 hybrid membrane for continuous antimicrobial treatment. *RSC Adv.* 10, 7360–7367. doi: 10.1039/d0ra00108b

Manger, D., Walshaw, M., Fitzgerald, R., Doughty, J., Wanyonyi, K., White, S., et al. (2017). Evidence summary: the relationship between oral health and pulmonary disease. *Br. Dent. J.* 222, 527–533. doi: 10.1038/sj.bdj.2017.315

Massoudinejad, M., Shahsavani, A., Kamarehie, B., Jafari, A., Ghaderpoori, M., Amini, M. M., et al. (2018). Highly efficient adsorption of fluoride from aqueous solutions by metal organic frameworks: modeling, isotherms, and kinetics. *Fluoride* 51, 355–365.

Matsumura, Y., Yoshikata, K., Kunisaki, S., and Tsuchido, T. (2003). Mode of bactericidal action of silver zeolite and its comparison with that of silver nitrate. *Appl. Environ. Microbiol.* 69, 4278–4281. doi: 10.1128/AEM.69.7.4278-4281.2003

McCusker, L. B., and Baerlocher, C. (2005). Zeolite structures. *Stud. Surf. Sci. Catal.* 157, 41–64. doi: 10.1016/S0167-2991(05)80005-9

Miao, W., Wang, J., Liu, J., and Zhang, Y. (2018). Self-cleaning and antibacterial zeolitic imidazolate framework coatings. *Adv. Mater. Interfaces* 5:1800167. doi: 10.1002/admi.201800167

Mima, E. G., Vergani, C. E., Machado, A. L., Massucato, E. M. S., Colombo, A. L., Bagnato, V. S., et al. (2012). Comparison of photodynamic therapy versus conventional antifungal therapy for the treatment of denture stomatitis: a randomized clinical trial. *Clin. Microbiol. Infect.* 18, E380–E388. doi: 10.1111/j.1469-0691.2012.03933.x

Mitra, S., Kandambeth, S., Biswal, B. P., Khayum, M. A., Choudhury, C. K., et al. (2016). Self-exfoliated guanidinium-based ionic covalent organic nanosheets (iCONs). *J. Am. Chem. Soc.* 138, 2823–2828. doi: 10.1021/jacs.5b13533

Mitra, S., Sasmal, H. S., Kundu, T., Kandambeth, S., Illath, K., Diìaz, D., et al. (2017). Targeted drug delivery in covalent organic nanosheets (CONs) via sequential postsynthetic modification. *J. Am. Chem. Soc.* 139, 4513–4520. doi: 10.1021/jacs.7b00925

Mohammadi, Z., Soltani, M. K., and Shalavi, S. (2014). An update on the management of endodontic biofilms using root canal irrigants and medicaments. *Iran. Endod. J.* 9, 89–97.

Mori, W., Takamizawa, S., Kato, C. N., Ohmura, T., and Sato, T. (2004). Molecular-level design of efficient microporous materials containing metal carboxylates: inclusion complex formation with organic polymer, gas-occlusion properties, and catalytic activities for hydrogenation of olefins. *Microporous Mesoporous Mater.* 73, 31–46. doi: 10.1002/chin.200505273

Nabipour, H., Hossaini Sadr, M., and Rezanejade Bardajee, G. (2017). Release behavior, kinetic and antimicrobial study of nalidixic acid from [Zn2(bdc)2(dabco)] metal-organic frameworks. *J. Coord. Chem.* 70, 2771–2784. doi: 10.1080/00958972.2017.1363391

Naseri, H., Sharifi, A., Ghaedi, M., Dashtian, K., Khoramrooz, S. S., Manzouri, L., et al. (2018). Sonochemical incorporated of cytosine in Cu-H2bpdc as an antibacterial agent against standard and clinical strains of *Proteus mirabilis* with rsbA gene. *Ultrason. Sonochem.* 44, 223–230. doi: 10.1016/j.ultsonch.2018.02.031

Nasrabadi, M., Ghasemzadeh, M. A., and Monfared, M. R. Z. (2019). The preparation and characterization of UiO-66 metal–organic frameworks for the delivery of the drug ciprofloxacin and an evaluation of their antibacterial activities. *New J. Chem.* 43, 16033–16040. doi: 10.1039/c9nj03216a

Nedeljkovic, I., Teughels, W., De Munck, J., Van Meerbeek, B., and Van Landuyt, K. L. (2015). Is secondary caries with composites a material-based problem? *Dent. Mater.* 31, e247–e277. doi: 10.1016/j.dental.2015.09.001

Nikawa, H., Hayashi, S., Nikawa, Y., Hamada, T., and Samaranayake, L. P. (1993). Interactions between denture lining material, protein pellicles and *Candida albicans*. *Arch. Oral. Biol.* 38, 631–634. doi: 10.1016/0003-9969(93)90132-6

Nikawa, H., Yamamoto, T., Hamada, T., Rahardjo, M., Murata, H., and Nakanoda, S. (1997). Antifungal effect of zeolite-incorporated tissue conditioner against *Candida albicans* growth and/or acid production. *J. Oral Rehabil.* 24, 350–357. doi: 10.1046/j.1365-2842.1997.d01-297.x

Nosrati, R., Olad, A., and Nofouzi, K. (2015). A self-cleaning coating based on commercial grade polyacrylic latex modified by TiO2/Ag-exchanged-zeolite-A nanocomposite. *Appl. Surf. Sci.* 346, 543–553. doi: 10.1016/j.apsusc.2015.04.056

Odabaş, M. E., Çinar, Ç., Akça, G., Araz, Ý., Ulusu, T., and Yücel, H. (2011). Short-term antimicrobial properties of mineral trioxide aggregate with incorporated silver-zeolite. *Dent. Traumatol.* 27, 189–194. doi: 10.1111/j.1600-9657.2011.00986.x

Omar, G. S., Wilson, M., and Nair, S. P. (2008). Lethal photosensitization of wound-associated microbes using indocyanine green and near-infrared light. *BMC Microbiol.* 8:111. doi: 10.1186/1471-2180-8-111

Papapanou, P. N. (1996). Periodontal diseases: epidemiology. *Ann. Periodontol.* 1, 1–36. doi: 10.1902/annals.1996.1.1.1

Papapanou, P. N., and Susin, C. (2017). Periodontitis epidemiology: is periodontitis under-recognized, over-diagnosed, or both? *Periodontology* 2000, 45–51. doi: 10.1111/prd.12200

Pihlstrom, B. L., Michalowicz, B. S., and Johnson, N. W. (2005). Periodontal diseases. *Lancet* 366, 1809–1820. doi: 10.1016/S0140-6736(05)67728-8

Popović, Z., Otter, M., Calzaferri, G., and De Cola, L. (2007). Selbstorganisation lebender systeme mit funktionalen nanomaterialien. *Angew. Chem.* 119, 6301–6304. doi: 10.1002/ange.200701019

Popovych, N., Kyriienko, P., Soloviev, S., Baran, R., Millot, Y., and Dzwigaj, S. (2016). Identification of the silver state in the framework of Ag-containing zeolite by XRD, FTIR, photoluminescence, 109Ag NMR, EPR, DR UV-vis, TEM and XPS investigations. *Phys. Chem. Chem. Phys.* 18, 29458–29465. doi: 10.1039/c6cp05263k

Prasetya, N., Himma, N. F., Sutrisna, P. D., Wenten, I., and Ladewig, B. P. (2019). A review on emerging organic-containing microporous material membranes for carbon capture and separation. *Chem. Eng. J.* 2019:123575. doi: 10.1016/j.cej.2019.123575

Qi, M., Chi, M., Sun, X., Xie, X., Weir, M. D., Oates, T. W., et al. (2019). Novel nanomaterial-based antibacterial photodynamic therapies to combat oral bacterial biofilms and infectious diseases. *Int. J. Nanomed.* 14:6937. doi: 10.2147/ijn.s212807

Rai, M., Yadav, A., and Gade, A. (2009). Silver nanoparticles as a new generation of antimicrobials. *Biotechnol. Adv.* 27, 76–83. doi: 10.1016/j.biotechadv.2008.09.002

Rainey, K., Michalek, S. M., Wen, Z. T., and Wu, H. (2018). Glycosyltransferase-mediated biofilm matrix dynamics and virulence of *Streptococcus mutans*. *Appl. Environ. Microbiol.* 85:e02247-18. doi: 10.1128/AEM.02247-18

Ramage, G., Tomsett, K., Wickes, B. L., López-Ribot, J. L., and Redding, S. W. (2004). Denture stomatitis: a role for Candida biofilms. *Oral Surg. Oral Med. Oral Pathol. Oral Radiol. Endod.* 98, 53–59. doi: 10.1016/j.tripleo.2003.04.002

Redfern, J., Geerts, L., Seo, J. W., Verran, J., Tosheva, L., and Wee, L. H. (2018). Toxicity and antimicrobial properties of ZnO@ZIF-8 embedded silicone against planktonic and biofilm catheter-associated pathogens. *ACS Appl. Nano Mater.* 1, 1657–1665. doi: 10.1021/acsanm.8b00140

Restrepo, J., Serroukh, Z., Santiago-Morales, J., Aguado, S., Gómez-Sal, P., Mosquera, M. E. G., et al. (2017). An antibacterial Zn–MOF with hydrazinebenzoate linkers. *Eur. J. Inorg. Chem.* 2017, 574–580. doi: 10.1002/ejic.201601185

Righolt, A., Jevdjevic, M., Marcenes, W., and Listl, S. (2018). Global-, regional-, and country-level economic impacts of dental diseases in 2015. *J. Dent. Res.* 97, 501–507. doi: 10.1177/0022034517750572

Rimoli, M. G., Rabaioli, M. R., Melisi, D., Curcio, A., Mondello, S., Mirabelli, R., et al. (2008). Synthetic zeolites as a new tool for drug delivery. *J. Biomed. Mater. Res. A* 87, 156–164. doi: 10.1002/jbm.a.31763

Ruparelia, J. P., Chatterjee, A. K., Duttagupta, S. P., and Mukherji, S. (2008). Strain specificity in antimicrobial activity of silver and copper nanoparticles. *Acta Biomater.* 4, 707–716. doi: 10.1016/j.actbio.2007.11.006

Saint-Cricq, P., Kamimura, Y., Itabashi, K., Sugawara-Narutaki, A., Shimojima, A., and Okubo, T. (2012). Antibacterial activity of silver-loaded "green zeolites". *Eur. J. Inorg. Chem.* 2012, 3398–3402. doi: 10.1002/ejic.201200476

Salehi, H., Mehrasa, M., Nasri-Nasrabadi, B., Doostmohammadi, M., Seyedebrahimi, R., Davari, N., et al. (2017). Effects of nanozeolite/starch thermoplastic hydrogels on wound healing. *J. Res. Med. Sci.* 22:110. doi: 10.4103/jrms.jrms_1037_16

Santo, C. E., Quaranta, D., and Grass, G. (2012). Antimicrobial metallic copper surfaces kill *Staphylococcus haemolyticus* via membrane damage. *Microbiologyopen* 1, 46–52. doi: 10.1002/mbo3.2

Sanz, M., del Castillo, A. M., Jepsen, S., Gonzalez-Juanatey, J. R., D'Aiuto, F., Bouchard, P., et al. (2020). Periodontitis and cardiovascular diseases: consensus report. *J. Clin. Periodontol.* 47, 268–288. doi: 10.1111/jcpe.13189

Schejn, A., Aboulaich, A., Balan, L., Falk, V., Lalevée, J., Medjahdi, G., et al. (2015). Cu^{2+}-doped zeolitic imidazolate frameworks (ZIF-8): efficient and stable catalysts for cycloadditions and condensation reactions. *Catal. Sci. Technol.* 5, 1829–1839. doi: 10.1039/c4cy01505c

Schneid, T. R. (1992). An *in vitro* analysis of a sustained release system for the treatment of denture stomatitis. *Spec. Care Dentist.* 12, 245–250. doi: 10.1111/j.1754-4505.1992.tb00458.x

Selwitz, R. H., Ismail, A. I., and Pitts, N. B. (2007). Dental caries. *Lancet* 369, 51–59. doi: 10.1016/S0140-6736(07)60031-2

Shearier, E., Cheng, P., Zhu, Z., Bao, J., Hu, Y. H., and Zhao, F. (2016). Surface defection reduces cytotoxicity of Zn(2-methylimidazole)2(ZIF-8) without compromising its drug delivery capacity. *RSC Adv.* 6, 4128–4135. doi: 10.1039/C5RA24336J

Shen, X., Zhang, Y., Ma, P., Sutrisno, L., Luo, Z., Hu, Y., et al. (2019). Fabrication of magnesium/zinc-metal organic framework on titanium implants to inhibit bacterial infection and promote bone regeneration. *Biomaterials* 212, 1–16. doi: 10.1016/j.biomaterials.2019.05.008

Simon-Yarza, T., Mielcarek, A., Couvreur, P., and Serre, C. (2018). Nanoparticles of metal-organic frameworks: on the road to *in vivo* efficacy in biomedicine. *Adv. Mater.* 30:1707365. doi: 10.1002/adma.201707365

Siqueira, J. F. (2002). Endodontic infections: concepts, paradigms, and perspectives. *Oral Surg. Oral Med. Oral Pathol. Oral Radiol. Endod.* 94, 281–293. doi: 10.1067/moe.2002.126163

Siqueira, J. F., and Rôças, I. N. (2004). Polymerase chain reaction–based analysis of microorganisms associated with failed endodontic treatment. *Oral Surg. Oral Med. Oral Pathol. Oral Radiol. Endod.* 97, 85–94. doi: 10.1016/s1079-2104(03)00353-6

Smeets, R., Henningsen, A., Jung, O., Heiland, M., Hammächer, C., and Stein, J. M. (2014). Definition, etiology, prevention and treatment of peri-implantitis-a review. *Head Face Med.* 10:34. doi: 10.1186/1746-160x-10-34

Song, Z., Wu, Y., Cao, Q., Wang, H., Wang, X., and Han, H. (2018). pH-responsive, light-triggered on-demand antibiotic release from functional metal–organic framework for bacterial infection combination therapy. *Adv. Funct. Mater.* 28:1800011. doi: 10.1002/adfm.201800011

Strassert, C. A., Otter, M., Albuquerque, R. Q., Höne, A., Vida, Y., Maier, B., et al. (2009). Photoactive hybrid nanomaterial for targeting, labeling, and killing antibiotic-resistant bacteria. *Angew. Chem. Int. Ed. Engl.* 48, 7928–7931. doi: 10.1002/anie.200902837

Taherzade, S. D., Soleimannejad, J., and Tarlani, A. (2017). Application of metal-organic framework Nano-MIL-100 (Fe) for sustainable release of doxycycline and tetracycline. *Nanomaterials* 7:215. doi: 10.3390/nano7080215

Tamames-Tabar, C., Cunha, D., Imbuluzqueta, E., Ragon, F., Serre, C., Blanco-Prieto, M. J., et al. (2014). Cytotoxicity of nanoscaled metal–organic frameworks. *J. Mater. Chem. B* 2, 262–271. doi: 10.1039/c3tb20832j

Tamames-Tabar, C., Imbuluzqueta, E., Guillou, N., Serre, C., Miller, S. R., Elkaïm, E., et al. (2015). A Zn azelate MOF: combining antibacterial effect. *CrystEngComm* 17, 456–462. doi: 10.1039/c4ce00885e

Thakare, S. R., and Ramteke, S. M. (2017). Fast and regenerative photocatalyst material for the disinfection of *E. coli* from water: silver nano particle anchor on MOF-5. *Catal. Commun.* 102, 21–25. doi: 10.1016/j.catcom.2017.06.008

Tonetti, M. S., Jepsen, S., Jin, L., and Otomo-Corgel, J. (2017). Impact of the global burden of periodontal diseases on health, nutrition and wellbeing of mankind: a call for global action. *J. Clin. Periodontol.* 44, 456–462. doi: 10.1111/jcpe.12732

Torres-Giner, S., Torres, A., Ferrándiz, M., Fombuena, V., and Balart, R. (2017). Antimicrobial activity of metal cation-exchanged zeolites and their evaluation on injection-molded pieces of bio-based high-density polyethylene. *J. Food Saf.* 37:e12348. doi: 10.1111/jfs.12348

Tosheva, L., Belkhair, S., Gackowski, M., Malic, S., Al-Shanti, N., and Verran, J. (2017). Rapid screening of the antimicrobial efficacy of Ag zeolites. *Colloids Surf. B Biointerfaces* 157, 254–260. doi: 10.1016/j.colsurfb.2017.06.001

Uchida, M. (1995). Antimicrobial zeolite and its application. *Chem. Ind.* 46, 48–54.

Unamuno, X., Imbuluzqueta, E., Salles, F., Horcajada, P., and Blanco-Prieto, M. J. (2018). Biocompatible porous metal-organic framework nanoparticles based on Fe or Zr for gentamicin vectorization. *Eur. J. Pharm. Biopharm.* 132, 11–18. doi: 10.1016/j.ejpb.2018.08.013

Valtchev, V., Majano, G., Mintova, S., and Pérez-Ramírez, J. (2013). Tailored crystalline microporous materials by post-synthesis modification. *Chem. Soc. Rev.* 42, 263–290. doi: 10.1039/c2cs35196j

Vos, T., Abajobir, A. A., Abate, K. H., Abbafati, C., Abbas, K., Abdallah, F., et al. (2017). Global, regional, and national incidence, prevalence, and years lived with disability for 328 diseases and injuries for 195 countries, 1990-2016: a systematic analysis for the Global Burden of Disease Study 2016. *Lancet* 390, 1211–1259. doi: 10.1016/s0140-6736(17)32154-2

Vyas, V. S., Vishwakarma, M., Moudrakovski, I., Haase, F., Savasci, G., Ochsenfeld, C., et al. (2016). Exploiting noncovalent interactions in an imine-based covalent organic framework for quercetin delivery. *Adv. Mater.* 28, 8749–8754. doi: 10.1002/adma.201603006

Wan, S., Guo, J., Kim, J., Ihee, H., and Jiang, D. (2008). A belt-shaped, blue luminescent, and semiconducting covalent organic framework. *Angew. Chem. Int. Ed. Engl.* 47, 8826–8830. doi: 10.1002/anie.200803826

Wan, S., Guo, J., Kim, J., Ihee, H., and Jiang, D. (2009). A photoconductive covalent organic framework: self-condensed arene cubes composed of eclipsed 2D polypyrene sheets for photocurrent generation. *Angew. Chem. Int. Ed. Engl.* 48, 5439–5442. doi: 10.1002/anie.200900881

Wang, J., Wang, Z., Guo, S., Zhang, J., Song, Y., Dong, X., et al. (2011). Antibacterial and anti-adhesive zeolite coatings on titanium alloy surface. *Microporous Mesoporous Mater.* 146, 216–222. doi: 10.1016/j.micromeso.2011.04.005

Wojciechowska, A., Gągor, A., Zierkiewicz, W., Jarząb, A., Dylong, A., and Duczmal, M. (2015). Metal–organic framework in an l-arginine copper (ii) ion polymer: structure, properties, theoretical studies and microbiological activity. *RSC Adv.* 5, 36295–36306. doi: 10.1039/c5ra02790j

Wuttke, S., Zimpel, A., Bein, T., Braig, S., Stoiber, K., Vollmar, A., et al. (2017). Validating metal-organic framework nanoparticles for their nanosafety in diverse biomedical applications. *Adv. Healthc. Mater.* 6:1600818. doi: 10.1002/adhm.201600818

Wyszogrodzka, G., Marszałek, B., Gil, B., and Dorożyński, P. (2016). Metal-organic frameworks: mechanisms of antibacterial action and potential applications. *Drug Discov. Today* 21, 1009–1018. doi: 10.1016/j.drudis.2016.04.009

Ximing, G., Bin, G., Yuanlin, W., and Shuanghong, G. (2017). Preparation of spherical metal–organic frameworks encapsulating Ag nanoparticles and study on its antibacterial activity. *Mater. Sci. Eng. C Mater. Biol. Appl.* 80, 698–707. doi: 10.1016/j.msec.2017.07.027

Xue, M., Li, B., Qiu, S., and Chen, B. (2016). Emerging functional chiral microporous materials: synthetic strategies and enantioselective separations. *Mater. Today* 19, 503–515. doi: 10.1016/j.mattod.2016.03.003

Yang, F., Dong, W., He, F., Wang, X., Zhao, S., and Yang, G. (2012). Osteoblast response to porous titanium surfaces coated with zinc-substituted hydroxyapatite. *Oral Surg. Oral Med. Oral Pathol. Oral Radiol.* 113, 313–318. doi: 10.1016/j.tripleo.2011.02.049

Yuan, X., Smith, R. J. Jr., Guan, H., Ionita, C. N., Khobragade, P., Dziak, R., et al. (2016). Hybrid biomaterial with conjugated growth factors and mesenchymal stem cells for ectopic bone formation. *Tissue Eng. Part A* 22, 928–939. doi: 10.1089/ten.TEA.2016.0052

Zhang, W., Du, L., Bi, F., and He, H. (2015). A novel SrTiO3/HZSM-5 photocatalyst prepared by sol–gel method. *Mater. Lett.* 157, 103–105. doi: 10.1016/j.matlet.2015.05.056

Zhang, X., Liu, L., Huang, L., Zhang, W., Wang, R., Yue, T., et al. (2019). The highly efficient elimination of intracellular bacteria via a metal organic framework (MOF)-based three-in-one delivery system. *Nanoscale* 11, 9468–9477. doi: 10.1039/c9nr01284b

Zhang, X., Sun, J., Liu, J., Xu, H., Dong, B., Sun, X., et al. (2018). Label-free electrochemical immunosensor based on conductive Ag contained EMT-style nano-zeolites and the application for α-fetoprotein detection. *Sens. Actuators B* 255, 2919–2926. doi: 10.1016/j.snb.2017.09.112

Zhang, Y., Zhang, X., Song, J., Jin, L., Wang, X., and Quan, C. (2019). Ag/H-ZIF-8 nanocomposite as an effective antibacterial agent against pathogenic bacteria. *Nanomaterials* 9:1579. doi: 10.3390/nano9111579

Zhao, F., Liu, H., Mathe, S. D., Dong, A., and Zhang, J. (2018). Covalent organic frameworks: from materials design to biomedical application. *Nanomaterials* 8:15. doi: 10.3390/nano8010015

Zhu, L., and Zhang, Y.-B. (2017). Crystallization of covalent organic frameworks for gas storage applications. *Molecules* 22:1149. doi: 10.3390/molecules22071149

Zhu, W., Liu, P., Xiao, S., Wang, W., Zhang, D., and Li, H. (2015). Microwave-assisted synthesis of Ag-doped MOFs-like organotitanium polymer with high activity in visible-light driven photocatalytic NO oxidization. *Appl. Catal. B* 17, 46–51. doi: 10.1016/j.apcatb.2015.02.003

Zhuang, W., Yuan, D., Li, J. R., Luo, Z., Zhou, H. C., Bashir, S., et al. (2012). Highly potent bactericidal activity of porous metal-organic frameworks. *Adv. Healthc. Mater.* 1, 225–238. doi: 10.1002/adhm.201100043

Conflict of Interest: The authors declare that the research was conducted in the absence of any commercial or financial relationships that could be construed as a potential conflict of interest.

frontiers
in Bioengineering and Biotechnology

ORIGINAL RESEARCH
published: 12 August 2020
doi: 10.3389/fbioe.2020.00948

An Evaluation of Norspermidine on Anti-fungal Effect on Mature *Candida albicans* Biofilms and Angiogenesis Potential of Dental Pulp Stem Cells

Yan He[1,2†], Yanfan Cao[2,3†], Yangfan Xiang[2], Fengting Hu[2], Fengyu Tang[2], Yanni Zhang[2], Abdullkhaleg Ali Albashari[2], Zhenjie Xing[2], Lihua Luo[2], Yan Sun[2], Qiang Huang[4]*, Qingsong Ye[2,4,5]* and Keke Zhang[2]*

[1] Laboratory for Regenerative Medicine, Tianyou Hospital, Wuhan University of Science and Technology, Wuhan, China, [2] School & Hospital of Stomatology, Wenzhou Medical University, Wenzhou, China, [3] Department of Pediatric Dentistry, School and Hospital of Stomatology, Wenzhou Medical University, Wenzhou, China, [4] School of Stomatology and Medicine, Foshan University, Foshan, China, [5] Center of Regenerative Medicine, Renmin Hospital of Wuhan University, Wuhan, China

Edited by:
Junchao Wei,
Nanchang University, China

Reviewed by:
Bo Jia,
Southern Medical University, China
Ting Sang,
Nanchang University, China
Fugui Zhang,
Massachusetts General Hospital and Harvard Medical School, United States

***Correspondence:**
Qingsong Ye
qingsongye@hotmail.com
Qiang Huang
fkyhq@126.com
Keke Zhang
kekezhang@foxmail.com

† These authors have contributed equally to this work and share first authorship

Specialty section:
This article was submitted to Biomaterials, a section of the journal Frontiers in Bioengineering and Biotechnology

Received: 02 June 2020
Accepted: 23 July 2020
Published: 12 August 2020

Citation:
He Y, Cao Y, Xiang Y, Hu F, Tang F, Zhang Y, Albashari AA, Xing Z, Luo L, Sun Y, Huang Q, Ye Q and Zhang K (2020) An Evaluation of Norspermidine on Anti-fungal Effect on Mature Candida albicans Biofilms and Angiogenesis Potential of Dental Pulp Stem Cells. Front. Bioeng. Biotechnol. 8:948. doi: 10.3389/fbioe.2020.00948

Norspermidine (Nspd) is a kind of polyamine molecule, which is common in eukaryotes and prokaryotes. It has been reported as a potential anti-biofilms agent of bacteria, but its anti-fungal effect remains unclear. *Candida albicans* (*C. albicans*) is a common opportunistic pathogen in oral cavity of human beings. *C. albicans* biofilm is often seen in dental caries. In this work, we aimed to study the effect of Nspd on mature *Candida albicans* biofilms and to investigate how Nspd would influence human dental pulp stem cells (DPSCs). Our biofilm assays indicated that 111.7 and 55.9 mM Nspd dispersed 48 h mature fungal biofilms and showed significant fungicidal effect. 27.9 and 14.0 mM Nspd showed moderate fungicidal effect. Live/dead staining echoed the fungicidal effect. 111.7–14.0 mM Nspd showed a dose- inhibitory effect on mature fungal biofilm, where 14.0 mM Nspd reduced the metabolic activity by half compared with blank control. Moreover, we demonstrated that 111.7–27.9 mM Nspd restrained the production of hyphae form of *C. albicans* via SEM. Low dose Nspd (27.9 and 14.0 mM) could significantly reduce virulence related gene expression *in C. albicans* biofilms. MTT assay displayed a dose effect relation between 2.5–0.08 mM Nspd and DPSCs viability, where 0.63 mM Nspd reduced the viable level of DPSCs to 75% compared with blank control. Live/dead staining of DPSCs did not show distinctive difference between 0.63 mM Nspd and blank control. Vascular differentiation assay showed capillary-like structure of inducted DPSCs culture with and without 0.63 mM Nspd suggesting that it did not significantly affect angiogenic differentiation of DPSCs. Nspd can penetrate remaining dentin at low level, which is confirmed by an *in vitro* caries model. In conclusion, our study indicated high dosage Nspd (111.7 and 55.9 mM) could effectively disrupt and kill mature fungal biofilms. Low dosage (27.9 and 14.0 mM) showed mild anti-fungal effect on mature *C. albicans* biofilms. Human DPSCs were tolerate to 0.08–0.63 mM Nspd, where viability was over 75%. 0.63 mM Nspd did not affect the proliferation and angiogenetic differentiation of DPSCs.

Keywords: norspermidine, *Candida albicans*, regenerative dentistry, anti-fungal effect, dental pulp stem cells, differentiation

INTRODUCTION

Candida albicans (*C. albicans*) is widespread in normal human microbiota and it is one of the most important fungi colonies asymptomatically residing in oral cavity (Mayer et al., 2013). It is also an opportunistic pathogen that can cause infection in immunocompromised individuals under certain circumstances and in healthy individuals with implanted medical and dental devices (Bachtiar et al., 2016; Lin et al., 2019). It can cause skin diseases, vaginal mucosal infections, meningitis, and systemic diseases when immunological functioning is disturbed (Nobile and Johnson, 2015). Also it is the main pathogen causing denture stomatitis and compromising the oral function. *C. albicans* adhered to dental surfaces and forms biofilms, it was closely related to cariogenic microbe (Liu et al., 2017). Investigations indicated that *C. albicans* has been frequently found in early childhood caries (Yang et al., 2012). There are other possible reasons causing caries in childhood, such as fixed orthodontic treatments (Hu et al., 2013). Morphological transition of *C. albicans* in dimorphic, hydrolytic enzymes secretion, invasins, thigmotropism and phenotypic switching, adhesion and biofilms formation are regard as virulence to make a contribution to its pathogenesis (Soll and Daniels, 2016; Solis et al., 2018). It is reported that the biofilm mode of *C. albicans* is responsible to most fungal infections in clinical settings, which anchors on surfaces of medical implants and spreads to remote tissue and organs via blood circulation. Biofilm formation starts with the adherence of yeast-form cells on surface, followed by proliferation of yeast-form cells (Ishchuk et al., 2019). Usually mature biofilm forms a robust and complicated structure with yeast, pseudohyphae and hyphae wrapped in extracellular matrix (Finkel and Mitchell, 2011; Metwalli et al., 2013).

Common drugs to treat the fungal infection clinically are fluconazole, amphotericin B and Caspofungin acetate, which can inhibit the formation of *C. albicans* biofilm at varying degrees (Uppuluri et al., 2011). Nevertheless, conventional infection control of *C. albicans* biofilm is ineffective in that a mature fungal biofilm is more resistant to these drugs and arrantly hard to be eradicated, which requires higher dosage and results in severe side effects and excessive medical expenditure (Van et al., 2018). Due to the structural characteristics, extracellular matrix of *C. albicans* biofilm could isolate anti-fungal drugs acting as barriers. The extracellular DNA and polysaccharides in the matrix were found to contribute to anti-fungal resistance (Davey and O'toole, 2000; Bjarnsholt et al., 2013). *C. albicans* cells in biofilm model are more resistant to anti-biotics compared with the planktonic fungi, up to more than 1,000 times higher (Tobudic et al., 2012). Moreover, the emergence of drug-resistant strains made it more difficult to treat the infections. It is very urgent to develop new anti-fungal or anti-biofilms agents in the post-anti-biotic era (Srivastava et al., 2018).

Polyamine was initially found to affect the activity of cyclin-dependent kinases during the DNA replication to regulate cell proliferation and it also had aliphatic groups that influence cell growth, proliferation, division and differentiation, as well as membrane stability (Oredsson, 2003; Igarashi and Kashiwagi, 2010). Norspermidine (Nspd), one kind of polyamines, has drawn an increasing attention for its potential against bacterial biofilms recently. The effect of Nspd on bacterial biofilms was species dependent and dose dependent. It showed inhibitory effects biofilms of many pathogens including *Pseudomonas aeruginosa* (*P. aeruginosa*), *Acinetobacter baumannii* (*A. baumannii*), *Staphylococcus epidermidis* (*S. epidermidis*), *Streptococcus mutans* (*S. mutans*), *Salmonella* and *Klebsiella pneumonia* (*K. pneumoniae*) (Figueiredo and Ferreira, 2014; Konai et al., 2014; Nesse et al., 2015; Qu et al., 2016; Wu et al., 2016; Ou and Ling, 2017; Sun et al., 2019). Nspd was displayed to show inhibition on planktonic form of *C. albicans* in polyamine free medium (Hamana et al., 1989). Being able to form biofilms is one of the most important virulence factors of *C. albicans.* Factors such as complicated biofilm architecture, extracellular matrix, enhanced expression of drug efflux pumps and metabolic plasticity made contributions to enhance the drug resistance of a mature fungal biofilm (Lynch and Robertson, 2008; Wu et al., 2015). Up to date, there was no knowledge about the effect of Nspd on fungal biofilms.

Deep caries irritates dental pulp and thus influence the dental pulp vitality. Dental pulp stem cells have become a promising source of stem cells. Dental pulp preservation has been increasingly important. Dental pulp stem cells (DPSCs) derived from the neural crest carry the characteristics of mesenchymal stem-ness. DPSCs and other odontogenic stem cells can proliferate and differentiate into multiple tissue cells (Chen et al., 2013; Luo et al., 2018). Therefore, DPSCs have been widely used in the field of regenerative medicine research, preclinical research, which includes oral diseases (Morsczeck et al., 2005); Also advanced technology, such as CBCT can assist the evaluation of the regeneration outcomes (Sun et al., 2014). Studies have showed various good regenerative potency of DPSC when co-cultured with drugs and scaffolds. In our study, Nspd was targeted to treat fungal infection caused by *C. albicans*. when treating dental caries with Nspd, it is important to assess the effect of Nspd on the proliferation and differentiation of DPSCs.

MATERIALS AND METHODS

Organism, Growth Condition

Candida albicans SC5314 (*C. albicans*) was obtained from the Institute of Stomatology (Wenzhou Medical University, China). *C. albicans* was cultured overnight routinely in Sabouraud Dextrose Broth (SDB; Solarbio Science & Technology Co., Ltd., China) for proliferation in aerobic circumstances. Morpholinepropanesulfonic acid (MOPS; Solarbio Science & Technology Co., Ltd., China) modified RPMI-1640 media (Thermo Fisher Scientific, United States) was used to support the minimal inhibitory concentration (MIC) assay and biofilm associated experiments. MIC was defined as the concentration at which *C. albicans* growth was visibly inhibited. The fungi and biofilms were statically cultured at 37°C aerobically (Oredsson, 2003).

For biofilm associated experiments, RPMI-1640 medium contained no Nspd was set as blank control, 10 × MIC of fluconazole against *C. albicans* SC5314 was used as positive control and 0.08% ethanol was set as vehicle control, as ethanol was used as solvent in preparing fluconazole (Seleem et al., 2016). The working cell densities of fungi were 5×10^3 and 5×10^5 CFU/ml for MIC of fluconazole against *C. albicans* and 48 h *C. albicans* biofilm formation, respectively. 96 well plates were used to culture *C. albicans* biofilms in most studies. If biofilms were formed in other system, specific description would be made to clarify. Nspd (Sigma-Aldrich Corporation, United States) dissolved in MOPS modified RPMI-1640 media was used to culture 48h old *C. albicans* biofilm for another 48h to investigate the effect of Nspd on mature *C. albicans* biofilms.

Biomass Assay

To investigate the effect of Nspd on *C. albicans* biofilm biomass, crystal violet assay was conducted as previously described (Peeters et al., 2008; Huo et al., 2011). Nspd (111.7, 55.9, 27.9, and 14.0 mM) conditioned growth media were added to 48h pre-formed *C. albicans* biofilms separately in 96-well plates and cultured for another 48h. Then biofilms were stained with 0.1% (w/v) crystal violet for qualitative analysis by capturing the biofilms images using a stereoscope (Nikon Corporation, Tokyo, Japan). To quantitatively assess the biomass, biofilms retained crystal violet was dislodged with 150 μl of 33.3% (v/v) acetic acid (Zhongxing Chemical reagent Co., Ltd., Zhejiang, China) for 10 min. 100 μl of dissolved solution were added to a new plate. Then absorbance was measured at 595 nm by a microplate reader (Thermo Fisher Scientific, United States).

Fungicidal Assessment

Colony forming unit (CFU) count was used to evaluate the fungicidal effect of Nspd on *C. albicans* biofilms. After 48 h Nspd treatment on the biofilms, phosphate buffer saline (PBS) was used to remove loosely attached cells. Fungi were thoroughly scraped off from the bottom of culture plates and re-suspended in 200 μl of sterile PBS by vortex. For CFU count, 10-fold gradient dilution was prepared and 100 μl *C. albicans* diluted suspension was inoculated on Sabouraud's Agar plates (SDA; Solarbio Science & Technology Co., Ltd., China) and cultured 24h before colony counting (Seneviratne et al., 2009). Log_{10} CFU/ml was calculated for the fungicidal comparison.

Fungal Metabolic Assessment – XTT Assay

2, 3-bis (2-methoxy-4-nitro-5-sulfo-phenyl)-2H-tetrazolium-5-carboxanilide (XTT; Invitrogen, Carlsbad, CA, United States) assay was used to detect the metabolic activity of *C. albicans* biofilms influenced by Nspd (Ramage et al., 2001). After washed twice with PBS, the biofilm was incubated with 150 μl XTT solution (0.5 mg/ml) at 37°C in darkness for 1 h. 100 μl of incubated solution were extracted for absorbance measurement at 490 nm by the microplate reader.

Live/Dead Staining of *C. albicans*

To detect the influence of Nspd on the vitality of *C. albicans* inside biofilms, live/dead staining was conducted using a LIVE/DEAD® BacLight$^{\text{TM}}$ Bacterial Viability Kits (Invitrogen Carlsbad, CA, United States) following the manufacturer's instruction as previous (Samaranayake et al., 2009). Briefly, biofilms were stained with SYTO 9 and propidium iodide (PI) at 37°C for 30 min in the darkness, a confocal laser scanning microscope (Nikon Corporation, Tokyo, Japan) was used to acquire biofilm images at 3 random sites on each sample using a 60 × oil immersion lens. The excitation/emission wavelength was set at 480/500 nm for SYTO 9 and 490/635 nm for PI.

Scanning Electron Microscope Imaging

To observe the morphological features of the biofilms by SEM, 10 mm × 10 mm × 3 mm acrylic resin chips (Jianchi Dental Equipment, Changzhi, China) were purchased and sterilized by ethylene oxide (Silva S. et al., 2013; Bachtiar et al., 2016). The acrylic resin chips were placed into 24-well plate to form 48h old *C. albicans* biofilms. Various dosages of Nspd were co-cultured with 48h old biofilms for another 48h. Biofilms were washed twice with PBS, fixed with 2.5% (w/v) glutaraldehyde (J&K Scientific, Co., Ltd., China) and dehydrated by gradient ethanol (Sangetha et al., 2009). The samples were sputter-coated with gold-palladium. Biofilm structure and the fungal morphology were imaged by SEM (Hitachi, Tokyo, Japan). The captured images were presented at 2000 × magnification.

Genes Expression

To explore the mechanism how Nspd influence the formation of biofilm, the expression level of *C. albicans* hyphal wall protein1 (*hwp1*), agglutinin-like sequence protein 3 (*als3)* and cell surface hydrophobicity (*csh1*) were studied. Hyphal proliferation and substratum adhesion related protein, Hwp1, plays a decisive role in *C. albicans* adhesion, virulence expression and pathogenesis (Feldman et al., 2016). The expression of *als3,* a hyphae-specific cell surface protein, played a decisive role in the adhesion of *C. albicans* biofilms formation (Feldman et al., 2016). The *csh1* is the first gene that has been proved to be important in the production of cell surface hydrophobicity mucin and it acts vitally in biofilms formation (Feldman et al., 2016).

RNA Isolation

14.0 and 27.9 mM Nspd were selected to challenge the 48 h old biofilms for 48 h. Then the biofilms were collected for RNA extraction using Trizol (Theiss et al., 2006). Concentration and purity of the extracted RNA were verified by Nanodrop 2000, and the integrity of RNA was confirmed by agarose gel electrophoresis.

Reverse Transcription

Reverse transcription was conducted to obtain cDNA by a PrimeScript$^{\text{TM}}$ RT reagent Kit with gDNA Eraser (Perfect Real Time) (Takara Bio Inc., Otsu, Japan) following the manufacturer's instructions.

Real-Time Quantitative PCR

TB Green® Premix Ex Taq$^{\text{TM}}$ II kit (Takara Bio Inc., Otsu, Japan) was used for qRT- PCR analysis (Li et al., 2018). The total reaction volume was 20.0 μl (10.0 μl 2 × SYBR Premix Ex Taq II, 0.8 μl forward primer, 0.8 μl reverse primer 0.4 μl reference dye II, 2.0 μl of cDNA and 6.0 μl sterilized distilled water). The reaction procedure was set as follows: pre-denaturation at 95°C for 30s, followed by 40 cycles of denaturation at 95°C for 5s, annealing at 55°C for 30s, extension at 72°C for 30s in a StepOnes plus (Life Technologies, United States). The results were analyzed by $2^{-\Delta\Delta Ct}$ method. *18S rRNA* was used as reference gene. Primers were: *18S rRNA* (F: 5′-CACGACGGAGTTTCACAAGA-3′; R: 5′-CGATGGAAGTTTGAGGCAAT-3′), *hwp1* (F: 5′-GCTCCTGCTCCTGAAATGAC-3′; R: 5′-CTGGAGCAATTGGTGAGGTT-3′), *als3* (F: 5′-CAACTTGGGTTATTGAAACAAAAACA-3′; R: 5′-AGAAACAGAAACCCAAGAACAACC-3′), *csh1* (F: 5′-CTGTCGGTACTATGAGATTG-3′; R: 5′-GATGAATAAACCCAACAACT-3′) (Feldman et al., 2016).

Cell Culture, Identification and Multilineage Differentiation

DPSCs were extracted, cultured and identified in accordance with our previous study (Luo et al., 2018). The use of DPSCs and protocols used in this study was independently reviewed and approved by the Ethics Committee of the School and Hospital of Stomatology, Wenzhou Medical University (No. WYKQ2018008). Cells from passage 3–5 were used in this study. 2 × 10^3 cells/well was seeded in the 96-well plates and 100 μl per well medium was added. If other seeding density or culture system were applied, separate description would be made. Complete α-modified Eagle's medium (α-MEM, Thermo Fisher Scientific, United States) was prepared with addition of 10% fetal bovine serum (FBS, Thermo Fisher Scientific, United States) and 1% antibiotics [100 IU/mL penicillin (Thermo Fisher Scientific, United States) and streptomycin (Thermo Fisher Scientific, United States)]. This complete α-MEM was also used as control. DPSCs were cultured at 37°C in 5% CO_2 70% humidified incubator. DPSCs were prepared in triplicate to minimize result variation.

Flow cytometry analysis was applied to confirm the immunophenotyping of DPSCs used in this study. When 80–90% confluence reached, stem cells were incubated with the following monoclonal antibodies: CD73, CD105, CD34, and CD45 (BioLegend, United States) for 30 min at 4°C in the darkness. Stained cells were washed three times and re-suspended in PBS with 1% BSA. Then the stem cells were analyzed with CytoFLEX flow cytometer (Beckman Coulter, California, United States).

Adipogenic differentiation: DPSCs were plated into 6-well plates with a density of 1.5 × 10^5 cells/well. When 100% confluence or post-confluence was achieved, OriCell TM mesenchymal stem cells adipogenic differentiation medium (Cyagen, United States) was used to induce adipogenic differentiation of DPSCs according to manufacturer's instructions. After 21 days of differentiation, cells were fixed with 4% PFA for 20 min and stained with oil red O for half an hour to identify the lipid droplets in adipose cells. Staining result was observed and analyzed by light microscope (TS100, Nikon, Japan).

Osteogenic differentiation: DPSCs were plated into 6-well plates with a density of 1.5 × 10^5 cells/well. Until 60—70% confluence, the medium was replaced with OriCell TM mesenchymal stem cell osteogenic differentiation medium (Cyagen, United States) and cultured for 21 days. Culture medium was renewed twice a week. After 3 weeks of induction, the cells were washed with PBS and fixed with 4% PFA for 20 min, then stained with alizarin red S (Cyagen, United States) at room temperature in the dark for 3–5 min to identify calcified tissue. Staining result was observed and analyzed by light microscope (TS100, Nikon, Japan).

Chondrogenic differentiation: 2.5 × 10^5 cells were collected by centrifugation at 1,000 rpm for 5 min. Then the cell pellets were cultured in chondrogenic medium in a humidified atmosphere with 37°C, 5% CO_2 for 28 days. During differentiation, culture medium was changed every 3 days. At the end of chondrogenic pellets' formation, tissue pellet was fixed with 4% PFA for 20 min and stained with Alcian blue to identify differentiated chondrocytes. Staining result was observed and analyzed by light microscope (TS100, Nikon, Japan).

DPSCs Metabolic Activity Assessment – MTT Assay

MTT assay was to define the cytotoxicity and determine the optimal concentration of Nspd for further experiments. The old media of 24h culture were replaced with complete α-MEM containing FBS, 1% antibiotics, streptomycin and added various concentrations of Nspd (0.0, 0.08, 0.16, 0.31, 0.63, 1.25, 2.5, 5.0 mM). Cell culture with the presence of Nspd was continued for 24h. Then the medium was removed and washed twice with PBS. 100 μl per well 0.5 mg/mL MTT solution was added and incubated at 37°C for 2h. The MTT solution was discarding and rinsed by PBS. 150 μl per well DMSO was used to dissolve the formation of crystals and transferred to a new plate. Optical density (OD) values of solution were measured photometrically at 570 nm by an absorbance microplate reader (Vikas et al., 2019).

Live/Dead Staining of DPSCs

To compare the vitality of DPSCs with and without the presence of low dosage of Nspd, live/dead staining was used to treat DPSCs that were cultured with serially diluted Nspd for 24h. Old media were removed and washed twice with PBS. A blend of 3 μl PI (1 mg/ml), 2 μl of Calcein AM (1 mg/ml) and 1 ml PBS was prepared and aliquoted. 100 μl per well of the mixture was added and incubated for 30 min in the dark at room temperature. PBS was used to replace the stain. Fluorescence microscope (Axiovert A1, Carl Zeiss, Germany) was used to visualize and capture images. Live cells exhibited green, and the dead appeared red (Yao and Flynn, 2018).

Capillary-Like Network Formation

To investigate the effect of Nspd on angiogenic differentiation of DPSCs, GelMA hydrogels was used as a scaffold structure

(Chen et al., 2012). Complete endothelial cell growth medium-2^{TM} (EGM-2^{TM}, containing 2% FBS, 0.4% hFGF-B, 0.1% VEGF, 0.1% hEGF, 0.1% R3-IGF-1, 0.1% Heparin, 0.1% ascorbic acid, 0.1% gentamicin/amphotericin-B, and 0.04% hydrocortisone) (Lonza Bioscience, Switzerland) with various concentrations of Nspd were added to the confluent DPSCs and GelMA in 96-well plates. After 7 day differentiation, cells were washed with PBS and fixed with 4% PFA for 15 min at room temperature. Cells were permeabilized with 0.1% Triton X-100 for 20 min and washed three times in PBS. Then the cells were incubated with Phalloidin-TRITC (Solarbio Science & Technology Co., Ltd., China) (1:200 with 1% BSA) for 1h in the dark at 37°C, followed by incubation with DAPI for 5 min. Phalloidin-TRITC was used to stain F-actin, one of the cytoskeletons, which is important to cell-to-cell and cell-to-matrix adhesion. DAPI was used to stain nuclei. The samples were analyzed through fluorescence microscopy (Nam et al., 2017).

Dental Caries Model

To study whether Nspd would permeate into pulp chamber and affect DPSCs inside the chamber, we introduced a dental caries model with teeth decay on the surface *in vitro* (**Figure 7A**, arrow on the right). The use of teeth and protocols described in this study was approved by the Ethics Committee of the School and Hospital of Stomatology, Wenzhou Medical University (No. WYKQ2020002). The pulp tissue was removed from extracted teeth via lateral access (**Figure 7A**, arrow on the left). Saline (100 μl per teeth in dental pulp tune) was added inside the pulp chamber. All access to external environment including the apical foramina was sealed. Then teeth (1 tooth/well) were placed in 24-well plate containing 116.7 mM of Nspd. The teeth were incubated at 37°C for 48 h.

Quantification of Nspd

After 48 h, liquid from sealed dental pulp chamber was extracted. To quantify the Nspd by gas chromatography (GC; Agilent Technologies, United States), the sample was diluted 250 times with methanol, recorded as dental samples. A standard Nspd solution was prepared with methanol to make Nspd at 330.68 ng/ml, served as control and recorded as substance group. Different dental samples and substance were detected by gas chromatography analysis (GC; Agilent Technologies, United States). Linear velocity of helium carrier gas was 40.0 cm/sec; Oxygen flow rate was 66.7 ml/min; Hydrogen flow rate was 16.7 ml/min; Nitrogen as auxiliary gas; split ratio was 39:1; Injector temperature was 280°C; Initial column temperature was 120°C and at a hating rate of 25°C/min to 260°C; The temperature of gasify room and detector were 300°C (Retention time: 10 min).

Statistical Analysis

One-way Analysis of Variance (ANOVA) was used to analyze the data, followed by the Tukey's multiple comparison tests. Statistical significance was set as $p < 0.05$.

RESULTS AND DISCUSSION

MIC of Fluconazole for *C. albicans*

The MIC of fluconazole against *C. albicans* was 8 μM. 80 μM fluconazole was used as positive control.

Nspd Reduced the Biomass of Mature *C. albicans* Biofilms

Crystal violet staining results showed that Nspd inhibited the biomass of mature *C. albicans* biofilms in a dose dependent manner. Nspd showed more inhibitory effect on pre-formed biofilms than fluconazole did, which merely reduced 16.44% when compared with blank control. 111.7 and 55.9 mM Nspd significantly reduced 31.45% and 27.80% biomass of the biofilm ($p < 0.05$) (**Figure 1A**). Vehicle group hardly affected the biomass ($p > 0.05$) indicating the reduction of biomass was contributed by Nspd.

According to previous studies, Nspd was suggested to disassemble mature biofilms through targeting extracellular polysaccharide in a large, old-aged microbial aggregates model (Si et al., 2014). Cardile et al. (2017) claimed 20 mM Nspd was effective in dispersing and inhibiting 24 h MRSA bacterial biofilm. However, the actual mechanism of the anti-biofilms effect of Nspd on *C. albicans* remained unknown. As cell structure of *C. albicans* is quite different from that of bacteria, the molecular mechanism of Nspd affecting the *C. albicans* biofilms might differ from that of bacteria.

Fungicidal Assessment

Colony forming unit results showed fungicidal effect of Nspd on pre-formed *C. albicans* biofilms. 14.0, 27.9, 55.9 and 111.7 mM Nspd significantly reduced 12.98%, 20.50%, 30.64%, and 66.37% Log_{10} CFU, respectively, when compared with blank control (**Figure 1B**). The fungal count was significantly decreased in Nspd treated at the concentration of 111.7 mM when compared to lower concentrations of Nspd, fluconazole and vehicle control groups ($p < 0.05$). Fluconazole only reduced 11.72% Log_{10} CFU when compared with the blank control group and showed no significant difference to 14.0 mM Nspd group ($p > 0.05$). Vehicle control showed no significant fungicidal effect ($p > 0.05$). The fungicidal ability of Nspd was significantly enhanced at 111.7 mM concentration when compared to other experiment and control groups. Antimicrobial effect of Nspd varied from bacterial strains, Cardile et al. studied the antimicrobial effect of 20 mM Nspd on planktonic bacterial growth in liquid media for 24 h. They reported that 20 mM Nspd could effectively kill *S. aureus*, could suppress the growth of *A. baumanii* and *K. pneumoniae*, and could not affect *P. aeruginosa* (Cardile et al., 2017).

Nspd Reduced the Viability and Metabolic Activity of *C. albicans* Biofilms

According to live/dead staining results, Nspd reduced the viability of *C. albicans* biofilms. There was more dead *C. albicans* (stained red) in Nspd containing groups when compared to blank control group (**Figure 2**). Fluconazole and vehicle control group could not inhibit *C. albicans* biofilms which had less

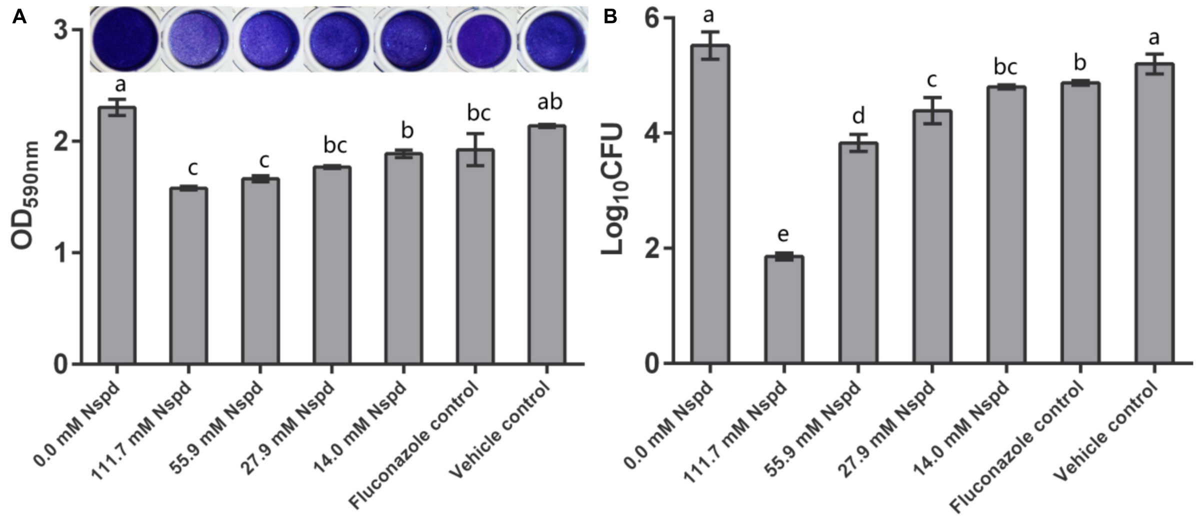

FIGURE 1 | *C. albicans* biofilm biomass determined by crystal violet assay and CFU count. **(A)** Quantitative analysis of biofilm biomass by crystal violet assay with inserted panel of representative *C. albicans* biofilm stained with crystal violet. 111.7 and 55.9 mM Nspd showed obvious removal effect on 48 h old mature fungal biofilms. Other Nspd, positive and vehicle controls showed moderate biofilm removal effect. **(B)** CFU count of *C. albicans* in biofilms after 48 h exposure to interventions. CFU counting indicated survival proportion of *C. albicans* in biofilm. 111.7 and 55.9 mM Nspd showed significant fungicidal effect on mature biofilms. Other Nspd and positive control groups showed mild fungicidal effect. Vehicle control, containing 0.08% ethanol, showed no fungicidal effect on mature biofilms. Data were presented in mean ± standard deviation and values with dissimilar letters were significantly different from each other; $p < 0.05$.

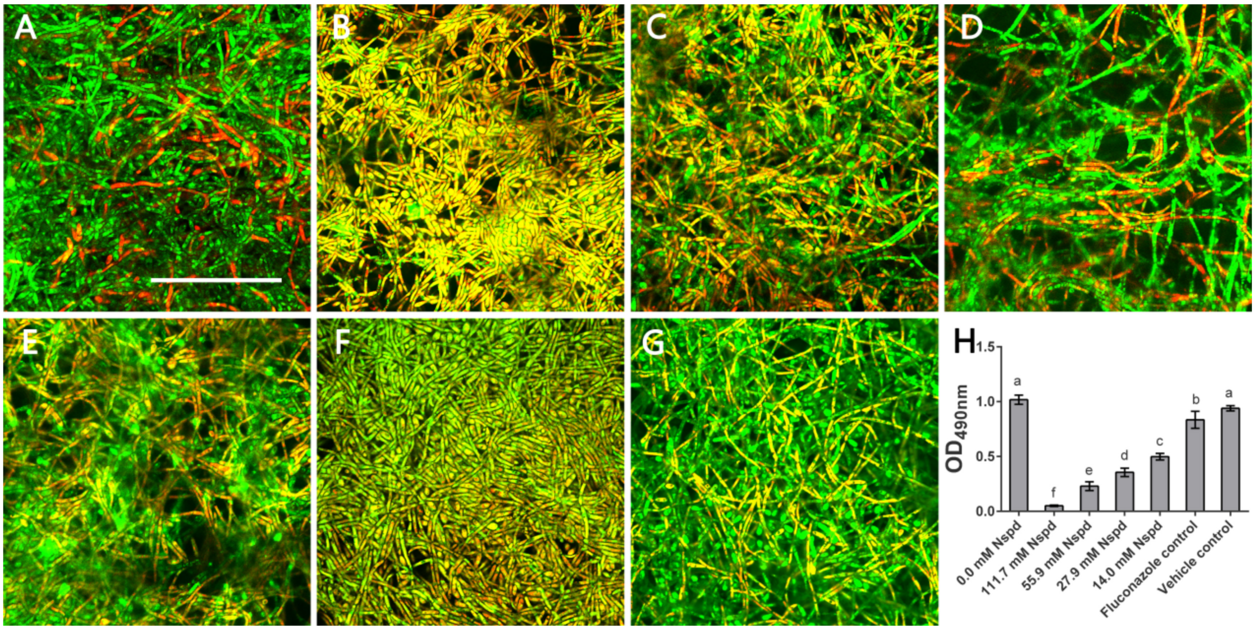

FIGURE 2 | Live/Dead staining and metabolic activity of *C. albicans* biofilms. Representative *C. albicans* biofilm images revealed by live/dead staining: **(A)** Blank control group (0 mM Nspd) showed few dead cells in a mature biofilm. **(B–E)** The number of dead cells (red) decreased as Nspd was diluted from 111.7 to 14.0 mM. **(F)** 80 μM fluconazole group and **(G)** vehicle group (0.08% ethanol), both displayed a few dead cells inside the biofilm. Live cells appeared as green and dead cells appeared as red; yellow/orange colors were the result of an overlap of fluorescent dyes; bar = 50 μm. **(H)** Metabolic activity of *C. albicans* biofilms was determined by XTT assay. A clear dosage effect relation was displayed in the metabolic level and dilution of Nspd. Nspd could significantly suppressed the metabolic activity of fungal cells in mature biofilm, much more effective than positive and vehicle controls. 14.0 mM Nspd could inhibit the metabolic activity level of mature fungal biofilm to half of the blank control's (0.0 mM). Data were presented in mean ± standard deviation and values with dissimilar letters were significantly different from each other; $p < 0.05$.

dead fungus (**Figures 2A,G**). The XTT results showed that Nspd showed significant inhibitory effect on the metabolic activity of *C. albicans* biofilms in a dose dependent manner when compared with bank control ($p < 0.05$) (**Figure 2H**). Fluconazole group affected metabolic activity of *C. albicans* in biofilm to a much less degree than Nspd containing groups did ($p < 0.05$), which

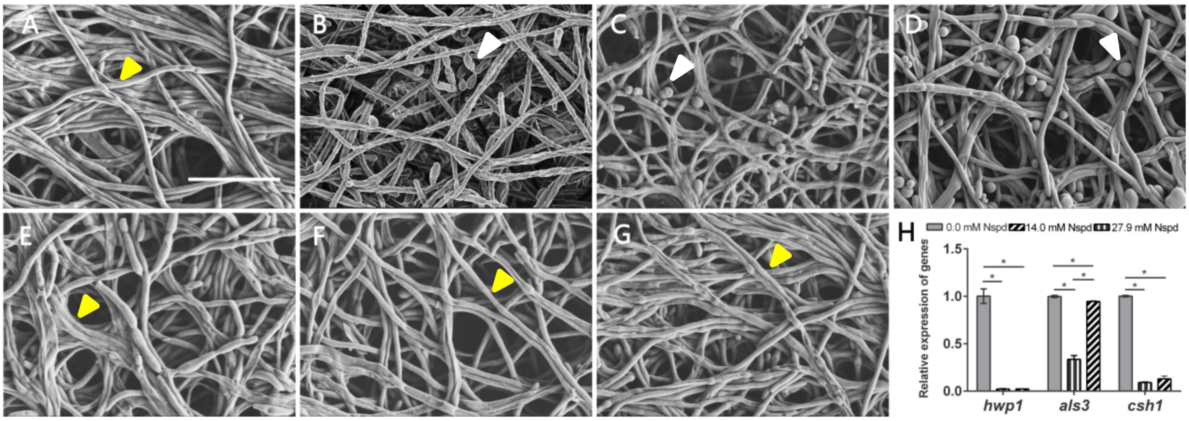

FIGURE 3 | SEM images of *C. albicans* biofilms and virulence related gene expression influenced by Nspd on the *C. albicans* biofilms. **(A–E)** SEM images of *C. albicans* biofilms challenged by Nspd at various concentrations (0, 111.7, 55.9, 27.9, and 14.0 mM, respectively). **(F)** 80 μM fluconazole. **(G)** Vehicle (0.08% ethanol). More yeasts (indicated by white arrows) were formed in 111.7 mM **(B)**, 55.9 mM **(C)**, and 27.9 mM **(D)** Nspd groups. There were no yeasts but hyphae form of fungal cells (indicated by yellow arrows) in mature biofilms of blank control **(A)**, 14.0 mM Nspd group **(E)**, 80 μM fluconazole **(F)**, and vehicle **(G)** groups. Bar = 20 μm. **(H)** Virulence related gene expression of *hwp1*, *als3,* and *csh1* revealed by qRT-PCR on 48 h mature *C. albicans* biofilms. Data were presented in mean ± standard deviation; *$p < 0.05$.

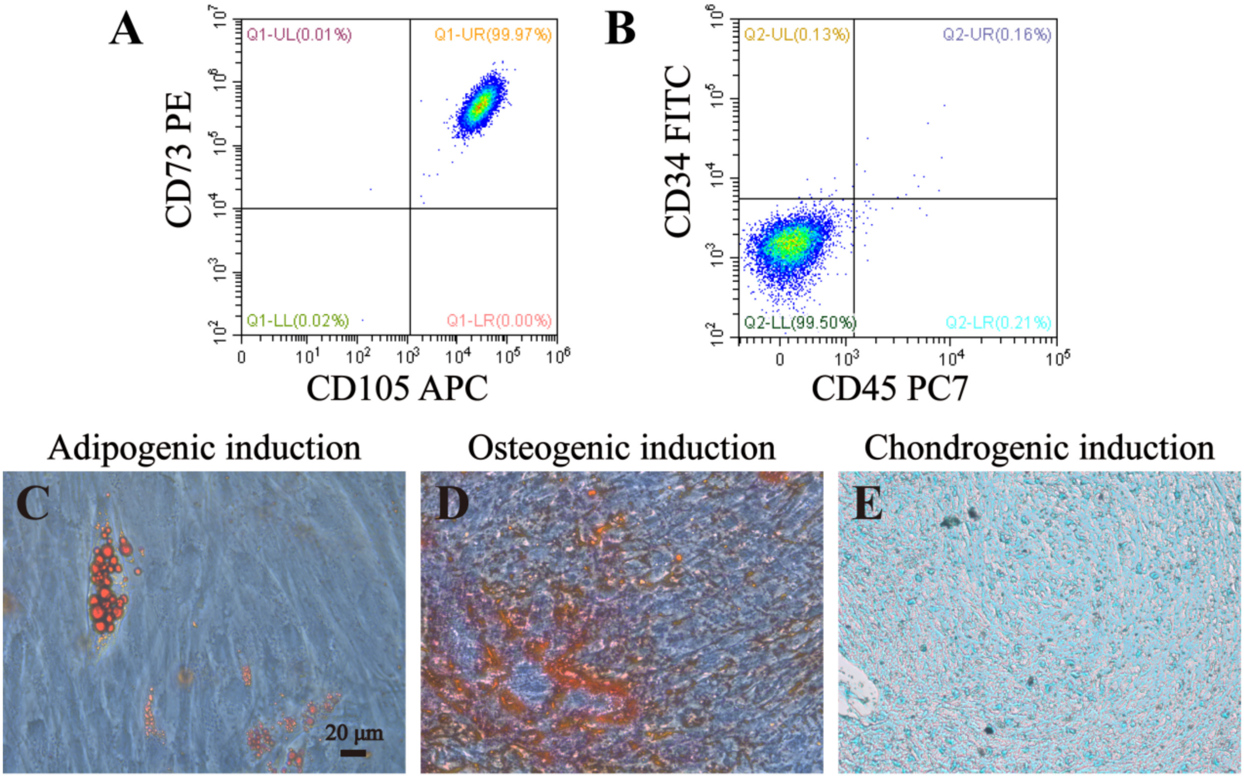

FIGURE 4 | Identification and lineage differentiation of DPSCs. **(A,B)** Flow cytometry confirmed that DPSCs isolated and cultured in present study positively expressed surface markers of mesenchymal stem cells (CD73 and CD105), and negatively expressed surface markers of hematopoietic stem cells (CD34 and CD45). **(C–E)** Multiple differentiation potency of DPSCs used in this study was assessed by osteogenic, adipogenic and chondrogenic experiments. Fat droplets (red in **C**), calcified nodules (red in **D**), and chondrocytes (blue in **E**) were presented after 21 or 28 days inductions. Bar = 20 μm.

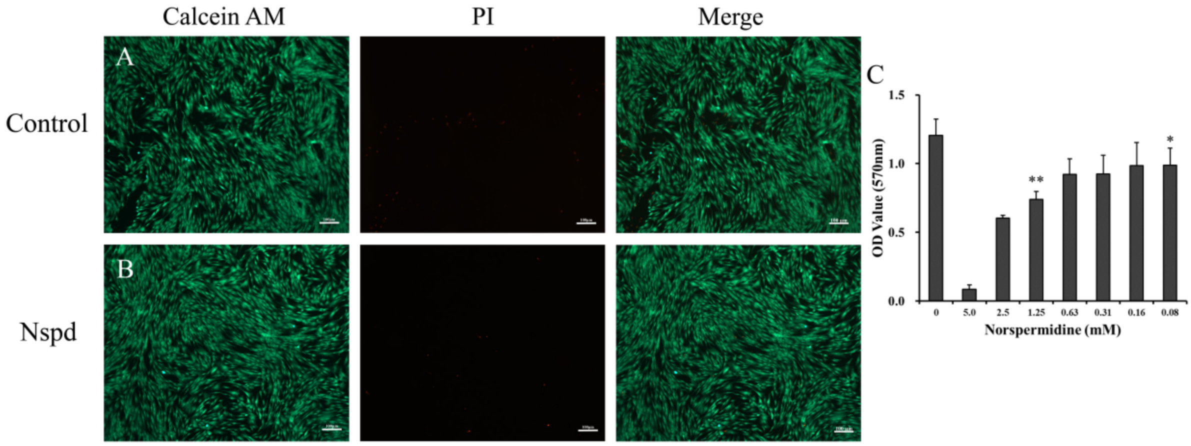

FIGURE 5 | Live/dead staining of DPSCs with and without Nspd and the cytotoxic of Nspd determined by MTT assay. **(A)** DPSCs cultured with α-MEM medium, the control. DPSCs were in spindle shapes and were well aligned in typical pattern. **(B)** DPSCs cultured with α-MEM medium containing 0.63 mM Nspd. Similar to those in the control, DPSCs were densely aligned. Calcein AM (green) was used to stain live stem cells and PI (red) was used to stain dead stem cells. Bar = 100 μm. **(C)** To identify an optimal concentration of Nspd for DPSCs study, Nspd at various concentrations (0, 5.0, 2.5, 1.25, 0.63, 0.31, 0.16, and 0.08 mM, respectively) were used to culture DPSCs for 24 h. Live/dead cell viability for DPSCs. MTT assay was used to assess the viability and proliferation rate of DPSCs with presence of Nspd. Data were presented in mean ± standard deviation. *represented 0.08, 0.16, 0.32, and 0.64 mM of Nspd were significantly different from control group, (0 mM). **represented the result was significantly different from the 0.63 mM Nspd group.

only reduced by 18.1% when compared with blank control. There was no significant difference between blank control and vehicle control. Hamana et al. (1989) reported that planktonic *C. albicans* did not grow with presence of 100 μM Nspd for 48 h. In our study, to effectively inhibit the vitality of *C. albicans* in mature biofilm, only 111.7 mM Nspd was successful after 48 h (**Figure 1B**). This suggested that biofilm mode of fungi did increase the resistance of antibiotics greatly.

The viability and metabolic activity are important for virulence effect of biofilm. Biofilm featuring the multicellular and complex structures may provide prevention strategies for fungus (Ramage et al., 2001). Yeast phase of *C. albicans* was a probable way of self-protection. We noted that compared with fluconazole, high dosage Nspd effectively inhibited the viability and metabolic activity of mature fungal biofilm.

Npsd Induced More Yeast Phase of *C. albicans* in Biofilm

The *C. albicans* biofilms formed on acrylic resin specimens were observed to assess biomass and fungal morphology by SEM (**Figure 3**). Different concentrations of Nspd could partially eliminate pre-formed *C. albicans* biofilm and this inhibitory effect on fungal biofilm gradually declined with the dilution of Nspd (**Figures 3A,G**). Also, there was more yeast form presented in Nspd groups when compared with blank control. While in 80 μM fluconazole, blank and vehicle controls, the proportion of yeast form seemed to have no difference.

Nspd seemed to be able to promote the expression of yeast phase. There existed higher proportion of yeast phase in pre-formed *C. albicans* biofilms in Nspd containing groups than that of blank control, especially in 111.7, 55.9, and 27.9 mM groups. Hypha and yeast are two different forms of *C. albicans*, and the morphological transition between hyphae and yeast forms is associated with the pathogenicity of *C. albicans.* Hypha, an important virulence attribute of *C. albicans*, shows more invasiveness compared to yeast and it promotes the host tissue penetration and leads to the establishment of systemic infections (Raut et al., 2013). It is reported that hyphal formation could be facilitated through a number of environmental factors

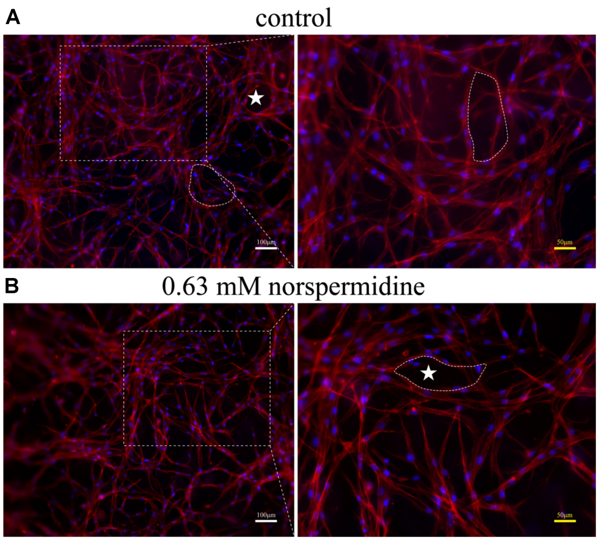

FIGURE 6 | Fluorescence images of capillary-like structure of DPSCs after 7 day angiogenic induction with and without Nspd cultured in GelMA. Differentiated DPSCs were stained with Phalloidin-TRITC (red) to specifically display F-actin, a capillary-like network structure and DAPI (blue) to display cell nuclei. **(A)** Inducted by growth medium as control; **(B)** Induced by media with 0.63 mM Nspd. In both groups, capillary-like network was observed (white stars). White bar = 100 μm, and yellow bar = 50 μm.

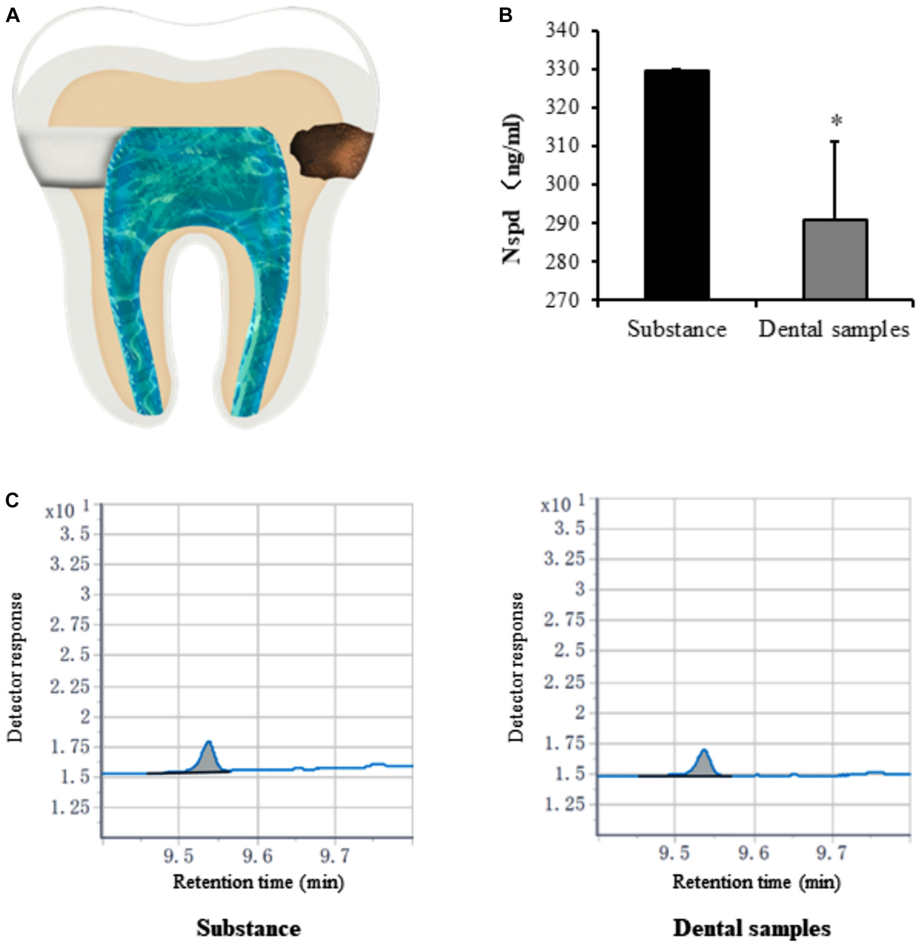

FIGURE 7 | Quantification of norspermidine in dental caries model *in vitro*. **(A)** The opening location of pulp chamber (left side) and Cavity of tooth (right side) in dental caries model. **(B)** Nspd was quantified according to the peak area detected with Agilent GC system. * represented dental samples group was significantly different from substance group. Data were presented in the mean ± standard deviation; $^{*}p < 0.05$. **(C)** Detector response of Nspd. Substance group was diluted 250 times with 0.63 mM Nspd, and the dental sample was also diluted 250 times.

such as serum or N-acetylglucosamine, neutral pH, CO_2, body temperature, starvation and embedded growth conditions (Vesely et al., 2017). Nspd can promote hyphal development through regulating the pH of the medium (da Silva Dantas et al., 2016). Yet our result showed more yeast formation in high dosage of Nspd groups which seemed conflicts. Previous studied suggested that yeast formation was believed to represent the cell form that primarily involves in dissemination (Saville et al., 2003). We proposed that at high concentration of Nspd, fungi tended to switch to a smaller yeast form to escape from where the environment did not favor the survival of *C. albicans*.

Nspd Reduced the Expression of Virulence-Related Genes

The expression of *hwp1* reduced to 2.2% and 2.3% in 27.9 mM Nspd and 14.0 mM Nspd groups when compared with blank control ($p < 0.05$) (**Figure 3H**). Also, the expression of *csh1* showed a similar situation to *hwp1* despite that *als3* had raised its expression at a concentration of 14.0 mM, which was slightly lower than that of the control group. Researchers had discovered the positive correlation between fungal hydrophobicity and biofilm formation in *C. albicans* (Silva-Dias et al., 2015). Also protein family is one of the most widely studied *C. albicans* virulence attributes and deletion of *als3* produces the greatest reduction in adhesive function. Moreover, als3 makes the largest contribution to adhesion to human cells (Lin et al., 2014). Those were consistent to our research findings. 27.9 and 14.0 mM Nspd had significantly decreased the expression of *csh1* (**Figure 3H**) resulting in obvious biomass volume reductions (**Figure 1A**). Our research also made an addition to the research of correlation between fungal hydrophobicity and biofilm metabolic activity in *C. albicans*, where Silva-Dias and co-workers did not find any correlation. Due to the difference in culture condition/substratum and fungal form, we were able to display a dramatic metabolic reduction in 27.9 and 14.0 mM Nspd groups where hydrophobicity had been down-regulated significantly (**Figure 2H**).

SEM images of mature *C. albicans* biofilm challenged by for 48h showed that there were less biofilms biomass and less proportion of hyphal formation. Silva-Dias claimed that yeast form of *C. albicans* had weaker adhesion than its hyphal form. This might explain our SEM and biomass findings. Challenged by Nspd, there were more yeasts (**Figure 3B**) than hyphae (**Figures 3A,G**) in *C. albicans* biofilm, confirmed by SEM observations; the biomass was less reduced at low Nspd dosage and at high dosage (**Figure 1A**).

Taken together, we claimed that Nspd was effective in treating a mature fungal biofilm via its downregulating on virulence related genes. In regenerative medicine and clinical practice, fungal related infection control often co-exists with the need for tissue regeneration. Stem cell therapy being one of promising cell source has become a research hot topic. The regenerative potential and clinical application of stem cells have been extensively studied. Accumulating evidence has proved that vascularization is an important step toward the success of tissue regeneration (Wang et al., 2010). Petri and co-works claimed that stem cell concentrates can be an alternative to segmental bone regeneration for long-bone defects are larger than 3 cm (Petri et al., 2013). Critical size long bone defect could be completely re-grown with the aid of vascularization. DPSCs were able to differentiate into functional endothelial cells. In this work, we aimed to test whether the presence of Nspd would affect the tissue regeneration potency of DPSCs.

DPSCs Identification and Lineage Differentiation

In order to identify DPSCs, flow cytometry and multilineage differentiation were performed. According to our result, DPSCs could express MSC-like marker CD73 and CD105, but negatively expressed CD34 and CD45, which is two of the surface markers of hematopoietic stem cells (**Figures 4A,B**). These data confirmed that DPSCs did have MSC-like immunophenotype. The results of multilineage differentiation confirmed a good regenerative potency upon adipogenic, osteogenic and chondrogenic inductions (**Figures 4C–E**).

DPSCs Could Proliferate and Differentiate Normally With the Presence of 0.63 mM Nspd

Fluorescent microscopic study on the DPSCs with the presence of Nspd showed that the morphology and vitality of the stem cells were not influenced compared with blank control (**Figures 5A,B**). Metabolic activity of DPSCs cultured with and without Nspd was revealed by MTT assay. In this study, we discovered that the metabolism of DPSCs were tolerant to Nspd at 0.63 mM and lower levels. When DPSCs were cultured with the highest tolerable 0.63 mM Nspd level, the vitality of DPSCs was reduced by 23.5% compared with that of the control. Although there was statistical difference between 0.63 mM group and control group ($p < 0.05$) (**Figure 5C**), the stem cells subject to 0.63 mM Nspd still held a fine vitality and proliferation ability. Cell viability varied with cell types. Cardile et al. reported that 1 mM Nspd reduced the viability of human keratinocytes to 70% and human fibroblasts to 80% compared with blank control in 24 h *in vitro* culture (Cardile et al., 2017). In our study, 1.25 mM Nspd reduced the viability of DPSCs to 60% compared with blank control, where it was significantly lower than that of 0.63 mM Nspd. 0.025 and 0.1 mM Nspd could inhibit some breast cancer cell lines in 24 h culture (Silva T. M. et al., 2013). Taken together, tissue cell tolerance of Nspd decreased in following order: fibroblasts > keratinocytes > DPSCs > some breast cancer cells.

Further, when DPSCs were undergone angiogenic differentiation, 0. 63 mM Nspd did not show obvious influence on differentiated cells and capillary-like network formation was observed (**Figure 6**). In both control and 0.63 mM Nspd groups, we could see well differentiate cells stretching and forming capillary-like structures in the co-cultured with GelMA hydrogels. Together, we defined a tolerable range of Npsd (0.63–0.08 mM) for *in vitro* cell culture of DPSCs; proved that DPSCs could be induced into endothelia like cells with the presence of Nspd at safe dosage.

Caries model experiment indicated that only small amounts of Nspd enter (significantly less than 0.63 mM) the pulp cavity (**Figures 7B,C**). Considering the clinical treatment will be taken to seal the dentinal tubules and other means, we assessed that Nspd application won't cause any side effect to pulp tissue regeneration.

CONCLUSION

Our project was the first to study the effect of Nspd on a 48 h old mature *C. albicans* biofilm with additional contribution to the mechanism study on the virulence characteristics of *C. albicans*. Our results showed that 111.7–14.0 mM Nspd showed a dose- inhibitory effect on this mature fungal biofilm. High concentration of Nspd (111.7 and 55.9 mM) inhibit the fungal viability in the mature biofilms and reduced the biomass and metabolic activity of these biofilms significantly. Medium concentration of Nspd (27.9 and 14.0 mM) displayed a moderate fungicidal effect and significantly suppressed the expression of virulence related genes. 111.7–27.9 mM Nspd restrained the production of hyphae form in mature biofilms. In biosafety study of Nspd with DPSCs, Nspd at 0.63 mM and lower was safe for DPSCs based angiogenic application. Based on our results, Nspd seemed to be a potential new drug against infections caused by *C. albicans* biofilms especially when dental pulp vitality or dental pulp regeneration was considered.

DATA AVAILABILITY STATEMENT

The raw data supporting the conclusions of this article will be made available by the authors, without undue reservation.

AUTHOR CONTRIBUTIONS

KZ, YH, and QY conceived the idea. The work was done by YH, YC, KZ, LL, YX, and FT. YZ, FH, AA, and ZX analyzed the data. KZ, QH, and QY discussed and interpreted the results. YH, YC, YS, and KZ wrote the manuscript. QH and QY critically revised the manuscript. All authors contributed to the article and approved the submitted version.

FUNDING

This project was funded by the National Natural Science Foundation of China (Nos. 81700960, 81701032, and 81871503), Zhejiang Provincial Natural Science Foundation of China (Nos. LGF19H140004 and LGF20H140001), and Wenzhou Technology Bureau Project (Nos. Y20190487 and Y20180163).

ACKNOWLEDGMENTS

We thank the Institute of Stem Cells and Tissue Engineering for providing SEM facility. We would also like to thank Wenzhou Medical University for providing CLSM facility and the technique help during Live/Dead staining work. The U-tooth Biotechnology Ltd. Co. is appreciated for providing technical support in culturing dental pulp stem cells.

REFERENCES

Bachtiar, E. W., Dewiyani, S., Akbar, S. M. S., and Bachtiar, B. M. (2016). Inhibition of *Candida albicans* biofilm development by unencapsulated *Enterococcus faecalis* 2. *J. Dent. Sci.* 11, 323–330. doi: 10.1016/j.jds.2016.03.012

Bjarnsholt, T., Alhede, M., Alhede, M., Eickhardt-Sørensen, S. R., Moser, C., Kühl, M., et al. (2013). The in vivo biofilm. *Trends Microbiol.* 21, 466–474. doi: 10.1016/j.tim.2013.06.002

Cardile, A. P., Woodbury, R. L., Sanchez, C. J. J., Becerra, S. C., Garcia, R. A., Mende, K., et al. (2017). Activity of norspermidine on bacterial biofilms of multidrug-resistant clinical isolates associated with persistent extremity wound infections. *Adv. Exp. Med. Biol.* 973, 53–70. doi: 10.1007/5584_2016_93

Chen, X., Zhang, T., Shi, J., Xu, P., Gu, Z., Sandham, A., et al. (2013). Notch1 signaling regulates the proliferation and self-renewal of human dental follicle cells by modulating the G1/S phase transition and telomerase activity. *PLoS One* 8:e69967. doi: 10.1371/journal.pone.0069967

Chen, Y. C., Lin, R. Z., Qi, H., Yang, Y., Bae, H., Melero-Martin, J. M., et al. (2012). Functional human vascular network generated in photocrosslinkable gelatin methacrylate hydrogels. *Adv. Funct. Mater.* 23, 2027–2039. doi: 10.1002/adfm.201101662

da Silva Dantas, A., Lee, K. K., Raziunaite, I., Schaefer, K., Wagener, J., Yadav, B., et al. (2016). Cell biology of *Candida albicans*–host interactions. *Curr. Opin. Microbiol.* 34, 111–118. doi: 10.1016/j.mib.2016.08.006

Davey, M. E., and O'toole, G. A. (2000). Microbial biofilms: from ecology to molecular genetics. *Microbiol. Mol. Biol. Rev.* 64, 847–867. doi: 10.1128/mmbr.64.4.847-867.2000

Feldman, M., Ginsburg, I., Al-Quntar, A., and Steinberg, D. (2016). Thiazolidinedione-8 alters symbiotic relationship in *C. albicans-S. mutans* dual species biofilm. *Front. Microbiol.* 7:140. doi: 10.3389/fmicb.2016.00140

Figueiredo, A. M., and Ferreira, F. A. (2014). The multifaceted resources and microevolution of the successful human and animal pathogen methicillin-resistant *Staphylococcus aureus*. *Mem. Inst. Oswaldo Cruz.* 109, 265–278. doi: 10.1590/0074-0276140016

Finkel, J. S., and Mitchell, A. P. (2011). Genetic control of *Candida albicans* biofilm development. *Nat. Rev. Microbiol.* 9, 109–118. doi: 10.1038/nrmicro2475

Hamana, K., Matsuzaki, S., Hosaka, K., and Yamashita, S. (1989). Interconversion of polyamines in wild-type strains and mutants of yeasts and the effects of polyamines on their growth. *FEMS Microbiol. Lett.* 61, 231–236. doi: 10.1016/0378-1097(89)90202-4

Hu, H., Li, C., Li, F., Chen, J., Sun, J., Zou, S., et al. (2013). Enamel etching for bonding fixed orthodontic braces. *Cochrane Database Syst. Rev.* 11:CD005516. doi: 10.1002/14651858.CD005516.pub2

Huo, L., Zhang, K., Ling, J., Peng, Z., Huang, X., Liu, H., et al. (2011). Antimicrobial and DNA-binding activities of the peptide fragments of human lactoferrin and histatin 5 against Streptococcus mutans. *Arch. Oral Biol.* 56, 869–876. doi: 10.1016/j.archoralbio.2011.02.004

Igarashi, K., and Kashiwagi, K. (2010). Modulation of cellular function by polyamines. *Int. J. Biochem. Cell Biol.* 42, 39–51. doi: 10.1016/j.biocel.2009.07.009

Ishchuk, O. P., Sterner, O., Strevens, H., Ellervik, U., and Manner, S. (2019). The use of polyhydroxylated carboxylic acids and lactones to diminish biofilm formation of the pathogenic yeast *Candida albicans*. *RSC Adv.* 9, 10983–10989. doi: 10.1039/C9RA01204D

Konai, M. M., Ghosh, C., Yarlagadda, V., Samaddar, S., and Haldar, J. (2014). Membrane active phenylalanine conjugated lipophilic norspermidine derivatives with selective antibacterial activity. *J. Med. Chem.* 57, 9409–9423. doi: 10.1021/jm5013566

Li, Y., Li, J., Yan, Y., Liu, W., Zhang, W., Gao, L., et al. (2018). Knock-down of CsNRT2.1, a cucumber nitrate transporter, reduces nitrate uptake, root length, and lateral root number at low external nitrate concentration. *Front. Plant Sci.* 9:722. doi: 10.3389/fpls.2018.00722

Lin, J., Oh, S. H., Jones, R., Garnett, J. A., Salgado, P. S., Rusnakova, S., et al. (2014). The peptide-binding cavity is essential for Als3-mediated adhesion of *Candida albicans* to human cells. *J. Biol Chem.* 289, 18401–18412. doi: 10.1074/jbc.M114.547877

Lin, M. Y., Yuan, Z. L., Hu, D. D., Hu, G. H., Zhang, R. L., Zhong, H., et al. (2019). Effect of loureirin A against *Candida albicans* biofilms. *Chin J. Nat. Med.* 17, 616–623. doi: 10.1016/S1875-5364(19)30064-0

Liu, S., Qiu, W., Zhang, K., Zhou, X., Ren, B., He, J., et al. (2017). Nicotine enhances interspecies relationship between *Streptococcus mutans* and *Candida albicans*. *Biomed. Res. Int.* 2017, 1–9. doi: 10.1155/2017/7953920

Luo, L., Albashari, A. A., Wang, X., Jin, L., Zhang, Y., Zheng, L., et al. (2018). Effects of transplanted heparin-poloxamer hydrogel combining dental pulp stem cells and bFGF on spinal cord injury repair. *Stem Cells Int.* 2018, 1–13. doi: 10.1155/2018/2398521

Lynch, A. S., and Robertson, G. T. (2008). Bacterial and fungal biofilm infections. *Annu. Rev. Med.* 59, 415–428. doi: 10.1146/annurev.med.59.110106.132000

Mayer, F. L., Wilson, D., and Hube, B. (2013). *Candida albicans* pathogenicity mechanisms. *Virulence* 4, 119–128. doi: 10.4161/viru.22913

Metwalli, K. H., Khan, S. A., Krom, B. P., and Jabra-Rizk, M. A. (2013). Streptococcus mutans, *Candida albicans*, and the human mouth: a sticky situation. *PLoS Pathog.* 9:e1003616. doi: 10.1371/journal.ppat.1003616

Morsczeck, C., Gotz, W., Schierholz, J., Zeilhofer, F., Kuhn, U., Mohl, C., et al. (2005). Isolation of precursor cells (PCs) from human dental follicle of wisdom teeth. *Matrix Biol.* 24, 155–165. doi: 10.1016/j.matbio.2004.12.004

Nam, H., Kim, G. H., Bae, Y. K., Jeong, D. E., Joo, K. M., Lee, K., et al. (2017). Angiogenic capacity of dental pulp stem cell regulated by SDF-1α-CXCR4 axis. *Stem Cells Int.* 2017, 1–10. doi: 10.1155/2017/8085462.8085462

Nesse, L. L., Berg, K., and Vestby, L. K. (2015). Effects of norspermidine and spermidine on biofilmformation by potentially pathogenic *Escherichia coli* and *Salmonella enterica* wild-type strains. *Appl. Environ. Microbiol.* 81, 2226–2232. doi: 10.1128/AEM.03518-14

Nobile, C. J., and Johnson, A. D. (2015). *Candida albicans* biofilms and human disease. *Annu. Rev. Microbiol.* 69, 71–92. doi: 10.1146/annurev-micro-091014-104330

Oredsson, S. M. (2003). Polyamine dependence of normal cell-cycle progression. *Biochem. Soc. Trans.* 31, 366–370. doi: 10.1042/bst0310366

Ou, M., and Ling, J. (2017). Norspermidine changes the basic structure of *S. mutans* biofilm. *Mol. Med. Rep.* 15, 210–220. doi: 10.3892/mmr.2016.5979

Peeters, E., Nelis, H. J., and Coenye, T. (2008). Comparison of multiple methods for quantification of microbial biofilms grown in microtiter plates. *J. Microbiol. Methods* 72, 157–165. doi: 10.1016/j.mimet.2007.11.010

Petri, M., Namazian, A., Wilke, F., Ettinger, M., Stübig, T., Brand, S., et al. (2013). Repair of segmental long-bone defects by stem cell concentrate augmented scaffolds: a clinical and positron emission tomography-computed tomography analysis. *Int. Orthop.* 37, 2231–2237. doi: 10.1007/s00264-013-2087-y

Qu, L., She, P., Wang, Y., Liu, F., Zhang, D., Chen, L., et al. (2016). Effects of norspermidine on *Pseudomonas aeruginosa* biofilm formation and eradication. *Microbiologyopen* 5, 402–412. doi: 10.1002/mbo3.338

Ramage, G., Vande, W. K., Wickes, B., and López-Ribot, J. L. (2001). Standardized method for in vitro antifungal susceptibility testing of *Candida albicans* biofilms. *Antimicrob. Agents Chemother.* 45, 2475–2479. doi: 10.1128/aac.45.9.2475-2479.2001

Raut, J. S., Shinde, R. B., Chauhan, N. M., and Karuppayil, S. M. (2013). Terpenoids of plant origin inhibit morphogenesis, adhesion, and biofilm formation by *Candida albicans*. *Biofouling* 29, 87–96. doi: 10.1080/08927014.2012.749398

Samaranayake, Y. H., Cheung, B. P., Parahitiyawa, N., Seneviratne, C. J., Yau, J. Y., Yeung, K. W., et al. (2009). Synergistic activity of lysozyme and antifungal agents against *Candida albicans* biofilms on denture acrylic surfaces. *Arch. Oral Biol.* 54, 115–126. doi: 10.1016/j.archoralbio.2008.09.015

Sangetha, S., Zuraini, Z., Suryani, S., and Sasidharan, S. (2009). In situ TEM and SEM studies on the antimicrobial activity and prevention of *Candida albicans* biofilm by *Cassia spectabilis* extract. *Micron* 40, 439–443. doi: 10.1016/j.micron.2009.01.003

Saville, S. P., Lazzell, A. L., Monteagudo, C., and Lopez-Ribot, J. L. (2003). Engineered control of cell morphology in vivo reveals distinct roles for yeast and filamentous forms of *Candida albicans* during infection. *Eukaryot Cell.* 2, 1053–1060. doi: 10.1128/ec.2.5.1053-1060.2003

Seleem, D., Benso, B., Noguti, J., Pardi, V., and Murata, R. M. (2016). In vitro and in vivo antifungal activity of lichochalcone-A against *Candida albicans* biofilms. *PLoS One* 11:e0157188. doi: 10.1371/journal.pone.0157188

Seneviratne, C. J., Silva, W. J., Jin, L. J., Samaranayake, Y. H., and Samaranayake, L. P. (2009). Architectural analysis, viability assessment and growth kinetics of *Candida albicans* and *Candida glabrata* biofilms. *Arch. Oral Biol.* 54, 1052–1060. doi: 10.1016/j.archoralbio.2009.08.002

Si, X., Quan, X., Li, Q., and Wu, Y. (2014). Effects of D-amino acids and norspermidine on the disassembly of large, old-aged microbial aggregates. *Water Res.* 54, 247–253. doi: 10.1016/j.watres.2014.02.007

Silva, S., Pires, P., Monteiro, D. R., Negri, M., Gorup, L. F., Camargo, E. R., et al. (2013). The effect of silver nanoparticles and nystatin on mixed biofilms of *Candida glabrata* and *Candida albicans* on acrylic. *Med. Mycol.* 51, 178–184. doi: 10.3109/13693786.2012.700492

Silva, T. M., Sara, A., Sunil, K. S., Maria, P. M., Lo, P., and Stina, O. (2013). Norspermidine and novel Pd (II) and Pt (II) polynuclear complexes of norspermidine as potential antineoplastic agents against breast cancer. *PLoS One* 8:e55651. doi: 10.1371/journal.pone.0055651

Silva-Dias, A., Miranda, I. M., Branco, J., Monteiro-Soares, M., Pina-Vaz, C., and Rodrigues, A. G. (2015). Adhesion, biofilm formation, cell surface hydrophobicity, and antifungal planktonic susceptibility: relationship among *Candida* spp. *Front. Microbiol.* 6:205. doi: 10.3389/fmicb.2015.00205

Solis, N. V., Park, Y. N., Swidergall, M., Daniels, K. J., Filler, S. G., and Soll, D. R. (2018). *Candida albicans* white-opaque switching influences virulence but not mating during oropharyngeal Candidiasis. *Infect. Immun.* 86, e774–e717. doi: 10.1128/IAI.00774-17

Soll, D. R., and Daniels, K. J. (2016). Plasticity of *Candida albicans* biofilms. *Microbiol. Mol. Biol. Rev.* 80, 565–595. doi: 10.1128/MMBR.00068-15

Srivastava, V., Singla, R. K., and Dubey, A. K. (2018). Emerging virulence, drug resistance and future anti-fungal drugs for *Candida pathogens*. *Curr. Top. Med. Chem.* 18, 759–778. doi: 10.2174/1568026618666180528121707

Sun, H., Wang, Y., Sun, C., Ye, Q., Dai, W., Wang, X., et al. (2014). Root morphology and development of labial inversely impacted maxillary central incisors in the mixed dentition: a retrospective cone-beam computed tomography study. *Am. J. Orthod. Dentofacial. Orthop.* 146, 709–716. doi: 10.1016/j.ajodo.2014.07.026

Sun, Y., Pan, Y., Sun, Y., Li, M., Huang, S., Qiu, W., et al. (2019). Effects of norspermidine on dual-species biofilms composed of *Streptococcus mutans* and *Streptococcus sanguinis*. *BioMed Res. Int.* 2019:1950790. doi: 10.1155/2019/1950790

Theiss, S., Ishdorj, G., Brenot, A., Kretschmar, M., Lan, C. Y., Nichterlein, T., et al. (2006). Inactivation of the phospholipase B gene PLB5 in wild-type *Candida albicans* reduces cell-associated phospholipase A2 activity and attenuates virulence. *Int. J. Med. Microbiol.* 296, 405–420. doi: 10.1016/j.ijmm.2006.03.003

Tobudic, S., Kratzer, C., Lassnigg, A., and Presterl, E. (2012). Antifungal susceptibility of *Candida albicans* in biofilms. *Mycoses* 55, 199–204. doi: 10.1111/j.1439-0507.2011.02076.x

Uppuluri, P., Srinivasan, A., Ramasubramanian, A., and Lopez-Ribot, J. L. (2011). Effects of fluconazole, amphotericin B, and caspofungin on *Candida albicans* biofilms under conditions of flow and on biofilm dispersion. *Antimicrob. Agents Chemother.* 55, 3591–3593. doi: 10.1128/AAC.01701-10

Van, D. P., Sjollema, J., Cammue, B. P., Lagrou, K., Berman, J., d'Enfert, C., et al. (2018). Methodologies for in vitro and in vivo evaluation of efficacy of antifungal and antibiofilm agents and surface coatings against fungal biofilms. *Microb. Cell* 5, 300–326. doi: 10.15698/mic2018.07.638

Vesely, E. M., Williams, R. B., Konopka, J. B., and Lorenz, M. C. (2017). N-acetylglucosamine metabolism promotes survival of *Candida albicans* in the phagosome. *mSphere* 2:e00357-17. doi: 10.1128/mSphere.00357-17

Vikas, B., Anil, S., and Remani, P. (2019). Cytotoxicity profiling of annona squamosa in cancer cell lines. *Asian Pac. J. Cancer Prev.* 20, 2831–2840. doi: 10.31557/APJCP.2019.20.9.2831

Wang, L., Fan, H., Zhang, Z. Y., Lou, A. J., Pei, G. X., Jiang, S., et al. (2010). Osteogenesis and angiogenesis of tissue-engineered bone constructed by prevascularized β-tricalcium phosphate scaffold and mesenchymal stem cells. *Biomaterials* 31, 9452–9461. doi: 10.1016/j.biomaterials.2010.08.036

Wu, H., Moser, C., Wang, H. Z., Høiby, N., and Song, Z. J. (2015). Strategies for combating bacterial biofilm infections. *Int. J. Oral Sci.* 7, 1–7. doi: 10.1038/ijos.2014.65

Wu, Y., Quan, X., Si, X., and Wang, X. (2016). A small molecule norspermidine in combination with silver ion enhances dispersal and disinfection of multi-species wastewater biofilms. *Appl. Microbil. Biotechnol.* 100, 5619–5629. doi: 10.1007/s00253-016-7394-y

Yang, X. Q., Zhang, Q., Lu, L. Y., Yang, R., Liu, Y., and Zou, J. (2012). Genotypic distribution of *Candida albicans* in dental biofilm of Chinese children associated with severe early childhood caries. *Arch. Oral Biol.* 57, 1048–1053. doi: 10.1016/j.archoralbio.2012.05.012

Yao, L., and Flynn, N. (2018). Dental pulp stem cell-derived chondrogenic cells demonstratedifferential cell motility in type I and type II collagen hydrogels. *Spine J.* 18, 1070–1080. doi: 10.1016/j.spinee.2018.02.007

Conflict of Interest: The authors declare that the research was conducted in the absence of any commercial or financial relationships that could be construed as a potential conflict of interest.

frontiers
in Bioengineering and Biotechnology

REVIEW
published: 14 August 2020
doi: 10.3389/fbioe.2020.00926

Recent Advances on Synthetic and Polysaccharide Adhesives for Biological Hemostatic Applications

Dawei Li[1]†, Jing Chen[2]†, Xing Wang[3,4]*, Mingming Zhang[5], Chunlin Li[1] and Jin Zhou[1]*

[1] Eighth Medical Center of the General Hospital of the Chinese People's Liberation Army, Beijing, China, [2] Department of Orthopedics, Aerospace Center Hospital, Beijing, China, [3] Beijing National Laboratory for Molecular Sciences, Institute of Chemistry, Chinese Academy of Sciences, Beijing, China, [4] University of Chinese Academy of Sciences, Beijing, China, [5] The People's Liberation Army Strategic Support Force Characteristic Medical Center, Beijing, China

OPEN ACCESS

Edited by:
Bing Han,
Peking University School and Hospital of Stomatology, China

Reviewed by:
Yun-Long Wu,
Xiamen University, China
Dawei Liu,
Peking University School and Hospital of Stomatology, China
Peng Sun,
Tsinghua University, China

***Correspondence:**
Xing Wang
wangxing@iccas.ac.cn
Jin Zhou
huoshan1975@sina.com

†These authors have contributed equally to this work

Specialty section:
This article was submitted to Biomaterials, a section of the journal Frontiers in Bioengineering and Biotechnology

Received: 14 June 2020
Accepted: 20 July 2020
Published: 14 August 2020

Citation:
Li D, Chen J, Wang X, Zhang M, Li C and Zhou J (2020) Recent Advances on Synthetic and Polysaccharide Adhesives for Biological Hemostatic Applications. Front. Bioeng. Biotechnol. 8:926. doi: 10.3389/fbioe.2020.00926

Rapid hemostasis and formation of stable blood clots are very important to prevent massive blood loss from the excessive bleeding for living body, but their own clotting process cannot be completed in time for effective hemostasis without the help of hemostatic materials. In general, traditionally suturing and stapling techniques for wound closure are prone to cause the additional damages to the tissues, activated inflammatory responses, short usage periods and inevitable second operations in clinical applications. Especially for the large wounds that require the urgent closure of fluids or gases, these conventional closure methods are far from enough. To address these problems, various tissue adhesives, sealants and hemostatic materials are placed great expectation. In this review, we focused on the development of two main categories of tissue adhesive materials: synthetic polymeric adhesives and naturally derived polysaccharide adhesives. Research of the high performance of hemostatic adhesives with strong adhesion, better biocompatibility, easy usability and cheap price is highly demanded for both scientists and clinicians, and this review is also intended to provide a comprehensive summarization and inspiration for pursuit of more advanced hemostatic adhesives for biological fields.

Keywords: hemostatic, hydrogel, adhesives, polysaccharides, tissue regeneration

INTRODUCTION

Traumatic closure, wound repair and regeneration of surgical damaged soft tissues often occur medically. Uncontrolled bleeding, as a main cause of trauma-related deaths, frequently occurs on the battlefield and in the operating room. It is reported that 50% of military deaths stem from the bleeding (Behrens et al., 2014). In general, coagulation is a complicated process of plasma transformation from an unstable platelet plug to stable and insoluble fibrin. At the initial stage, formation of initial platelet plug can bind to the injured endothelium to achieve the stable adhesion and trigger the aggregation of locally activated platelets to form a hemostatic plug and stop the bleeding. Then, coagulation cascade, including intrinsic and extrinsic coagulation pathways with start-up modes and contributory coagulation factors, is activated immediately to accomplish hemostasis. Although body's own coagulation process played important roles in preventing the excessive bleeding from the death, formation of stable blood clots or insoluble fibrin including primary hemostasis and clotting cascades process are always required a long time to accomplish the hemostasis. In other words, without the assistance of hemostatic devices and hemostatic agents, hemostasis cannot be timely conducted especially in emergency situations. Traditionally, sutures and staples are two main methods of achieving wound closure or implant fixation, whereas they can easily cause the additional trauma, leakage and lack of tissue integration due to the obviously inherent mismatch between body tissues and fixture compliances (Ghobril and Grinstaff, 2015).

Hemostatic agents, sealants, adhesives and their compositions shall meet a wide range of requirements. In 2008, safety, efficacy, usability, cost, and Food and Drug Administration (FDA) approval are required as five main necessities for use all over the world (Spotnitz and Burks, 2008, 2010), and other specific requirements like biodegradability, biocompatibility, mechanics, swelling ratio, stability, qualified water tightness, adjustable adhesion, and enhanced ability of healing process through the delivery of growth factors or active drugs are also be focused for actual usage. Accordingly, ideal hemostatic agents should simultaneously have abilities with rapid hemostasis, good biocompatibility, well-matched degradation, no adverse effects on wound healing and conducive to accelerating the healing process (Howe and Cherpelis, 2013; Qin et al., 2015; Dowling et al., 2016; Momeni and Filiaggi, 2016). Furthermore, the important issues of quality, manufacturing cost, stability, swelling rate, safety and adjustable mechanics should also be considered and addressed (Hsu et al., 2015).

Until now, a varied of polysaccharide-derived hemostatic materials, like fibrinogen, albumin, thrombin, gelatin, collagen, chitosan, cellulose, dextran alginate, starch, and hyaluronic acid, have been well-developed as local hemostatic agents, tissue adhesives and sealants in biomedical fields (Low et al., 1993; Liu, 2000; Milkes et al., 2002; Hung-Hsing and David, 2003; Oz et al., 2003; Sabel and Stummer, 2004; Liu et al., 2005; Lew and Weaver, 2008; Azargoon et al., 2011; Pozza and Millner, 2011; Rajagopal and Hakim, 2011; Fortelny et al., 2012; Vyas and Saha, 2013; Behrens et al., 2015; Zeng et al., 2016). While the synthesized hemostatic materials of isocyanate, polyethylene glycol and catechol monomers exhibit favorable adhesion and antibacterial properties for wide applications (Napoleone et al., 2009; Bochyńska et al., 2013; Boerman et al., 2017). In addition, some inorganic hemostatic materials including kaolin, mineral zeolite, montmorillonite, and bioactive glass are attributed to their high pore structure and fast water absorption (Gerlach et al., 2010; Ran et al., 2010; Arnaud et al., 2011; Pourshahrestani et al., 2016). So far, biodegradable self-assembling peptide hydrogels are another kind of hemostasis that possess a similar morphology to fibrin clots for capturing the blood components (Saini et al., 2016). Although there are a series of synthetic polymer and polysaccharide-based hemostatic materials on the market (**Table 1**), some important issues of biosafety, hemostatic effect and high cost still greatly limit their widespread biomedical applications. For instance, famous blood functional components of fibrinogen and thrombin, biologically derived hemostatic agents, have expensive costs, short-shelf life, and potential side-effects of virus contamination (DeAnglis et al., 2017). For the synthetic adhesives, some obvious disadvantage of non-biodegradability and potential cytotoxicity should be issued as applied in clinical use. For inorganic hemostatic materials, high exothermic reactivity and poor biodegradability can easily cause thermal damage and inflammatory reactions for the clinical patients.

In the present review, we will describe the current polymeric adhesives and hemostatic sealant in surgical toolkits including the commercially available materials and recently reported adhesives in literatures for wound closure as well as their respective advantages and drawbacks. From a point of view of polymer chemistry, polymeric hemostatic materials will be divided into two categories: synthetic adhesive (polycyanoacrylates, poly(ethylene glycol), polyurethanes and polyesters) and polysaccharide (chitosan, cellulose, alginate, hyaluronic acid, starch, and chondroitin). Although we are intended to quantitatively compare these various biomaterials, unfortunately many reports are only provided with the qualitative results at various test conditions. Therefore, the purpose of this review is to highlight the scientific progress over the years and further summarize the surgical applications of most crucial adhesives and sealing biomaterials from the synthetic and polysaccharide adhesives, thereby proposing the importance, necessity and urgency of continuous research of advanced bio-adhesives for the biological hemostatic applications.

SYNTHETIC POLYMERS-BASED HEMOSTATIC ADHESIVES

Polycyanoacrylates

Cyanoacrylate-derived tissue adhesives are a series of synthetic sealants with instantaneously strong adhesion force and rapid adhesive time, which are simply polymerized at room temperature without any harsh conditions of solvent, heating, light, catalyst, pressure, etc. In this process, cyanoacrylates can be easily generated within seconds by exposure to a small amount of water to initiate the polymerization and form strong bond interactions to yield polycyanoacrylate adhesives in a single-component system. The mechanism of the cyanoacrylate tissue adhesion is ascribed to the rapid formation of covalent bonds between the cyanoacrylate and amine groups within the tissue proteins (e.g., primary amine of lysine). As it is applied to tissues, cyanoacrylate monomer will penetration into cracks of tissue surface in order that a firm bond between the tissue and the glue is rapidly formed. In addition, mechanical interlocking force between the cyanoacrylate glue and tissues also plays vital roles in strength enhancement. Importantly, these cyanoacrylate adhesives are even useful on the moist and porous substrates (Tseng et al., 1990; Celik et al., 1991; Evans et al., 1999; Fortelny et al., 2007).

However, fast degradation of polycyanoacrylates via the hydrolysis effects generates a lot of toxic products (cyanoacetate and formaldehyde) that can result in severely inflammatory responses and wound infection for the cells and tissues (Trott, 1997). The degradation rate decreases with steric hindrance of long alkyl chains of cyanoacrylate polymers (**Figure 1**), and thus shorter chains of polycyanoacrylate derivatives can cause higher concentrations of toxic products for endanger

TABLE 1 | Commercially available synthetic polymer and polysaccharide-based tissue adhesives.

Commercial Product	Approved Indications	Constituents
FocalSeal-L (Focal Inc.), replaced AdvaSeal (Sawhney et al., 1993)	Sealing lung air leaks	Photopolymerizable PEG-co-poly (lactic acid)/poly(trimethy lene carbonate)
DuraSeal (Covidien), DuraSeal Xact (Preul et al., 2003; Cosgrove et al., 2007)	Adjunct to sutures for dural repair; anti-adhesion (SprayShield); retina reattachment; nerve sciatic anastomosis; vascular closure	Tetra-NHS- PEG and trilysine
CoSeal (Cohesion Technologies) (Wallace et al., 2001)	Adjunct hemostasis in vascular surgery; inhibiting suture line bleeding	Tetra-NHS-PEG and tetra-SH-PEG
SprayGel (Covidien) (Dunn et al., 2001b; Ferland et al., 2001; Johns et al., 2003)	Adhesion barrier in gynecological and colorectal procedures	Tetra-NHS-PEG and tetra-NH_2-derivatized PEG
TissuGlu® (Gilbert et al., 2008)	Prevention of seroma formation under skin flaps	Lysine di/tri isocyanate-PEG polymers
TissuePatch (TissueMed) (Kettlewell et al., 2007; von der Brelie et al., 2012; Ferroli et al., 2013)	Air leakage in thoracic surgery; sealing and reinforcing soft tissues adjunct to sutures; dural repair in cranial surgery, adjunct to sutures	Poly-((N-vinylpyrrolidone)$_{50}$-co-(acrylic acid)$_{25}$-co-(acrylic acid N-hydroxysuccin imide ester)$_{25}$)
HemCon Bandage Pro (Jayakumar et al., 2011)	Hemostasis; antibacterial barrier	Chitosan
Commercially unavailable (Ono et al., 2000; Ishihara, 2002; Ishihara et al., 2002)	Sealing suture lines in aorta and intestine; incision sealing in trachea	2% of amines of chitosan substituted lactobionic acid, p-azido-benzoic acid
Actamax (Bhatia et al., 2007b)	Adhesion prevention; tissue sealing	Dextran aldehyde, 8-arm-NH_2-PEG functionalized with tris(2-aminoethyl) amine
CS Glue (commercially unavailable) (Wang et al., 2007)	Connecting biomaterial to cartilage	Chondroitin sulfate functionalized with both aldehyde and acrylate groups

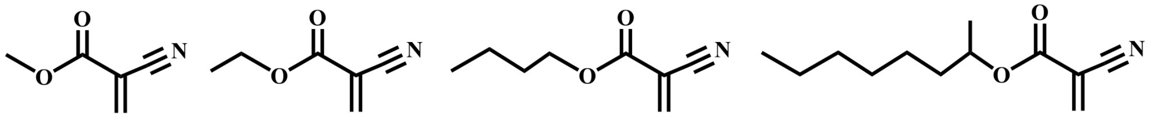

FIGURE 1 | Cyanoacrylate monomers for tissue adhesives, including methyl-cyanoacrylate, ethyl-cyanoacrylate, butyl cyanoacrylate and octyl cyanoacrylate. Reproduced from Singer et al. (2008) with permission from Copyright 2008 Elsevier.

the human health. Besides, polymercyanoacrylate adhesives possess weak mechanical strength, for example, the ethyl- and butyl-cyanoacrylates become brittle and fragile after the polymerization, which cannot be suitable for the use of long incisions or skin creases (Singer et al., 2008; Dragu et al., 2009).

Although some cyanoacrylate tissue adhesives are approved by FDA and commercially used for the closure of a local skin incision and barrier of a microbial penetration, they remain the inflammatory responses that may inhibit the collagen reconstruction and wound repair (Montanaro et al., 2001; Singer et al., 2008; Bhatia, 2010).

Poly(ethylene glycol)

Poly(ethylene glycol) (PEG) is hydrophilic and biocompatible polymer with a stealth-like behavior *in vivo*, and can be employed as another important class of tissue adhesives (Knop et al., 2010; Wang et al., 2015, 2018; Cao et al., 2018; Bian et al., 2020; Li et al., 2020; Tang et al., 2020; Yu et al., 2020). There are three main kinds of PEG-based tissue adhesives, including the photopolymerizable adhesives (FocalSeal®, successor of AdvaSeal), PEG-trilysine adhesives (DuraSealTM) and functionalized PEG with two component adhesives (CoSeal®, SprayGel). The first PEG-based adhesive consists of an ABA-triblock polymer, wherein PEG block is middle and poly(lactic acid) (PLA) or poly(glycolic acid) (PGA) blocks are outer via ring opening polymerization of lactide or glycolide with a bifunctional PEG macroinitiator in **Figure 2A**, followed by the end-functionalized modification of photopolymerizable acrylate moieties. In aqueous solutions, these copolymers self-assemble into the micellar gels, enabling the fast photopolymerization due to the high density of acrylate concentrations within the hydrophobic area. Although this hydrogel is non-adhesive to tissues, it still exhibits strong adhesion even on the smooth surface, which ascribes to the creation of interpenetrating networks with the tissue proteins and generation of an adhered complex after the direct polymerization in contact to tissue.

Based on the self-assembly principle in aqueous solutions, FocalSeal® is approved as a commercial sealant by the FDA in 2000 to seal air leaks after the lung surgery (Anonymous and Confluent Surgical Inc, 2004). To improve its mechanical properties, a second ABA triblock copolymer of poly(trimethylene carbonate) (PTMC)-PEG-PTMC is added (**Figure 2B**) to form the hydrogels by crosslinking acrylate groups with more than 80 wt% of water content after the photopolymerization (Macchiarini et al., 1999; Anonymous and Focal Inc, 2000; Quinn, 2005). After the hydrolysis of ester bonds and degradation of sealant hydrogels, the degraded products of LA and PEG are released, metabolized and cleared through the kidneys (Macchiarini et al., 1999). Furthermore, other PEG sealants are also reported according to the same principle, such

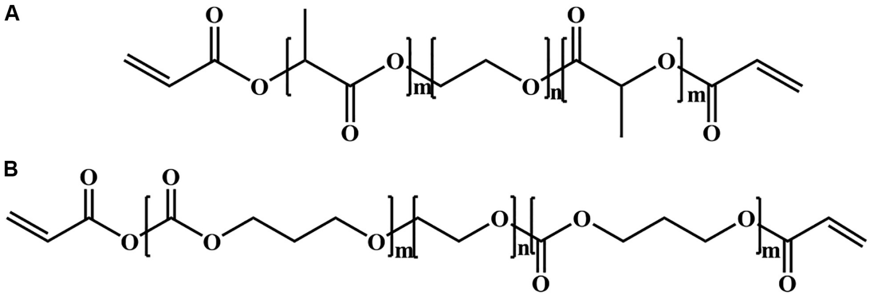

FIGURE 2 | Two different building blocks of photopolymerizable copolymer for PEG photopolymerizable tissue adhesives with **(A)** PLA-PEG-PLA and **(B)** PTMC-PEG-PTMC diacrylates.

as poly(propylene fumarate) (PPF)-PEG-PPF, poly(succinic acid) (PSA)-PEG-PSA, etc. (Suggs et al., 1998; Tanaka et al., 1999; Nivasu et al., 2004). However, on account of the irradiation condition for these PEG photopolymerizable tissue adhesives, they are not fully safe for usage *in vivo* and not widespread securely. Also, these produced free radicals in the polymerization may bring about unknown hazard and side reaction to the tissues.

The second PEG-based tissue adhesive, known as DuraSealTM Dural Sealant device, is first used to prevent cerebrospinal fluid (CSF) leakage for the cranial surgery (Cosgrove et al., 2007). DuraSeal is formed as two varied components are touched, which is composed of a tetra-amine crosslinker of trilysine at a dissolved sodium borate buffer (pH 10.2) and a tetra-armed PEG (M_n = 10 kDa) capped with N-hydroxy succinimide-esters (NHS) in a sodium phosphate buffer (pH 4.0) in **Figure 3**. As two components are simultaneously sprayed to the tissues, amine groups of trilysine are quickly reacted with NHS groups to generate amide bonds crosslinked network (**Figure 4**). Notably, upon application of this DuraSeal adhesive to the tissues, the amine and thiol groups of proteins in tissue surface can also simultaneously react with NHS-functionalized polymer, generating the strong covalent adhesion to the tissues (Boogaarts et al., 2005).

Similarly, along with the ester hydrolysis and the enzymatic degradation of lysine ingredients, DuraSealTM can degrade after 4–8 weeks with the removal of degradation byproducts through the renal clearance from the body (Ghobril and Grinstaff, 2015). However, the drawback of these tissue adhesives is high swelling ratio that may hinder the use in bone regeneration because of the potential oppression to the nerves (Lee et al., 2010). A modified two compound adhesive DuraSealTM of Xact Adhesion Barrier and Sealant System can decrease the swelling behaviors by inserting more crosslinkers to change ratio of PEG versus trilysine and obtain a higher crosslinking degrees (Anonymous and Confluent Surgical Inc, 2009). A inconvenient downside of DuraSeal is the required two-component design that can easily cause the syringe clogging in the mixed component process if these tissue adhesives are not applied immediately enough.

The third PEG-based adhesive is another two-component tissue sealant of PEG-PEG adhesives, analogous to CoSeal® Surgical Sealant. It is composed of a 20% (w/v) solution of a tetra-PEG-SH in a pH 9.6 of sodium phosphate/sodium carbonate buffer and a second 20% (w/v) solution of a tetra-PEG-NHS in pH 6.0 of sodium phosphate buffer in **Figure 5** (Goode et al., 2001). Once mixing these two PEG solutions, thiol can react with NHS groups to generate a thioester bond and form a well-organized crosslinked network within 3 s along with the simultaneous formation of a small number of disulfide linkages. During this process, a transamidation reaction occurs between amines and thioesters to form the covalent bonds in the tetra-PEG network between the adhesives and tissues (Wallace et al., 2001). Noted that even though the CoSeal® adhesive is applied onto the non-reactive surfaces, the produced adhesions are still highly stiff because the permeation of liquids flow into the crack and fracture of materials. The degradation time of this hydrogel was within several weeks due to the hydrolysis of glutarate esters and thioesters (Goode et al., 2001). Compared to the DuraSeal with amide bonds, faster degradation ascribes to the unstable thioester groups. However, this PEG-PEG hydrogel still possesses high swelling ratio and relatively weak adhesion to the surrounding tissues (Saunders et al., 2009). SprayGel adhesion barrier system is another developed example of PEG-PEG sealants, which is also composed of two reactive tetra-PEG-NHS and tetra-PEG-NH_2 solutions. Once mixing two solutions together, the adhesives are also quickly formed and degraded after 5–7 days with the excretion to outside of body by the renal clearance (Dunn et al., 2001a; Ferland et al., 2001; Johns et al., 2003).

Polyurethanes

These synthetic polyurethanes are widely applied for various adhesives due to the excellent thermal stability in the physiological temperature and the absence of hemolysis (Ferreira et al., 2007), wherein TissuGlu® is a popularly surgical adhesive to bind abdominal tissues. However, a common side effect of abdominal surgery is a subcutaneous effusion under the skin to cause the seroma, which requires to drain regularly to clear fluids. In general, the abdominal skin must be reattached to the underlying layer during the abdominal surgery, but meanwhile an imperfect connection may cause the gaps between the subcutaneous tissues and the skins. Postoperative effusion may ascribe to the presence of this cavity.

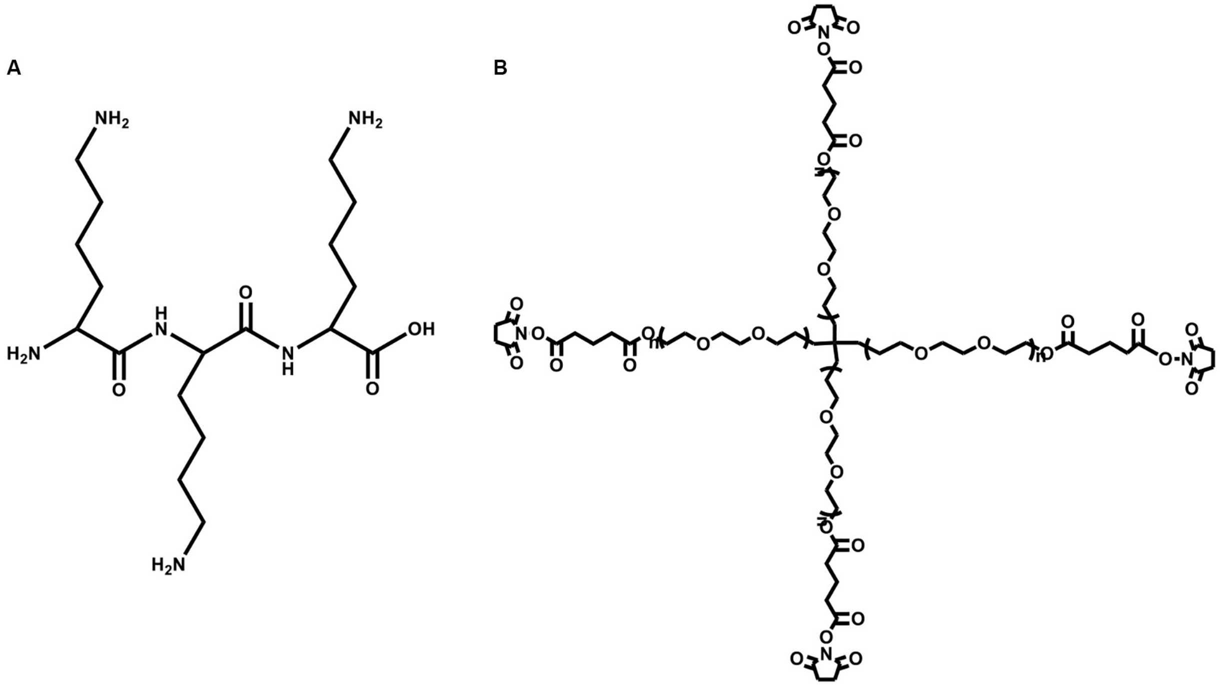

FIGURE 3 | The structures of **(A)** trilysine and **(B)** pentaerythritol poly(ethylene glycol) ether succinimidyl glutarate.

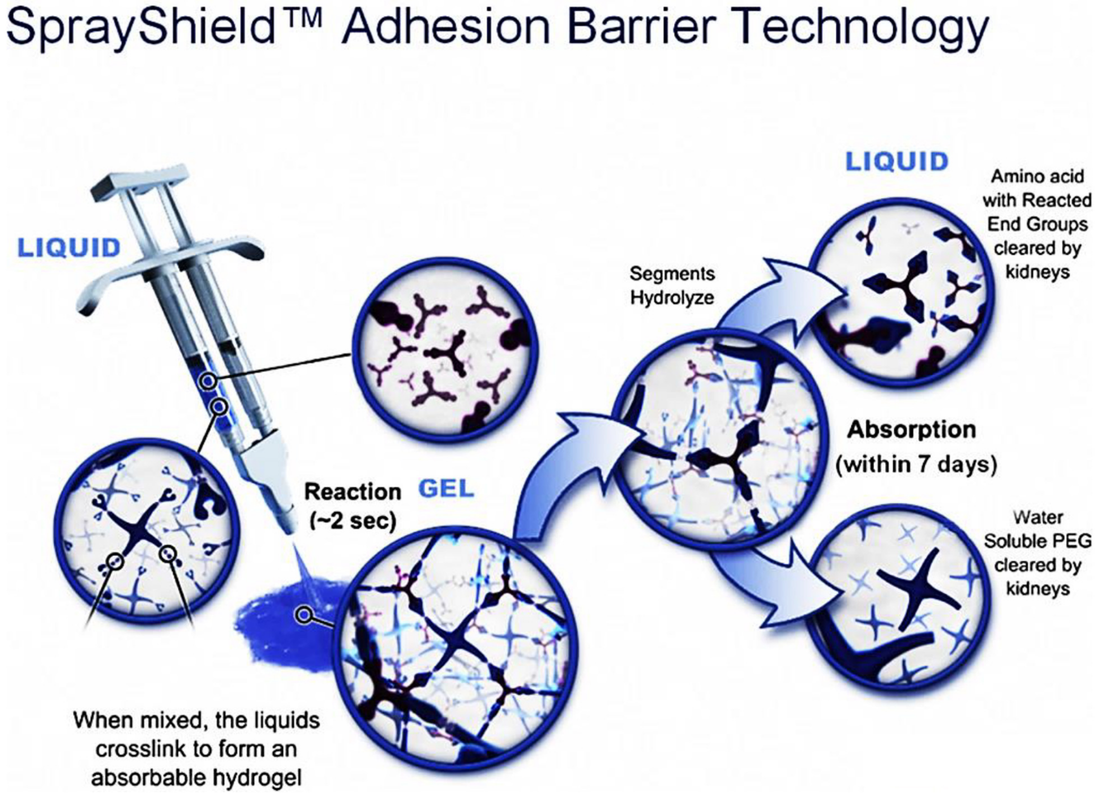

FIGURE 4 | A schematic overview of DuraSealTM with a two-component system of tetra-PEG and trilysine. Reproduced from Ghobril and Grinstaff (2015) with permission from Copyright 2015 Royal Society of Chemistry.

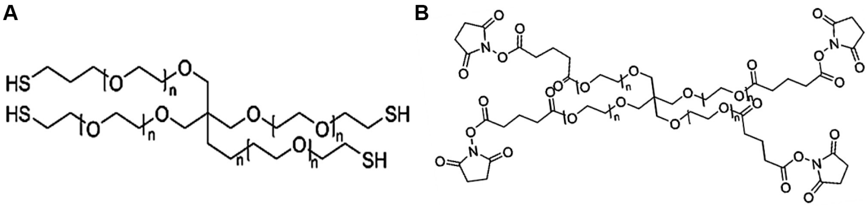

FIGURE 5 | The chemical structures of **(A)** pentaerythritol poly(ethylene glycol) ether tetrathiol and **(B)** pentaerythritol poly(ethylene glycol) ether tetrasuccinimidyl glutarate.

As a result, TissuGlu® adhesive are widely used to shorten the space cavities via the formation of a bond among these tissue layers (Gilbert et al., 2008).

TissuGlu® surgical adhesive consists of a hyperbranched macromolecules with isocyanate groups and ca. 50 wt% of lysine, and the polyurethane prepolymer can be generated via an organized combination of lysine diisocyanate and triisocyanate with diols and polyols (Beckman, 2011). When this prepolymer is touched with water within the tissue, it hydrolyzes into an amine through the isocyanate group and reacts with the surplus isocyanates to construct the crosslinking networks through the urethane bonds, which requires as long as 25 min to provide enough surgeons time to close the abdominal skin. On account of the hydrolysis effect and enzymatic degradation of lysine-based bonds, this surgical adhesive can give rise to many byproducts of glycerol, lysine, ethanol, and carbon dioxide with the ready clearness from the body. Trials on human patients have shown that TissuGlu® adhesive is biocompatible enough to achieve the reduction of fluid accumulation extents (Walgenbach et al., 2012; Ohlinger et al., 2018). Afterward, a new single component of Sylys® surgical sealant is developed using the urethane chemistry by Cohera Medical Inc., which can provide supports after anastomosis to prevent the leakage.

Polyurethanes can also be widely applied for the wound hemostasis, bone fixation and vascular graft sealants (Lipatova, 1986; Phaneuf et al., 2001; Ferreira et al., 2008b). Since vascular graft can slightly permeate into the blood and induce the leak to the whole body, these polyurethane sealants are required to tight the water for actual applications. For example, a polyurethane product has been prepared by the reaction of 4,4-diphenylmethane diisocyanate (MDI) and poly(tetramethylene ether glycol) (PTMEG) followed by adding the 2,2-bis(hydroxymethyl)-propionic acid (DHMPA) in **Figure 6** (Phaneuf et al., 2001). Besides, the sealant should also be bound with proteins within the bloodstream to provide the effective blood-biomaterial interactions. To date, no vivo papers are yet demonstrated, which may ascribe to the accumulation problem of hydrophobic and stable character of PTMEG *in vivo*.

Polyesters

Aliphatic polyesters like polycaprolactone (PCL) and polylactic acid-glycolic acid (PLGA) are significantly applied as tissue adhesives for various biomedical applications. Ferreira et al. (2008b) functionalized PCL with isophorone diisocyanate (IPD) and hexamethyldiisocyanate (HDI) to obtain several tissue reactive polymers. After placing them between two gelatin pieces and separating gelatin sheets, the adhesive tests found that the IPD-modified PCL can effectively bind to the gelatin parts without affecting the adhesive sections. However, HDI-modified PCL exhibited failure adhesive properties because of lower NCO concentration within polymers (Ferreira et al., 2008b). Besides for the dependence on the chain entanglements of linear chains, the absence of crosslinks was the main reason for the potential limitation. Although some adhesive strength of PCL-based materials had been developed by means of strong interpenetration between the polymeric crosslinking networks and the tissues, few literatures of *in vivo* tests are reported so far (Ferreira et al., 2008a).

Two examples of PLGA-based adhesives are so-called TissuePatchTM for the prevention of air leakage after lung surgery and TissuePatchDuralTM for the prevention of fluid leakage after brain surgery (von der Brelie et al., 2012; Ferroli et al., 2013). These adhesive patches are composed of poly((N-vinylpyrrolidone)$_{50}$-(acrylic acid)$_{25}$-(acrylicacid NHS-ester)$_{25}$) and PLGA with multiple layers. TissuePatchTM contains four layers, of which the second and third layers are NHS-functional polymers, and the first and fourth layers are PLGA, interspersed with NHS functional polymers (Kettlewell et al., 2007). As this adhesive patch is attached to the tissue proteins, it can be reacted with the amine to form an amide bond between the patch and tissue within a minute. The adhesive tape can degrade after the hydrolysis of amide bond and PLGA *in vivo* for 50 days (Della Puppa et al., 2010). The main advantage is ease of use without tedious preparation before the operation.

POLYSACCHARIDE-BASED HEMOSTATIC ADHESIVES

Polysaccharides are a kind of naturally derived polymers with sugar building blocks, which possess more exceptional advantages on the rich source of naturally raw materials, biodegradability, biosafety, good biocompatibility, no immune response or histologic reaction *in vivo*, etc. More importantly, these polysaccharide-based biomaterials can be feasibly synthesized and modified through simple physical and chemical methods for the hemostatic applications (Basu et al., 2015). Early in 1940s, Frantz (1948) prepared a locally absorbable hemostatic agent by oxidizing the cellulose, and then developed hemostatic alginate agents. Afterward, with the development of

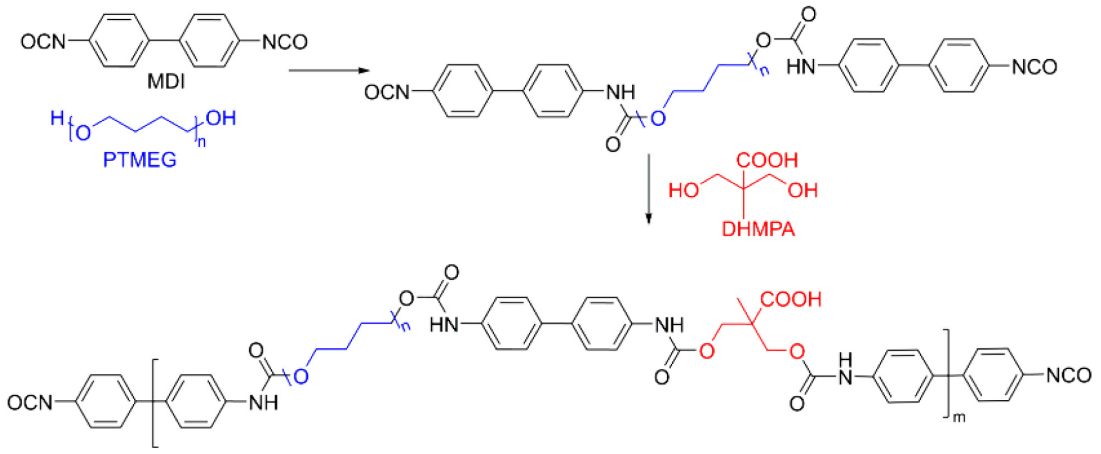

FIGURE 6 | A typical polyurethane with the main components of MDI (black), PTMEG (blue), and DHMPA (red). Reproduced from Phaneuf et al. (2001) with permission from Copyright 2001 Elsevier.

TABLE 2 | Polysaccharide-based hemostatic adhesives.

Main component	Active ingredients	Clotting mechanism
Chitosan (Malette et al., 1983)	Positive amino groups	Adsorb positively charged platelets and red blood cells
Cellulose (Cheng et al., 2013)	Carboxyl groups	Binding iron ions in hemoglobin, activation of clotting factor VIII and promote platelet adhesion
Dextran (Bouten et al., 2014)	Hydroxyl in the ortho	Provide polyaldehyde seats
Alginate (Hama et al., 2010)	Linear polysaccharides	Rapid glue formation with tissue adhesion
Starch (Antisdel et al., 2009)	Polydextrose with numerous hydroxyl groups	Rapid water absorption and platelet coagulation
Hyaluronic acid (An et al., 2019)	Acid mucopolysaccharide	Carry a lot of water

science and technology in the clinic field, polysaccharide-based biomaterials have produced a series of hemostatic agents tissue adhesives and sealants with good biosafety and biodegradability *in vivo* (Lewis et al., 2015). In this section, we will investigate and discuss some typical polysaccharide-based materials like chitosan, cellulose, alginate, hyaluronic acid and starch for the hemostatic applications (**Table 2**).

Chitosan

Chitosan (CS), a positively charged polysaccharide from chitin deacetylation, has greatly applied values in the biomedical fields owing to its good biodegradability, non-toxicity, antibiosis and non-antigenicity (Liu et al., 2020). In the 1980s, Malette et al. (1983) used the chitosan powders to apply for the hemostasis of open wounds due to the electrostatic interaction with the erythrocytes and manual compression to accelerate blood clotting (Brandenberg et al., 1984). FDA has approved two hemostatic agents of CloSur PAD and Hemcon chitosan, which can stop blood loss via the platelet aggregation effects (Lan et al., 2015; Kavitha Sankar et al., 2017). It is mentioned that varied degrees of deacetylation (DDA) and molecular weights (Mw) of chitosan display distinct hemostatic properties, so a mixed component of chitosan with variational DDA (75–88%) and Mw (8.6–247 kDa) is generally required (Hattori and Ishihara, 2015). Although chitosan hemostasis can accelerate erythrocyte adhesion and platelet activation, they also restrain the activation of contact system that is related to the intrinsic coagulation cascade and eventual thrombin formation, just like a double-edged sword in the hemostatic application (He et al., 2013).

On account of the high reactive amine groups within the chitosan backbone, CS is easily modified for improving the hemostatic efficacy (Yang et al., 2018). Dowling et al. (2016) synthesized the dodecyl-modified chitosan (HM-CS) via reacting with the amino groups. Dodecyl-modified chitosan was made into the self-expanding foam with a sprayed behavior from a gas tank. When the injured area was incompressible like the internal injuries in the trunk, this product could treat bleeding. Once spraying the foam into the open cavity, it could quickly form a barrier to prevent blood out of the cavity, which relied on the physical wrap of blood components into the formation of clusters via the hydrophobic interactions. Notably, this hemostasis foam could stop bleeding quickly without additionally external pressure. Yin et al. (2020) synthesized a nanofibrous polyvinyl alcohol (PVA)/quaternary ammonium N-halamine chitosan (CSENDMH) membrane for the hemostasis dressing. This membrane with a bead-free network and porous structure exhibited a good water absorption and excellent blood clotting abilities for the effective hemostatic applications (Yin et al., 2020). Zhang et al. (2020) designed a composite sponge of hydroxybutyl chitosan (HBC) and diatom-biosilica (DB) to improve the hemostatic effects (**Figure 7**). By means of its porous structures, good biocompatibility and fast fluid absorbability,

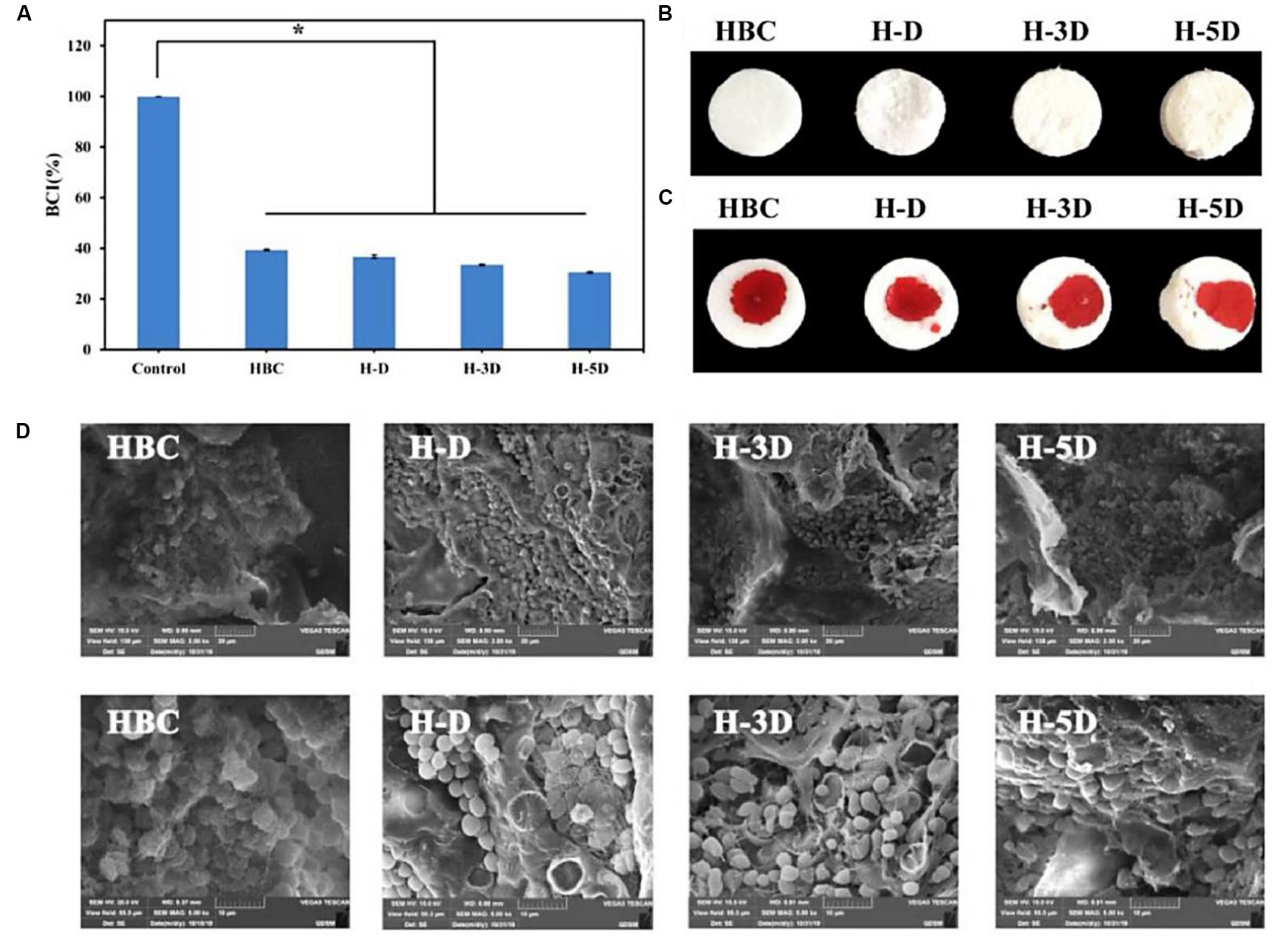

FIGURE 7 | (A) BCI ration of HBC, H-D, H-3D, and H-5D. The data represent mean ± SD (*n* = 3), $p < 0.05$. The photo of composite sponges **(B)** without and **(C)** with blood. **(D)** SEM of red blood cell aggregation on HBC and H-Ds. Reproduced from Zhang et al. (2020) with permission from Copyright 2020 Elsevier.

H-D exhibited effective hemostasis effect with a shorten clotting time of 70% compared to the controls, because strong interface effect from H-D could induce the red blood cell absorption, active the inherent blood clotting pathway and accelerate the blood coagulation (Zhang et al., 2020). Liu et al. (2014) prepared a porous chitosan sponge by introduction of the halloysite nanotubes, which could significantly improve the clotting efficiency and promote the would repair than the pure CS. Kumar et al. (2012) reported a composite bandage with the main components of porous CS hydrogel/zinc oxide nanoparticles, which could increase swelling property, blood clotting rate and antibacterial ability.

Cellulose

Cellulose, a main component of plant cell wall, is a kind of D-glucopyranose homopolysaccharide. In particular, cellulose oxide (OC), also known as cellulose oxide, is a denatured polysaccharide by the chemical modification of cellulose. Cellulose and its derivatives are popularly utilized as absorbable wound dressings and hemostatic products due to their excellent biocompatibility, biodegradability and low costs (Cheng et al., 2013; Metaxa et al., 2014; Kwak et al., 2015; Mertaniemi et al., 2016). Cellulose oxide can quickly absorb the liquids, entrap the platelets and erythrocyte, increase the concentration of clotting factors and speed up the clotting process as it is employed at the bleeding sites, facilitating the fibrin clots and blocking blood flow effectively (Hutchinson et al., 2013). Meanwhile, their carboxyl groups can initiate the coagulation by self-activation of coagulation factor XII.

Although OC had been extensively investigated as a hemostatic agent, it possessed obvious clinical disadvantages originating from the low pH of many carboxyl groups, which significantly limited the sensitive tissue (nervous and cardiac systems) therapy (Ohta et al., 2015). To address this problem, scientists have spent efforts on the improvement of its hemostatic applications. Demirekin et al. (2015) reported a potassium and sodium salt of ORC in the presence of metal ions to effectively accelerate the blood coagulation and inhibit bacterial infection. In addition, introduction of other polysaccharide is an effective method to enhance the hemostatic therapy. For example, He et al. (2014) reported a hemostatic agent by blending the chitosan on the surface of ORC gauze, exhibiting satisfactory hemostatic effect compared to the traditional ORC gauze. In addition, Karahaliloglu et al. (2017) fabricated a bilayer of wound dressing with CS and bacterial cellulose blends in the sublayer of and silk fibroin (SF) in the upper layer. When it was applied in the wound, the sublayer bacterial cellulose can quickly absorb a lot of liquid in the blood and the upper layer of SF can rapidly cause the platelet adhesion, which ascribed to the similar hierarchical structure to collagen/elastin fibers with high surface area/volume areas. Compared with the control of standard gauze, this bilayer dressing presented the highly effective hemostatic effect both *in vitro* and *in vivo* (Karahaliloglu et al., 2017).

Dextran

Dextran, a biocompatible polysaccharide, is composed of an α-1,6-linked D-glucopyranose residue. Like other polysaccharides, dextran has a large number of hydroxyl groups in its anhydroglucose unit with facile chemical modification. In addition, its high water absorption endowed the dextran with hemostatic function as a tissue adhesive agent (Bouten et al., 2014; Yan et al., 2017). Generally, $NaIO_4$ is used to oxidize the adjacent diols of dextran into aldehyde groups, which can be chemically crosslinked with the amino groups of biomaterials or tissue proteins, exhibiting strong adhesive force for tissue sealants. When the dextran is oxidized less than 60%, it can slowly bind into the tissues, because the tissue-material adhesion force, local inflammation and systemic tissue toxicity is extensively relied on the number and density of aldehyde groups (Bhatia et al., 2007a). Liu et al. (2019) designed a kind of aldehyde dextran (PDA) sponge with good water absorption and adhesive behaviors (**Figure 8**). After optimization of pore size, PDA sponge displayed the quick blood absorption, powerful tissue adhesion and effective hemostasis on the rabbit models, because the quick coagulation process of PDA sponge could accelerate the wound block, cell aggregation and cell initiation without the need for coagulation cascade activation (Liu et al., 2019).

Artzi et al. (2009, 2011) prepared a kind of sealant consisting of star-shaped PEG-NH_2 and Dex-CHO with various molecular weights and aldehyde oxidation degrees, exhibiting effective tissue adhesion behaviors after chemical modification. Du et al. (2019) reported a novel hydrogel dressing comprising hydrophobicity-modified CS and oxidized dextran. After the analysis of gelation behavior, self repair and rheological property, this hydrogel dressing presented good hemostatic and antibacterial activity in a rat hemorrhaging liver model, which demonstrated its multifunctional activities on the improvement of hemorrhagic and infected wound therapy (Du et al., 2019).

Although sealants and tissue adhesives based on oxidized dextran have been extensively investigated, the formation of imine bonds is an equilibrium reaction with instability in aqueous solutions. Wang et al. (2012) have developed a tissue glue consisting of the aldehyde dextran and gelatin. Incorporation of 2-isocyanoethyl methacrylate into the architectural backbone of dextran hydrogel can significantly increase the crosslinking degree along with formation of a dense intermolecular network, thus improving the mechanical strength and stability of biocompatible hydrogels (Wang et al., 2012).

Alginate

Alginate consists of α-L-glucuronic acid and β-D-mannuroic acid monomers. On account of its good biocompatibility and biodegradability, alginate is easily formed to an ionic hydrogel or a microsphere crosslinked by Ca^{2+} ions (e.g., calcium alginate) for biomedical applications (Hama et al., 2010; Kinaci et al., 2013; Pinkas and Zilberman, 2014; van Elk et al., 2015). Once calcium alginate comes to contact with blood, Ca^{2+} ions can release in exchange for sodium ions, which can simultaneously accelerate platelet aggregation to activate the coagulation process and serve as a cofactor in the coagulation cascade. In addition, by means of the high water absorption, the modified CA can quickly attach the materials onto wound with a suitable hemostatic property. Shi et al. (2016) designed a kind of biodegradable and hemostatic composite microspheres comprising carboxymethyl chitosan, sodium alginate and collagen, which possessed high-efficient hemostatic property via the feasible platelet adherence, aggregation and activation.

The drug loading capacity of alginate microspheres has also attracted people's attention. Rong et al. (2015) prepared a thrombin-loaded alginate calcium microsphere via the emulsion crosslinking technique, which can transport the hemostatic agent for the blunt injury and abdominal solid viscera bleeding. Zhai et al. (2019) demonstrated a co-assembly system of peptide binding compound and alginatewith attractive cell adhesions, which exhibited the effective hemostatic property without adding other growth factors (**Figure 9**). This composite hydrogel can quickly stop bleeding after adding whole blood *in vitro*, and reduce the bleeding volume of the mouse liver puncture model to about 18% of the untreated group. Meanwhile, it promoted the migration of fibroblasts and accelerates wound healing speed of the mouse full-thickness skin defect model, which was developed into the promising nanocomposite materials for a variety of biomedical applications (Zhai et al., 2019). Huang et al. (2019) prepared a hemostatic composite (SACC) microsphere via the crosslinked technology of sodium alginate (SA), carboxymethyl chitosan (CMC) and collagen. On account of generic and narrow sphere shape, rough surface and high-water absorption, SACC showed better hemostatic effects than that of CMC and SA using the bleeding rat models. In addition, SACC exhibited good biocompatibility and biodegradability by histomorphological and immunofluorescent results, which can be used in the future clinical hemostasis applications (Huang et al., 2019).

Starch

Starch is a widely natural polymer with high water solubility and low cost. Starch can be modified into the gelatinized starch, grafted starch and crosslinked starch by means of simply chemical methods, and degraded into oligosaccharides, maltose and glucose by plasma amylase *in vivo*. In recent years, starch microspheres (DSMs) are widely applied in the temporary blockage of blood vessels in combination with cytotoxic drugs in the treatment of malignant tumors. HemoStase and Arista are two commercially available starch-based hemostatic agents (Humphreys et al., 2008; Antisdel et al., 2009). To overcome its insufficient drawback for the severe bleeding,

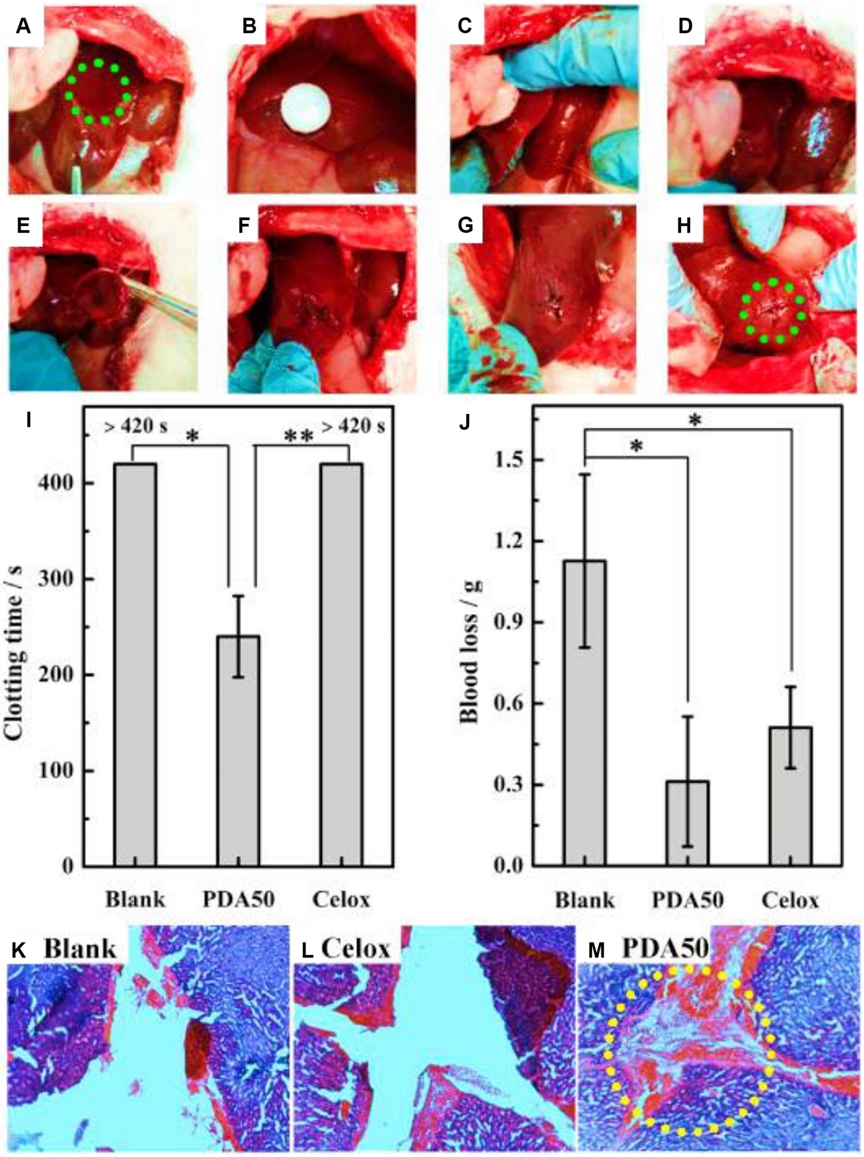

FIGURE 8 | Hemostasis of liver injury using the rabbit model. **(A)** Creation of liver injury in the left medial lobe. **(B–D)** Treatment with PDA sponge. **(E–G)** Hemostasis maintained after removal of sponge. **(H)** Hemostasis kept even squeezing the wound. **(I,J)** Coagulation time and blood loss of liver injury. **(K–M)** Histopathology of liver trauma. Reproduced from Liu et al. (2019) with permission from Copyright 2019 Elsevier.

DSMs can be used in combination with recombinant factor VIIa, fibrinogen or thrombin to improve its hemostatic effect (Bjorses and Holst, 2007). However, these derivative agents may improve viral infections in clinical use. For example, Bjorses et al. (2011) tailored surface properties (negative/positive charge and hydrophilic/hydrophobic ratio) of DSMs to affect the material/blood interactions, showing superior hemostatic capacity *in vivo*.

In addition, incompressible bleed still faces great challenges for irregular wound treatments. Yang et al. (2019) synthesized a hemostatic starch/PEG hemostatic sponge (TRAP-Sp) with good water absorption, passive hemostatic performance and rapid self-healing property to absorb the plasma, concentrate blood cells and improve the blood coagulation (**Figure 9**). Once applied and contacted with blood, this hemostatic sponge could quickly expand pressure onto the injured sites with outstanding mechanics and superior resilience (Yang et al., 2019).

Hyaluronic Acid

Hyaluronic acid (HA) consisting of D-glucuronic acid and N-acetyl-D-glucosamine is a linear non-sulfated polysaccharide, which can facilitate cell adhesion and migration because of excellent water retention and inherent swelling property *in vivo*, which contribute to the suitable conditions for wound repair and accelerate the collagen secretion from wound surface via the fibroblast proliferation effect. An et al. (2019) developed

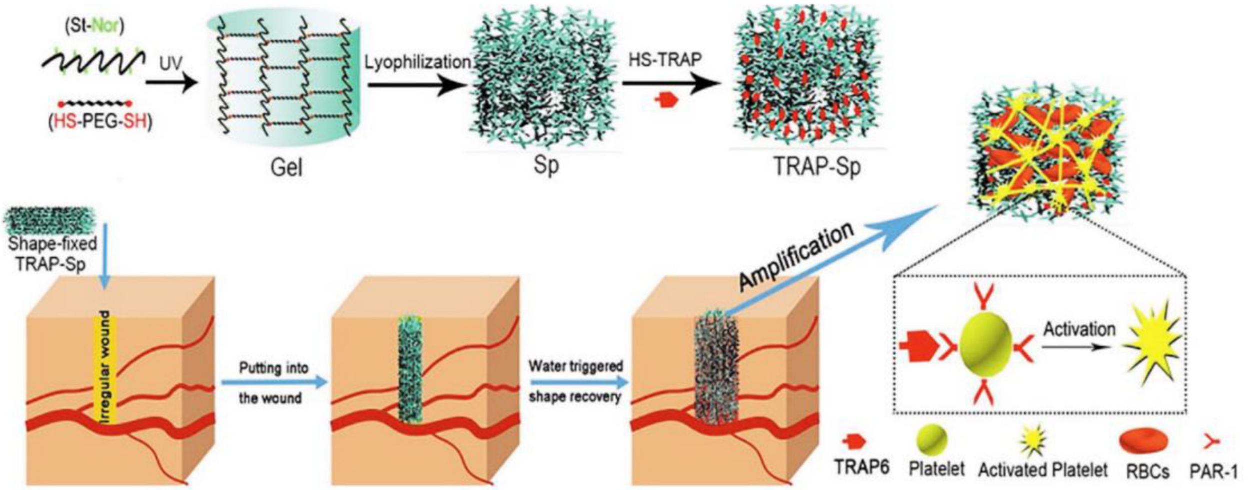

FIGURE 9 | . Preparation of TRAP-Sp with macroporous structures and reasonable mechanical properties. Reproduced with permission. Reproduced from Yang et al. (2019) with permission from Copyright 2019 Elsevier.

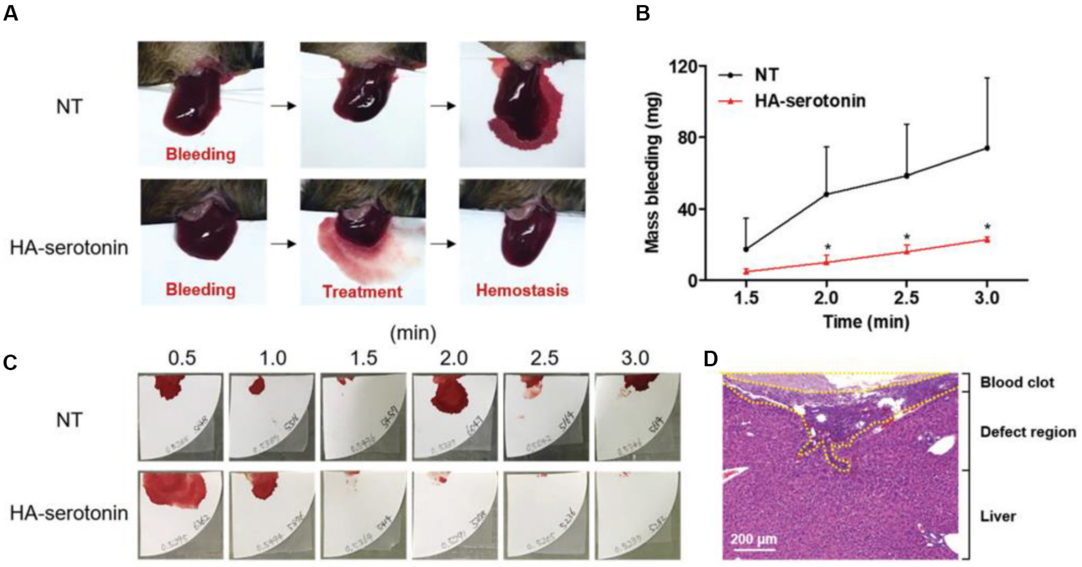

FIGURE 10 | (A) HA-serotonin-mediated hemostasis in a liver hemorrhage model of Factor VIII-deficient hemophilia mice without treatment (NT, top) and treatment by hemostatic adhesives (HA-serotonin, bottom). **(B)** Accumulated blood loss from hemophilia mice after bleeding without any treatment (NT, black) and treatment of hemostatic adhesives (HA-serotonin, red) ($n = 3$, $^*p < 0.05$ versus NT group). **(C)** Photographs of the blood absorbed papers from non- and HA-serotonin-treated hemophilia mice every 30 s up to 3 min. **(D)** H&E staining of damaged liver harvested from HA-serotonin-treated hemophilia mice for 3 days. Scale bar = 200 mm. Reproduced from An et al. (2019) with permission from Copyright 2019 Royal Society of Chemistry.

a new class of hemostatic adhesive using serotonin-conjugated HA hydrogel system, wherein the serotonin could promote the hemostasis of blood clotting in platelets. Inspired by platelet clotting mechanism, the serotonin-conjugated HA hydrogel showed superior hemostatic ability in normal and hemophilic lesions than the commercially fibrinolytic agents, which could prevent the abnormal post-hemostatic tissue adhesion in a rat model (**Figure 10**; An et al., 2019).

Luo et al. (2019) prepared two kind of injectable hydrogels of self-crosslinking gelatin and hyaluronic acid/gelatin for the hemorrhage control, which possessed good stability, low cytotoxicity, favorable bursting strength and excellent hemostatic ability compared to commercial fibrin glue (Luo et al., 2019). Hong et al. (2019) had developed a strongly adhesive hemostatic hydrogel for repairing arterial and cardiac hemorrhages. After ultraviolet irradiation of methyacrylated HA, it could quickly form the hydrogel, adhere and seal the bleeding arteries and heart walls. These repairs could withstand higher blood pressures than those of most traditionally clinical settings. Notably, hydrogel could prevent the hypertensive bleed from a 4–5 mm of incision wound in a pig carotid artery and hypertensive bleeding from a 6 mm of heart penetrating hole in a pig heart, presenting greatly clinical advantages for the wound sealants.

FUTURE OUTLOOK AND CONCLUSION

In this review, synthetic and polysaccharide adhesives have shown outstanding performance and multifunctionality when compared to the commercially available hemostatic polymers, but many challenges remain unresolved. One of the key issues is that the existed adhesives are lack of sufficient adhesion strength to replace the sutures, especially for the fragile tissues that need to close the leakage of liquids or gases. For synthetic polymers-based hemostatic adhesives, although the cyanoacrylate-based adhesive exhibited the incomparable hemostatic property than any other hemostatic agents, the biocompatibility profile of this cyanoacrylate did not meet the standardized guidelines to speed up regulatory approval process. Poly(ethylene glycol)-based hemostatic hydrogels have been used as a biodegradable adhesive to possess more advantages of being free of any human/animal materials, being safe and well-tolerated, and having a tight covalent bond and adhesion force to the surface of wet tissue. However, they often significantly swell *in vivo* and have undesirable mechanical strength for their applicability. In addition, PEG-based hydrogels are needed to produce *in situ* with two ingredients, which are relatively difficult to store separately as freeze-drying products and handle for usage. On account of the fast crosslinking of PEG hydrogels, these two ingredients are needed to first dissolve and then mix together through a dual syringe spray with a short handling time. Besides, these PEG hydrogel adhesives are quite expensive for limitation of wide use in the clinic applications. Therefore, great challenges about the synthetic adhesives is to design and prepare multifunctional polymers that simultaneous possessed safe, high strength and strong adhesion onto the tissues.

Polysaccharide-based adhesives have more advantages of intrinsic biocompatibility, safety and biodegradability, but they are always required to be modified to improve the solubility (e.g., chitin and chitosan) and further crosslinked with other polysaccharides. The huge benefits of polysaccharide-based adhesives are their widely biomedical fields from the former closing dura and corneal incisions to the current cartilage injures of glues and hemostatic products in regenerative medicine. As for the future research of polysaccharide-based hemostatic materials, pursuits of multifunctionality, and more advanced technologies are vital factors that should be issued. On the one hand, proven physic-chemical modification methods can furnish the polysaccharide with powerful adhesions with the tissue surfaces to acquire the directly rapid hemostasis without fully relying on the activation of coagulation process itself and inducement of inherent systemic emboli and thromboses. Furthermore, intelligent polysaccharide-based hemostatic materials should also facilitate the whole sequential processes of hemostatic, analgesia, anti-infection, inflammation, proliferation, remodeling, and healing functions to promote the long-term care of wound until body recovery. On the other hand, more advance techniques are urgently needed to endow the polysaccharide-based hemostatic materials with facile usages and great potentials. For example, by means of layer-by-layer self-assembly, electrostatic spinning, and reverse emulsion polymerization technologies, more inorganic nanomaterials can be blended into the biocompatible polysaccharide to well-organized into inorganic-organic hybrid biomaterials to directly and high-effectively activate the coagulation cascade and improve the hemostatic performance.

Future biomedical adhesives should be required with environmental stimulus responsiveness, which can respond to changes in the externally applied stimuli, such as pH, light, electricity, temperature and magnetism, or other active biomolecules (glucose, enzyme, etc.) within their surroundings. In this case, these changes can tailor the bioadhesives to release the encapsulated drug particles and improve the adhesive properties. Besides, scientists should also do consult the end-users about the feasibility and practicality of hemostatic materials in designing and fabricating novel adhesives. Researchers and clinicians need to work more closely together to develop high-level biological adhesives, identify unmet requirements and prioritize their design for further clinical applications on the market.

AUTHOR CONTRIBUTIONS

XW and JZ initiated the project. DL, JC, MZ, and CL searched the database, wrote, and finalized the manuscript. XW and JZ made suggestions and revised the article. All authors reviewed and commented on the entire manuscript.

FUNDING

This work was supported by the National Natural Science Foundation of China (NSFC, 81972081 and 51973226), the Beijing Novel Program (Z181100006218059), Military Medical Science and Technology Youth Cultivation Project (20QNPY109), and Military Medical Youth Growth Program of PLA General Hospital (QNC19028).

REFERENCES

An, S., Jeon, E. J., Jeon, J., and Cho, S. W. (2019). A serotonin-modified hyaluronic acid hydrogel for multifunctional hemostatic adhesives inspired by a platelet coagulation mediator. *Mater. Horiz.* 6, 1169–1178. doi: 10.1039/c9mh00157c

Anonymous, and Confluent Surgical Inc (2004). *FDA Executive Summary DuraSeal Dural Sealant System*, Vol. 47. Waltham, MA: Confluent Surgical Inc, 040034.

Anonymous, and Confluent Surgical Inc (2009). *FDA Executive Summary for DuraSeal Xact Sealant System*, Vol. 47. Waltham, MA: Confluent Surgical Inc, 080013.

Anonymous, and Focal Inc (2000). *FDA Summary of safety and effectiveness data FocalSeal*, Vol. 14. Lexington, MA: Focal Inc, 990028.

Antisdel, J. L., West-Denning, J. L., and Sindwani, R. (2009). Otolaryngol. effect of microporous polysaccharide hemospheres (MPH) on bleeding after endoscopic sinus surgery: randomized controlled study. *Head Neck Surg.* 141, 353–357. doi: 10.1016/j.otohns.2009.06.078

Arnaud, F., Teranishi, K., Okada, T., Parreno-Sacdalan, D., Hupalo, D., McNamee, G., et al. (2011). Comparison of combat gauze and traumastat in two severe groin injury models. *J. Surg. Res.* 169, 92–98. doi: 10.1016/j.jss.2009.09.004

Artzi, N., Shazly, T., Baker, A. B., Bon, A., and Edelman, E. R. (2009). Aldehyde-amine chemistry enables modulated biosealants with tissue-specific adhesion. *Adv. Mater.* 21, 3399–3403. doi: 10.1002/adma.200900340

Artzi, N., Zeiger, A., Boehning, F., Ramos, A., Vliet, K. V., and Edelman, E. R. (2011). Tuning adhesion failure strength for tissue-specific applications. *Acta Biomater.* 7, 67–74. doi: 10.1016/j.actbio.2010.07.008

Azargoon, H., Williams, B. J., Solomon, E. S., Kessler, H. P., He, J., and Spears, R. (2011). Assessment of hemostatic efficacy and osseous wound healing using hemcon dental dressing. *J. Endod.* 37, 807–811. doi: 10.1016/j.joen.2011.02.023

Basu, A., Kunduru, K. R., Abtew, E., and Domb, A. J. (2015). Polysaccharide-based conjugates for biomedical applications. *Bioconjugate. Chem.* 26, 1396–1412. doi: 10.1021/acs.bioconjchem.5b00242

Beckman, E. J. (2011). *One-Part Moisture-Curable Tissue Sealant*. US Patent No WO 2011/150199 A2. Leeds: Tissuemed Ltd.

Behrens, A. M., Lee, N. G., Casey, B. J., Srinivasan, P., Sikorski, M. J., Daristotle, J. L., et al. (2015). Biodegradable-polymer-blend-based surgical sealant with body-temperature-mediated adhesion. *Adv. Mater.* 27, 8056–8061. doi: 10.1002/adma.201503691

Behrens, A. M., Sikorski, M. J., and Kofinas, P. (2014). Hemostatic strategies for traumatic and surgical bleeding. *J. Biomed. Mater. Res. Part A* 102, 4182–4194. doi: 10.1002/jbm.a.35052

Bhatia, S. K. (2010). *Traumatic Injuries*. New York, NY: Springer, 213–258.

Bhatia, S. K., Arthur, S. D., Chenault, H. K., Figuly, G. D., and Kodokian, G. K. (2007a). Polysaccharide-based tissue adhesives for sealing corneal incisions. *Curr. Eye Res.* 32, 1045–1050. doi: 10.1080/02713680701767876

Bhatia, S. K., Arthur, S. D., Chenault, H. K., and Kodokian, G. K. (2007b). Interactions of polysaccharide-based tissue adhesives with clinically relevant fibroblast and macrophage cell lines. *Biotechnol. Lett.* 29, 1645–1650.

Bian, J., Xia, Y. X., Sang, L. Y., Zhu, C. X., Li, Y. X., Li, G. Y., et al. (2020). Recyclable colorimetric probe: in-situ fabrication of highly stable HPEI-AuNPs for selective Ag^+ detection. *New J. Chem.* 44, 5438–5447. doi: 10.1039/d0nj00497a

Bjorses, K., Faxalv, L., Montan, C., Wildt-Persson, K., Fyhr, P., Holst, J., et al. (2011). In vitro and in vivo evaluation of chemically modified degradable starch microspheres for topical haemostasis. *Acta Biomater.* 7, 2558–2565. doi: 10.1016/j.actbio.2011.03.003

Bjorses, K., and Holst, J. (2007). Various local hemostatic agents with different modes of action; an in vivo comparative randomized vascular surgical experimental Study. *Eur. J. Vasc. Endovasc. Surg.* 33, 363–370. doi: 10.1016/j.ejvs.2006.10.011

Bochyńska, A. I., Sharifi, S., van Tienen, T. G., Buma, P., and Grijpma, D. W. (2013). Development of tissue adhesives based on amphiphilic isocyanate-terminated trimethylene carbonate block copolymers. *Macromol. Symp.* 334, 40–48. doi: 10.1002/masy.201300101

Boerman, M. A., Roozen, E., Sanchez-Fernandez, M. J., Keereweer, A. R., Felix Lanao, R. P., Bender, J. C. M. E., et al. (2017). Next generation hemostatic materials based on NHS-ester functionalized poly(2-oxazoline)s. *Biomacromolecules* 18, 2529–2538. doi: 10.1021/acs.biomac.7b00683

Boogaarts, J. D., Grotenhuis, J. A. A., Bartels, R. H. M., and Beems, T. (2005). Use of a novel absorbable hydrogel for augmentation of dural repair: results of a preliminary clinical study. *Neurosurgery* 57, 146–151. doi: 10.1227/01.neu.0000164384.05351.59

Bouten, P. J. M., Zonjee, M., Bender, J., Yauw, S. T. K., van Goor, H., van Hest, J. C. M., et al. (2014). The chemistry of tissue adhesive materials. *Prog. Polym. Sci.* 39, 1375–1405.

Brandenberg, G., Leibrock, L. G., Shuman, R., Malettz, W. G., and Quigley, H. (1984). Chitosan: a new topical hemostatic agent for diffuse capillary bleeding in brain tissue. *Neurosurgery* 15, 9–13. doi: 10.1227/00006123-198407000-00004

Cao, Q. C., Wang, X., and Wu, D. C. (2018). Controlled cross-linking strategy for formation of hydrogels, microgels and nanogels. *Chin. J. Polym. Sci.* 36, 8–17. doi: 10.1007/s10118-018-2061-7

Celik, H., Caner, H., Tahta, K., Ozcan, O. E., Erbengi, A., and Onol, B. (1991). Nonsuture closure of arterial defect by vein graft using isobutyl-2-cyanoacrylate as a tissue adhesive. *J. Neurosurg. Sci.* 35, 83–87.

Cheng, W., He, J., Wu, Y., Song, C., Xie, S., Huang, Y., et al. (2013). Preparation and characterization of oxidized regenerated cellulose film for hemostasis and the effect of blood on its surface. *Cellulose* 20, 2547–2558. doi: 10.1007/s10570-013-0005-5

Cosgrove, G. R., Delashaw, J. B., Grotenhuis, J. A. A., Tew, J. M., Van Loveren, H., Spetzler, R. F., et al. (2007). Safety and efficacy of a novel polyethylene glycol hydrogel sealant for watertight dural repair. *J. Neurosurg.* 106, 52–58. doi: 10.3171/jns.2007.106.1.52

DeAnglis, A. P., Nur, I., Gorman, A. J., and Meidler, R. (2017). A method to measure thrombin activity in a mixture of fibrinogen and thrombin powders. *Blood Coagul. Fibrinolysis* 28, 134–138.

Della Puppa, A., Rossetto, M., and Scienza, R. (2010). Use of a new absorbable sealing film for preventing postoperative cerebrospinal fluid leaks: remarks on a new approach. *Br. J. Neurosurg.* 24, 609–611. doi: 10.3109/02688697.2010.500413

Demirekin, Z. B., Sezer, U. A., Karatopuk, D. U., and Sezer, S. (2015). Development of metal ion binded oxidized regenerated cellulose powder as hemostatic agent: a comparative study with in vivo performance. *Ind. Eng. Chem. Res.* 54, 4906–4914. doi: 10.1021/ie504985b

Dowling, M. B., Chaturvedi, A., MacIntire, I. C., Javvaji, V., Gustin, J., Raghavan, S. R., et al. (2016). Determination of efficacy of a novel alginate dressing in a lethal arterial injury model in swine. *Injury* 47, 2105–2109. doi: 10.1016/j.injury.2016.05.003

Dragu, A., Unglaub, F., Schwarz, S., Beier, J. P., Kneser, U., and Bach, A. D. (2009). Foreign body reaction after usage of tissue adhesives for skin closure: a case report and review of the literature. *Arch. Orthop. Trauma. Surg.* 129, 167–169. doi: 10.1007/s00402-008-0643-5

Du, X. C., Liu, Y. J., Wang, X., Yan, H. Y., Wang, L. N., Qu, L. J., et al. (2019). Injectable hydrogel composed of hydrophobically modified chitosan/oxidized-dextran for wound healing. *Mater. Sci. Eng. C* 104:109930. doi: 10.1016/j.msec.2019.109930

Dunn, R., Lyman, M. D., Edelman, P. G., and Campbell, P. K. (2001a). BioGlue and Dermabond save time, leak less, and are not mechanically inferior to two-layer and modified one-layer vasovasostomy. *Fertil. Steril.* 75, 411–416.

Dunn, R., Lyman, M. D., Edelman, P. G., and Campbell, P. K. (2001b). Evaluation of the SprayGel^{TM} adhesion barrier in the rat cecum abrasion and rabbit uterine horn adhesion models. *Fertil. Steril.* 75, 411–416. doi: 10.1016/s0015-0282(00)01677-0

Evans, C. E., Lees, G. C., and Trail, I. A. (1999). Cytotoxicity of cyanoacrylate adhesives to cultured tendon cells. *J. Hand. Surg.* 24, 658–661. doi: 10.1054/jhsb.1999.0279

Ferland, R., Mulani, D., and Campbell, P. K. (2001). Evaluation of a sprayable polyethylene glycol adhesion barrier in a porcine efficacy model. *Hum. Reprod.* 16, 2718–2720.

Ferreira, P., Coelho, J. F. J., and Gil, M. H. (2008a). Development of a new photocrosslinkable biodegradable bioadhesive. *Int. J. Pharm.* 352, 172–181. doi: 10.1016/j.ijpharm.2007.10.026

Ferreira, P., Silva, A. F., Pinto, M. I., and Gil, M. H. (2008b). Development of a biodegradable bioadhesive containing urethane groups. *J. Mater. Sci. Mater. Med.* 19, 111–120. doi: 10.1007/s10856-007-3117-3

Ferreira, P., Pereira, R., Coelho, J. F. J., Silva, A. F. M., and Gil, M. H. (2007). Modification of the biopolymer castor oil with free isocyanate groups to be applied as bioadhesive. *Int. J. Biol. Macromol.* 40, 144–152. doi: 10.1016/j.ijbiomac.2006.06.023

Ferroli, P., Acerbi, F., Broggi, M., Schiariti, M., Albanese, E., Tringali, G., et al. (2013). Novel impermeable adhesive membrane to reinforce dural closure: a preliminary retrospective study on 119 consecutive high-risk patients. *World Neurosurg.* 79, 551–557. doi: 10.1016/j.wneu.2011.09.022

Fortelny, R. H., Petter-Puchner, A. H., Glaser, K. S., and Redl, H. (2012). Use of fibrin sealant (Tisseel/Tissucol) in hernia repair: a systematic review. *Surg. Endosc.* 26, 1803–1812. doi: 10.1007/s00464-012-2156-0

Fortelny, R. H., Petter-Puchner, A. H., Walder, N., Mittermayr, R., Öhlinger, W., Heinze, A., et al. (2007). Cyanoacrylate tissue sealant impairs tissue integration of macroporous mesh in experimental hernia repair. *Surg. Endosc.* 21, 1781–1785. doi: 10.1007/s00464-007-9243-7

Frantz, V. K. (1948). Experimental studies of alginates as hemostatics. *Ann. Surg.* 127, 1165–1172. doi: 10.1097/00000658-194806000-00005

Gerlach, T., Grayson, J. K., Pichakron, K. O., Sena, M. J., DeMartini, S. D., Clark, B. Z., et al. (2010). Preliminary study of the effects of smectite granules (WoundStat) on vascular repair and wound healing in a swine survival model. *J. Trauma* 69, 1203–1209. doi: 10.1097/ta.0b013e3181c452b5

Ghobril, C., and Grinstaff, M. W. (2015). The chemistry and engineering of polymeric hydrogel adhesives for wound closure: a tutorial. *Chem. Soc. Rev.* 44, 1820–1835. doi: 10.1039/c4cs00332b

Gilbert, T. W., Badylak, S. F., Gusenoff, J., Beckman, E. J., Clower, D. M., Daly, P., et al. (2008). Lysine-derived urethane surgical adhesive prevents seroma formation in a canine abdominoplasty model. *Plast. Reconstr. Surg.* 122, 95–102. doi: 10.1097/prs.0b013e31817743b8

Goode, J. L., Harvey, E., Chandeysson, P., Zhou, S., Das, S., Durfor, C., et al. (2001). Review memorandum: cohesion technologies: CoSeal Surgical Sealant. P 010022, 8.

Hama, C., Umeda, T., Musha, Y., Koda, S., and Itatani, K. (2010). Preparation of novel hemostatic material containing spherical porous hydroxyapatite/alginate granules. *J. Ceram. Soc.* 118, 446–450. doi: 10.2109/jcersj2.118.446

Hattori, H., and Ishihara, M. (2015). Changes in blood aggregation with differences in molecular weight and degree of deacetylation of chitosan. *Biomed. Mater.* 10:015014. doi: 10.1088/1748-6041/10/1/015014

He, J., Wu, Y., Wang, F., Cheng, W., Huang, Y., and Fu, B. (2014). Hemostatic, antibacterial and degradable performance of the water-soluble chitosan-coated oxidized regenerated cellulose gauze. *Fibers Polym.* 15, 504–509. doi: 10.1007/s12221-014-0504-5

He, Q., Gong, K., Ao, Q., Ma, T., Yan, Y., Gong, Y., et al. (2013). Positive charge of chitosan retards blood coagulation on chitosan films. *J. Biomater. Appl.* 27, 1032–1045. doi: 10.1177/0885328211432487

Hong, Y., Zhou, F. F., Hua, Y. J., Zhang, X. Z., Ni, C. Y., Pan, D. H., et al. (2019). A strongly adhesive hemostatic hydrogel for the repair of arterial and heart bleeds. *Nat. Commun.* 10:2060.

Howe, N., and Cherpelis, B. (2013). Obtaining rapid and effective hemostasis: part I. Update and review of topical hemostatic agents. *J. Am. Acad. Dermatol.* 69, 659.e1–659.e17. doi: 10.1016/j.jaad.2013.07.014

Hsu, B. B., Conway, W., Tschabrunn, C. M., Mehta, M., Perez-Cuevas, M. B., Zhang, S., et al. (2015). Clotting mimicry from robust hemostatic bandages based on self-assembling peptides. *ACS Nano* 9, 9394–9406. doi: 10.1021/acsnano.5b02374

Huang, H., Chen, H. S., Wang, X. L., Qiu, F. X., Liu, H. H., Lu, J. W., et al. (2019). Degradable and bioadhesive alginate-based composites: an effective hemostatic agent. *ACS Biomater. Sci. Eng.* 5, 5498–5505. doi: 10.1021/acsbiomaterials.9b01120

Humphreys, M. R., Lingeman, J. E., Terry, C., Castle, E. P., Andrews, P. E., Gettman, M. T., et al. (2008). Renal injury and the application of polysaccharide hemospheres: a laparoscopic experimental model. *J. Endourol.* 22, 1375–1381.

Hung-Hsing, C., and David, F. T. (2003). BioGlue: albumin/Glutaraldehyde sealant in cardiac surgery. *J. Card. Surg.* 18, 500–503. doi: 10.1046/j.0886-0440.2003.00304.x

Hutchinson, R. W., George, K., Johns, D., Craven, L., Zhang, G., and Shnoda, P. (2013). Hemostatic efficacy and tissue reaction of oxidized regenerated cellulose hemostats. *Cellulose* 20, 537–545. doi: 10.1007/s10570-012-9828-8

Ishihara, M. (2002). Photo-crosslinkable chitosan hydrogel as a wound dressing and a biological adhesive. *Trends Glycosci. Glyc.* 14, 331–341.

Ishihara, M., Nakanishi, K., Ono, K., Sato, M., Kikuchi, M., Saito, Y., et al. (2002). Photocrosslinkable chitosan as a dressing for wound occlusion and accelerator in healing process. *Biomaterials* 23, 833–840. doi: 10.1016/s0142-9612(01)00189-2

Jayakumar, R., Prabaharan, M., Kumar, P. T. S., Nair, S. V., and Tamura, H. (2011). Biomaterials based on chitin and chitosan in wound dressing applications. *Biotechnol. Adv.* 29, 322–337. doi: 10.1016/j.biotechadv.2011.01.005

Johns, D. A., Ferland, R., and Dunn, R. (2003). Initial feasibility study of a sprayable hydrogel adhesion barrier system in patients undergoing laparoscopic ovarian surgery. *J. Am. Assoc. Gynecol. Laparosc.* 10, 334–338. doi: 10.1016/s1074-3804(05)60257-5

Karahaliloglu, Z., Demirbilek, M., Ulusoy, I., Guemueskaya, B., and Denkbas, E. B. (2017). Active nano/microbilayer hemostatic agents for diabetic rat bleeding model. *J. Biomed. Mater. Res. Part B* 105, 1573–1585. doi: 10.1002/jbm.b.33696

Kavitha Sankar, P. C., Rajmohan, G., and Rosemary, M. J. (2017). Physico-chemical characterisation and biological evaluation of freeze dried chitosan sponge for wound care. *Mater. Lett.* 208, 130–132. doi: 10.1016/j.matlet.2017.05.010

Kettlewell, G., Mandley, D. J., Fortune, D. H., Thompson, I., and Morris, D. (2007). *Tissue Adhesive Formulations*. US Patent No WO 2007/099370 A2. Available online at: http://www.freepatentsonline.com/EP1837038.pdf

Kinaci, E., Basak, F., and Dincel, O. (2013). Efficacy of calcium alginate in prevention of hepatic parenchymal bleeding: an experimental study. *J. Gastroenterol. Hepatol. Res.* 2, 593–596.

Knop, K., Hoogenboom, R., Fischer, D., and Schubert, U. S. (2010). Poly(ethylene glycol) in drug delivery: pros and cons as well as potential alternatives. *Angew. Chem. Int. Ed.* 49, 6288–6290.

Kumar, P. T., Lakshmanan, V. K., Anilkumar, T. V., Ramya, C., Reshmi, P., Unnikrishnan, A. G., et al. (2012). Flexible and microporous chitosan Hydrogel/Nano ZnO composite bandages for wound dressing: in vitro and in vivo evaluation. *ACS Appl. Mater. Interfaces* 4, 2618–2629. doi: 10.1021/am300292v

Kwak, M. H., Kim, J. E., Go, J., Koh, E. K., Song, S. H., Son, H. J., et al. (2015). Bacterial cellulose membrane produced by *Acetobacter* sp. A10 for burn wound dressing applications. *Carbohydr. Polym.* 122, 387–398. doi: 10.1016/j.carbpol.2014.10.049

Lan, G., Lu, B., Wang, T., Wang, L., Chen, J., Yu, K., et al. (2015). Chitosan/gelatin composite sponge is an absorbable surgical hemostatic agent. *Colloids Surf. B* 136, 1026–1034. doi: 10.1016/j.colsurfb.2015.10.039

Lee, G., Lee, C. K., and Bynevelt, M. (2010). DuraSeal-hematoma: concealed hematoma causing spinal cord compression. *Spine* 35, 1522–1524.

Lew, W. K., and Weaver, F. A. (2008). Clinical use of topical thrombin as a surgical hemostat. *Biologics* 2, 593–599.

Lewis, K. M., Atlee, H., Mannone, A., Lin, L., and Goppelt, A. (2015). Efficacy of hemostatic matrix and microporous polysaccharide hemospheres. *J. Surg. Res.* 193, 825–830. doi: 10.1016/j.jss.2014.08.026

Li, D. W., Zhou, J., Zhang, M. M., Ma, Y. Z., Yang, Y. Y., Han, X., et al. (2020). Long-term delivery of alendronate through injectable Tetra-PEG hydrogel to promote osteoporosis therapy. *Biomater. Sci.* 8, 3138–3146. doi: 10.1039/d0bm00376j

Lipatova, T. E. (1986). Medical polymer adhesives. *Adv. Polym. Sci.* 79, 65–93. doi: 10.1007/3-540-16422-7_7

Liu, C. Y., Liu, X., Liu, C. Y., Wang, N., Chen, H. L., Yao, W. H., et al. (2019). A highly efficient, in situ wet-adhesive dextran derivative sponge for rapid hemostasis. *Biomaterials* 205, 23–37. doi: 10.1016/j.biomaterials.2019.03.016

Liu, H. T. (2000). Wound care following CO2 laser resurfacing using kaltostat. duoderm, and telfa for dressings. *Dermatol. Surg.* 26, 341–344. doi: 10.1046/j.1524-4725.2000.99131.x

Liu, H. Y., Wang, X., Cao, Y. X., Yang, Y. Y., Yang, Y. T., Gao, Y. F., et al. (2020). Freezing-tolerant, highly sensitive strain and pressure sensors assembled from ionic conductive hydrogels with dynamic cross-links. *ACS Appl. Mater. Interfaces* 12, 25334–25344. doi: 10.1021/acsami.0c06067

Liu, M., Shen, Y., Ao, P., Dai, L., Liu, Z., and Zhou, C. (2014). The improvement of hemostatic and wound healing property of chitosan by halloysite nanotubes. *RSC Adv.* 4, 23540–23553. doi: 10.1039/c4ra02189d

Liu, P., Zhao, J., Fan, W., Liu, M., and Li, Y. (2005). Clinical application of a novel hemostatic material Arista AH in spine surgery. *Acta Acad. Med. Mil. Tertiae* 23, 82–84.

Low, R. K., Moran, M. E., and Goodnight, J. E. (1993). Microfibrillar collagen hemostat during laparoscopically directed liver biopsy. *J. Laparoendosc. Surg.* 3, 415–420. doi: 10.1089/lps.1993.3.415

Luo, J. W., Liu, C., Wu, J. H., Lin, L. X., Fan, H. M., Zhao, D. H., et al. (2019). In situ injectable hyaluronic acid/gelatin hydrogel for hemorrhage control. *Mater. Sci. Eng. C* 98, 628–634. doi: 10.1016/j.msec.2019.01.034

Macchiarini, P., Wain, J., Almy, S., and Dartevelle, P. (1999). Experimental and clinical evaluation of a new synthetic, absorbable sealant to reduce air leaks in thoracic operations. *J. Thorac. Cardiovasc. Surg.* 117, 751–758. doi: 10.1016/s0022-5223(99)70296-5

Malette, W. G., Quigley, H. J., Gaines, R. D., Johnson, N. D., and Rainer, W. G. (1983). Chitosan: a new hemostatic. *Ann. Thorac. Surg.* 36, 55–58. doi: 10.1016/s0003-4975(10)60649-2

Mertaniemi, H., Escobedo-Lucea, C., Sanz-Garcia, A., Gandia, C., Makitie, A., Partanen, J., et al. (2016). Human stem cell decorated nanocellulose threads for biomedical applications. *Biomaterials* 82, 208–220. doi: 10.1016/j.biomaterials.2015.12.020

Metaxa, A. F., Efthimiadou, E. K., and Kordas, G. (2014). Cellulose-based drug carriers for cancer therapy: cytotoxic evaluation in cancer and healthy cells. *Mater. Lett.* 132, 432–435. doi: 10.1016/j.matlet.2014.06.134

Milkes, D. E., Friedland, S., Lin, O. S., Reid, T. R., and Soetikno, R. M. (2002). A novel method to control severe upper GI bleeding from metastatic cancer with a hemostatic sealant: the CoStasis surgical hemostat. *Gastrointest. Endosc.* 55, 735–740. doi: 10.1067/mge.2002.122796

Momeni, A., and Filiaggi, M. J. (2016). Degradation and hemostatic properties of polyphosphate coacervates. *Acta Biomater.* 41, 328–341. doi: 10.1016/j.actbio.2016.06.002

Montanaro, L., Arciola, C. R., Cenni, E., Ciapetti, G., Savioli, F., Filippini, F., et al. (2001). Cytotoxicity, blood compatibility and antimicrobial activity of two cyanoacrylate glues for surgical use. *Biomaterials* 22, 59–66. doi: 10.1016/s0142-9612(00)00163-0

Napoleone, C. P., Valori, A., Crupi, G., Ocello, S., Santoro, F., Vouhé, P., et al. (2009). An observational study of CoSeal for the prevention of adhesions in pediatric cardiac surgery. *Interact Cardiovasc Thorac Surg.* 9, 978–982. doi: 10.1510/icvts.2009.212175

Nivasu, V. M., Reddy, T. T., and Tammishetti, S. (2004). In situ polymerizable polyethyleneglycol containing polyesterpolyol acrylates for tissue sealant applications. *Biomaterials* 25, 3283–3291. doi: 10.1016/j.biomaterials.2003.09.091

Ohlinger, R., Gieron, L., Rutkowski, R., Kohlmann, T., Zygmunt, M., and Unger, J. (2018). The use of TissuGlu(R) surgical adhesive for mastectomy with or without lymphonodectomy. *InVivo* 32, 625–631.

Ohta, S., Nishiyama, T., Sakoda, M., Machioka, K., Fuke, M., Ichimura, S., et al. (2015). Development of carboxymethyl cellulose nonwoven sheet as a novel hemostatic agent. *J. Biosci. Bioeng.* 119, 718–723. doi: 10.1016/j.jbiosc.2014.10.026

Ono, K., Saito, Y., Yura, H., Ishikawa, K., Kurita, A., Akaike, T., et al. (2000). Photocrosslinkable chitosan as a biological adhesive. *J. Biomed. Mater. Res.* 49, 289–295. doi: 10.1002/(sici)1097-4636(200002)49:2<289::aid-jbm18>3.0.co;2-m

Oz, M. C., Rondinone, J. F., and Shargill, N. S. (2003). Floseal matrix: new generation topical hemostatic sealant. *J. Card. Surg.* 18, 486–493. doi: 10.1046/j.0886-0440.2003.00302.x

Phaneuf, M. D., Dempsey, D. J., Bide, M. J., Quist, W. C., and Logerfo, F. W. (2001). Coating of Dacron vascular grafts with an ionic polyurethane: a novel sealant with protein binding properties. *Biomaterials* 22, 463–469. doi: 10.1016/s0142-9612(00)00202-7

Pinkas, O., and Zilberman, M. (2014). Effect of hemostatic agents on properties of gelatin–alginate soft tissue adhesives. *J. Biomater. Sci.* 25, 555–573. doi: 10.1080/09205063.2014.881681

Pourshahrestani, S., Zeimaran, E., Djordjevic, I., Kadri, N. A., and Towler, M. R. (2016). Inorganic hemostats: the state-of-the-art and recent advances. *Mater. Sci. Eng. C* 58, 1255–1268. doi: 10.1016/j.msec.2015.09.008

Pozza, M., and Millner, R. W. (2011). Celox (chitosan) for haemostasis in massive traumatic bleeding: experience in Afghanistan. *Eur. J. Emerg. Med.* 18, 31–33. doi: 10.1097/mej.0b013e32833a5ee4

Preul, M. C., Bichard, W. D., Muench, T. R., and Spetzler, R. F. (2003). Multimodality treatment of giant intracranial arteriovenous malformations. *Neurosurgery* 53, 1–12.

Qin, X., Labuda, K., Chen, J., Hruschka, V., Khadem, A., Liska, R., et al. (2015). Development of synthetic platelet-activating hydrogel matrices to induce local hemostasis. *Adv. Funct. Mater.* 25, 6606–6617. doi: 10.1002/adfm.201501637

Quinn, J. V. (2005). *Tissue Adhesives in Clinical medicine*. Hamilton, Ontario: Decker Inc., 185.

Rajagopal, P., and Hakim, N. (2011). The use of a powdered polysaccharide hemostat (HemoStase) in live donor nephrectomies controls bleeding and reduces postoperative complications. *Transplant. Proc.* 43, 424–426. doi: 10.1016/j.transproceed.2011.01.079

Ran, Y., Hadad, E., Daher, S., Ganor, O., Kohn, J., Yegorov, Y., et al. (2010). QuikClot combat gauze use for hemorrhage control in military trauma: january 2009 Israel defense force experience in the gaza strip-a preliminary report of 14 cases. *Prehosp. Disaster. Med.* 25, 584–588. doi: 10.1017/s1049023x00008797

Rong, J., Liang, M., Xuan, F., Sun, J., Zhao, L., Zhen, H., et al. (2015). Alginate-calcium microsphere loaded with thrombin: a new composite biomaterial for hemostatic embolization. *Int. J. Biol. Macromol.* 75, 479–488. doi: 10.1016/j.ijbiomac.2014.12.043

Sabel, M., and Stummer, W. (2004). The use of local agents: surgicel and Surgifoam. *Eur. Spine J.* 13, 97–101.

Saini, A., Serrano, K., Koss, K., and Unsworth, L. D. (2016). Evaluation of the hemocompatibility and rapid hemostasis of (RADA)$_4$ peptide-based hydrogels. *Acta Biomater.* 31, 71–79. doi: 10.1016/j.actbio.2015.11.059

Saunders, M. M., Baxter, Z. C., Abou-Elella, A., Kunselman, A. R., and Trussell, J. C. (2009). BioGlue and Dermabond save time, leak less, and are not mechanically inferior to two-layer and modified one-layer vasovasostomy. *Fertil. Steril.* 91, 560–565. doi: 10.1016/j.fertnstert.2007.12.006

Sawhney, A. S., Pathak, C. P., and Hubbell, J. A. (1993). Bioerodible hydrogels based on photopolymerized poly(ethylene glycol)-co-poly(.alpha.-hydroxy acid) diacrylate macromers. *Macromolecules* 26, 581–587. doi: 10.1021/ma00056a005

Shi, X., Fang, Q., Ding, M., Wu, J., Ye, F., Lv, Z., et al. (2016). Microspheres of carboxymethyl chitosan, sodium alginate and collagen for a novel hemostatic in vitro study. *J. Biomater. Appl.* 30, 1092–1102. doi: 10.1177/0885328215618354

Singer, A. J., Quinn, J. V., and Hollander, J. E. (2008). The cyanoacrylate topical skin adhesives. *Am. J. Emerg. Med.* 26, 490–496. doi: 10.1016/j.ajem.2007.05.015

Spotnitz, W. D., and Burks, S. (2008). Hemostats, sealants, and adhesives: components of the surgical toolbox. *Transfusion* 48, 1502–1516. doi: 10.1111/j.1537-2995.2008.01703.x

Spotnitz, W. D., and Burks, S. (2010). State-of-the-art review: hemostats, sealants, and adhesives II: update as well as how and when to use the components of the surgical toolbox. *Clin. Appl. Thromb. Hemost.* 16, 497–514. doi: 10.1177/1076029610363589

Suggs, L. J., Krishnan, R. S., Garcia, C. A., Peter, S. J., Anderson, J. M., and Mikos, A. G. (1998). In vitro and in vivo degradation of poly(propylene fumarate-co-ethylene glycol) hydrogels. *J. Biomed. Mater. Res.* 42, 312–320. doi: 10.1002/(sici)1097-4636(199811)42:2<312::aid-jbm17>3.0.co;2-k

Tanaka, K., Takamoto, Sh, Ohtsuka, T., Kotsuka, Y., and Kawauchi, M. (1999). Application of advaseal for acute aortic dissection: experimental study. *Ann. Thorac. Surg.* 68, 1308–1310.

Tang, G. K., Zhou, B. Y., Li, F., Wang, W. H., Liu, Y., Wang, X., et al. (2020). Advances of naturally-derived and synthetic hydrogels for intervertebral disc regeneration. *Front. Bioeng. Biotechnol.* 8:745. doi: 10.3389/fbioe.2020.00745

Trott, A. T. (1997). Cyanoacrylate tissue adhesives: an advance in wound care. *J. Am. Med. Asso.* 277, 1559–1560. doi: 10.1001/jama.277.19.1559

Tseng, Y. C., Tabata, Y., Hyon, S. H., and Ikada, Y. (1990). In vitro toxicity test of 2-cyanoacrylate polymers by cell culture method. *J. Biomed. Mater. Res.* 24, 1355–1367. doi: 10.1002/jbm.820241007

van Elk, M., Ozbakir, B., Barten-rijbroek, A. D., Storm, G., Nijsen, F., Hennink, W. E., et al. (2015). Alginate microspheres containing temperature sensitive liposomes (TSL) for MR-Guided embolization and triggered release of doxorubicin. *PLoS One* 10:e0141626. doi: 10.1371/journal.pone.0141626

von der Brelie, C., Soehle, M., and Clusmann, H. R. (2012). Intraoperative sealing of dura mater defects with a novel, synthetic, self adhesive patch: application experience in 25 patients. *Br. J. Neurosurg.* 26, 231–235. doi: 10.3109/02688697.2011.619597

Vyas, K. S., and Saha, S. P. (2013). Comparison of hemostatic agents used in vascular surger. *Expert Opin. Biol. Ther.* 13, 1663–1672. doi: 10.1517/14712598.2013.848193

Walgenbach, K. J., Bannasch, H., Kalthoff, S., and Rubin, J. P. (2012). Randomized, prospective study of TissuGlu§surgical adhesive in the management of wound drainage following abdominoplasty. *Aesthetic. Plast. Surg.* 36, 491–496. doi: 10.1007/s00266-011-9844-3

Wallace, D. G., Cruise, G. M., Rhee, W. M., Schroeder, J. A., Prior, J. J., Ju, J., et al. (2001). A tissue sealant based on reactive multifunctional polyethylene glycol. *J. Biomed. Mater. Res.* 58, 545–555. doi: 10.1002/jbm.1053

Wang, D. A., Varghese, S., Sharma, B., Strehin, I., Fermanian, S., Gorham, J., et al. (2007). Multifunctional chondroitin sulphate for cartilage tissue–biomaterial integration. *Nat. Mater.* 6, 385–392. doi: 10.1038/nmat1890

Wang, T., Nie, J., and Yang, D. (2012). Dextran and gelatin based photocrosslinkable tissue adhesive. *Carbohydr. Polym.* 90, 1428–1436. doi: 10.1016/j.carbpol.2012.07.011

Wang, X., Gao, P. Y., Yang, Y. Y., Guo, H. X., and Wu, D. C. (2018). Dynamic and programmable morphology and size evolution via a living hierarchical self-assembly strategy. *Nat. Commun.* 9:2772.

Wang, X., Yang, Y. Y., Gao, P. Y., Yang, F., Shen, H., Guo, H. X., et al. (2015). Synthesis, self-assembly and photoresponsive behavior of tadpole-shaped azobenzene polymers. *ACS Macro Lett.* 4, 1321–1326. doi: 10.1021/acsmacrolett.5b00698

Yan, C., Yang, T., Zhu, S., and Wu, H. (2017). Synthesis and properties of poly(DEX-GMA/AAc) microgel particle as a hemostatic agent. *J. Mater. Chem. B* 5, 3697–3705. doi: 10.1039/c7tb00768j

Yang, X., Liu, W., Shi, Y., Xi, G., Wang, M., Liang, B., et al. (2019). Peptide-immobilized starch/PEG sponge with rapid shape recovery and dual-function for both uncontrolled and noncompressible hemorrhage. *Acta Biomater.* 99, 220–235. doi: 10.1016/j.actbio.2019.08.039

Yang, Y. Y., Wang, X., Yang, F., Wang, L. N., and Wu, D. C. (2018). Highly elastic and ultratough hybrid ionic-covalent hydrogels with tunable structures and mechanics. *Adv. Mater.* 30:1707071. doi: 10.1002/adma.201707071

Yin, M. L., Wang, Y. F., Zhang, Y., Ren, X. H., Qiu, Y. Y., and Huang, T. S. (2020). Novel quaternarized N-halamine chitosan and polyvinyl alcohol nanofibrous membranes as hemostatic materials with excellent antibacterial properties. *Carbohyd. Polym.* 232:115823. doi: 10.1016/j.carbpol.2019.115823

Yu, T. T., Wang, H. F., Zhang, Y. F., Wang, X., and Han, B. (2020). The Delivery of RNA-interference therapies based on engineered hydrogels for bone tissue regeneration. *Front. Bioeng. Biotechnol.* 8:445. doi: 10.3389/fbioe.2020.00445

Zeng, Z., Mo, X., He, C., Morsi, Y., El-Hamshary, H., and El-Newehy, M. (2016). An in situ forming tissue adhesive based on poly(ethylene glycol)-dimethacrylate and thiolated chitosan through the Michael reaction. *J. Mater. Chem. B* 4, 5585–5592. doi: 10.1039/c6tb01475e

Zhai, Z. R., Xu, K. M., Mei, L. X., Wu, C., Liu, J., Liu, Z. Q., et al. (2019). Co-assembled supramolecular hydrogels of cell adhesive peptide and alginate for rapid hemostasis and efficacious wound healing. *Soft. Matter.* 15, 8603–8610. doi: 10.1039/c9sm01296f

Zhang, K. C., Li, J., Wang, J., Mu, Y. Z., Sun, X. J., Su, C., et al. (2020). Hydroxybutyl chitosan/diatom-biosilica composite sponge for hemorrhage control. *Carbohyd. Polym.* 236:116051. doi: 10.1016/j.carbpol.2020.116051

Conflict of Interest: The authors declare that the research was conducted in the absence of any commercial or financial relationships that could be construed as a potential conflict of interest.

frontiers
in Bioengineering and Biotechnology

ORIGINAL RESEARCH
published: 27 August 2020
doi: 10.3389/fbioe.2020.01038

E-quality Control in Dental Metal Additive Manufacturing Inspection Using 3D Scanning and 3D Measurement

Liang Du[1], Yiwen Lai[1], Chunwang Luo[1], Yong Zhang[1], Jun Zheng[2]*, Xiaohong Ge[2]* and Yuangang Liu[3]*

[1] School of Electrical Engineering and Automation, Xiamen University of Technology, Xiamen, China, [2] School of Materials Science and Engineering, Xiamen University of Technology, Xiamen, China, [3] College of Chemical Engineering, Huaqiao University, Xiamen, China

OPEN ACCESS

Edited by:
Junchao Wei,
Nanchang University, China

Reviewed by:
Chao Feng,
Ocean University of China, China
Mingqiang Li,
Sun Yat-sen University, China
Lihua Li,
Jinan University, China

***Correspondence:**
Jun Zheng
2016000031@xmut.edu.cn
Xiaohong Ge
xhge@xmut.edu.cn
Yuangang Liu
ygliu@hqu.edu.cn

Specialty section:
This article was submitted to
Biomaterials,
a section of the journal
Frontiers in Bioengineering and
Biotechnology

Received: 23 June 2020
Accepted: 11 August 2020
Published: 27 August 2020

Citation:
Du L, Lai Y, Luo C, Zhang Y,
Zheng J, Ge X and Liu Y (2020)
E-quality Control in Dental Metal
Additive Manufacturing Inspection
Using 3D Scanning and 3D
Measurement.
Front. Bioeng. Biotechnol. 8:1038.
doi: 10.3389/fbioe.2020.01038

3D printed metal crowns can be used for dental restorations. The main quality control challenge of these dental metal is the method of quality inspection. Electronic quality is a process by which the quality of the process and the parts produced can be checked online, thereby improving the process and reducing the time it takes for the entire process. Here, we propose a combination of 3D scanning and 3D measurement for 3D inspection of metal crowns. The data extracted from the 3D printed metal crowns were used as case studies to prove the proposed methodology. The obtained results confirm that the new method has very high classification accuracy compared with the traditional inspection methods, and thus yields excellent results. Moreover, the proposed approach is capable to archive 3D models of the parts and achieve rapid quality control. This paper forms the basis for solving many other similar problems that occur in 3D printing related industries.

Keywords: E-quality, dental restoration, metal materials, 3D scanning, 3D measurement

INTRODUCTION

Selective laser melting (SLM) technology can quickly prepare metal crowns suitable for the individual needs of different patients (Huang et al., 2015; Buican et al., 2017). However, the choice of different materials and the setting of process parameters may cause defects in printed crowns. In this case, the E-quality control system was developed which is benefit to perform quality inspections reliably, accurately and in a very short time (Liverani et al., 2017).

Traditional methods to achieve and ensure quality standards are mainly through statistical process control (SPC) procedures (Zhai et al., 2004). However, the product quality in the sequential manufacturing process is affected by various factors, and it is difficult to set the optimal manufacturing specifications for SPC (Kang et al., 1999). Traditional SPC and six sigma techniques must adhere to statistical assumptions such as the normality of the variable distribution, constant variance of the variables, and so on. However, it is difficult to satisfy all these assumptions in practice. Based on some shortcomings of current statistical methods, a hybrid data mining method based on the combination of rough set theory, fuzzy set theory, genetic algorithm and agent based technology is proposed. Compared with standard statistical tools that use population based methods, the Rough Set Theory (RST) uses an individual approach based on an object model, which is a very useful tool for analyzing quality control issues (Kusiak, 2001). In addition, Fuzzy Set Theory (FST) has proven its function in many applications, especially for the control of complex non-linear systems that may be difficult to model analytically (Huang et al., 2008). The Genetic algorithm (GA) is based on the overall solution rather than a single solution (Goldberg, 1989). In order to solve the shortcomings of these statistical methodologies in the quality control of dental metal, the proposed approach expects to provide a way to optimize prediction for the lowest defective rate.

Recent work has shown that 3D dental models can be obtained through 3D scanning, which can be used for rapid prototyping, parts inspection and dimensional control (Munera et al., 2012; Javaid et al., 2019). This type of technology can use light as a probe, which does not damage the sample during analysis, ensuring that the measurement technology will not deform the object (Zhang and Alemzadeh, 2007). Therefore, it is of great significance to obtain 3D reconstruction of dental models. However, the related research mainly focused on reconstruction and measurement of plaster dental models or casting dental models, while there are few studies on dental metal models manufactured by SLM (Sinescu et al., 2008; Zhou and Fan, 2017; Song et al., 2018; Yang et al., 2018). We already have a case of E-quality control of automotive parts, but we still face some challenges for the E-quality control of metal crowns manufactured by SLM.

This paper presents a 3D E-quality control system that integrates 3D scanning and 3D reconstruction to perform fast quality control inspections of complex dental metal parts. The systems then compare the scanned 3D models of produced parts with the scanned 3D models of the standard parts to provide accurate and timely measurement feedback for quality control, thereby helping to prove that the produced products meet the required specifications.

METHODOLOGY

The 3D E-quality Control System

The 3D E-quality control system advances the basic research to address the aforementioned issues through the use of integration of cyber communication, virtual prototyping, 3D scanning, and machine vision system. The hardware is mainly composed of the 3D scanning system and the machine vision system. These equipment and systems provide the foundation for the project. The software consists of Intelligent Graphical User Interface (i.e., Application Program Interface) embedded with 3D reconstruction and 3D measurement algorithms. The overall framework of the 3D E-quality control system is shown in **Figure 1**. Firstly, the inspection support system (ISS) uses a 3D scanner to scan the metal crowns to generate high-resolution 2D images and accurate 3D models for inspection. The 3D scanning System based on Structured light is used to capture high-resolution 2D images of parts from different angles with blue light patterns. After these images have been produced, they are used to construct accurate 3D models which will be saved in the PC and compared with the standard 3D model later for the comparison is implemented, the contrast and difference between two parts will be identified. Finally, the inspection outcomes will be reported as Pass, Rework, and Discard.

3D Reconstruction

The scanning process of metal crowns is carried out by using a 3D scanner. The scanner is the medium of data capture. The purpose of the 3D scanner is to measure and record the relative distance between the surface of the object and a known point in space. This geometric data is expressed in the form of point cloud data (Sinescu et al., 2008). In order to generate accurate 3D models for inspection, 3D reconstruction of metal crowns is required. The structured light used in the scanning process is blue, and the light pattern consists of a series of stripes. In capturing, the grating projection device projects several pieces of structured light with a specific code onto the metal crowns, and the two cameras at a certain angle simultaneously acquire corresponding images. Because of noise and limited resolution of the projector, the scanning of structured light will introduce some high frequency offset and noise. We use bilateral noise reduction to smooth the structured light scanning surface, then create a surface normal maps from the smoothed grid, and use high-pass filtering to extract the high frequency details of the estimated normals (Mallick et al., 2005) (see **Figure 2**).

Finally, we use the embossing process in Zickler et al. (2002) to optimize the mesh vertices to match this combined normal map. We obtain diffuse and specular normals from gradient illumination. For the polarization pattern, a separate linear polarizer is placed on each light. The linear polarizer is installed on the servo motor in front of the camera, which can quickly flip the polarizer between its horizontal and vertical directions at its diagonal (Mallick et al., 2005).

While using normals to improve the geometry, we found the measured position from the distance image. Reference to the pixel coordinates on the camera will cause the natural parameterization of the corresponding surface. Therefore, under perspective projection, the coordinates of the surface points can be represented by the depth function Z (x, y). That is to say, given the pixel coordinates, the position of the corresponding surface point P (x, y) has only one degree of freedom Z (x, y):

$$P\left(x,y\right)=\left[-\frac{x}{f_x}Z\left(x,y\right),-\frac{y}{f_y}Z\left(x,y\right),-\frac{x}{f_x}Z\left(x,y\right)\right]^T \tag{1}$$

Where f_x and f_y are the focal length of the camera in pixels. The challenge we face is to find a depth function that matches our estimate of the position and normal of each point. To this end, we select a depth function to minimize the sum of two error terms: position error E^p and normal error E^n. Then define the position error as the sum of the square of the distance between the optimized position and the measured position:

$$\left|\left|P_i-P_j^m\right|\right|^2=\mu_i^2(Z_i-Z_i^m)^2,\ where\,\mu_i^2=\left(\frac{x_i}{f_x}\right)^2+\left(\frac{y_i}{f_y}\right)^2+1 \tag{2}$$

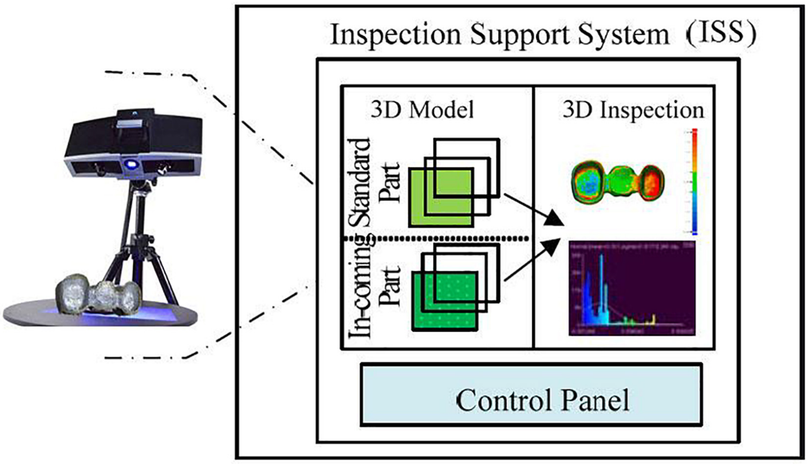

FIGURE 1 | The framework of the 3D E-quality control systems.

The surface tangents T_x and T_y at a given pixel can be expressed as a linear function of the depth value and its partial derivative:

$$T_x = \frac{\partial P}{\partial x} = \left[-\frac{1}{f_x}\left(x\frac{\partial Z}{\partial x} + Z\right), -\frac{1}{f_x}y\frac{\partial Z}{\partial x}, \frac{\partial Z}{\partial x}\right]^T \tag{3}$$

$$T_y = \frac{\partial P}{\partial y} = \left[-\frac{1}{f_x}x\frac{\partial Z}{\partial y}, -\frac{1}{f_y}\left(y\frac{\partial Z}{\partial y} + Z\right), \frac{\partial Z}{\partial y}\right]^T \tag{4}$$

Then define the normal error as

$$E^n = \sum_i \left[T_x(P_i) \cdot N_i^c\right]^2 + \left[T_y(P_i) \cdot N_i^c\right]^2 \tag{5}$$

The best surface is as follows:

$$\arg\min_Z \gamma E^p + (1-\gamma)E^n \tag{6}$$

where the parameter $\gamma \in [0, 1]$ controls the degree of influence of position and normals in optimization.

3D Measurement Application Programming Interface (API)

Remote access can be achieved through an application programming interface (API). The purpose of API development is to provide a graphical user interface (GUI) to allow the user to establish and control communication lines with Web-enabled devices. As a result, the API allows the user to view, measure or operate dental metal parts through the machine vision system (MVS), webcam, and "remote desktop" provided by Microsoft® Windows. The current 3D measurement API using point clouds to perform 3D inspections to measure the geometric elements of metal crown parts, such as contours, surfaces, boundaries, etc. It extracts features directly from the point cloud and provides feedback such as standard deviation (mean error), tolerance and distribution. Also it gets color mapping from surfaces or contours comparison and label edition on particular points for inspection. The inspector then can classify the part into Pass or Fail categories. The 2D inspection function can show the inspector the high-resolution images taken during the scanning process that are used to generate the accurate 3D model. The 2D inspection function can also lead the inspector to the Machine Vision System (MVS) for traditional 2D inspection (see **Figures 3**, **4**).

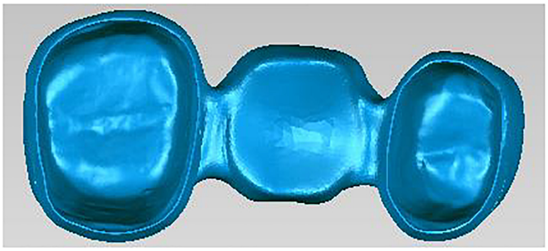

FIGURE 2 | Scanned geometry of metal crowns.

Registration of 3D Measurement

Before doing 3D measurement, we need to register the two models to be compared. The first step is to scale the two models to make sure they are expressed in the same units. First, select an accurate element that is visible in the two metal crown models, such as edges, surfaces, or other elements. Then, measure the distance D_{max} between two specific points on the model on a larger scale, and then repeat the process on the other model, and obtain the corresponding distance D_{min}. Finally, the scale factor $S_f = D_{max}/D_{min}$ is calculated and applied to the smaller model in the f_x, f_y, and f_z fields of the 3D measurement API modification tool. In the second step, we roughly register the two models with translate and rotation tool of the API, and then use the Iterative Closest Point (ICP) algorithm to precisely register and finish the superimposition of the two models (**Figure 5**).

The default method for calculating the distance between two point clouds is "nearest neighbor distance." For each

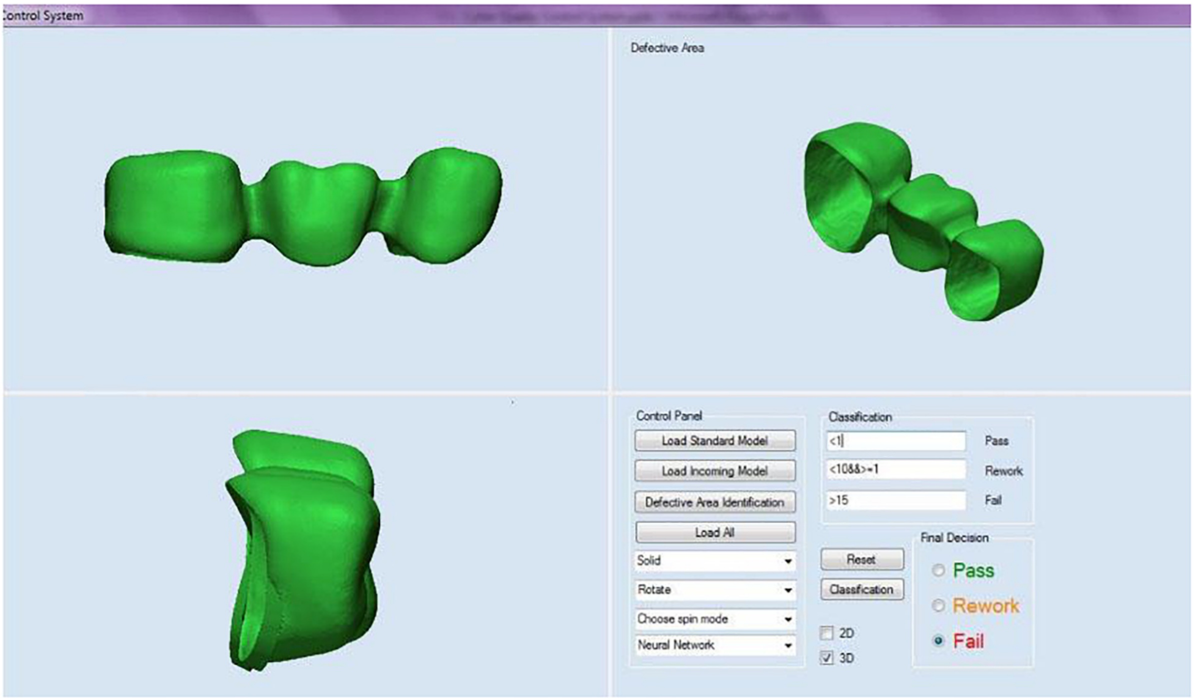

Classification
<1 Pass
<10&&>=1 Rework
>15 Fail

Solid
Rotate
Choose spin mode
Neural Network

☐ 2D
☑ 3D

Final Decision
○ Pass
○ Rework
● Fail

FIGURE 3 | 3D quality control API.

point of the compared cloud, the API searches for the closest point in the reference cloud and calculates their (Euclidean) distance. If the reference point cloud is dense enough, an approximation of the distance from the comparison cloud to the base surface represented by the reference cloud can be accepted. However, if the reference cloud is not dense enough, the nearest neighbor distance may sometimes be inaccurate. Therefore, the 3D measurement API uses an intermediate method that can better approximate the true distance of the reference surface. When determining the closest point in the reference cloud, the idea is to locally model the reference cloud surface by fitting a mathematical model, e.g., Delaunay triangulation, located at the "nearest" point and its neighbors. The distance from each point in the comparison cloud to the closest point in the reference cloud will be replaced by the distance to the model (**Figure 6**). Statistically, this is more accurate and less dependent on cloud sampling.

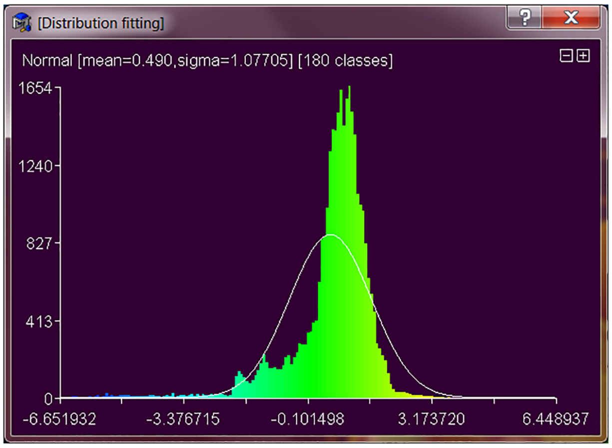

FIGURE 4 | Distribution from 3D measurement.

EXPERIMENT AND ANALYSIS

This case study involves the occurrence of two common defects in dental crown parts printed by SLM technology and the change on dimensions after forming. If the minimum strength requirements are not met, metallurgical defects may cause parts to crack. These requirements may be accomplished, but if appearance becomes the main requirement, they may be affected by such defects. Shrinkage is an important aspect to consider in the metal powder forming process, as it is essential for good fit and function of the final product. The final inspection of the process includes a visual inspection and a first inspection by the person in charge. Coordinate measuring machines may also be used to ensure dimensional accuracy of the final product. If defects are found, parts may be repaired manually, or in case if it cannot be repaired, it must be scrapped. Defects may occur randomly or simultaneously due to many factors. Therefore, checks are required to ensure that there are no other issues either with the forming process parameters, the materials or equipment used. If dimensional accuracy is not accomplished, parts are simply scrapped.

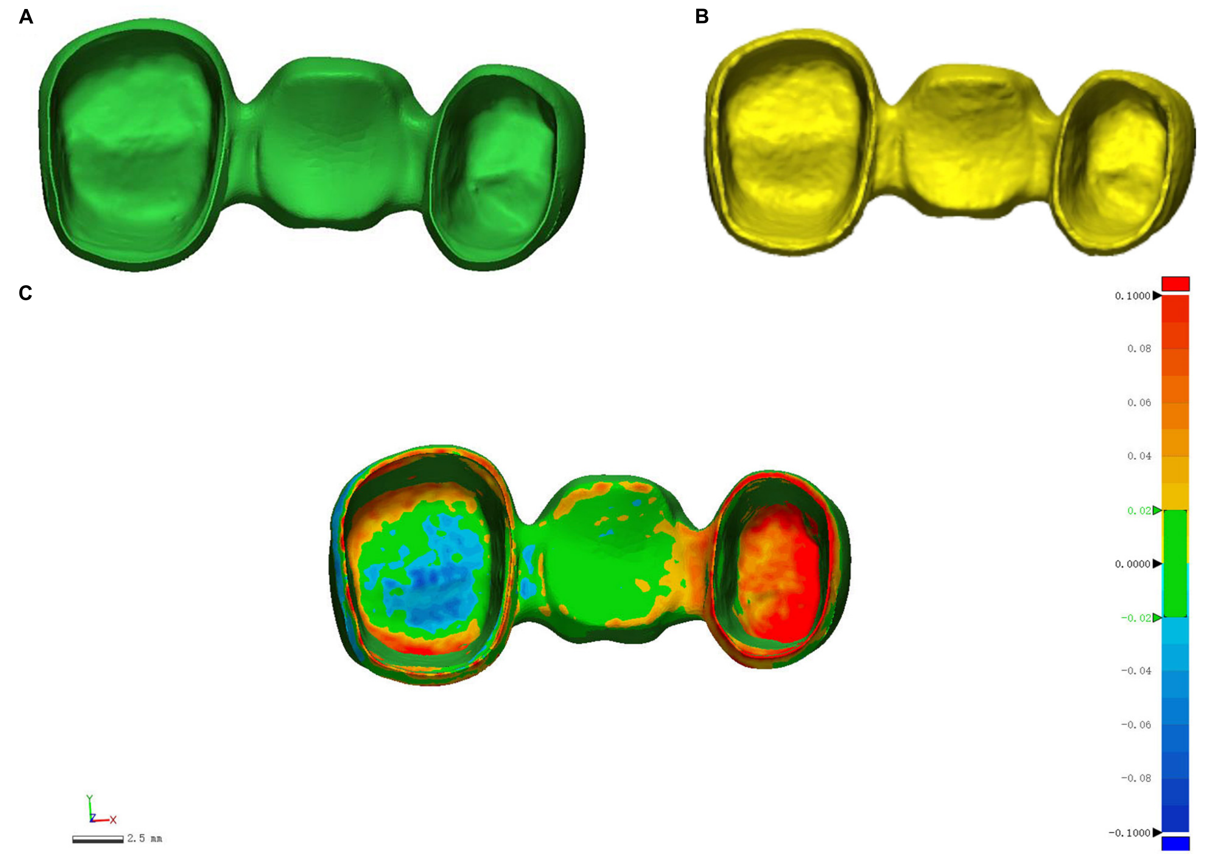

FIGURE 5 | Register the two metal crown models before 3D measurement using the ICP algorithm. **(A)** Standard metal crown model; **(B)** Scanned metal crown model; **(C)** Registered metal crown models.

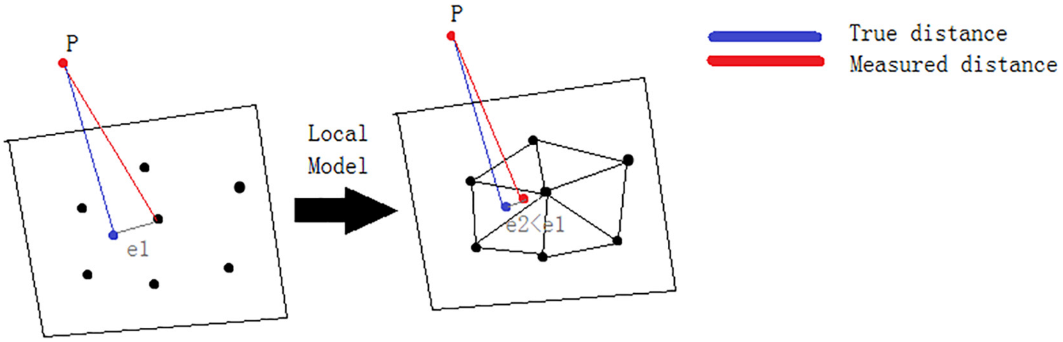

FIGURE 6 | A local model is used to calculate the distance between two point clouds.

Selective laser melting process is a method of directly forming metal components, which has been widely used in medical, automotive, aerospace and other industries (Yadroitsev and Smurov, 2010; Hedberg et al., 2014). In the medical field, metal crowns are made of metal powder materials, usually cobalt chromium alloys or titanium alloys, depending on the characteristics and specifications of the materials (Averyanova et al., 2011; Xu et al., 2014). When designing dental parts, it must be very carefully designed for the patient to wear. Before this process, the small features of the parts, powder materials, process parameters, are some of the important points to take into account (Delgado et al., 2012; Zhang et al., 2012).

The key process parameters affecting the quality of metal crowns in SLM are shown in **Figure 7**. Laser power has an important influence on the quality of metal powder melting during rapid forming. If laser power is too low, the energy irradiated on the metal powder will be small, resulting in the powder cannot be completely melted, causing defects such as

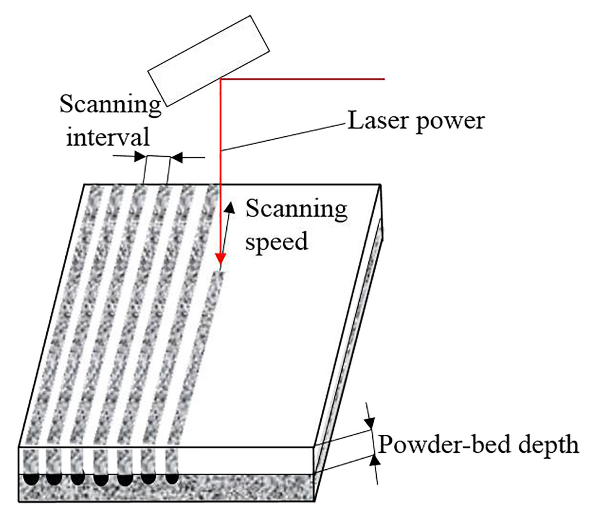

FIGURE 7 | Key process parameters affecting metal crowns quality in SLM.

spheroidization and pores. However, if laser power is too high, excessive melting will occur, resulting in warping, deformation and cracking of the formed parts, which will have an adverse effect on the forming quality (Zhang et al., 2017). Scanning speed refers to the moving speed of the laser spot on the powder bed, which directly affects the interaction time between laser and metal powder. Scanning interval refers to the distance between two adjacent parallel scan lines, which determines the overlap between melt channels. Smallar powder-bed depth is generally beneficial to improve the forming quality, but at the cost of reducing processing efficiency. These important parameters are related to energy density, reflecting the complexity and difficulty of SLM process parameters control (Cherry et al., 2015).

When setting different process parameters to print dental parts, some defects may appear in the process. At this point, all employees involved in the process are trained to identify these issues. This means that quality control is dependent on a human being been able to identify such defects. Depending on the defect, the part may not meet its requirements and may not function as expected. There may be little details easily fixable, but there may be other details that cannot be resolved at all.

Some appearance defects may include spheroidization, warpage, shrinkage, cracking, among others (Kang and Ma, 2017). We will focus on two of cosmetic defects: balling and warpage (**Figure 8**).

Since the laser melting channel has a tendency to reduce the surface energy under the action of surface tension, it is easy to form a balling phenomenon in the SLM process (Dai and Gu, 2015). The balling phenomenon is mainly caused by too low and too high energy density. The spheroidization on the sintering surface during SLM processing is the main reason for the existence of pores. The best energy density can be obtained by adjusting the process parameters so as to reduce the porosity of the sintered surface (Li et al., 2012; Galy et al., 2018).

Shrinkage and warpage are caused by residual stress (Liu et al., 2016). Such defects can be avoided by reducing the

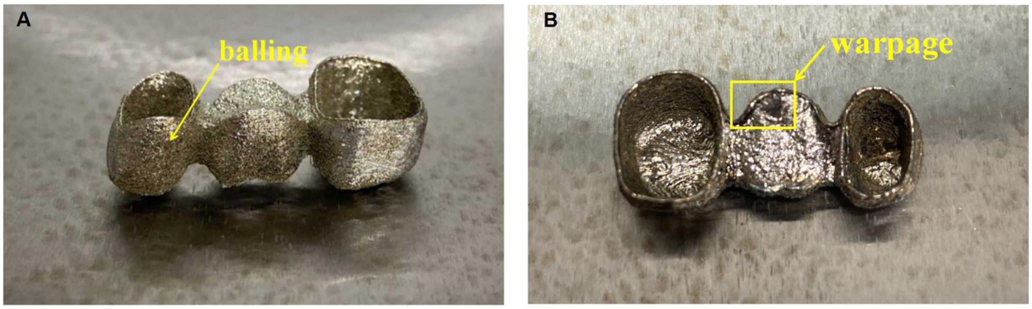

FIGURE 8 | Cosmetic defects: **(A)** Balling, **(B)** Warpage.

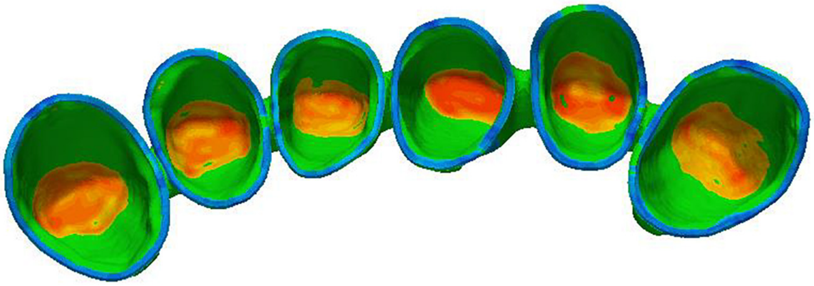

FIGURE 9 | The green surface in the half-bridge crown is the key area for quality control.

generation of residual stresses. Residual stress is an inevitable metallurgical defect when SLM processing metal parts. The main reason for its existence is the high temperature gradient during processing, and preheating the substrate can reduce residual stress (Salmi et al., 2017). At the same time, the warpage of parts can be reduced by optimizing the support structure and process parameters.

If a good quality control plan is not established and personnel are not properly trained to detect defective parts in a timely manner, scrapped parts may waste a lot of time and cost. It is required to find any defects before the parts are delivered or used so that they can be repaired, reworked or scrapped.

In order to solve the problem of surface metallurgical defects, some points need to be clarified (Olakanmi et al., 2015; Taib et al.,

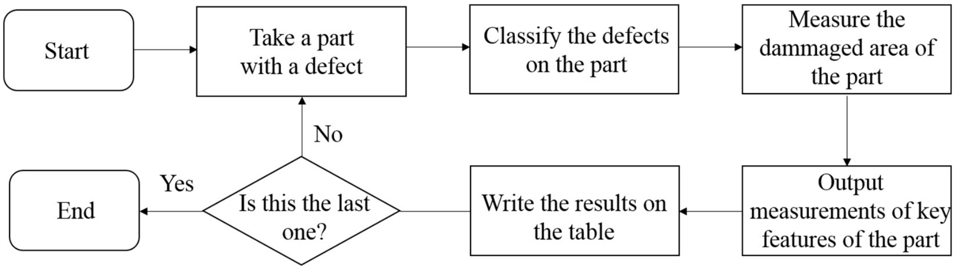

FIGURE 10 | 3D printed metal crowns quality control flowchart.

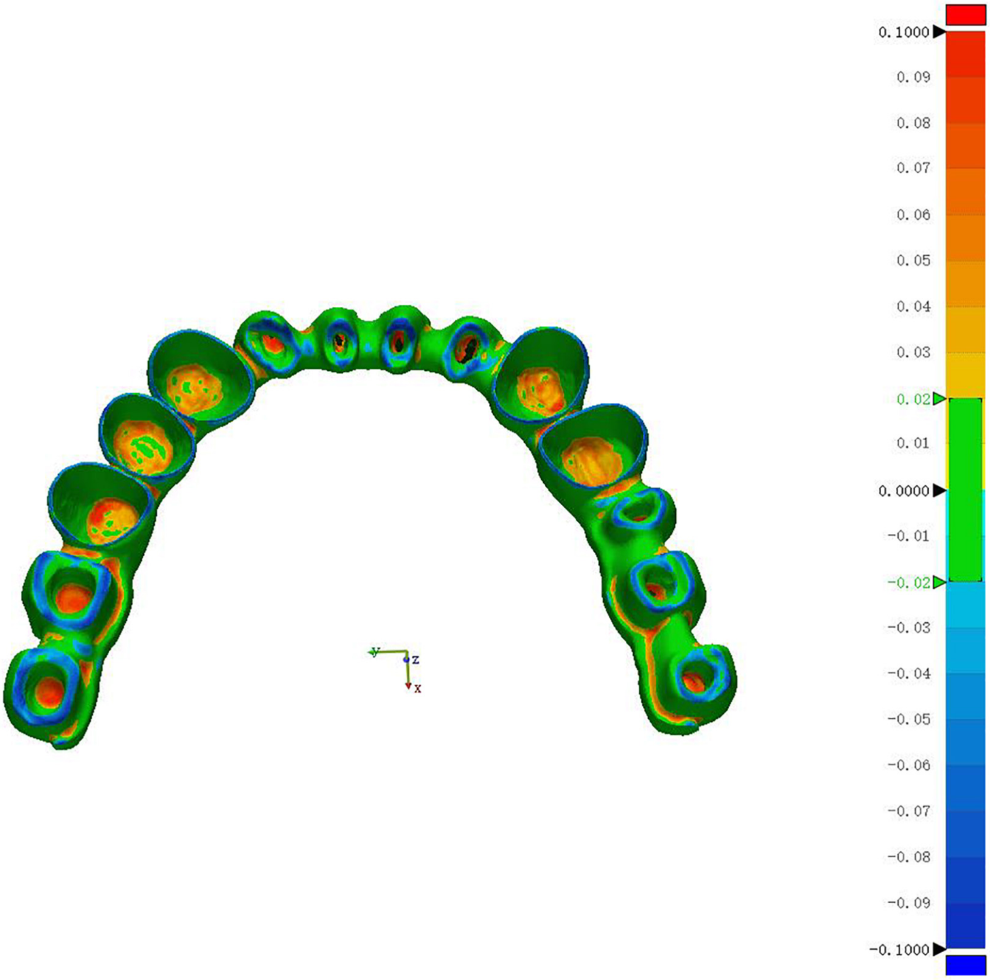

FIGURE 11 | 3D Measurement of dental metal parts.

2016). First, you should check the exact location and shape of the defect and find out when it is really obvious. Then, we need to specify if the defect occurs once every time or irregularly, if it is always exists at a certain position of the metal crowns, if we can predict the defect and if it only happens with one 3D printer or others. If we are capable to identify defects on time, we can ensure that appropriate measures are taken to avoid major losses due to insufficient information.

To demonstrate the proposed methodologies of E-quality control in an industrial setting, metal crowns containing different types of defects including spheroidization, holes, cracking, and warpage were used for testing. This part requires certain specifications about size and durability. If it does not meet these specifications, such as cracking or deformation, it must be scrapped. If the dimensional accuracy of metal crown parts does not meet the requirements, it will not be suitable for patients to wear and cause discomfort. It is necessary to investigate what causes this problem. It depends on what kind of defects the parts have so as to make targeted technical improvements.

Design of Experiments

A half-bridge crown model is shown in **Figure 9**. These parts have a tolerance limit of ± 0.25 mm. Parts with dimensions outside this range will be rejected. The green surface is important because the green surface is mainly the internal surface profile of the metal crowns.

Twenty metal crown parts were printed on the WXL-120 SLM equipment, and some of them exceeded tolerance limits for each size. Each type of dental metal part is mixed together for inspection. The test flow chart is shown in **Figure 10** below. Although these parts does not pose any serious measurement challenges, it presents a moderate level of complexity for the requirement of our work. The 3D measurement of dental metal parts is shown in **Figure 11**.

Classification Analysis

The following tables show the comparison of the classification analysis using 2D Machine Vision System, 3D Quality Control System and the efficiency test results. From **Table 1** and **Table 2**, we can see that the 2D Machine Vision System can achieve accuracy of 0.85 and with precision of 0.875 while the 3D Quality Control System can achieve both accuracy and precision of 1 compared with the actual efficiency test results. With 3D E-quality control, all 20 dental metal parts are predicted correctly, resulting in 100% classification accuracy.

TABLE 1 | The confusion matrix of the 2D Machine Vision System (MVS) classification results.

	Predicted	
Actual Efficiency Test	**Pass**	**Fail**
Pass	14	2
Fail	1	3

TABLE 2 | The confusion matrix of the 3D Quality Control System (QCS) classification results.

	Predicted	
Actual Efficiency Test	**Pass**	**Fail**
Pass	16	0
Fail	0	4

CONCLUSION

This paper proposes a 3D E-quality control system, which integrates 3D scanning and 3D reconstruction functions, and can perform rapid quality control inspection on complex metal crown parts manufactured by SLM. The scanner based on structured light can provide traceable data and accurate 3D models of 3D printed complex parts, thereby providing manufacturers with proof of compliance. The system captures millions of data points in just a few minutes to represent the true and complete geometry of complex metal crown parts. The systems then compare the scanned 3D models to computer aided design (CAD) models to provide accurate and timely measurement feedback for quality control, thereby helping to prove that the produced products meet the required specifications. The data extracted from the 3D printed metal crowns was used as a case study to prove the proposed methodology. The results show that, compared with traditional detection approach, this approach has better effect and higher classification accuracy. Through this approach, the following conclusions can be drawn: (1) Measuring the whole part can better ensure that the requirements are met and improve overall quality. (2) Scan and store 3D models of complex parts for technicians to view, analyze and measure later. (3) Create accurate digital models of existing components for redesign. (4) Help replicate complex parts, tooling or parts that are no longer produced.

DATA AVAILABILITY STATEMENT

The raw data supporting the conclusions of this article will be made available by the authors, without undue reservation.

AUTHOR CONTRIBUTIONS

All the authors were involved in this work. JZ and XG conceived the idea of the study. CL and YZ designed and performed the experiments. YLi helped with the experiments and provided constructive discussions. JZ provided the financially supporting for this work. YLa analyzed the data. LD, JZ, and YLi interpreted the data and wrote the manuscript. All authors contributed to the article and approved the submitted version.

ACKNOWLEDGMENTS

We sincerely thank the Xiamen Wuxinglong Technology Co., Ltd. for providing us the infrastructure needed to carry out our research work.

REFERENCES

Averyanova, M., Bertrand, P., and Verquin, B. (2011). Manufacture of Co-Cr dental crowns and bridges by selective laser Melting technology. *Virtual Phys. Prototy.* 6, 179–185. doi: 10.1080/17452759.2011.619083

Buican, G. R., Oancea, G., and Martins, R. F. (2017). Study on SLM manufacturing of teeth used for dental tools testing. *MATEC Web Conf.* 94:03002. doi: 10.1051/matecconf/20179403002

Cherry, J. A., Davies, H. M., Mehmood, S., Lavery, N. P., Brown, S. G. R., and Sienz, J. (2015). Investigation into the effect of process parameters on microstructural and physical properties of 316L stainless steel parts by selective laser melting. *Int. J. Adv. Manuf. Technol.* 76, 869–879. doi: 10.1007/s00170-014-6297-2

Dai, D., and Gu, D. (2015). Tailoring surface quality through mass and momentum transfer modeling using a volume of fluid method in selective laser melting of TiC/AlSi10Mg powder. *Int. J. Mach. Tool. Manu.* 88, 95–107. doi: 10.1016/j.ijmachtools.2014.09.010

Delgado, J., Ciurana, J., and Rodríguez, C. A. (2012). Influence of process parameters on part quality and mechanical properties for DMLS and SLM with iron-based materials. *Int. J. Adv. Manuf. Technol.* 60, 601–610. doi: 10.1007/s00170-011-3643-5

Galy, C., Le Guen, E., Lacoste, E., and Arvieu, C. (2018). Main defects observed in aluminum alloy parts produced by SLM: from causes to consequences. *Addit. Manuf.* 22, 165–175. doi: 10.1016/j.addma.2018.05.005

Goldberg, D. E. (1989). *Genetic Algorithms in Search, Optimization and Machine Learning*. Reading, MA: Addison-Wesley.

Hedberg, Y. S., Qian, B., Shen, Z., Virtanen, S., and Wallinder, I. O. (2014). In vitro biocompatibility of CoCrMo dental alloys fabricated by selective laser melting. *Dent. Mater.* 30, 525–534. doi: 10.1016/j.dental.2014.02.008

Huang, C. C., Fan, Y. N., Tseng, T. L., Lee, C. H., and Chuang, H. F. (2008). "A hybrid data mining approach to quality assurance of manufacturing process," in *Proceedings of the IEEE International Conference on Fuzzy Systems (IEEE World Congress on Computational Intelligence)*, Hong Kong, 818–825. doi: 10.1109/FUZZY.2008.4630465

Huang, Z., Zhang, L., Zhu, J., and Zhang, X. (2015). Clinical marginal and internal fit of metal ceramic crowns fabricated with a selective laser melting technology. *J. Prosthet. Dent.* 113, 623–627. doi: 10.1016/j.prosdent.2014.10.012

Javaid, M., Haleem, A., and Kumar, L. (2019). Current status and applications of 3D scanning in dentistry. *Clin. Epidemiol. Global Health* 7, 228–233. doi: 10.1016/j.cegh.2018.07.005

Kang, B. S., Choe, D. H., and Park, S. C. (1999). Intelligent process control in manufacturing industry with sequential processes. *Int. J. Prod. Econ.* 6061, 583–590. doi: 10.1016/s0925-5273(98)00178-9

Kang, J., and Ma, Q. (2017). The role and impact of 3D printing technologies in casting. *China Foundry* 14, 157–168. doi: 10.1007/s41230-017-6109-z

Kusiak, A. (2001). Rough set theory: a data mining tool for semiconductor manufacturing. *IEEE Trans. Electron. Packag. Manuf.* 24, 44–50. doi: 10.1109/6104.924792

Li, R., Liu, J., Shi, Y., Wang, L., and Jiang, W. (2012). Balling behavior of stainless steel and nickel powder during selective laser melting process. *Int. J. Adv. Manuf. Technol.* 59, 1025–1035. doi: 10.1007/s00170-011-3566-1

Liu, Y., Yang, Y., and Wang, D. (2016). A study on the residual stress during selective laser melting (SLM) of metallic powder. *Int. J. Adv. Manuf. Technol.* 87, 647–656. doi: 10.1007/s00170-016-8466-y

Liverani, E., Toschi, S., Ceschini, L., and Fortunato, A. (2017). Effect of selective laser melting (SLM) process parameters on microstructure and mechanical properties of 316L austenitic stainless steel. *J. Mater. Process. Technol.* 249, 255–263. doi: 10.1016/j.jmatprotec.2017.05.042

Mallick, S. P., Zickler, T. E., Kriegman, D. J., and Belhumeur, P. N. (2005). "Beyond lambert: reconstructing specular surfaces using color," in *Proceedings of the IEEE Computer Society Conference on Computer Vision and Pattern Recognition (CVPR'05)*, San Diego, CA, 619–626. doi: 10.1109/CVPR.2005.88

Munera, N., Lora, G. J., and Garcia-Sucerquia, J. (2012). Evaluation of fringe projection and laser scanning for 3d reconstruction of dental pieces. *Dyna* 79, 65–73. doi: 10.1016/j.mssp.2011.05.010

Olakanmi, E. O., Cochrane, R., and Dalgarno, K. (2015). A review on selective laser sintering/melting (SLS/SLM) of aluminium alloy powders: processing, microstructure, and properties. *PrMS* 74, 401–477. doi: 10.1016/j.pmatsci.2015.03.002

Salmi, A., Atzeni, E., Iuliano, L., and Galati, M. (2017). Experimental analysis of residual stresses on AlSi10Mg parts produced by means of Selective Laser Melting (SLM). *Proc. CIRP* 62, 458–463. doi: 10.1016/j.procir.2016.06.030

Sinescu, C., Negrutiu, M., Faur, N., Negru, R., Romînu, M., and Cozarov, D. (2008). Dental scanning in CAD/CAM technologies: laser beams. *Progr. Biomed. Opt. Imaging Proc. SPIE* 6843:13. doi: 10.1117/12.764829

Song, L. M., Lin, W. W., Yang, Y. G., Zhu, X. J., Guo, Q. H., and Yang, H. D. (2018). Fast 3D reconstruction of dental cast model based on structured light. *Optoelectron. Lett.* 14, 457–460. doi: 10.1007/s11801-018-8076-z

Taib, M., Adnan, Z., Harun, W. S. W., Ghani, S. A. C., Ab Rashid, M. F. F., Omar, M. A., et al. (2016). Dimensional accuracy study of open cellular structure CoCrMo alloy fabricated by selective laser melting process. *Adv. Mat. Res.* 1133, 280–284. doi: 10.4028/www.scientific.net/AMR.1133.280

Xu, D., Xiang, N., and Wei, B. (2014). The marginal fit of selective laser melting–fabricated metal crowns: an in vitro study. *J. Prosthet. Dent.* 112, 1437–1440. doi: 10.1016/j.prosdent.2014.05.018

Yadroitsev, I., and Smurov, I. (2010). Selective laser melting technology: from the single laser melted track stability to 3D parts of complex shape. *Phys. Proc.* 5, 551–560. doi: 10.1016/j.phpro.2010.08.083

Yang, S., Shi, X., Zhang, G., and Lv, C. (2018). A dual-platform laser scanner for 3D reconstruction of dental pieces. *Engineering* 4, 796–805. doi: 10.1016/j.eng.2018.10.005

Zhai, J., Xu, X., Xie, C., and Luo, M. (2004). Fuzzy control for manufacturing quality based on variable precision rough set. *Proc. World Congr. Intelligent Control Autom. WCICA* 3, 2347–2351. doi: 10.1109/WCICA.2004.1342013

Zhang, B., Huang, Q., Gao, Y., Luo, P., and Zhao, C. (2012). Preliminary study on some properties of Co-Cr dental alloy formed by selective laser melting technique. *J. Wuhan. Univ. Technol.* 27, 665–668. doi: 10.1007/s11595-012-0525-0

Zhang, B., Li, Y., and Bai, Q. (2017). Defect formation mechanisms in selective laser melting: a review. *Chin. J. Mech. Eng.* 30, 515–527. doi: 10.1007/s10033-017-0121-5

Zhang, L., and Alemzadeh, K. (2007). "A 3-dimensional vision system for dental applications," in *Proceedings of the Annual International Conference of the IEEE Engineering in Medicine and Biology Society*, Lyon, 3369–3372. doi: 10.1109/IEMBS.2007.4353053

Zhou, H., and Fan, Q. (2017). 3D Reconstruction and SLM Survey for Dental Implants. *J. Mech. Med. Biol.* 17:1750084. doi: 10.1142/S0219519417500841

Zickler, T. E., Belhumeur, P. N., and Kriegman, D. J. (2002). Helmholtz stereopsis: exploiting reciprocity for surface reconstruction. *IJCV* 49, 215–227. doi: 10.1023/A:1020149707513

Conflict of Interest: The authors declare that the research was conducted in the absence of any commercial or financial relationships that could be construed as a potential conflict of interest.

frontiers
in Bioengineering and Biotechnology

REVIEW
published: 17 September 2020
doi: 10.3389/fbioe.2020.587658

Recent Advances of Chitosan-Based Injectable Hydrogels for Bone and Dental Tissue Regeneration

Guoke Tang[1,2,3†], Zhihong Tan[2†], Wusi Zeng[2], Xing Wang[4,5*], Changgui Shi[1], Yi Liu[1,3], Hailong He[1], Rui Chen[1*] and Xiaojian Ye[1,3*]

[1] Department of Orthopedic Surgery, Changzheng Hospital, Second Military Medical University, Shanghai, China, [2] Department of Spine Surgery, The Affiliated Zhuzhou Hospital of Xiangya School of Medicine, Central South University (CSU), Hunan, China, [3] Department of Orthopedics, Tongren Hospital, Shanghai Jiao Tong University School of Medicine, Shanghai, China, [4] Beijing National Laboratory for Molecular Sciences, Institute of Chemistry, Chinese Academy of Sciences, Beijing, China, [5] University of Chinese Academy of Sciences, Beijing, China

Edited by:
Bing Han,
Peking University School and Hospital of Stomatology, China

Reviewed by:
Hao Hu,
Qingdao University, China
Payam ZarrinTaj,
Oklahoma State University, United States
Xun Sun,
Tianjin Hospital, China

***Correspondence:**
Xing Wang
wangxing@iccas.ac.cn
Rui Chen
chenruiwal@smmu.edu.cn
Xiaojian Ye
xjyespine@smmu.edu.cn

†These authors have contributed equally to this work

Specialty section:
This article was submitted to Biomaterials, a section of the journal Frontiers in Bioengineering and Biotechnology

Received: 27 July 2020
Accepted: 24 August 2020
Published: 17 September 2020

Citation:
Tang G, Tan Z, Zeng W, Wang X, Shi C, Liu Y, He H, Chen R and Ye X (2020) Recent Advances of Chitosan-Based Injectable Hydrogels for Bone and Dental Tissue Regeneration.
Front. Bioeng. Biotechnol. 8:587658.
doi: 10.3389/fbioe.2020.587658

Traditional strategies of bone repair include autografts, allografts and surgical reconstructions, but they may bring about potential hazard of donor site morbidity, rejection, risk of disease transmission and repetitive surgery. Bone tissue engineering (BTE) is a multidisciplinary field that offers promising substitutes in biopharmaceutical applications, and chitosan (CS)-based bone reconstructions can be a potential candidate in regenerative tissue fields owing to its low immunogenicity, biodegradability, bioresorbable features, low-cost and economic nature. Formulations of CS-based injectable hydrogels with thermo/pH-response are advantageous in terms of their high-water imbibing capability, minimal invasiveness, porous networks, and ability to mold perfectly into an irregular defect. Additionally, CS combined with other naturally-derived or synthetic polymers and bioactive agents has proven to be an effective alternative to autologous bone and dental grafts. In this review, we will highlight the current progress in the development of preparation methods, physicochemical properties and applications of CS-based injectable hydrogels and their perspectives in bone and dental regeneration. We believe this review is intended as starting point and inspiration for future research effort to develop the next generation of tissue-engineering scaffold materials.

Keywords: chitosan, injectable hydrogel, responsiveness, bone repair, dental tissue regeneration

INTRODUCTION

Bone, composed of collagen and calcium phosphate apatite crystals, is a well-known internal support system in higher vertebrates, which provides the rigidity, strength and a certain degree of elasticity to the living body. In recent years, on account of the increase of population aging, accidental injury, disease, trauma, obesity and weak physical activity in internal and external

---

Abbreviations: ACP, amorphous calcium phosphate; ALN, alendronate; ASP, aspirin; BCP, biphasic calcium phosphate; β-GP, β-sodium glycerophosphate; bFGF, basic fibroblast growth factor; BMPs, morphogenetic proteins; BMP-2, bone morphogenetic protein 2; BMP-7, bone morphogenetic protein-7; BTE, bone tissue engineering; CMCh, carboxymethyl chitosan; CS, chitosan; DPSCs, dental pulp stem cells; ECM, extracellular matrix; EPO, erythropoietin; GP, β-glycerophosphate; MCS, maleilated chitosan; MSCs, mesenchymal stem cells; NIPAAm, N-isopropylacrylamide; NPs, nanoparticles; nBG, bioactive glass NP; ORN, ornidazole; PEGDA, poly(ethylene glycol) diacrylate; PVA, poly(vinyl alcohol); VEGF, vascular endothelial growth factor.

mediators, bone disorders and diseases are on the rise worldwide (Amin et al., 2014; Saravanan et al., 2016; Baldwin et al., 2019; Wang et al., 2019; Yu et al., 2020). Although natural curing is a stable and reliable process, Patients with bone traumas always suffer from impaired healing and rehabilitation. Traditional healing strategy includes the autografts, allografts and xenografts that are employed as bone substitutes to promote bone repair. However, these grafts have many disadvantages in repetitive manipulation process, high cost, surgery wound, immune rejection and potential infectious diseases (Visser et al., 2019). The advent of Bone Tissue Engineering (BTE) brings about the advanced development of bone regeneration at the defect host site without any post-operative complications (e.g., morbidity and immunogenicity). BTE is structured around four key components: (1) osteoblasts generate a bone tissue matrix; (2) biocompatible backbone mimic the extracellular matrix (ECM); (3) vascularization process offer nutrients and wastes transport and (4) morphogenesis signals guide the cell activation (Amini et al., 2012; Guo and Ma, 2014). Thereby, bone tissue engineering material requires favorable properties (e.g., osteoinduction and osseointegration), which can promote the progenitor cell differentiation to osteoblasts, support bone growth and facilitate bone fusion to form new bone tissue. In addition, BTE materials should have chemical and mechanical stabilities, non-thrombosis, easy sterilization and facile manufacturability in the host environment. For example, alveolar bone defects are urgently needed to be regenerated by relying on the advanced BTE materials to bring about a positive impact on dental tissue engineering for the periodontal therapy (Hench and Polak, 2002; Stevens, 2008).

Natural polymers with good biocompatibility and biodegradability have a variety of characteristics and advantageous properties for living tissues and cells (Li et al., 2020a). As a representative, chitosan (CS), deacetylated form of chitin (**Figure 1**), is a naturally linear cationic heteropolymer extracted from the shrimp or crab shells. It has analogous compositions and structures to glycosaminoglycans, and renders high biocompatibility, good biodegradability and minimal immune response to tissues and cells (Kavya et al., 2013; Ran et al., 2016; Yang et al., 2016; Atak et al., 2017; Keller et al., 2017). Its physical properties are mainly relied on the molecular weight, degree of deacetylation and purity (Ngo and Kim, 2014). For example, owing to the cationic attribute, CS possesses outstanding antimicrobial activity against both Gram-positive and Gram-negative bacteria, which is relied on the type and degree of deacetylation of chitosan as well as the other extrinsic environmental conditions, but its antimicrobial mechanism has not yet been fully understood. Due to the presence of protonated amino groups of the D-glucosamine residues (**Figure 1A**), CS can form a non-Newtonian, shear-thinning fluid in most diluted acidic solutions at a pH below 6.5 (pKa value ∼6.3), and further contributes to the complexes with metal ions, polymers, lipids, proteins, DNA, etc. (Berillo et al., 2012, 2014; Zhou et al., 2015; Saravanan et al., 2016; Berillo and Cundy, 2018; Yang et al., 2018; Liu H.Y. et al., 2020). In addition, CS-based hydrogels can be chemically crosslinked by glutaraldehyde, oxidized dextran or other carbohydrates and genipin due to the reductive amination between the amino and aldehyde groups in mild conditions (Berillo et al., 2012; Akilbekova et al., 2018; Lu et al., 2018; Chen et al., 2019). Although CS hydrogel has many advantages, its mechanical properties are weak. Thus, it should be combined with other functional materials to promote the osteogenic differentiation and tissue regeneration (Deepthi et al., 2016; Saravanan et al., 2016; Bao et al., 2020).

CS-BASED HYDROGELS

Hydrogel has a three-dimensional porous and interconnected structure that can create a biocompatible ECM microenvironment for cell attachment and proliferation, which can be served as a potential bone supportive system to enhance remodeling at defect sites (Ko et al., 2013; Liu et al., 2017; Wang et al., 2017a, 2020b; Xu et al., 2020a,b). On account of the long and painful invasive surgery for the clinical application of implanted hydrogels, injectable hydrogels are required to have capacities to fill irregularly shaped defects in a non-invasive way, which are recognized as a high-quality and less invasive alternative surgical strategy in BTE (Li et al., 2020b). When the precursor solution containing drugs, cells and/or biomolecules is injected into the subcutaneous region of defective site, composite hydrogels can be quickly formed via the physically or chemically crosslinking reaction with close correlations to the surrounding environments (Yang J.A. et al., 2014; Cao et al., 2018; Wang et al., 2018a; Bao et al., 2019; Liu B.C. et al., 2020). Especially, CS-based injectable hydrogels can be actuated by physical or chemical stimuli via the sol-gel transition. Besides, CS-based injectable hydrogels can deliver cells, drugs and other bioactive molecules, and thus receiving an amount of recognition in fields of cosmetics, food, drug/gene delivery and bone regeneration (**Figure 1B**; Zheng et al., 2010; Vo et al., 2016; Menon et al., 2018; Yang et al., 2018; Lavanya et al., 2020).

Preparation Techniques of CS-Based Hydrogels

Hydrogels are generally fabricated via crosslinking the polymer network through physical and chemical strategies. Based on these two basic approaches, there are various preparation techniques for construction of hydrogel configurations. On the one hand, physical crosslinkers mainly include the hydrophobic-hydrophobic, host-guest, ionic or electrostatic, crystallization and stereo complex interactions, which can cause the formation of polymer network in mild conditions (Hoffman, 2012; Sivashanmugam et al., 2015; Fan et al., 2019; Zhu C.X. et al., 2019; Wang et al., 2020a). Physically crosslinked hydrogels possess great advantages in biological applications because of the absence of chemical crosslinkers that may bring about the unpredictable and potential toxicity for the tissues, but their reversible architectures, poor stability and low mechanics greatly limited the scope of applications (Zhang et al., 2013; Maitra and Shukla, 2014; Parhi, 2017; Li et al., 2018). On the other hand, chemical crosslinkers are constructed by the covalent linkage of polymer chains together within the network using high-effective synthetic methods, such as click chemistry, Schiff base reaction,

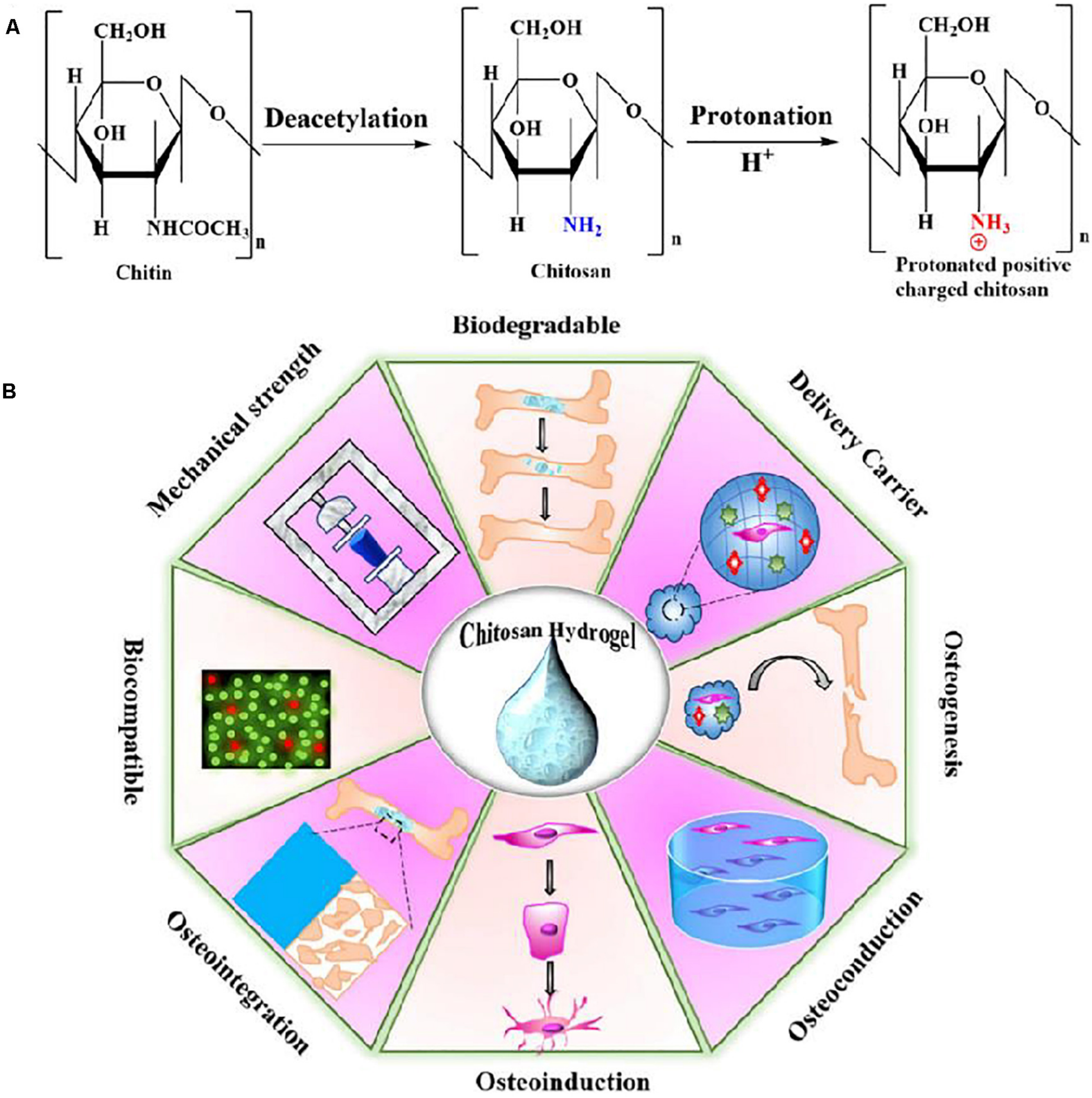

FIGURE 1 | (A) The chemical structures for the chitin, noncharged form of chitosan and protonated positive-charged chitosan. **(B)** Schematic representation of physio-chemical and biological properties of CS-based hydrogel. Reproduced from Lavanya et al. (2020) with permission from Copyright 2020 Elsevier.

free radical polymerization, etc. (Hennink and van Nostrum, 2012; Wang et al., 2013; Zhang J.F. et al., 2019). On account of the permanent and irreversible junctions among polymeric chains, chemically crosslinking hydrogels possess stable structures and excellent mechanics for tissue engineering fields. However, toxic chemical agents and difficult sterilization may produce adverse effects and certain insecurities.

Physico-Chemical Properties of CS-Based Injectable Hydrogels

In recent years, the application of injectable in-situ forming hydrogels in orthopedics has been widely investigated by many scientists (Gyawali et al., 2013). Unlike the prefabricated stents that require surgical implantation, injectable hydrogels can be *in situ* injected into the defect sites to fill in any geometric deformities using the minimally invasive surgery methods. Hydrogel is usually used for confronting bone defects in non-weight bearing parts or injured bone tissue through delivering and releasing the therapeutic biomolecules and agents once the stimulus response that triggers its physical and/or chemical properties has been changed. On account of numerous hydroxy and amine groups within the cationic CS framework, CS can be feasibly modified to improve its multifunction, such as antibacterial property, solubility, stimulus-response, adhesion and degradation behaviors (Lavanya et al., 2020). Therefore, CS-based injectable hydrogels possess more advantages on the tailor of topological structures, biodegradability behaviors, cytocompatibility and adhesive force, which can be widespread used as effective biopharmaceutical materials to promote bone regeneration (Liu et al., 2017; Shariatinia and Jalali, 2018).

Chitosan is usually combined with other natural-derived or synthetic biomaterials via the covalent and/or non-covalent bonds, yielding a varied of multifunctional hydrogels. Wherein, physical gelation is a typical approach for fabrication of CS-based hydrogels with good biocompatibility and gradual degradability to promote the cell-materials interactions and stimulate the proliferation and differentiation of osteoprogenitor cells (Berger et al., 2004). Therefore, development of CS-based injectable hydrogels would allow for the effective therapy for the bone regeneration, especially for the irregular defective sites of bone tissue. Based on this physical gelation of CS-based injectable hydrogel, environmentally responsive injectable hydrogels, such as pH, light and temperature, are widely used for repair of large bone defect, because an externally applied trigger for gelation can easily tailor sol-gel transition with the facile permeation into the defect sites and quick gelation *in situ* to fully seal the injury. Recently, Li et al. (2015) prepared a series of soluble UV-crosslinkable CS-based injectable hydrogels by modification of amine groups of CS with methacrylic anhydride in the absence of any activators. These methacryloyl groups improved the CS solubilization in water by impairing intra-/intermolecular hydrogen bonds and provided the crosslinkable CS derivatives. Xia et al. (2017) reported a photopolymerized injectable water-soluble maleilated chitosan (MCS)/poly(ethylene glycol) diacrylate (PEGDA) hydrogels, which had faster gelation rate, higher compressive strength than MCS hydrogel under UV radiation. Control of the MCS/PEGDA ratio could tailor the swelling behavior and mechanical properties of composite hydrogels that could promote the L929 cells attachment and tissue regeneration. Instead of UV light, Hu et al. (2012) prepared CS hydrogels crosslinked under visible light for tissue engineering. By tailoring three various blue light initiators (camphorquinone, fluorescein and riboflavin), methacrylate glycol CS can form the CS hydrogels under the visible light (400–500 nm at 500 mW cm^{-2}), displaying good mechanical properties and less damages to cells than energetic UV light. Further, diverse therapeutic agents or drugs can be encapsulated into these temperature and pH-responsive injectable hydrogels to form the multifunctional hydrogels in tissue engineering and drug delivery systems. For example, Qi et al. (2013) incorporated the bone morphogenetic proteins (BMPs) and mesenchymal stem cells (MSCs)/osteoprogenitors into CS-based injectable hydrogels. The thermo-sensitive CS/poly (vinyl alcohol) (PVA) composite hydrogel can offer the strength support and tailored degradation time, which induced the tissue repair via the space conduction and occupation of defect part. In addition, compared to the pure CS hydrogel, introduction of non-degradable PVA could obviously postpone the degradation and prolong the self-healing term of tissue within the defect center.

Besides, rheological properties also play vital roles in injectable CS-based hydrogels, especially for the gelation, firmness and durability of crosslinking network, which provide intriguing guidance on the effective selection of appropriate chitosan for wide application. Many studies on rheological properties of chitosan in solution have been conducted to characterize the effects various parameters such as polymer concentration, degree of deacetylation, concentrated chitosan, chitosan and vinyl polymers, temperature, shearing and storage time, and addition of other polymers/nanoparticles on the viscoelastic behaviors, which are closely relative to a peculiar mechanism of association with the double-chain strands connected network (Hwang and Shin, 2000; Chen et al., 2003; Martiínez et al., 2004; Lewandowska, 2009; El-hefian and Yahaya, 2010; Racine et al., 2017). Until now, injectable hydrogels are widely applied for tissue engineering and orthopedic applications. Unlike surgical implantation methods, pre-fabricated hydrogel can be injected into any geometries of defect bearing sites using minimally invasive procedures and quick *in situ* gelation through a sol-gel transition once exposure to a simulative change. In addition, injectable hydrogels can also be blended with other biomolecules, therapeutic agents and cells to form multifunctional carriers to repair the bone and dental tissues (**Figure 2**; Saravanan et al., 2019).

pH-Responsive CS-Based Injectable Hydrogels

Chitosan and its derivatives are a series of natural biopolymers with good biocompatibility, pH sensitivity, enzymatic biodegradability and polycationic attributes. Especially, tailor the protonation/deprotonation of $-NH_2$ group can obviously furnish CS-based injectable hydrogels with pH-responsive behaviors (Xu and Matysiak, 2017). Lower pH can protonate amine group to induce the electrostatic repulsion, and thus the polymer chains can easily expand and interact with water molecules to effectively improve the water-solubility. In contrast, higher pH can deprotonate the $-NH_2$ group and cause the collapse of globular structure, severely impairing the water-solubility of CS. In this case, the water solubility and swelling property of CS-based hydrogels is mainly relied on the its pKa value and external pH conditions (Rizwan et al., 2017). Therefore, CS-based injectable hydrogels possess the innate pH response that has been attracted considerable attentions in the bone regeneration process. In addition, incorporation of various polymers with CS can improve this pH responsiveness. Nevertheless, CS has poor solubility in alkaline and neutral solutions as well as the insufficient mechanical performance. To overcome these limitations, various physical or chemical modification strategies have been well-developed to make CS soluble without impairing its other properties.

For instance, Rogina et al. (2017) demonstrated a pH-responsive CS-hydroxyapatite hydrogel with a gelling agent of $NaHCO_3$. Tailoring of $NaHCO_3$ can achieve the quick gelation of CS-hydroxyapatite-based hydrogel within 4 min, which exhibited good viability for cell proliferation and differentiation as a potential cell carrier. Zhao et al. (2019) developed a composite CMCh-ACP hydrogel via combining the carboxymethyl chitosan (CMCh) and amorphous calcium phosphate (ACP). Incorporation of an acidifier of glucono δ-lactone could endow pH-responsive injectable hydrogels with

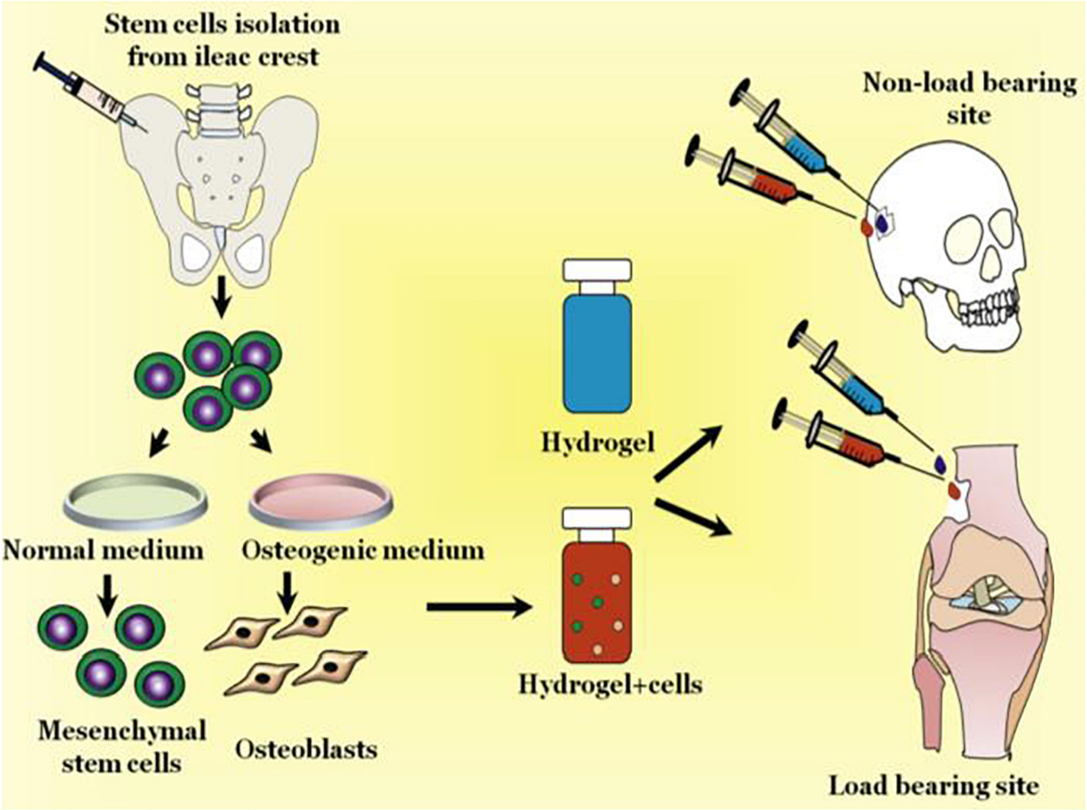

FIGURE 2 | Schematic representation of injectable hydrogels for treating bone loss at defective sites. Reproduced from Saravanan et al. (2019) with permission from Copyright 2019 Elsevier.

good biocompatibility and effective cell adhesion/proliferation, which upregulated the expression of bone markers and enhanced the new bone regeneration (**Figure 3**).

Thermo-Responsive CS-Based Injectable Hydrogels

Chitosan itself has not thermosensitive behaviors, and thermo-responsive CS-based hydrogels are generally fabricated via introducing the thermo-responsive polymers into CS-based hydrogels (Argüelles-monal et al., 2018). In views of simple regulation and easy utilization for *in vitro* and *in vivo* testing, temperature is recognized as a typical stimulus for the hydrogel system. In recent years, ideally thermo-responsive CS injectable hydrogels with the sol-gel transition at a physiological temperature have been developed in application of tissue engineering because of their temperature response, attractive moldable ability, tailorable rheological property, excellent biocompatibility and biodegradability to the cells and tissues, which can provide suitable manipulation and enhance cellular activity for bone and dental regenerations. In addition, encapsulation of diverse polymers (natural and synthetic polymers), bioactive molecules and nanoparticles can also expand the functional properties of CS injectable hydrogels for biomedical applications (Mohebbi et al., 2019; Zarrintaj et al., 2019; Bagheri et al., 2020; Khalili et al., 2020; Mahmodi et al., 2020; Nourbakhsh et al., 2020). For example, CS/β-glycerophosphate (GP) hydrogel is a famous scaffold for wide-range delivery of growth factors, cells, small drugs and nucleic acid. Since cationic CS chains can be connected with negatively charged GP molecules via the electrostatic attraction and hydrogen bonds, injectable CS/GP hydrogels can achieve structural optimization systems with a sol-gel transition temperature of 37°C for the bone regeneration (**Figure 4**; Dhivya et al., 2015; Saravanan et al., 2019).

The gelation mechanism of this thermo-responsive CS/GP hydrogel has been detailedly elucidated as follows (Chenite et al., 2001). Firstly, on account of poor solubility of CS in neutral and basic solutions, CS solutions above pH 6.2 can result in the immediate formation of hydrated gel-like precipitate as well as the occurrence of phase separation of CS at pH >6 to form a hydrogel. Maintaining CS solution within a physiological pH (6.8–7.2) in the presence of GP polyol salt could generate a thermo-responsive injectable hydrogel, which kept a sol state at room temperature and transferred into a gel state at physiological temperature (cloud point of $\geq$37°C). Incorporation of GP components into CS solutions can reduce electrostatic repulsion between phosphate groups of GP and amino groups of CS, enhance CS-CS hydrophobic interactions

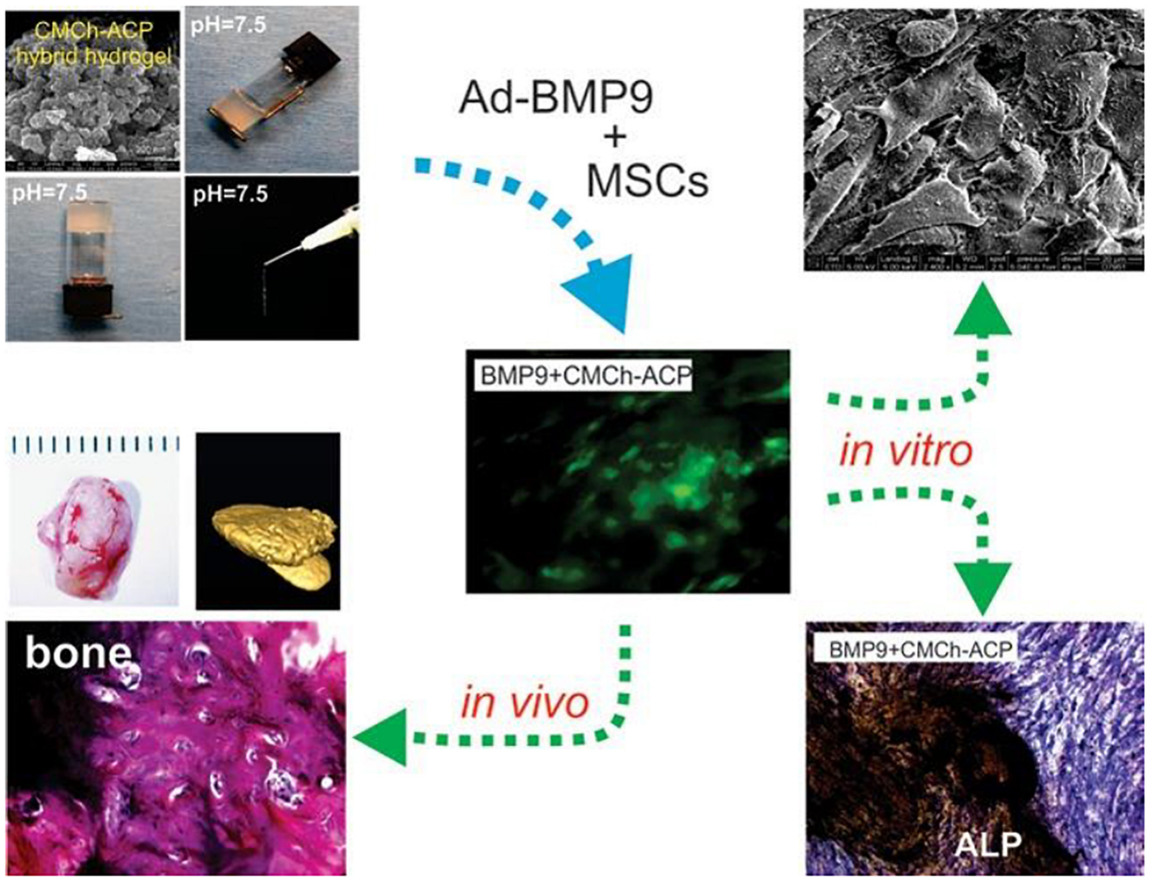

FIGURE 3 | Schematic representation of pH-responsive CS-based hydrogels for bone tissue engineering. Reproduced from Zhao et al. (2019) with permission from Copyright 2019 American Chemical Society.

and increase hydrogen bonding effects between CS chains during gel formation, and therefore the pH range can be modulated from 7.0 to 7.4 and the sol-gel transition temperature can be tailored at 37°C. The temperature dependence of CS/GP hydrogels has been investigated by the rheological studies. Owing to the hydrophobic interactions between CS chains and glycerol groups, CS chains aggregation can be prevented by the CS-water interactions at low temperature. Once upon heating, water molecules are partially removed from the glycerol moieties and CS chains can associate and aggregate into a gel formation. In this CS/GP gelling system, temperature rise can also tailor CS-CS hydrophobic interactions in addition to the regulation of electrostatic forces, because the orientation of dipolar water molecules surrounding CS polymer chains is effectively limited via increasing the vibrational and rotational energy of water molecules. These energized water molecules are removed around the CS polymeric chains, thereby causing the interconnection among dehydrated hydrophobic segments. At low temperatures, CS displays a helical structure due to the presence of intramolecular hydrogen bonds and the masking of physical connections. At high temperature, the decreasing number of intramolecular hydrogen bonds allows the CS molecules to unfold and facilitate the gelation. Thus, pH and temperature are significantly important factors for this thermo-responsive CS/GP injectable hydrogels.

Polymers Introducing the CS-Based Injectable Hydrogels

Incorporation of various polymers like naturally-derived (e.g., alginate, hyaluronic acid, collagen, starch, and silk fibroin) and synthetic macromolecules [e.g., poly(vinylalcohol), polyethylene glycol and polycaprolactone] into CS hydrogels can further improve their multifunctionality and thermo-responsive behaviors for effective bone repair. For example, Bagheri et al. (2019) prepared a kind of electroactive hydrogel based on chitosan–aniline oligomer and agarose, wherein the aniline oligomer can tailor the swelling, degradation rate, thermal and conductive properties of CS-based hydrogels. Owing to its conductivity, control of the electrical stimulus can manipulate the on-demand drug release that may promote the cell activity, growth and proliferation. Chen et al. (2013) prepared a biocompatible injectable thermo-responsive HA-CPN/BCP hydrogel based on a hyaluronic acid-g-chitosan-g-poly (N-isopropylacrylamide) containing biphasic calcium phosphate (BCP) ceramic microparticles. The HA-CPN/BCP possessed better biocompatibility with human fetal osteoblast cell

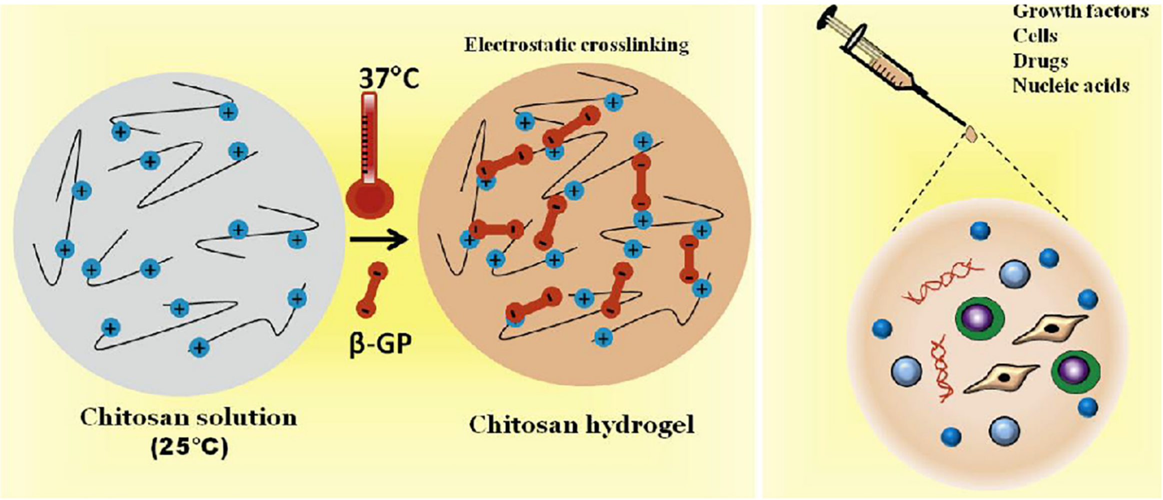

FIGURE 4 | Schematic representation of thermal-responsive CS/β-GP hydrogels encapsulating with various growth factors, cells, drugs and nucleic acids for bone tissue engineering. Reproduced from Saravanan et al. (2019) with permission from Copyright 2019 Elsevier.

attachment, proliferation and osteoblastic differentiation. In addition, higher mechanical strength and elasticity of these thermo-responsive injected hydrogels was benefited for calcium deposition, extracellular matrix mineralization and generation of ectopic bone tissue. Additionally, incorporation of synthetic polymers endows the CS hydrogels with multifunction to achieve the advanced regulation. Wu et al. (2018) constructed a thermo-sensitive NIPAAm-g-CS hydrogel with disulfide crosslinkers throughout the networks (**Figure 5**), and found that three types of cells exhibited excellent biocompatibility with favorable cell attachment, growth and proliferation.

Bioactive Molecules Encapsulated CS-Based Injectable Hydrogels

Over the last decade, CS-based hydrogels have been functionalized via loading bioactive molecules into drug delivery systems, compelling the bioactive molecules to locally deliver into target sites with adequate dose for a desired period. Encapsulation of hydrophobic and hydrophilic molecules like bioactive factors, drugs, proteins, amino acid, and nucleic acids into CS-based responsive hydrogels can construct smart delivery system and bone regenerative medicine. Wherein, these bioactive molecules [e.g., bone morphogenetic protein 2 (BMP-2) and vascular endothelial growth factor (VEGF)] can keep long stability and half-life with low adverse effects while thermo-responsive injectable hydrogels can effectively prolong the localized drug or growth factor release in a sophisticated delivery system (Tiffany et al., 2012; Faikrua et al., 2014; Mi et al., 2017). In this case, these bioactive molecules-encapsulated CS-based hydrogels can modulate and promote cell differentiation, proliferation, migration, recruitment and angiogenesis. For example, Li et al. (2017) demonstrated a thermo-responsive CS/CSn (pDNA-BMP2)-GP hydrogel system of CS-based hydrogel with pDNA-BMP2 for alveolar bone regeneration. The sustained release of pDNA-BMP2 could affect the osteocytes growth within the lacunae, increase trabecular thickness and promote trabecular bone formation. Apart from these growth factors, CS-based hydrogels could deliver bone resorption inhibitors of alendronate (ALN) to treat the Paget's disease and osteoporosis. Nafee et al. (2017) prepared ALN-loaded CS/β-GP hydrogel with injectable and thermo-reversible gelation behaviors. These biodegradable and biocompatible hydrogels expressed less inflammatory responses and faster proliferation of granulation tissue via controlling ALN drug release for 65 days.

Nanoparticles Encapsulated CS-Based Injectable Hydrogels

Incorporation of functional nanoparticles (NPs) into hydrogels can increase the mechanical, biological, and chemical properties and therefore expand their applications. Especially, metal/metal-oxide NPs (e.g., Au, Ag, and Fe_3O_4), inorganic/ceramic NPs (e.g., hydroxyapatite, calcium phosphate, silica and silicates), and polymeric NPs (natural/synthetic polymers, dendrimers and hyperbranched polyesters) can promote the osteogenic differentiation and mineralization for bone regeneration (Moorthi et al., 2014; Wang et al., 2014, 2016, 2017b, 2018b; Yang Y.Y. et al., 2014; Yang et al., 2015, 2021; Thoniyot et al., 2015; Ko et al., 2018; Min et al., 2018; Bian et al., 2020; Fan et al., 2020). For example, Radwan et al. (2020) prepared CS-based calcium phosphate composite scaffolds with embedded moxifloxacin hydrochloride. Composite hydrogels delivered the antibiotic drugs for 3 days and induced the cell differentiation and osteoblasts proliferation, benefiting for bone tissue formations using the osteomyelitis-induced animal model. Moreira et al. (2018, 2019) constructed a novel thermo-responsive CS/gelatin/nBG-based composite hydrogel by combining CS-gelatin with bioactive glass NP (nBG), on account of its capacity to bond with living tissues, these thermo-responsive composite hydrogels possessed enhanced osteoblasts proliferation and angiogenesis-related gene expressions, thus promoting cell

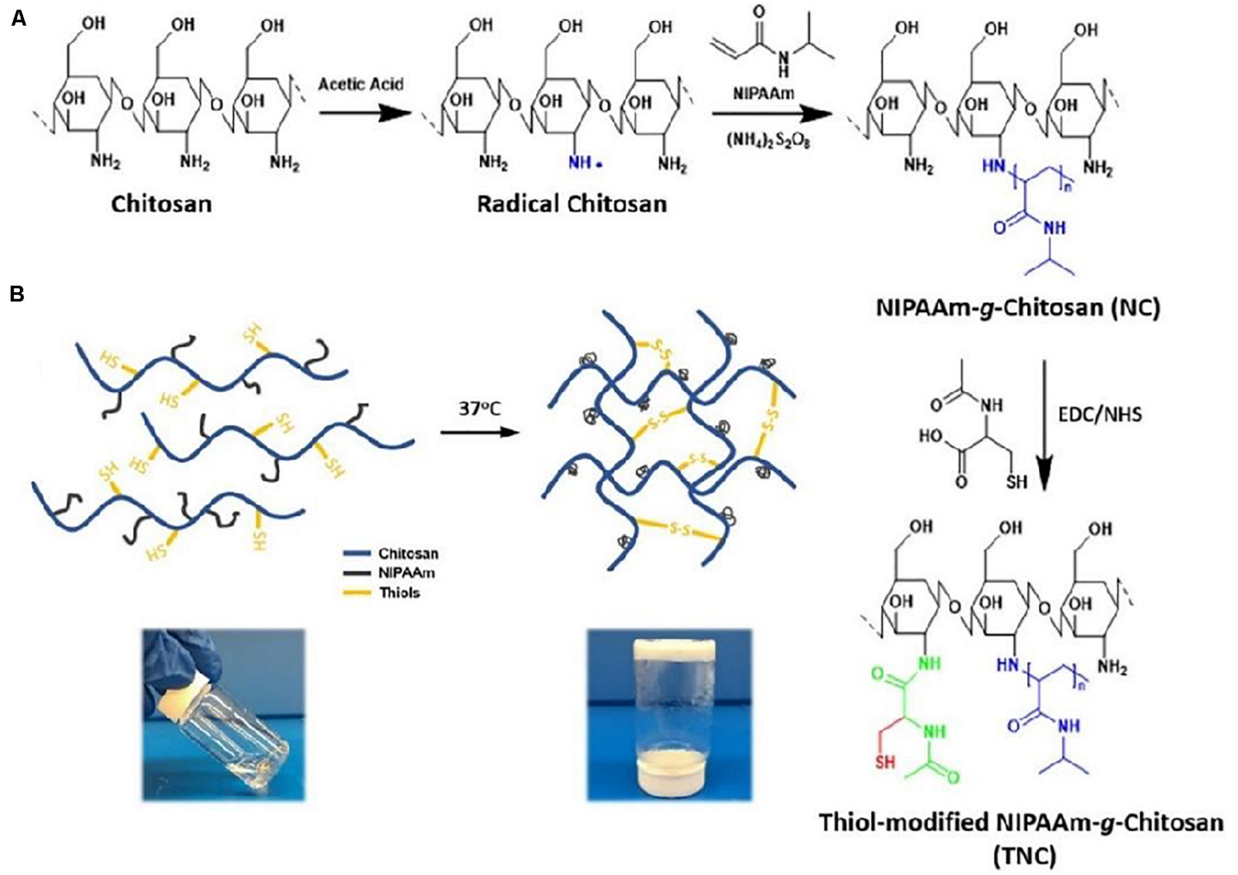

FIGURE 5 | (A) Synthetic preparation of NIPAAm-g-CS. **(B)** Gelation mechanism of physical cross-linking (helix-coil structure) and chemical cross-linking (disulfide bonds). Reproduced from Wu et al. (2018) with permission from Copyright 2018 Elsevier.

proliferation activity and bone regeneration. Additionally, introducing metallic NPs into injectable hydrogels can facilitate bone cell growth and expand bone regeneration applications. For example, when the Au NPs and κ-carrageenan poly(NIPAM) were mixed into the CS-based injectable hydrogels, Pourjavadi et al. (2019) found these Au NPs-incorporated injectable hydrogels were conductive that could enhance cell attachment and proliferation to accelerate bone tissue growth through MG-63 cell viability assay, presenting a great potential application in tissue engineering.

CS-Based Hydrogels for Bone Regeneration

Bone tissues are highly functional connective that can constitute the human skeleton, provide the mechanical support, protect internal organs and participate in many physiological activities (Arvidson et al., 2011). Once it is injured, bone tissues can undergo the self-repair process by stimulating MSCs toward osteogenic differentiation and forming the neo-angiogenesis for small size of bone defect, but large-size defects should require bone grafts in the clinical procedures (Gómez-Barrena et al., 2015; Loi et al., 2016). On account of low immunogenicity, physiological inertia, osteoconductivity and osteogenesis, CS-based hydrogels can significantly promote cell proliferation and cell adhesion, presenting great application prospects in bone tissue regeneration (Jiang et al., 2019). In addition, to improve its mechanics and multiple function, CS-based hydrogels are always required to be mixed with other synthetic or natural polymers and bioactive pharmacological molecules to construct multifunctional biomaterials scaffolds. For example, Oudadesse et al. (2020) proposed a nBG-loaded hybrid CS-based hydrogel using freeze-gelation method. The surface area, porosity and mechanical properties of BGN/CH composite hydrogel could be tailored by altering the BGN proportion, which could favor the generation of apatite layer on the surface to promote the direct bone bonding with the implanted hydrogels. Zhang Y.H. et al. (2019) developed a biodegradable hybrid DN hydrogel via interspersing a methacrylated gelatin network into a nanocomposite hydrogel comprised of methacrylated chitosan and polyhedral oligomeric silsesquioxane. Based on its easy manipulation and excellent mechanics, hybrid DN hydrogels could preferentially guide the MSCs toward the osteogenic differentiation *in vitro* and accelerate new bone regeneration *in situ* using a rat of calvarial defects. These advantageous characteristics and attractive capacities endowed

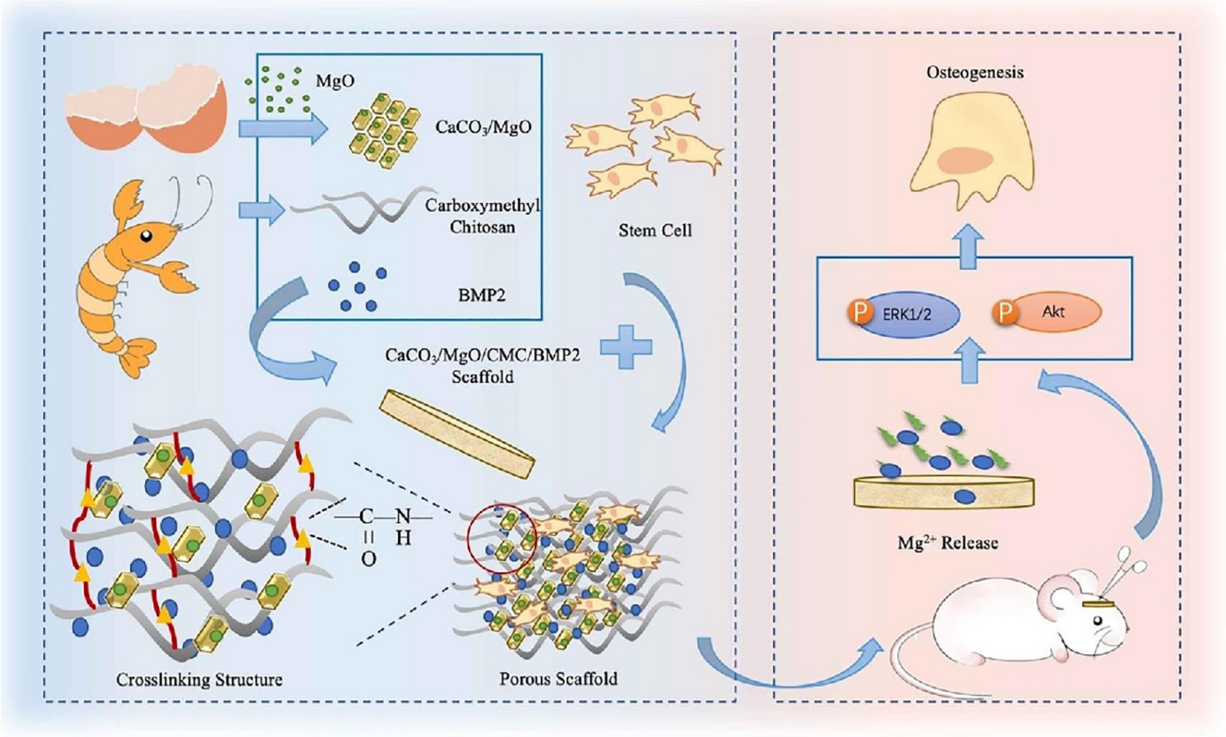

FIGURE 6 | Schematic preparation of $CaCO_3$/MgO/CMC/BMP2 scaffolds and their applications *in vivo*. Reproduced from Huang et al. (2020) with permission from Copyright 2020 Elsevier.

these functional DN hydrogels with great potentials for stem cell therapy and tissue engineering application. It is noted that tunable osteogenesis and degradation rates are important for repairing the bone defect. Huang et al. (2020) prepared a novel composite $CaCO_3$/MgO/CMC/BMP2 scaffold with high mechanical strength, mineralization ability, biomimetic activity and osteogenic differentiation. The sustainable release of Mg^{2+} and BMP2 played an important role in activating the phosphorylation of ERK1/2 and Akt pathways, which guided the osteogenesis formation using an in-situ rat calvarial defect model (**Figure 6**).

CS-Based Hydrogels for Dental Repair

Periodontal Regeneration

Periodontitis is a chronic inflammation of periodontal support tissues caused by the local bacterial infection. The age of onset was after 35 years old. If gingivitis is not treated in time, the inflammation can spread from gingival to the periodontal membrane and alveolar bone, thus forming the periodontitis. Due to no obvious conscious symptoms and easy to be ignored at initial stage, once the symptoms are more serious, treatment of such pathology is a great challenge for the clinician (Cortellini and Tonetti, 2015; Larsson et al., 2015; Kinane et al., 2017; Roi et al., 2019; Xu et al., 2020a,b). In general, reducing the inflammation is a key to control the infection for periodontal therapy, but traditional mechanical treatments like scaling and root planin are closely connected with the wound repair. In addition, non-surgical treatment alone is insufficient for adjuvant therapy (Abdul Rahman et al., 2019; Harmouche et al., 2019). Therefore, use of local delivery of active drugs has been utilized as an effective strategy to address the inflammation and promote tissue repair (Morand et al., 2017; Batool et al., 2018; Petit et al., 2019). By means of the injectable chitosan hydrogels with modulable physico-chemical properties, CS-based delivery system can be employed as reliable vehicle to release the encapsulated active drugs (e.g., statins, doxycycline, antibiotics, and antiseptics) at the disease site within periodontal pockets (Özdoğan et al., 2018). Simultaneous anti-inflammation and periodontium regeneration is vital for terminating the alveolar bone resorption. Based on this, Xu et al. (2019) proposed a thermo-responsive CS-based injectable hydrogel with the main components of CS, β-sodium glycerophosphate (β-GP) and gelatin. After tailoring the continuous release behavior of aspirin (ASP) and erythropoietin (EPO), CS/β-GP/gelatin@ASP/EPO scaffolds exerted pharmacological roles of anti-inflammation and periodontium regeneration, indicating the suitable candidate for dental treatment in the clinical fields (**Figure 7**). Zang et al. (2019) also prepared a thermo-sensitive bone morphogenetic protein-7 (BMP-7) and ornidazole (ORN)-encapsulated CS/β-GP composite hydrogel. The BMP-7 and ORN molecules could be stably and sustainably released from the hydrogels, displaying the significantly antimicrobial activity and improved osteoclasts ability than that of control groups. The results indicated

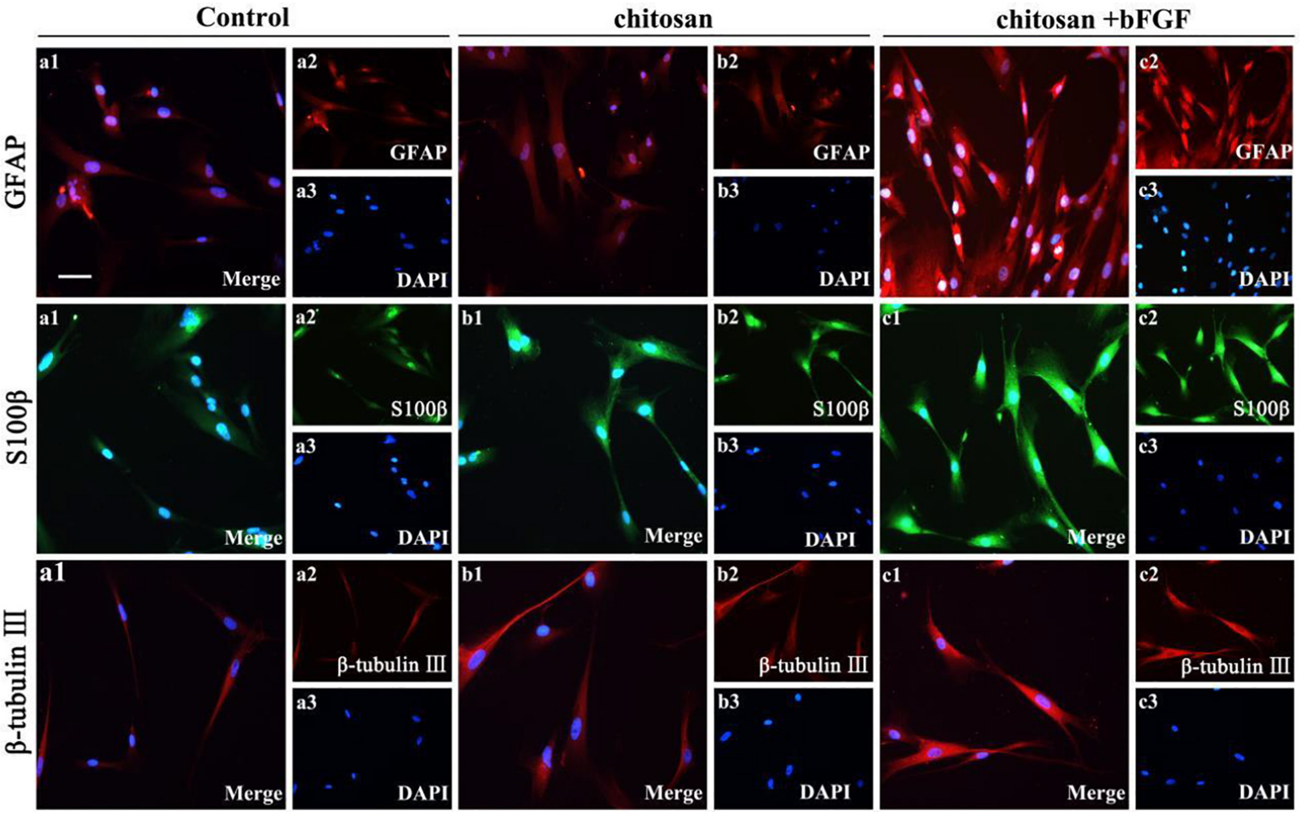

FIGURE 7 | Schematic illustration of the preparation and application of the CS/β-GP/gelatin hydrogels. Reproduced from Xu et al. (2019) with permission from Copyright 2019 Elsevier.

that CS/β-GP hydrogels with the controllable delivery of BMP-7 and ORN were valuable and promising for the periodontal therapy.

Dental-Pulp Regeneration

Dental-pulp mainly consists of nerves, blood vessels, lymph and connective tissue, as well as odontoid cells lining periphery of the pulp, aiming to form dentin with the ability of nutrition, feeling and defense. The pulp nerve is particularly sensitive to external stimuli and can produce unbearable pain. In general, dental-pulp regeneration strategy aim to achieve the regeneration of connective tissue, dentin tooth root edification, vascularization and innervation (Keller et al., 2015). Based on the smart drug delivery system, hydrogels are used to deliver active molecules and carry competent cells within the endodontic compartment for the endodontic treatment, which required adequate viscosity and injectable nature of hydrogels to quick adhesion and gelation in the whole root canal system. Recently, it is reported that CS-based hydrogels are widely developed for dental-pulp regeneration, because they can promote proliferation, migration and odontoblastic differentiation of dental pulp stem cells (DPSCs) and MSCs both *in vitro* and *in vivo* (Bordini et al., 2019; Ducret et al., 2019; Zhu N. et al., 2019). For example, Zhang et al. found that when the DPSCs were cultured in CS-based hydrogels containing basic fibroblast growth factor (bFGF) for 7 days, GFAP, S100β and β-tubulin III levels were significantly increased than the control and pure chitosan groups, indicating the non-toxic CS hydrogels carry and transport the therapeutic cells effectively to the recipient area and great potential for the DPSCs survival and dental-pulp regeneration (**Figure 8**; Zheng et al., 2020).

It is well-known that VEGF plays a crucial role in reparative dentin formation, whereas its constant administrations remains problematic within the body. Wu et al. (2019) conducted a VEGF-loaded injectable CS/β-GP composite hydrogel with a sustained drug release behavior. After cultured DPSCs with CS/β-GP hydrogel, CCK-8 assay found that DPSCs could keep cell adhesion and proliferation activity. Along with the continual release of VEGF from the VEGF/CS/β-GP hydrogel, odontogenic differentiation capacities were significantly improved, which could be utilized as an ideal drug carrier for the pulp capping therapy.

FUTURE OUTLOOK AND CONCLUSION

Chitosan, a deacetylated form of chitin, is widely utilized as a positive-charged and low-cost natural polymer for bone and dental tissue engineering applications. On account of the excellent biocompatibility, good biodegradability and

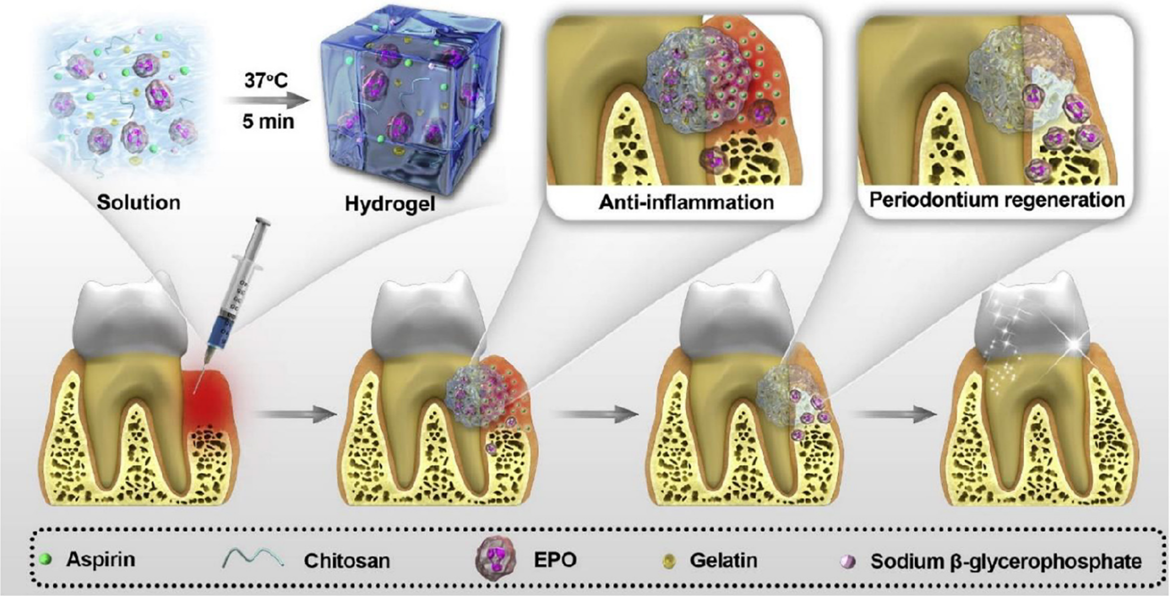

FIGURE 8 | Effect of chitosan/bFGF scaffolds on neural differentiation of DPSCs. Immunofluorescence staining of GFAP, S100β and β-tubulin III. Reproduced from Zheng et al. (2020) with permission from Copyright 2020 Informa Healthcare.

adjustable physico-chemical properties, in this review, we briefly summarized the various physio-chemical properties of CS-based injectable hydrogels for bone repair and explored in depth the updated progress of CS-based hydrogels with more innate advantages to promote cell attachment, spreading, proliferation and differentiation, thus benefiting for the tissue repair and regenerative medicine for the last two decades. To improve the mechanical characteristics, physicochemical and biological properties, CS-based hydrogels are required to combine with other natural or synthetic polymers, which can create a series of environmentally responsive and injectable hydrogels for biomedical engineering applications. In addition, incorporation of bioactive molecules with CS-based hydrogels can induce the angiogenesis and vascularization, accelerate bone repair and promote periodontal tissue engineering. We believe that further research on chitosan and the search for new variations in its use with other polymers will reveal greater prospects in biomedical applications.

Although CS-based hydrogels are possible alternative for current clinical practices of bone defect repair with vast array of beneficial properties, there is some clinical limitation for bone and dental regeneration. One major limitation is the standardization of molecular weight distribution, raw material resources and commercial production. High molecular weight may cause potential inflammation as a bone graft, and cell wall-derived CS may be more reliable than that from seafood due to the varieties and reproducibility of fungal and marine sources all over the world. In addition, CS-based hydrogels as bone scaffolds are their infancy in experimental research with limited studies and insufficient clinical utility. Therefore, further research should be focused on the establishment of uniform standards and invention of advanced technology to expand potential clinical applications. Additionally, improvement of higher loading capacity and controlled release of bioactive molecules into CS-based hydrogels will be a prime research objective upon implantation for clinical applications. Going forward clinical research is the combination of CS-based hydrogels with different biofabrication techniques like electrospinning, microspheres and 3D-printing for building a multifaceted and multilayered bone graft in bone regeneration and fracture management.

Thus, we believed that along with clear elucidation of the molecular and signaling mechanisms on bone and dental regeneration, CS-based hydrogels will spark broader interests in the scientific community to create more tailormade tissue-engineering scaffolds with optimum characteristics and advanced properties like natural bones to combat large bone defects in clinical therapeutics.

AUTHOR CONTRIBUTIONS

RC, XW, and XY initiated the project. GT, ZT, WZ, CS, YL, and HH searched the data base. GT, XW, and XY wrote, revised, and finalized the manuscript. All authors contributed to the article and approved the submitted version.

FUNDING

This work was supported by the National Natural Science Foundation of China (51973226 and 81772445), and the Hunan Province Science and Technology Department (2017SK51001).

REFERENCES

Abdul Rahman, N., Nickles, K., Gallenbach, K., Dannewitz, B., Ramich, T., and Scharf, S., et al. (2019). Five-year stability of clinical attachment after regenerative treatment of infrabony defects compared to controls. *J. Clin. Periodontol.* 46, 650–658.

Akilbekova, D., Shaimerdenova, M., Adilov, S., and Berillo, D. (2018). Biocompatible scaffolds based on natural polymers for regenerative medicine. *Int. J. Biol. Macromol.* 114, 324–333. doi: 10.1016/j.ijbiomac.2018.03.116

Amin, S., Achenbach, S. J., Atkinson, E. J., Khosla, S., and Melton, I. I. I. L. J. (2014). Trends in fracture incidence: a population-based study over 20 years. *J. Bone Miner. Res.* 29:581. doi: 10.1002/jbmr.2072

Amini, A. R., Laurencin, C. T., and Nukavarapu, S. P. (2012). Bone tissue engineering: recent advances and challenges. *Crit. Rev. Biomed. Eng.* 40, 363–408. doi: 10.1615/critrevbiomedeng.v40.i5.10

Argüelles-monal, W. M., Lizardi-mendoza, J., Daniel, F. Q., and Montiel-herrera, M. (2018). Chitosan derivatives: introducing new functionalities with a controlled molecular architecture for innovative materials. *Polymers* 10:342. doi: 10.3390/polym10030342

Arvidson, K., Abdallah, B. M., Applegate, L. A., Baldini, N., Cenni, E., Gomez-Barrena, E., et al. (2011). Bone regeneration and stem cells. *J. Cell Mol. Med.* 15, 718–746.

Atak, B. H., Buyuk, B., Huysal, M., Isik, S., Senel, M., Metzger, W., et al. (2017). Preparation and characterization of amine functional nano-hydroxyapatite/chitosan bionanocomposite for bone tissue engineering applications. *Carbohydr. Polym.* 164, 200–213. doi: 10.1016/j.carbpol.2017.01.100

Bagheri, B., Zarrintaj, P., Samadi, A., Zarrintaj, R., Ganjali, M. R., Saeb, M. R., et al. (2020). Tissue engineering with electrospun electro-responsive chitosan-aniline oligomer/polyvinyl alcohol. *Int. J. Biol. Macromol.* 147, 160–169. doi: 10.1016/j.ijbiomac.2019.12.264

Bagheri, B., Zarrintaj, P., Surwase, S. S., Baheiraei, B., Saeb, M. R., Mozafari, M., et al. (2019). Self-gelling electroactive hydrogels based on chitosan-aniline oligomers/agarose for neural tissue engineering with on-demand drug release. *Coll. Surf. B* 184:110549. doi: 10.1016/j.colsurfb.2019.110549

Baldwin, P., Li, D. J., Auston, D. A., Mir, H. S., Yoon, R. S., and Koval, K. J. (2019). Autograft, allograft, and bone graft substitutes: clinical evidence and indications for use in the setting of orthopaedic trauma surgery. *J. Orthop. Trauma* 33, 203–213. doi: 10.1097/bot.0000000000001420

Bao, W. R., Li, M. L., Yang, Y. Y., Wan, Y., Wang, X., Bi, N., et al. (2020). Advancements and frontiers in high performance of natural hydrogels for cartilage tissue engineering. *Front. Chem.* 8:53. doi: 10.3389/fchem.2020.00053

Bao, W. R., Lyu, J. R., Li, C. L., Zhang, J. F., Sun, T. N., Wang, X., et al. (2019). Fabrication of customized nanogel carriers from a UV-triggered dynamic self-assembly strategy. *Front. Chem.* 7:769. doi: 10.3389/fchem.2020.00769

Batool, F., Strub, M., Petit, C., Bugueno, I. M., Bornert, F., Clauss, F., et al. (2018). Periodontal tissues, maxillary jaw bone, and tooth regeneration approaches: from animal models analyses to clinical applications. *Nanomaterials* 8:337. doi: 10.3390/nano8050337

Berger, J., Reist, M., Mayer, J. M., Felt, O., and Gurny, R. (2004). Structure and interactions in chitosan hydrogels formed by complexation or aggregation for biomedical applications. *Eur. J. Pharm. Biopharm.* 57, 35–52. doi: 10.1016/s0939-6411(03)00160-7

Berillo, D., and Cundy, A. (2018). 3D-macroporous chitosan-based scaffolds with in situ formed Pd and Pt nanoparticles for nitrophenol reduction. *Carbohydr. Polym.* 192, 166–175. doi: 10.1016/j.carbpol.2018.03.038

Berillo, D., Elowsson, L., and Kirsebom, H. (2012). Oxidized dextran as crosslinker for chitosan cryogel scaffolds and formation of polyelectrolyte complexes between chitosan and gelatin. *Macromol. Biosci.* 12, 1090–1099. doi: 10.1002/mabi.201200023

Berillo, D., Mattiasson, B., and Kirsebom, H. (2014). Cryogelation of chitosan using noble-metal ions: in situ formation of nanoparticles. *Biomacromolecules* 15, 2246–2255. doi: 10.1021/bm5003834

Bian, J., Xia, Y. X., Sang, L. Y., Zhu, C. X., Li, Y. X., Li, G. Y., et al. (2020). A recyclable colorimetric probe: in-situ fabrication of highly stable HPEI-AuNPs for selective Ag+ detection. *New J. Chem.* 44, 5438–5447. doi: 10.1039/d0nj00497a

Bordini, E. A. F., Cassiano, F. B., Silva, I. S. P., Usberti, F. R., Anovazzi, G., Pacheco, L. E., et al. (2019). Synergistic potential of 1α,25-dihydroxyvitamin D3 and calcium-aluminate-chitosan scaffolds with dental pulp cells. *Clin. Oral Investig.* 24, 663–674. doi: 10.1007/s00784-019-02906-z

Cao, Q. C., Wang, X., and Wu, D. C. (2018). Controlled cross-linking strategy for formation of hydrogels, microgels and nanogels. *Chin. J. Polym. Sci.* 36, 8–17. doi: 10.1007/s10118-018-2061-7

Chen, J. P., Tsai, M. J., and Liao, H. T. (2013). Incorporation of biphasic calcium phosphate microparticles in injectable thermoresponsive hydrogel modulates bone cell proliferation and differentiation. *Colloids Surf. B* 110, 120–129. doi: 10.1016/j.colsurfb.2013.04.028

Chen, Y. C., Wang, C. H., Lai, L. S., and Lin, K. W. (2003). Rheological properties of chitosan Chenite and its interaction with porcine myofibrillar proteins as influenced by chitosan's degree of deacetylation and concentration. *J. Food Sci.* 68, 826–831. doi: 10.1111/j.1365-2621.2003.tb08250.x

Chen, Y. R., Zhou, Z. X., Zhang, J. Y., Yuan, F. Z., Xu, B. B., Guan, J., et al. (2019). Low-molecular-weight heparin-functionalized chitosan-chondroitin sulfate hydrogels for controlled release of TGF-β3 and in vitro neocartilage formation. *Front. Chem.* 7:745. doi: 10.3389/fchem.2020.00745

Chenite, A., Buschmann, M., Wang, D., Chaput, C., and Kandani, N. (2001). Rheological characterisation of thermogelling chitosan/glycerol-phosphate solutions. *Carbohydr. Polym.* 46, 39–47. doi: 10.1016/s0144-8617(00)00281-2

Cortellini, P., and Tonetti, M. S. (2015). Clinical concepts for regenerative therapy in intrabony defects. *Periodontol.* 68, 282–307. doi: 10.1111/prd.12048

Deepthi, S., Venkatesan, J., Kim, S. K., Bumgardner, J. D., and Jayakumar, R. (2016). An overview of chitin or chitosan/nano ceramic composite scaffolds for bone tissue engineering. *Int. J. Biol. Macromol.* 93, 1338–1353. doi: 10.1016/j.ijbiomac.2016.03.041

Dhivya, S., Saravanan, S., Sastry, T. P., and Selvamurugan, N. (2015). Nanohydroxyapatite-reinforced chitosan composite hydrogel for bone tissue repair in vitro and in vivo. *J. Nanobiotech.* 13:40.

Ducret, M., Montembault, A., Josse, J., Pasdeloup, M., Celle, A., Benchrih, R., et al. (2019). Design and characterization of a chitosan-enriched fibrin hydrogel for human dental pulp regeneration. *Dent. Mater.* 35, 523–533. doi: 10.1016/j.dental.2019.01.018

El-hefian, E. A., and Yahaya, A. H. (2010). Rheological study of chitosan and its blends: an overview. *Maejo Int. J. Sci. Tech.* 4, 210–220.

Faikrua, A., Wittaya-areekul, S., Oonkhanond, B., and Viyoch, J. (2014). A thermosensitive chitosan/corn starch/β-glycerol phosphate hydrogel containing TGF-β1 promotes differentiation of MSCs into chondrocyte-like cells. *Tis. Eng. Reg. Med.* 11, 355–361. doi: 10.1007/s13770-014-0030-y

Fan, D. Y., Wang, Q., Zhu, T. J., Wang, H. F., Liu, B. C., Wang, Y. F., et al. (2020). Recent advances of magnetic nanomaterials in bone tissue repair. *Front. Chem.* 8:124. doi: 10.3389/fchem.2020.00124

Fan, L. F., Wang, X., Cao, C. Q., Yang, Y. Y., and Wu, D. C. (2019). POSS-based supramolecular amphiphilic zwitterionic complexes for drug delivery. *Biomater. Sci.* 7, 1984–1994. doi: 10.1039/c9bm00125e

Gómez-Barrena, E., Rosset, P., Lozano, D., Stanovici, J., Ermthaller, C., and Gerbhard, F. (2015). Bone fracture healing: cell therapy in delayed unions and nonunions. *Bone* 70, 93–101. doi: 10.1016/j.bone.2014.07.033

Guo, B., and Ma, P. X. (2014). Synthetic biodegradable functional polymers for tissue engineering: a brief review. *Sci. China Chem.* 57, 490–500. doi: 10.1007/s11426-014-5086-y

Gyawali, D., Nair, P., Kim, H. K., and Yang, J. (2013). Citrate-based biodegradable injectable hydrogel composites for orthopedic applications. *Biomater. Sci.* 1, 52–64. doi: 10.1039/c2bm00026a

Harmouche, L., Courval, A., Mathieu, A., Petit, C., Huck, O., Severac, F., et al. (2019). Impact of tooth-related factors on photodynamic therapy effectiveness during active periodontal therapy: a 6-months split-mouth randomized clinical trial. *Photodiagnosis Photodyn.* 27, 190–194.

Hench, L. L., and Polak, J. M. (2002). Third-generation biomedical materials. *Science* 295, 1014–1017. doi: 10.1126/science.1067404

Hennink, W. E., and van Nostrum, C. F. (2012). Novel crosslinking methods to design hydrogels. *Adv. Drug Delivery Rev.* 64, 223–236. doi: 10.1016/j.addr.2012.09.009

Hoffman, A. S. (2012). Hydrogels for biomedical applications. *Adv. Drug Deliv. Rev.* 64, 18–23.

Hu, J. L., Hou, Y. P., Park, H., Choi, B., Hou, S. Y., Chung, A., et al. (2012). Visible light crosslinkable chitosan hydrogels for tissue engineering. *Acta Biomater.* 8, 1730–1738. doi: 10.1016/j.actbio.2012.01.029

Huang, Y. Z., Ji, Y. R., Kang, Z. W., Li, F., Ge, S. F., Yang, D. P., et al. (2020). Integrating eggshell-derived CaCO3/MgO nanocomposites and chitosan into a biomimetic scaffold for bone regeneration. *Chem. Eng. J.* 395:125098. doi: 10.1016/j.cej.2020.125098

Hwang, J. K., and Shin, H. H. (2000). Rheological properties of chitosan solutions. *Korea Aust. Rheol. J.* 12, 175–179.

Jiang, T., Ji, H., Zhang, L., Wang, Y., and Zhou, H. (2019). Chitosan oligosaccharide exerts anti-allergic effect against shrimp tropomyosin-induced food allergy by affecting Th1 and Th2 cytokines. *Int. Arch. Allergy Immunol.* 180, 10–16. doi: 10.1159/000500720

Kavya, K. C., Jayakumar, R., Nair, S., and Chennazhi, K. P. (2013). Fabrication and characterization of chitosan/gelatin/nSiO2 composite scaffold for bone tissue engineering. *Int. J. Biol. Macromol.* 59, 255–263. doi: 10.1016/j.ijbiomac.2013.04.023

Keller, L., Offner, D., Schwinté, P., Morand, D., Wagner, Q., Gros, C., et al. (2015). Active nanomaterials to meet the challenge of dental pulp regeneration. *Materials* 8, 7461–7471. doi: 10.3390/ma8115387

Keller, L., Regiel-Futyra, A., Gimeno, M., Eap, S., Mendoza, G., Andreu, V., et al. (2017). Chitosan-based nanocomposites for the repair of bone defects. *Nanomedicine* 13, 2231–2240. doi: 10.1016/j.nano.2017.06.007

Khalili, R., Zarrintaj, P., Jafari, S. H., Vahabi, H., and Saeb, M. R. (2020). Electroactive poly (p-phenylene sulfide)/r-Graphene Oxide/Chitosan as a novel potential candidate for tissue engineering. *Int. J. Biol. Macromol.* 154, 18–24. doi: 10.1016/j.ijbiomac.2020.03.029

Kinane, D. F., Stathopoulou, P. G., and Papapanou, P. N. (2017). Periodontal diseases. *Nat. Rev. Dis. Primers* 3:17038.

Ko, D. Y., Shinde, U. P., Yeon, B., and Jeong, B. (2013). Recent progress of in situ formed gels for biomedical applications. *Prog. Polym. Sci.* 38, 672–701. doi: 10.1016/j.progpolymsci.2012.08.002

Ko, W., Lee, J. S., and Hwang, Y. (2018). Injectable hydrogel composite containing modified gold nanoparticles: implication in bone tissue regeneration. *Int. J. Nanomed.* 13, 7019–7031. doi: 10.2147/ijn.s185715

Larsson, L., Decker, A., Nibali, L., Pilipchuk, S., Berglundh, T., and Giannobile, W. V. (2015). Regenerative medicine for periodontal and peri-implant diseases. *J. Dent. Res.* 95, 255–266. doi: 10.1177/0022034515618887

Lavanya, K., Viji Chandran, S., Balagangadharan, K., and Selvamurugan, N. (2020). Temperature- and pH-responsive chitosan-based injectable hydrogels for bone tissue engineering. *Mater. Sci. Eng. C* 111:110862. doi: 10.1016/j.msec.2020.110862

Lewandowska, K. (2009). Rheological properties of chitosan acetate blends with vinyl polymers. *Prog. Chem. Appl. Chitin Dravit.* 14, 41–48.

Li, B. Q., Wang, L., Xu, F., Gang, X. M., Demirci, U., Wei, D. Q., et al. (2015). Hydrosoluble, UV-crosslinkable and injectable chitosan for patterned cell-laden microgel and rapid transdermal curing hydrogel in vivo. *Acta Biomater.* 22, 59–69. doi: 10.1016/j.actbio.2015.04.026

Li, D. W., Chen, J., Wang, X., Zhang, M. M., Li, C. L., and Zhou, J. (2020a). Recent advances on synthetic and polysaccharide adhesives for biological hemostatic applications. *Front. Bioeng. Biotechnol.* 8:926. doi: 10.3389/fbioe.2020.00926

Li, D. W., Zhou, J., Zhang, M. M., Ma, Y. Z., Yang, Y. Y., Han, X., et al. (2020b). Long-term delivery of alendronate through injectable tetra-PEG hydrogel to promote osteoporosis therapy. *Biomater. Sci.* 8, 3138–3146. doi: 10.1039/d0bm00376j

Li, H., Ji, Q., Chen, X., Sun, Y., Xu, Q., Deng, P., et al. (2017). Accelerated bony defect healing based on chitosan thermosensitive hydrogel scaffolds embedded with chitosan nanoparticles for the delivery of BMP2 plasmid DNA. *J. Biomed. Mat. Res. A* 105, 265–273. doi: 10.1002/jbm.a.35900

Li, X., Sun, Q., Li, Q., Kawazoe, N., and Chen, G. (2018). Functional hydrogels with tunable structures and properties for tissue engineering applications. *Front. Chem.* 6:499. doi: 10.3389/fchem.2020.00499

Liu, H. Y., Wang, X., Cao, Y. X., Yang, Y. Y., Yang, Y. T., Gao, Y. F., et al. (2020). Freezing-tolerant, highly sensitive strain and pressure sensors assembled from ionic conductive hydrogels with dynamic cross-links. *ACS Appl. Mater. Interf.* 12, 25334–25344. doi: 10.1021/acsami.0c06067

Liu, B. C., Zhao, Y. R., Zhu, T. J., Gao, S., Ye, K. F., Zhou, F., et al. (2020). Biphasic double-network hydrogel with compartmentalized loading of bioactive glass for osteochondral defect repair. *Front. Bioeng. Biotechnol.* 8:752. doi: 10.3389/fchem.2020.00752

Liu, M., Zeng, X., Ma, C., Yi, H., Ali, Z., Mou, X., et al. (2017). Injectable hydrogels for cartilage and bone tissue engineering. *Bone Res.* 5:17014.

Loi, F., Córdova, L. A., Pajarinen, J., Lin, T., Yao, Z., and Goodman, S. B. (2016). Inflammation, fracture and bone repair. *Bone* 86, 119–130. doi: 10.1016/j.bone.2016.02.020

Lu, H. T., Lu, T. W., Chen, C. H., Lu, K. Y., and Mi, F. L. (2018). Development of nanocomposite scaffolds based on biomineralization of N,O-carboxymethyl chitosan/fucoidan conjugates for bone tissue engineering. *Int. J. Biol. Macromol.* 120, 2335–2345. doi: 10.1016/j.ijbiomac.2018.08.179

Mahmodi, G., Zarrintaj, P., Taghizadeh, A., Taghizadeh, M., Manouchehri, S., Dangwal, S., et al. (2020). From microporous to mesoporous mineral frameworks: An alliance between zeolite and chitosan. *Carbohyd. Res.* 489:107930. doi: 10.1016/j.carres.2020.107930

Maitra, J., and Shukla, V. K. (2014). Cross-linking in hydrogels-a review. *Am. J. Polym. Sci.* 4, 25–31.

Martiínez, A., Chornet, E., and Rodrigue, D. (2004). Steady-shear rheology of concentrated chitosan solutions. *J. Texture Stud.* 35, 53–74. doi: 10.1111/j.1745-4603.2004.tb00822.x

Menon, A. H., Soundarya, S. P., Sanjay, V., Chandran, S. V., Balagangadharan, K., and Selvamurugan, N. (2018). Sustained release of chrysin from chitosan-based scaffolds promotes mesenchymal stem cell proliferation and osteoblast differentiation. *Carbohydr. Polym.* 195, 356–367. doi: 10.1016/j.carbpol.2018.04.115

Mi, L., Liu, H., Gao, Y., Miao, H., and Ruan, J. (2017). Injectable nanoparticles/hydrogels composite as sustained release system with stromal cell-derived factor-1α for calvarial bone regeneration. *Int. J. Biol. Macromol.* 101, 341–347. doi: 10.1016/j.ijbiomac.2017.03.098

Min, J. H., Patel, M., and Koh, W. (2018). Incorporation of conductive materials into hydrogels for tissue engineering applications. *Polymers* 10:1078. doi: 10.3390/polym10101078

Mohebbi, S., Nezhad, M. N., Zarrintaj, P., Jafari, S. H., Gholizadeh, S. S., Saeb, M. R., et al. (2019). Chitosan in biomedical engineering: a critical review. *Curr. Stem Cell Res. Trans.* 14, 93–116. doi: 10.2174/1574888x13666180912142028

Moorthi, A., Parihar, P. R., Saravanan, S., Vairamani, M., and Selvamurugan, N. (2014). Effects of silica and calcium levels in nanobioglass ceramic particles on osteoblast proliferation. *Mater. Sci. Eng. C.* 43, 458–464. doi: 10.1016/j.msec.2014.07.040

Morand, D. N., Davideau, J. L., Clauss, F., Jessel, N., Tenenbaum, H., and Huck, O. (2017). Cytokines during periodontal wound healing: potential application for new therapeutic approach. *Oral Dis.* 23, 300–311. doi: 10.1111/odi.12469

Moreira, C. D., Carvalho, S. M., Sousa, R. G., Mansur, H. S., and Pereira, M. M. (2018). Nanostructured chitosan/gelatin/bioactive glass in situ forming hydrogel composites as a potential injectable matrix for bone tissue engineering. *Mater. Chem. Phys.* 218, 304–316. doi: 10.1016/j.matchemphys.2018.07.039

Moreira, C. D. F., Carvalho, S. M., Florentino, R. M., França, A., Okano, B. S., Rezende, C. M. F., et al. (2019). Injectable chitosan/gelatin/bioactive glass nanocomposite hydrogels for potential bone regeneration: in vitro and in vivo analyses. *Int. J. Biol. Macromol.* 132, 811–821. doi: 10.1016/j.ijbiomac.2019.03.237

Nafee, N., Zewail, M., and Boraie, N. (2017). Alendronate-loadedbiodegradable smart hydrogel: a promising injectable depot formulation for osteoporosis. *J. Drug Target.* 26, 563–575. doi: 10.1080/1061186x.2017.1390670

Ngo, D. H., and Kim, S. K. (2014). Antioxidant effects of chitin, chitosan, and their derivatives. *Adv. Food Nutr. Res.* 73, 15–31.

Nourbakhsh, M., Zarrintaj, P., Jafari, S. H., Hosseini, S. M., Aliakbari, S., Pourbadie, H. G., et al. (2020). Fabricating an electroactive injectable hydrogel based on pluronic-chitosan/aniline-pentamer containing angiogenic factor for functional repair of the hippocampus ischemia rat model. *Mater. Sci. Eng. C* 117:111328. doi: 10.1016/j.msec.2020.111328

Oudadesse, H., Najem, S., Mosbahi, S., Rocton, N., Refifi, J., El Feki, H., et al. (2020). Development of hybrid scaffold: Bioactive glass nanoparticles/chitosan for tissue engineering applications. *J. Biomed. Mater. Res. A* doi: 10.1002/jbm.a.37043

Özdoğan, A. I., Ilarslan, Y. D., Kösemehmetoğlu, K., Akca, G., Kutlu, H. B., Comerdov, E., et al. (2018). In vivo evaluation of chitosan based local delivery systems for atorvastatin in treatment of periodontitis. *Int. J. Pharm.* 550, 470–476. doi: 10.1016/j.ijpharm.2018.08.058

Parhi, R. (2017). Cross-linked hydrogel for pharmaceutical applications: a review. *Adv. Pharm. Bull.* 7, 515–530. doi: 10.15171/apb.2017.064

Petit, C., Batool, F., Bugueno, I. M., Schwinté, P., Benkirane-Jessel, N., and Huck, O. (2019). Contribution of statins towards periodontal treatment: a review. *Mediat. Inflamm.* 2019:6367402.

Pourjavadi, A., Doroudian, M., Ahadpour, A., and Azari, S. (2019). Injectable chitosan/κ-carrageenan hydrogel designed with au nanoparticles: a conductive scaffold for tissue engineering demands. *Int. J. Biol. Macromol.* 126, 310–317. doi: 10.1016/j.ijbiomac.2018.11.256

Qi, B. W., Yu, A. X., Zhu, S. B., Zhou, M., and Wu, G. (2013). Chitosan/poly (vinyl alcohol) hydrogel combined with Ad-hTGF-β1 transfected mesenchymal stem cells to repair rabbit articular cartilage defects. *Exper. Bio. Med.* 238, 23–30. doi: 10.1258/ebm.2012.012223

Racine, L., Texiera, I., and Auzély-Veltyb, R. (2017). Chitosan-based hydrogels: recent design concepts to tailor properties and functions. *Polym. Int.* 66, 981–998. doi: 10.1002/pi.5331

Radwan, N. H., Nasr, M., Ishak, R. A. H., Abdeltawab, N. F., and Awad, G. A. S. (2020). Chitosan-calcium phosphate composite scaffolds for control of post-operative osteomyelitis: fabrication, characterization, and in vitro-in vivo evaluation. *Carbohyr. Polym.* 244:116482. doi: 10.1016/j.carbpol.2020.116482

Ran, J., Hu, J., Sun, G., Chen, S., Jiang, P., Shen, X., et al. (2016). A novel chitosan-tussah silk fibroin/nano-hydroxyapatite composite bone scaffold platform with tunable mechanical strength in a wide range. *Int. J. Biol. Macromol.* 93, 87–97. doi: 10.1016/j.ijbiomac.2016.08.062

Rizwan, M., Yahya, R., Hassan, A., Yar, M., Azzahari, A. D., Selvanathan, V., et al. (2017). pH sensitive hydrogels in drug delivery: brief history, properties, swelling and release mechanism. *Mat. Select. Appl.* 9:137. doi: 10.3390/polym9040137

Rogina, A., Ressler, A., Matiæ, I., Ferrer, G. G., Marijanoviæ, I., Ivankoviæ, M., et al. (2017). Cellular hydrogels based on pH-responsive chitosan-hydroxyapatite system. *Carbohydr. Polym.* 166, 173–182. doi: 10.1016/j.carbpol.2017.02.105

Roi, A., Ardelean, L. C., Roi, C. I., Boia, E. R., Boia, S., and Rusu, L. C. (2019). Oral bone tissue engineering: advanced biomaterials for cell adhesion, proliferation and differentiation. *Materials* 12:2296. doi: 10.3390/ma12142296

Saravanan, S., Leena, R. S., and Selvamurugan, N. (2016). Chitosan based biocomposite scaffolds for bone tissue engineering. *Int. J. Biol. Macromol.* 93:1354. doi: 10.1016/j.ijbiomac.2016.01.112

Saravanan, S., Vimalraj, S., Thanikaivelan, P., Banudevi, S., and Manivasagam, G. (2019). A review on injectable chitosan/beta glycerophosphate hydrogels for bone tissue regeneration. *Int. J. Biol. Macromol.* 12, 38–54. doi: 10.1016/j.ijbiomac.2018.10.014

Shariatinia, Z., and Jalali, A. M. (2018). Chitosan-based hydrogels: preparation, properties and applications. *Int. J. Biol. Macromol.* 115, 194–220. doi: 10.1016/j.ijbiomac.2018.04.034

Sivashanmugam, A., Arun Kumar, R., Vishnu Priya, M., Nair, S. V., and Jayakumar, R. (2015). An overview of injectable polymeric hydrogels for tissue engineering. *Eur. Polym. J.* 72, 543–565. doi: 10.1016/j.eurpolymj.2015.05.014

Stevens, M. M. (2008). Biomaterials for bone tissue engineering. *Mater. Today* 11, 18–25.

Thoniyot, P., Tan, M. J., Karim, A. A., and Young, D. J. (2015). Nanoparticle-hydrogel composites: concept, design, and applications of these promising, multi-functional materials. *Adv. Sci.* 2:1400010. doi: 10.1002/advs.201400010

Tiffany, N. V. O., Kasper, F. K., and Mikos, A. G. (2012). Strategies for controlled delivery of growth factors and cells for bone regeneration. *Adv. Drug Deliv. Rev.* 64, 1292–1309. doi: 10.1016/j.addr.2012.01.016

Visser, N. J., Rezaie, E. S., Friedrich, P. F., Kotsougiani, D., Shin, A. Y., and Bishop, A. T. (2019). Effects of surgical angiogenesis on segmental bone reconstruction with cryopreserved massive-structural allografts in a porcine tibia model. *J. Orthop. Res.* 37, 1698–1708. doi: 10.1002/jor.24318

Vo, T. N., Shah, S. R., Lu, S., Tatara, A. M., Lee, E. J., Roh, T. T., et al. (2016). Injectable dual-gelling cell-laden composite hydrogels for bone tissue engineering. *Biomaterials* 83, 1–11. doi: 10.1016/j.biomaterials.2015.12.026

Wang, S. J., Jiang, D., Zhang, Z. Z., Chen, Y. R., Yang, Z. D., Zhang, J. Y., et al. (2019). Biomimetic nanosilica-collagen scaffolds for in situ bone regeneration: toward a cell-free, one-step surgery. *Adv. Mater.* 31:1904341. doi: 10.1002/adma.201904341

Wang, X., Gao, P. Y., Wang, J., Yang, Y. Y., You, Y. Z., and Wu, D. C. (2020a). A robust strategy for precise fabrication of rigid-flexible coupling dendrimers toward self-coordinated hierarchical assembly. *CCS Chem.* 2, 1093–1194. doi: 10.31635/ccschem.020.202000238

Wang, X., Gao, P. Y., Yang, Y. Y., Guo, H. X., and Wu, D. C. (2018a). Dynamic and programmable morphology and size evolution via a living hierarchical self-assembly strategy. *Nat. Commun.* 9:2772.

Wang, X., Li, D., Yang, F., Shen, H., Li, Z. B., and Wu, D. C. (2013). Controlled cross-linking strategy: from hybrid hydrogels to nanoparticle macroscopic aggregates. *Polym. Chem.* 4, 4596–4600. doi: 10.1039/c3py00811h

Wang, X., Wang, J., Yang, Y. Y., Yang, F., and Wu, D. C. (2017a). Fabrication of multi-stimuli responsive supramolecular hydrogels based on host-guest inclusion complexation of a tadpole-shaped cyclodextrin derivative with the azobenzene dimer. *Polym. Chem.* 8, 3901–3909. doi: 10.1039/c7py00698e

Wang, X., Yang, Y., Fan, L. F., Yang, F., and Wu, D. C. (2018b). POSS-embedded supramolecular hyperbranched polymers constructed from a 1→7 branching monomer with controllable morphology transitions. *Sci. China Chem.* 61, 311–318. doi: 10.1007/s11426-017-9168-3

Wang, X., Yang, Y. Y., Gao, P. Y., Li, D., Yang, F., Guo, H. X., et al. (2014). POSS dendrimers constructed from a 1→7 branching monomer. *Chem. Commun.* 50, 6126–6129. doi: 10.1039/c4cc01859a

Wang, X., Yang, Y. Y., Shi, Y., and Jia, F. (2020b). Editorial: smart hydrogels in tissue engineering and regenerative medicine. *Front. Chem.* 8:245. doi: 10.3389/fchem.2020.00245

Wang, X., Yang, Y. Y., Yang, F., Shen, H., and Wu, D. C. (2017b). pH-triggered decomposition of polymeric fluorescent vesicles to induce growth of tetraphenylethylene nanoparticles for long-term live cell imaging. *Polymer* 118, 75–84. doi: 10.1016/j.polymer.2017.04.064

Wang, X., Yang, Y. Y., Zhuang, Y. P., Gao, P. Y., Yang, F., Shen, H., et al. (2016). Fabrication of pH-responsive nanoparticles with an AIE feature for imaging intracellular drug delivery. *Biomacromolecules* 17, 2920–2929. doi: 10.1021/acs.biomac.6b00744

Wu, S., Zhou, Y. C., Yu, Y., Zhou, X., Du, W., Wan, M., et al. (2019). Evaluation of chitosan hydrogel for sustained delivery of VEGF for odontogenic differentiation of dental pulp stem cells. *Stem Cells Int.* 2019:1515040.

Wu, S. W., Liu, X., Miller, I. I. A. L., Cheng, Y. S., Yeh, M. L., and Lu, L. (2018). Strengthening injectable thermo-sensitive NIPAAm-g-chitosan hydrogels using chemical crosslinking of disulfide bonds as scaffolds for tissue engineering. *Carbohydr. Polym.* 192, 308–316. doi: 10.1016/j.carbpol.2018.03.047

Xia, Y., Zhou, Y. S., Dong, Q., Yang, H. J., Liu, X., Gu, S. J., et al. (2017). Photopolymerized injectable water-soluble maleilated chitosan/poly(ethylene glycol) diacrylate hydrogels as potential tissue engineering scaffolds. *J. Photopolym. Sci. Technol.* 30, 33–40. doi: 10.2494/photopolymer.30.33

Xu, B. B., Ye, J., Yuan, F. Z., Zhang, J. Y., Chen, Y. R., Fan, B. S., et al. (2020a). Advances of stem cell-laden hydrogels with biomimetic microenvironment for osteochondral repair. *Front. Bioeng. Biotechnol.* 8:247. doi: 10.3389/fchem.2020.00247

Xu, B. B., Yuan, F. Z., Lin, L., Ye, J., Fan, B. S., Zhang, J. Y., et al. (2020b). The higher inherent therapeutic potential of biomaterial-based hDPSCs and hEnSCs for pancreas diseases. *Front. Bioeng. Biotechnol.* 8:636. doi: 10.3389/fchem.2020.00636

Xu, H. C., and Matysiak, S. (2017). Effect of pH on chitosan hydrogel polymer network structure. *Chem. Commun.* 53, 7373–7376. doi: 10.1039/c7cc01826f

Xu, X. W., Gu, Z. Y., Chen, X., Shi, C., Liu, C. W., Liu, M., et al. (2019). An injectable and thermosensitive hydrogel: promoting periodontal regeneration by controlled-release of aspirin and erythropoietin. *Acta Biomater.* 86, 235–246. doi: 10.1016/j.actbio.2019.01.001

Yang, J. A., Yeom, J., Hwang, B. W., Hoffman, A. S., and Hahn, S. K. (2014). In situ-forming injectable hydrogels for regenerative medicine. *Prog. Polym. Sci.* 39, 1973–1986. doi: 10.1016/j.progpolymsci.2014.07.006

Yang, Y. Y., Wang, X., Hu, Y., Hu, H., Wu, D. C., and Xu, F. J. (2014). Bioreducible POSS-based star-shaped polymer for efficient gene delivery. *ACS Appl. Mater. Interf.* 6, 1044–1052. doi: 10.1021/am404585d

Yang, Y. Y., Hu, H., Wang, X., Yang, F., Shen, H., Xu, F. J., et al. (2015). Acid-labile poly(glycidyl methacrylate)-based star gene vectors. *ACS Appl. Mater. Interf.* 7, 12238–12248. doi: 10.1021/acsami.5b02733

Yang, Y. Y., Wang, X., Yang, F., Shen, H., and Wu, D. C. (2016). A universal soaking strategy to convert composite hydrogels into extremely tough and rapidly recoverable double-network hydrogels. *Adv. Mater.* 28, 7178–7184. doi: 10.1002/adma.201601742

Yang, Y. Y., Wang, X., Yang, F., Wang, L. N., and Wu, D. C. (2018). Highly elastic and ultratough hybrid ionic-covalent hydrogels with tunable structures and mechanics. *Adv. Mater.* 30:1707071. doi: 10.1002/adma.201707071

Yang, Y. Y., Yang, Y. T., Cao, X. Y., Wang, X., Chen, Y. R., Liu, H. Y., et al. (2021). Anti-freezing, resilient and tough hydrogels for sensitive and large-range strain and pressure sensors. *Chem. Eng. J.* 403:126431. doi: 10.1016/j.cej.2020.126431

Yu, T. T., Wang, H. F., Zhang, Y. F., Wang, X., and Han, B. (2020). The delivery of RNA-interference therapies based on engineered hydrogels for bone tissue regeneration. *Front. Bioeng. Biotechnol.* 8:445. doi: 10.3389/fchem.2020.00445

Zang, S. Q., Mu, R., Chen, F., Wei, X. C., Zhu, L., Han, B. Y., et al. (2019). Injectable chitosan/beta-glycerophosphate hydrogels with sustained release of BMP-7 and ornidazole in periodontal wound healing of class III furcation defects. *Mater. Sci. Eng. C* 99, 919–928. doi: 10.1016/j.msec.2019.02.024

Zarrintaj, P., Jouyandeh, M., Ganjali, M. R., Hadavand, B. S., Mozafari, M., Sheiko, S. S., et al. (2019). Thermo-sensitive polymers in medicine: a review. *Eur. Polym. J.* 117, 402–423.

Zhang, H., Zhang, F., and Wu, J. (2013). Physically crosslinked hydrogels from polysaccharides prepared by freeze-thaw technique. *React. Funct. Polym.* 73, 923–928. doi: 10.1016/j.reactfunctpolym.2012.12.014

Zhang, Y. H., Chen, M. J., Tian, J., Gu, P., Cao, H. L., Fan, X. Q., et al. (2019). In situ bone regeneration enabled by a biodegradable hybrid double-network hydrogel. *Biomater. Sci.* 7, 3266–3276. doi: 10.1039/c9bm00561g

Zhang, J. F., Luo, Z. P., Wang, W. J., Yang, Y. Y., Li, D. W., and Ma, Y. Z. (2019). One-pot synthesis of bio-functionally water-soluble POSS derivatives via efficient click chemistry methodology. *React. Funct. Polym.* 140, 103–110. doi: 10.1016/j.reactfunctpolym.2019.04.013

Zhao, C., Qazvini, N. T., Sadati, M., Zeng, Z., Huang, S., Losada, A., et al. (2019). A pH-triggered, self-assembled, and bioprintable hybrid hydrogel scaffold for mesenchymal stem cell-based bone tissue engineering. *ACS Appl. Mater. Interf.* 11, 8749–8762. doi: 10.1021/acsami.8b19094

Zheng, K., Feng, G. J., Zhang, J. L., Xing, J., Huang, D., Lian, M., et al. (2020). Basic fibroblast growth factor promotes human dental pulp stem cells cultured in 3D porous chitosan scaffolds to neural differentiation. *Int. J. Neurosci.* 5, 1–9. doi: 10.1080/00207454.2020.1744592

Zheng, L., Ao, Q., Han, H., Zhang, X., and Gong, Y. (2010). Evaluation of the chitosan/glycerol-betaphosphate disodium salt hydrogel application in peripheral nerve regeneration. *Biomed. Mater.* 5:35003.

Zhou, H. Y., Jiang, L. J., Cao, P. P., Li, J. B., and Chen, X. G. (2015). Glycerophosphate-based chitosan thermosensitive hydrogels and their biomedical applications. *Carbohydr. Polym.* 117, 524–536. doi: 10.1016/j.carbpol.2014.09.094

Zhu, N., Chatzistavrou, X., Ge, L., Qin, M., Papagerakis, P., and Wang, Y. (2019). Biological properties of modified bioactive glass on dental pulp cells. *J. Dent.* 83, 18–26. doi: 10.1016/j.jdent.2019.01.017

Zhu, C. X., Xia, Y. X., Zai, Y. Y., Dai, Y. Q., Liu, X. Y., Bian, J., et al. (2019). Adsorption and desorption behaviors of HPEI and thermoresponsive HPEI based gels on anionic and cationic dyes. *Chem. Eng. J.* 369:863. doi: 10.1016/j.cej.2019.03.169

Conflict of Interest: The authors declare that the research was conducted in the absence of any commercial or financial relationships that could be construed as a potential conflict of interest.

frontiers in Bioengineering and Biotechnology

ORIGINAL RESEARCH
published: 01 December 2020
doi: 10.3389/fbioe.2020.595579

Electrospinning With Lyophilized Platelet-Rich Fibrin Has the Potential to Enhance the Proliferation and Osteogenesis of MC3T3-E1 Cells

Jing Nie[1,2,3], Shumei Zhang[1,3], Peng Wu[4], Yuangang Liu[5]* and Yanjun Su[1,2,3]**

[1] Stomatological Hospital of Xiamen Medical College, Xiamen, China, [2] Xiamen Key Laboratory of Stomatological Disease Diagnosis and Treatment, Xiamen, China, [3] Engineering Research Center for Stomatological Biomaterials, Xiamen Medical College, Xiamen, China, [4] Technology Innovation Center for Exploitation of Marine Biological Resources, Third Institute of Oceanography, Ministry of Natural Resources, Xiamen, China, [5] College of Chemical Engineering, Huaqiao University, Xiamen, China

Edited by:
Jianxun Ding,
Changchun Institute of Applied Chemistry (CAS), China

Reviewed by:
Hae-Won Kim,
Institute of Tissue Regeneration Engineering (ITREN), South Korea
Binghong Luo,
Jinan University, China
Li Xie,
Sichuan University, China

***Correspondence:**
Jing Nie
drnie@foxmail.com
Yuangang Liu
ygliu@hqu.edu.cn
Yanjun Su
isorat@163.com

Specialty section:
This article was submitted to Biomaterials, a section of the journal Frontiers in Bioengineering and Biotechnology

Received: *17 August 2020*
Accepted: *12 November 2020*
Published: *01 December 2020*

Citation:
Nie J, Zhang SM, Wu P, Liu YG and Su YJ (2020) Electrospinning With Lyophilized Platelet-Rich Fibrin Has the Potential to Enhance the Proliferation and Osteogenesis of MC3T3-E1 Cells. Front. Bioeng. Biotechnol. 8:595579. doi: 10.3389/fbioe.2020.595579

Platelet-rich fibrin (PRF) as a reservoir of various growth factors plays an essential role in wound healing and tissue engineering at present. Electrospinning technology is an efficient approach to acquire artificial scaffold which has large specific surface area and high porosity. The goal of this study was to investigate the potential of electrospinning on the proliferation and osteogenesis of osteogenic precursor cells *in vitro*, with lyophilized PRF added as a component for electrospinning preparation. The surface structure of lyophilized PRF and nanofibers were investigated, and the proliferation, osteogenesis of MEC3T3-E1 cells with lyophilized PRF or nanofibers extract were studied. The results showed that the diameters of the lyophilized PRF pores were 1.51 ± 0.75 μm, and lyophilized PRF medium promoted the proliferation and osteocalcin (OCN) and osteopontin (OPN) genes expression of MEC3T3-E1 cells. Furthermore, the diameters of the polyvinyl alcohol/sodium alginate/lyophilized PRF (PVA/SA/PRF) fibers were 201.14 ± 40.14 nm. Compared to PVA/SA nanofibers extract and control medium, PVA/SA/PRF nanofibers extract also enhanced the proliferation and mineralization activity of MEC3T3-E1 cells. These results might be instructive to future therapeutics with PVA/SA/PRF electrospinning for bone tissue engineering or other applications.

Keywords: lyophilized platelet-rich fibrin, electrospinning, osteogenesis, cell proliferation, MEC3T3-E1

INTRODUCTION

Platelets are rich in various bioactive factors and present excellent potential in tissue regeneration. Platelet-rich fibrin (PRF) is a second-generation platelet concentrate to replace platelet-rich plasma (PRP), and has become an attractive strategy in tissue grafting and regenerative medicine because it has abundant tissue healing-promoting cytokines and interleukins (ILs), including transforming growth factor beta 1 (TGF-β1), basic fibroblast growth factor (bFGF), platelet derived growth factor (PDGF), vascular endothelial growth factor (VEGF), IL-6, IL-8, IL-11, and so on

(Masuki et al., 2016). Furthermore, PRF has been verified to increase tissue retention, quality, and neovascularized capillary density of grafted fat (Xiong et al., 2019). In addition, PRF has also been demonstrated to facilitate the regeneration of bone, periodontal tissue, and dental pulp (Chang and Zhao, 2011; Ji et al., 2015; You et al., 2019).

As the second-generation platelet concentrate, PRF is considered as an outstanding natural biomaterial scaffold based on fibrin. However, either used as a scaffold for tissue engineering or as a medical dressing for clinical application, fresh PRF encountered some limitations for its further application. For instance, it is not suitable for storage or transit in liquid nitrogen or on dry ice (Morris, 2005). Therefore, previous studies underline the preparation for immediate use (Choukroun et al., 2006). Furthermore, the gelatinous morphology of the fresh PRF lacks stable shape and resistance to compression. Fortunately, vacuum freeze-drying technology could address the issue of PRF storage. Freeze-drying decreases the moisture of the PRF to a minimum, and vacuum environment reduces the possibility of oxidation, denaturation and contamination (Walters et al., 2014). The two points mentioned above suggest that freeze-drying has the potential to keep the morphology of PRF and the stability of biological properties of PRF proteins, especially various growth factors (Nakajima et al., 2012). Moreover, previous study demonstrated that, compared to fresh PRF, lyophilized PRF presented better cell proliferation-promoting capacity *in vitro*, and better histocompatibility and bone regeneration *in vivo* (Li et al., 2014).

Electrospinning technology is a simple and efficient approach to acquire fibers at nanometer and micron scale (Greiner and Wendorff, 2007; Bhardwaj and Kundu, 2010). Electrospinning has the advantages of large specific surface area, high porosity, and low cost. In addition, it has been wildly studied or used in regenerative medicine, tissue engineering, medical wound dressing, and delivery of controlled drug release (Sill and von Recum, 2008). Furthermore, the ordered arrangement of nanofibers could produce complex three-dimensional (3D) multiscale and ultrathin fibrous scaffolds, and the microfabricated scaffolds could maintain cell viability better than plain scaffolds (Chen et al., 2017; Asencio et al., 2018). As new materials (such as bioactive substance) are added for preparation, electrospinning is expected to be an ideal biological scaffold. We therefore sought to further explore the biological potential of electrospinning with lyophilized PRF added as one of the materials.

Herein, we investigate the surface structure of lyophilized PRF and its effect on promoting cell proliferation and osteogenesis of MEC3T3-E1 cells. After mixing polyvinyl alcohol (PVA) and sodium alginate (SA) polymers with lyophilized PRF, we produce PVA/SA/PRF electrospinning and explore the surface morphology of the nanofibers. The effects of PVA/SA/PRF nanofibers extract on promoting cell proliferation and osteogenesis of MEC3T3-E1 cells are also investigated. Based on these results, we want to shed light on the possible strategies for tissue engineering (especially bone regeneration) or other applications with PVA/SA/PRF electrospinning.

MATERIALS AND METHODS

Preparation of Lyophilized PRF of Mouse

The care and experimental procedures of the animals in our study were compatible with animal ethical care guideline of Xiamen Medical College, and conformed to the Guide for the Care and Use of Laboratory Animals from the National Institutes of Health. C57/BL6 mice (18–22 g) 4–6 weeks of age were anesthetized with ether, and blood was collected from eye socket. The mouse blood was centrifuged at 400 *g* for 10 min and let to sit for 5 min at room temperature, then the PRF gel layers were collected, and the blood clots at the bottom of PRF gel layers were removed. The pure PRF was frozen and stored at −80°C. The frozen PRF was then freeze-dried for 48 h at −80°C using an Alpha2-4LDplus lyophilizer (Christ, Germany). The lyophilized PRF was used in the following experiments.

Surface Structure of Lyophilized PRF

Visualization of lyophilized PRF surface structure was achieved using a scanning electron microscope. Lyophilized PRF was fixed using 4% glutaraldehyde for 60 min. After dehydration with gradient alcohol series (30, 50, 70, 80, 90, 95, and 100%) for 15 min each, the samples were dried by hexamethyldisilazane and sputtered with gold palladium using a sputter coater. Dried lyophilized PRF samples were examined by scanning electron microscopy (SEM, ZEISS, Germany), and the diameters of 100 random pores were selected and analyzed by ImageJ (NIH, United States).

Cell Culture of MEC3T3-E1

MEC3T3-E1 cells (preosteoblast cell line of mouse calvaria bone) were purchased from the Cell Bank of Chinese Academy of Sciences (Shanghai, China). MEC3T3-E1 cells were cultivated in Minimum Essential Medium α (MEMα, Gibco, United States) supplemented with 10% fetal bovine serum (FBS, Gibco, United States), $NaHCO_3$ (1.5 g/L, Sigma, United States), inositol (43.2 mg/L, Sigma, United States), folic acid (8.82 mg/L, Sigma, United States), and β-mercaptoethanol (7.8 mg/L, Sigma, United States) in a humidified atmosphere at 37°C with 5% CO_2. The cultivation medium was replaced every 2 days.

Cell Proliferation Assay of Lyophilized PRF

To prepare the lyophilized PRF medium, 50 mg of lyophilized PRF was added into 3 mL of MEMα containing 100 units/mL penicillin and 100 mg/mL streptomycin. After incubation for 24 h at 4°C, the medium was centrifuged (400 *g*) for 5 min and then the supernatant was collected and filtered with a 0.22 μm filter. Then 10% FBS was added into the medium. A Cell Counting Kit-8 (CCK-8, Dojindo, Japan) was used to evaluate the proliferation ability of the MEC3T3-E1 cells cultivated in lyophilized PRF medium, and MEMα supplement with 10% FBS was set as the control medium group. A total of 3×10^3 cells was seeded in each well of a 96-well plate. After cultivation in the control medium for 24 h, the medium was replaced with lyophilized PRF medium and cultivated for 1, 3, and 5 days, the cultivation medium was changed to 100 μL of control medium with 10 μL of CCK-8 solution. After being incubated for 2 h in a humidified atmosphere at 37°C with 5% CO_2, the absorbance of the supernatant at 450 nm was examined with a spectrophotometer (Thermo, United States).

Detection of Osteogenic Genes Expression

A total of 5×10^4 cells was seeded in each well of a six-well plate. After cultivation in the control medium for 24 h, the medium was replaced with lyophilized PRF medium and cultivated for 5 days. The cells were collected for quantitative reverse transcription polymerase chain reaction (qRT-PCR) analysis. Total RNA was extracted using TriZol (Thermo, United States). The complementary DNA (cDNA) synthesis was performed using a RevertAid First Strand cDNA Synthesis Kit (Thermo, United States) on an MJ Research PTC-200 Peltier Thermal Cycler (Bio-Rad, United States). The qRT-PCR analysis was performed on a CFX96 Touch Real-Time PCR Detection System (Bio-Rad, United States). All of the procedures followed the manufacturers' protocols and were described previously (Yang et al., 2020). We monitored the expression of osteocalcin (OCN) and osteopontin (OPN) for osteogenesis of MEC3T3-E1 cells. PCR primer sequences and PCR products sizes are listed in **Table 1**. Primer sequences were designed and blasted at Primer BLAST website[1]. The expression of GAPDH was used as reference for normalization. $\Delta\Delta$ Ct calculation method was used to calculate and quantify the relative expression levels (Livak and Schmittgen, 2001). Three parallel replicates were prepared.

Preparation and Observation of PVA/SA/PRF Nanofibers

9 g of PVA (Sigma, United States) and 1 g of SA (Sigma, United States) were added into 90 mL of deionized water, and the PVA/SA solution was stirred at 600 revolutions per minute (rpm) for 8 h. Then 50 mg of lyophilized PRF was added into the solution. After being treated with ultrasound for 1 h, the PVA/SA/PRF solution was stirred at 600 rpm for 4 h. The PVA/SA solution without lyophilized PRF was set as control group. The PVA/SA/PRF solution or PVA/SA solution was put in 5 mL injection syringes with a 21G needle. The solutions were fabricated using an electrospinning machine at a static voltage of 20 kilovolt (kV). The distance of receiving board and flat pinhead was 25 cm, and the solution flow rate was 0.1 mL/h. The PVA/SA/PRF nanofibers and PVA/SA nanofibers were dried in a vacuum freeze drier. The surface structure of the nanofibers was observed using a scanning electron microscope, and the operating procedures were the same as mentioned in Section "Surface Structure of Lyophilized PRF." For the measurement of the diameters of 100 random fibers, fast Fourier transform (FFT) of the SEM images and analysis of the spectral intensity distribution of the electrospinning were performed using ImageJ (NIH, United States). In particular, the spectral intensity distribution was obtained from the summation of gray value of 360 points in a 360° radial direction of the circle using ImageJ with oval profile, and the center of the circle is also the center of the FFT image.

TABLE 1 | Oligonucleotide primer sequences for RT-PCRs.

Target gene	Primer sequence (forward, reverse)
OCN	Sense 5′-ATGATGGAAGGCTCATGGTTG-3′
	Antisense 5′-TGTTGGCGTACAGGTAATAGAA-3′
OPN	Sense 5′-TCCTGGCACCTACCTAAAACAGCA-3′
	Antisense 5′-CTACACTCTCGGCATTCACTTTGG-3′
GAPDH	Sense 5′-GGTGAAGGTCGGTGTGAACG-3
	Antisense 5′-CTCGCTCCTGGAAGATGGTG-3′

Cell Proliferation Assay of Nanofibers Extract

To prepare the PVA/SA/PRF and PVA/SA nanofibers extract, 50 mg of PVA/SA/PRF nanofibers or 50 mg of PVA/SA nanofibers was added into 3 mL MEMα (with 100 units/mL penicillin and 100 mg/mL streptomycin), respectively. After incubation for 24 h at 4°C, the medium was centrifuged (400 *g*) for 5 min, then the supernatant was collected and filtered with a 0.22 μm filter. Then 10% FBS was added into the medium. MEMα supplemented with 10% was set as the control medium group. CCK-8 (Dojindo, Japan) was used to evaluate the proliferation ability of the MEC3T3-E1 cells cultivated in PVA/SA/PRF and PVA/SA nanofibers extract, and the operating procedures were the same as described in Section "Cell Proliferation Assay of Lyophilized PRF."

Osteogenic Differentiation Assay of PVA/SA/PRF Nanofibers Extract

The osteogenesis differentiation capacity of MEC3T3-E1 influenced by PVA/SA/PRF nanofibers extract medium was evaluated by Alizarin Red S staining. A total of 1×10^5 MEC3T3-E1 cells were seeded in each well of 12-well plates with PVA/SA/PRF nanofibers extract and PVA/SA nanofibers extract. After cultivation for 21 days, the supernatant was removed and washed with PBS for three times, and the cells were fixed in 4% paraformaldehyde for 30 min. After being washed with PBS for three times, the fixed cells were incubated in 0.1% Alizarin Red S solution (Sigma, United States) for 30 min, and then washed with distilled water twice. The images of the stained cells were acquired under a microscope (Olympus, Japan), and spectrophotometric analysis was performed using ImageJ (NIH, United States).

Statistical Analysis

The data are presented as mean ± standard deviation (SD). An independent-samples *t*-test analysis of variance was used to analyze the differences between the groups. Statistical calculations were performed with IBM SPSS Statistics 26 software (IBM, United States). $P < 0.05$ is considered statistically significant.

---

[1] https://www.ncbi.nlm.nih.gov/tools/primer-blast/index.cgi

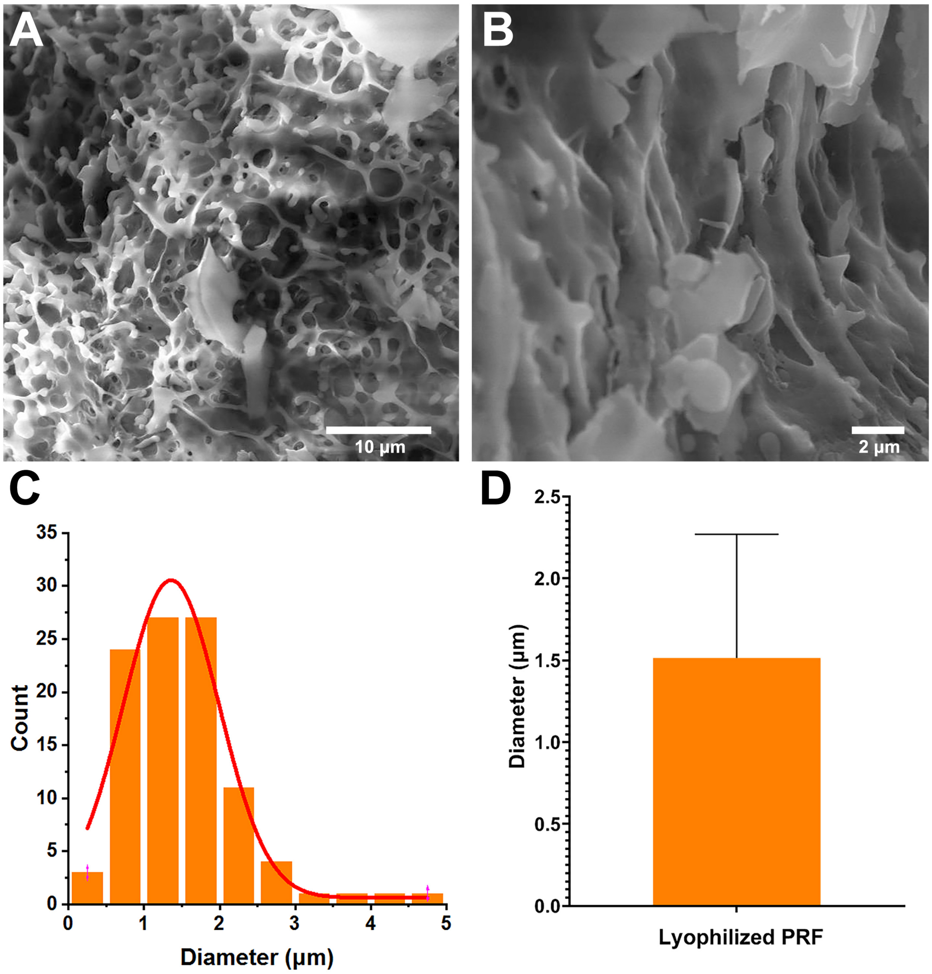

FIGURE 1 | Surface parameters of lyophilized PRF. **(A)** Surface morphology of lyophilized PRF (4000×). **(B)** Surface morphology of lyophilized PRF (10,000×). **(C)** The diameter distribution of pores. **(D)** The diameters of the pores were 1.51 ± 0.75 nm.

RESULTS

Morphological Characteristics of Lyophilized PRF

To evaluate the surface parameters of lyophilized PRF, the surface morphology of cut samples was detected by SEM. The SEM image showed that lots of cavities were present in the lyophilized PRF (**Figures 1A,B**). The image analysis results revealed that the diameters of pores were mainly distributed in the range of 0.75∼1.75 μm (78%) (**Figure 1C**), and the distribution of the pore diameters accorded with a GaussAmp fitting curve [$y = 0.60 + 29.93 \times \exp(-0.5 \times ((x-1.36)/0.63)^2$, $R^2 = 0.96$]. The diameters of the pores were 1.51 ± 0.75 μm (**Figure 1D**).

Lyophilized PRF Promoted the Proliferation of MEC3T3-E1 Cells

After cultivation for 1 day, the CCK-8 results revealed that lyophilized PRF medium promoted the proliferation of MEC3T3-E1 cells. After 3 days, the proliferation ability of MEC3T3-E1 cells in lyophilized PRF medium still was approximately 35% higher than that in control medium. The CCK-8 results on the fifth day showed that the excellent potential of the proliferation ability was kept to the end of experimental time point (**Figure 2A**).

Lyophilized PRF Increased the Gene Expressions of OCN and OPN

The qRT-PCR assay was used to determine the effect of lyophilized PRF on osteogenic differentiation of MEC3T3-E1 cells, and the results revealed that the expression level of OCN in PRF medium was threefold higher than that in control group. Meanwhile, OPN expression in PRF medium was also approximately twofold higher than that in control group (**Figure 2B**).

Surface Features of PVA/SA/PRF Nanofibers

Scanning electron microscopy assay was also used to determine the surface parameters of PVA/SA and

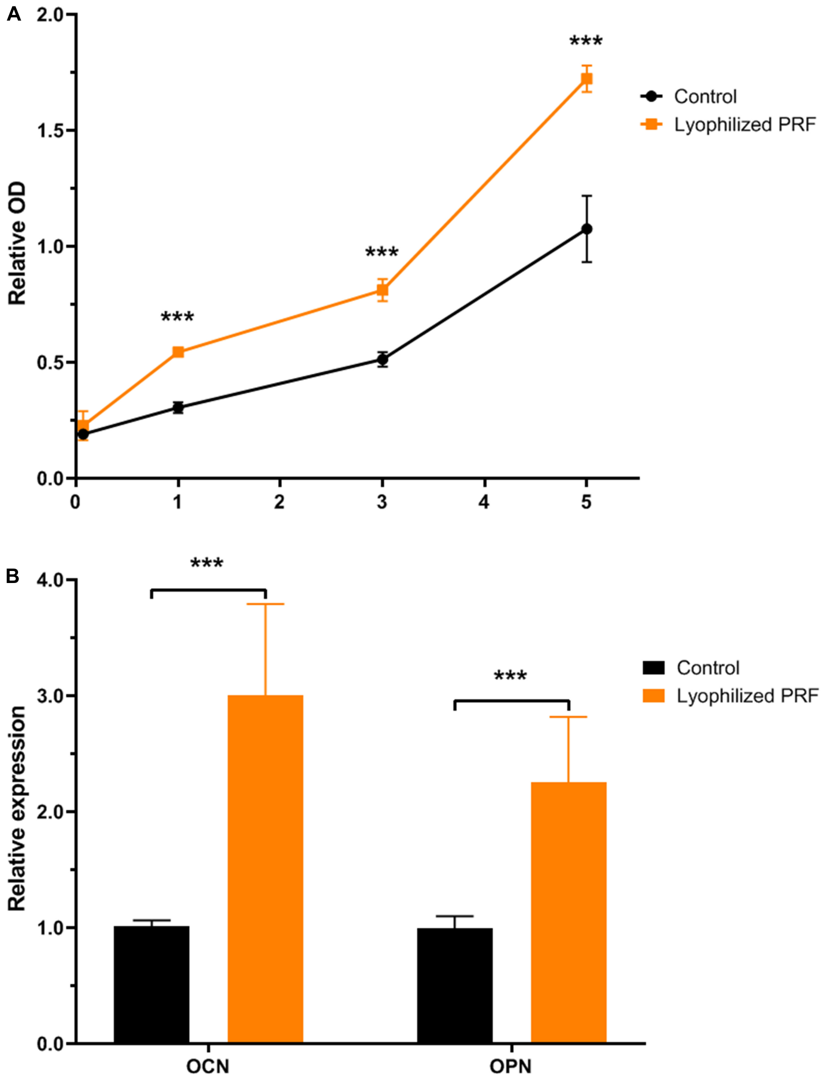

FIGURE 2 | The effect of lyophilized PRF on the proliferation and differentiation potential of MEC3T3-E1 cells. **(A)** The growth kinetics of MEC3T3-E1 cells in control and lyophilized PRF medium. The result showed that lyophilized PRF medium promoted MEC3T3-E1 cells proliferation. **(B)** The differentiation potential of MEC3T3-E1 cells in control and lyophilized PRF medium. The result revealed that lyophilized PRF medium could increase the gene expressions of OCN and OPN. ***$P < 0.001$.

PVA/SA/PRF nanofibers. The SEM image showed that the fibers of PVA/SA/PRF were lager than PVA/SA fibers (**Figures 3A,B**). The image analysis results revealed that the diameters of PVA/SA fibers were mainly distributed in the range of 100∼150 nm (58%), and the distribution of the fiber diameters accorded with a GaussAmp fitting curve [$y = 1.52 + 57.60 \times \exp(-0.5 \times ((x-131.26)/30.58)^2$, $R^2 = 0.99$]. While the diameters of PVA/SA/PRF fibers were mainly distributed in the range of 150∼250 nm (83%), and the distribution of the fiber diameters accorded with a GaussAmp fitting curve [$y = 1.09 + 52.04 \times \exp(-0.5 \times ((x-196.29)/35.41)^2$, $R^2 = 0.99$] (**Figure 3C**). The diameters of the PVA/SA fibers and PVA/SA/PRF fibers were 138.66 ± 46.20 vs. 201.14 ± 40.14 nm (**Figure 3D**). The FFT image showed a large difference between the gray value distribution of PVA/SA/PRF fibers and that of PVA/SA fibers (**Figure 4A**). The radial sums of PVA/SA FFT image showed that the gray value of spectral intensity distribution ranged from 55,400 to about 60,000, while the gray value of spectral intensity distribution of PVA/SA/PRF ranged from 60,400 to about 65,700 (**Figure 4B**). The spectral intensity distribution at 360° radius direction also demonstrated the diversity between PVA/SA/PRF fibers and PVA/SA fibers.

PVA/SA/PRF Nanofibers Extract Promoted the Proliferation of MEC3T3-E1 Cells

Cell Counting Kit-8 assay was also used to evaluate the proliferation ability of MEC3T3-E1 cells and the cytotoxicity of the PVA/SA and PVA/SA/PRF nanofibers extract. Compared with PVA/SA nanofibers extract and control groups,

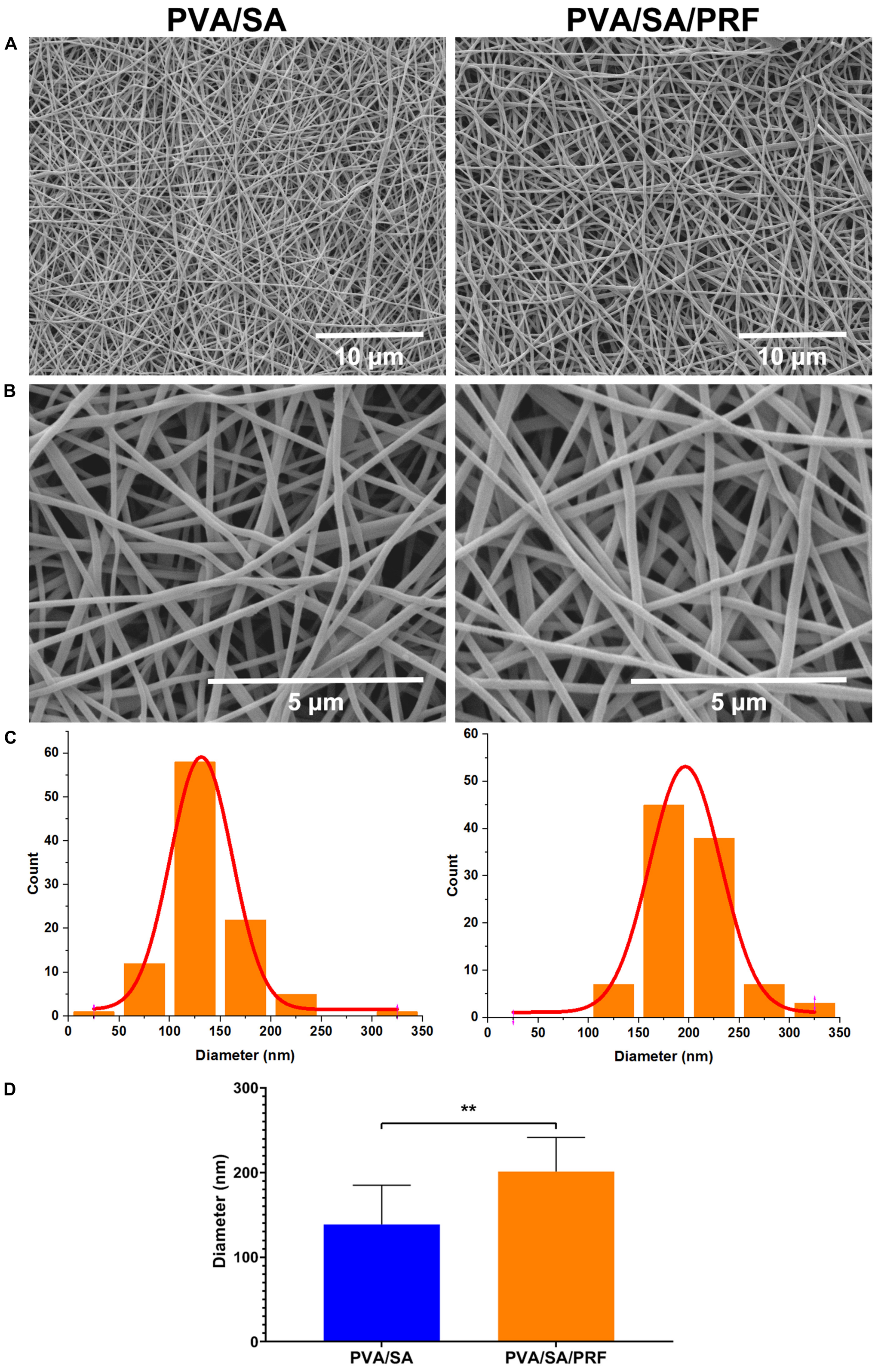

FIGURE 3 | Surface features of nanofibers of PVA/SA and PVA/SA/PRF. **(A)** Surface morphology of nanofibers of PVA/SA and PVA/SA/PRF (6000×). **(B)** Surface morphology of nanofibers of PVA/SA and PVA/SA/PRF (24,000×). **(C)** The diameter distribution of PVA/SA and PVA/SA/PRF fibers. **(D)** The diameters of the PVA/SA fibers and PVA/SA/PRF fibers were 138.66 ± 46.20 and 201.14 ± 40.14 nm, respectively. $^{**}P < 0.01$.

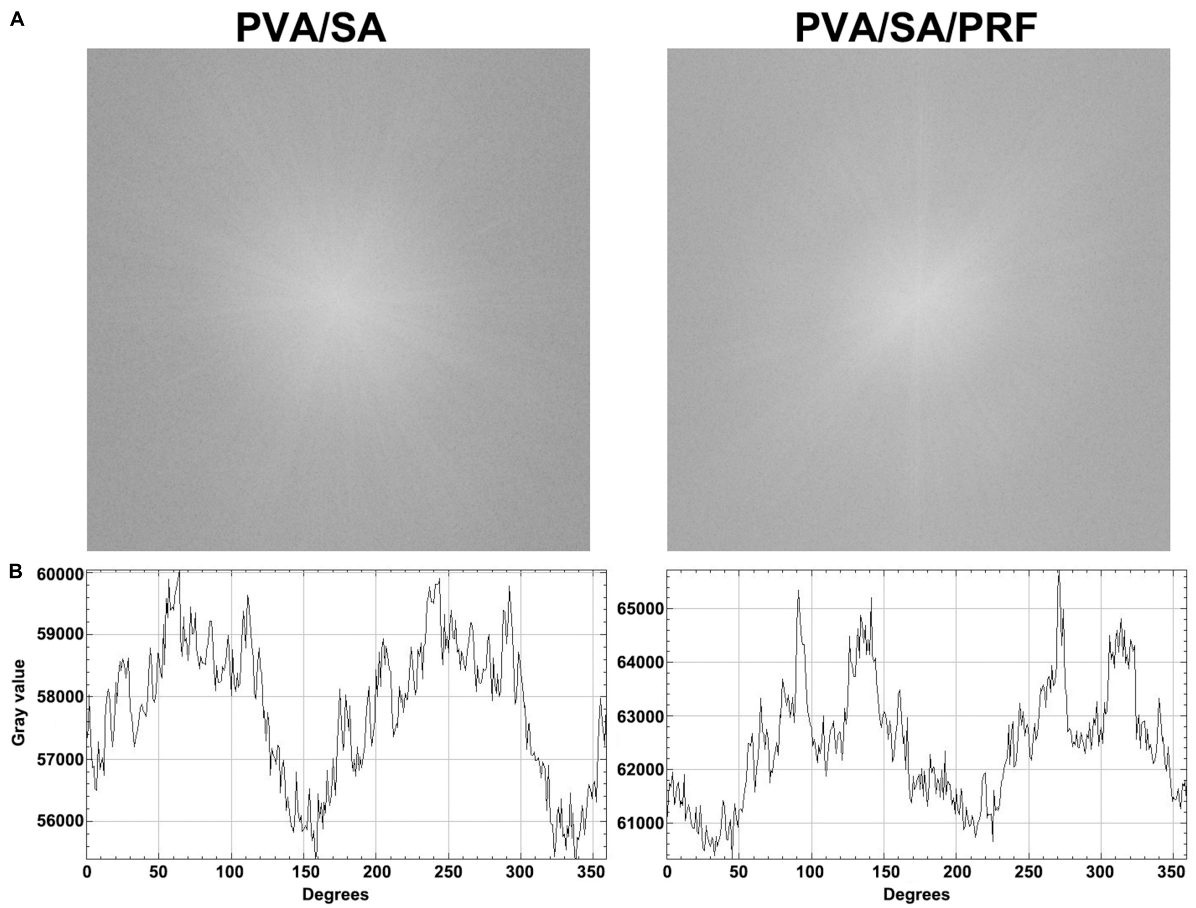

FIGURE 4 | The FFT image and spectral intensity distribution of PVA/SA and PVA/SA/PRF nanofibers. **(A)** The FFT was performed for PVA/SA and PVA/SA/PRF nanofibers. **(B)** The spectral intensity distribution demonstrated the diversity between PVA/SA/PRF fibers and PVA/SA fibers.

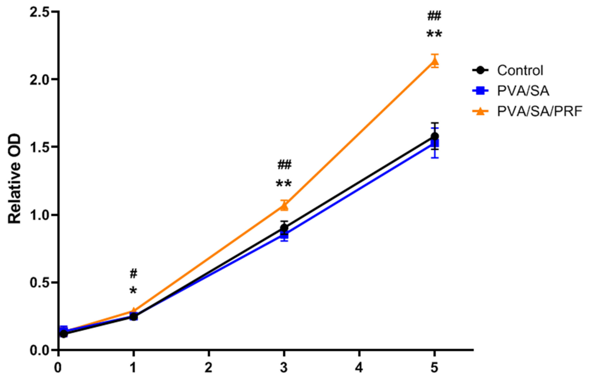

FIGURE 5 | The effect of PVA/SA and PVA/SA/PRF nanofibers extract on the proliferation ability of MEC3T3-E1 cells. PVA/SA/PRF nanofibers extract promoted the proliferation ability of MEC3T3-E1 cells obviously. $^{*}P < 0.05$ (PVA/SA/PRF vs. Control); $^{**}P < 0.01$ (PVA/SA/PRF vs. Control); $^{\#}P < 0.05$ (PVA/SA/PRF vs. PVA/SA); $^{\#\#}P < 0.01$ (PVA/SA/PRF vs. PVA/SA).

PVA/SA/PRF nanofibers extract promoted the proliferation ability of MEC3T3-E1 cells obviously on the first, third, and fifth day of the experimental time points. Meanwhile, there was no significant difference on the proliferation of MEC3T3-E1 cells between PVA/SA nanofibers extract and control medium in the duration of 7 days (**Figure 5**).

PVA/SA/PRF Nanofibers Extract Enhanced Osteogenic Differentiation

Alizarin Red S was used to stain the calcified nodules accumulated by osteogenic differentiation of MEC3T3-E1 cells. The results revealed that, compared with PVA/SA nanofibers extract and control groups, the relative optical density (OD) in PVA/SA/PRF nanofibers extract increased significantly. However, compared with control group, PVA/SA electrospinning extract medium did not enhance osteogenic differentiation of MEC3T3-E1 cells (**Figure 6**).

DISCUSSION

Platelet-rich fibrin and electrospinning technology are promising therapeutic intervention in tissue engineering and have been widely studied (Oryan et al., 2016; Dohle et al., 2018; Nemati et al., 2019; Udomluck et al., 2019). Bone tissue engineering is an alternative therapeutic strategy to repair

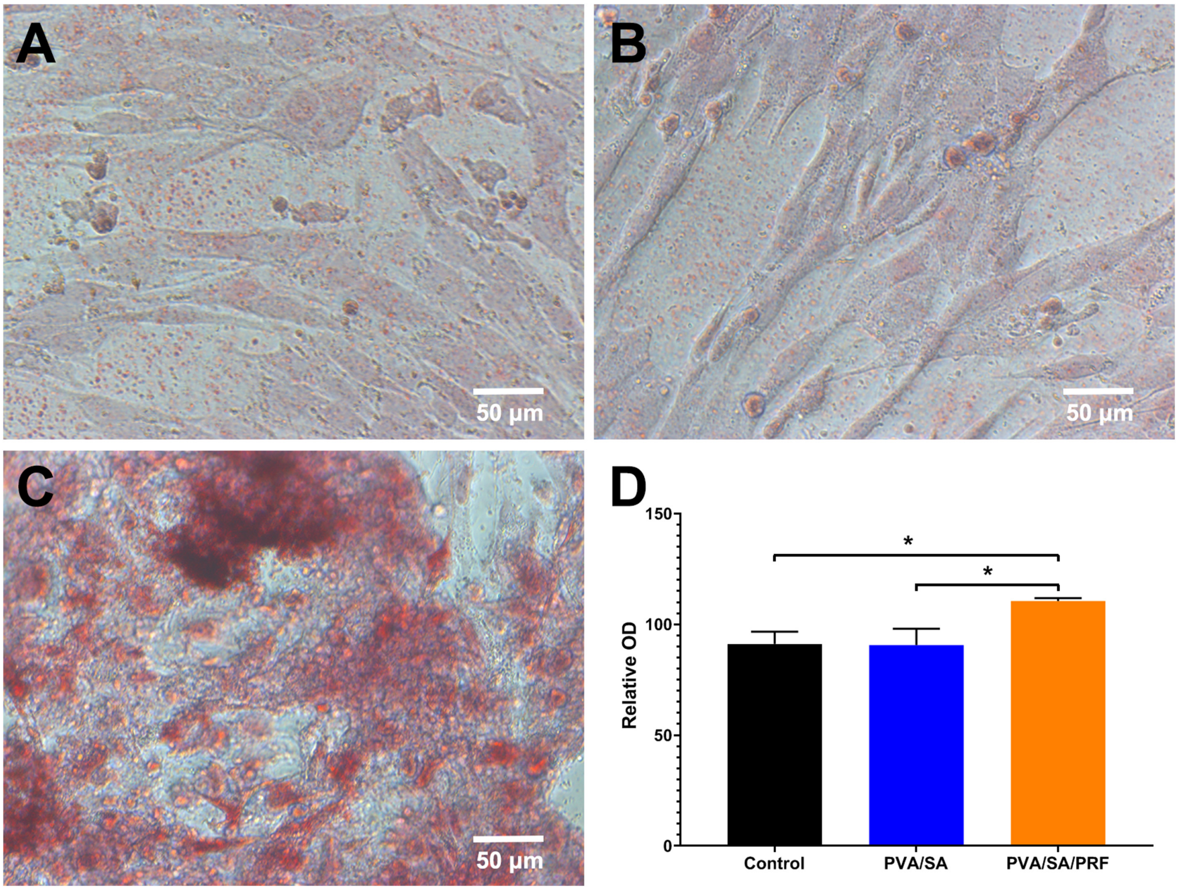

FIGURE 6 | The effect of PVA/SA and PVA/SA/PRF nanofibers extract on the osteogenic differentiation of MEC3T3-E1 cells. **(A)** Osteogenic differentiation of MEC3T3-E1 cells in control medium. **(B)** Osteogenic differentiation of MEC3T3-E1 cells in PVA/SA nanofibers extract. **(C)** Osteogenic differentiation of MEC3T3-E1 cells in PVA/SA/PRF nanofibers extract, and many stained calcified nodules could be observed in this group. **(D)** The spectrophotometric analysis results of the Alizarin Red S staining images. *$P < 0.5$.

damaged bone (Nemati et al., 2019; Udomluck et al., 2019). The purpose of this study was to investigate the biological characteristics of lyophilized PRF and its electrospinning, and explore the potential of PVA/SA nanofibers with lyophilized PRF added as the biomaterial for bone tissue engineering. The data from the present study demonstrated that both lyophilized PRF and PVA/SA/PRF nanofibers could promote the proliferation and mineralization activity of MEC3T3-E1 cells.

Platelet-rich plasma is plasma with a higher concentration of platelets, and has been used for wound healing and tissue engineering (Andreone and den Hollander, 2019). To overcome the disadvantages such as coagulopathies and allergic reactions after addition of bovine thrombin, PRF as the second generation of platelet products was developed. In fact, previous report demonstrated that PRF presents better capacity than PRP to alleviate the negative effect of drugs on the proliferation, migration, and viability of osteoblasts and oral fibroblasts as expect (Steller et al., 2019). However, PRF also has several limitations, not the least of which is that it requires the preparation for immediate use (Morris, 2005; Choukroun et al., 2006). Fortunately, vacuum freeze-drying technology addressed the issue of PRF storage and could maintain or even enhance the biological functions of PRF (Pietramaggiori et al., 2006; Nakajima et al., 2012; Li et al., 2014). It was speculated that the enhancement of biological function was due to the enlargement of pore size and improvement of cytokines release (Li et al., 2014). In addition, our data demonstrated that the diameters of the pores of our lyophilized PRF from mouse were 1.51 ± 0.75 μm, which are smaller than the 8.06 ± 0.31 μm of lyophilized PRF but larger than 0.6 ± 0.13 μm of fresh PRF from pig in a previous study (Li et al., 2014). The results suggested that the species of the source might influence the pore size of lyophilized PRF.

The present study indicated that lyophilized PRF promoted the proliferation and increased the OCN and OPN gene expressions of MEC3T3-E1 cells when compared to MEMα supplement with 10% FBS, suggesting that lyophilized PRF contains more nutriments than FBS for MEC3T3-E1 cells. These biological functions to promote proliferation and mineralization were attributed to the ability of the vacuum freeze-drying technology to maintain the bioactivity of the cytokines including abundant growth factors in the PRF. Growth factors play a critical role in tissue engineering (Udomluck et al., 2019). As one of the three elements for tissue engineering, many growth factors are well-studied including bone morphogenetic proteins (BMP2 to BMP8), TGF-β, PDGF, FGF, and so on (Gittens and Uludag, 2001; De Witte et al., 2018; Kim et al., 2018). In particular, bFGF, also known as FGF-2, has been used for the clinical regenerative treatment of osteonecrosis of the femoral head, demonstrating its safety and efficacy (Kuroda et al., 2019). It is interesting that plenty of growth factors for bone tissue engineering were involved in the cytokine profiles of PRF (Masuki et al., 2016). The growth factors in lyophilized PRF might assist each other in strengthening the mineralization activity of MEC3T3-E1 cells.

Electrospinning technology provides a potential and efficient platform to acquire nanofibers used as artificial biological scaffold for bone tissue engineering (Greiner and Wendorff, 2007; Bhardwaj and Kundu, 2010; Udomluck et al., 2019). Electrospinning has the advantages of large specific surface area, high porosity, and low cost, which meets the requirements of bone tissue scaffold to integrate a mass of bone related cells for forming bone like tissues (Yoshimoto et al., 2003; Udomluck et al., 2019). Moreover, growth factors were added for preparation, and the growth factors could be sustainably released from the electrospinning nanofibers (Sahoo et al., 2010). Herein, we intended to combine both the advantages of the lyophilized PRF and electrospinning technology to mimic the nature of the extracellular matrix. We speculated that while lyophilized PRF was added for electrospinning nanofibers preparation, plenty of the growth factors could be released from the electrospinning and benefit bone tissue formation. Our data demonstrated that the diameters of the traditional PVA/SA fibers were 138.66 ± 46.20 nm, but after lyophilized PRF being added, the diameters of the fibers were enlarged to 201.14 ± 40.14 nm. The FFT analysis also showed that gray value of spectral intensity distribution range went from 55,400∼60,000 to 60,400∼65,700. These results indicated that lyophilized PRF added as a component of the electrospinning material modified the physical properties of the nanofibers, especially the surface characteristics, which might be important for bone tissue engineering.

Previous studies focused on surface modification for enhancing cellular behavior in tissue engineering (high proliferation rate or bone formation), which indicated that proliferation and mineralization activity of the bone related cells is important for bone tissue engineering (Nandakumar et al., 2013; Lee et al., 2016; Udomluck et al., 2019). Electrospinning nanofibers with sustained release of growth factors have the great potential to create a beneficial microenvironment for bone tissue formation, including promoting migration and differentiation of osteoblasts by angiogenic, inflammatory, and bone formation enhancement (Sui et al., 2007; Vo et al., 2012). It is interesting that the cytokines from PRF also have similar biological functions for tissue regenerative medicine, such as anti-inflammation effects, promoting osteogenic differentiation and vascularization (Pietramaggiori et al., 2006; You et al., 2019; Nasirzade et al., 2020; Xie et al., 2020; Zhang et al., 2020). In present study, we investigated the effect of extract of PVA/SA/PRF nanofibers on proliferation and osteogenesis of osteogenic precursor cells (MEC3T3-E1 cells) *in vitro*. The results showed that PVA/SA/PRF nanofibers extract presented an extraordinary capacity to promote the proliferation and mineralization activity of MEC3T3-E1 cells in contrast to PVA/SA nanofibers extract and control medium, which demonstrated that PVA/SA/PRF nanofibers could maintain the bioactivity of proliferation and osteogenesis-promoting cytokines, and release them to the medium.

CONCLUSION

This study investigated the biological properties of lyophilized PRF, as promoting MEC3T3-E1 cells proliferation and mineralization induction. In addition, lyophilized PRF added into PVA/SA polymers as a component for electrospinning preparation could modify the physical properties of the electrospinning nanofibers. Moreover, PVA/SA/PRF nanofibers extract also promoted the proliferation and mineralization activity of MEC3T3-E1 cells in contrast to PVA/SA nanofibers extract and control medium. These results indicated that PVA/SA/PRF nanofibers might maintain the characteristics of lyophilized PRF for enhancing proliferation and mineralization, which might be a candidate scaffold for bone tissue engineering.

DATA AVAILABILITY STATEMENT

The original contributions presented in the study are included in the article/supplementary material. Further inquiries can be directed to the corresponding author/s.

ETHICS STATEMENT

The animal study was reviewed and approved by the Ethics Committee of Stomatological Hospital of Xiamen Medical College.

AUTHOR CONTRIBUTIONS

PW performed the 1 assay. JN, YS, and SMZ performed the 2–8 assay. YJS gathered and analyzed the research data. JN conceptualized and designed the study, wrote the manuscript, and reviewed and revised the final manuscript. YL critically reviewed and revised the manuscript for important intellectual content. All authors contributed for the development of this manuscript, approved the final version of the manuscript as submitted, and agreed to be accountable for all aspects of the work in ensuring that questions related to the accuracy or integrity of any part of the work.

FUNDING

This study was supported by Pilot Project of Fujian provincial Program Science and Technology Program (2017D0015).

REFERENCES

Andreone, A., and den Hollander, D. (2019). A retrospective study on the use of dermis micrografts in platelet-rich fibrin for the resurfacing of massive and chronic full-thickness burns. *Stem Cells Int.* 2019:8636079. doi: 10.1155/2019/8636079

Asencio, I. O., Mittar, S., Sherborne, C., Raza, A., Claeyssens, F., and MacNeil, S. (2018). A methodology for the production of microfabricated electrospun membranes for the creation of new skin regeneration models. *J. Tissue Eng.* 9:2041731418799851. doi: 10.1177/2041731418799851

Bhardwaj, N., and Kundu, S. C. (2010). Electrospinning: a fascinating fiber fabrication technique. *Biotechnol. Adv.* 28, 325–347. doi: 10.1016/j.biotechadv.2010.01.004

Chang, Y. C., and Zhao, J. H. (2011). Effects of platelet-rich fibrin on human periodontal ligament fibroblasts and application for periodontal infrabony defects. *Aust. Dent. J.* 56, 365–371. doi: 10.1111/j.1834-7819.2011.01362.x

Chen, H., Malheiro, A. D. B. F. B., van Blitterswijk, C., Mota, C., Wieringa, P. A., and Moroni, L. (2017). Direct writing electrospinning of scaffolds with multidimensional fiber architecture for hierarchical tissue engineering. *ACS Appl. Mater. Interf.* 9, 38187–38200. doi: 10.1021/acsami.7b07151

Choukroun, J., Diss, A., Simonpieri, A., Girard, M. O., Schoeffler, C., Dohan, S. L., et al. (2006). Platelet-rich fibrin (PRF): a second-generation platelet concentrate. Part IV: clinical effects on tissue healing. *Oral Surg. Oral Med. Oral Pathol. Oral Radiol. Endod.* 101, e56–e60. doi: 10.1016/j.tripleo.2005.07.011

De Witte, T. M., Fratila-Apachitei, L. E., Zadpoor, A. A., and Peppas, N. A. (2018). Bone tissue engineering via growth factor delivery: from scaffolds to complex matrices. *Regen. Biomater.* 5, 197–211. doi: 10.1093/rb/rby013

Dohle, E., El Bagdadi, K., Sader, R., Choukroun, J., James Kirkpatrick, C., and Ghanaati, S. (2018). Platelet-rich fibrin-based matrices to improve angiogenesis in an in vitro co-culture model for bone tissue engineering. *J. Tissue Eng. Regen. Med.* 12, 598–610. doi: 10.1002/term.2475

Gittens, S. A., and Uludag, H. (2001). Growth factor delivery for bone tissue engineering. *J. Drug Target* 9, 407–429. doi: 10.3109/10611860108998776

Greiner, A., and Wendorff, J. H. (2007). Electrospinning: a fascinating method for the preparation of ultrathin fibers. *Angew Chem. Int. Ed. Engl.* 46, 5670–5703. doi: 10.1002/anie.200604646

Ji, B., Sheng, L., Chen, G., Guo, S., Xie, L., Yang, B., et al. (2015). The combination use of platelet-rich fibrin and treated dentin matrix for tooth root regeneration by cell homing. *Tissue Eng. Part A* 21, 26–34. doi: 10.1089/ten.tea.2014.0043

Kim, S., Lee, S., and Kim, K. (2018). Bone tissue engineering strategies in co-delivery of bone morphogenetic protein-2 and biochemical signaling factors. *Adv. Exp. Med. Biol.* 1078, 233–244. doi: 10.1007/978-981-13-0950-2_12

Kuroda, Y., Kawai, T., Goto, K., and Matsuda, S. (2019). Clinical application of injectable growth factor for bone regeneration: a systematic review. *Inflamm. Regen.* 39:20. doi: 10.1186/s41232-019-0109-x

Lee, H., Lim, S., Birajdar, M. S., Lee, S. H., and Park, H. (2016). Fabrication of FGF-2 immobilized electrospun gelatin nanofibers for tissue engineering. *Int. J. Biol. Macromol.* 93(Pt B), 1559–1566. doi: 10.1016/j.ijbiomac.2016.07.041

Li, Q., Reed, D. A., Min, L., Gopinathan, G., Li, S., Dangaria, S. J., et al. (2014). Lyophilized platelet-rich fibrin (PRF) promotes craniofacial bone regeneration through Runx2. *Int. J. Mol. Sci.* 15, 8509–8525. doi: 10.3390/ijms15058509

Livak, K. J., and Schmittgen, T. D. (2001). Analysis of relative gene expression data using real-time quantitative PCR and the $2^{-\Delta\Delta C_T}$ method. *Methods* 25, 402–408. doi: 10.1006/meth.2001.1262

Masuki, H., Okudera, T., Watanebe, T., Suzuki, M., Nishiyama, K., Okudera, H., et al. (2016). Growth factor and pro-inflammatory cytokine contents in platelet-rich plasma (PRP), plasma rich in growth factors (PRGF), advanced platelet-rich fibrin (A-PRF), and concentrated growth factors (CGF). *Int. J. Implant Dent.* 2:19. doi: 10.1186/s40729-016-0052-4

Morris, G. J. (2005). The origin, ultrastructure, and microbiology of the sediment accumulating in liquid nitrogen storage vessels. *Cryobiology* 50, 231–238. doi: 10.1016/j.cryobiol.2005.01.005

Nakajima, Y., Kawase, T., Kobayashi, M., Okuda, K., Wolff, L. F., and Yoshie, H. (2012). Bioactivity of freeze-dried platelet-rich plasma in an adsorbed form on a biodegradable polymer material. *Platelets* 23, 594–603. doi: 10.3109/09537104.2011.645923

Nandakumar, A., Tahmasebi Birgani, Z., Santos, D., Mentink, A., Auffermann, N., van der Werf, K., et al. (2013). Surface modification of electrospun fibre meshes by oxygen plasma for bone regeneration. *Biofabrication* 5:015006. doi: 10.1088/1758-5082/5/1/015006

Nasirzade, J., Kargarpour, Z., Hasannia, S., Strauss, F. J., and Gruber, R. (2020). Platelet-rich fibrin elicits an anti-inflammatory response in macrophages in vitro. *J. Periodontol.* 91, 244–252. doi: 10.1002/JPER.19-0216

Nemati, S., Kim, S. J., Shin, Y. M., and Shin, H. (2019). Current progress in application of polymeric nanofibers to tissue engineering. *Nano Converg.* 6:36. doi: 10.1186/s40580-019-0209-y

Oryan, A., Alidadi, S., and Moshiri, A. (2016). Platelet-rich plasma for bone healing and regeneration. *Expert Opin. Biol. Ther.* 16, 213–232. doi: 10.1517/14712598.2016.1118458

Pietramaggiori, G., Kaipainen, A., Czeczuga, J. M., Wagner, C. T., and Orgill, D. P. (2006). Freeze-dried platelet-rich plasma shows beneficial healing properties in chronic wounds. *Wound Repair Regen.* 14, 573–580. doi: 10.1111/j.1743-6109.2006.00164.x

Sahoo, S., Ang, L. T., Goh, J. C., and Toh, S. L. (2010). Growth factor delivery through electrospun nanofibers in scaffolds for tissue engineering applications. *J. Biomed. Mater. Res. A* 93, 1539–1550. doi: 10.1002/jbm.a.32645

Sill, T. J., and von Recum, H. A. (2008). Electrospinning: applications in drug delivery and tissue engineering. *Biomaterials* 29, 1989–2006. doi: 10.1016/j.biomaterials.2008.01.011

Steller, D., Herbst, N., Pries, R., Juhl, D., and Hakim, S. G. (2019). Positive impact of Platelet-rich plasma and Platelet-rich fibrin on viability, migration and proliferation of osteoblasts and fibroblasts treated with zoledronic acid. *Sci. Rep.* 9:8310. doi: 10.1038/s41598-019-43798-z

Sui, G., Yang, X., Mei, F., Hu, X., Chen, G., Deng, X., et al. (2007). Poly-L-lactic acid/hydroxyapatite hybrid membrane for bone tissue regeneration. *J. Biomed. Mater. Res. A* 82, 445–454. doi: 10.1002/jbm.a.31166

Udomluck, N., Koh, W. G., Lim, D. J., and Park, H. (2019). Recent developments in nanofiber fabrication and modification for bone tissue engineering. *Int. J. Mol. Sci.* 21:99. doi: 10.3390/ijms21010099

Vo, T. N., Kasper, F. K., and Mikos, A. G. (2012). Strategies for controlled delivery of growth factors and cells for bone regeneration. *Adv. Drug Deliv. Rev.* 64, 1292–1309. doi: 10.1016/j.addr.2012.01.016

Walters, R. H., Bhatnagar, B., Tchessalov, S., Izutsu, K. I., Tsumoto, K., and Ohtake, S. (2014). Next generation drying technologies for pharmaceutical applications. *J. Pharm. Sci.* 103, 2673–2695. doi: 10.1002/jps.23998

Xie, Y., Chen, M., Chen, Y., Xu, Y., Sun, Y., Liang, J., et al. (2020). Effects of PRP and LyPRP on osteogenic differentiation of MSCs. *J. Biomed. Mater. Res. A* 108, 116–126. doi: 10.1002/jbm.a.36797

Xiong, S., Qiu, L., Su, Y., Zheng, H., and Yi, C. (2019). Platelet-rich plasma and Platelet-rich fibrin enhance the outcomes of fat grafting: a comparative study. *Plast. Reconstr. Surg.* 143, 1201e–1212e. doi: 10.1097/PRS.0000000000005624

Yang, C., Chen, Y., Zhong, L., You, M., Yan, Z., Luo, M., et al. (2020). Homogeneity and heterogeneity of biological characteristics in mesenchymal stem cells from human umbilical cords and exfoliated deciduous teeth. *Biochem. Cell Biol.* 98, 415–425. doi: 10.1139/bcb-2019-0253

Yoshimoto, H., Shin, Y. M., Terai, H., and Vacanti, J. P. (2003). A biodegradable nanofiber scaffold by electrospinning and its potential for bone tissue engineering. *Biomaterials* 24, 2077–2082. doi: 10.1016/s0142-9612(02)00635-x

You, J. S., Kim, S. G., Oh, J. S., and Kim, J. S. (2019). Effects of platelet-derived material (Platelet-Rich Fibrin) on bone regeneration. *Implant Dent.* 28, 244–255. doi: 10.1097/ID.0000000000000877

Zhang, J., Yin, C., Zhao, Q., Zhao, Z., Wang, J., Miron, R. J., et al. (2020). Anti-inflammation effects of injectable platelet-rich fibrin via macrophages and dendritic cells. *J. Biomed. Mater. Res. A* 108, 61–68. doi: 10.1002/jbm.a.36792

Conflict of Interest: The authors declare that the research was conducted in the absence of any commercial or financial relationships that could be construed as a potential conflict of interest.

frontiers
in Bioengineering and Biotechnology

REVIEW
published: 08 December 2020
doi: 10.3389/fbioe.2020.618931

Current Trends of Targeted Drug Delivery for Oral Cancer Therapy

Mingming Zhang[1†], *Jianqin Liang*[2†], *Yanyu Yang*[3*], *Huize Liang*[1], *Huaping Jia*[1*] *and Dawei Li*[4*]

[1] Strategic Support Force Characteristic Medical Center of Chinese People's Liberation Army, Beijing, China, [2] The 8th Medical Center, General Hospital of the Chinese People's Liberation Army, Beijing, China, [3] College of Materials Science and Engineering, Zhengzhou University, Zhengzhou, China, [4] The 4th Medical Center, General Hospital of the Chinese People's Liberation Army, Beijing, China

Oral cancer is an aggressive tumor that invades the local tissue and can cause metastasis and high mortality. Conventional treatment strategies, e.g., surgery, chemotherapy, and radiation therapy alone or in combinations, possess innegligible issues, and significant side and adverse effects for the clinical applications. Currently, targeting drug delivery is emerging as an effective approach for oral delivery of different therapeutics. Herein we provide a state-of-the-art review on the current progress of targeting drug delivery for oral cancer therapy. Variously oral delivery systems including polymeric/inorganic nanoparticles, liposomes, cyclodextrins, nanolipids, and hydrogels-based forms are emphasized and discussed, and biomimetic systems with respect to oral delivery like therapeutic vitamin, exosomes, proteins, and virus-like particles are also described with emphasis on the cancer treatment. A future perspective is also provided to highlight the existing challenges and possible resolution toward clinical translation of current oral cancer therapies.

Keywords: oral cancer, drug delivery, nanoparticles, nanotechnology, OSCC (oral squamous cell carcinoma)

OPEN ACCESS

Edited by:
Bing Han,
Peking University School and Hospital of Stomatology, China

Reviewed by:
Yun-Long Wu,
Xiamen University, China
Qin Xiaoyuun,
Zhengzhou University of Light Industry, China

Correspondence:
Yanyu Yang
yyyang@zzu.edu.cn
Huaping Jia
jiahuaping12@126.com
Dawei Li
ldw309@126.com

† These authors have contributed equally to this work

Specialty section:
This article was submitted to Biomaterials, a section of the journal Frontiers in Bioengineering and Biotechnology

Received: *19 October 2020*
Accepted: *19 November 2020*
Published: *08 December 2020*

Citation:
Zhang M, Liang J, Yang Y, Liang H, Jia H and Li D (2020) Current Trends of Targeted Drug Delivery for Oral Cancer Therapy. Front. Bioeng. Biotechnol. 8:618931. doi: 10.3389/fbioe.2020.618931

INTRODUCTION

Oral cancer refers to tumors that occur in the lips, hard palate, upper, and lower alveolar ridges, anterior two-thirds of the tongue, sublingual, buccal mucosa, posterior deltoid muscle of molars, and oral cavity (Vogel et al., 2010). More than 90% of oral cancers are carcinomas with squamous differentiation from the mucosal epithelium, thus called oral squamous cell carcinoma (OSCC), which is the sixth most common cancer worldwide with ∼50% of the 5-year survival rate (Rivera, 2015; Manikandan et al., 2016). In 2018, 354,864 new cases of lip and oral cavity cancer were identified, and 177,384 people died from these types of cancer (Bray et al., 2018). Besides for the genetic and epigenetic mechanisms for the OSCC, environmental factors mainly including excessive alcohol intake and tobacco usage have significant roles in the multifactorial disease and carcinogenesis. In addition, human papillomavirus (HPV) associated with oropharyngeal squamous cell carcinoma and other factors (e.g., circadian clock disruption) also plays an important role in the initiation and progression of the OSCC therapy (Heck et al., 2009; Majchrzak et al., 2014; Nirvani et al., 2018; Adeola et al., 2019). Conventional therapy strategies for oral cancer mainly include surgery, chemotherapy and radiation therapy alone or in combinations, and have made important progress in oral cancer treatment, but these modalities possess innegligible issues and significant side and adverse effects. For instance, chemotherapy can cause nausea, vomiting, hair loss, infections and diarrhea in patients while radiation therapy can also bring about transient or permanent damage to healthy tissues, thus severely affecting the well-being and life quality.

Pathophysiology of oral cancer is important factor that should be intensively studied, wherein the genomic pathway plays a role in OSCC, that is, changes in the genome lead to changes in the expression of proteins, chemical mediators, and enzymes. Carcinogenesis is a process with multiple steps, which are characterized by the continuous stimulation of additional genetic defects and clonal expansion. Because oncogene was activated and tumor suppressor gene was inactivated, OSCC causes abnormal cell proliferation and death. Genetic changes mainly include gene amplification, oncogene overexpression, mutation, deletion and hypermethylation, leading to the inactivation of specific genes (e.g., p53 tumor suppressor genes).

In current therapies, anticancer drugs (e.g., 5-fluorouracil, paclitaxel, cisplatin, and docetaxel) are used alone or in combination, which have been employed in chrono-chemotherapy for oral cancer treatment (Catimel et al., 1994; Baselga et al., 2005; Bonner et al., 2006; Agüeros et al., 2009; Haddad et al., 2009). However, they are highly toxic to normal cells as intravenously administered with non-specific tissue distribution within the bodies, easily causing greater damages to healthy tissues with severely adverse reactions (Kruijtzer et al., 2002). In addition, low solubility, permeability, and poor bioavailability of these anticancer drugs in bodily fluids are also noted as limitations for oral chemotherapy. Therefore, development of new therapeutic regimen or modifications of current approaches are significantly urgent for improvement of human health and survival against the oral cancer and tissues.

To overcome the disadvantages of current treatment techniques, scientific community has turned toward nanotechnology to develop new and more effective nanotechnology-based drug carrier systems to optimize oral, buccal, and intravenous treatment routes. An innovative approach to improve the efficacy is the targeted drug delivery system that has great potentials to increase drug bioavailability and bio-distribution at the site of the primary tumor, showing promise in overcoming the complications of conventional anticancer agents and enhancing the therapeutic efficacy. Especially, naturally derived and synthetic polymers are exploited as two common candidates for delivering the chemotherapeutic agents into the tumor site, and the targeted drug delivery system is capable of releasing a bioactive molecule at a specific site to improve individual health outcomes for oral cancer. Thus, it is promising that targeted drug delivery system has the ability to reduce the severity/extent of side effects of some chemotherapeutic drugs, which can be exploited as a novel therapeutic strategy in oral, head, and neck cancer patients and beyond.

This review is aimed to summarize the current most relevant findings related to different drug delivery system for oral cancer therapy, and provide some potential of anticancer drug delivery approaches. Future perspectives and therapeutic strategies are also suggested. We believe this overview can be useful for promoting novel strategies that can be implemented in clinical management and applied pre-clinically for oral cancer therapy in the future.

NANOTECHNOLOGY-BASED CARRIERS FOR ORAL CANCER THERAPY

To address the issues of conventional chemotherapeutic agents, molecularly targeted therapies are urgently required for improving the drug efficiency and reducing the potential toxicity. Therefore, by means of the novel controlled nanodelivery systems, the drug-loaded nanoparticles with optimal size can express the smart manipulation of drug release behaviors once the microenvironment is slightly changed, which is utilized for the targeted therapy. Nanotechnology-based drug carriers have allowed for the selective methodologies for OSCC treatment (Huang et al., 2011; Calixto et al., 2014). Compared to the chemotherapeutic agents, targeted drug delivery systems are widely used for the controlled drug release with advanced advantages on improved therapeutic effect and reduced side effects, which can significantly amplify the main properties of the bioactive agent: absorption, metabolism, distribution and elimination. Various nanotechnology-based carriers based on nanoparticles, liposomes, cyclodextrins, nanolipids, and hydrogels are discussed here with their respective characteristics. In addition, biomimetic nanoparticles like vitamins, exosomes, peptides/proteins, and virus-like particles have also been utilized as potential carriers of chemotherapeutic agents for oral cancer therapy.

Nanoparticles for Oral Cancer Therapy

On account of the adjustable chemical and physical characteristics, nanoparticles show an increase in popularity on targeted drug delivery system with enhanced bioactivity and effective therapy, thus reducing its systemic toxicity for oral cancer therapy. These carriers mainly comprising of polymeric and inorganic nanoparticles can kill cancer cells by loading, stabilizing, and delivering the chemotherapeutic drugs with various loading contents and release profiles (Poonia et al., 2017).

Polymeric Nanoparticles for Oral Cancer Therapy

An ideal drug carrier should possess favorable biocompatibility, biodegradability and controlled drug release behaviors at specific sites. Naturally derived and synthetic polymers [e.g., polysaccharides, polycaprolactone (PCL), poly(lactic acid) (PLA), poly(glycolic acid) (PGA), and polyethylene glycol (PEG)] are series of suitable biomaterials for preparation of polymeric nanoparticles by many techniques like nanoprecipitation, emulsifications, and self-assembly (Panyam et al., 2002; Ravikumara et al., 2013; Du et al., 2014; Wang et al., 2015, 2016, 2018, 2019; Desai, 2018; Yang et al., 2018; Sun et al., 2019; Li et al., 2020; Zhou et al., 2020). They can be modified as chemo-preventive agents to be directly delivered into the affected sites within the oral cavity, so the malignant conversion is effectively prevented from oral epithelial dysplasia to frank carcinoma. For example, Endo et al. prepared a kind of polymeric nanoparticles to reduce the toxicity of cisplatin and improve OSCC therapy based on a PEG-poly(glutamic acid) block copolymer (Endo et al., 2013; Madhulaxmi et al., 2017). These cisplatin-loaded nanoparticles could activate the caspase-3 and caspase-7 pathways to induce apoptosis and killed the oral cancers. Compared to the oral cisplatin in solution, controlled release of cisplatin from nanoparticles could obviously decrease the nephrotoxicity and neurotoxicity both *in vitro* and *in vivo*. Zhu et al. developed an effective chemotherapeutic system for achieving co-delivery of anticancer drug sodium arsenite ($NaAsO_2$) and MTH1 inhibitor TH287 for the OSCC therapy (Li et al., 2017). By means of the self-assembly of an amphiphilic cationic hyperbranched poly(amine-ester) (HPAE), pH-sensitive HPAE nanoparticles were prepared in solutions that simultaneously encapsulated the $NaAsO_2$ and TH287. Under acidic microenvironments within the tumors, both of $NaAsO_2$ and TH287 were quickly released from nanoparticles, displaying effective inhibition of tumor proliferation by *in vitro* results (**Figure 1**).

Inorganic Nanoparticles for Oral Cancer Therapy

Inorganic nanoparticles are extensively employed due to their low toxicity, high tolerance of organic solvents and good bioavailability, and thus these inorganic nanoparticles (e.g., Au NPs, Ag NPs) have been applied in diagnostic and therapeutic fields for tumors with high efficacy, especially for their unique photo-thermal functions for oral cancer therapy (Subramani and Ahmed, 2012; Senapati et al., 2018). Sayed et al. described a design of an anti-epithelial growth factor receptor (EGFR) antibody-conjugated Au NPs for the therapeutic application of the OSCC therapy. *In vitro* experiments displayed that OSCC cells did not require high energy to produce photothermal destruction for anti-EGFR/Au conjugates, and clinical results showed that near-infrared (NIR) laser light could allow for effective delivery of anti-EGFR/Au conjugates into the malignant cells with the deep penetration, because Au NPs on the surface could be easily modified to absorb the NIR, thereby achieving the maximal therapeutic effects (El-Sayed et al., 2006). Lucky et al. prepared a kind of biocompatible up-conversion nanoparticles with encapsulation of PEGylated titanium dioxide (TiO_2), which enhanced tissue penetration using NIR and effectively targeted the EGFRs on the surface of OSCC cells to inhibit the tumor proliferation (Lucky et al., 2016; Marcazzan et al., 2018). For the inorganic nanoparticles systems, this photodynamic therapy (PDT) strategy was benefited for the oral cancer that required the deep penetration of antitumor drugs in the clinical practice.

Combinational (Polymeric-Inorganic) Nanoparticles for Oral Cancer Therapy

Combinational drug treatment is recognized as advanced therapeutic benefits for the targeted drug delivery system that allows for the reduced toxicity and improved therapeutic efficacy. Darwish et al. prepared a combinational chemo-photothermal therapy with vincristine (VCR) as phytochemical anticancer and plasmonic gold nanorods (GNRs) as photothermal reagents for the OSCC therapy (Darwish et al., 2020). Based on the self-assembly of amphiphilic poly (DL-lactide-co-glycolide) (PLGA)-PEG polymers, VCR was physically encapsulated into the polymeric corona through the chem-covalently assembly around silica coated gold nanorods (GNRs). The breakage of amide linkages impelled the sustainable VCR release under acidic intracellular environments, revealing the prepared combinational therapeutic nanoprobes were identified as promising candidates for potentially clinical translation (**Figure 2**).

Liposomes for Oral Cancer Therapy

Liposomes are a series of single- or multi-layer microscopic particles with the main component of a membrane-like lipid, phospholipids and cholesterol (Mezei and Gulasekharam, 1980; Ribeiro de Souza et al., 2012). Liposomes, as the non-toxic for the normal tissues or cells, are the most widely used drug delivery system to increase its accumulation at target sites, which have gained significant attention for the administration of drug release and utilization of drug delivery with highly efficient therapy (Lian and Ho, 2001). For example, Figueiró Longo et al. prepared a kind of liposomes that could tailor the release of aluminum phthalocyanine chloride using Swiss mice by the photodynamic therapy, exhibiting the effective treatment for the oral cancer (Figueiró Longo et al., 2012). Tedesco et al. proposed a kind of mixed lipid vesicles (LVs) based on the various ratios of 1,2-distearoyl-sn-glycero-3-phosphocholine and 1,2-dioleoyl-sn-glycero-3-phosphocholine for targeted drug delivery (Calori and Tedesco, 2016). These LVs could keep stability in solutions for more than 50 days. On account of the aluminum-phosphate specific interactions, LVs bonded with the AlClPc molecules that could distribute in the cellular organelles and suffer a disaggregation process after uptake by the OSCC, which could guide us for future deep study on the intracellular mechanism of PDT for oral cancer therapy (**Figure 3**).

Cyclodextrins for Oral Cancer Therapy

Cyclodextrins (CD), a family of cyclic oligosaccharides, are derived from the enzymatic degradation of starch, which can complex hydrophobic guest molecules (e.g., anticancer drugs of docetaxel, cisplatin, methotrexate, and paclitaxel) via the host-gust inclusion interactions (Rajewski and Stella, 1996). The interior lipophilic cavity prevents the hydrophobic molecules while the exterior polar surface contributes to the solubilising effects in aqueous solutions. Thus, these cyclodextrins and their derivatives are widely utilized as versatile multifunctional excipients with highly therapeutic efficiency and pharmacological activity for the targeted drug delivery system (Szente and Szejtli, 1999; Vyas and Saraf, 2008). Wang et al. reported a kind of soluble supramolecular complexes via the phospholipid compound technology and a hydroxypropyl-beta-cyclodextrin (HP-β-CD) inclusion technique, which obviously improved the solubility and oral bioavailability of two curcuminoids (**Figure 4**; Wang H. et al., 2020). The preparation of these supramolecular complexes was simple and the gastrointestinal absorption capacity was enhanced, expressing great potentials in the oral delivery for cargoes.

Nanolipids for Oral Cancer Therapy

Although nanoparticles are significantly applied for oral cancer, their potential cytotoxicity and low internalization into the tumor cells limit the therapeutic efficiency (Hoshyar et al.,

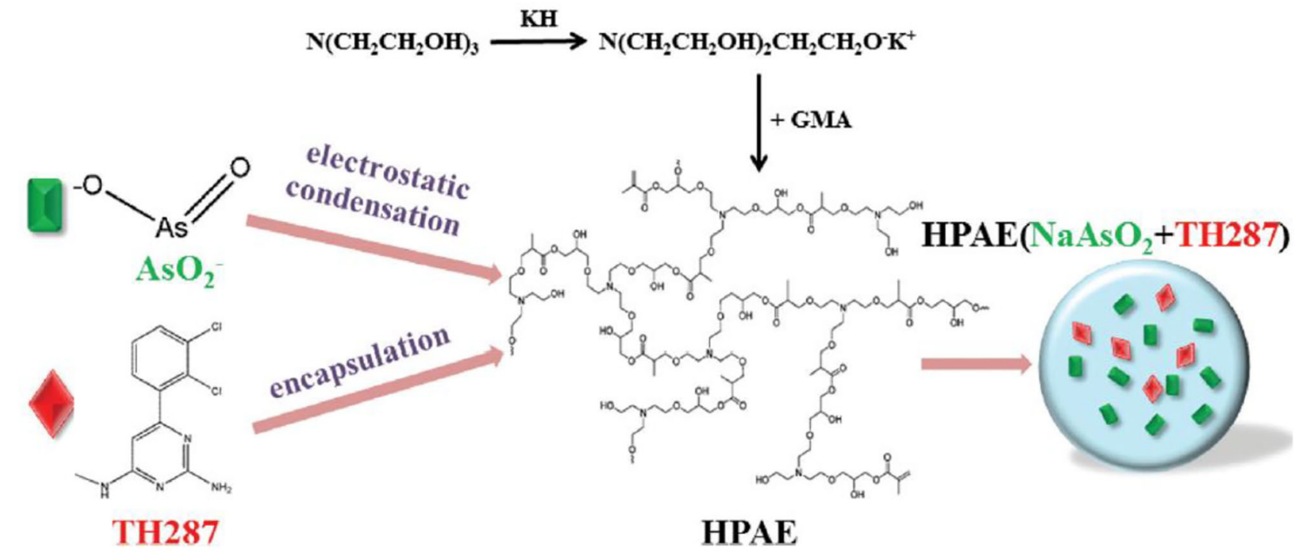

FIGURE 1 | Schematic fabrication of ($NaAsO_2$+TH287)-loaded HPAE nanoparticles. Reproduced from Li et al. (2017) with permission from Copyright 2017 Royal Society of Chemistry.

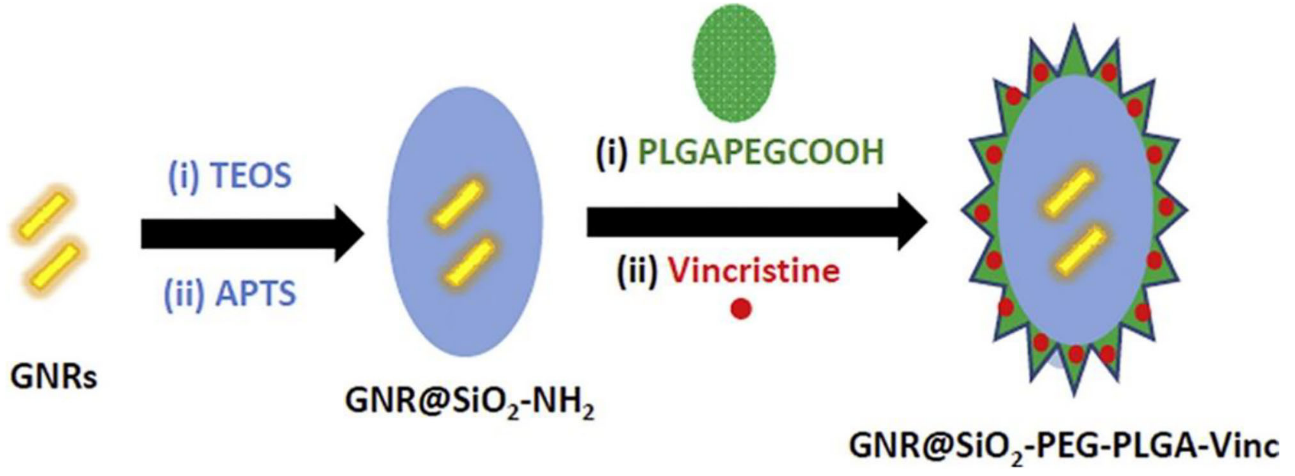

FIGURE 2 | Schematic combination (chemo-photothermal) therapeutic model for oral squamous carcinoma. Reproduced from Darwish et al. (2020) with permission from Copyright 2020 Elsevier.

2016). Nanolipid-based carriers are well-fabricated and widely applied to overcome this limitation for oral cancer therapy. These nanostructured lipid carriers consisting of solid and liquid lipids within a core matrix can distort their crystalline structures, provide the sufficient space and accommodate the local chemopreventive drugs in the amorphous clusters (Beloqui et al., 2016). Based on these advantages, nanolipids can improve the bioavailability, solubility and stability of drug carriers for therapeutic OSCC applications (Liu et al., 2011; Zhang et al., 2011; Iida et al., 2013; Zlotogorski et al., 2013).

Hydrogels for Oral Cancer Therapy

Hydrogels have a three-dimensional (3D) porous and interconnected structures that not only provide a biocompatible microenvironment for cell attachment and proliferation but also possess many unique advantages on the targeted drug delivery systems (Maitra and Kumar Shukla, 2014; Cao et al., 2018; Ketabat et al., 2018; Bao et al., 2019; Wang X. et al., 2020; Xu et al., 2020; Yan et al., 2020). Compared to the nanoparticle-based carriers, hydrogels provide sustained or triggered administration of both hydrophilic and hydrophobic agents and other biomolecules. In addition, hydrogel carriers allow for the

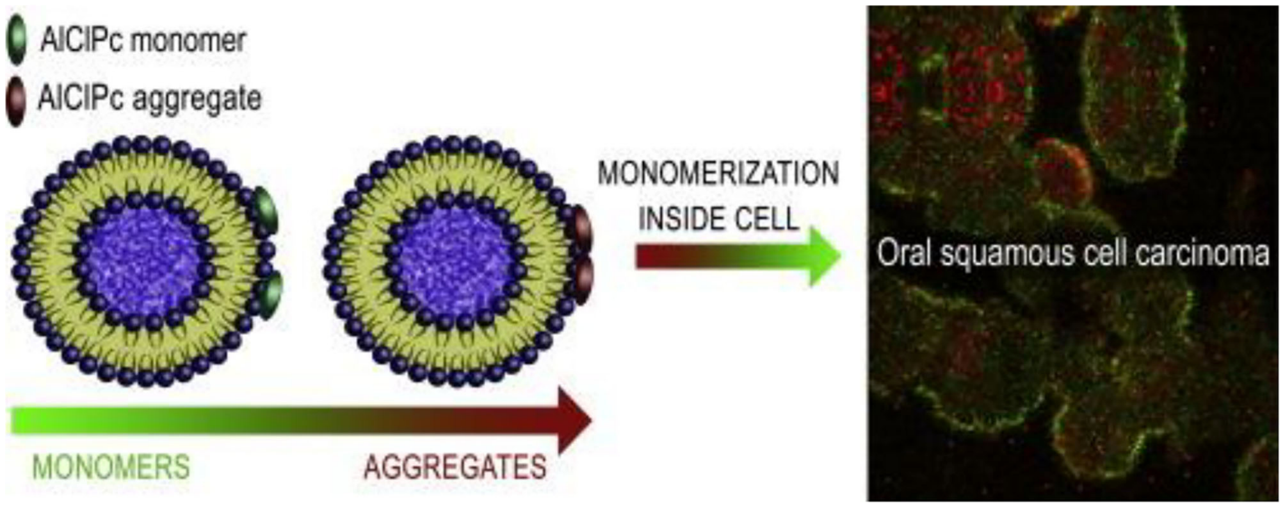

FIGURE 3 | Schematic image of lipid vesicles loading aluminum phthalocyanine chloride. Reproduced from Calori and Tedesco (2016) with permission from Copyright 2016 Elsevier.

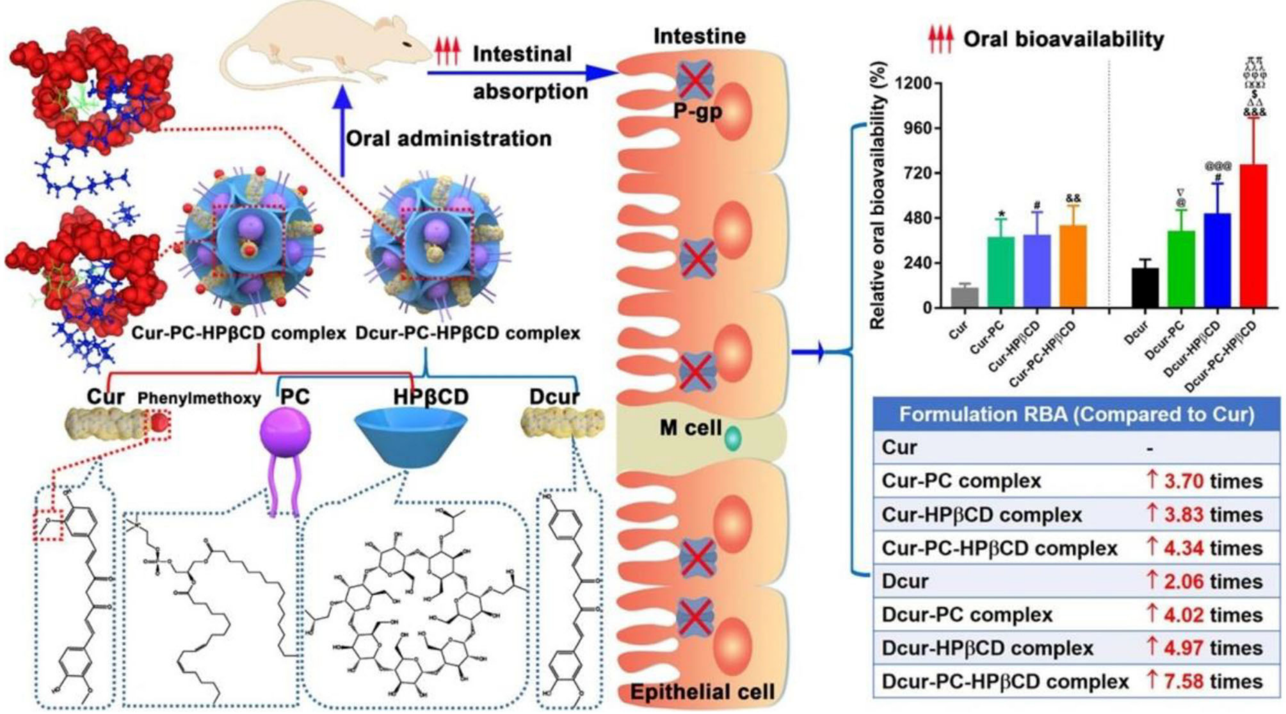

Formulation RBA (Compared to Cur)	
Cur	-
Cur-PC complex	↑ 3.70 times
Cur-HPβCD complex	↑ 3.83 times
Cur-PC-HPβCD complex	↑ 4.34 times
Dcur	↑ 2.06 times
Dcur-PC complex	↑ 4.02 times
Dcur-HPβCD complex	↑ 4.97 times
Dcur-PC-HPβCD complex	↑ 7.58 times

FIGURE 4 | Schematic image of HP-β-CD supramolecular complexes for oral delivery of curcuminoids. Reproduced from Wang H. et al. (2020) with permission from Copyright 2020 Elsevier.

co-administration of multiple drugs for achieving the synergistic anti-cancer effects with high drug loading content and low drug resistance (Li and Mooney, 2016; Ketabat et al., 2017; Sepantafar et al., 2017; Liu B. C. et al., 2020; Liu H. Y. et al., 2020; Tang et al., 2020; Yang et al., 2021). Another unique advantage is localized application for the targeted drug delivery systems, by which various hydrogel formulations can directly be implanted into the injury lesion location that can avoid the intravenous injection of small nanoparticles in the blood circulation. In this case, hydrogel carriers can tailor the drug release periods for a long time (several months) by controlling the hydrogel architectures, network pores, and gelation mechanisms (physical

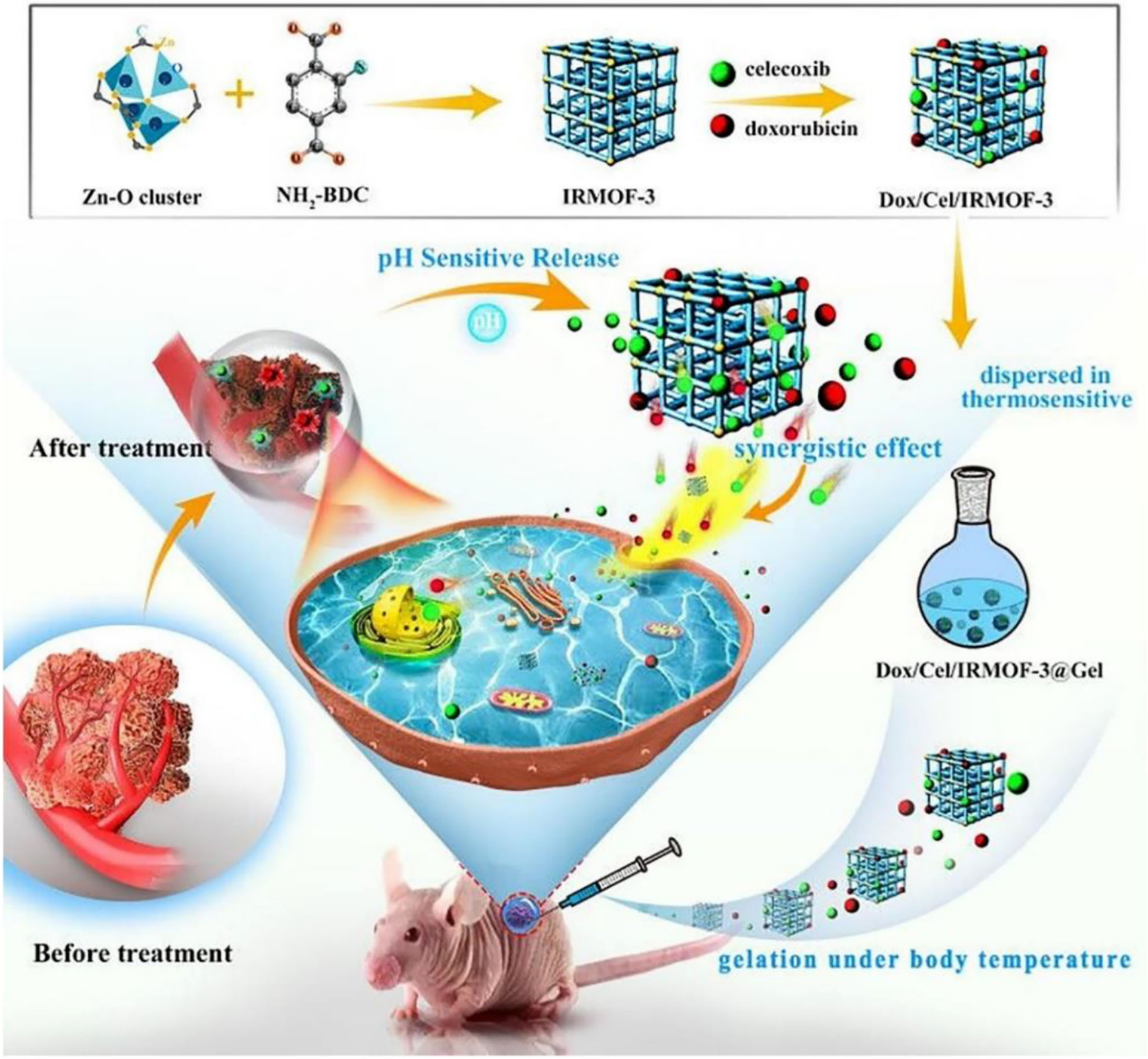

FIGURE 5 | Schematic illustration of DOX/Cel/MOFs@Gel as a novel injectable hydrogel for local dual drug delivery. Reproduced from Tan et al. (2020) with permission from Copyright 2020 Elsevier.

and chemical gelation) (Koutsopoulos and Zhang, 2012). For example, Tan et al. prepared an injectable thermosensitive hydrogel consisting of metal-organic frameworks (MOFs), doxorubicin (DOX) and celecoxib for oral cancer therapy (Tan et al., 2020). The loaded celecoxib possessed antiangiogenetic property that could improve the oral cancer therapy with the synergistic effect of DOX. In this system, DOX/Cel/MOFs@Gel exhibited high drug-loading capacity, pH-responsive release profile, and excellent tumor inhibition behavior by the *in vitro* and *in vivo* results (**Figure 5**). These injectable hydrogels had low toxicity and no apparent injury to the other tissues, possessing great potentials for fabrication of injectable implant platform for local oral cancer therapy.

BIOMIMETIC NANOPARTICLES FOR ORAL CANCER THERAPY

Although natural or synthetic materials have been applied as targeted drug carriers for the therapeutics, their low drug payloads, oral bioavailability, and delivery efficiency are still highly challenging that should be issued. Conclusively,

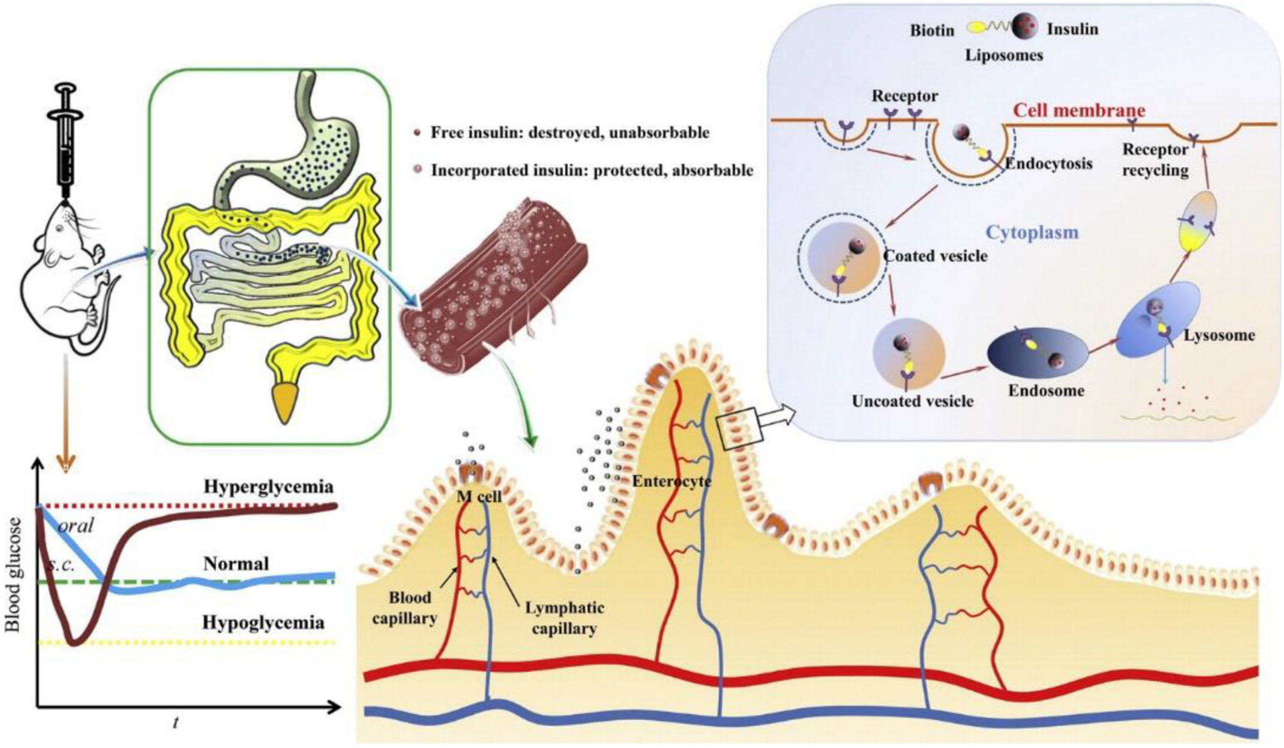

FIGURE 6 | Schematic images of the biotinylated liposomes with hypoglycemic effect and enhanced oral bioavailability of insulin for the oral delivery. Reproduced from Zhang et al. (2014) with permission from Copyright 2014 Elsevier.

biomimetic strategies are here investigated to illustrate the structure-property of biomimetic carriers to improve the bioavailability and targeting capability of therapeutic drugs.

Vitamin-Coated Nanoparticles for Oral Cancer Therapy

Vitamin B12 (VB12), due to the absorption pathway by receptor-mediated endocytosis, can form a complex with an intrinsic factor in the stomach, which are easily modified into the nanoparticles to improve the oral delivery efficiency. For example, Chalasani et al. found that compared with the pure nanoparticles, covalent conjugation of VB12 to insulin-loaded dextran caused a higher pharmacological availability using streptozotocin-induced diabetic animals. Similarly, VB12-modified nanoparticles based on trimethyl-chitosan or calcium phosphate improved the oral absorption of insulin (Chalasani et al., 2007a,b; Verma et al., 2016). In addition, Vitamin B7 is a non-endogenous vitamin and absorbed by Na^+-dependent and carrier-mediated endocytic mechanisms.

Wu et al. prepared a targeting biotinylated liposome for the oral insulin delivery, which effectively improved the drug bioavailability through the favorable cellular uptake and rapid gastrointestinal transport (Zhang et al., 2014). Vitamin B9, i.e., folic acid (FA), possessed unique abilities of high affinity and specificity to the folate receptor to increase the cellular uptake contents (**Figure 6**). By means of caveolinmediated endocytosis and modification with amphiphilic copolymers, an oral targeted delivery nanovehicle was fabricated and applied for the cancer therapy (Zheng et al., 2009; Liu et al., 2013).

Exosomes for Oral Cancer Therapy

Exosomes secreted by various cells (e.g., dendritic cells, macrophages, mesenchymal stem cells, endothelial, and epithelial cells) possess variously nanosized dimensions and natural formation, and therefore they have attracted great attentions by many researchers for the biological applications in recent years. Importantly, exosomes can deliver various biomolecules or chemotherapeutic agents for the intercellular exchange because of their effective adhesion abilities onto the cell membrane, suggestive of their potential roles as a novel vehicle for targeted drug delivery applications (Batrakova and Kim, 2015; Jiang and Gao, 2017; Zhao et al., 2020). For example, Tomita et al. demonstrated the a THP-1 and primary human macrophages (PHM)-derived exosomes to investigate the effects and sensitivity of macrophage secreted exosomes using 5 fluorouracil (5 FU) and cis diamminedichloroplatinum (CDDP) on the OSCC therapy (Tomita et al., 2020). The results found that these macrophage-derived exosomes decreased the proliferative inhibitory effects of 5 FU and CDDP and apoptosis in OSCC cells through activation of AKT/GSK-3β signaling pathway, playing important roles in reducing the sensitivity to chemotherapeutic agents in OSCC cells and improving the chemosensitivity of the tumor microenvironment in oral cancer. However, the exosomes also possess several limitations for the truly clinical applications, such as the effective separation and rigorous process for the purity, low loading capacity for the drug delivery and potential adverse immune for the biosafety (Ha et al., 2016), which should be addressed for the oral cancer therapy.

Peptides/Proteins for Oral Cancer Therapy

Synthetic peptides are also issued for the oral targeted delivery. Typically, CSKSSDYQC (CSK) peptide was employed to improve the hypoglycemic effect because of its goblet cell-targeting capacity (Sang et al., 2008). The studies found that CSK peptide-decorated chitosan NPs could effectively increase the oral bioavailability of other peptides and small agents by targeting intestinal goblet cells and promoting intestinal cellular uptake for oral delivery (Chen et al., 2018). Du et al. reported transferrin receptor specific nanocarriers conjugated with functional peptide, which increased intracellular uptake, alter intracellular trafficking, and enhance transcytosis in polarized cells for targeted oral drug delivery (Du et al., 2013).

Virus-Like Particles (VLPs) for Oral Cancer Therapy

VLPs are generally obtained by the self-assembly of viral capsids or viral-derived envelope proteins. On account of the surface biophysical and chemical properties, VLPs are easily regulated by altering VLP proteins through genetic and chemical engineering to provide their multifunction (Yang et al., 2019). Although VLPs are fully addressed to be effective as oral antigen carriers in immunization, they remain to be confirmed whether they have superior delivery characteristics in other oral cancer treatments (Chien et al., 2018; Ren et al., 2018; Serradell et al., 2019).

FUTURE OUTLOOK AND CONCLUSION

Considerable issues and advances have been developed with various nanotechnological strategies for oral cancer therapy. Based on these targeted drug delivery systems with tailored structures and various physicochemical properties, these carriers can load anticancer cargoes to target the malignant cells with high efficiency and less damage to the healthy cells, presenting a site-specific delivery behavior. Various forms of drug delivery have been deeply studied in this review as treatment options for the oral cancer, including polymeric/inorganic nanoparticles, liposomes, cyclodextrins, nanolipids, hydrogels, and several biomimetic forms. Taking advantages of their delicate regulations of structure-property relationship, most of these carriers expressed great potential alternative to overcome the limitations associated with oral drugs and conventional formulations. Nevertheless, for the currently targeted drug delivery systems, few clinic investigations were intensively performed thus far, which disclosed that improvement of clinical efficiency, well-control of drug release and reduction of side effects are highly challenging.

One of the main hindrances is the relatively complicated structures for most of drug carrier for the commercializations, causing severe problems like time-consuming and costly production. Even though, high-loading drug doses and ideal drug release profiles from these systems for the oral cancer therapy are still a major goal due to varied cellular mechanisms in OSCC scenario. In addition, other nanotechnologies on treatment of oral cancer should be introduced, such as ultrasounds, PTD, or PTT. For example, ultrasound-guided drug delivery has been a promising system to treat tumors since the ultrasound technology is simple, non-invasive, readily available, and spatial tailor of cargoes to the targeted sites with the high precision, which can be fabricated to respond to the thermal, mechanical effects of ultrasound or a combination of both.

Another important issue that needs to be solved in all cancer types, including oral cancer, is related to the clinic trials. Currently, most investigations are still focused on *in vitro* or *in vivo* studies. It is urgent to remind both clinicians and scientists to develop a full awareness of all the relative factors involved in the innovative strategy and guide appropriate clinical trials design, and further studies are needed to turn the concepts of nanotechnology toward practical applications in a multidisciplinary environment for oral cancer therapy. For instance, an advent of personalized medicine will lead to the advanced therapeutic outcomes, lower costs and high survival rates that benefit for both oncologists and patients in the near future.

AUTHOR CONTRIBUTIONS

YY and HJ initiated the project. MZ, JL, HL, and DL searched the data base, wrote, and finalized the manuscript. YY and DL made important suggestions and helped revising the paper. All authors reviewed and commented on the entire manuscript.

FUNDING

This work was supported by the National Natural Science Foundation of China (81972081), the Beijing Novel Program (Z181100006218059), Military Medical Science and Technology Youth Cultivation Project (20QNPY109), and Military Medical Youth Growth Program of PLA General Hospital (QNC19028).

REFERENCES

Adeola, H. A., Papagerakis, P., and Papagerakis, S. (2019). System biology approaches and precision oral health: a circadian clock perspective. *Front. Physiol.* 10:399. doi: 10.3389/fphys.2019.00399

Agüeros, M., Ruiz-Gatón, L., Vauthier, C., Bouchemal, K., Espuelas, S., Irache, J. M., et al. (2009). Combined hydroxypropylbeta-cyclodextrin and poly(anhydride) nanoparticles improve the oral permeability of paclitaxel. *Eur. J. Pharm. Sci.* 38, 405–413. doi: 10.1016/j.ejps.2009.09.010

Bao, W. R., Lyu, J. R., Li, C. L., Zhang, J. F., Sun, T. N., Wang, X., et al. (2019). Fabrication of customized nanogel carriers from a UV-triggered dynamic self-assembly strategy. *Front. Chem.* 7:769. doi: 10.3389/fchem.2019.00769

Baselga, J., Trigo, J. M., Bourhis, J., Tortochaux, J., Cortés-Funes, H., Hitt, R., et al. (2005). Phase II multicenter study of the antiepidermal growth factor receptor monoclonal antibody cetuximab in combination with platinum-based chemotherapy in patients with platinum-refractory metastatic and/or recurrent squamous cell carcinoma of the head and neck. *J. Clin. Oncol.* 23, 568–5577. doi: 10.1200/JCO.2005.07.119

Batrakova, E. V., and Kim, M. S. (2015). Using exosomes, naturally-equipped nanocarriers, for drug delivery. *J. Control. Release* 219, 396–405. doi: 10.1016/j.jconrel.2015.07.030

Beloqui, A., Solinís, M. Á., Rodríguez-Gascón, A., Almeida, A. J., and Préat, V. (2016). Nanostructured lipid carriers: promising drug delivery systems for future clinics. *Nanomed. Nanotechnol. Biol. Med.* 12, 143–161. doi: 10.1016/j.nano.2015.09.004

Bonner, J. A., Harari, P. M., Giralt, J., Azarnia, N., Shin, D. M., Cohen, R. B., et al. (2006). Radiotherapy plus cetuximab for squamous-cell carcinoma of the head and neck. *N. Engl. J. Med.* 354, 567–578. doi: 10.1056/NEJMoa053422

Bray, F., Ferlay, J., Soerjomataram, I., Siegel, R. L., Torre, L. A., and Jemal, A. (2018). Global cancer statistics 2018: GLOBOCAN estimates of incidence and mortality worldwide for 36 cancers in 185 countries. *CA Cancer J. Clin.* 68, 394–424. doi: 10.3322/caac.21492

Calixto, G., Bernegossi, J., Fonseca-Santos, B., and Chorilli, M. (2014). Nanotechnology-based drug delivery systems for treatment of oral cancer: a review. *Int. J. Nanomed.* 9, 3719–3735. doi: 10.2147/IJN.S61670

Calori, I. R., and Tedesco, A. C. (2016). Lipid vesicles loading aluminum phthalocyanine chloride: formulation properties and disaggregation upon intracellular delivery. *J. Photochem. Photobiol. B-Biol.* 160, 240–247. doi: 10.1016/j.jphotobiol.2016.03.050

Cao, C. Q., Wang, X., and Wu, D. C. (2018). Controlled cross-linking strategy for formation of hydrogels, microgels and nanogels. *Chinese J. Polym. Sci.* 36, 8–17. doi: 10.1007/s10118-018-2061-7

Catimel, G., Verweij, J., Mattijssen, V., Hanauske, A., Piccart, M., Wanders, J., et al. (1994). Docetaxel (Taxotere): an active drug for the treatment of patients with advanced squamous cell carcinoma of the head and neck. *EORTC early clinical trials group. Ann Oncol.* 5, 533–537. doi: 10.1093/oxfordjournals.annonc.a058908

Chalasani, K. B., Russell-Jones, G. J., Jain, A. K., Diwan, P. V., and Jain, S. K. (2007b). Effective oral delivery of insulin in animal models using vitamin B12-coated dextran nanoparticles. *J. Control. Release* 122, 141–150 doi: 10.1016/j.jconrel.2007.05.019

Chalasani, K. B., Russell-Jones, G. J., Yandrapu, S. K., Diwan, P. V., and Jain, S. K. (2007a). A novel vitamin B12-nanosphere conjugate carrier system for peroral delivery of insulin. *J. Controlled Release* 117, 421–429. doi: 10.1016/j.jconrel.2006.12.003

Chen, G., Svirskis, D., Lu, W., Ying, M., Huang, Y., and Wen, J. (2018). N-trimethyl chitosan nanoparticles and CSKSSDYQC peptide: N-trimethyl chitosan conjugates enhance the oral bioavailability of gemcitabine to treat breast cancer. *J. Control. Release* 277, 142–153. doi: 10.1016/j.jconrel.2018.03.013

Chien, M. H., Wu, S. Y., and Lin, C. H. (2018). Oral immunization with cell-free self-assembly virus-like particles against orange-spotted grouper nervous necrosis virus in grouper larvae, Epinephelus coioides. *Vet. Immunol. Immunopathol.* 197, 69–75. doi: 10.1016/j.vetimm.2018.01.012

Darwish, W. M., Abdoon, A. S., Shata, M. S., and Elmansy, M. (2020). Vincristine-loaded polymeric corona around gold nanorods for combination (chemo-photothermal) therapy of oral squamous carcinoma. *Reactive Funct. Polymers*. 151:104575. doi: 10.1016/j.reactfunctpolym.2020.104575

Desai, K. G. H. (2018). Polymeric drug delivery systems for intraoral site-specific chemoprevention of oral cancer. *J. Biomed. Mater. Res. Part B Appl. Biomater*. 106, 1383–1413. doi: 10.1002/jbm.b.33943

Du, F., Meng, H., Xu, K., et al. (2014). CPT loaded nanoparticles based on betacyclodextrin-grafted poly(ethylene glycol)/poly(L-glutamic acid) diblock copolymer and their inclusion complexes with CPT. *Colloids Surf. B Biointerfaces* 113, 230–236. doi: 10.1016/j.colsurfb.2013.09.015

Du, W., Fan, Y., Zheng, N., He, B., Yuan, L., Zhang, H., et al. (2013). Transferrin receptor specific nanocarriers conjugated with functional 7peptide for oral drug delivery. *Biomaterials* 34, 794–806. doi: 10.1016/j.biomaterials.2012.10.003

El-Sayed, I. H., Huang, X., and El-Sayed, M. A. (2006). Selective laser photo-thermal therapy of epithelial carcinoma using anti-EGFR antibody conjugated gold nanoparticles. *Cancer Lett.* 239, 129–135. doi: 10.1016/j.canlet.2005.07.035

Endo, K., Ueno, T., Kondo, S., Wakisaka, N., Murono, S., Ito, M., et al. (2013). Tumor-targeted chemotherapy with the nanopolymer-based drug NC-6004 for oral squamous cell carcinoma. *Cancer Sci*. 104, 369–374. doi: 10.1111/cas.12079

Figueiró Longo, J. P., Muehlmann, L. A., Velloso, N. V., Simioni, A. R., Lozzi, S. P., de Oliveira Cavalcanti, C. E., et al. (2012). Effects of photodynamic therapy mediated by liposomal aluminum-phthalocyanine chloride on chemically induced tongue tumors. *Chemotherapy* 1:103. doi: 10.4172/2167-7700.1000103

Ha, D., Yang, N., and Nadithe, V. (2016). Exosomes as therapeutic drug carriers and delivery vehicles across biological membranes: current perspectives and future challenges. *Acta Pharm. Sin. B.* 6, 287–296. doi: 10.1016/j.apsb.2016.02.001

Haddad, R., Sonis, S., Posner, M., Wirth, L., Costello, R., Braschayko, P., et al. (2009). Randomized phase 2 study of concomitant chemoradiotherapy using weekly carboplatin/paclitaxel with or without daily subcutaneous amifostine in patients with locally advanced head and neck cancer. *Cancer* 115, 4514–4523. doi: 10.1002/cncr.24525

Heck, J. E., Berthiller, J., Vaccarella, S., Winn, D. M., Smith, E. M., Shan'gina, O., et al. (2009). Sexual behaviours and the risk of head and neck cancers: a pooled analysis in the International Head and Neck Cancer Epidemiology (INHANCE) consortium. *Int. J. Epidemiol*. 39, 166–181. doi: 10.1093/ije/dyp350

Hoshyar, N., Gray, S., Han, H., and Bao, G. (2016). The effect of nanoparticle size on in vivo pharmacokinetics and cellular interaction. *Nanomedicine* 11, 673–692. doi: 10.2217/nnm.16.5

Huang, H., Barua, S., Sharma, G., Dey, S. K., and Rege, K. (2011). Inorganic nanoparticles for cancer imaging and therapy. *J. Control. Release*. 155, 344–357. doi: 10.1016/j.jconrel.2011.06.004

Iida, S., Shimada, J., and Sakagami, H. (2013). Cytotoxicity induced by docetaxel in human oral squamous cell carcinoma cell lines. *In Vivo* 27, 321–332.

Jiang, X. C., and Gao, J. Q. (2017). Exosomes as novel bio-carriers for gene and drug delivery. *Int. J. Pharm*. 521, 167–175. doi: 10.1016/j.ijpharm.2017.02.038

Ketabat, F., Karkhaneh, A., Mehdinavaz Aghdam, R., and Hossein Ahmadi Tafti, S. (2017). Injectable conductive collagen/alginate/polypyrrole hydrogels as a biocompatible system for biomedical applications. *J. Biomater. Sci. Polym. Ed*. 28, 794–805. doi: 10.1080/09205063.2017.1302314

Ketabat, F., Khorshidi, S., and Karkhaneh, A. (2018). Application of minimally invasive injectable conductive hydrogels as stimulating scaffolds for myocardial tissue engineering. *Polym. Int*. 67, 975–982. doi: 10.1002/pi.5599

Koutsopoulos, S., and Zhang, S. (2012). Two-layered injectable self-assembling peptide scaffold hydrogels for long-term sustained release of human antibodies. *J. Control. Release* 160, 451–458. doi: 10.1016/j.jconrel.2012.03.014

Kruijtzer, C. M., Beijnen, J. H., and Schellens, J. H. (2002). Improvement of oral drug treatment by temporary inhibition of drug transporters and/or cytochrome P450 in the gastrointestinal tract and liver: an overview. *Oncologist* 7, 516–530. doi: 10.1634/theoncologist.7-6-516

Li, D. W., Zhou, J., Zhang, M. M., Ma, Y. Z., Yang, Y. Y., Han, X., et al. (2020). Long-term delivery of alendronate through injectable tetra-peg hydrogel to promote osteoporosis therapy. *Biomater. Sci.* 8, 3138–3146. doi: 10.1039/D0BM00376J

Li, J., and Mooney, D. J. (2016). Designing hydrogels for controlled drug delivery. *Nat. Rev. Mater*. 1:16071. doi: 10.1038/natrevmats.2016.71

Li, X., Li, L., Huang, Y., Liu, B., Chi, H. R., Shi, L. L., et al. (2017). Synergistic therapy of chemotherapeutic drugs and MTH1 inhibitors using a pH-sensitive polymeric delivery system for oral squamous cell carcinoma. *Biomater. Sci.* 5, 2068–2078. doi: 10.1039/C7BM00395A

Lian, T., and Ho, R. J. (2001). Trends and developments in liposome drug delivery systems. *J. Pharm. Sci.* 90, 667–680. doi: 10.1002/jps.1023

Liu, B. C., Zhao, Y. R., Zhu, T. J., Gao, S., Ye, K. F., Zhou, F., et al. (2020). Biphasic double-network hydrogel with compartmentalized loading of bioactive glass for osteochondral defect repair. *Front. Bioeng. Biotechnol*. 8:752. doi: 10.3389/fbioe.2020.00752

Liu, D., Liu, Z., Wang, L., Zhang, C., and Zhang, N. (2011). Nanostructured lipid carriers as novel carrier for parenteral delivery of docetaxel. *Colloids Surf. B Biointerfaces* 85, 262–269. doi: 10.1016/j.colsurfb.2011.02.038

Liu, H. Y., Wang, X., Cao, Y. X., Yang, Y. Y., Yang, Y. T., Gao, Y. F., et al. (2020). Freezing-tolerant, highly sensitive strain and pressure sensors assembled from ionic conductive hydrogels with dynamic cross-links. *ACS Appl. Mater. Interfaces* 12, 25334–25344. doi: 10.1021/acsami.0c06067

Liu, X., Zhang, Y., Ma, D., Tang, H., and Yao, S. (2013). Biocompatible multi-walled carbon nanotube-chitosan–folic acid nanoparticle hybrids as GFP gene delivery materials. *Colloids Surf. B*. 111, 224–231. doi: 10.1016/j.colsurfb.2013.06.010

Lucky, S. S., Idris, N. M., Huang, K., Kim, J., Li, Z., Thong, P. S. P., et al. (2016). *In vivo* biocompatibility, biodistribution and therapeutic efficiency of titania coated upconversion nanoparticles for photodynamic therapy of solid oral cancers. *Theranostics*. 6, 1844–1865. doi: 10.7150/thno.15088

Madhulaxmi, M., Iyer, K., Periasamy, R., Gajendran, P., and Lakshmi, T. (2017). Role of cisplatin in oral squamous cell carcinoma-a review. *J Adv Pharm Educ Res*. 7, 39–42.

Maitra, J., and Kumar Shukla, V. (2014). Cross-linking in hydrogels-a review. *Am. J. Polym. Sci*. 4, 25–31. doi: 10.5923/j.ajps.20140402.01

Majchrzak, E., Szybiak, B., Wegner, A., Pienkowski, P., Pazdrowski, J., Luczewski, L., et al. (2014). Oral cavity and oropharyngeal squamous cell carcinoma in young adults: a review of the literature. *Radiol. Oncol*. 48, 1–10. doi: 10.2478/raon-2013-0057

Manikandan, M., Rao, A. K. D. M., Arunkumar, G., Manickavasagam, M., Rajkumar, K. S., Rajaraman, R., et al. (2016). Oral squamous cell carcinoma: microRNA expression profiling and integrative analyses for elucidation of tumourigenesis mechanism. *Mol. Cancer*. 15:28. doi: 10.1186/s12943-016-0512-8

Marcazzan, S., Varoni, E. M., Blanco, E., Lodi, G., and Ferrari, M. (2018). Nanomedicine, an emerging therapeutic strategy for oral cancer therapy. *Oral Oncol*. 76, 1–7. doi: 10.1016/j.oraloncology.2017.11.014

Mezei, M., and Gulasekharam, V. (1980). Liposomes-a selective drug delivery system for the topical route of administration. *Lotion dosage form. Life Sci*. 26, 1473–1477 doi: 10.1016/0024-3205(80)90268-4

Nirvani, M., Khuu, C., Utheim, T. P., Sand, L. P., and Sehic, A. (2018). Circadian clock and oral cancer. *Mol. Clin. Oncol*. 8, 219–226. doi: 10.3892/mco.2017.1518

Panyam, J., Zhou, W. Z., Prabha, S., Sahoo, S. K., and Labhasetwar, V. (2002). Rapid endo-lysosomal escape of poly(DL-lactide-co-glycolide) nanoparticles: implications for drug and gene delivery. *FASEB J*. 16, 1217–1226 doi: 10.1096/fj.02-0088com

Poonia, M., Ramalingam, K., Goyal, S., and Sidhu, K. S. (2017). Nanotechnology in oral cancer: a comprehensive review. *J. Oral Maxillofac. Pathol*. 3, 407–414. doi: 10.4103/jomfp.JOMFP_29_17

Rajewski, R. A., and Stella, V. J. (1996). Pharmaceutical applications of cyclodextrins. 2. *In vivo* drug delivery. *J. Pharm. Sci*. 85, 1142–1168. doi: 10.1021/js960075u

Ravikumara, N. R., Tiyaboonchai, W., and Madhusudhan, B. (2013). Fabrication and characterization of genistein encapsulated poly (D, L) lactic acid nanoparticles for pharmaceutical application. *Curr. Nanosci*. 9, 293–302. doi: 10.2174/1573413711309020021

Ren, Z., Zhao, Y., Liu, J., Ji, X., Meng, L., Wang, T., et al. (2018). Inclusion of membrane-anchored LTB or flagellin protein in H5N1 virus-like particles enhances protective responses following intramuscular and oral immunization of mice. *Vaccine* 36, 5990–5998. doi: 10.1016/j.vaccine.2018.08.053

Ribeiro de Souza, A. L., Kiill, C. P., dos Santos, F. K., et al. (2012). Nanotechnologybased drug delivery systems for dermatomycosis treatment. *Curr. Nanosci*. 8:512–519. doi: 10.2174/157341312801784311

Rivera, C. (2015). Essentials of oral cancer. *Int J Clin Exp Pathol*. 8, 11884–11894. doi: 10.5281/zenodo.192487

Sang, K. K., Woo, J. H., Kim, M. K., Woo, S. S., Choi, J. H., Lee, H. G., et al. (2008). Identification of a peptide sequence that improves transport of macromolecules across the intestinal mucosal barrier targeting goblet cells. *J. Biotechnol*. 135, 210–216. doi: 10.1016/j.jbiotec.2008.01.021

Senapati, S., Mahanta, A. K., Kumar, S., and Maiti, P. (2018). Controlled drug delivery vehicles for cancer treatment and their performance. *Signal Transduct. Target. Ther*. 3:7. doi: 10.1038/s41392-017-0004-3

Sepantafar, M., Maheronnaghsh, R., Mohammadi, H., Radmanesh, F., Hasani-sadrabadi, M. M., Ebrahimi, M., et al. (2017). Engineered hydrogels in cancer therapy and diagnosis. *Trends Biotechnol*. 35, 1074–1087. doi: 10.1016/j.tibtech.2017.06.015

Serradell, M. C., Rupil, L. L., Martino, R. A., Prucca, C. G., Carranza, P. G., Saura, A., et al. (2019). Efficient oral vaccination by bioengineering virus-like particles with protozoan surface proteins. *Nat. Commun*. 10:361. doi: 10.1038/s41467-018-08265-9

Subramani, K., and Ahmed, W. (2012). *Nanoparticulate Drug Delivery Systems for Oral Cancer Treatment, 1st Edn.* Amsterdam: Elsevier Inc.

Sun, G. F., Liu, J. H., Wang, X., Li, M., Cui, X., Zhang, L. C., et al. (2019). Fabrication of dual-sensitive poly(β-hydroxyl amine) micelles for controlled drug delivery. *Eur. Polym. J*. 114:338–345. doi: 10.1016/j.eurpolymj.2019.02.048

Szente, L., and Szejtli, J. (1999). Highly soluble cyclodextrin derivatives: chemistry, properties, and trends in development. *Adv. Drug Deliv. Rev*. 36, 17–28 doi: 10.1016/S0169-409X(98)00092-1

Tan, G. Z., Zhong, Y. T., Yang, L. L., Jiang, Y. D., Liu, J. Q., and Ren, F. (2020). A multifunctional MOF-based nanohybrid as injectable implant platform for drug synergistic oral cancer therapy. *Chem. Eng. J*. 390:124446. doi: 10.1016/j.cej.2020.124446

Tang, G. K., Zhou, B. Y., Li, F., Wang, W. H., Liu, Y., Wang, X., et al. (2020). Advances of naturally-derived and synthetic hydrogels for intervertebral disc regeneration. *Front. Bioeng. Biotechnol*. 8:745. doi: 10.3389/fbioe.2020.00745

Tomita, R., Sasabe, E., Tomomura, A., and Yamamoto, T. (2020). Macrophage-derived exosomes attenuate the susceptibility of oral squamous cell carcinoma cells to chemotherapeutic drugs through the AKT/GSK-3beta pathway. *Oncol. Rep*. 44, 1905–1916 doi: 10.3892/or.2020.7748

Verma, A., Sharma, S., Gupta, P. K., Singh, A., Teja, B. V., Dwivedi, P., et al. (2016). Vitamin B12 functionalized layer by layer calcium phosphate nanoparticles: a mucoadhesive and pH responsive carrier for improved oral delivery of insulin. *Acta Biomater*. 31, 288–300. doi: 10.1016/j.actbio.2015.12.017

Vogel, D. W. T., Zbaeren, P., and Thoeny, H. C. (2010). Cancer of the oral cavity and oropharynx. *Cancer Imaging*. 10, 62–72. doi: 10.1102/1470-7330.2010.0008

Vyas, A., and Saraf, S. (2008). Cyclodextrin based novel drug delivery systems. *J. Incl. Phenom. Macrocycl. Chem*. 62, 23–42. doi: 10.1007/s10847-008-9456-y

Wang, H., Luo, J. C., Zhang, Y. H., He, D., Jiang, R., Xie, X. M., et al. (2020). Phospholipid/hydroxypropyl-beta-cyclodextrin supramolecular complexes are promising candidates for efficient oral delivery of curcuminoids. *Int. J. Pharm*. 582:119301. doi: 10.1016/j.ijpharm.2020.119301

Wang, S. J., Jiang, D., Zhang, Z. Z., Chen, Y. R., Yang, Z. D., Zhang, J. Y., et al. (2019). Biomimetic nanosilica-collagen scaffolds for in situ bone regeneration: toward a cell-free, one-step surgery. *Adv. Mater*. 31:1904341. doi: 10.1002/adma.201904341

Wang, X., Gao, P. Y., Yang, Y. Y., Guo, G. X., and Wu, D. C. (2018). Dynamic and programmable morphology and size evolution via a living hierarchical self-assembly strategy. *Nat. Commun*. 9:2772. doi: 10.1038/s41467-018-05142-3

Wang, X., Yang, Y. Y., Gao, P. Y., Yang, F., Shen, H., Guo, H. X., et al. (2015). Synthesis, self-assembly and photoresponsive behavior of tadpole-shaped azobenzene polymers. *ACS Macro Lett*. 4, 1321–1326. doi: 10.1021/acsmacrolett.5b00698

Wang, X., Yang, Y. Y., Shi, Y., and Jia, F. (2020). Editorial: smart hydrogels in tissue engineering and regenerative medicine. *Front. Chem*. 8:245. doi: 10.3389/fchem.2020.00245

Wang, X., Yang, Y. Y., Zuo, Y. F., Yang, F., Shen, H., and Wu, D. C. (2016). Facile creation of fret systems from a ph-responsive AIE fluorescent vesicle. *Chem. Commun*. 52, 5320–5323. doi: 10.1039/C6CC01706A

Xu, B. B., Ye, J., Yuan, F. Z., Zhang, J. Y., Chen, Y. R., Fan, B. S., et al. (2020). Advances of stem cell-laden hydrogels with biomimetic microenvironment for osteochondral repair. *Front. Bioeng. Biotechnol*. 8:247. doi: 10.3389/fbioe.2020.00247

Yan, X., Chen, Y. R., Song, Y. F., Ye, J., Yang, M., Xu, B. B., et al. (2020). Advances in the application of supramolecular hydrogels for stem cell delivery and cartilage tissue engineering. *Front. Bioeng. Biotechnol*. 8:847. doi: 10.3389/fbioe.2020.00847

Yang, G., Chen, S., and Zhang, J. (2019). Bioinspired and biomimetic nanotherapies for the treatment of infectious diseases. *Front. Pharmacol*. 10:751. doi: 10.3389/fphar.2019.00751

Yang, Y. Y., Wang, X., Yang, F., Wang, L. N., and Wu, D. C. (2018). Highly elastic and ultratough hybrid ionic-covalent hydrogels with tunable structures and mechanics. *Adv. Mater*. 30:1707071. doi: 10.1002/adma.201707071

Yang, Y. Y., Yang, Y. T., Cao, Y. X., Wang, X., Chen, Y. R., Liu, H. Y., et al. (2021). Anti-freezing, resilient and tough hydrogels for sensitive and large-range strain and pressure sensors. *Chem. Eng. J*. 403:126431. doi: 10.1016/j.cej.2020.126431

Zhang, T., Chen, J., Zhang, Y., Shen, Q., and Pan, W. (2011). Characterization and evaluation of nanostructured lipid carrier as a vehicle for oral delivery of etoposide. *Eur. J. Pharm. Sci*. 43, 174–179. doi: 10.1016/j.ejps.2011.04.005

Zhang, X., Qi, J., Lu, Y., He, W., Li, X., and Wu, W. (2014). Biotinylated liposomes as potential carriers for the oral delivery of insulin. *Nanomedicine* 10, 167–176. doi: 10.1016/j.nano.2013.07.011

Zhao, X. G., Zhao, Y. H., Sun, X., Xing, Y., Wang, X., and Yang, Q. (2020). The immunomodulatory property of MSCs and MSC-derived exosomes in osteoarthritis. *Front. Bioeng. Biotechnol.* 11:1912. doi: 10.3389/fbioe.2020.575057

Zheng, Y., Cai, Z., Song, X., Chen, Q., Bi, Y., Li, Y., et al. (2009). Preparation and characterization of folate conjugated N-trimethyl chitosan nanoparticles as protein carrier targeting folate receptor: *in vitro* studies. *J. Drug Target.* 17, 294–303. doi: 10.1080/10611860902737920

Zhou, Z. X., Chen, Y. R., Zhang, J. Y., Jiang, D., Yuan, F. Z., Mao, Z. M., et al. (2020). Facile strategy on hydrophilic modification of poly (ε-caprolactone) scaffolds for assisting tissue-engineered meniscus constructs *in vitro*. *Front. Pharmacol.* 11:471. doi: 10.3389/fphar.2020.00471

Zlotogorski, A., Dayan, A., Dayan, D., Chaushu, G., Salo, T., and Vered, M. (2013). Nutraceuticals as new treatment approaches for oral cancer-I: curcumin. *Oral Oncol.* 49, 187–191. doi: 10.1016/j.oraloncology.2012.09.015

Conflict of Interest: The authors declare that the research was conducted in the absence of any commercial or financial relationships that could be construed as a potential conflict of interest.

frontiers
in Bioengineering and Biotechnology

REVIEW
published: 18 December 2020
doi: 10.3389/fbioe.2020.620537

Biologically Modified Polyether Ether Ketone as Dental Implant Material

Zhangyu Ma[1†], *Xingyu Zhao*[2†], *Jing Zhao*[3], *Zhilong Zhao*[1], *Qihui Wang*[1] *and Congxiao Zhang*[1*]

[1] Department of Stomatology, The First Hospital of Jilin University, Changchun, China, [2] Department of Bone and Joint Surgery, The First Hospital of Jilin University, Changchun, China, [3] Department of Stomatology, China-Japan Friendship Hospital, Beijing, China

Polyether ether ketone (PEEK) is a non-toxic polymer with elastic modulus close to human bone. Compared with metal implants, PEEK has advantages such as evasion of stress shielding effect, easy processing, and similar color as teeth, among others. Therefore, it is an excellent substitute material for titanium dental orthopedic implants. However, PEEK's biological inertia limits its use as an implant. To change PEEK's biological inertia and increase its binding ability with bone tissue as an implant, researchers have explored a number of modification methods to enhance PEEK's biological activities such as cellular compatibility, osteogenic activity, and antibacterial activity. This review summarizes current biological activity modification methods for PEEK, including surface modification and blending modification, and analyzes the advantages and disadvantages of each modification method. We believe that modified PEEK will be a promising dental and orthopedic implant material.

Keywords: Polyether ether ketone, surface modification, blending modification, biological activity, dental orthopedic implants

OPEN ACCESS

Edited by:
Junchao Wei,
Nanchang University, China

Reviewed by:
Youmei Bao,
Yale University, United States
Kun Zhou,
Boston Children's Hospital,
United States

****Correspondence:***
Congxiao Zhang
zhangcongxiao@jlu.edu.cn

† These authors have contributed equally to this work

Specialty section:
This article was submitted to Biomaterials,
a section of the journal
Frontiers in Bioengineering and Biotechnology

Received: *23 October 2020*
Accepted: *16 November 2020*
Published: *18 December 2020*

Citation:
Ma Z, Zhao X, Zhao J, Zhao Z, Wang Q and Zhang C (2020) Biologically Modified Polyether Ether Ketone as Dental Implant Material. Front. Bioeng. Biotechnol. 8:620537. doi: 10.3389/fbioe.2020.620537

INTRODUCTION

Polyether ether ketone (PEEK) is a member of the polyaryletherketone family, which has an aromatic backbone combining the ketone and ether functional groups between the aryl rings. It is a high-performance engineering plastic with many excellent properties (Williams, 2008) such as chemical stability, excellent heat resistance and machinability, frictional resistance, good biocompatibility, elastic modulus close to human bone, and good X-ray penetration (Toth et al., 2006; Kurtz and Devine, 2007; Zhao et al., 2013; Wang et al., 2014; Abdullah et al., 2015; **Figure 1**). Owing to PEEK's excellent mechanical properties, minimal immunotoxicity, and overall good processing performance (Toth et al., 2006; Kurtz and Devine, 2007; Zhao et al., 2013; Wang et al., 2014; Abdullah et al., 2015), it has become an alternative to metal implants and the preferred material for plastic and trauma surgery since the late 1990s (Kurtz and Devine, 2007). PEEK can overcome some of the limitations of metal implants such as stress shielding and metal allergy. PEEK is currently used as an orthopedic implant in clinical practice and has achieved good results (Song et al., 2010, 2011).

In recent years, based on several extensive PEEK research studies, its excellent performance has also attracted the attention of researchers in the field of stomatology. PEEK has similar mechanical properties to the hard tissue of the tooth and bone and its color is similar to that of the tooth, reflecting its great potential as a material for fixed prosthodontics (Ouyang et al., 2016). At present, there have been some research studies on PEEK as the restoration material for fixed-definition dental bridge brackets, implant abutments, and implants (Santing et al., 2012; Tannous et al., 2012;

Najeeb et al., 2016). However, when used as an implant, PEEK has insufficient biological activity and cannot form good osseointegration with the surrounding bone tissue. These defects severely limit the practical clinical application of PEEK. Therefore, in recent years, various modification methods that can enhance PEEK's biological activities such as cell compatibility, osteogenic activity, and antibacterial ability have become research hotspots. This paper reviews the biological modification methods of PEEK. The classification of PEEK modification is shown in **Figure 2**, which is mainly divided into surface modification and blending modification. Surface modification includes physical modification, chemical modification, and composite modification, which are a series of modification methods to improve PEEK's biological activity by changing its surface morphology and active ingredients. Blending modification includes various modification methods to improve PEEK biological activity by mixing PEEK with hydroxyapatite (HA), carbonfiber (CF), zinc oxide (ZnO), and other bioactive substances to prepare composite materials. These modification methods will be reviewed in this paper.

SURFACE MODIFICATION

As bone implant materials, the cytocompatibility on the surface of the materials is very important. The implant materials with good cytocompatibility can form good bone binding with the surrounding tissues after being implanted into the human body. The physical and chemical structure of the surface of bioactive materials can significantly affect the cytocompatibility of the surface. Generally, bioactive materials with rougher surface structure and better hydrophilicity are more conducive to the adhesion and proliferation of cells on the surface of the material, so that the material can form good bone binding with surrounding tissues. Surface modification methods are aimed at constructing biologically active structures or introducing biologically active substances on the PEEK surface by various means to increase the roughness and hydrophilicity of the material surface. These methods only act on PEEK surface without changing PEEK's mechanical properties. According to the properties of modification methods, surface modification methods can be divided into three types: physical surface modification, chemical surface modification, and composite surface modification.

Physical Surface Modification

This is a relatively simple method. Common physical modification methods include plasma treatment, neutral atomic beam technology, acid corrosion, and various surface coatings. These methods improve the biological activity of PEEK by constructing cell-based structures on the surface or by coating the surface with active substances.

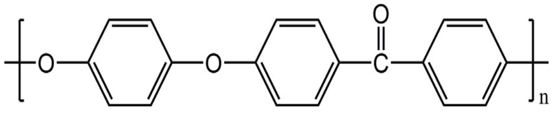

FIGURE 1 | PEEK's molecular structure.

Plasma Treatment

Plasma treatment refers to the use of N_2, NH_3, O_2, Ar, H_2, and other gas plasma treatment PEEK surface. This method improves the surface hydrophilicity, biological activity, and biocompatibility of PEEK by changing its surface morphology or forming functional groups with biological activity on PEEK surface. Novotna et al. (2015) modified PEEK surface by argon plasma and prepared samples with argon plasma processing time of 120, 240, and 480 s. After modification, the author systematically studied the changes of PEEK surface morphology before and after modification. The results showed that the roughness of the modified samples increased significantly, and as shown in **Table 1**, the hydrophilicity and oxygen content of the modified samples were significantly enhanced, while the rough surface, good hydrophilicity, and oxygen-containing active groups could promote the adhesion and growth of cells. The authors then introduced mouse fibroblasts and human osteoblasts on different sample surfaces to observe the growth of these two kinds of cells before and after modification. *In vitro* cell experiments showed that plasma treatment could significantly enhance cell adhesion, proliferation, and metabolic activities of the two cell lines. These results showed that the biological activity of PEEK surface was significantly improved by argon plasma treatment. The modified PEEK surface was more conducive to cell adhesion and proliferation as well as osteogenic differentiation, so it is easier to form a good bone binding with the surrounding tissues as an implant.

In the study by Waser-Althaus et al. (2014), PEEK surface was treated with oxygen and ammonia plasma with a power of 10, 50, 100, and 200 W for 5 min; further, carboxylic acid, ester, and amine functional groups were introduced to increase the hydrophilicity of the material and change the surface morphology. Compared with pure PEEK, both plasma treatments could change PEEK surface morphology and increase PEEK hydrophilicity and protein adsorption capacity, but oxygen plasma treatment was significantly more effective than ammonia plasma treatment under the same conditions. These results show that the modification ability of different plasmas is different, and the surface structure of the sample can affect the hydrophilicity of the sample surface and the protein adsorption ability. The authors inoculated adipose tissue-derived mesenchymal stem cells (adMSCs) onto PEEK samples and conducted a series of cell experiments to evaluate the effect of plasma treatment on cell proliferation and differentiation. The cellular experiment results showed that compared with pure PEEK, treated PEEK significantly enhanced adhesion, proliferation, and osteogenic differentiation of adMSCs. These results indicated that plasma treatment can effectively enhance the biological activity of PEEK surface. These results showed that PEEK treated with oxygen and ammonia plasma could better bind to bone tissue, achieving the modification purpose of improving PEEK biological activity and promoting bone binding formation around the implant.

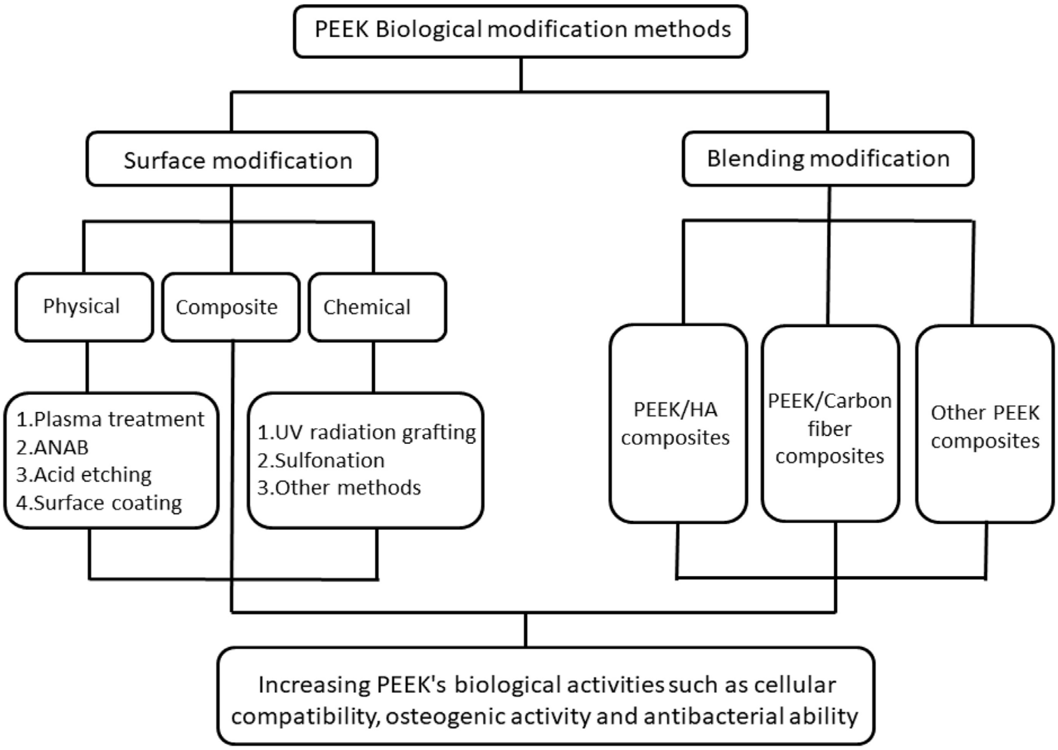

FIGURE 2 | The classification of PEEK's biological modification methods.

Surface modification methods for plasma treatment are repeatable, cheap, and simple to operate and can be applied to the modification of materials of various shapes and structures. However, the resultant modification effect lasts for a limited time, and the modified sample surface can only maintain the biological activity for a short period (Petlin et al., 2017). To increase the duration of the modification effect, researchers have been developing and studying new modification methods, among which the modification effect of the accelerated neutral atomic beam modification method can last for a long time and has less influence on the structure of the material.

Accelerated Neutral Atom Beam

Accelerated neutral atom beam (ANAB) technology is an ultra-shallow surface treatment technique that accelerates positively charged gas clusters by high electric potential, controlling the average energy of individual atoms between 10 eV per atom and 100 eV per atom. Because the energy carried by each atom is very small, the influence of these atoms on the structure of the material when they act on the surface is far less than that of other modification methods. The modification depth of the surface of the material is only 2–3 nm (Kirkpatrick et al., 2013; Ajami et al., 2017). Therefore, this modification method is favored by many researchers.

TABLE 1 | Contact angle and X-ray photoelectron spectroscopy (XPS) elemental analysis results.

	WCA (°)		Element concentration (at%)	
Sample	**15 min**	**14 days**	**C (1 s)**	**O (1 s)**
PEEK	79.5 ± 2.4	79.5 ± 2.4	88.8	11.2
PEEK/120 s	23.2 ± 1.8	55.1 ± 2.2	67.3	32.7
PEEK/240 s	21.8 ± 1.3	48.3 ± 1.9	60.1	39.9
PEEK/480 s	18.9 ± 1.7	64.7 ± 2.1	51.4	48.6

Khoury et al. (2013) used an intense beam of cluster-like packets of accelerated unbonded neutral argon gas atoms to modify PEEK and conducted a series of cellular and animal-model experiments. The surface roughness and hydrophilicity of the modified samples increased with ANAB technology. Human fetal osteoblast cells (hFOBs) were inoculated on PEEK surface before and after modification and on the surface of titanium alloy in cell experiments. The results showed that the cell proliferation of cells on modified PEEK surface was significantly better than that of cells on unmodified PEEK surface, and the number of modified PEEK surface cells was similar to that of titanium alloy, the most commonly used clinical implant material. To further explore the biological activity of the modified samples, the authors conducted *in vivo* experiments to prepare the critical skull defect model of rats, and implanted the PEEK samples, before and after modification, into the defect for 4 weeks to observe the binding of the samples to the surrounding tissues. The results of animal experiments are shown in **Figure 3**. There was only a small amount of fibrous tissue around the unmodified pure PEEK sample, while the

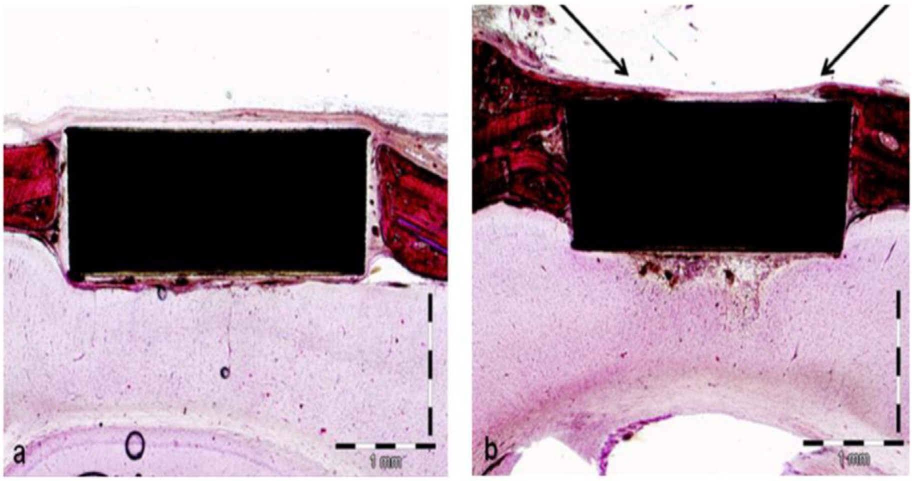

FIGURE 3 | The tissue growth around unmodified pure PEEK sample **(a)** and ANAB-modified sample **(b)**.

bone tissue around the ANAB modified sample was significantly increased. These results confirmed that ANAB technology can enhance PEEK biological activity by changing PEEK surface topography and increasing roughness, which is conducive to the formation of binding of PEEK implants to surrounding tissue and bone.

In another study by Khoury et al. (2017), ANAB technology was used to modify PEEK. In this experiment, the number of surfactant groups in each sample group was measured, and the results showed that the number of surface-active groups in the sample group modified by ANAB method was significantly higher than that of the unmodified sample group and the plasma-treated sample group. These results proved that both ANAB modification and plasma modification could increase PEEK bioactivity by forming hydroxyl and carboxyl groups on PEEK surface; the modification effect of ANAB technology was better than that of plasma treatment. Subsequent *in vitro* biological experiments and animal experiments showed that ANAB-technology modified samples were more conducive to mineral deposition, effectively improved the ability of cell adhesion and proliferation, and the expression of genes related to cell osteogenesis; they also formed good bone binding in animals. These results indicated that ANAB technology can effectively improve PEEK biological activity, which may be enhanced by introducing various active groups on PEEK surface.

These studies have proved that ANAB technology can increase PEEK surface roughness by changing PEEK surface morphology. Introduction of the hydroxyl, carboxyl, and other active groups on PEEK surface could further effectively improve PEEK's cellular compatibility and bone binding ability. Compared with the gas plasma surface modification technology, the controllable operation of ANAB on the surface of materials is between 2 and 3 nm (Ajami et al., 2017), which has little influence on the structure of PEEK and has long-term stability. However, the cost is high and the operation is complex.

Acid Etching

A previous study (Wong et al., 2009; Wang et al., 2019) showed that the porousstructure on the surface of bone implants is conducive to the formation of bone binding. Acid etching surface modification method refers to the corrosion of PEEK with strong acid such as concentrated sulfuric acid, and the preparation of porous structure conducive to cell growth on PEEK surface to enhance PEEK biological activity and facilitate the modification of PEEK surface bone binding. Therefore, Torstrick et al. (2018) adopted acid etching to form a porous structure on PEEK surface. The pore morphometrics data are shown in **Table 2**. The data showed that the pores were uniform in size and intercorrelated internally. To study the effect of porous structure on PEEK biological activity, MC3T3 cells were simultaneously inoculated on smooth unmodified PEEK, porous PEEK, and plasma-sprayed, titanium-coated PEEK. After a 14-day culture, calcium content, osteocalcin content, vascular endothelial growth factor (VEGF) secretion, alkaline phosphatase activity, and DNA content were measured. The results are shown in **Figure 4**. Increased calcium and osteocalcin content and decreased DNA content of cells on porous PEEK surface represent increased cell-mediated mineralization and enhanced osteogenic differentiation activity of the cells on the porous PEEK surface. However, the

TABLE 2 | Porous PEEK pore morphometrics.

	Porous PEEK
Porosity (%)	68.7 ± 0.5
Pore size (μm)	340 ± 8
Strut spacing (μm)	244 ± 2
Strut thickness (μm)	114 ± 2
Pore depth (μm)	523 ± 17
Inter-connectivity (%)	99.96 ± 0.01

Mean ± SE for all values.

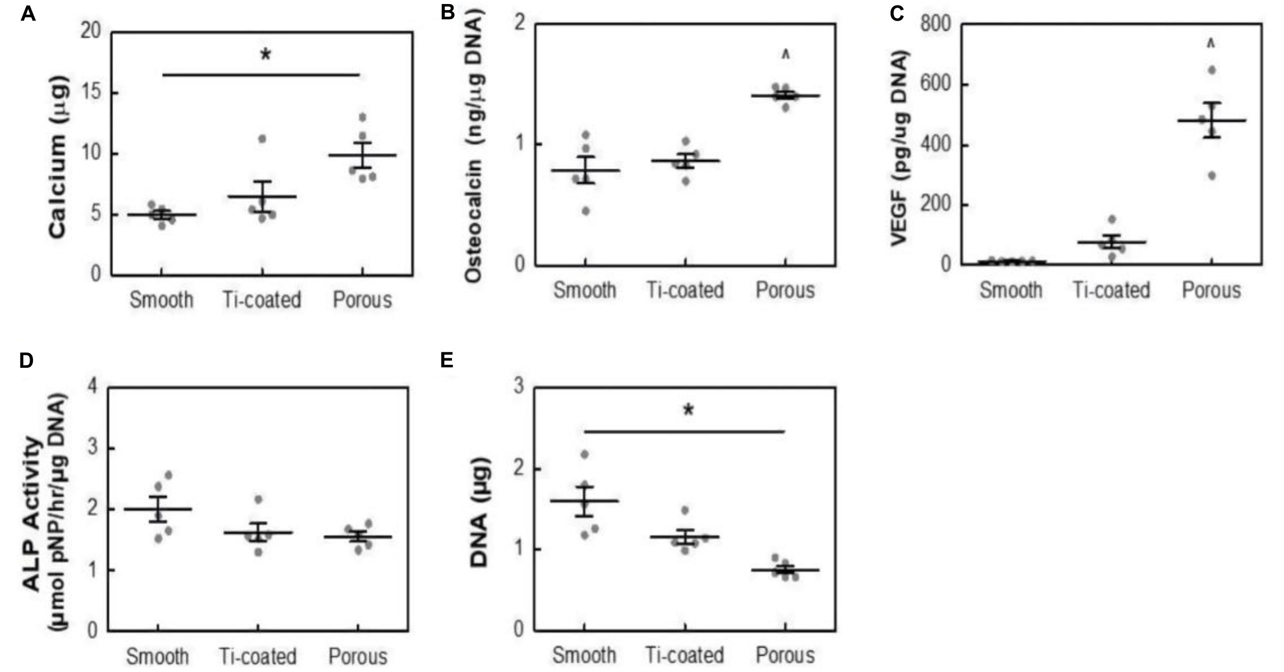

FIGURE 4 | Calcium content **(A)**, osteocalcin **(B)**, VEGF **(C)**, ALP Activity **(D)**, and DNA content **(E)** of MC3T3 cultures in osteogenic media at 14 days. All data are from identical sample wells, except for calcium, which was from parallel cultures. $^*p < 0.05$, $^\wedge p < 0.05$ vs. other groups (two-way ANOVA, Tukey's test, $n = 5$). Mean ± SE.

increased secretion of vascular endothelial influencing factor may be the result of lack of oxygen in the deep pores. Alkaline phosphatase is a marker of early osteogenic differentiation, so there was no significant difference in alkaline phosphatase activity between different sample groups at 14 days. To further investigate the *in vivo* osseointegration ability of porous PEEK, the authors implanted different samples into the proximal tibia of rats, and observed the bone binding of each group 8 weeks later by computed tomography (CT), histological analysis, and pull-out tests. The results indicated that the osseointegration ability with surrounding tissues of the three samples showed the trend in the order of porous PEEK > titanium-coated PEEK > smooth pure PEEK implants, with porous PEEK implants requiring the greatest extractive force than the other two samples. These results indicate that the porous structure can effectively improve PEEK's bone-binding ability, and the porous structure can intermesh with the bone, providing better bone binding strength *in vivo*.

Hieda et al. (2017) treated the PEEK scaffold with 70% porosity with concentrated sulfuric acid and potassium carbonate solution successively, formed a porous foam structure on the surface of the scaffold, and then implanted the scaffold material into the femur of rabbits. At the time points of 4, 8, and 12 weeks, respectively, they studied the bone binding of different samples *in vivo* through micro-CT and various staining methods. The results of CT and von Kossa staining are shown in **Figure 5**. The results showed that mature bone tissue had grown in the modified scaffold sample after 4 weeks, while only a small amount of bone tissue appeared around the scaffold in the unmodified sample. At 8 and 12 weeks, mature bone grafts also appeared in the unmodified scaffold; however, the area of bone tissue was lower than that in the modified PEEK scaffold. These results indicate that the porous structure can effectively improve the osteogenic activity of PEEK implants. In general, the acid etching modification method is simple to operate, but PEEK's structure is destroyed during the modification, which affects its excellent mechanical properties.

Surface Coating

In addition to plasma treatment, neutral atom beam technique, and acid treatment to improve PEEK bioactivity by introducing active groups or changing surface morphology, researchers have also adopted many different methods to prepare bioactive coatings on PEEK surface to achieve modification. The literature on modification of PEEK surface coating is summarized in **Table 3**.

Chemical Surface Modification Methods

Chemical surface modification mainly refers to the chemical reaction between PEEK and various biologically active substances, and the introduction of biologically active substances or groups on PEEK surface in the form of various chemical bonds, in order to achieve the purpose of modification. The binding strength between PEEK and the active substance bound by chemical bonds is better than the physical method, and there are many biologically active substances to choose from.

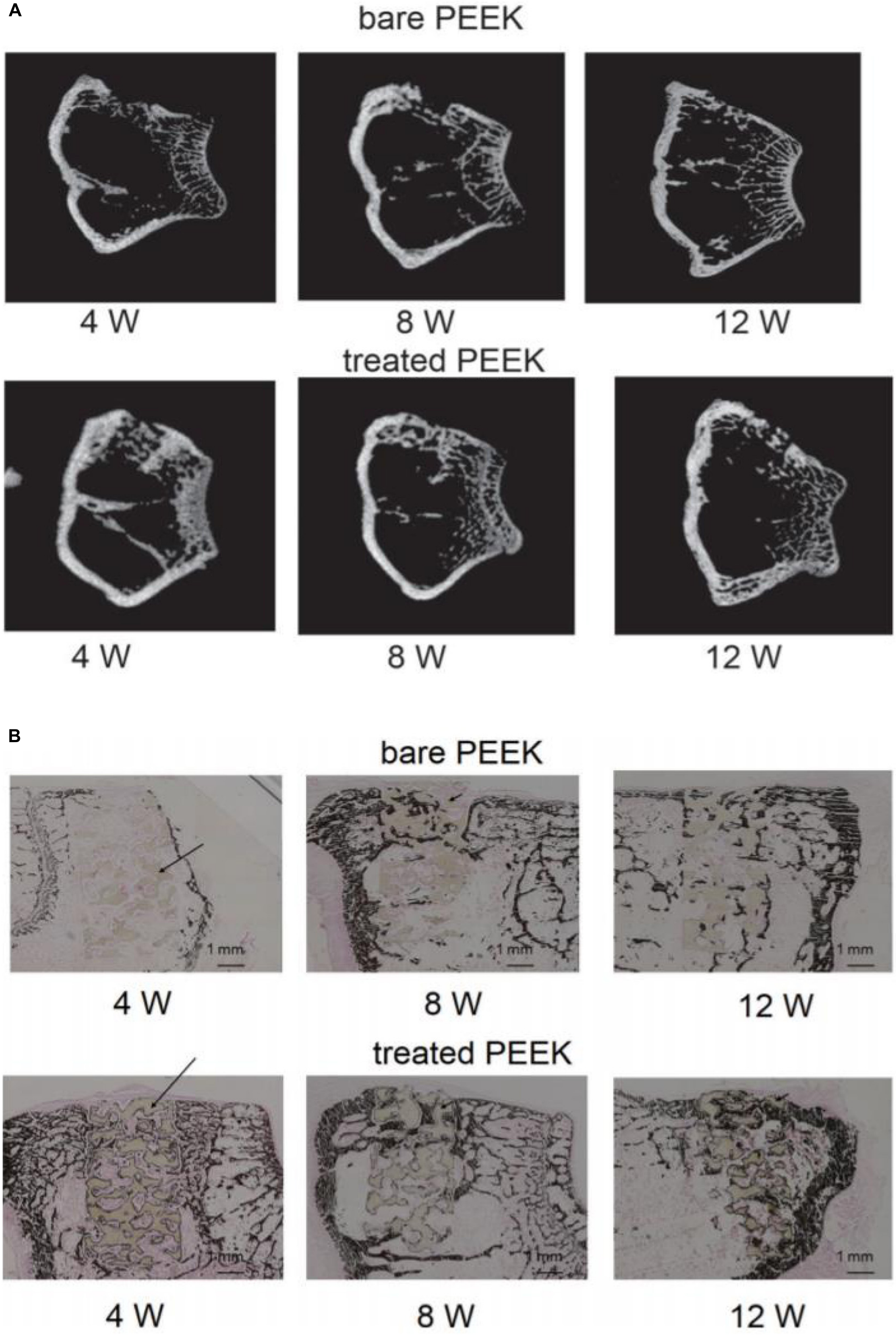

FIGURE 5 | Micro computed tomography (micro-CT) images **(A)** and von Kossa staining images **(B)** at 4, 8, and 12 weeks after surgery. Dark brown staining represents bone tissue and black arrows show the PEEK materials in the bone defect.

TABLE 3 | Examples of surface coating modification literature.

Coating material	Method	Modification effect	Advantages	Disadvantages	Authors
Ti	Plasma-spray	Enhances osteogenic activity	Simple operation and low cost	Insufficient bonding strength of coating and high temperature may damage PEEK's original structure (Stiles-Shields et al., 2015)	Hwang et al., 2015
Ti	Electron beam deposition	Enhances proliferation and osteogenic differentiation of human mesenchymal stromal cells and Mc3t3-e1	High coating accuracy	Low efficiency and high cost	Han et al., 2010; Elschner et al., 2015
TiO_2	High-power pulsed magnetron sputtering	Enhances cytocompatibility of PEEK surface	The coating is more stable and has better mechanical properties	PEEK surface structure is damaged during modification	Yang et al., 2015
TiO_2	Sol-gel method	Enhances ability of bone integration	No damage to PEEK surface structure	Long reaction time and high cost	Shimizu et al., 2016; Shimizu et al., 2017
TiO_2	Arc ion plating	Enhances osteogenic properties	Simple operation and low cost	The coating is not uniform and has large particles	Tsou et al., 2015
HA	Spin coating	Enhances the ability of bone integration	Low cost and uniform coating	Limited preparation efficiency	Barkarmo et al., 2013
HA	Cold Spraying	Enhances the proliferation and osteogenic differentiation of human bone marrow mesenchymal stem cells	The bonding strength of the coating is better	The cost is high and the operation is dangerous	Lee et al., 2013
Nano ZrP	Spin coating	Enhances the ability of bone integration	Low cost and uniform coating	Limited preparation efficiency	Kjellin et al., 2020
Nano Si_3N_4	Suspension coating and melt bonding	Enhances the ability of cytocompatibility and bone integration	Excellent modification effect	Complex modification steps	Dai et al., 2019

Ultraviolet Radiation Grafting

Ultraviolet (UV) radiation grafting is a simple chemical modification method. UV irradiation can break the carbonyl chemical bonds in PEEK's main chain structure and generate free radicals, which can induce polymerization of bioactive olefins and other monomers, thus grafting various bioactive substances onto the PEEK surface. This method is relatively simple to operate and has low cost of irradiation equipment. Besides, this modification does not affect the structure and properties of the material, and there is a chemical bond between the active substance and PEEK, which is stronger than the simple physical bond in physical modification. More active substances can be selected for chemical modification than the simple physical modification. Therefore, many researchers introduced various active substances into PEEK's surface by this method and explored the changes of PEEK biological activity before and after modification.

Ma Z. et al. (2020) grafted sodium polystyrene sulfonate onto PEEK surface by UV-induced grafting, thereby achieving the purpose of improving PEEK biological activity. The specific experimental procedure is shown in **Figure 6**. By controlling the UV exposure time, the modified samples were prepared with the grafting amount ranging from 0.59 ± 0.07 to 5.08 ± 0.21 mmol/cm^2. Characterization tests showed that sodium polystyrene sulfonate was successfully grafted on PEEK surface and distributed evenly. *In vitro*-simulated mineralization test results showed that the mineral deposition capacity of PEEK surface was significantly improved after modification, and the Ca/P ratio of the deposited mineral was very close to that of calcium phosphate in human bone. The *in vitro* experiments also showed that the proliferation, spread, extracellular matrix secretion, calcification, alkaline phosphatase activity, and osteogene-related gene expression of modified PEEK surface cells were stronger than those of unmodified PEEK cells, and this trend increased with the graft amount. These results indicate that sodium polystyrene sulfonate grafted to PEEK surface by UV irradiation can effectively improve PEEK osteogenic activity, which is a positive significance for the clinical application of PEEK as an implant.

Owing to the complexity of the *in vivo* environment, simple *in vitro* cell experiments could not fully reflect the osseo-binding effect of the implant *in vivo*. Thus, after the phosphate group was grafted onto the PEEK surface by UV-induced one-step method, Zheng et al. (2019) conducted not just *in vitro* experiments but also animal experiments to further investigate the osseointegration of PEEK implant in animals. Characterization tests proved that UV irradiation successfully grafts phosphate groups to the PEEK surface without changing PEEK surface morphology and structure, effectively increasing PEEK surface hydrophilicity. The *in vitro* experiment results showed that the adhesion, proliferation, extracellular matrix mineralization, activity of osteogenic enzymes, and content of osteogenic-related genes were significantly increased in cells grown on the modified PEEK surface compared to those grown on the unmodified PEEK surface. The rabbit proximal tibia defect

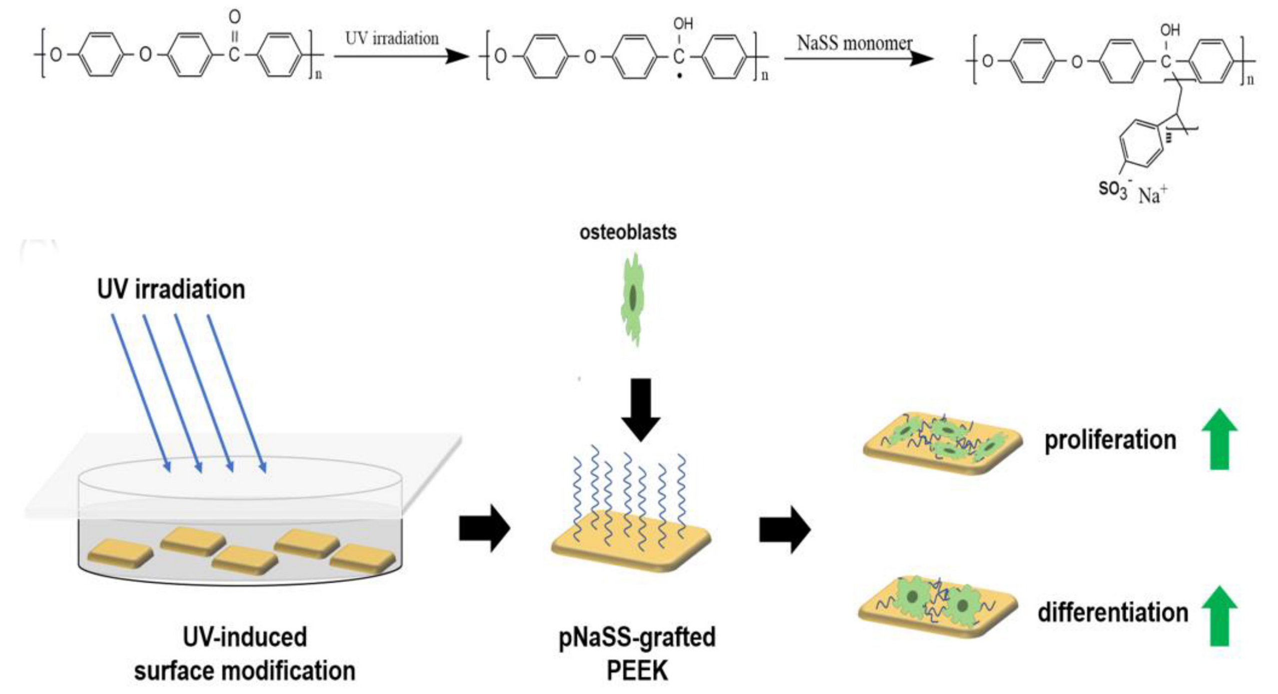

FIGURE 6 | Preparation route and *in vitro* evaluations of pNaSS-grafted PEEK.

model was used to evaluate the *in vivo* biological activity of a different sample set of PEEK. In rabbits with tibial implants, the histological results after 12 weeks showed that the modified PEEK around the implant bone formation was significantly higher than that of the unmodified implant. The statistical analysis found that the modified sample of bone–implant contact ratio can reach 45%, the bone–implant contact ratio of the unmodified sample ratio was only 25%. These results indicate that this modification method can improve PEEK's biological activity simply and effectively.

In addition to sodium polystyrene sulfonate and phosphate groups, a number of active substances are grafted onto PEEK surfaces. Zhao et al. (2017b) and Yousaf et al. (2014) also grafted polyacrylic acid, polyvinyl phosphonic acid, polybutyl acrylate, and other polymers on PEEK surface through UV irradiation. The results of these studies all showed that PEEK's biological activity was significantly enhanced and the osteogenic capacity was improved after the introduction of the active substance. It shows that this modification method is feasible and effective.

Sulfonation Treatment

Sulfonated surface modification is a modification method that forms a porous structure on the surface of PEEK by concentrated sulfuric acid treatment or other methods and introduces a sulfonic acid group to enhance the biological activity of PEEK. The traditional sulfonation method directly treats PEEK with concentrated sulfuric acid solution to achieve sulfonation effect. Wan et al. (2020) recently discovered a new sulfonation method, which uses sulfur trioxide fumigation PEEK to achieve sulfonation. The effect of fumigation and sulfonation on PEEK structure is much less than that of traditional concentrated sulfuric acid sulfonation.

Zhao et al. (2013) sulfonated PEEK with traditional sulfonation method. According to different subsequent treatment methods, the modified samples were divided into high-sulfur samples treated with water and low-sulfur samples treated with water and acetone. The results of *in vitro* and animal experiments showed that the sulfonated samples with low sulfur concentration had stronger ability of cell proliferation, differentiation, and bone integration *in vivo* than the sulfonated samples with high sulfur concentration. Ouyang et al. (2016) also sulfonated PEEK using traditional methods, and obtained samples with different sulfur content after heat treatment under different conditions. For a dental implant, excellent antibacterial performance is essential in addition to good osteogenic activity. Therefore, the author not only conducted cytology test, but also conducted antibacterial experiment, and found that the modified samples can promote the proliferation and osteogenesis of mesenchymal stem cells of differentiation, and had a good resistance to *Staphylococcus aureus* and *Escherichia coli*. They then explored the effect of sulfur content on this modification. The results showed that, with the increase of sulfur content, the antibacterial activity of the samples increased, but the osteogenic ability decreased. Subsequently, the authors conducted animal experiments using a mouse femur defect model, and the result trend was consistent with the results of cell and antibacterial experiments *in vitro*. These results showed that sulfonated samples had good osteogenic ability and antibacterial property, but the release of sulfur from high-sulfur samples may lead to low pH around implants to inhibit the growth of cells to some extent, so it is very important to control the sulfur content of the modified samples to achieve the optimum osteogenesis and antibacterial ability.

In addition to the traditional sulfonation modification concentrated sulfuric acid, Wan et al. (2020) recently adopted a new gas fumigation method for sulfonation of PEEK. This method adopts gas fumigation of PEEK to form a microporous structure on its surface, and introduces a sulfonic group to obtain sulfonated PEEK with different sulfur content by controlling the fumigation time. Compared with the traditional method, this method can achieve sulfonation without destroying the structure of PEEK. The specific experimental process is shown in **Figure 7**. The fumigated sulfonated PEEK surface has uniform pores between 6 and 14 μm, and the modified material has good hydrophilicity, protein adsorption, and mineralization abilities, as well as good cytocompatibility, which can effectively promote cell adhesion, proliferation, and differentiation. These results indicate that the pore structure formed by fumigation on PEEK surface is significantly smaller and more uniform than that formed by conventional sulfonation methods. Moreover, this modification method effectively improves PEEK's biological activity, and is a modified sulfonation method, which is worthy of further exploration regarding the effect of this method on PEEK's antibacterial ability and biological activity *in vivo*.

The operation steps of the sulfonated surface modification method are relatively simple, and can form a porous structure conducive to cell growth on the PEEK surface, introduce sulfonic acid groups with biological activity, and improve PEEK's antibacterial and osteogenic capabilities. However, the concentrated sulfuric acid and other modified reagents are dangerous to handle, so the experiment has certain limitations. Moreover, the traditional sulfonation modification method can destroy PEEK's structure and inhibit the growth of PEEK surface cells when the sample surface contains too much sulfur.

Other Chemical Modification Methods

In addition to the ultraviolet irradiation graft and sulfonation modification, the researchers also adopted a variety of chemical substances to undergo reduction and hydrolysis reactions with PEEK, and introduced carboxyl, amino, and other active tubular groups on PEEK surface to achieve modification.

Zheng et al. (2015) reduced the carbonyl group on the surface of PEEK to a hydroxyl group, and then treated the hydroxylated pretreated PEEK sample with organosilane solution to form the functional surface layer of carboxyl group (–COOH). *In vitro* cell experiments showed that compared with hydroxylated PEEK and unmodified pure PEEK, carboxyl introduced on the surface of PEEK samples could better promote cell adhesion, spread, and proliferation. These results indicated that the introduction of carboxyl groups effectively enhanced the biological activity of PEEK surface.

Mahjoubi et al. (2017) introduced phosphate groups to the PEEK surface through a two-step diazo chemistry method. The modified samples had good hydrophilicity and mineral deposition ability. Further, the author tested the adhesion strength of the HA deposited on the surface of the sample with means of a scratch test. The results showed that the adhesion strength of the HA deposited on the surface of the modified sample with phosphate was stronger than the HA deposited on the unmodified PEEK surface. *In vitro* experiments showed that the samples with phosphate groups introduced on the surface could significantly improve the metabolic activity, and extracellular matrix mineralization of MC3T3-E1 cells. Animal experimental results showed that 3 months after modified PEEK implantation into rat skulls, the unmodified PEEK implant was surrounded by fibrous tissue, while there was no fibrous tissue around the modified PEEK implant and no evidence of mineral deposition, indicating that the introduction of phosphate groups could significantly enhance the osseointegration ability of PEEK implant.

Infection is a common complication of implantation; hence, as a bone implant material, in addition to good bone-binding ability, antibacterial ability is also indispensable. He M. et al. (2019) chlorinated PEEK and then grafted two types of quaternary ammonium salts on PEEK surface through chemical reaction to obtain S-PEEK and C-PEEK samples modified by quaternary ammonium salt. Fourier transform infrared analysis, contact angle, and other characterization results proved that the two ammonium salts were successfully grafted onto PEEK surface and significantly improved its hydrophilicity. The antibacterial activity of the modified samples was evaluated by bacteriostatic circle test and plate colony-counting methods. As shown in **Figure 8**, obvious bacteriostatic rings appeared around the two modified samples, and the morphology of bacteria at high magnification showed that the surface of *E. coli* and *S. aureus* in contact with the modified samples was damaged, which proved that the antibacterial mechanism of quaternary ammonium salt was by contact sterilization. The results of plate colony counting showed that the antibacterial rates of the two modified samples against *S. aureus* and *E. coli* were >98 and >48%, respectively, which proved that the quaternary ammonium salt-modified PEEK could effectively improve the antibacterial ability of PEEK.

Such modification methods have the advantages of simple operation and low cost. However, given PEEK's stable property, it is difficult to react with other substances, so the modification methods available at present are very limited. However, after the introduction of active groups on the surface, PEEK surface reactivity increases, making it easier to introduce other bioactive substances on PEEK's surface, which is also one of the advantages of this surface modification method.

Composite Surface Modification Methods

The human body environment is very complex. As an intramedullary implant material, PEEK's single physical or chemical modification sometimes fails to meet clinical needs. Therefore, based on the original single physical or chemical modification, researchers adopted other modification methods to further introduce more active substances to more effectively improve PEEK's biological activity and further improve the binding ability between the implant and surrounding tissues. This kind of surface modification method is the composite surface modification method. Wiacek et al. (2016a,b) introduced

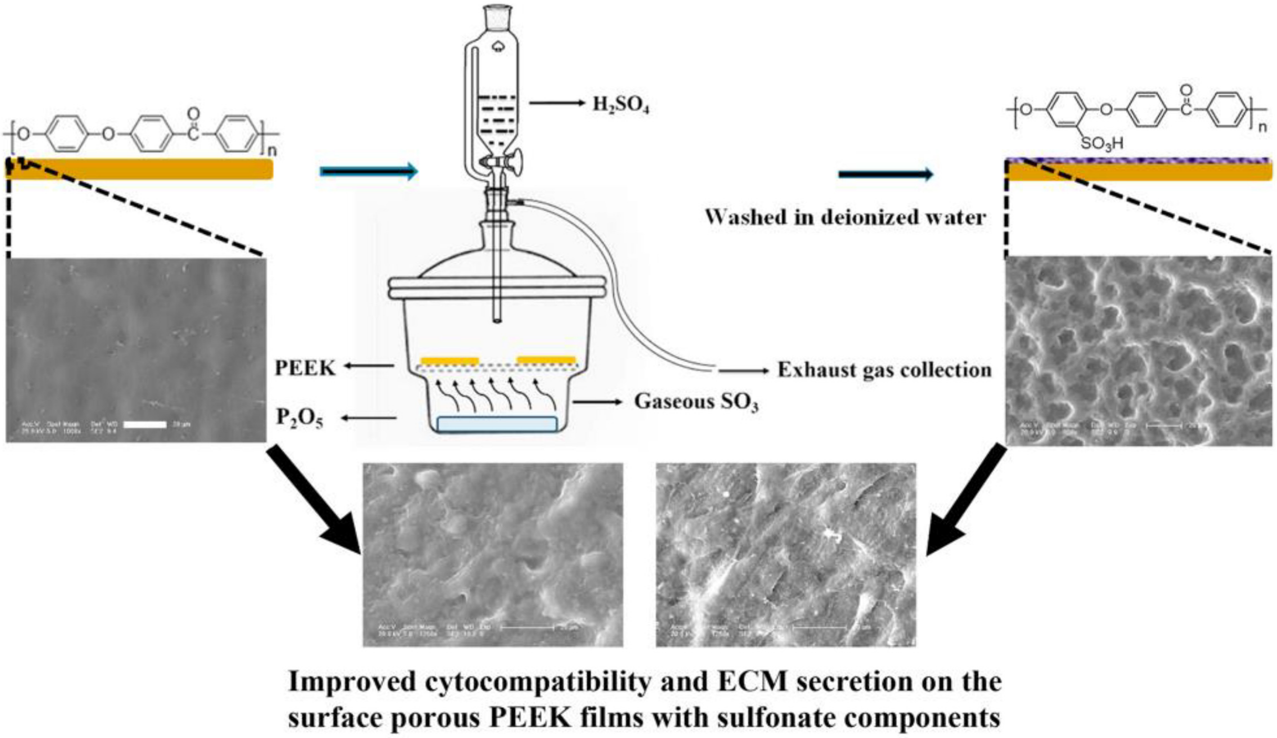

FIGURE 7 | Schematic diagram of fabricating surface porous PEEK implants by gaseous SO_3-induced controllable sulfonation.

a coating of chitosan with antibacterial properties and good biological activity onto the surface of nitrogen-plasma-modified PEEK and tested the physicochemical properties and biological activities of the modified material. Experimental results showed that after nitrogen plasma treatment at low temperature, the surface roughness, free energy, and adhesion of the modified samples were obviously improved, and the adhesion stability of the chitosan coating on the PEEK surface could be greatly improved. Therefore, the modified PEEK surface could ensure a stable chitosan coating. The results of the contact angle and mechanical properties showed that the mechanical properties of PEEK did not change before and after the composite modification, while the hydrophilicity was significantly improved.

Pure porous structure can only increase PEEK's biological activity to a limited extent. Therefore, some researchers choose to introduce more active substances on PEEK's surface after acid modification to obtain a better modification effect. Sun et al. (2018) treated PEEK with concentrated sulfuric acid to create a porous structure on the PEEK surface, then introduced different concentrations of bone morphogenetic proteins-2 (BMP-2) into the porous sample surface. The samples were divided into BMP2-25, BMP2-50, and BMP2-100 groups according to different concentrations of BMP-2 solution added on each PEEK sample surface. Various characterization results showed that BMP-2 was successfully fixed in PEEK's porous structure, and the hydrophilicity of the loaded BMP-2 protein sample was significantly enhanced and increased with the protein content. The release test results of BMP-2 protein showed that the release time of high-content samples was up to 28 days. The *in vitro* experimental results showed that the proliferation, adhesion, collagen secretion, alkaline phosphatase activity, and extracellular matrix calcification of the loaded protein samples were stronger than those of the control group. In this study, the author further introduced BMP-2, an active substance promoting osteoblastic differentiation of cells, into the sulfonated PEEK surface, which further enhanced the biological activity of the PEEK surface, reduced the adverse effect of sulfonated modified samples on cell growth and obtained better modification effect than simple sulfonated modification.

In addition to BMP-2, other active substances have also been introduced into the porous PEEK surface for better biological activity. Wan et al. (2019) also pretreated PEEK with concentrated sulfuric acid and prepared a porous structure conducive to bone integration on the material surface. Two growth factors—IGF-1 and BMP-2—were fixed on the porous surface of PEEK material through a polydopamine (pDA) coating to construct a biologically active PEEK implant material. Characterization tests showed that PEEK surface showed homogeneous pores with pore size between 0.24 and 0.74 μm after sulfuric acid treatment. After dopamine fixation, the hydrophilicity and protein adsorption ability of the sample surface were significantly enhanced. Cell experiments showed that after the two growth factors were fixed on the PEEK surface, the adhesion, proliferation, and spread of the growing cells on the PEEK surface became better, and the activity of osteoblast-related

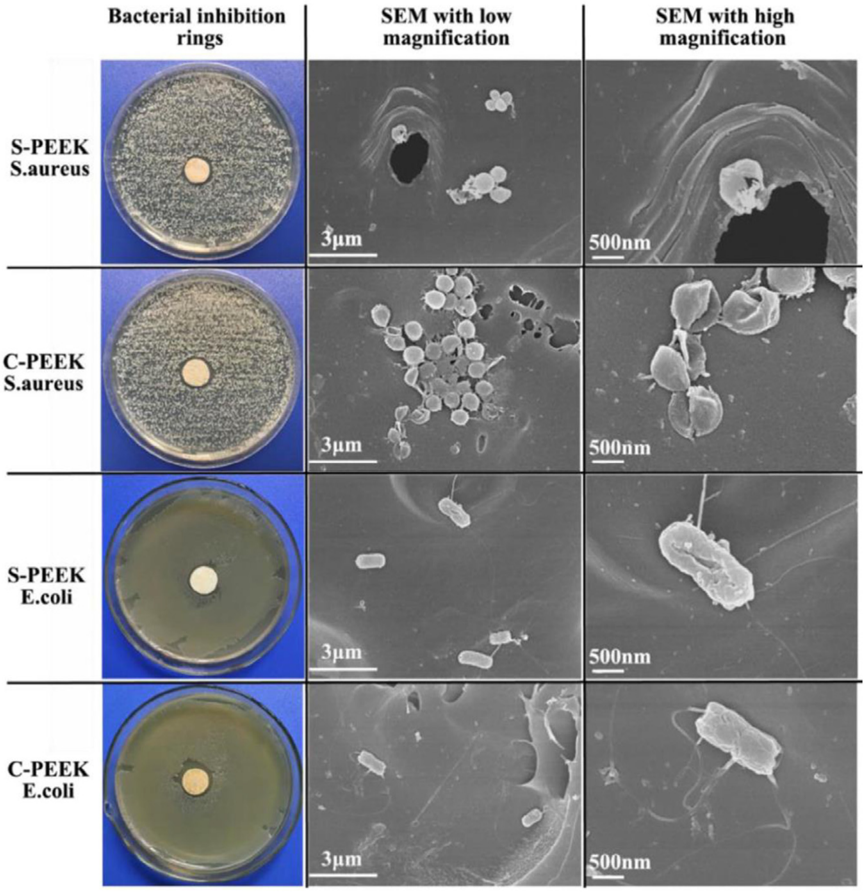

FIGURE 8 | The bacterial inhibition rings and SEM images with low and high magnifications.

enzyme alkaline phosphatase and cellular matrix calcification also increased. Chen et al. (2012) and Sun et al. (2012) induced graft copolymerization of polyacrylic acid onto PEEK surface by UV irradiation to introduce carboxyl groups, then fixed bovine serum albumin (BSA) on the PEEK surface after graft activation. Experimental results showed that the biological activity of the modified PEEK surface was significantly improved.

As dental implant material, in addition to good cellular compatibility, good antibacterial ability is also essential. Ding et al. (2019) selected nitric acid and sulfuric acid in a ratio of 1:1 to treat PEEK surface, and constructed a three-dimensional porous structure conducive to bone growth on the PEEK surface. Then, chemical grafting was used to graft ethylenediamine, which has antibacterial activity, on the porous PEEK surface. The specific reaction mechanism is shown in **Figure 9**. Scanning electron microscopy, atomic force microscope, energy-dispersive spectroscopy, contact angle, and other characterization results showed that the amino group was successfully grafted onto porous PEEK surface, and the pores of the sample surface were evenly distributed, and the hydrophilicity was obviously enhanced. *In vitro* antibacterial tests and cytological testing showed that the composite modified samples showed excellent resistance ability to *E. coli* and *S. aureus*, and the modified samples had good cytocompatibility and osteogenic activity The rabbit femoral defect model was used in animal experiments, and the osseointegration of implants in different sample groups was evaluated by push-out tests and histological examination. The results showed that the composite modified samples were most closely bound to the surrounding tissues and required the greatest extrudability. Histological staining results at 1 month of implantation also showed no inflammatory response around the composite modified sample and the newest bone formation. These results proved that this modification method combines the advantages of the two methods and achieves better modification effect.

By combining sulfonation modification and surface coating modification, He X. et al. (2019) constructed a porous structure by sulfonation treatment on PEEK surface, and then introduced the hydrogel drug loading system of chlorogenic acid (CGA)/bone-induced growth factorinto the porous PEEK surface to further improve PEEK's biological activity and antibacterial ability. The specific modification process is shown in **Figure 10**. The antibacterial experiment and *in vitro* cytological test results showed that the compound modification effectively improved PEEK's antibacterial ability and promoted the proliferation, adhesion, and osteogenic differentiation of cells growing on the

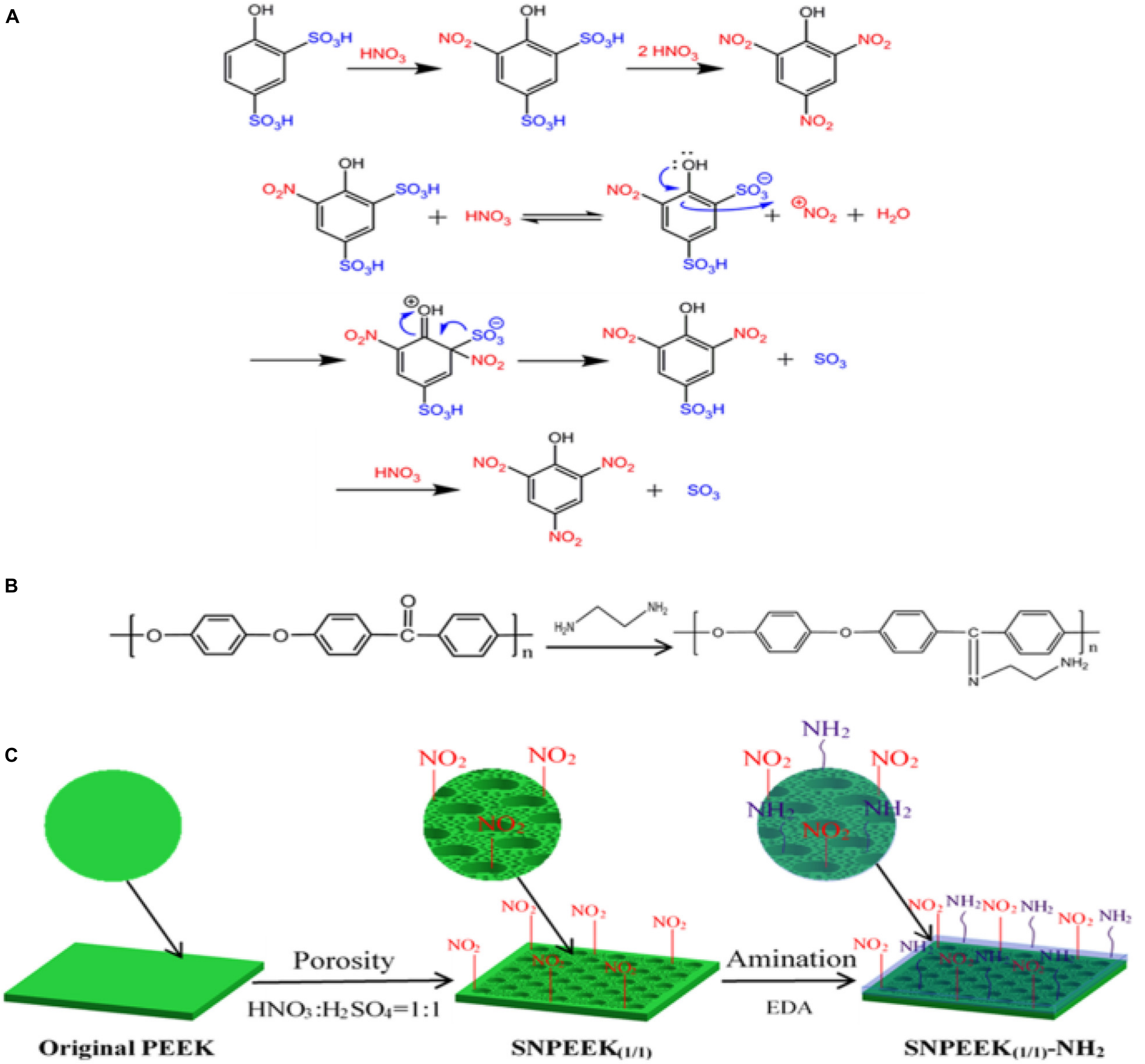

FIGURE 9 | (A) Taking the preparation of picric acid from 4-hydroxybenzene-1, 3-disulfonic acid as an example, the mechanism of substituting the sulfonic acid group with nitrite for PEEK modification was expounded. **(B)** Grafting reaction between the EDA and ketone carbonyl group of PEEK. **(C)** Schematic diagram for the modification process of the PEEK surface.

PEEK surface. Kuroda et al. (2018) treated PEEK by sulfuric acid etching and ultraviolet irradiation, and the experimental results showed that modified PEEK's bone binding ability was improved and could inhibit bacterial adhesion. In summary, the composite modification can combine the advantages of various modification methods to further improve PEEK's biocompatibility.

BLENDING MODIFICATION

Polyether ether ketone is a kind of dental implant material with good physical and chemical properties and elastic modulus close to human bone, which makes it a good application prospect in implant field. However, PEEK's biological inertia limits its ability to form good bone binding with bone tissue. Therefore, various modification methods have been used to improve its biological activity. In addition to the surface modification mentioned above, blending modification methods are also possible. Blending modification is carried out to prepare composite materials by mixing various biological active substances with PEEK to improve its biological activity. This method can effectively improve PEEK's biological activities (such as bone formation activity) or antibacterial ability, but mixing other materials into PEEK may have a certain impact on its structure and mechanical properties. Common bioactive substances that can be mixed with PEEK include HA and carbon fiber (CF).

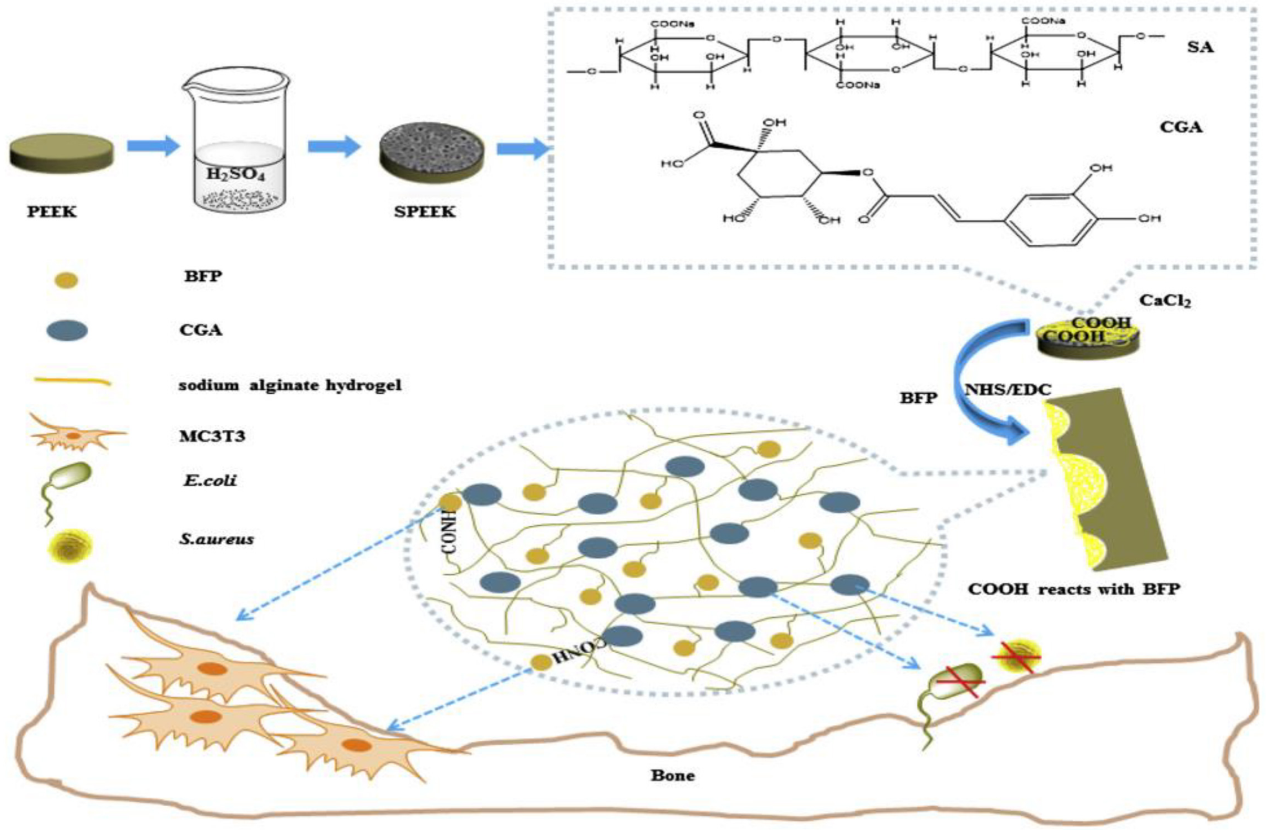

FIGURE 10 | A preparation schematic of the drug-loaded/grafted peptide sodium alginate hydrogel bridging system, that endows SPEEK with dual biological applications: osteogenesis and antibacterial activity.

PEEK/HA Composites

Hydroxyapatite is a bioactive substance with good biocompatibility and bone conductivity, whose ratio of calcium and phosphorus is similar to human bone. It can combine well with bone tissue (Zhang et al., 2019; Zhu et al., 2020; Zhao et al., 2021). Therefore, researchers often mix HA and PEEK to prepare composite material to improve the latter's biocompatibility. Walsh et al. (2016) prepared an HA and PEEK blend material, then prepared tibial cortical bone defect of sheep and spongy bone defect of tibia and femur, implanted pure PEEK and PEEK/HA composite materials into the defect respectively, and observed the osseointegration by histological detection at 4 and 12 weeks. The results showed that the interface of fibrous tissue was formed around the unmodified sample, while the new bone was formed around the composite and formed bone binding with the surrounding tissue. Then, the authors implanted the composite material into sheep as intervertebral fusion nails and compared it with the allogeneic bone material and pure PEEK material. The results showed that the allograft bone was fractured and reabsorbed, fibrous tissue interfaces were formed around PEEK, and the PEEK/HA composite formed good bone binding at 12 weeks. These results showed that HA significantly improved PEEK's osteogenic capacity.

The bioactivity of nano hydroxyapatite (N-HA) is better than that of HA alone. Therefore, Zhao et al. (2016) mixed N-HA with PEEK to prepare a composite material with a content of 40% N-HA. Subsequently, human osteoblast-like cells MG-63 were inoculated on the surface of the sample before and after modification to observe the cytocompatibility of the cells before and after modification. It was found that the cell adhesion ability and alkaline phosphatase activity on the surface of n-HA/PEEK composite material were higher than those of the PEEK sample group, but the cell proliferation ability was lower than that of pure PEEK. Proteomics analysis was used to explain that this phenomenon was caused by the increase in the amount of calcium-related proteins and the decrease in the amount of RNA-related proteins in the composite sample group. These results suggested that n-HA can enhance PEEK's ability to promote cell adhesion and osteogenic differentiation.

Hydroxyapatite is brittle (Ma et al., 2014a), and it always destroy PEEK's excellent mechanical properties after blending with PEEK. To enhance the mechanical properties of composite materials, Ma J. et al. (2020) used a 3D braiding, self-retention, hot pressing method to prepare an N-HA and PEEK blending material. The nHA/PEEK composites with an nHA content of 6.5 and 14.5 wt% were prepared. *In vitro* characterization tests showed that the hydrophilicity and mineralization of the composites were significantly stronger than those of pure PEEK materials. The mechanical properties of composites were evaluated by a series of mechanical tests. The results showed that owing to the impact of the braided structure, the elastic modulus, hardness, and bending strength of the composite were higher than those of the PEEK sample, and the fracture toughness of the sample with low nHA content was also significantly enhanced. Meanwhile, *in vitro* cytological test results showed that the introduction of nHA effectively improved PEEK's cell adhesion and proliferation abilities. The above results showed that PEEK's biological activity could be significantly improved after blending with HA. Although HA is rather brittle and has poor mechanical properties, with the continuous development of research, new preparation methods of mixed materials that can reduce the impact of HA on the mechanical properties of PEEK are being constantly discovered; thus, HA/PEEK composites have a good research prospect.

PEEK/Carbon Fiber Composites

Carbon fiber has the advantages of high strength and high temperature and corrosion resistance and is usually blended with PEEK to enhance its mechanical properties. Yan M. et al. (2018) prepared CF/PEEK composites by selective laser sintering, and the mechanical results showed that the tensile strength and elastic modulus of PEEK/CF composites were significantly higher than pure PEEK, effectively improving PEEK mechanical properties. Zhao et al. (2017a) prepared PEEK/CF composites by the vacuum hot pressing method and detected the contact angle and friction coefficient of different samples. The results showed that compared with pure PEEK, CF/PEEK's surface contact angle decreased, hydrophilicity increased, friction coefficient decreased, and wear resistance increased.

To study the specific modification effect of introducing CF into PEEK, Qin et al. (2019) prepared a series of PEEK/CF composites with different CF contents and studied the mechanical properties, thermal properties, and cytotoxicity of the composites. The results showed that compared with pure PEEK, the mechanical properties and thermal properties of CF were significantly enhanced, but they were slightly toxic to cells within a week. The results showed that CF-enhanced PEEK could effectively improve the mechanical properties of PEEK, but the biocompatibility of composite materials was somewhat limited. Therefore, Yan J. H. et al. (2018) introduced a graphene coating on the CF-reinforced PEEK (CFR/PEEK) surface to enhance the biological activity of CFR/PEEK scaffolds. Characterization tests showed that the graphene coating was successfully introduced onto the surface of the CFR/PEEK stent and enhanced the hydrophilicity of the CFR/PEEK material. *In vitro* cytological tests showed that the graphene-coated scaffold surface was more conducive to cell adhesion, proliferation, and osteogenic differentiation, showing good biological activity. In animal experiments, the rabbit femoral condyle defect model was used, and the results of three-dimensional imaging of the formation of new stock around the implant at 4, 8, and 12 weeks as well as histological staining results showed that the graphene-coated implant scaffolds had stronger osteogenic activity.

In addition to graphene, HA was also used to improve the biocompatibility of CF/PEEK composites. Liu et al. (2011) introduced HA which has good biological activity on CF/PEEK and prepared PEEK/HA/CF composites and studied the biocompatibility of the composites by co-culture with osteoblasts *in vitro*. The results showed that the composite was non-toxic to osteoblasts, the cells grew well on the surface of the composite, and the differentiation ability of the surface cells of the composite was improved compared with the control group. These results indicated that the PEEK/HA/CF composite had good cytocompatibility *in vitro*. Furthermore, the results showed that CF could significantly improve PEEK mechanical properties. Although it has limited ability to improve PEEK's biological activity, other bioactive substances such as HA or graphene can be further introduced to enhance PEEK's mechanical properties and simultaneously improve its biological activity.

Other PEEK Composites

In addition to HA and CF, studies have identified a number of bioactive materials for PEEK blends, such as zinc oxide, bioactive glass, titanium dioxide particles, and nano-silicates.

Zinc oxide nanoparticles are multi-functional inorganic nanoparticles with excellent mechanical and biological properties. Studies showed that ZnO exhibits significant antibacterial activity (Yamamoto, 2001). Diez-Pascual and Diez-Vicente (2014) and Diez-Pascual et al. (2014) first modified the surface of ZnO nanoparticles, and then prepared PEEK/ZnO nanocomposites to study the mechanical and antibacterial properties of composites. The results show that PEEK/ZnO nanocomposites prepared by modified nano-ZnO have better mechanical properties than those prepared by unmodified nano-ZnO., but PEEK/ZnO nanocomposites had good antibacterial properties against *E. coli* and *S. aureus* regardless of whether ZnO was modified. The antibacterial property enhanced with the increase in the ZnO content, and the best antibacterial property was obtained at 7.5 wt% of the modified nanoparticles. Hao et al. (2018) synthesized PEEK/ZnO nanocomposites by conventional melting blending and compression molding and studied the properties of the composites. The results showed that the mechanical properties and thermal stability of the composites were significantly improved and the composites had good cellular compatibility.

In addition to ZnO, TiO_2, Al_2O_3, MoS_2, nanometer calcium silicate (n-CS), and other active substances were also used to prepare mixed materials with PEEK to improve its biological and mechanical properties. Wu et al. (2012) prepared PEEK/TiO_2 composite material and through biological detection, found that its cellular compatibility was enhanced compared with pure PEEK; moreover, the osteoblasts were more likely to stick to the exposed position of TiO_2 particles. Kuo et al. (2005) prepared PEEK/SiO_2 and PEEK/Al_2O_3 composites with nanometer SiO_2 and Al_2O_3 particles respectively, and studied the mechanical properties of the composites. The results showed that when the introduced particle mass fraction was 5.0–7.5%, the hardness, elastic modulus, and tensile strength of the composites could be significantly improved. Lv et al. (2020) mixed molybdenum disulfide (MoS_2, MS) nanosheets with

PEEK to prepare MS/PEEK composites with an MS content of 4 and 8 wt%, and studied the tribological and mechanical properties and cellular compatibility of the composites. The results showed that the surface of the composite became rougher and hydrophilic, the mechanical properties were enhanced, and the modification effect improved with increasing MS content. Cytological tests showed that the growth of rat bone marrow mesenchymal cells on the surface of composite material was better than that of the pure PEEK sample group, indicating that MS could effectively improve PEEK's mechanical properties and cellular compatibility. Ma et al. (2014b) prepared n-CS/PEEK bioactive composite by compound injection molding method. The mechanical properties, hydrophilicity, bioactivity, and cytocompatibility of the composites were studied. The results showed that compared with pure PEEK, the mechanical properties, hydrophilicity, and mineralization ability of the composite were significantly improved. The results of cell experiments showed that n-CS/PEEK composites significantly promoted the ability of cell attachment, proliferation, diffusion, and osteogenic differentiation.

These results indicate that various blend modifications can enhance PEEK biological activity by introducing active substances or changing PEEK surface morphology, but most of the studies have been limited to *in vitro* experiments, and further *in vivo* and clinical trials are needed to verify the modification effect.

CONCLUSION

Polyether ether ketone and its composites play an important role in the field of oral repair given their excellent physical and chemical properties as well as biological properties. Its machinability enables PEEK to accurately manufacture various kinds of implants with complex structures. Its excellent properties such as stable chemical properties, good biosecurity, and elastic modulus are close to human dense bone and therefore make it an excellent oral implant potential material. The biological modification methods described above are all aimed at improving PEEK's biological activity. Each modification method has its advantages and disadvantages. Despite considerable experimental studies, modification technologies are still immature and lack sufficient clinical data to prove the clinical efficacy of these modification methods. Therefore, future research should focus on the development of more efficient and practical modification methods and clinical practice, and the exploration of PEEK modification methods to address different branches of stomatology.

AUTHOR CONTRIBUTIONS

All authors listed have made a substantial, direct and intellectual contribution to the work, and approved it for publication.

ACKNOWLEDGMENTS

We thank the financial support from the Program of Scientific Development of Jilin Province (20180414043GH and 20190304112YY), the program of Jilin University (3R2201543428), and the program of the First Hospital of Jilin University (01032140001, 04023720002, and JDYYJC002).

REFERENCES

Abdullah, M. R., Goharian, A., Abdul Kadir, M. R., and Wahit, M. U. (2015). Biomechanical and bioactivity concepts of polyetheretherketone composites for use in orthopedic implants-a review. *J. Biomed. Mater. Res. Part A* 103, 3689–3702. doi: 10.1002/jbm.a.35480

Ajami, S., Coathup, M. J., Khoury, J., and Blunn, G. W. (2017). Augmenting the bioactivity of polyetheretherketone using a novel accelerated neutral atom beam technique. *J. Biomed. Mater. Res. Part B Appl. Biomater.* 105, 1438–1446. doi: 10.1002/jbm.b.33681

Barkarmo, S., Wennerberg, A., Hoffman, M., Kjellin, P., Breding, K., Handa, P., et al. (2013). Nano-hydroxyapatite-coated PEEK implants: a pilot study in rabbit bone. *J. Biomed. Mater. Res. Part A* 101, 465–471. doi: 10.1002/jbm.a.34358

Chen, R. C., Sun, H., Li, A., and Xu, G. Z. (2012). UV-induced self-initiated graft polymerization of acrylamide onto poly(ether ether ketone). *Chem. Res. Chin. Univ.* 28, 162–165.

Dai, Y., Guo, H., Chu, L., He, Z., Wang, M., Zhang, S., et al. (2019). Promoting osteoblasts responses in vitro and improving osteointegration in vivo through bioactive coating of nanosilicon nitride on polyetheretherketone. *J. Orthop. Translat.* 24, 198–208. doi: 10.1016/j.jot.2019.10.011

Diez-Pascual, A. M., and Diez-Vicente, A. L. (2014). Development of nanocomposites reinforced with carboxylated poly(ether ether ketone) grafted to zinc oxide with superior antibacterial properties. *ACS Appl. Mater. Interfaces* 6, 3729–3741. doi: 10.1021/am500171x

Diez-Pascual, A. M., Xu, C., and Luque, R. (2014). Development and characterization of novel poly(ether ether ketone)/ZnO bionanocomposites. *J. Mater. Chem. B* 2, 3065–3078. doi: 10.1039/c3tb21800g

Ding, R., Chen, T., Xu, Q., Wei, R., Feng, B., Weng, J., et al. (2019). Mixed modification of the surface microstructure and chemical state of polyetheretherketone to improve its antimicrobial activity, hydrophilicity, cell adhesion, and bone integration. *ACS Biomater. Sci. Eng.* 6, 842–851. doi: 10.1021/acsbiomaterials.9b01148

Elschner, C., Noack, C., Preissler, C., Krause, A., Scheler, U., and Hempel, U. (2015). In vitro response of human mesenchymal stromal cells to titanium coated peek films and their suitability for magnetic resonance imaging. *J. Mater. Sci. Technol.* 31, 427–436. doi: 10.1016/j.jmst.2014.10.012

Han, C.-M., Lee, E.-J., Kim, H.-E., Koh, Y.-H., Kim, K. N., Ha, Y., et al. (2010). The electron beam deposition of titanium on polyetheretherketone (PEEK) and the resulting enhanced biological properties. *Biomaterials* 31, 3465–3470. doi: 10.1016/j.biomaterials.2009.12.030

Hao, L., Hu, Y., Zhang, Y., Wei, W., Hou, X., Guo, Y., et al. (2018). Enhancing the mechanical performance of poly(ether ether ketone)/zinc oxide nanocomposites to provide promising biomaterials for trauma and orthopedic implants. *RSC Adv.* 8, 27304–27317. doi: 10.1039/c8ra01736k

He, M., Hou, Y., Jiang, Y., Li, Y., Zou, Q., Chen, C., et al. (2019). Quaternization on polyetheretherketone and its antimicrobial activity. *Mater. Lett.* 235, 242–245. doi: 10.1016/j.matlet.2018.10.024

He, X., Deng, Y., Yu, Y., Lyu, H., and Liao, L. (2019). Drug-loaded/grafted peptide-modified porous PEEK to promote bone tissue repair and eliminate bacteria. *Colloids Surf B Biointerfaces* 181, 767–777. doi: 10.1016/j.colsurfb.2019.06.038

Hieda, A., Uemura, N., Hashimoto, Y., Toda, I., and Baba, S. (2017). In vivo bioactivity of porous polyetheretherketone with a foamed surface. *Dent. Mater. J.* 36, 222–229. doi: 10.4012/dmj.2016-277

Hwang, W.-C., Myers, H. F., Chiu, E., Mak, E., Butner, J. E., Fujimoto, K., et al. (2015). culturally adapted cognitive-behavioral therapy for chinese americans with depression: a randomized controlled trial. *Psychiatric Services* 66, 1035–1042. doi: 10.1176/appi.ps.201400358

Khoury, J., Kirkpatrick, S. R., Maxwell, M., Cherian, R. E., Kirkpatrick, A., and Svrluga, R. C. (2013). Neutral atom beam technique enhances bioactivity of PEEK. *Nucl. Instrum. Methods Phys. Res. Section B- Beam Interact. Mater. Atoms* 307, 630–634. doi: 10.1016/j.nimb.2012.11.087

Khoury, J., Maxwell, M., Cherian, R. E., Bachand, J., Kurz, A. C., Walsh, M., et al. (2017). Enhanced bioactivity and osseointegration of PEEK with accelerated neutral atom beam technology. *J. Biomed. Mater. Rese. Part B Appl. Biomater.* 105, 531–543. doi: 10.1002/jbm.b.33570

Kirkpatrick, A., Kirkpatrick, S., Walsh, M., Chau, S., Mack, M., Harrison, S., et al. (2013). Investigation of accelerated neutral atom beams created from gas cluster ion beams. *Nucl. Instrum. Methods Phys. Res. Section B Beam Interact. Mater. Atoms* 307, 281–289. doi: 10.1016/j.nimb.2012.11.084

Kjellin, P., Vikingsson, L., Danielsson, K., Johansson, P., and Wennerberg, A. (2020). A nanosized zirconium phosphate coating for PEEK implants and its effect in vivo. *Materialia* 10:100645. doi: 10.1016/j.mtla.2020.100645

Kuo, M. C., Tsai, C. M., Huang, J. C., and Chen, M. (2005). PEEK composites reinforced by nano-sized SiO2 and Al2O3 particulates. *Mater. Chem. Phys.* 90, 185–195. doi: 10.1016/j.matchemphys.2004.10.009

Kuroda, K., Igarashi, K., Kanetaka, H., and Okido, M. (2018). Surface modification of PEEK and its osteoconductivity and anti-inflammatory properties. *J. Biomater. Nanobiotechnol.* 09, 233–243. doi: 10.4236/jbnb.2018.93013

Kurtz, S. M., and Devine, J. N. (2007). PEEK biomaterials in trauma, orthopedic, and spinal implants. *Biomaterials* 28, 4845–4869. doi: 10.1016/j.biomaterials.2007.07.013

Lee, J. H., Jang, H. L., Lee, K. M., Baek, H.-R., Jin, K., Hong, K. S., et al. (2013). In vitro and in vivo evaluation of the bioactivity of hydroxyapatite-coated polyetheretherketone biocomposites created by cold spray technology. *Acta Biomater.* 9, 6177–6187. doi: 10.1016/j.actbio.2012.11.030

Liu, X., Deng, C., Liu, J., Li, J., and Sui, G. (2011). Research on the extracorporeal cytocompatibility of a composite of HA, carbon fiber and polyetheretherketone. *Sheng Wu Yi Xue Gong Cheng Xue Za Zhi* 28, 1159–1164.

Lv, X., Wang, X., Tang, S., Wang, D., Yang, L., He, A., et al. (2020). Incorporation of molybdenum disulfide into polyetheretherketone creating biocomposites with improved mechanical, tribological performances and cytocompatibility for artificial joints applications. *Colloids Surf B Biointerfaces* 189:110819. doi: 10.1016/j.colsurfb.2020.110819

Ma, J., Li, Z. J., Xue, Y. Z. B., Liang, X. Y., Tan, Z. J., and Tang, B. (2020). Novel PEEK/nHA composites fabricated by hot-pressing of 3D braided PEEK matrix. *Adv. Compos. Hybrid Mater.* 3, 156–166. doi: 10.1007/s42114-020-00147-3

Ma, Z., Li, L., Shi, X., Wang, Z., Guo, M., Wang, Y., et al. (2020). Enhanced osteogenic activities of polyetheretherketone surface modified by poly(sodium p-styrene sulfonate) via ultraviolet-induced polymerization. *J. Appl. Polym. Sci.* 137:49157. doi: 10.1002/app.49157

Ma, R., Fang, L., Luo, Z., Weng, L., Song, S., Zheng, R., et al. (2014a). Mechanical performance and in vivo bioactivity of functionally graded PEEK–HA biocomposite materials. *J. Sol Gel Sci. Technol.* 70, 339–345. doi: 10.1007/s10971-014-3287-7

Ma, R., Tang, S., Tan, H., Qian, J., Lin, W., Wang, Y., et al. (2014b). Preparation, characterization, in vitro bioactivity, and cellular responses to a polyetheretherketone bioactive composite containing nanocalcium silicate for bone repair. *ACS Appl. Mater. Interfaces* 6, 12214–12225. doi: 10.1021/am504409q

Mahjoubi, H., Buck, E., Manimunda, P., Farivar, R., Chromik, R., Murshed, M., et al. (2017). Surface phosphonation enhances hydroxyapatite coating adhesion on polyetheretherketone and its osseointegration potential. *Acta Biomater.* 47, 149–158. doi: 10.1016/j.actbio.2016.10.004

Najeeb, S., Zafar, M. S., Khurshid, Z., and Siddiqui, F. (2016).). Applications of polyetheretherketone (PEEK) in oral implantology and prosthodontics. *J. Prosthod. Res.* 60, 12–19. doi: 10.1016/j.jpor.2015.10.001

Novotna, Z., Reznickova, A., Rimpelova, S., Vesely, M., Kolska, Z., and Svorcik, V. (2015). Tailoring of PEEK bioactivity for improved cell interaction: plasma treatment in action. *Rsc Adv.* 5, 41428–41436. doi: 10.1039/c5ra03861h

Ouyang, L. P., Zhao, Y. C., Jin, G. D., Lu, T., Li, J. H., Qiao, Y. Q., et al. (2016). Influence of sulfur content on bone formation and antibacterial ability of sulfonated PEEK. *Biomaterials* 83, 115–126. doi: 10.1016/j.biomaterials.2016.01.017

Petlin, D. G., Tverdokhlebov, S. I., and Anissimov, Y. G. (2017). Plasma treatment as an efficient tool for controlled drug release from polymeric materials: a review. *J. Control. Release* 266, 57–74. doi: 10.1016/j.jconrel.2017.09.023

Qin, W., Li, Y., Ma, J., Liang, Q., and Tang, B. (2019). Mechanical properties and cytotoxicity of hierarchical carbon fiber-reinforced poly (ether-ether-ketone) composites used as implant materials. *J. Mech. Behav. Biomed. Mater.* 89, 227–233. doi: 10.1016/j.jmbbm.2018.09.040

Santing, H. J., Meijer, H. J. A., Raghoebar, G. M., and Özcan, M. (2012). Fracture strength and failure mode of maxillary implant-supported provisional single crowns: a comparison of composite resin crowns fabricated directly over peek abutments and solid titanium abutments. *Clin. Implant Dent. Related Res.* 14, 882–889. doi: 10.1111/j.1708-8208.2010.00322.x

Shimizu, T., Fujibayashi, S., Yamaguchi, S., Otsuki, B., Okuzu, Y., Matsushita, T., et al. (2017). In vivo experimental study of anterior cervical fusion using bioactive polyetheretherketone in a canine model. *PLoS One* 12:e0184495. doi: 10.1371/journal.pone.0184495

Shimizu, T., Fujibayashi, S., Yamaguchi, S., Yamamoto, K., Otsuki, B., Takemoto, M., et al. (2016). Bioactivity of sol-gel-derived TiO2 coating on polyetheretherketone: in vitro and in vivo studies. *Acta Biomater.* 35, 305–317. doi: 10.1016/j.actbio.2016.02.007

Song, K. J., Choi, B. W., Kim, G. H., and Song, J. H. (2010). Usefulness of polyetheretherketone (PEEK) cage with plate augmentation for anterior arthrodesis in traumatic cervical spine injury. *Spine J.* 10, 50–57. doi: 10.1016/j.spinee.2009.08.458

Song, K. J., Kim, G. H., and Choi, B. Y. (2011). Efficacy of PEEK cages and plate augmentation in three-level anterior cervical fusion of elderly patients. *Clin. Orthop. Surg.* 3, 9–15. doi: 10.4055/cios.2011.3.1.9

Stiles-Shields, C., Corden, M. E., Kwasny, M. J., Schueller, S. M., and Mohr, D. C. (2015). Predictors of outcome for telephone and face-to-face administered cognitive behavioral therapy for depression. *Psychol. Med.* 45, 3205–3215. doi: 10.1017/s0033291715001208

Sun, H., Chen, R. C., Li, A., and Xu, G. Z. (2012). Immobilization of bovine serum albumin on poly(ether ether ketone) for surface biocompatibility improvement. *Chem. Res. Chin. Univ.* 28, 353–357.

Sun, Z., Ouyang, L., Ma, X., Qiao, Y., and Liu, X. (2018). Controllable and durable release of BMP-2-loaded 3D porous sulfonated polyetheretherketone (PEEK) for osteogenic activity enhancement. *Colloids Surf B Biointerfaces* 171, 668–674. doi: 10.1016/j.colsurfb.2018.08.012

Tannous, F., Steiner, M., Shahin, R., and Kern, M. (2012). Retentive forces and fatigue resistance of thermoplastic resin clasps. *Dent. Mater.* 28, 273–278. doi: 10.1016/j.dental.2011.10.016

Torstrick, F. B., Lin, A. S. P., Potter, D., Safranski, D. L., Sulchek, T. A., Gall, K., et al. (2018). Porous PEEK improves the bone-implant interface compared to plasma-sprayed titanium coating on PEEK. *Biomaterials* 185, 106–116. doi: 10.1016/j.biomaterials.2018.09.009

Toth, J. M., Wang, M., Estes, B. T., Scifert, J. L., Seim, H. B., and Turner, A. S. (2006). Polyetheretherketone as a biomaterial for spinal applications. *Biomaterials* 27, 324–334. doi: 10.1016/j.biomaterials.2005.07.011

Tsou, H.-K., Chi, M.-H., Hung, Y.-W., Chung, C.-J., and He, J.-L. (2015). In Vivo osseointegration performance of titanium dioxide coating modified polyetheretherketone using arc ion plating for spinal implant application. *Biom. Res. Int.*2015:328943.

Walsh, W. R., Pelletier, M. H., Bertollo, N., Christou, C., and Tan, C. (2016). Does PEEK/HA enhance bone formation compared with PEEK in a sheep cervical fusion model? *Clin. Orthop. Related Res.* 474, 2364–2372. doi: 10.1007/s11999-016-4994-x

Wan, T., Jiao, Z., Guo, M., Wang, Z., Wan, Y., Lin, K., et al. (2020). Gaseous sulfur trioxide induced controllable sulfonation promoting biomineralization and osseointegration of polyetheretherketone implants. *Bioact. Mater.* 5, 1004–1017. doi: 10.1016/j.bioactmat.2020.06.011

Wan, T., Li, L. L., Guo, M., Jiao, Z. X., Wang, Z. L., Ito, Y., et al. (2019). Immobilization via polydopamine of dual growth factors on polyetheretherketone: improvement of cell adhesion, proliferation, and osteo-differentiation. *J. Mater. Sci.* 54, 11179–11196. doi: 10.1007/s10853-018-03264-z

Wang, C., Wang, J., Zeng, L., Qiao, Z., Liu, X., and Liu, H. (2019). Fabrication of electrospun polymer nanofibers with diverse morphologies. *Molecules* 24:834. doi: 10.3390/molecules24050834

Wang, H. Y., Lu, T., Meng, F. H., Zhu, H. Q., and Liu, X. Y. (2014). Enhanced osteoblast responses to poly ether ether ketone surface modified by water plasma immersion ion implantation. *Colloids and Surfaces B Biointerfaces* 117, 89–97. doi: 10.1016/j.colsurfb.2014.02.019

Waser-Althaus, J., Salamon, A., Waser, M., Padeste, C., Kreutzer, M., Pieles, U., et al. (2014). Differentiation of human mesenchymal stem cells on plasma-treated polyetheretherketone. *J. Mater. Sci. Mater. Med.* 25, 515–525. doi: 10.1007/s10856-013-5072-5

Wiacek, A. E., Terpilowski, K., Jurak, M., and Worzakowska, M. (2016a). Effect of low-temperature plasma on chitosan-coated PEEK polymer characteristics. *Eur. Polym. J.* 78, 1–13. doi: 10.1016/j.eurpolymj.2016.02.024

Wiacek, A. E., Terpilowski, K., Jurak, M., and Worzakowska, M. (2016b). Low-temperature air plasma modification of chitosan-coated PEEK biomaterials. *Polym. Test.* 50, 325-334. doi: 10.1016/j.eurpolymj.2016.02.024

Williams, D. (2008). The role of nitric oxide in biocompatibility. *Med. Dev. Technol.* 19, 10–18, 10.

Wong, K. L., Wong, C. T., Liu, W. C., Pan, H. B., Fong, M. K., Lam, W. M., et al. (2009). Mechanical properties and in vitro response of strontium-containing hydroxyapatite/polyetheretherketone composites. *Biomaterials* 30, 3810–3817. doi: 10.1016/j.biomaterials.2009.04.016

Wu, X., Liu, X., Wei, J., Ma, J., Deng, F., and Wei, S. (2012). Nano-TiO2/PEEK bioactive composite as a bone substitute material: in vitro and in vivo studies. *Int. J. Nanomed.* 7, 1215–1225. doi: 10.2147/ijn.s28101

Yamamoto, O. (2001). Influence of particle size on the antibacterial activity of zinc oxide. *Int. J. Inorganic Mater.* 3, 643–646. doi: 10.1016/s1466-6049(01)00197-0

Yan, J. H., Wang, C. H., Li, K. W., Zhang, Q., Yang, M., Di-Wu, W. L., et al. (2018). Enhancement of surface bioactivity on carbon fiber-reinforced polyether ether ketone via graphene modification. *Int. J. Nanomed.* 13, 3425–3440. doi: 10.2147/ijn.s160030

Yan, M., Tian, X., Peng, G., Li, D., and Zhang, X. (2018). High temperature rheological behavior and sintering kinetics of CF/PEEK composites during selective laser sintering. *Compos. Sci. Technol.* 165, 140–147. doi: 10.1016/j.compscitech.2018.06.023

Yang, Y.-J., Tsou, H.-K., Chen, Y.-H., Chung, C.-J., and He, J.-L. (2015). Enhancement of bioactivity on medical polymer surface using high power impulse magnetron sputtered titanium dioxide film. *Mater. Sci. Eng. C Mater. Biol. Appl.* 57, 58–66. doi: 10.1016/j.msec.2015.07.039

Yousaf, A., Farrukh, A., Oluz, Z., Tuncel, E., Duran, H., Dogan, S. Y., et al. (2014). UV-light assisted single step route to functional PEEK surfaces. *React. Funct. Polym.* 83, 70–75. doi: 10.1016/j.reactfunctpolym.2014.07.011

Zhang, Y. B., Liu, X. C., Zeng, L. D., Zhang, J., Zuo, J. L., Zou, J., et al. (2019). Polymer fiber scaffolds for bone and cartilage tissue engineering. *Adv. Funct. Mater.* 29:1903279. doi: 10.1002/adfm.201903279

Zhao, D., Zhu, T., Li, J., Cui, L., Zhang, Z., Zhuang, X., et al. (2021). Poly(lactic-co-glycolic acid)-based composite bone-substitute materials. *Bioact. Mater.* 6, 346–360. doi: 10.1016/j.bioactmat.2020.08.016

Zhao, M., Li, H., Liu, X., Wei, J., Ji, J., Yang, S., et al. (2016). Response of human osteoblast to n-HA/PEEK-quantitative proteomic study of bio-effects of nano-hydroxyapatite. *Composite* 6:22832.

Zhao, X., Xiong, D., and Wu, X. (2017a). Effects of surface oxidation treatment of carbon fibers on biotribological properties of CF/PEEK materials. *J. Bionic Eng.* 14, 640–647. doi: 10.1016/s1672-6529(16)60430-4

Zhao, X., Xiong, D. S., Wang, K., and Wang, N. (2017b). Improved biotribological properties of PEEK by photo-induced graft polymerization of acrylic acid. *Mater. Sci. Eng. C Mater. Biol. Appl.* 75, 777–783. doi: 10.1016/j.msec.2017.02.147

Zhao, Y., Wong, H. M., Wang, W., Li, P., Xu, Z., Chong, E. Y. W., et al. (2013). Cytocompatibility, osseointegration, and bioactivity of three-dimensional porous and nanostructured network on polyetheretherketone. *Biomaterials* 34, 9264–9277. doi: 10.1016/j.biomaterials.2013.08.071

Zheng, Y., Liu, L., Xiao, L., Zhang, Q., and Liu, Y. (2019). Enhanced osteogenic activity of phosphorylated polyetheretherketone via surface-initiated grafting polymerization of vinylphosphonic acid. *Colloids Surf B Biointerfaces* 173, 591–598. doi: 10.1016/j.colsurfb.2018.10.031

Zheng, Y. Y., Xiong, C. D., Wang, Z. C., and Zhang, L. F. (2015). Enhanced osteoblast cells adhesion, spreading, and proliferation to surface-carboxylated poly(etheretherketone). *J. Bioact. Comp. Polym.* 30, 302–318. doi: 10.1177/0883911515572494

Zhu, T., Cui, Y., Zhang, M., Zhao, D., Liu, G., and Ding, J. (2020). Engineered three-dimensional scaffolds for enhanced bone regeneration in osteonecrosis. *Bioact. Mater.* 5, 584–601. doi: 10.1016/j.bioactmat.2020.04.008

Conflict of Interest: The authors declare that the research was conducted in the absence of any commercial or financial relationships that could be construed as a potential conflict of interest.

frontiers
in Bioengineering and Biotechnology

ORIGINAL RESEARCH
published: 18 December 2020
doi: 10.3389/fbioe.2020.610284

Customized Borosilicate Bioglass Scaffolds With Excellent Biodegradation and Osteogenesis for Mandible Reconstruction

Peng Zhang[1,2], Kang Yang[3], Ziyu Zhou[1,2], Xingrong Zhu[1,2], Wenchao Li[4,5], Chuanliang Cao[4,5], Kui Zhou[4,5], Lan Liao[1,2]* and Fanrong Ai[4,5]*

[1] School of Stomatology, Nanchang University, Nanchang, China, [2] The Key Laboratory of Oral Biomedicine, Jiangxi Province, Nanchang, China, [3] School of Pharmacy, Nanchang University, Nanchang, China, [4] School of Mechatronics Engineering, Nanchang University, Nanchang, China, [5] Nanchang Municipal Key Laboratory of 3D Bioprinting Technology and Equipment, Nanchang, China

OPEN ACCESS

Edited by:
Bing Han,
Peking University School and Hospital of Stomatology, China

Reviewed by:
Bin Duan,
University of Nebraska Medical Center, United States
Saeid Kargozar,
Mashhad University of Medical Sciences, Iran

***Correspondence:**
Lan Liao
liaolan5106@163.com
Fanrong Ai
afr3755875@126.com

Specialty section:
This article was submitted to Biomaterials, a section of the journal Frontiers in Bioengineering and Biotechnology

Received: *25 September 2020*
Accepted: *06 November 2020*
Published: *18 December 2020*

Citation:
Zhang P, Yang K, Zhou Z, Zhu X, Li W, Cao C, Zhou K, Liao L and Ai F (2020) Customized Borosilicate Bioglass Scaffolds With Excellent Biodegradation and Osteogenesis for Mandible Reconstruction. Front. Bioeng. Biotechnol. 8:610284. doi: 10.3389/fbioe.2020.610284

Graft reconstruction of the mandible is an important approach that aims at improving the appearance and functionality of defected mandibles. The traditional implant materials are generally bioinert, non-degradable, and that they lack favorable pore structures for cell proliferation, which limit their clinical application. In this study, we used boron-containing bioactive glass which was combined with a three-dimensional (3D) printing technology to construct an osteoinductive implant scaffold, according to the imaging instructions of CT scan on bone defects. Here, the boron-containing bioglass scaffold (B-BGs) was prepared through sol-gel processing and a 3D print technique. Different boron content of borosilicate bioglass was prepared by incorporating B_2O_3 (molar: 19.4 and 38.8%) into 58S bioglass to replace parts of SiO_2. For fabricated mandible implants through three-dimensional 3D printing of B-BGs (size: 8 × 2 mm; pore size: 250 μm) modified with borosilicate bioglass powder and sodium alginate. Notably, the compressive strength of the B-BGs was about 3.8 Mpa, which supported mandibular activity. Subsequently, the excellent biocompatibility of B-BGs was confirmed using cytotoxicity *in vitro* studies. Finally, data from *in vivo* experiments demonstrated that the B-BGs could promote bone regeneration and they could almost get completely degraded within 4 weeks. Our results showed that the boron-containing bioglass could repair mandibular defects.

Keywords: borosilicate bioglass, mandible reconstruction, degradation, osteogenesis, 3D printing

INTRODUCTION

Mandibular defects usually occur after bone tumor resections, osteomyelitis, trauma, and congenital deformities and are accompanied by tissue destruction and alveolar bone absorption, causing insufficient bone mass (Khan et al., 2015; Brown et al., 2016; Beth-Tasdogan et al., 2017). Regardless of their etiology, they can cause severe alteration on the mandibular contour, which could also impact its morphology, and function. Surgical reconstruction of segmental mandibular remains a significant clinical problem because of the limited self-repair capacity of the mandibles (Khan et al., 2015; Nickel et al., 2018; Sculean et al., 2019).

Clinically, to promote the healing of fractures and large defects autologous or allogeneic bone transplantation methods are still the most popular options (Myeroff and Archdeacon, 2011; Fillingham and Jacobs, 2016). However, the use of these materials also imposes many limitations. First, the use of the allogeneic bone transplantation method could trigger immune reactions and possible disease transmissions, which is challenging for patients diagnosed with tumors or are suffering from severe infections (O'Sullivan et al., 2017). Secondly, due to donor limitations, it is often challenging to obtain a graft with a compatible shape and size to the damaged site. However, some inert implant materials, like titanium alloy materials, seem to avoid these risks. Nevertheless, the overall implant success rate of titanium and its alloy is only 93.0–96.6% after 6 months, which is inevitably accompanied by the possibility of implant-related complications such as screw loosening and steel plate breakage (Mestas et al., 2016; Bormann et al., 2018). These disadvantages result in the traditional inert materials being nearly difficult to reconstruct well in the defect (Namm et al., 2018; Ramadanov et al., 2020).

It is therefore deemed critical that a more effective treatment strategy to fast restore the function and morphology of the mandible is required. The ideal mandibular repair material requires macropore and micropore structures that are similar to the bone to support vascular endogenesis, proliferation of the cell, regeneration of the bone, and cytokine exchange, and secondly, it should be compatible with the defect to support mandibular activity (Kim et al., 2017; Zhang et al., 2019; Chen et al., 2020). The three-dimensional printing technology has emerged as a promising modality with considerable advantages in customizing the implants to meet diverse individual needs. This technique has been used in bone and joint repair, and vascular reconstruction (Lim, 2017; Shi et al., 2017; Pan et al., 2020). In our study, an improved bioactive glass combined with a 3D printing technique was used in the construction of an osteoinductive implant scaffold. Here, we first used a biocompatible sodium alginate solution as a solvent to dissolve the toxicity and irritation caused by the residue of traditional organic solvents and accomplish rapid prototyping ability through adjusting the different sodium alginate and bioglass ratios. Subsequently, the 3D printing technique used CT scan data from the defect sites, to generate B-BGs that mimic the structure and shape these sites.

Although tooth loss is usually attributed to trauma, tumors, etc. it is usually accompanied by the destruction and absorption of alveolar bone, which results in insufficient bone mass, particularly in the upper anterior teeth region. This makes it difficult for the traditional inert materials to reconstruct well in the defect. Different studies have suggested a series of promoting materials that have osteoinduction and vascular regeneration properties. For instance, bioglass has osteoinductive properties, and its ionic products may prompt osteoblast activity, which is deliberated to be caused through the over-expression of osteoblast-related genes present in it. Other materials like VEGF, PuF, etc. promote an increase in bone mass. Also, this bioglass promotes the proliferation of cells through IGF and glutamic acid synthesis. As a trace element, boron (B) has been considered essential for bone physiology. It is playing a regulatory role in the metabolism of various micronutrients such as calcium, phosphorus, aluminum and molybdenum. Moreover, it is reported that incorporation of B in bioactive glass could boost osteogenesis *in vitro* and *in vivo*. Therefore, it has received massive attention and is used in bone defect replacement repair caused by tumors and osteoporosis (Hoppe et al., 2011; Zeimaran et al., 2015).

In this study, a B-BG was obtained from boron which completely replaced sodium. Studies from previous articles have confirmed its osteoinductive aptitude and degradation characteristics (Xia et al., 2019; Deilmann et al., 2020; Houaoui et al., 2020; Li et al., 2020). Also, implants that were hard to degrade were described to cause long-term inflammatory reactions, and stress shielding occurs, which results in bone resorption and implant loosening due to mechanical properties that do not match that of the natural bone (Fedorowicz et al., 2007; Xu et al., 2020). However, the degradable bioactive glass can avoid the stress shielding effect and offer a place for new growth of bone as the material degrades. Notably, a good degradable implant must have a degradation rate that matches that of bone repair (Han et al., 2016; Yang et al., 2019). Reports have indicated that the traditional 58S bioglass, can only degrade 8% within 28 days, whereas the time taken by the conventional mandible repair technique is only 4–6 weeks, hence it inhibits the regeneration of the bone during its late-stage (Bak et al., 2010; Wong et al., 2010; Shuai et al., 2016). Nevertheless, the slow rate in degradation of the 58S bioglass could be as a result of the high dense mineral layer. For it to accelerate the degradation rate, studies have shown that the use of boron instead of silicon in the bioglass helps (Sanz-Herrera and Boccaccini, 2011; Moonesi Rad et al., 2019). With the introduction of the seed-soil theory, studies have also considered that angiogenesis is a vital guarantee for bone reconstruction and even long-term survival of implants. The osteoinduction effect of the boron-doped bioglass has been reported extensively, and some recent articles have shown that it can promote vascular remodeling (Westhauser et al., 2019). In our experiment, the boron-doped bioglass was used and its degradation rate and bioactivity improved for better mandibular repair.

MATERIALS AND METHODS

Synthesis of Boron-Contain Bioactive Glass

First, the B-BG was synthesized according to our previously developed methods (Ai et al., 2020). Then, ethanol was briefly dissolved in deionized water under constant magnetic stirring followed by the addition of the respective amounts of the individual precursors. Notably, the precursors were added as stated in the order below and each precursor was ensured that it completely dissolved before the next one was added. Tetraethyl orthosilicate (TEO, Aladdin, Shanghai, China), calcium nitrate tetrahydrate (Aladdin, Shanghai, China), triethyl phosphate (TEP, Aladdin, Shanghai, China), and Trinbutyl Borate (TBB, Aladdin, Tianjin, China) were used as precursors for SiO_2, CaO, P_2O_5, and B_2O_3, respectively. Subsequently, nitric acid (Macklin, Shanghai, China) was added to catalyze the hydrolysis reaction

TABLE 1 | The weight percentage (wt.%) of Boron-containing bioglass composition.

Batch	58S-0B	58S-1B	58S-2B
Weight percentage (wt.%)			
SiO_2	58.2	38.8	19.4
CaO	32.6	32.6	32.6
P_2O_5	9.2	9.2	9.2
B_2O_3	0	19.4	38.8

and the resulting solution stirred for 24 h at room temperature. Next, this solution was aged and dried for 48 h at a temperature of 80°C. The resulting gel was dried and calcinated for 2 h at a temperature of 800°C and a heating rate of 1°C min−1 and then naturally cooled in the furnace. **Table 1** illustrates the different compositions that were used in the preparation of Boron-containing Bioactive glass samples such as 0B, 1B, and 2B. The calcined product was ground in a mortar and pestle to obtain a fine powder which was sieved through a 200 mesh (75 μm).

Fabrication and Characterization of 3D Printed Scaffolds

To prepare ink for 3D printing, B-BG powders and 30 wt% sodium alginate (SA, Macklin, Shanghai, China) were mixed to obtain an aqueous solution, which was stirred thoroughly to get a well-mixed composite mixture. Here, the scaffolds were produced using an Inkjet 3D Printer. Next, the ink was printed through a nozzle using a layer-by-layer method. Notably, the printing extrusion speed set at 0.007 mm/s, and layer height and wire spacing set at 0.45 and 1.2 mm, respectively. Consequently, the prepared bioglass scaffolds were dried at room temperature and sintered at 800°C for 6 h.

Then, the selection of scaffold samples with a diameter of 8 mm and a height of 2 mm was done to test different mechanical properties. Afterward, the stress-strain curve of the B-BGs and that of the hydroxyapatite scaffold were measured using a Universal Testing Machine (SUNS, CMT560503050100, Shenzhen, China), and the compressive strength was calculated based on the obtained stress-strain curves. Subsequently, a Scanning electron microscope (JEOL Ltd, JSM-6701F03040700, Tokyo, Japan) was used to collect the surface structure and morphology of the stent. Lastly, X-Ray diffraction (Materials Talks, Empyrean 03030502, Netherlands) was performed to characterize the composition of hydroxyapatite and bioglass scaffold crystals and the formation of crystals throughout the process of bioglass mineralization.

In vitro Mineralization

The mechanism of bone-like apatite formation was investigated by soaking B-BGs in a simulated body fluid (SBF, Servicebio, Wuhan, China), in the mass ratio of 1: 100 and kept at 37°C. Next, the B-BGs were tested for mineralization after 42 days of immersion using the XRD analysis.

In vitro Cell Experiments

Sprague Dawley (SD) rats used in this experiment were procured from the Jiangxi University of Traditional Chinese Medicine. All animal experiments were approved by the Ethical Committee of the Second Affiliated Hospital of Nanchang University. To perform *in-vitro* cell experiments, the rat bone marrow mesenchymal stem cells (rBMSC) were first extracted, as outlined in previous studies (Yao et al., 2019). These cells were maintained in Dulbecco's Modified Eagle's Medium (DMEM/F-12, BI, Israel) which was supplemented with 10% fetal bovine serum (FBS, BI, Israel) and 1% penicillin-streptomycin (P/S, Thermo Fisher Scientific, MA, USA). Next, the B-BGs ionic dissolution product was prepared according to the ISO10993-5 standard protocol. In a nutshell, 1 g of the scaffold was added to 5 ml of DMEM/F-12 without serum, then incubated for 24 h at 37°C, and the ionic dissolution product was collected and stored at 4°C. Subsequently, the effect of the B-BGs ionic dissolution product on cell proliferation and survival was assessed using the cck-8 assay (Beyotime, Shanghai, China). Briefly, the rBMSC were seeded in 96-well plates at an initial density of 3×10^3 cells /well with different B-BGs ionic extracts concentrations following the manufacturer's recommendations. Notably, all cell cultures were performed at 37°C under a humidified atmosphere of 5% CO_2. Subsequently, at days 1, 3, and 7, serum-free medium supplemented with 10% cck-8 was added to each well. Consequently, the cells were incubated for 2 h at 37°C, and their absorbance measured at 450 nm using a microplate reader to evaluate their cell viability. Then, we used a dead cell staining kit (Yeason, Shanghai, China) to directly observe live/dead cells. Here, we inoculated 5×10^3 rBMSC in a 24-well plate, and used a diluted extract in the ratio of 1: 2 to simulate the fate of cells in close contact with the scaffold. Imaging of live/dead cells on days 1, 3, and 7 were performed using a fluorescence microscope (TE2000, Nikon, Japan) under an excitation light wavelength of 490 and 535 nm, respectively.

In vivo Animal Experiments

Male New Zealand white rabbit (3.5–4.0 kg) were purchased from the Department of Animal Science of Nanchang University and used to construct a rabbit mandibular defect model which directly assesses the effect and toxicity of the stent on mandibular repair. In summary, these rabbits were first anesthetized using 10% chloral hydrate (2.5 ml/kg). Next, the submandibular area was shaved, sterilized and the rabbits laid on a sterile sheet. Their skin was cut in sections, to separate the muscle and periosteum to expose the bone surface. Subsequently, a trephine bur was used to cut a circular defect (8 × 2 mm) in the region of the exposed mandibular.

The 12 New Zealand white rabbits were divided into three treatment groups: 1B- BGs, hydroxyapatite scaffolds, and blank control. The resulting scaffold was filled into the defect and sutured. Within 1 week after the operation, antibiotics were administered to the experimental animals. After 2 and 4 weeks, the rabbits were sacrificed using an intravenous injection of pentobarbital and their lower jaws were collected.

Imaging and Pathology Examination

The mandibular specimens were taken at the 4th and 8th weeks postoperatively, and they were scanned using a CT tomography at a voltage of 80 kVp and a current of 80 mA. After the initial calibration against known density standards, each complete mandible was scanned in a chilled dH_2O solution. Using the MicroView 2.2 software (GE Healthcare, Milwaukee, WI), two different regions of interest (ROIs) were identified for each hemi-mandible at the anterior and posterior bone graft interfaces as follows; the coronal plane was centered at the interface between the native bone and the iliac crest bone graft, which remained identifiable after graft incorporation. From this initial position, 20 frames were splined both anteriorly and posteriorly for a total of 40 consecutive frames per ROI. Next, several rotations and cropping of non-bone space were performed to guarantee uniform data measurement. Then, bone mineral density (BMD), bone volume fraction (BVF), and tissue mineral density (TMD) metrics were obtained from each of the ROI. After bone analysis, data on the anterior and posterior ROI from each animal were averaged for subsequent statistical analysis. Consequently, to assess bone density, bone volume fraction, trabecular bone separation, and bone thickness, CT scan images were then imported into a medical image processing software (Mimics 16.0; Materialize). Subsequently, to assess bone regeneration and inflammation, the obtained specimens from the hard tissue microtome were stained using a Hematoxylin-Eosin/HE Staining Kit which was procured from Solarbio, Shanghai, China. Lastly, to obtain an objective pathological evaluation, the pathological analysis of the slices was double-blinded by three experienced pathology-related practitioners.

Statistical Analysis

All data were expressed as mean ± standard deviation for at least three independent experiments. The differences between the control and experimental groups were compared using the Kruskal-Wallis one-way analysis of variance (ANOVA) and *t*-test to calculate statistical significance (Graphpad prism 8.0.1).

RESULTS AND DISCUSSION

Characterization and *in vitro* Mineralization of B-BGs

Hydroxyapatite, one form of calcium phosphate coating, has been widely used as a biocompatible scaffold for bioengineered bone implants (Wang et al., 2020; Yu et al., 2020; Zhu et al., 2020). However, it seems to have some certain type of acidity, whereas most reports have indicated that an alkaline environment inhibits the production of osteoclasts and promotes the proliferation of osteoblasts, thus reducing bone resorption (Arnett and Dempster, 1986; Arnett, 2008; Galow et al., 2017). On the other hand, bioglass contains alkali metals, which could slowly maintain a certain alkaline condition in the body fluid environment for a long time (El-Rashidy et al., 2017), hence, there could be a probability that it is a better material for the regeneration of bones. The SEM image analysis shows that this bioglass scaffold has a complete macrostructure, and a uniform pore size of 0.25 mm is formed through printing, which has a rough surface morphology that allows proper cell attachment. Besides, higher magnification microscopic images have shown that the pores ranged in size from several microns to tens of microns on the surface of this bioglass scaffold, whereas, as illustrated in **Figures 1A–D**, the hydroxyapatite scaffold only had a uniform pore size of about 1 μm which was observed on its surface. Our study hypothesized that this difference could be attributed to the volatilization of the solvent and the non-linear shrinkage of the bioglass, compared to the formation of crystals during the calcination of the hydroxyapatite. Moreover, the hypothesis that hydroxyapatite mainly exists in the form of crystals which hinder the exchange of cytokines in body fluids was confirmed from the X-ray powder diffraction results. Five characteristic peaks (peaks at 22.861°, 31.786°, and 34.054°) of the hydroxyapatite are clearly observed and conformed to the characteristic peaks of standard card No. Here, only a small amount of crystals will be generated, even after the B-BGs are sintered at high temperature (**Figure 1G**). As illustrated in **Figures 1E,F**, the weakening of the compressive strength and stress-strain curve of the B-BGs compared with that of HAs shown the important role of microstructures on mechanical properties. In this study, the compressive strength of B-BG was ∼1.2 MPa, much lower than 4.0 MPa of the hydroxyapatite scaffold. As shown in **Figure 1H**, after soaked in SBF, the B-BGs exhibited many additional new XRD signals, which are the characteristic peaks hydroxyapatite. Which confirmed the *in vitro* mineralization experiments indicated that after 42 days of immersion, most of the undegraded B-BGs became newly generated hydroxyapatite. Additionally, the inert materials that are hard to degrade can cause secondary fractures because of the unmatched strength of these materials and that of the new bone. During the movement of the mandible, the implanted scaffold wears out forming free particles, which cause embolism or inflammation (Koff et al., 2019; Qiu et al., 2020). However, the biodegradable glass can circumvent this problem.

In vitro Cell Compatibility

Since it is the first step in the process of bone reconstruction, this study further analyzed the fate of mesenchymal cells-osteoblasts which is crucial in repairing defective bones. Here, we identified that the optimal pH for the proliferation of osteoblasts was 8.4 (**Figure 2C**), and that it is a major mechanism by which the bioglass scaffold promotes bone repair (Galow et al., 2017; Zamani et al., 2019). The long-term cytotoxicity of scaffolds from the BMSC were measured using the CCK-8 assay. These cells were treated with increasing concentrations of the scaffold ionic dissolution product at days 1, 3, and 7. Although there was no significant difference in all these days compared to the blank group, the alkaline environment which was above the stated physiological pH did not cause great damage to these cells. As illustrated in **Figure 2**, the B-BGs exhibited a certain level of toxicity in the high-concentration of ionic dissolution products, but still, they have a higher biocompatibility than hydroxyapatite (**Figures 2B,C**). To simulate the fate of the cells in close contact with the scaffold, a scaffold ionic dissolution product ratio of 1: 8 was used. Then, cell viability was tested

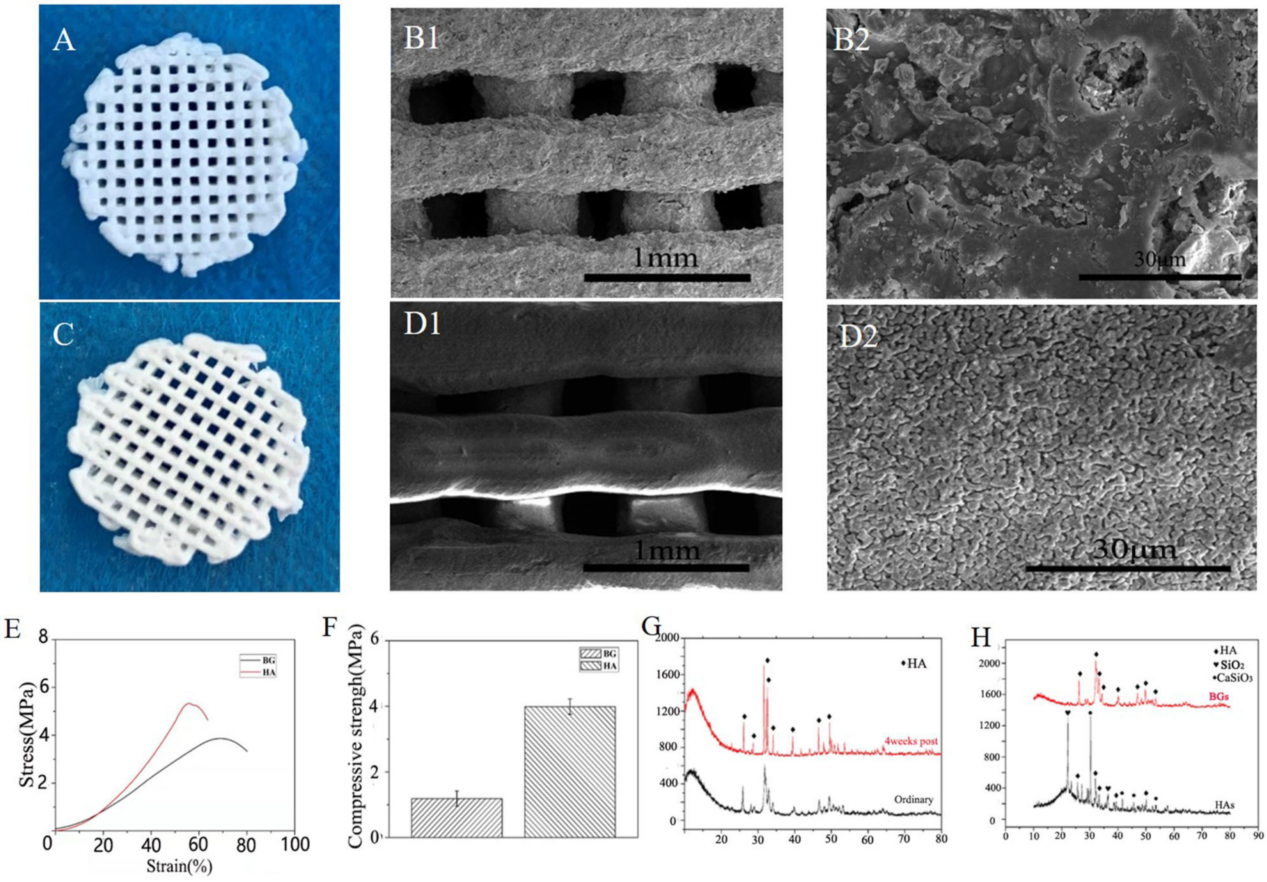

FIGURE 1 | Characterization and *in vitro* degradation of the B-BGs and HAs. **(A)** Photo and **(B)** SEM images of B-BGs; **(C)** photo and **(D)** SEM images of HAs**; (E)** the stress-strain curve of the B-BGs and Has; **(F)** compressive strength of the B-BGs and HAs; **(G)** The x-ray diffraction patterns of the ordinary and 4 weeks of the B-BGs; **(H)** The x-ray diffraction patterns of the B-BGs and Has.

using either live or dead cell staining techniques (**Figure 2A**). On the first day, the cells showed a round shape instead of the fusiform shape that is common to many mesenchymal stem cells, and this could be attributed to the fact that the plated cells did not fully extend on their first day of culture. However, from the normal spindle cells, flat and large cells appeared after 3 days of culture and this could be due to active osteoblasts, differentiated cohort cells, epithelial cell contamination, or the intolerance of the epithelial cells to alkali. Therefore, as illustrated in **Figure 1A**, this study affirms the first two speculations.

In vivo Osteogenesis of the Scaffold

The most direct evidence to evaluate the ability of the scaffold in promoting bone repair is through direct osteogenesis conducted in animals. This study exemplifies that small-animal models presents several challenges and limitations during the reconstruction of the mandible. Furthermore, we performed *in vivo* experiments to test the strength of the mandibles that were repaired using the bioglass implant. As illustrated in **Figure 1E**, our study established that despite the low strength of the boron-containing bioglass scaffold, all the experimental animals could eat on their own within 3 days after surgery. This shows that the bioglass scaffold can still perform certain functions under specific size defects in place of the defected bone. CT scans and *in vitro* jaw images show that the B-BGs have the fastest ability for bone repair mechanism. Here, results also showed that in the second week, it had degraded and repaired most of the defect structure. **Figure 4** shows that in the fourth week of the defect image, the defect repaired using the 1B scaffold had the most complete and smooth structure. The quantitative CT scan results are illustrated in **Figure 3** which shows that the B-BG-repaired defects have the following characteristics of the bone; highest density, volume fraction, and trabecular thickness compared to both the hydroxyapatite and the blank control groups. This indicated that the B-BGs produced the new bone mass during the repair process (**Figures 3A–D,F–H,J**). In all the above cases, we observed mild oozing from the oral incision site, perhaps due to the underlying mild inflammation that occurred 2 weeks after surgery. Nevertheless, this was completely

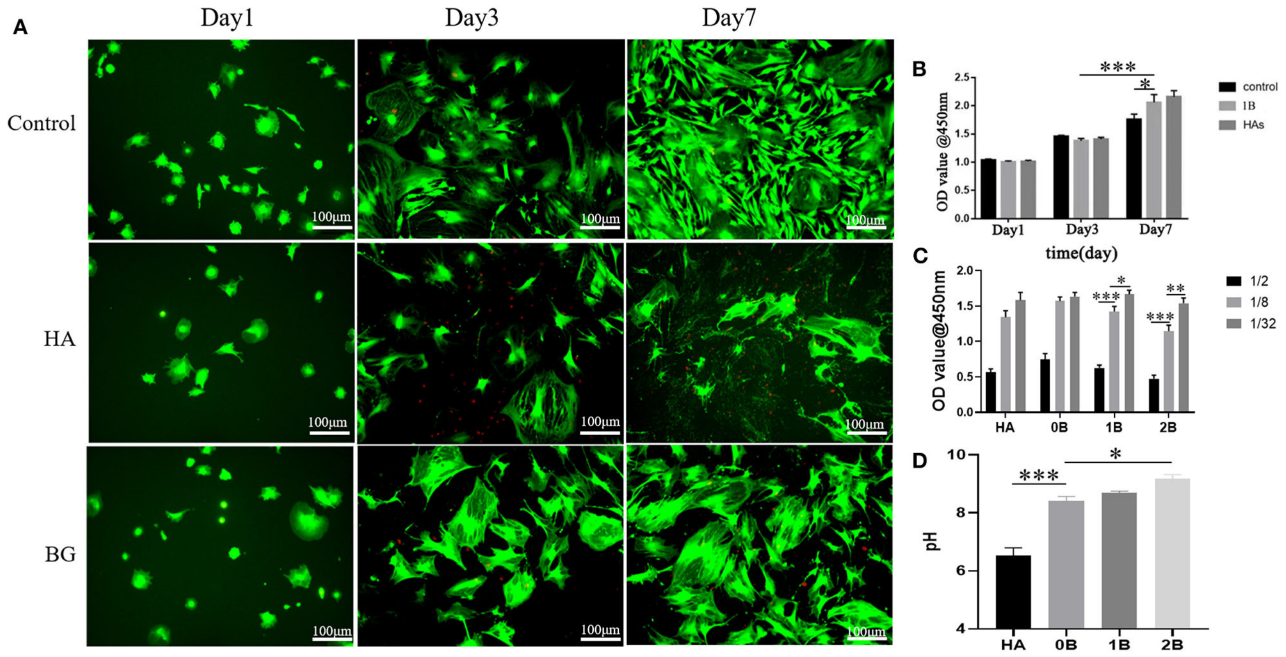

FIGURE 2 | *In vitro* cytotoxicity evaluation of BMSCs using the CCK8 assay and the Live/dead cell staining technique. **(A)** Live/dead cell staining for BMSCs with treatment of media (control), has an ionic dissolution product (HA), and 1B-BGs ionic dissolution product (BG); **(B)** Cell survival rate at different exposure time using different treatments; **(C)** Cell survival rate at different concentration of ionic dissolution products; **(D)** the pH value of different ionic dissolution products. **P* < 0.05, ***P* < 0.01, and ****P* < 0.001.

resolved through the 4-weeks recheck examination. A short-term BMP-induced inflammation is commonly reported and it begins on the 3rd day after surgery, peaks at 1 week, and typically resolves 2–3 weeks postoperatively (Lee et al., 2012). This response is anticipated as the bioglass scaffold exhibits chemotactic activity for inflammatory cells such as mononuclear and poly-morphonuclear cells and osteoclast-like cells. From our study, we, therefore, conclude that the general dose and method of application that uses the bioglass scaffold is viable, despite the minimal inflammation and mild oozing, hence, it is clinically appropriate as it resolves defects spontaneously by the 4th week after surgery.

The CT scan image formed a more complete bone tissue result. The boron-containing bioglass scaffold has the lowest trabecular bone separation. This means that the new one has the strongest strength and can efficiently treat the mandibular defects caused by bone resorption or other systemic diseases (**Figures 3E,I**). The methylene blue/magenta staining results further confirmed the CT scan results. Here, the B-BGs had the most osteoblasts (yellow arrows), more new bones (green arrows), and the least empty bone pockets (red arrows), nevertheless it is also observed in slices even in the fourth week after surgery. However, they partially contained undegraded material (white arrow). This could be due to the deficiencies of the sol-gel method used in the preparation of bioglass itself, that is, it is easy for insoluble calcium salts and silicates to be produced during the preparation process of bioglass scaffolds (**Figure 4**).

When deciding on the best facial reconstructive procedures, it is important to remember that the ultimate goals of mandibular reconstruction are to restore speech, masticatory function, swallowing, respiration, and to preserve facial features. In this study, we prepared a boron-containing bioglass using the sol-gel method and used Sodium alginate as a solvent to prepare a bone defect repair bracket that can be quickly printed. Notably, when this technique is combined with CT three-dimensional reconstruction technology, it is likely to quickly customize repair brackets with special sizes and structures according to the patient defects through 3D printing. Through the boron-substituted bioglass scaffolds, we found bioglass with a higher and faster degradation rate, and can slowly mineralize in body fluids to promote bone reconstruction. Besides, it has a certain strength that supports the normal functioning of the defective mandible. Also, it has good bone induction ability and can quickly repair damaged mandibles. Moreover, it promotes bone reconstruction and slows down its resorption, so that the new bone has a higher strength. In future work, we can improve the strength of the biological glass scaffold so that it can be applied to larger defects.

CONCLUSION

In this study, borosilicate bio-glass scaffolds matched with the defects were prepared by using CT scanning data combined with 3D printing technology according to the shape and

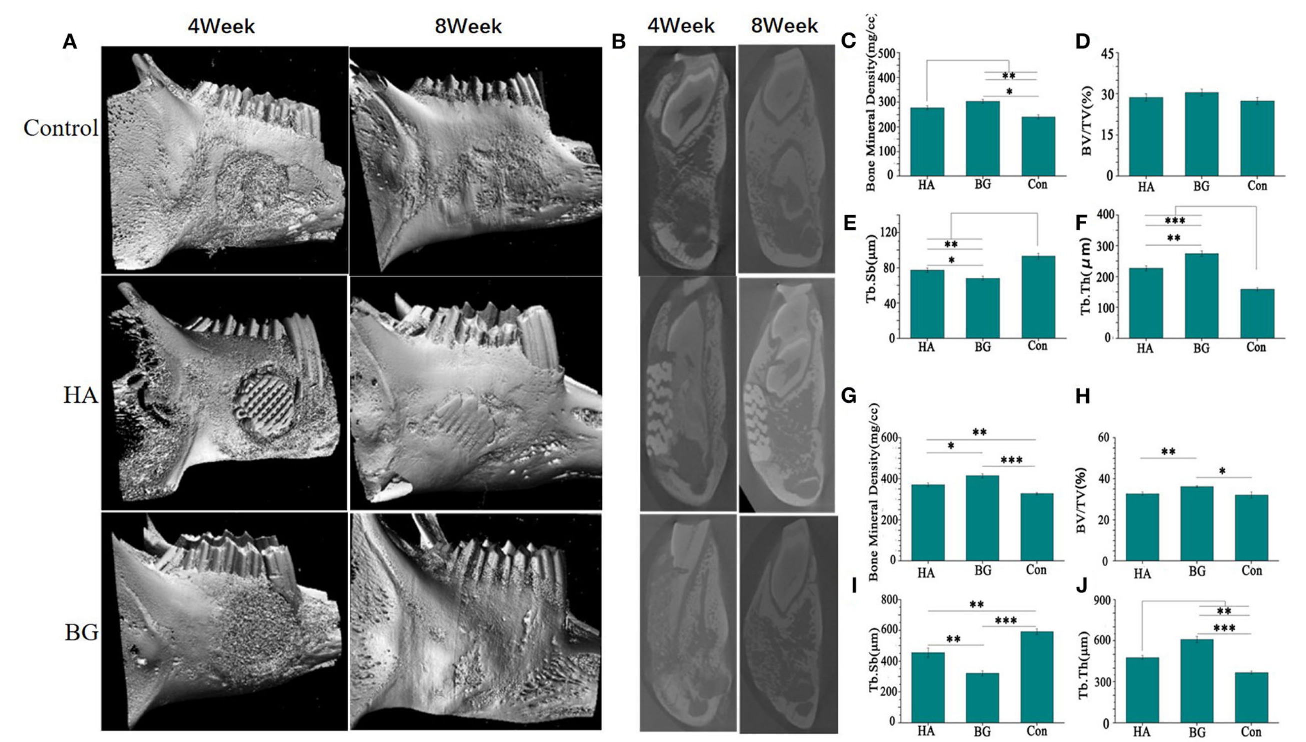

FIGURE 3 | The CT scan image**(A)** and sagittal image **(B)** of the harvested mandible healed for 4 weeks and 8 weeks; The bone mineral density (BMD) after 4 weeks **(C)** and 8 weeks **(G)**; The bone volume density (BV/TV) after 4 weeks **(D)** and 8 weeks **(H)**; The trabecular separation, (Tb.Sp) after 4 weeks **(E)** and 8 weeks **(I)**; The trabecular thickness(Tb.Th) after 4 weeks **(F)** and 8 weeks **(J)**. $^*P < 0.05$, $^{**}P < 0.01$, and $^{***}P < 0.001$.

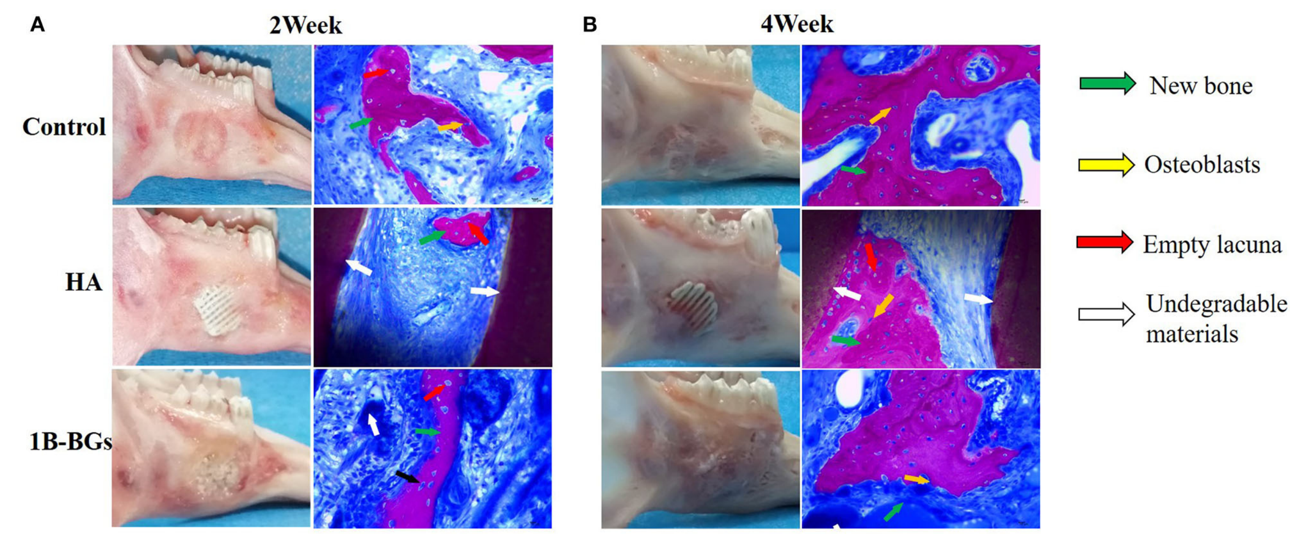

FIGURE 4 | Lower jaw tissue harvested after 2 and 4 weeks of treatment. Image of lower jaw and HE staining pictures after **(A)** 2 weeks and **(B)** 4 weeks of treatment. The osteoblasts (yellow arrows), new bones (green arrows), empty bone pockets (red arrows), and undegraded material (white arrow) were marked.

size of the mandibular defects. we have demonstrated that 3D of printed boron-containing bioactive glass scaffolds have good biocompatibility. their pore structure provides transport channels for nutrients and metabolites for cell growth, facilitates cell proliferation and promotes bone regeneration. almost completely degraded within 4 weeks after transplantation, with the gradual degradation of materials, new tissues adapted to the morphology and function of their own bone tissue are formed to repair the defective tissue. All in all, B bio-glass provides new hope for the repair of mandibular defects.

DATA AVAILABILITY STATEMENT

The raw data supporting the conclusions of this article will be made available by the authors, without undue reservation.

ETHICS STATEMENT

The animal study was reviewed and approved by Ethical Committee of Laboratory Animal Science Department, Nanchang University.

AUTHOR CONTRIBUTIONS

PZ, KY, and LL contributed to conception and design, data acquisition, analysis, interpretation, and drafting of the manuscript. ZZ and XZ contributed to data acquisition and drafting of the manuscript. WL, CC, and KZ contributed to interpretation and critical revision of the manuscript. FA contributed to conception and design, interpretation, and critical revision of the manuscript. All authors gave final approval and agreed to be accountable for all aspects of the work.

FUNDING

This work was jointly supported by the Science and Technology Project of Jiangxi Health Commission (No. 20203407).

REFERENCES

Ai, F., Chen, L., Yan, J., Yang K., Li. S., Duan, H., et al. (2020). Hydroxyapatite scaffolds containing copper for bone tissue engineering. *J. Sol Gel Sci. Techn.* 95, 168–179. doi: 10.1007/s10971-020-05285-0

Arnett, T. R. (2008). Extracellular pH regulates bone cell function. *J. Nutr*. 138, 415S—418S. doi: 10.1093/jn/138.2.415S

Arnett, T. R., Dempster, D. W. (1986). Effect of ph on bone-resorption by rat osteoclasts *in vitro*. *Endocrinology* 119, 119–124. doi: 10.1210/endo-119-1-119

Bak, M., Jacobson, A. S., Buchbinder, D., and Urken, M. L. (2010). Contemporary reconstruction of the mandible. *Oral Oncol.* 46, 71–76. doi: 10.1016/j.oraloncology.2009.11.006

Beth-Tasdogan, N. H., Mayer, B., Hussein, H., and Zolk, O. (2017). Interventions for managing medication-related osteonecrosis of the jaw. *Cochrane Database Syst. Rev*. 10:CD012432. doi: 10.1002/14651858.CD012432.pub2

Bormann, K., Gellrich, N., Kniha, H., Schild, S., Weingart, D., and Gahlert, M. (2018). A prospective clinical study to evaluate the performance of zirconium dioxide dental implants in single-tooth edentulous area: 3-year follow-up. *BMC Oral Health*. 18:181. doi: 10.1186/s12903-018-0636-x

Brown, J. S., Barry, C., Ho, M., and Shaw, R. (2016). A new classification for mandibular defects after oncological resection. *Lancet Oncol.* 17, E23–E30. doi: 10.1016/S1470-2045(15)00310-1

Chen, Z., Yan, X., Yin, S., Liu, L., Liu, X., Zhao, G., et al. (2020). Influence of the pore size and porosity of selective laser melted Ti6Al4V ELI porous scaffold on cell proliferation, osteogenesis and bone ingrowth. *Mater. Sci. Eng. C Mater. Biol. Appl.* 106:110289. doi: 10.1016/j.msec.2019.110289

Deilmann, L., Winter, O., Cerrutti, B., Bradtmüller, H., Herzig, C., Limbeck, A., et al. (2020). Effect of boron incorporation on the bioactivity, structure, and mechanical properties of ordered mesoporous bioactive glasses. *J. Mater. Chem. B* 8, 1456–1465. doi: 10.1039/C9TB01805K

El-Rashidy, A. A., Roether, J. A., Harhaus, L., Kneser, U., and Boccaccini, A. R. (2017). Regenerating bone with bioactive glass scaffolds: A review of *in vivo* studies in bone defect models. *Acta Biomater*. 62, 1–28. doi: 10.1016/j.actbio.2017.08.030

Fedorowicz, Z., Nasser, M., Newton, J. T., and Oliver, R. J. (2007). Resorbable versus titanium plates for orthognathic surgery. *Cochrane Database Syst. Rev*. 18:CD006204. doi: 10.1002/14651858.CD006204.pub2

Fillingham, Y., and Jacobs, J. (2016). Bone grafts and their substitutes. *Bone Joint J.* 98B, 6–9. doi: 10.1302/0301-620X.98B.36350

Galow, A., Rebl, A., Koczan, D., Bonk, S. M., Baumann, W., and Gimsa, J. (2017). Increased osteoblast viability at alkaline pH *in vitro* provides a new perspective on bone regeneration. *Biochem. Biophys. Rep*. 10, 17–25. doi: 10.1016/j.bbrep.2017.02.001

Han, J., Wan, P., Ge, Y., Fan, X., Tan, L., Li, J., et al. (2016). Tailoring the degradation and biological response of a magnesium-strontium alloy for potential bone substitute application. *Mater. Sci. Eng. C Mater. Biol. Appl.* 58, 799–811. doi: 10.1016/j.msec.2015.09.057

Hoppe, A., Güldal, N. S., and Boccaccini, A. R. (2011). A review of the biological response to ionic dissolution products from bioactive glasses and glass-ceramics *Biomaterials* 32, 2757–2774. doi: 10.1016/j.biomaterials.2011.01.004

Houaoui, A., Lyyra, I., Agniel, R., Pauthe, E., Massera, J., and Boissiere, M. (2020). Dissolution, bioactivity and osteogenic properties of composites based on polymer and silicate or borosilicate bioactive glass. *Mater. Sci. Eng. C Mater. Biol. Appl.* 107:110340. doi: 10.1016/j.msec.2019.110340

Khan, A. A., Morrison, A., Hanley, D. A., Felsenberg, D., McCauley, L. K., O'Ryan, F., et al. (2015). Diagnosis and management of osteonecrosis of the jaw: a systematic review and international consensus. *J. Bone Miner. Res.* 30, 3–23. doi: 10.1002/jbmr.2405

Kim, H. D., Amirthalingam, S., Kim, S. L., Lee, S. S., Rangasamy, J., and Hwang, N. S. (2017). Biomimetic materials and fabrication approaches for bone tissue engineering. *Adv. Healthc. Mater*. 6:1700612. doi: 10.1002/adhm.201700612

Koff, M. F., Esposito, C., Shah, P., Miranda, M., Baral, E., Fields, K., et al. (2019). MRI of THA correlates with implant wear and tissue reactions: a cross-sectional study. *Clin. Orthop. Relat. Res.* 477, 159–174. doi: 10.1097/CORR.0000000000000535

Lee, K., Taghavi, C. E., Murray, S. S., Song, K., Keorochana, G., and Wang, J. C. (2012). BMP induced inflammation: a comparison of rhBMP-7 and rhBMP-2. *J. Orthop. Res.* 30, 1985–1994. doi: 10.1002/jor.22160

Li, C., Hao, W., Wu, C., Li, W., Tao, J., Ai, F., et al. (2020). Injectable and bioactive bone cement with moderate setting time and temperature using borosilicate bio-glass-incorporated magnesium phosphate. *Biomed. Mater.* 15:045015. doi: 10.1088/1748-605X/ab633f

Lim, G. B. (2017). Vascular disease treatment of ischaemic vascular disease with 3D-printed vessels. *Nat. Rev. Cardiol.* 14, 442–443. doi: 10.1038/nrcardio.2017.101

Mestas, G., Alarcon, M., and Chambrone, L. (2016). Long-term survival rates of titanium implants placed in expanded alveolar ridges using split crest procedures: a systematic review. *Int. J. Oral Maxillofac. Implants.* 31, 591–599. doi: 10.11607/jomi.4453

Moonesi Rad, R., Pazarçeviren, E., Ece Akgün, E., Evis, Z., Keskin, D., Sahin, S., et al. (2019). *In vitro* performance of a nanobiocomposite scaffold containing boron-modified bioactive glass nanoparticles for dentin regeneration. *J. Biomater. Appl.* 33, 834–853. doi: 10.1177/0885328218812487

Myeroff, C., and Archdeacon, M. (2011). Autogenous bone graft: donor sites and techniques. *J. Bone Joint Surg. Am.* 93A, 2227–2236. doi: 10.2106/JBJS.J.01513

Namm, J. D., Morris, R. P., Speck, F. L., and Lindsey, R. W. (2018). The impact of eccentric diaphyseal plate and screw placement on the risk of peri-implant fracture. *J. Bone Joint Surg. Am*. 100, 1765–1770. doi: 10.2106/JBJS.18.00024

Nickel, J. C., Iwasaki, L. R., Gonzalez, Y. M., Gallo, L. M., and Yao, H. (2018). Mechanobehavior and ontogenesis of the temporomandibular joint. *J. Dent. Res.* 97, 1185–1192. doi: 10.1177/0022034518786469

O'Sullivan, E. D., Battle, R. K., Zahra, S., Keating, J. F., Marson, L. P., and Turner, D. M. (2017). Allosensitization following bone graft. *Am. J. Transpl.* 17, 2207–2211. doi: 10.1111/ajt.14231

Pan, S., Yin, J., Yu, L., Zhang, C., Zhu, Y., Gao, Y., et al. (2020). 2D MXene-integrated 3D-printing scaffolds for augmented osteosarcoma phototherapy and accelerated tissue reconstruction. *Adv. Sci.* 7:1901511. doi: 10.1002/advs.201901511

Qiu, J., Peng, P., Xin, M., Wen, Z., Chen, Z., Lin, S., et al. (2020). ZBTB20-mediated titanium particle-induced peri-implant osteolysis by promoting macrophage inflammatory responses. *Biomater. Sci.* 8, 3147–3163. doi: 10.1039/D0BM00147C

Ramadanov, N., Toma, I., Herkner, H., Klein, R., Behringer, W., and Matthes, G. (2020). Factors that influence the complications and outcomes of femoral neck fractures treated by cannulated screw fixation. *Sci. Rep*. 10:758. doi: 10.1038/s41598-020-57696-2

Sanz-Herrera, J. A., and Boccaccini, A. R. (2011). Modelling bioactivity and degradation of bioactive glass based tissue engineering scaffolds. *Int. J. Solids Struct.* 48, 257–268. doi: 10.1016/j.ijsolstr.2010.09.025

Sculean, A., Stavropoulos, A., and Bosshardt, D. D. (2019). Self-regenerative capacity of intra-oral bone defects. *J. Clin. Periodontol.* 46, 70–81. doi: 10.1111/jcpe.13075

Shi, W., Sun, M., Hu, X., Ren, B., Cheng, J., Li, C., et al. (2017). Structurally and functionally optimized silk-fibroin-gelatin scaffold using 3d printing to repair cartilage injury *in vitro* and *in vivo*. *Adv. Mater.* 29:1701089. doi: 10.1002/adma.201701089

Shuai, C., Cao, Y., Dan, G., Gao, C., Feng, P., and Wu, P. (2016). Improvement in degradability of 58s glass scaffolds by ZnO and beta-TCP modification. *Bioengineered* 7:342–351. doi: 10.1080/21655979.2016.1197032

Wang, Q., Tang, Y., Ke, Q., Yin, W., Zhang, C., Guo, Y., et al. (2020). Magnetic lanthanum-doped hydroxyapatite/chitosan scaffolds with endogenous stem cell-recruiting and immunomodulatory properties for bone regeneration. *J. Mater. Chem. B*. 8, 5280–5292. doi: 10.1039/D0TB00342E

Westhauser, F., Widholz, B., Nawaz, Q., Tsitlakidis, S., Hagmann, S., Moghaddam, A., et al. (2019). Favorable angiogenic properties of the borosilicate bioactive glass 0106-B1 result in enhanced *in vivo* osteoid formation compared to 45S5 Bioglass. *Biomater. Sci*. 7, 5161–5176. doi: 10.1039/C9BM01220F

Wong, R. C., Tideman, H., Kin, L., and Merkx, M. A. (2010). Biomechanics of mandibular reconstruction: a review. *Int. J. Oral Maxillofac. Surg.* 39, 313–319. doi: 10.1016/j.ijom.2009.11.003

Xia, L., Ma, W., Zhou, Y., Gui, Z., Yao, A., Wang, D., et al. (2019). Stimulatory effects of boron containing bioactive glass on osteogenesis and angiogenesis of polycaprolactone: *in vitro* study. *Biomed Res. Int.* 2019:8961409. doi: 10.1155/2019/8961409

Xu, X., Wang, C., Shou, W., Du, Z., Chen, Y., Li, B., et al. (2020). Physical realization of elastic cloaking with a polar material. *Phys. Rev. Lett.* 124:114301. doi: 10.1103/PhysRevLett.124.114301

Yang, D., Xiao, J., Wang, B., Li, L., Kong, X., and Liao, J. (2019). The immune reaction and degradation fate of scaffold in cartilage/bone tissue engineering. *Mater. Sci. Eng. C* 104:109927. doi: 10.1016/j.msec.2019.109927

Yao, M., Gao, F., Xu, R., Zhang, J., Chen, Y., and Guan, F. (2019). A dual-enzymatically cross-linked injectable gelatin hydrogel loaded with BMSC improves neurological function recovery of traumatic brain injury in rats. *Biomater. Sci.* 7, 4088–4098. doi: 10.1039/C9BM00749K

Yu, L., Rowe, D. W., Perera, I. P., Zhang, J., Suib, S. L., Xin, X., et al. (2020). Intrafibrillar mineralized collagen-hydroxyapatite-based scaffolds for bone regeneration. *ACS Appl. Mater. Interfaces* 12, 18235–18249. doi: 10.1021/acsami.0c00275

Zamani, D., Mortarzadeh, F., and Bizari, D. (2019). Alginate-bioactive glass containing Zn and Mg composite scaffolds for bone tissue engineering. *Int. J. Biol. Macromol.* 137, 1256–1267. doi: 10.1016/j.ijbiomac.2019.06.182

Zeimaran, E., Pourshahrestani, S., Djordjevic, I., Pingguan-Murphy, B., Kadri, N. A., and Towler, M. R. (2015). Bioactive glass reinforced elastomer composites for skeletal regeneration: a review. *Mater. Sci. Eng. C Mater. Biol. Appl.* 53, 175–188. doi: 10.1016/j.msec.2015.04.035

Zhang, Q., Wu, W., Qian, C., Xiao, W., Zhu, H., Guo, J., et al. (2019). Advanced biomaterials for repairing and reconstruction of mandibular defects. *Mater. Sci. Eng. C Mater. Biol. Appl.* 103:109858. doi: 10.1016/j.msec.2019.109858

Zhu, Y., Li, Z., Zhang, Y., Lan, F., He, J., and Wu, Y. (2020). The essential role of osteoclast-derived exosomes in magnetic nanoparticle-infiltrated hydroxyapatite scaffold modulated osteoblast proliferation in an osteoporosis model. *Nanoscale*. 12, 8720–8726. doi: 10.1039/D0NR00867B

Conflict of Interest: The authors declare that the research was conducted in the absence of any commercial or financial relationships that could be construed as a potential conflict of interest.

frontiers in Bioengineering and Biotechnology

ORIGINAL RESEARCH
published: 07 January 2021
doi: 10.3389/fbioe.2020.621601

Enhanced Osseointegration by the Hierarchical Micro-Nano Topography on Selective Laser Melting Ti-6Al-4V Dental Implants

Tianyu Shu*[1,2†], *Yuchen Zhang*[1†], *Guo Sun*[1], *Yang Pan*[1], *Gang He*[3], *Yilong Cheng*[4], *Ang Li*[1,5]* and *Dandan Pei*[1,6]

[1] Key Laboratory of Shaanxi Province for Craniofacial Precision Medicine Research, College of Stomatology, Xi'an Jiaotong University, Xi'an, China, [2] State Key Laboratory of Military Stomatology, School of Stomatology, The Fourth Military Medical University, Xi'an, China, [3] Frontier Institute of Science and Technology, Xi'an Jiaotong University, Xi'an, China, [4] School of Chemistry, Xi'an Jiaotong University, Xi'an, China, [5] Department of Periodontology, College of Stomatology, Xi'an Jiaotong University, Xi'an, China, [6] Department of Prosthodontics, College of Stomatology, Xi'an Jiaotong University, Xi'an, China

OPEN ACCESS

Edited by:
Jianxun Ding,
Changchun Institute of Applied Chemistry, Chinese Academy of Sciences, China

Reviewed by:
Fucong Tian,
Augusta University, United States
Jianfeng Zhou,
Peking University School of Stomatology, China
Hongye Yang,
Wuhan University, China

***Correspondence:**
Ang Li
drliang@mail.xjtu.edu.cn
Dandan Pei
peidandan1986@126.com

†These authors have contributed equally to this work

Specialty section:
This article was submitted to Biomaterials, a section of the journal Frontiers in Bioengineering and Biotechnology

Received: *26 October 2020*
Accepted: *30 November 2020*
Published: *07 January 2021*

Citation:
Shu T, Zhang Y, Sun G, Pan Y, He G, Cheng Y, Li A and Pei D (2021) Enhanced Osseointegration by the Hierarchical Micro-Nano Topography on Selective Laser Melting Ti-6Al-4V Dental Implants. Front. Bioeng. Biotechnol. 8:621601. doi: 10.3389/fbioe.2020.621601

Currently, selective laser melting (SLM) has been thriving in implant dentistry for on-demand fabricating dental implants. Based on the coarse microtopography of SLM titanium surfaces, constructing nanostructure to form the hierarchical micro-nano topography is effective in enhancing osseointegration. Given that current nanomodification techniques of SLM implants, such as anodization and hydrothermal treatment, are facing the inadequacy in costly specific apparatus and reagents, there has been no recognized nanomodified SLM dental implants. The present study aimed to construct hierarchical micro-nano topography on self-made SLM dental implants by a simple and safe inorganic chemical oxidation, and to evaluate its contribution on osteoblastic cells bioactivity and osseointegration. The surface chemical and physical parameters were characterized by FE-SEM, EDS, profilometer, AFM, and contact angle meter. The alteration on bioactivity of MG-63 human osteoblastic cells were detected by qRT-PCR. Then the osseointegration was assessed by implanting implants on the femur condyle of New Zealand Rabbits. The hierarchical micro-nano topography was constituted by the microrough surface of SLM implants and nanoneedles (diameter: 20∼50 nm, height: 150∼250 nm), after nanomodifying SLM implants in 30% hydrogen peroxide and 30% hydrochloride acid (volume ratio 1:2.5) at room temperature for 36 h. Low chemical impurities content and high hydrophilicity were observed in the nanomodified group. Cell experiments on the nanomodified group showed higher expression of mitophagy related gene (PINK1, PARKIN, LC3B, and LAMP1) at 5 days and higher expression of osteogenesis related gene (Runx2 and OCN) at 14 days. In the early stage of bone formation, the nanomodified SLM implants demonstrated higher bone-to-implant contact. Intriguingly, the initial bone-to-implant contact of nanomodified SLM implants consisted of more mineralized bone with less immature osteoid. After the cessation of bone formation, the bone-to-implant contact of nanomodified SLM implants was equal to untreated SLM implants and marketable TixOs implants. The overall findings indicated that the inorganic chemical oxidized hierarchical micro-nano topography could enhance the bioactivity of osteoblastic cells, and consequently promote the peri-implant bone formation and mineralization of SLM dental implants. This study sheds some light on improvements in additive manufactured dental implants.

Keywords: selective laser melting, dental implant, surface, hierarchical micro-nano topography, osseointegration

INTRODUCTION

Globally, over 275 million people were suffering from edentulous malady (Vos et al., 2016). As a routine procedure for replacing missing teeth, implant denture had demonstrated significant oral functional rehabilitation and excellent long-term prognosis (Bosshardt et al., 2017; Buser et al., 2017). Current dental implants were manufactured by traditional metal fabrication processes like forging, casting, hot rolling, and machining (Andani et al., 2014). Such implants were limited by fixed specification on macro design and dimension, that sometimes necessitated costly and invasive bone augmentation surgery (Oliveira and Reis, 2019). For on-demand dental implants fabrication, the selective laser melting (SLM), as one of additive manufacturing techniques, had shown great facilitations on product customization and cost control (Trevisan et al., 2018). Besides, due to the higher microroughness of SLM titanium surfaces could accommodate cell attachment and bone-to-implant mechanical anchorage (Dos Santos et al., 2019; Liu et al., 2019), SLM dental implants had demonstrated similar even better osseointegration than traditional dental implants (Oliveira and Reis, 2019). However, titanium and its alloys were bioinert (Bhargav et al., 2018). Modifying SLM dental implants to accelerate osseointegration was still an important issue.

The hierarchical micro-nano surface topography, due to its similarity with the multi-ordered structure of human bone, had become a better choice for intrabony biomaterials (Cui et al., 2019; Zhang et al., 2019). It had been proven that the bioactivity of SLM dental implants, including *in vitro* mesenchymal stem cells adherence, proliferation, differentiation, and *in vivo* osseointegration could be improved by the hierarchical micro-nano topography (Ferraris et al., 2011, 2019; Gulati et al., 2017; H. Wang et al., 2018; Yu et al., 2018). An up to date research had verified that the osteogenesis promoting effect of nanomodified SLM implants was strongly related to the integrin α2-PI3K-AKT signaling axis (Zheng et al., 2020). Today, SLM titanium surfaces could be nanomodified *via* anodization (Gulati et al., 2017), hydrothermal (H. Wang et al., 2018; Yu et al., 2018), or inorganic chemical treatments (Ferraris et al., 2011, 2019). These surface modifications enabled additional nanotopography while preserving the nature microroughness of SLM surfaces, and consequently constituted the hierarchical micro-nano topography. However, both anodization and hydrothermal treatment were under the need of specific apparatus and reagents. The current inorganic chemical treatment was also facing the limitation of dangerous hydrofluoride acid. There was no certified nanotextured SLM dental implant product yet.

In this study, we introduced the osseointegration of nanotextured SLM implants modified by an improved inorganic chemical oxidation method. Such protocol could be used to construct the hierarchical micro-nano topography on the surface of self-made SLM Ti-6al-4V dental implants in a simple and safe manner. For certifying the validity of nanomodification, we characterized the topography, roughness, chemical components, and wettability of modified and untreated SLM titanium surfaces. *In vitro* osteogenesis, mitochondrial dynamics and *in vivo* osseointegration were examined by MG-63 human osteoblastic cell culturing and animal experiments. A commercially available SLM dental implant (TixOs, Leader Implants, Italy) was used as the control group due to its favorable clinical case reports (Mangano et al., 2012, 2017). As the result, for SLM implants with hierarchical micro-nano topography, promoted bioactivity of osteoblastic cells was found at the gene expression level, and improved peri-implant bone formation and mineralization were proven by bone histomorphometric analysis. In brief, this paper tried to facilitate the development of hierarchical micro-nano topography for future SLM dental implants.

MATERIALS AND METHODS

SLM Implants Fabrication and Surface Modification

The raw material of SLM was Ti-6Al-4V powder in 25∼45 μm diameter. At first, the computer-aided design (CAD) model of an implant with 3.75 mm diameter and 6.0 mm height was designed in Solidworks 2015 and then exported to the printer (SLM-150, Hanbang, Guangzhou, China) in the STL format. Key SLM parameters include laser power (300 W), scanning rate (500 mm/s), line width (60 μm), and layer thickness (50 μm). Finally, SLM implants were ultrasonic cleaned in distilled water for 15 min, as the SLM-UT (untreated) group in this study. Half of SLM implants were selected randomly to be nanomodified. These implants were immersed in a mixture solution (volume ratio 1:2.5) of 30% hydrogen peroxide and 30% hydrochloride acid at room temperature. After 36 h, these nanomodified implants were rinsed with distilled water thoroughly, as the SLM-CO (chemical oxidized) group. For cell experiments, untreated and nanomodified SLM Ti-6Al-4V chips (10 mm × 10 mm × 1 mm) were also fabricated by the same working condition of SLM-UT and SLM-CO groups.

Surface Characterization

The surface topography was characterized by a field emission scanning electronic microscope (FE-SEM; Hitachi S-4800, Japan). The surface arithmetical mean height (S_a) at micro and nano scale were detected, respectively, by a 3D profilometer

(PS50, NANOVEA, United States) in a 400 μm × 400 μm area and an atomic force microscope (AFM; 5500, Agilent, United States) in a 2.5 μm × 2.5 μm area. The surface chemical composition was analyzed by an energy-dispersive X-ray spectrometer (EDS; EDAX, United States). The surface wettability with distilled water in the air was detected by an optical contact angle meter (DSA100, Kruss, Germany).

Cell Experiments

MG-63 Cells Seeding and Culturing

The SLM-UT and SLM-CO chips were sterilized by ultraviolet irradiation for 30 min and placed individually into the 24-well plate (Corning, United States). The human MG-63 osteoblastic cells (ATCC CRL1427, United States) were cultured in Dulbecco's Modified Eagle Medium (Gibco, United States) supplemented with 10% Fetal bovine serum (Gibco, United States) and 0.5% Anti-anti (Gibco, United States) at a primary density of 2×10^4 cells/well. Cells were incubated in a humidified atmosphere of 5% CO_2 at 37°C. The culture medium was renewed every 2 days.

MTT Assay

The cell proliferation level was evaluated by the MTT [3-(4,5-Dimethylthiazol-2-yl)2,5-diphenyltetrazolium bromide] assay at 1, 3, and 5 days after cell seeding. At each time point, SLM-UT and SLM-CO chips were transferred to new wells and incubated at 37°C with a culture medium containing MTT (0.5 mg/ml) for 4 h in dark. Next, the intracellular purple formazan product of each sample was dissolved using 375 μL dimethyl sulfoxide (DMSO). After smoothly oscillated for 15 min, 150 μL supernate in each sample was transferred to a 96-well plate (Corning, United States). The absorbance at 570 nm of each well was quantified by a spectrophotometer (Multiskan FC, Thermo, United States).

Alizarin Red Staining

After cell seeding for 14 days, SLM-UT and SLM-CO chips were washed with distilled water twice and fixed in 3.7% formaldehyde at room temperature for 10 min. To make mineralized nodules visualized, the chips were immersed in a 2% Alizarin red S solution (pH 4.2) at 37 °C and washed with distilled water after 30 min.

Quantitative Real-Time PCR

The Quantitative Real-time PCR (qRT-PCR) assay was performed to study the effect of nanomodified SLM implants on the expression of genes related to osteogenesis and mitochondrial dynamics. After seeding MG-63 cells for 5 and 14 days, respectively, total RNA was extracted by Trizol reagent (Invitrogen, United States). The quantity and quality of the RNA were measured by a nano spectrophotometer (DS-11, DeNovix, United States). Then, cDNA was synthesized through a reverse transcription premix kit (AG11706, Accurate Biotechnology, China). The glyceraldehyde-3-phosphate dehydrogenase (GAPDH) was used as the housekeeping gene. For investigating the mitochondrial dynamics, the relative expressions of peroxisome proliferator-activated receptor-γ coactivator-1 α and β (PGC-1α and PGC-1β), DNA polymerase γ (POLγ), mitochondrial transcription factor A (TFAM), mitofusin-1 (MFN1), mitofusin-2 (MFN2), dynamin-related protein-1 (DRP1), mitochondrial fission protein-1 (FIS1), phosphatase-and-tensin homolog-induced putative kinase 1 (PINK1), PARKIN, microtubule-associated protein-1 light-chain 3-B (LC3B), and lysosomal-associated membrane protein 1 (LAMP1) were measured at 5 days. For comparing the osteogenesis effect, the relative expressions of Runt-related transcription factor 2 (Runx2) and osteocalcin (OCN) were measured at 14 days. Primer sequences were listed in **Table 1** and synthesized by Sangon Biotech (Shanghai, China). The qRT-PCR procedure was performed by using SYBR green PCR reaction mix kit (AG11701, Accurate Biotechnology, China) on the real-time PCR system (AB 7500, Applied Biosystems, United States). Results were calculated using the $2^{-\Delta\Delta Ct}$ method and presented as fold regulations relative to the control.

Animal Experiment

Animal Surgical Operation

A rational animal model was vital for an animal experiment. The bone structure of rabbit femoral condyle was similar to that of human alveolar bone, which was spongy cancellous bone wrapped by thin cortical bone (Wu et al., 2019). Hence, the New Zealand Rabbit was widely used in evaluating dental implant functions (Wancket, 2015). The experiment protocol was approved by The Laboratory Animal Care and Welfare Committee, Fourth Military Medical University (No. 2018-K9-020). Male New Zealand Rabbits (weight 3.25 ± 0.25 kg) were obtained from the Junxing Biomedical (Xi'an, China), and were housed in a temperature-controlled room with 12 h alternating light-dark cycle at The Laboratory Animal Center, State Key Laboratory of Military Stomatology (Xi'an, China). Fodder and water were given ad labium. All rabbits were acclimatized for 7 days before the operation. For anesthesia, the xylazine hydrochloride injection (Huamu Veterinary Medicine, Jilin, China) at 0.1 mL/kg were intramuscularly injected, followed by a slow intravenous injection of 3% pentobarbital sodium (Sigma, United States) at 0.8 mL/kg. Benzylpenicillin sodium (Harbin Pharmaceutical Group Holding, Harbin, China) at 800,000 U was intramuscularly injected as a prophylactic antibiotic. Rabbits were then transferred to a thermostatic operating table to avoid hypothermia. We used a parapatellar incision to expose the outside surface of the femoral condyle in a minimal wound (**Supplementary Figure 1**). The planting hole (diameter: 3.75 mm, depth: 6.0 mm) was prepared by intermittent drilling at a speed of 800 rpm and rinsed with normal saline at 4°C. After douching implant holes with normal saline thoroughly, implants were rotated into holes slowly. Then the surgical field was irrigated by 80,000 U gentamicin and sutured in layers. During post-operation 5 days, all rabbits received wound disinfection with iodine and intramuscularly injecting benzylpenicillin sodium 800,000 U per 24 h.

Specimen Harvesting

Specimens were harvested at post-operation 2, 4, and 8 weeks. Each time point included 10 SLM-UT, 10 SLM-CO, and 5 TixOs implants. Rabbits were euthanized with a lethal dose of

TABLE 1 | Primer sequences used in quantitative real-time PCR.

Gene	Forward sequence	Reverse sequence
GAPDH	GCACCGTCAAGGCTGAGAAC	TGGTGAAGACGCCAGTGGA
Runx2	AGGCAGTTCCCAAGCATTTCATCC	TGGCAGGTAGGTGTGGTAGTGAG
OCN	CGCTACCTGTATCAATGGCTGG	CTCCTGAAAGCCGATGTGGTCA
PGC-1α	CAGAGAGTATGAGAAGCGAGAG	AGCATCACAGGTATAACGGTAG
PGC-1β	TTCAGACAGAACGCCAAGCATCC	CAGCACCTCGCACTCCTCAATC
POLγ	GCACCGTCAAGGCTGAGAAC	CAAGTCATTCAGACCCAGCTTGTA
TFAM	GAGGTGGTTTTCATCTGTCTTGG	CAACGCTGGGCAATTCTTCT
MFN1	GTGGCAAACAAAGTTTCATGTG	CACTAAGGCGTTTACTTCATCG
MFN2	GTGCTTCTCCCTCAACTATGAC	ATCCGAGAGAGAAATGGAACTC
DRP1	GAGATGGTGTTCAAGAACCAAC	CAATAACCTCACAATCTCGCTG
FIS1	AGTACGCCTGGTGCCTGGTG	GCTGTTCCTCCTTGCTCCCTTTG
PINK1	GGACGCTGTTCCTCGTTA	ATCTGCGATCACCAGCCA
PARKIN	AACCGGTACCAGCAGTATGG	TTCGCAGGTGACTTTCCTCT
LC3B	AGCAGCATCCAACCAAAA	CTGTGTCCGTTCACCAACAG
LAMP1	GTGTCTGCTGGACGAGAACA	TAGCCTGCGTGACTCCTCTT

pentobarbital sodium. Femur condyles of all rabbits were cut off carefully and then trimmed as implant-containing bone blocks (1.5 cm × 1.5 cm × 0.6 cm) by a bone tissue cutting machine (312, EXAKT, Germany). Then, all implant-containing bone blocks were immediately fixed in 4% formaldehyde for at least 72 h.

Micro CT

A micro X-ray 3D imaging system (Y.Cheetah, YXLON, Germany) was used to scanning the peri-implant bone structure, in the regime 55.6 μA and 90 kV. The isotropic resolution of scanning is 9 μm. Raw data were imported into VG Studio MAX 3.0.2 (Volume Graphics, Germany) and reconstructed *via* beam hardening correction and ring artifact elimination. The region of interest (ROI) was selected as a 72 μm thick shell appressed with the implant surface (**Supplementary Figure 2**). Such ROI contained all cancellous bone in contact with implant surfaces, which could reflect the three-dimensional bone-to-implant contact. Then the BV/TV, BS/BV, Tb.Th, Tb.N, and Tb.Sp of each sample was calculated based on the ROI to detect the amount, morphology, trabecular thickness, trabecular separation, and trabecular number, respectively, according to the bone histomorphometry guide by The Histomorphometry Nomenclature Committee of The American Society for Bone and Mineral Research (Dempster et al., 2013).

Undecalcified Histology Sections

After micro CT scanning, bone blocks were dehydrated in gradient ethanol solutions and embedded in the light-curing embedding resin (Technovit 7200 VLC, Kulzer, Germany). Using an undecalcified hard tissue microtome (300CP, EXAKT, Germany), primary sections in 200 μm thickness were prepared firstly. Then, primary sections were grinded and polished to the final thickness of 20∼30 μm using a hard tissue grinding system (400CS, EXAKT, Germany). Finally, Toluidine Blue O was used for staining sections. The osteoid was labeled as light blue while mature bone was deeper blue (Mouraret et al., 2014). Using the Bioquant Osteo 2019 software (Bioquant, United States), the bone-to-implant contact (BIC) was calculated by the length ratio of the bone-to-implant contact zone and intrabony implant perimeter (**Supplementary Figure 3A**). Also, the volume and surface fraction of osteoid was quantified by OV/BV and OS/BS, in the wound chamber between adjacent intrabony implant threads (**Supplementary Figure 3B**; Berglundh et al., 2003; Dempster et al., 2013).

Statistical Analysis

Data of qRT-PCR and bone histomorphometric analysis were expressed as mean ± standard deviation (SD). In cell experiments, three parallel samples in each group were used, and a multiple *t*-test with Benjamini, Krieger, and Yekutieli's *post hoc* was used for analyzing the significant difference. For comparing the osseointegration of SLM-UT, SLM-CO, and TixOs implants at 2, 4, and 8 weeks, a two-way analysis of variance (two-way ANOVA) with Tukey's *post hoc* was conducted in the animal experiment. The value of $P < 0.05$ was considered statistically significant.

RESULTS

Surface Topography and Roughness

The surface topography of SLM-UT, SLM-CO, and TixOs implants under FE-SEM were shown in **Figure 1**. At low magnifications, surfaces of three SLM implants were rich in randomly distributed balling structures (diameter: 10∼30 μm). At higher magnifications, the surface of SLM-CO implants displayed nanoneedles (diameter: 20∼50 nm, height: 150∼250 nm). No specific nanostructure was observed on the surface of SLM-UT implants. Groove submicrostructures (width: 0.17∼2.17 μm) were observed on the surface of TixOs implants, without specific nanostructure either. **Figure 2** illustrated the reconstructed 3D view of each implant by the profilometer and AFM, which was consistent with the FE-SEM observation. The S_a at micro and nano scales were

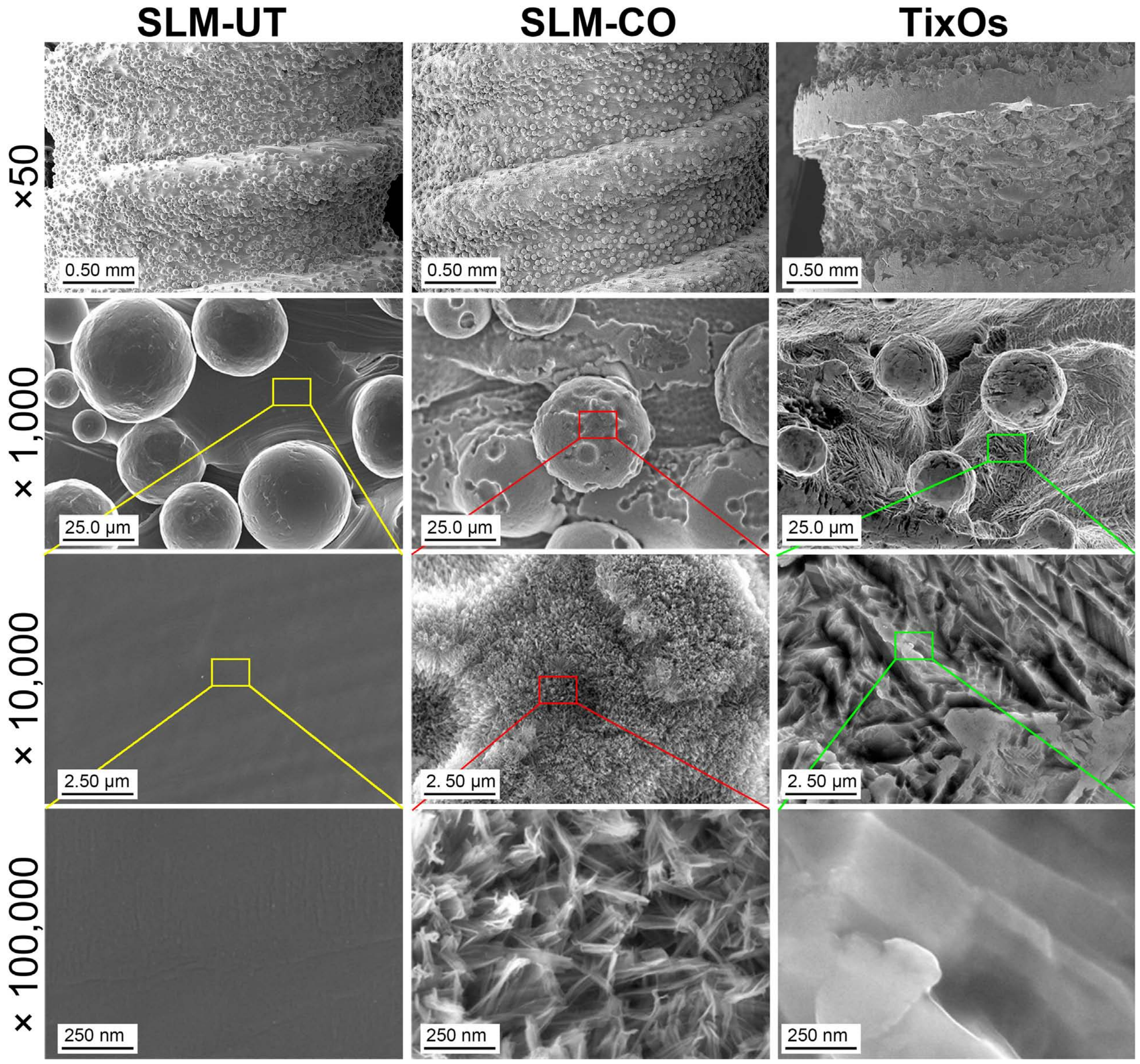

FIGURE 1 | Surface topography of three implants by the field emission scanning electron microscope.

calculated and listed in **Table 2**. The sequence of microroughness was SLM-UT>TixOs>SLM-CO, and of nanoroughness was SLM-CO > TixOs > SLM-UT.

Surface Chemical Composition and Wettability

The multi-curve-stack lines by Y offsets of EDS showed the composition of the chemical elements (**Figure 3**). Ti, Al, and V were detected on the surface of SLM-UT implants. Ti, O, and N were detected on the surface of SLM-CO implants. Ti, Al, V, C, and O were detected on the surface of TixOs implants. The weight percentage of each element were listed in **Table 3**. A video of the wetting process showed enhanced wettability of nanomodified SLM titanium surfaces (Movie 1). Both distilled water and blood could spread over quickly on SLM-CO rather than keeping relative static on SLM-UT and TixOs surfaces. To describe this striking contrast quantitatively, **Figure 4** showed the contact angle of three implants with distilled water in the air. The contact angle of SLM-UT and TixOs surfaces were higher than 90°, and of SLM-CO was less than 5°.

Cell Proliferation and Osteogenesis *in vitro*

The MG-63 cells proliferation measured by MTT assay was shown in **Figure 5A**. At 1, 3, and 5 days after cell seeding, the formazan solution absorbance of SLM-UT and SLM-CO surfaces

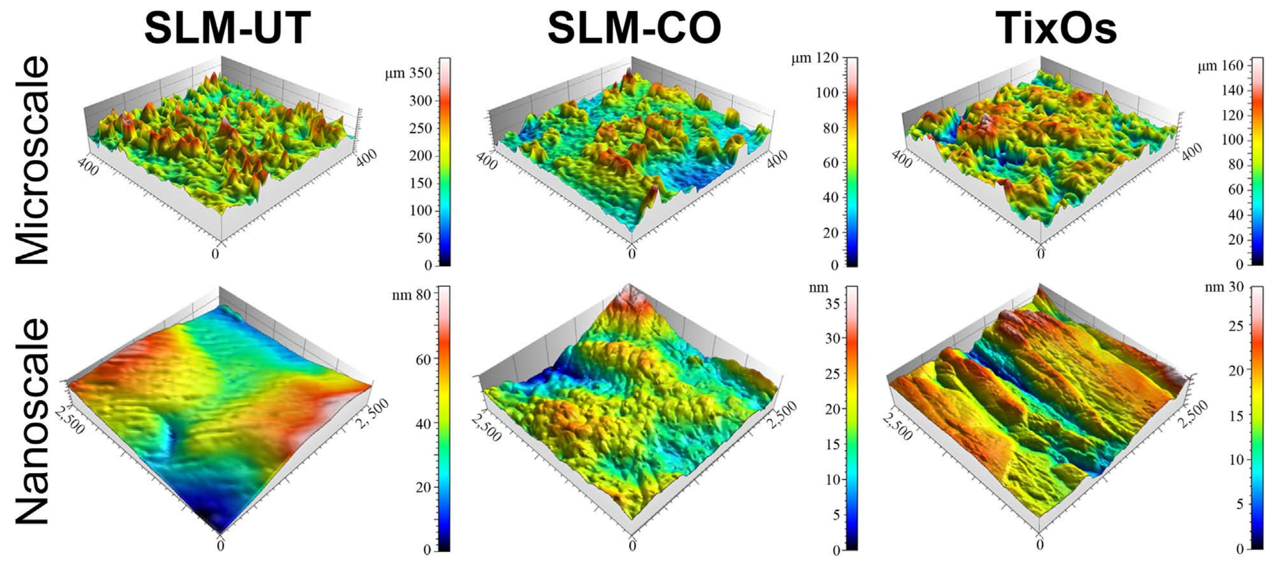

FIGURE 2 | Surface three-dimensional reconstruction view of three implants by the profilometer (at microscale) and atomic force microscope (at nanoscale).

TABLE 2 | The S_a at micro and nano scale of three implants in this study.

	S_a at microscale (μm)	S_a at nanoscale (nm)
SLM-UT	28.28	7.57
SLM-CO	12.82	54.33
TixOs	19.49	31.67

TABLE 3 | The surface chemical composition (weight percentage) of three implants in this study.

	Ti	O	Al	V	Other elements
SLM-UT	89.4%	–	6.3%	4.3%	–
SLM-CO	63.0%	34.1%	–	–	2.9% N
TixOs	79.8%	4.5%	5.6%	4.6%	5.4% C

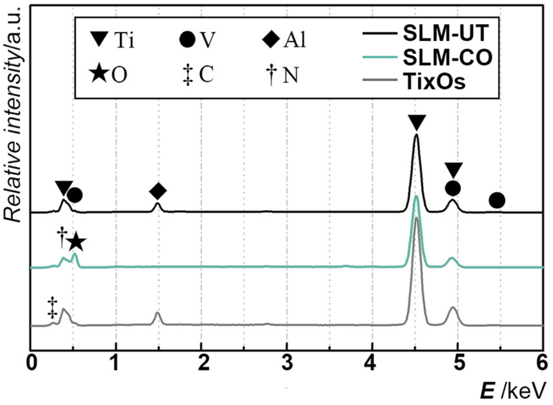

FIGURE 3 | The elements component of three implants, illustrated by the multi-curve-stack lines by Y offsets graph of energy-dispersive X-ray spectrometry.

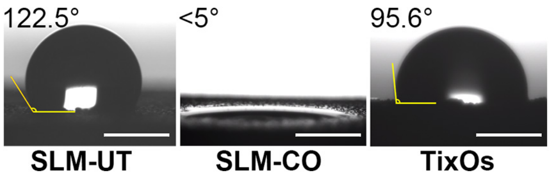

FIGURE 4 | The contact angle in the air with distilled water of three implants (bar = 0.5 mm).

both increased gradually. No significant difference existed between the two groups, implying that MG-63 cell proliferation was not affected on nanomodified SLM titanium surfaces.

At 5 days after cell seeding, significantly upregulated mitophagy markers (PINK1, PARKIN, LC3B, and LAMP1) of the SLM-CO surface were observed (**Figure 5B**). No significant difference was found on mitochondrial biogenesis (PGC-1α, PGC-1β, POLγ, and TFAM), fusion (MFN1 and MFN2), and fission (DRP1 and FIS1) markers between SLM-UT and SLM-CO surfaces. After culturing for 14 days, **Figure 5C** showed the relative expression level of Runx2 and OCN were upregulated significantly on SLM-CO surfaces. At the same time point, **Figure 5D** illustrated the photograph of alizarin red staining. The mineralized nodules on SLM-UT surfaces were sporadic and point-like, while on SLM-CO surfaces were larger and more continuous. These data indicated that the osteogenesis of MG-63 cells could be promoted by the nanomodified SLM titanium surfaces.

Osseointegration *in vivo*

The micro CT rendering graphic, accompanied with bone structural parameters of peri-implant bone were shown in **Figure 6**. The overall trend was the amount of peri-implant

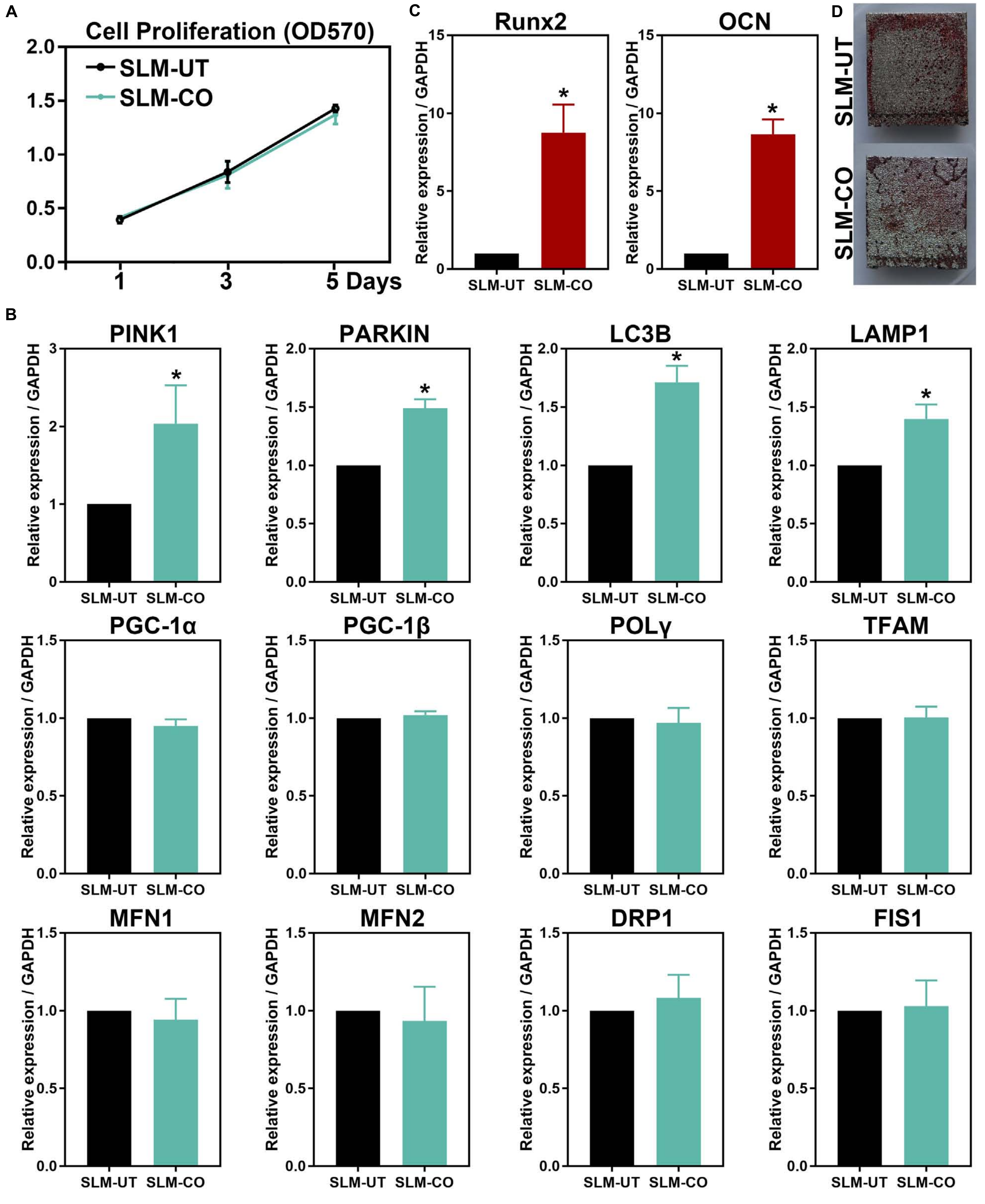

FIGURE 5 | The MG-63 cells proliferation, osteogenesis, and mitochondrial dynamics. **(A)** No significant difference in cell proliferation between SLM-UT and SLM-CO surfaces. **(B)** Upregulated relative gene expression of Runx2 and OCN at 14 days. **(C)** More continuous mineralization nodules of the SLM-CO surface. **(D)** Upregulated mitophagy related gene expression of the SLM-CO surface (*$P < 0.05$). No significant difference existed in mitochondrial biogenesis (PGC-1α, PGC-1β, POLγ, and TFAM), fission (DRP1 and FIS1), and fusion (MFN1 and MFN2) related gene expression ($P > 0.05$).

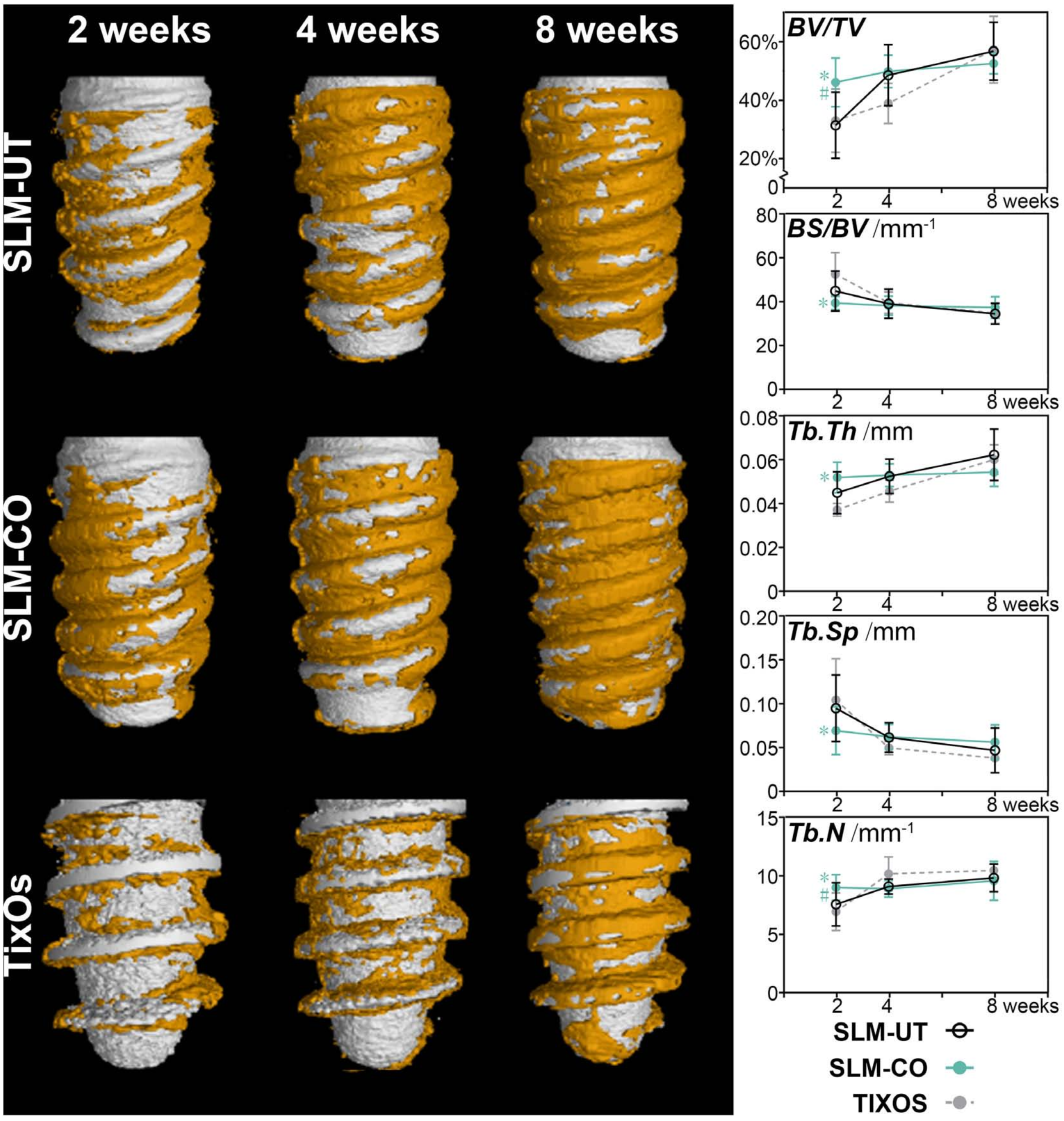

FIGURE 6 | The time sequence of osseointegration showed by micro-CT and the corresponding quantitative analysis of bone structural parameters (*significant difference between SLM-CO and TixOs, $P < 0.05$, $^{\#}$significant difference between SLM-CO and SLM-UT, $P < 0.05$).

bone of three implants was gradually increasing from 2 to 8 weeks after surgical implantation. At the time point of 2 weeks, the peri-implant bone of SLM-CO implants demonstrated a higher amount and density than SLM-UT and TixOs implants. Quantitatively, the BV/TV, Tb.Th, and Tb.N of SLM-CO implants at 2 weeks were significantly higher than SLM-UT and TixOs implants. The BS/BV and Tb.Sp of SLM-CO implants at 2 weeks were significantly lower than SLM-UT and TixOs implants. At 4 and 8 weeks, no significant differences of bone structural parameters were found between surfaces of SLM-UT, SLM-CO, and TixOs implants.

The utmost advantages of histological sections were including tissue response information than micro CT (Bissinger et al., 2017). Hence, we further quantified the mineralization level of peri-implant bone by undecalcified histology sections. As **Figure 7** illustrated, immature osteoid and woven bone at 2 weeks were gradually replaced by parallel-fiber bone, and finally transformed to mature lamellar bone at 8 weeks. The morphology of peri-implant bone was discrete and thin at 2 weeks, and become relatively continuous at 8 weeks. Quantitatively, the BIC of SLM-CO implants was significantly higher than SLM-UT and TixOs implants at 2 weeks and demonstrated no significant difference between 2 and 4 weeks. The most striking result was that the OV/BV and OS/BS of SLM-CO implants were significantly lower than SLM-UT implants at 2 weeks, which implied enhanced initial bone mineralization on nanomodified SLM dental implants. At 4 and 8 weeks, no significant differences of BIC, OV/BV, and OS/BS was found between SLM-UT, SLM-CO, and TixOs implants.

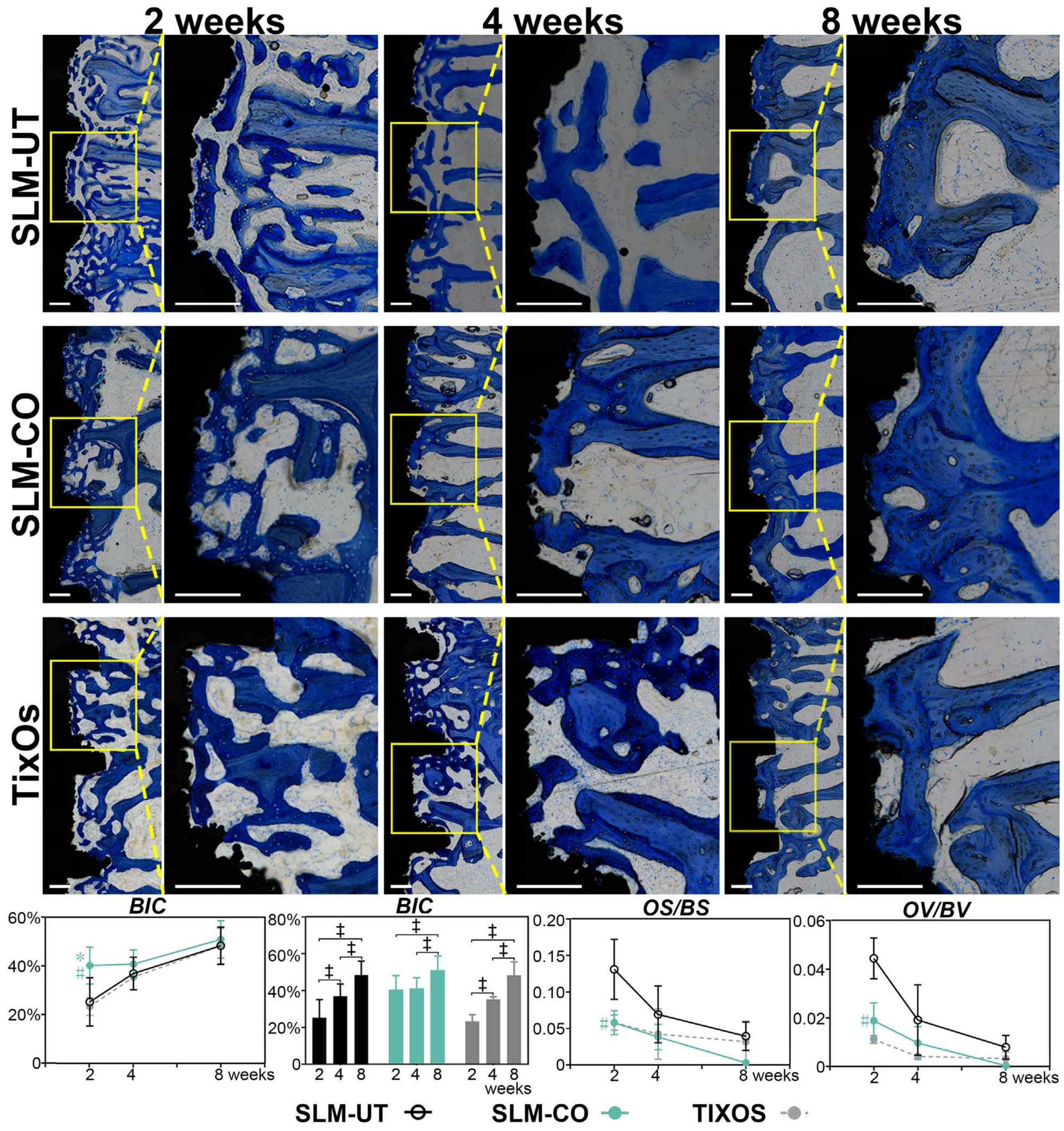

FIGURE 7 | The time sequence of osseointegration showed by Toluidine Blue O stained undecalcified histological sections and the corresponding quantitative analysis of bone-to-implant contact (BIC) and osteoid content (‡significant difference of BIC between different time points, $P < 0.05$, *significant difference between SLM-CO and TixOs, $P < 0.05$, $^{\#}$significant difference between SLM-CO and SLM-UT, $P < 0.05$).

DISCUSSION

In this study, according to bone histomorphology, it was proved that the peri-implant bone formation and mineralization could be promoted by the hierarchical micro-nano topography based on SLM dental implants. Besides, the *in vitro* effects on mitochondrial dynamics and osteogenesis was investigated as a possible mechanism in enhancing osseointegration. Some issues will be discussed next.

The SLM was a layer-by-layer fabrication process that used a laser to melt and fuse specific regions of metal powder (Yap et al., 2015). Universally, the natural surface topography of SLM titanium implants was coarse balling structures with a diameter of tens of microns (Ahmed, 2019). In implant dentistry, it had been recommended that both micro and nano topography could enhance osseointegration. The major contribution of the microtopography was improving cell compatibility and bone-to-implant mechanical interlocking (Gittens et al., 2011;

Albrektsson and Wennerberg, 2019), while the positive effect of the nanotopography was enhancing the initial adsorption of key proteins in tissue healing (Rupp et al., 2018; Albrektsson and Wennerberg, 2019; Ferraris et al., 2019). Combining advantages of microtopography and nanotopography, the hierarchical surface micro-nano topography had demonstrated its superiority in enhancing osseointegration of SLM titanium implants (Xu et al., 2016; Yu et al., 2018, 2019). This trend could also be revealed by enhanced osteogenic gene expression, BIC, and BV/TV in this study. The denser peri-implant bone of nanomodified SLM implants than untreated SLM and TixOs implants might contribute to strengthening the bone-to-implant mechanical anchorage. Osteoid was believed as the signal of new bone formation, and the amount of which decreased while new bone becoming mineralized and mature (Stadlinger et al., 2009; Ocana et al., 2017). We found less osteoid beside nanomodified SLM implants than untreated SLM implants at 2 weeks. Considering the higher BIC of nanomodified SLM titanium implants, this finding confirmed that the hierarchical surface micro-nano topography could promote peri-implant bone mineralization of SLM implants. No significant difference in osteoid content existed between the TixOs and SLM-CO group. A possible reason might be the submicron grooves on surfaces of TixOs implants could promote peri-implant bone mineralization. In conclusion, the histological evidence in this study could support the significance of hierarchical micro-nano topography on inorganic chemical oxidized SLM implants.

In cell experiments, the advantages of hierarchical micro-nano topography based on SLM titanium surfaces were also proven. Mitochondria acted as the potential target of nanomaterials and played an essential role in the energy metabolism of eukaryotic cells (Shen et al., 2018). Balanced mitochondrial dynamics could facilitate natural homeostasis of tissue function (Li et al., 2017). Detailly, mitochondrial biogenesis, fusion, and fission could keep mitochondria healthy, while fission and mitophagy could segregate and remove damaged mitochondria (Ni et al., 2015; Shen et al., 2018). Mitophagy was an evolutionarily conserved cellular process to stabilize cell energy metabolism by removing dysfunctional or superfluous mitochondria (Ashrafi and Schwarz, 2013; Palikaras et al., 2018). Also, the process of mitophagy was proven to participate in the cell-mediated biomineralization process. To be specific, the amorphous calcium phosphate, which was the precursor in biomineralization, could trigger mitophagy to transport intracellularly *via* the autophagosome and released to the extracellular matrix *via* exocytosis (Pei et al., 2018). In this study, with the relative expression of mitophagy-related gene upregulated at 5 days, the osteogenesis-related gene expression of SLM-CO group was promoted, which was consistent with other relevant studies (Hyzy et al., 2016; H. Wang et al., 2018; Yu et al., 2018). These results confirmed our conjecture that the hierarchical micro-nano topography could influence cell bioactivity for better osteogenesis performance.

Implant surface modifications were closely influencing osseointegration (Bosshardt et al., 2017). Physical, chemical, or biological techniques were used in surface modification of dental implants (Liu et al., 2019). In general, controlling surface roughness has been the holy grail of implant surface modification, avoiding limitations on detachment or potential toxicity of extra materials coating (Modaresifar et al., 2019). To form hierarchical micro-nano topography, plenty of techniques had been used in increasing the nanoroughness of microrough SLM titanium implants. Anodization was to induce nanopores or nanotubes on the anode metal surface under the assistance of electric field and temperature (Minagar et al., 2012; Q. Wang et al., 2020). The other process, hydrothermal treatment, was to prepare titanium oxide layer with nanotopography *via* surface crystallization procedure within an elevated temperature and aqueous media (Ali et al., 2020; Bencina et al., 2020). However, these techniques strongly depended on specific apparatus like electrochemical reactors or teflon-lined autoclaves. Lately, an inorganic chemical modification protocol was investigated, which simply used hydrofluoride acid and peroxide hydrogen to create nanotopography on titanium surfaces (Ferraris et al., 2011). Such modification had been demonstrated to improve osteoblasts progenitors' adhesion, proliferation, and extracellular matrix deposition of additive manufactured titanium implants (Ferraris et al., 2019), but its *in vivo* osseointegration had not been reported yet. In this study, we utilized an improved protocol of inorganic chemical oxidation to create nanotopography on SLM Ti-6Al-4V implant surfaces. Without expensive equipment and dangerous reagents, using hydrochloride acid and peroxide hydrogen at room temperature was relatively safe and low-cost. The surface topography of SLM-CO implants was similar to which of hydrothermal treated (Xu et al., 2016; Yu et al., 2018) or inorganic chemical oxidized (Ferraris et al., 2011) SLM implants in previous studies. Moreover, these nanoneedles could form extracellular matrix-like nanonets. Such nanonets structure had been proven to promote the alkaline phosphatase activity in osteogenesis than anodized nanotubes on SLM titanium surfaces (Xu et al., 2016). The relative higher value of nano-S_a could also reflect the existence of nanotopography of SLM-CO implants.

Considering that almost all surface modifications could alter the surface chemical and physical character (Dohan Ehrenfest et al., 2011; Albrektsson and Wennerberg, 2019), we further measured chemical element components and contact angle of different surfaces. The surface chemical elements component of SLM-CO implants was close to that of other nanomodified SLM titanium surfaces modified by anodization (64.11% titanium and 29.50% oxygen) and hydrothermal treatment (51.69% titanium and 43.53% oxygen) (Xu et al., 2016). Also, the absence of aluminum and vanadium on the SLM-CO surface kept consistence with anodized and hydrothermal treated SLM surface (Xu et al., 2016), which implied the formation of titanium oxide layer. Moreover, 2.9% nitrogen was found at the surface of SLM-CO implants, which was less than the impurity content of TixOs implants. The surface hydrophilicity was an important physical character influenced by surface modification, which could promote the initial blood wetting, protein adsorption, and subsequent wound healing process (Minagar et al., 2013; Chambrone et al., 2015; Calciolari et al., 2018; Donos et al., 2018; Kitajima et al., 2020). Generally, the osteogenesis stimulating effect of hydrophilic titanium surfaces was suggested (Gittens et al., 2014; Rupp et al., 2018). While the contact angle of SLM-UT and TixOs implants were similar to which of pure titanium (about 90°(Gittens et al., 2014)), the contact angle of SLM-CO implants was less than 5° and close to which of other nanomodified SLM implants (Hyzy et al., 2016). These results implied the benign chemical and physical characteristics of hierarchical surface micro-nano topography on SLM-CO implants.

In general, peri-implant new bone formation and mineralization of SLM titanium implants were successfully enhanced by the hierarchical micro-nano topography. The up-regulation of mitophagy level might serve as the facilitation. Two possible issues should be investigated in further study. Firstly, the enhancement of mitophagy was only studied at the gene expression level in the current study. Future works should be organized with more molecular biological methods. Secondly, the results of animal experiments on New Zealand rabbits could not be applied to clinical treatments. The human osseointegration of nanomodified SLM dental implants still needs to be evaluated through rigorous clinical trials and compared with conventional dental implants.

DATA AVAILABILITY STATEMENT

The original contributions presented in the study are included in the article/**Supplementary Material**, further inquiries can be directed to the corresponding authors.

ETHICS STATEMENT

The animal study was reviewed and approved by The Laboratory Animal Care and Welfare Committee, Fourth Military Medical University.

AUTHOR CONTRIBUTIONS

DP and AL provided the original research idea and constructive guidance. TS, YZ, YC, and GH fabricated the materials. TS, YZ, GS, and YP performed the experiments and organized the data. TS, YZ, GS, YC, GH, DP, and AL interpreted the data and wrote the manuscript. AL provided the financial support for this work. All authors contributed to the article and approved the submitted version.

FUNDING

The authors appreciated the support by the National Natural Science Foundation of the People's Republic of China (81870798), the Fundamental Research Funds for the Central Universities (xtr012019007), and the Opening Research from State Key Laboratory of Military Stomatology (2017KA01).

ACKNOWLEDGMENTS

The authors feel grateful to Tao Zhou (State Key Laboratory for Manufacturing Systems Engineering, Xi'an Jiaotong University) for his assistance with micro CT.

SUPPLEMENTARY MATERIAL

The Supplementary Material for this article can be found online at: https://www.frontiersin.org/articles/10.3389/fbioe.2020.621601/full#supplementary-material

REFERENCES

Ahmed, N. (2019). Direct metal fabrication in rapid prototyping: a review. *J. Manufact. Process.* 42, 167–191. doi: 10.1016/j.jmapro.2019.05.001

Albrektsson, T., and Wennerberg, A. (2019). On osseointegration in relation to implant surfaces. *Clin. Implant. Dent. Relat. Res.* 21(Suppl. 1), 4–7. doi: 10.1111/cid.12742

Ali, N., Ali, F., Khurshid, R., Ikramullah, Ali, Z., Afzal, A., et al. (2020). TiO2 nanoparticles and Epoxy-TiO2 nanocomposites: a review of synthesis, modification strategies, and photocatalytic potentialities. *J. Inorgan. Organometal. Polym. Mater.* 30, 4829–4846. doi: 10.1007/s10904-020-01668-6

Andani, M. T., Shayesteh Moghaddam, N., Haberland, C., Dean, D., Miller, M. J., and Elahinia, M. (2014). Metals for bone implants. Part 1. Powder metallurgy and implant rendering. *Acta Biomater.* 10, 4058–4070. doi: 10.1016/j.actbio.2014.06.025

Ashrafi, G., and Schwarz, T. L. (2013). The pathways of mitophagy for quality control and clearance of mitochondria. *Cell Death Differ.* 20, 31–42. doi: 10.1038/cdd.2012.81

Bencina, M., Iglic, A., Mozetic, M., and Junkar, I. (2020). Crystallized TiO2 nanosurfaces in biomedical applications. *Nanomaterials (Basel)* 10:1121. doi: 10.3390/nano10061121

Berglundh, T., Abrahamsson, I., Lang, N. P., and Lindhe, J. (2003). De novo alveolar bone formation adjacent to endosseous implants. *Clin. Oral Implants Res.* 14, 251–262. doi: 10.1034/j.1600-0501.2003.00972.x

Bhargav, A., Sanjairaj, V., Rosa, V., Feng, L. W., and Fuh Yh, J. (2018). Applications of additive manufacturing in dentistry: a review. *J. Biomed. Mater. Res. B Appl. Biomater.* 106, 2058–2064. doi: 10.1002/jbm.b.33961

Bissinger, O., Probst, F. A., Wolff, K. D., Jeschke, A., Weitz, J., Deppe, H., et al. (2017). Comparative 3D micro-CT and 2D histomorphometry analysis of dental implant osseointegration in the maxilla of minipigs. *J. Clin. Periodontol.* 44, 418–427. doi: 10.1111/jcpe.12693

Bosshardt, D. D., Chappuis, V., and Buser, D. (2017). Osseointegration of titanium, titanium alloy and zirconia dental implants: current knowledge and open questions. *Periodontology 2000* 73, 22–40. doi: 10.1111/prd.12179

Buser, D., Sennerby, L., and De Bruyn, H. (2017). Modern implant dentistry based on osseointegration: 50 years of progress, current trends and open questions. *Periodontology 2000* 73, 7–21. doi: 10.1111/prd.12185

Calciolari, E., Hamlet, S., Ivanovski, S., and Donos, N. (2018). Pro-osteogenic properties of hydrophilic and hydrophobic titanium surfaces: Crosstalk between signalling pathways in in vivo models. *J. Periodont. Res.* 53, 598–609. doi: 10.1111/jre.12550

Chambrone, L., Shibli, J. A., Mercurio, C. E., Cardoso, B., and Preshaw, P. M. (2015). Efficacy of standard (SLA) and modified sandblasted and acid-etched (SLActive) dental implants in promoting immediate and/or early occlusal loading protocols: a systematic review of prospective studies. *Clin. Oral Implants Res.* 26, 359–370. doi: 10.1111/clr.12347

Cui, Y., Zhu, T., Li, D., Li, Z., Leng, Y., Ji, X., et al. (2019). Bisphosphonate-functionalized scaffolds for enhanced bone regeneration. *Adv. Healthc Mater.* 8:e1901073. doi: 10.1002/adhm.201901073

Dempster, D. W., Compston, J. E., Drezner, M. K., Glorieux, F. H., Kanis, J. A., Malluche, H., et al. (2013). Standardized nomenclature, symbols, and units for bone histomorphometry: a 2012 update of the report of the ASBMR Histomorphometry Nomenclature Committee. *J. Bone Miner. Res.* 28, 2–17. doi: 10.1002/jbmr.1805

Dohan Ehrenfest, D. M., Vazquez, L., Park, Y. J., Sammartino, G., and Bernard, J. P. (2011). Identification card and codification of the chemical and morphological characteristics of 14 dental implant surfaces. *J. Oral Implantol.* 37, 525–542. doi: 10.1563/AAID-JOI-D-11-00080

Donos, N., Horvath, A., Mezzomo, L. A., Dedi, D., Calciolari, E., and Mardas, N. (2018). The role of immediate provisional restorations on implants with a hydrophilic surface: a randomised, single-blind controlled clinical trial. *Clin. Oral Implants Res.* 29, 55–66. doi: 10.1111/clr.13038

Dos Santos, L. C. P., Malheiros, F. C., and Guarato, A. Z. (2019). Surface parameters of as-built additive manufactured metal for intraosseous dental implants. *J. Prosthet. Dent.* 124, 217–222. doi: 10.1016/j.prosdent.2019.09.010

Ferraris, S., Cochis, A., Cazzola, M., Tortello, M., Scalia, A., Spriano, S., et al. (2019). Cytocompatible and anti-bacterial adhesion nanotextured titanium oxide layer on titanium surfaces for dental and orthopedic implants. *Front. Bioeng. Biotechnol.* 7:103. doi: 10.3389/fbioe.2019.00103

Ferraris, S., Spriano, S., Pan, G., Venturello, A., Bianchi, C. L., Chiesa, R., et al. (2011). Surface modification of Ti-6Al-4V alloy for biomineralization and specific biological response: Part I, inorganic modification. *J. Mater. Sci. Mater. Med.* 22, 533–545. doi: 10.1007/s10856-011-4246-2

Gittens, R. A., McLachlan, T., Olivares-Navarrete, R., Cai, Y., Berner, S., Tannenbaum, R., et al. (2011). The effects of combined micron-/submicron-scale surface roughness and nanoscale features on cell proliferation and differentiation. *Biomaterials* 32, 3395–3403. doi: 10.1016/j.biomaterials.2011.01.029

Gittens, R. A., Scheideler, L., Rupp, F., Hyzy, S. L., Geis-Gerstorfer, J., Schwartz, Z., et al. (2014). A review on the wettability of dental implant surfaces II: Biological and clinical aspects. *Acta Biomater.* 10, 2907–2918. doi: 10.1016/j.actbio.2014.03.032

Gulati, K., Prideaux, M., Kogawa, M., Lima-Marques, L., Atkins, G. J., Findlay, D. M., et al. (2017). Anodized 3D-printed titanium implants with dual micro- and nano-scale topography promote interaction with human osteoblasts and osteocyte-like cells. *J. Tissue Eng. Regen. Med.* 11, 3313–3325. doi: 10.1002/term.2239

Hyzy, S. L., Cheng, A., Cohen, D. J., Yatzkaier, G., Whitehead, A. J., Clohessy, R. M., et al. (2016). Novel hydrophilic nanostructured microtexture on direct metal laser sintered Ti-6Al-4V surfaces enhances osteoblast response in vitro and osseointegration in a rabbit model. *J. Biomed. Mater. Res. A* 104, 2086–2098. doi: 10.1002/jbm.a.35739

Kitajima, H., Hirota, M., Iwai, T., Hamajima, K., Ozawa, R., Hayashi, Y., et al. (2020). Computational fluid simulation of fibrinogen around dental implant surfaces. *Int. J. Mol. Sci.* 21:660. doi: 10.3390/ijms21020660

Li, Q., Gao, Z., Chen, Y., and Guan, M. X. (2017). The role of mitochondria in osteogenic, adipogenic and chondrogenic differentiation of mesenchymal stem cells. *Protein Cell* 8, 439–445. doi: 10.1007/s13238-017-0385-7

Liu, Y., Rath, B., Tingart, M., and Eschweiler, J. (2019). Role of implants surface modification in osseointegration: a systematic review. *J. Biomed. Mater. Res. A* 108, 470–484. doi: 10.1002/jbm.a.36829

Mangano, C., Mangano, F. G., Shibli, J. A., Ricci, M., Perrotti, V., d'Avila, S., et al. (2012). Immediate loading of mandibular overdentures supported by unsplinted direct laser metal-forming implants: results from a 1-year prospective study. *J. Periodontol.* 83, 70–78. doi: 10.1902/jop.2011.110079

Mangano, F., Mangano, C., Piattelli, A., and Iezzi, G. (2017). Histological evidence of the osseointegration of fractured direct metal laser sintering implants retrieved after 5 years of function. *Biomed. Res. Int.* 2017:9732136. doi: 10.1155/2017/9732136

Minagar, S., Berndt, C. C., Wang, J., Ivanova, E., and Wen, C. (2012). A review of the application of anodization for the fabrication of nanotubes on metal implant surfaces. *Acta Biomater.* 8, 2875–2888. doi: 10.1016/j.actbio.2012.04.005

Minagar, S., Wang, J., Berndt, C. C., Ivanova, E. P., and Wen, C. (2013). Cell response of anodized nanotubes on titanium and titanium alloys. *J. Biomed. Mater. Res. A* 101, 2726–2739. doi: 10.1002/jbm.a.34575

Modaresifar, K., Azizian, S., Ganjian, M., Fratila-Apachitei, L. E., and Zadpoor, A. A. (2019). Bactericidal effects of nanopatterns: a systematic review. *Acta Biomater.* 83, 29–36. doi: 10.1016/j.actbio.2018.09.059

Mouraret, S., Hunter, D. J., Bardet, C., Brunski, J. B., Bouchard, P., and Helms, J. A. (2014). A pre-clinical murine model of oral implant osseointegration. *Bone* 58, 177–184. doi: 10.1016/j.bone.2013.07.021

Ni, H. M., Williams, J. A., and Ding, W. X. (2015). Mitochondrial dynamics and mitochondrial quality control. *Redox Biol.* 4, 6–13. doi: 10.1016/j.redox.2014.11.006

Ocana, R. P., Rabelo, G. D., Sassi, L. M., Rodrigues, V. P., and Alves, F. A. (2017). Implant osseointegration in irradiated bone: an experimental study. *J. Periodont. Res.* 52, 505–511. doi: 10.1111/jre.12416

Oliveira, T. T., and Reis, A. C. (2019). Fabrication of dental implants by the additive manufacturing method: a systematic review. *J. Prosthet. Dent.* 122, 270–274. doi: 10.1016/j.prosdent.2019.01.018

Palikaras, K., Lionaki, E., and Tavernarakis, N. (2018). Mechanisms of mitophagy in cellular homeostasis, physiology and pathology. *Nat. Cell Biol.* 20, 1013–1022. doi: 10.1038/s41556-018-0176-2

Pei, D. D., Sun, J. L., Zhu, C. H., Tian, F. C., Jiao, K., Anderson, M. R., et al. (2018). Contribution of mitophagy to cell-mediated mineralization: revisiting a 50-year-old conundrum. *Adv. Sci.* 5:1800873. doi: 10.1002/advs.201800873

Rupp, F., Liang, L., Geis-Gerstorfer, J., Scheideler, L., and Huttig, F. (2018). Surface characteristics of dental implants: a review. *Dent. Mater.* 34, 40–57. doi: 10.1016/j.dental.2017.09.007

Shen, Y., Wu, L., Qin, D., Xia, Y., Zhou, Z., Zhang, X., et al. (2018). Carbon black suppresses the osteogenesis of mesenchymal stem cells: the role of mitochondria. *Part. Fibre Toxicol.* 15:16. doi: 10.1186/s12989-018-0253-5

Stadlinger, B., Lode, A. T., Eckelt, U., Range, U., Schlottig, F., Hefti, T., et al. (2009). Surface-conditioned dental implants: an animal study on bone formation. *J. Clin. Periodontol.* 36, 882–891. doi: 10.1111/j.1600-051X.2009.01466.x

Trevisan, F., Calignano, F., Aversa, A., Marchese, G., Lombardi, M., Biamino, S., et al. (2018). Additive manufacturing of titanium alloys in the biomedical field: processes, properties and applications. *J. Appl. Biomater. Funct. Mater.* 16, 57–67. doi: 10.5301/jabfm.5000371

Vos, T., Allen, C., Arora, M., Barber, R., Bhutta, Z., Brown, A., et al. (2016). Global, regional, and national incidence, prevalence, and years lived with disability for 310 diseases and injuries, 1990–2015: a systematic analysis for the Global Burden of Disease Study 2015. *Lancet* 388, 1545–1602. doi: 10.1016/S0140-6736(16)31678-6

Wancket, L. M. (2015). Animal models for evaluation of bone implants and devices: comparative bone structure and common model uses. *Vet. Pathol.* 52, 842–850. doi: 10.1177/0300985815593124

Wang, H., Zhang, X., Wang, H., Zhang, J., Li, J., Ruan, C., et al. (2018). Enhancing the osteogenic differentiation and rapid osseointegration of 3D printed Ti6Al4V implants via nano-topographic modification. *J. Biomed. Nanotechnol.* 14, 707–715. doi: 10.1166/jbn.2018.2551

Wang, Q., Zhou, P., Liu, S., Attarilar, S., Ma, R. L., Zhong, Y., et al. (2020). Multi-scale surface treatments of titanium implants for rapid osseointegration: a review. *Nanomaterials (Basel)* 10:1244. doi: 10.3390/nano10061244

Wu, Y., Feng, F., Xin, H., Li, K., Tang, Z., Guo, Y., et al. (2019). Fracture strength and osseointegration of an ultrafine-grained titanium mini dental implant after macromorphology optimization. *ACS Biomater. Sci. Eng.* 5, 4122–4130. doi: 10.1021/acsbiomaterials.9b00406

Xu, J. Y., Chen, X. S., Zhang, C. Y., Liu, Y., Wang, J., and Deng, F. L. (2016). Improved bioactivity of selective laser melting titanium: Surface modification with micro-/nano-textured hierarchical topography and bone regeneration performance evaluation. *Mater. Sci. Eng. C Mater. Biol. Appl.* 68, 229–240. doi: 10.1016/j.msec.2016.05.096

Yap, C. Y., Chua, C. K., Dong, Z. L., Liu, Z. H., Zhang, D. Q., Loh, L. E., et al. (2015). Review of selective laser melting: materials and applications. *Appl. Phys. Rev.* 2:041101. doi: 10.1063/1.4935926

Yu, M., Lin, Y., Liu, Y., Zhou, Y., Liu, C., Dong, L., et al. (2018). Enhanced osteointegration of hierarchical structured 3D-printed titanium implants. *ACS Appl. Bio Mater.* 1, 90–99. doi: 10.1021/acsabm.8b00017

Yu, M., Liu, Y., Yu, X., Li, J., Zhao, W., Hu, J., et al. (2019). Enhanced osteogenesis of quasi-three-dimensional hierarchical topography. *J. Nanobiotechnol.* 17:102. doi: 10.1186/s12951-019-0536-5

Zhang, Y. B., Liu, X. C., Zeng, L. D., Zhang, J., Zuo, J. L., Zou, J., et al. (2019). Polymer fiber scaffolds for bone and cartilage tissue engineering. *Adv. Funct. Mater.* 29:20. doi: 10.1002/adfm.201903279

Zheng, H., Tian, Y., Gao, Q., Yu, Y., Xia, X., Feng, Z., et al. (2020). Hierarchical micro-nano topography promotes cell adhesion and osteogenic differentiation via integrin alpha2-PI3K-AKT signaling axis. *Front. Bioeng. Biotechnol.* 8:463. doi: 10.3389/fbioe.2020.00463

Conflict of Interest: The authors declare that the research was conducted in the absence of any commercial or financial relationships that could be construed as a potential conflict of interest.

The handling editor declared a past co-authorship with one of the authors YC.

frontiers in Materials

REVIEW
published: 11 January 2021
doi: 10.3389/fmats.2020.615225

Adhesion of Teeth

Zhilong Zhao[1†], *Qihui Wang*[1†], *Jing Zhao*[2], *Bo Zhao*[1], *Zhangyu Ma*[3] *and Congxiao Zhang*[1]*

[1]Department of Stomatology, The First Hospital of Jilin University, Changchun, China, [2]Department of Stomatology, China-Japan Union Hospital, Beijing, China, [3]Nanyang Medical College, Nanyang, China

Dental bonding materials are widely used in dentistry and there are several available kinds. However, in recent years, there has been no further research into dental bonding materials, with most dentists focusing on dental implants and orthodontics. In this paper, we systematically review the technology of tooth bonding in recent years and summarize the existing literature for potential innovation and direction of future research. First, the theoretical research on dental assembly materials and bonding mechanism was reviewed. Then, we reviewed the bonding of teeth, the bonding of metal alloy prosthesis, and the measurement of bond strength. Finally, the future development of dental bonding technology was evaluated. It is hoped that more dentists will be able to treat patients and update research on bonding materials in the field of teeth bonding to bring a new era to the restoration of teeth in the future.

Keywords: adhesion, tooth, dental, restoration, bonding, prosthesis

Edited by:
Junchao Wei,
Nanchang University, China

Reviewed by:
Mingqiang Li,
Sun Yat-sen University, China
Hu Wang,
Sichuan University, China

***Correspondence:**
Congxiao Zhang
zhangcongxiao@jlu.edu.cn

†These authors have contributed equally to this work

Specialty section:
This article was submitted to Biomaterials, a section of the journal Frontiers in Materials

Received: *08 October 2020*
Accepted: *26 November 2020*
Published: *11 January 2021*

Citation:
Zhao Z, Wang Q, Zhao J, Zhao B, Ma Z and Zhang C (2021) Adhesion of Teeth. Front. Mater. 7:615225. doi: 10.3389/fmats.2020.615225

INTRODUCTION

As we all know, when our teeth are broken by force or because of dental caries, we need to use bonding materials or filling materials. Over the years, a lot of changes have taken place in the dental materials. We aim to tell you how these materials have improved and restored teeth through such a review.

Adhesion is defined as the sticking of two surfaces to one another. Dental adhesion depends on the properties of components: assembly materials such as cement and adhesive, the tooth, and prosthesis. The mode of adhesion can be divided into two main categories: mechanical and chemical. Mechanical adhesion relies on mechanical interlocking which provides retention and a durable form of bonding. Chemical adhesion involves the modification of the surface etch, and two dissimilar surfaces are connected by an active monomer. This article will have a global review of dental assembly materials, mechanism of adhesion, adhesive bonding to teeth, and prosthesis.

DENTAL ASSEMBLY MATERIALS

Cement

The definition of cement or adhesive is mainly defined by its curing methods. Cement includes acid base reaction curing materials. The most common forms are acidic liquids and alkaline powders. The liquid is composed of an aqueous solution of polyacrylic acidor a copolymer of acrylic acid and other unsaturated carboxylic acids. The powder is fluoroaluminosilicate glass. Their properties depend on the nature of liquid and powder.

Table 1 shows the classification of dental cements. Silicate cement is discarded due to its low mechanical properties, high cytotoxicity, and high solubility. Zinc polycarboxylate has the worst cohesion. Because of their poor mechanical properties, they are used less. The compressive strength of zinc orthophosphate is slightly lower than that of glass ionomer cement (Sofan et al., 2017).

TABLE 1 | Classification of dental cements.

Conventional dental cement	Zinc phosphate cement Zn_3 $(PO_4)_2$
	Zinc oxide eugenol cement (ZnO)
	Polycarboxylate cement ($ZnCO_3$)
	Glass ionomer cement (GIC)
Resin base cement	Resin cement
	Resin-modified ionomer cement

In dental application, both glass ionomer cement (GIC) and zinc polycarboxylate cement provide direct adhesion to tooth and can provide fluoride release, but the latter is more radiopaque and biocompatible than GIC (Wetzel et al., 2020).

Polycarboxylate cement also sets according to an acid–base reaction. The powder is composed of mainly zinc oxide (ZnO), magnesium oxide (MgO), bismuth (Bi_2O_3) and aluminum oxide (Al_2O_3). It may also contain stannous fluoride (SnF_2) where disappearance of fluoride improves the shear bond strength (SBS) of the orthodontic bracket (Khargekar et al., 2019).

Zinc oxide (ZnO) particles have been used for temporal or permanent luting cement because of their excellent mechanical strength and biocompatibility. ZnO nanoparticles have distinct optical and antibacterial properties and a high surface-to-volume ratio (Nguyen et al., 2019).

Typically, GICs are reacted by fluoride-containing silicate glass and polyalkenoic acids. **Figure 1** shows the manufacturing method of GIC. Fluoride is one of ionic constituents that are released from the glass during the setting reaction. Polyacid-modified resin composites (compomers) claim to combine the mechanical and aesthetic properties of composites with the fluoride-releasing advantages of conventional GICs so the resultant material is a low-fluoride-releasing resin composite that contains vinyl groups that can be polymerized by visible light-activated initiators. Polyacrylic acid pretreatment significantly increases the micro-SBS (μSBS) of all cements (Paing et al., 2020). All these cements have relatively low cohesion and are relatively fragile. Although these weak properties limit the marking of conventional cement, they indicate that one of the main characteristics of cement is the ease of removal of excess cement (Shahid et al., 2010).

Adhesives

The adhesive is composed of powder and liquid and is mostly an organic polymer that comprises methacrylate matrix, wherein the matrix does or does contain mineral filler (**Table 2**).

The resin matrix is made of two methacrylic acid monomers. The most common ones are bis-GMA, UDMA, or methyl methacrylate (MMA). Ethylene glycol (TEGDMA) derivatives are usually added to reduce the high viscosity provided by bis-GMA. The filler includes colloidal particles of glass silicon such as SiO_2, B_2O_3, Na_2O_3, Al_2O_3, which is obviously sub-micron size (particle size: 10–40 nm). They account for 30–65% of the adhesive volume. The volume ratio of filler to matrix has a major effect on adhesive properties. Therefore, the increase of this ratio will reduce the removal of polymerization and increase viscosity. To form a cohesive structure, a strong chemical bond must be formed between the matrix and the filler. Otherwise, each interface will be the preferred location for the initiation of cracks.

After the redox reaction, the polymerization initiator activates the curing phenomenon. The initiation always takes place after the redox reaction. The reaction produces free radicals that attack the double bond of the methacrylic group, which leads to polymerization. When the adhesive is chelating, it is usually triggered by a pair of amine peroxide. **Figure 2** shows the progress of initiation of amine peroxide.

The adhesive is then packaged into two pastes, each paste containing one element and in contact with each other when mixed.

MECHANISM OF ADHESION

To choose the proper adhesive, it is important to understand the mechanism of adhesion and the surface energies of all the substrates, and how well the adhesive will wet out. Surface energy is a physical property of the surface of a material that determines whether an adhesive will make intimate contact and provide a bond. The adhesive interactions between an adhesive and a substrate not only concern the actual area of contact (adhesion zone) of the adhesive and substrate but also concern the state of the adhesive in the vicinity of the surface of the substrate (transition zone). **Figure 3** shows the structure of the adhesive joint and effect of surface energy.

The Concept of Surface State, Surface, Surface Energy, and Adsorption

To better understand the mechanism of adhesion, it is necessary to redefine some concepts of surface state that include all the interactions that help to connect two main bodies. A good distinction must be made between the notion of cohesion, which includes all interactions that help to bind the two bodies, and adhesion, which corresponds to the force or energy of separation of an assembly.

The components (atoms, ions, molecules) between the surface and the internal do not have the same number. This result in an imbalance: the distance between atoms is greater than that of

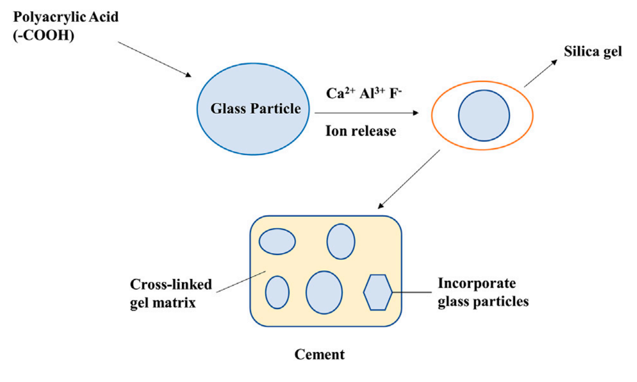

FIGURE 1 | Manufacturing method of glass ionomer cement (GIC).

TABLE 2 | Composition of dental adhesives.

Composition	
Powder	**Liquid**
Resin matrix (Diacrylate monomer, Bis-GMA, UDMA, TEGDMA)	Methyl methacrylate
Inorganic fillers	Tertiary amine
Coupling agent (organosilane)	4-META, MDP
Chemical or photo initiator or activator	
Camphorquinone, tertiary amine, benzoyl peroxide	
Catalyst: Tributylborane (TBB)	

equilibrium; different levels of electronics; and an energetic state higher than that inside the body.

These characteristics explain the particular reactivity of the surface to its environment. Therefore, the surface energy must be defined, which is equivalent to the work required (W) to form a new area unit of the material (A).

$$dW = \gamma dA$$

where γ is represented by J/m^2.

At the liquid/gas interface, the surface energy corresponds to surface tension. In accordance with the law of thermodynamics, the surface will naturally seek to reduce its energy levels. The components that make up the solid surface do not have the same freedom of movement as the liquid surface. These interface connections are matched with adsorption and reduce the energy of the surface by exchanging connections with the external environment.

In this case, physical adsorption includes weak bonds (2–42 kJ/mol) such as van der Waals or hydrogen bond; whereas, chemisorption includes strong bond by electronic transfers at the interfaces such as ionic and covalent bonds (100–1,000 kJ/mol).

All the chemical, structural, and topographic properties of the material surface are combined into the surface state. In practice, the surface is always full of defects and heterogeneity.

(1) Chemical heterogeneity is linked not only to the nature of different species that constitute the structure or material but also to the existence of adsorbed hetero atoms.
(2) Structural heterogeneity with some amorphous or crystalline characteristics and sequences of related defects.
(3) Morphological and topographical heterogeneity of substrates that have never been ideally smoothed can have a porous and absorbent appearance.

Adhesion and Wetting

When a material is deposited in the liquid phase on a substrate, it is spread and linked to the two materials to form bonds. Physical adhesion is only possible when the intermolecular distance is ≤7 Å.

The spreading of liquid corresponds to wetting and depends on three interfacial energies:

(1) The surface energy of the substrate (γS)
(2) The surface energy in saturation of liquid vapor (γL)
(3) The solid-liquid interfacial energy which corresponds to the bonds (γSL)

Wetting for the liquid and wettability for the substrate are inversely proportional to γL and γS, respectively.

The adhesion, linked to γL and γS, is given by Dupré's law (**Figure 4**):

$$WA = \gamma L + \gamma S - \gamma SL$$

By setting the equation of the quality of the forces at equilibrium, we find Young's law:

$$\gamma S = \gamma L.\cos\theta + \gamma SL$$

where θ is the contact angle

$$\begin{aligned} WA &= \gamma L + \gamma S - \gamma SL \\ WA &= \gamma L + (\gamma L.\cos\theta + \gamma SL) - \gamma SL \\ WA &= \gamma L(1 + \cos\theta) \end{aligned}$$

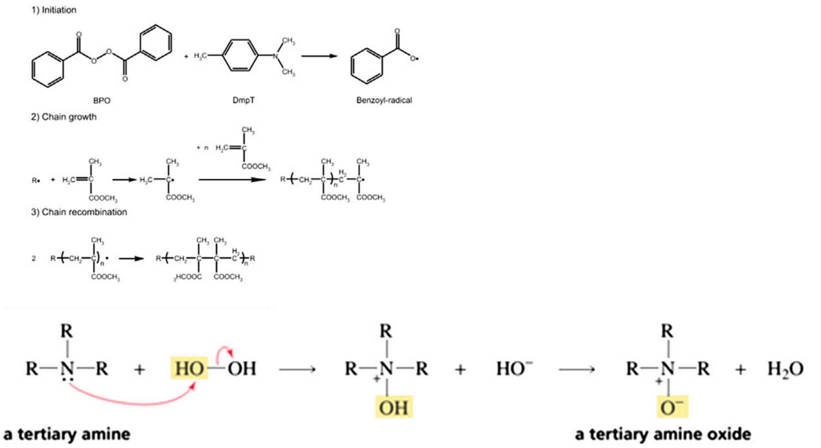

FIGURE 2 | Progression of initiation of amine peroxide.

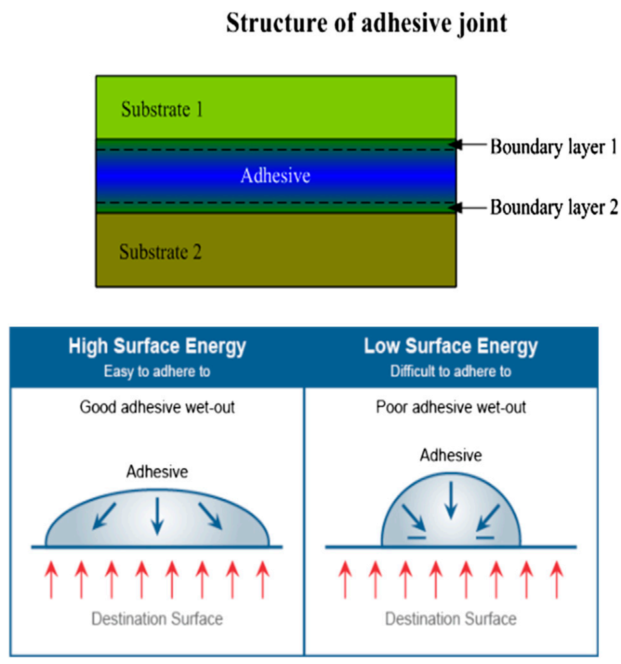

FIGURE 3 | Structure of adhesive joint and effect of surface energy.

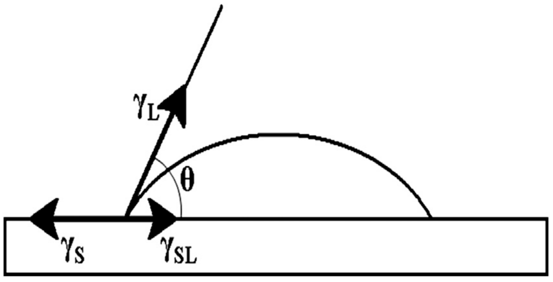

FIGURE 4 | Dupré's law.

The contact angle must be defined at equilibrium. This will be recorded by the contact angle according to time. The curve is hyperbolic and its limit gives us the value of θ.

Contrary to expectation, viscosity does not affect the wettability but only the spreading kinetics.

$$v = \gamma L/2\eta$$

where v is the spreading speed, γL is the surface tension of the liquid, and η is the viscosity.

Liquid Surface Tension and/or Viscosity

It is obvious that a liquid adhesive will moisten the surface faster than a high-viscosity adhesive. The importance of this extension kinetics is relative, because the flow rate of most adhesive resins on an etched enamel is several centimeters per second. Therefore, the viscosity only affects a very fast kinetics.

Therefore, for two liquids of the same nature but different viscosity applied on the same surface and when $t \rightarrow 0$, the contact angle of the most viscous contact angle is greater than that of the other, but when $t \rightarrow \infty$, the angle is the same.

The roughness has a positive influence on interlocking when contact angle (θ) is $<90°$ and has a negative influence when $\theta > 90°$ (**Figure 5**).

However, since all the real surfaces are not ideal, the Wenzel model was developed to describe the contact angles on the real surface where the new angle provides a roughness index (ρ) which corresponds to the real contact provided by the rough topography—Wenzel equation:

$$\rho = \cos\theta' / \cos\theta$$

Where θ' is the apparent contact angle and θ is the equilibrium contact angle on an ideal solid without roughness.

The capillary rise represents a special case of adhesive spreading, which is affected by capillary pressure.

$$\mathrm{Pc} = 2\gamma \mathrm{L}\cos\theta / r$$

where γL is the surface tension of the adhesive and r is the capillary radius.

This characteristic is largely responsible for the quality of the resin/etched enamel interface, particularly for a transverse section of prisms.

Adhesion Theory

There is no single theory to explain adhesion, but it is commonly divided into mechanical interlocking, physical bonding, and chemical bonding (**Figure 6**).

Mechanical Interlocking

Mechanical interlocking happens when two dissimilar phases attach to one another by mechanical force only. This typically requires a rough surface where the other material can penetrate.

Physical Bonding

Physical adhesion means a very small interaction distance. The liquid expansion on the substrate becomes a basic component. This theory is associated with the micro or macro bond of mechanical anchors through low link (hydrophilic or hydrophobic) physical adsorption. When the liquid is wetted,

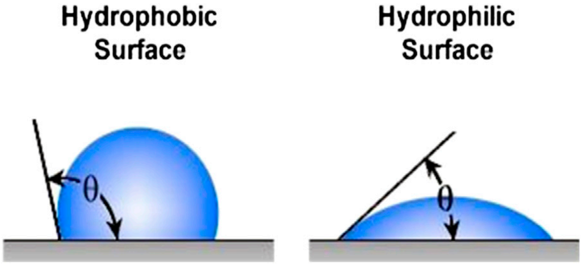

FIGURE 5 | Correlation between contact angle (θ) and roughness.

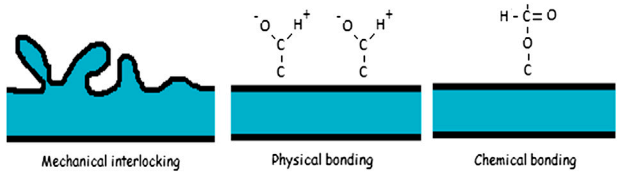

FIGURE 6 | Schematic of three kinds of adhesion theory.

the interaction may be considered a response to the theory of physical adhesion.

Biomaterial surface properties including chemical, topographic, and wettability regulate the cell response. Control of inflammation will inform the design of surface modification procedures to direct the immune response and enhance the success of implanted materials (Hotchkiss et al., 2016; Qiu et al., 2020; Sang et al., 2020).

Intern-Diffusion Theory

The model is illustrated by polymer-polymer adhesion. The diffusion of one polymer into another polymer increased the degree of adhesion. Brown emphasized this interaction, which is considered to be the "Velcro" of molecules. There are two basic criteria for this diffusion:

1. Thermodynamic criteria: molecules must be compatible in terms of hydrophobicity and hydrophobicity (van der Spoel et al., 2006).
2. Dynamic criteria: macromolecules must have sufficient mobility. In addition, the molecule diameter and the distance of intermolecular space must be compatible with internal diffusion. Even if the thermodynamic criteria are valid, a 200 Å polymer will not diffuse the membrane protein with intermolecular spaces of 150 Å (Ando and Skolnick, 2010).

Therefore, the importance of diffusion medium and solvent and the viscosity of the material are also discussed.

This is the theory of the principle of dental hybrid layer.

Chemical Bonding

Chemical bonding which is much stronger than physical bonding includes covalent, ionic, and metallic bonding. Chemical bonding is responsible for cohesive forces inside the material itself.

Electrostatic Theory and Acid-Base Theory

The basis of the electrostatic theory of adhesion is the difference in electronegativity of adhering materials. The surface has its structural defects and heterogeneity in electronic community generating a low range (1–2 nm) but very strong field (>108 V m^{-1}). Adhesive force is attributed to the transfer of electrons across the interface creating positive and negative charges that attract one another. The electrostatic forces at the interface account for resistance to separation of the adhesive and the substrate.

The surface of a substrate has plurality of polar sites, which have the acidity of the electron donor and/or the alkalinity of the electron acceptor. These sites can be linked to the reverse polarity activity of adhesives. Therefore, the polar connection will result from the load transfer between the base donor position and the adhesive acceptor position, and vice versa.

ADHESION TO TEETH

Paradoxically, the vast majority of adhesives do not have adhesive ability to the surfaces. Only a few adhesives have adhesive ability because of active monomers such as 4-methacryl ethyl triacrylate (4-META) or 10-methacryl decyl phenyl phosphate (10-MDP).

Therefore, a coupling agent is used to adhere to the dental surface. The coupling agent involves a reactive polar group, which can be connected with dental tissue on one hand and an adhesive material on the other hand (HEMA).

Adhesion to Enamel

The conventional resins that are highly hydrophobic have no adhesive ability to dental surface.

The solution for bonding these surfaces is by creating favorable surface topography for anchorage, finding a coupling agent to bind to the dental tissues and the adhesive.

Phosphoric acid etching can clean the enamel surface, improve the surface energy of the substrate, and improve the wettability of the adhesive. On the other hand, acid etching produces a roughness (up to 50 microns) where resin can penetrate. In fact, this highly mineralized tissue has a composite structure which leads to selective etching of certain hydroxyapatite phases (Sato et al., 2018).

The depth and quality of etching will depend on some parameters as listed below:

(1) Acid properties

Phosphoric acid treatment seems to be the best for enamel etching. However, if we want to bond to enamel and dentin, the choice of acid is affected by dentin treatment, and the dentin must also be etched. Compared with the enamel, the complexity of the dentin adhesion has led to the development of other adhesives based on other acids, minerals (2.5% nitric acid), or organic compounds (10% maleic acid and 10% citric acid). It is used to etch enamel and dentin at the same time (total etch). However, the effectiveness of these acids does not seem equal to that of phosphoric acid (Benetti et al., 2019; Markovic et al., 2019).

(2) Concentration

Generally, 10–60% of the phosphoric acid solution seems to have similar adhesiveness. However, the acid concentration affects the depth of relief. In addition, the white appearance after etching is only obtained from a concentration of 20% (Ajaj et al., 2020). The concentration of 35% appears to be optimal.

(3) Consistency

A study showed that gels are as effective as liquid solutions. Therefore, we prefer colored gels that allow precise operation and good visual control (Cardenas et al., 2018).

(4) Application time

It seems the same bonding value between 5 and 37% phosphoric acid etching in the range of 15 s to 1 min. It proves good tolerance of enamel etching with different prosthesis (Cardenas et al., 2018; Sai et al., 2018).

It should be noted that contamination of the etched substrate with salivary or blood proteins can affect the quality of the bonding. Because the molecules are adsorbed on the surface, a simple rinsing is insufficient to eliminate these molecules. Therefore, it seems reasonable to have a new etching. Clinically, this has proved the importance of using the oral rubber dam to avoid the contamination.

Therefore, adhesion to enamel responds to two mechanisms: the first is physicochemical by increasing the wettability and surface area, and the second is the micromechanical, where the adhesive has penetrated and hardened the roughness produced by the acid.

Dentin Adhesion

Because the structure of dentin is complex, there are many problems regarding bonding with dentin.

1. Dentin are hydrophilic and saturated oxygen.
2. Dentin continues to form throughout life.
3. Mineral phase (70%), organic phase (20%).
4. Its complex structure varies from the depth of the tubule. In fact, near the dentinoenamel junction, only 1% dentinal tube is present on the dental surface and 22% dentinal tube is near the pulp.
5. Dentin is covered by dentin mud. It should be noted that the removal of dentin by milling creates a deposit smear layer.

Therefore, these obstacles make it difficult to develop reliable dental adhesive systems.

General Principles

To implement the hybridization protocol, three basic components are needed:

(1) A conditioner

The application of the conditioner corresponds to acid etching. This reaction is acid-based with hydroxyapatite and smear layer, resulting in dissolution. It allows to eliminate the dentin mud and contaminants, open the tubules, demineralize the peri- and inter-tubular dentins over a thickness (1–5 μm) and form a dense collagen network. Many types of acids have been proposed to etch dentin, such as Maleic acid ($C_4H_4O_4$HOOCCH=CHCOOH), Oxalic acid ($C_2H_2O_4$ HOOC-COOH), Tartaric acid (HOOC-CHOH-CHOH-COOH$C_4H_6O_6$), or Ethylenediaminetetraacetic acid (EDTA).

Glutaraldehyde ($C_5H_8O_2$) is known for its ability to interconnect with collagen and is sometimes incorporated into the conditioner.

Hybridization involves infiltration of the collagen network with adhesive resin. The problem is to find a way to infiltrate this hydrophobic resin into this highly hydrophilic network.

(2) A primer or coupling agent.

The primer permits the opening of the inter-fibrillar space because of the hydrophilic monomers dissolved in a specific solvent which fix the collagen in a humid environment. These monomers have a methacrylate group at one end and a reactive group at the other end. The reactive group can interact with the polar molecules of the dentin, such as the hydroxyapatite of the apatite or the amine of collagen. The most commonly used is HEMA which has a positive effect on dentin adhesion. It is necessary to infiltrate the primer because the drying dentin surface would cause collage collapse.

The solvent can be alcohol or acetone, which can help the active monomer penetrate into the network and also eliminate the water.

(3) An adhesive resin

The last step is to apply the adhesive resin, which must penetrate into the tubules and infiltrate into intercellular protein networks.

Application of Bonding System

Paradoxically, the vast majority of adhesives do not have adhesive ability to the surfaces. Only a few adhesives have this ability because of the active monomers, such as 4-methacryl ethyl triacrylate (4-META) or 10-methacryl decyl phenyl phosphate (10-MDP).

Therefore, a coupling agent is used to adhere to the dental surface. The coupling agent involves a reactive polar group, which can be connected with dental tissue on one end and with adhesive material on the other end (HEMA).

Since the vast majority of adhesives do not have adhesive ability, the bonding is done by forming a mixing layer between the teeth or the porcelain and the adhesive (HEMA).

Nevertheless, there exist active monomers such as (4-META, 10-MDP, and 11-methacrylic oxygen-1, 1-eleven alkane two carboxylic acid (MAC 10) with adhesive ability.

On using 4-META, the dentin was treated by 10% citric acid and 3% ferric chloride. Citric acid allows opening of the dentinal tubules and collagen network. Ferric chloride can help form polar sites and enhance affinity to 4-META. It is forbidden to use H_3PO_4 on dentin because it creates low bonding value with 4 META-MMA resin, changes collagen nature, and prevents the penetration of monomers. Polymerization is initiated by three-N-butyl borane (TBB). This initiation mode is unique, because unlike the peroxide amine, dibromobenzene tribromide is not inhibited by oxygen and water, rather activated.

PMMA provides good viscoelastic properties and provides stress relaxation ability through reversible deformation. Therefore, the interfacial stress is reduced.

ADHESION TO METAL ALLOY PROSTHESIS

In order to fix a dental prosthesis to teeth, it is necessary to obtain a strong and durable adhesion on both sides. Adhesives based on hydrophobic monomers such as bis-GMA and UDMA do not have durable adhesion to alloy and to ceramic. Adhesives with reactive monomers such as 4-META or 10-MDP have the ability to spontaneously adhere to metal surfaces, especially to non-precious alloys. However, the adhesion value seems to be sensitive to long-term degradation, especially hydrolysis. Therefore, we show different technologies on metal and ceramic, both for conventional and reactive adhesives.

Surface Mechanical Reconstruction

Micro Mechanical Maintenance

Rochette suggested in 1973 that metal splint should be bonded on etched enamel. The metal splint was punched so that the resin can be mechanically fixed and maintained. However, the disadvantage of this technology was that on the one hand, the surface of the exposed adhesives increased, resulting in wear and penetration, while on the other hand, the metal surface greatly reduced. Therefore, with the improvement of adhesive quality and development of metal surface preparation, the signs of macromechanical technology gradually disappeared.

Micro Mechanical Retention

The principle is to change the topography of the metal surface without changing its chemical composition.

Alumina sandblasting (Al_2O_3, 50–250 micron) is a simple treatment method, which on the one hand can purify the surface contaminants of the possible adsorbents, thereby enhancing the surface tension. On the other hand, it can create a kind of roughness i.e., favorable for micromechanical retention.

A study showed that alumina sandblasting achieves bonding performance for non-precious metal alloy. For those adhesives without adhesive ability, the sandblasting cannot provide enough retention.

Electrolytic or Acid Etching

This technology was developed in the early 1980s, providing substrate compatible with conventional adhesives. It only applies to non-noble alloys (Ni-Cr, Cr-Co) with eutectic microstructure, allowing one part of the two phases to dissolved to produce high roughness surfaces. Therefore, owing to the micromechanical bonding provided by the surface, the method obtained high strength resin adhesion. However, it has been pointed out that the efficiency of Cr-Co alloy is lower than that of Ni-Cr alloy. In addition, some studies also showed that the results of Ni-Cr were poor.

Because electrolysis etching requires special equipment and high skill, acid etching has become a popular method. This method simply includes the application of high concentration hydrogen fluoride hydrogel (HF).

Because of the lack of effective electrolytic etching, a fine salt crystal layer is deposited on the metal surface before making the resin model. Once the resin is polymerized, the salt crystals were dissolved away from the resin, leaving a reproductible cap.

Chemical Changement for Noble Alloy

The poor bonding quality between the noble alloy and the adhesive is related to the low surface reactivity. We can modify the surface by chemical method and make it suitable for bonding.

Tin Deposit

The principle is to depose tin microcrystals onto the alloy surface, giving it a gray appearance. Tin is chemically linked to the surface to create micromechanical retention and forms polar bonds with the reactive groups of the adhesive.

However, the coupling between tin deposition (electronegativity) and the noble alloy substrate (electropositivity) may lead to corrosion and degradation of the joint.

Silica Deposit

The following two methods have been worked out:

(1) Thermochemical deposition

The Silicoater MD (Heraeus Kulzer) system consists of siloxane application: tetramethoxy silane, thermal dissolving in propane air flame or in an oven to deposit 0.5-micron siloxane.

(2) Tribochemical deposit

The surface is sanded with special powder containing alumina covered with colloidal silica under high pressure. The energy generated by the impact of pressurized silica particles on the metal surface leads to the binding of silica. These systems include the ROCATEC the COJET 3M ESPE system.

After silica deposition, the surface is treated with silane. It can be connected to the free hydroxyl (-OH) group and play an intermediate role between the silica layer and the adhesive resin. Regardless of the alloy and adhesive used, this method improves both the bonding value and the resistance to degradation.

Chemical Improvement

The poor bonding quality between the noble alloy and the self-etching adhesive is related to the low surface reactivity. We can chemically alter the surface and make it more suitable for bonding adhesives.

After silicon deposition, the surface is treated with silane. It can be connected to the free hydroxyl group (-OH) and play an intermediate role between the silica layer and the resin.

As explained earlier, regardless of the alloy and adhesive used, these methods improve both the bonding value and provide better resistance to degradation.

Metal Primers

Active monomers, such as those listed in **Table 2**, have the ability to react with the surface oxide of non-noble alloys such as Ni-Cr, Cr-Co, or steel, thereby providing strong and stable adhesion (Ikemura et al., 2011; Al Bakkar et al., 2016). The MDP seemed to be the most effective monomer. For example, for Superbond, metal primer is a liquid (MMA monomer +5% 4-META) activated by TBB, with a significantly improved bonding value.

Because noble alloy surfaces have little or no oxide, the primer based on acid monomers will be ineffective. Similarly, adhesives based on 4-META, 10-MDP have poor adhesion to precious alloys. The adhesion can be improved by applying specific primers.

These are based on a coupling agent using bifunctional monomers. The bifunctional monomer has methacrylic groups at one end and thiol groups (-SH) at the other end. On the sanded metal surface, the sulfide group (S^{2-}) reacts with the noble alloy to form a strong chemical combination.

It is worth noting that these preparations are developed for specific types of adhesives and are not always able to withstand penetration. The metal primer 6- (4-vinylbenzyl-n-propyl) amino-1,3,5-triazine-2,4-dithione (VBATDT) is suitable for 4-META resin, but not for conventional methyl-based low-temperature adhesives. On the contrary, the AMPS monomer ($C_7H_{13}NO_4S$) designed for conventional resin is very poor in bonding with 4-META resin.

Ultraviolet irradiation (UVI) processing efficiently increases the bond strength between porcelain and the Ti surface (Kumasaka et al., 2018). Because of the high strength of noble alloy surface, the acid monomer will not be effective. It can be concluded that alloy primer containing both the vinyl-thione monomer (VBATDT) and hydrophobic phosphate monomer (MDP) is effective for bonding the Ag-Zn-Sn-In alloy and pure Ag, Zn, and Sn (Imamura et al., 2018).

For highly translucent zirconia, chemical pre-treatment with an MDP-containing primer improved bonding efficacy of 4-META/MMA-TBB resin (Shimizu et al., 2018).

The polymerization kinetics of composites is material dependent which affects their contraction stress and clinical performance (Wang et al., 2019).

Ceramic Bonding

Traditional resins have no natural affinity to ceramics because ceramics are hydrophilic like resins, especially due to surface hydroxyl groups. By combining the technology with the application of coupling agents, the film surface can be adhered with ceramics.

However, improving the mechanical and optical quality of adhesives and ceramics is very important to improve the reliability of ceramic bonding.

Therefore, the adhesion of ceramics is controlled by combining the acid retaining micro-computer retention agent and the chemical retention agent through the coupling agent (Blatz et al., 2018). For computer-aided design (CAD)/computer-aided manufacturing (CAM)-fabricated, high-strength ceramics, proper pretreatment of the bonding surfaces and application of primers or composite resins that contain special adhesive monomers are necessary (Yoshihara et al., 2016; Dapieve et al., 2020).

Ceramic surface treatment by primer containing monobond can promote micromechanical interlocking and chemical bonds for lithium disilicate ($Li_2O_5Si_2$) (vitroceramique) restorations.

The application of fluorofluoric acid for ceramic will greatly increase the roughness. In fact, in an enhanced Feldspathic ceramic with highly heterogeneous structure, the acid will preferably attack the crystalline phase. Hydrofluoric acid etching changes the pore pattern, crystal structure, roughness, and wettability of silica-based glass ceramics (**Figure 7**) (Ramakrishnaiah et al., 2016; El-Damanhoury and Gaintantzopoulou, 2018). Another study proved that the ceramic primer promoted the fatigue performance of lithium silicate ceramic (Dapieve et al., 2020; Fonzar et al., 2020). Phosphoric acid is completely ineffective for ceramic etching, but it can be used as a cleaning agent.

Some defects of hydrogen fluoride should be noted:

(1) This is a very toxic substance and needs to be handled with great care.
(2) If the residue is not completely neutralized before bonding, the residue can spread after the event and cause tissue damage.
(3) Even in gel form, it tends to burn because it may not bite the edges, which may have an adverse effect on the sealing of the edges.
(4) On the other hand, the bite mark beyond the boundary is a marginal factor of plate maintenance and inflammation.

When the two materials are chemically incompatible, the cured solution is a coupling agent that has intermediate properties between the two substrates-silane (SiH_4). As a result, condensation reaction occurs between the silane and the hydroxyl groups of the substrate on the surface of the ceramic surface, and the water molecules are released. Therefore, silane molecules are linked to the ceramic surface by covalent bonding.

Theoretically, the aim is to provide a monolayer of silane, but there is actually a gap composed of several silane and oligomer layers, which are basically connected with ceramic or resin that may damage the hydrolytic stability of the adhesive bonding. This method has greatly improved the hydrolytic stability of seals. Before applying silane, the prosthetic components must be carefully cleaned with alcohol, acetone, or phosphoric acid. Some silanes are packed in methyl form, which need acid activation, and then mixed in two liquids shortly before application.

MEASUREMENT OF BOND STRENGTH

Among the various methods used to test the bond strength of a joint, the shear and tensile tests are common. Regardless of the test used, many variable parameters influence the bond strength, including the interface geometry (Thoppul et al., 2009), force loading (Souza et al., 2015), and speed of the test (Abreu et al.,

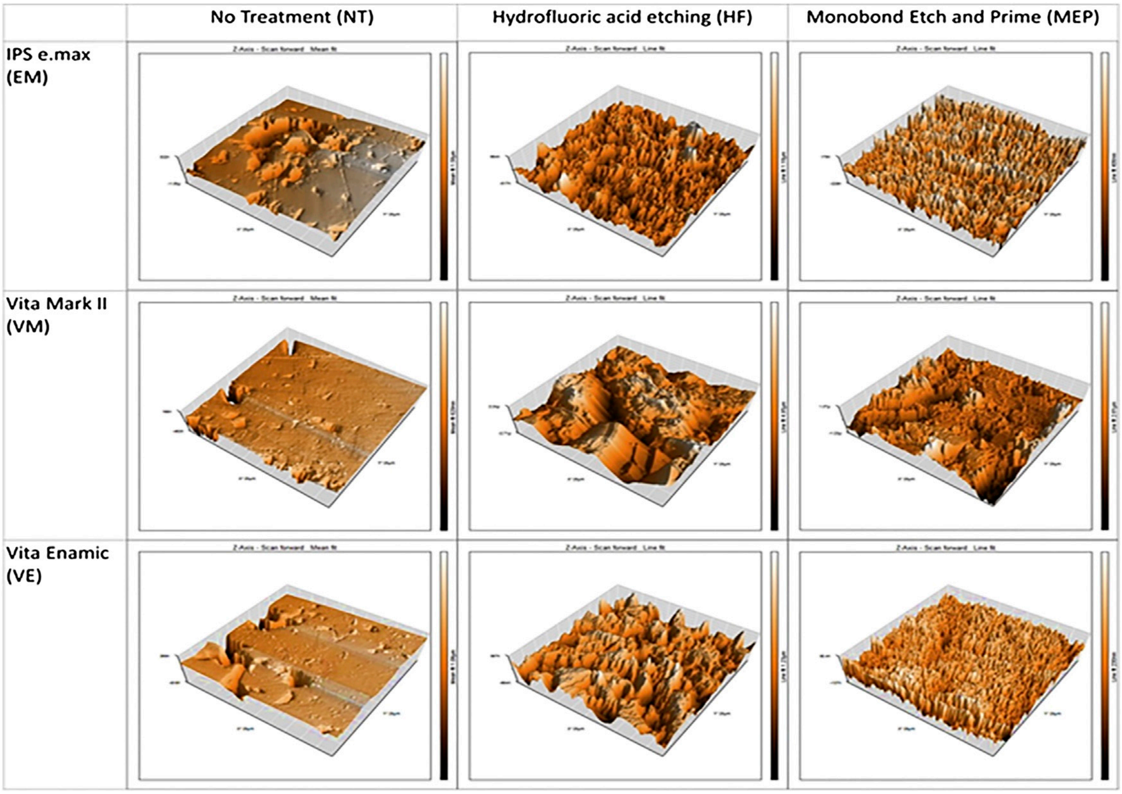

FIGURE 7 | Micrographs of the materials tested after no treatment (NT), hydrofluoric acid etching/Monobond Plus (HFMP) or self-etching ceramic primer Monobond Etch and Prime (MEP) pretreatment.

2011). This variability, which makes comparison among studies virtually impossible, may be due to sensitivity to the geometry of the interface (Thoppul et al., 2009), the loading of the force (Souza et al., 2015), and the solicitation speed of the test (Abreu et al., 2011). Additionally, the clinical and laboratory performances of dental adhesives rarely coincide, because dental adhesion tests are incapable of separating the effects of adhesive composition, substrate properties, joint geometry, and loading type on the measured bond strength (Jancar, 2011). Therefore, to evaluate the inherent material properties of an adhesive joint, tests measuring the adherence energy have been proposed. The concept behind these tests is to initiate and propagate a crack through the bonded interface in a stable manner (Bechtle et al., 2010).

The double cantilever beam (DCB) test and the notchless triangular prism (NTP) are two approaches that may be used to evaluate the adherence energy of a bonded joint. Theoretically, the data obtained by these tests are independent of the specimen geometry and provide a real, characteristic value of the bonding joints. The mechanics and principles of the DCB test have been described in detail in a previous study (Blaysat et al., 2015). The DCB test is a cleavage test that measures the value of Gc, which is an energy value that reflects the durability of the metal/resin interface. The DCB method provides valuable insights into how the microstructure enhances the toughness of the dental composite (De Souza et al., 2011). The DCB test was recently successfully applied to evaluate the mode I fracture energy of hydrated and thermally dehydrated cortical bone tissues of the young bovine femur, which has a composition similar to that of human dentine (Kageyama et al., 1987). Moreover, results from the DCB test have shown a good correlation with clinical findings (Dastjerdi et al., 2013).

In 1965, Irwin (1958) reported that the stress field around a sharp crack in a linear-elastic material could be uniquely defined by the stress intensity factor K, and that fracture occurs when the value of K exceeds some critical value of the fracture toughness, Kc. Thus, K is a stress field parameter i.e., material-independent, whereas KC reflects an inherent material property. K1C is the critical stress intensity fracture value for crack growth in the material during mode I. The NTP was derived from the chevron-notched short rod (CNSR, ASTM E1304-89) to develop a new method for evaluating the fracture property of materials. Bubsey detailed the mechanics of the NTP test in 1982 (Bubsey et al., 1982), and the test was first applied to dental biomaterials by Ruse in 1996 (Ruse and Feduik, 1996). The NTP test measures the toughness of the interface in bond joints (K1C). According to finite element analysis, the K1C values of poly (methyl methacrylate) obtained by the NTP correlate well with values obtained by the CNSR (Bubsey et al., 1982). These results suggest that the NTP test may be used to determine the fracture mechanics of bulk materials and adhesive interfaces.

CONCLUSION AND FUTURE PROSPECTS

Though dental bonding system are becoming simplified and more efficacy, dentists still must follow manufacturer's direction, adhere to the correct sequence of steps and observe the proper application times of each step. Though fewer bottles are needed, dentists should understand that not all structure is the same and not all material, be it composite, porcelain, zirconia or metal, can be treated similarly.

It is hoped that more dentists will be able to preserve natural teeth and update research on bonding materials in the field of dental bonding in the future. Perhaps the innovative technology of dental bonding materials will bring great impetus to the field of dental bonding research.

AUTHOR CONTRIBUTIONS

ZZ and QW wrote the manuscript with support from JZ, BZ, ZM, and CZ. All authors contributed to the general discussion.

FUNDING

This work was supported by the Program of Scientific Development of Jilin Province (20180414043GH and 20190304112YY), the program of Jilin University (3R2201543428), and the program of the First Hospital of Jilin University (01032140001, 04023720002, and JDYYJC002).

REFERENCES

Abreu, C. W., Santos, J. F. F., Passos, S. P., Michida, S. M. A., Takahashi, F. E., and Bottino, M. A. (2011). The influence of cutting speed and cutting initiation location in specimen preparation for the microtensile bond strength test. *J. Adhesive Dent* 13 (3), 221–226. doi:10.3290/j.jad.a21540

Ajaj, M. T., Al-Khateeb, S., and Al-Batayneh, O. B. (2020). Effect of different acid etchants on the remineralization process of white-spot lesions: an *in vitro* study. *Am. J. Dent* 33 (1), 43–47.

Al Bakkar, H., Spintzyk, S., Schille, C., Schweizer, E., Geis-Gerstorfer, J., and Rupp, F. (2016). Influence of a bonding agent on the bond strength between a dental Co–Cr alloy and nine different veneering porcelains. *Biomed. Tech* 61 (5), 509–517. doi:10.1515/bmt-2015-0101

Ando, T., and Skolnick, J. (2010). Crowding and hydrodynamic interactions likely dominate *in vivo* macromolecular motion. *Proc. Natl. Acad. Sci. U.S.A* 107 (43), 18457–18462. doi:10.1073/pnas.1011354107

Bechtle, S., Fett, T., Rizzi, G., Habelitz, S., Klocke, A., and Schneider, G. A. (2010). Crack arrest within teeth at the dentinoenamel junction caused by elastic modulus mismatch. *Biomaterials* 31 (14), 4238–4247. doi:10.1016/j.biomaterials.2010.01.127

Benetti, A. R., Michou, S., Larsen, L., Peutzfeldt, A., Pallesen, U., and van Dijken, J. W. V. (2019). Adhesion and marginal adaptation of a claimed bioactive, restorative material. *Biomater. Investig. Dent* 6 (1), 90–98. doi:10.1080/26415275.2019.1696202

Blatz, M. B., Vonderheide, M., and Conejo, J. (2018). The effect of resin bonding on long-term success of high-strength ceramics. *J. Dent. Res* 97 (2), 132–139. doi:10.1177/0022034517729134

Blaysat, B., Hoefnagels, J. P. M., Lubineau, G., Alfanob, M., and Geersa, M. G. D. (2015). Interface debonding characterization by image correlation integrated with Double Cantilever Beam kinematics. *Int. J. Solid Struct* 55, 79–91. doi:10.1016/j.ijsolstr.2014.06.012

Bubsey, R. T., Munz, D., Pierce, W. S., and Shannon, J. L. (1982). Compliance calibration of the short rod chevron-notch specimen for fracture-toughness testing of brittle materials. *Int. J. Fract* 18 (2), 125–133. doi:10.1007/BF00019637

Cardenas, A. F. M., Siqueira, F. S. F., Bandeca, M. C., Costa, S. O., Lemos, M. V. S., Feitora, V. P., et al. (2018). Impact of pH and application time of meta-phosphoric acid on resin-enamel and resin-dentin bonding. *J. Mech. Behav. Biomed. Mater* 78, 352–361. doi:10.1016/j.jmbbm.2017.11.028

Dapieve, K. S., Machry, R. V., Pilecco, R. O., Kleverlaan, C. J., Pereira, G. K. R., Venturini, A. B., et al. (2020). One-step ceramic primer as surface conditioner: effect on the load-bearing capacity under fatigue of bonded lithium disilicate ceramic simplified restorations. *J. Mech. Behav. Biomed. Mater* 104, 9. doi:10.1016/j.jmbbm.2020.103686

Dastjerdi, A. K., Tan, E., and Barthelat, F. (2013). Direct measurement of the cohesive law of adhesives using a rigid double cantilever beam technique. *Exp. Mech* 53 (9), 1763–1772. doi:10.1007/s11340-013-9755-0

De Souza, J. A., Goutianos, G., Skovgaard, M., and Sørensen, B. F. (2011). Fracture resistance curves and toughening mechanisms in polymer based dental composites. *J. Mech. Behav. Biomed. Mater* 4 (4), 558–571. doi:10.1016/j.jmbbm.2011.01.003

El-Damanhoury, H. M., and Gaintantzopoulou, M. D. (2018). Self-etching ceramic primer versus hydrofluoric acid etching: etching efficacy and bonding performance. *J. Prosthodont. Res* 62 (1), 75–83. doi:10.1016/j.jpor.2017.06.002

Fonzar, R. F., Goracci, C., Carrabba, M., Louca, C., Ferrari, M., and Vichi, A. (2020). Influence of acid concentration and etching time on composite cement adhesion to lithium-silicate glass ceramics. *J. Adhes. Dent* 22 (2), 175–182. doi:10.3290/j.jad.a44282

Hotchkiss, K. M., Reddy, G. B., Hyzy, S. L., Schwartz, Z., Boyan, B. D., and Navarrete, R. O. (2016). Titanium surface characteristics, including topography and wettability, alter macrophage activation. *Acta Biomater* 31, 425–434. doi:10.1016/j.actbio.2015.12.003

Ikemura, K., Fujii, T., Negoro, N., Endo, T., and Kadoma, Y. (2011). Design of a metal primer containing a dithiooctanoate monomer and a phosphonic acid monomer for bonding of prosthetic light-curing resin composite to gold, dental precious and non-precious metal alloys. *Dent. Mater. J* 30 (3), 300–307. doi:10.4012/dmj.2010-163

Imamura, N., Kawaguchi, T., Shimizu, H., and Takahashi, Y. (2018). Effect of three metal priming agents on the bond strength of adhesive resin cement to Ag-Zn-Sn-In alloy and component metals. *Dent. Mater. J* 37 (2), 301–307. doi:10.4012/dmj.2017-139

Irwin, G. R. (1958). "Fracture," in *Elasticity and Plasticity/Elastizität und Plastizität*. Editor S. Flügge (Berlin, Heidelberg, Germany: Springer Berlin Heidelberg), 551–590.

Jancar, J. (2011). Bond strength of five dental adhesives using a fracture mechanics approach. *J. Mech. Behav. Biomed. Mater* 4 (3), 245–254. doi:10.1016/j.jmbbm.2010.09.004

Kageyama, K., Kobayashi, T., and Chou, T. W. (1987). Analytical compliance method for mode-I interlaminar fracture-toughness testing of composites. *Composites* 18 (5), 393–399. doi:10.1016/0010-4361(87)90364-8

Khargekar, N. R., Kalathingal, J. H., Sam, G., Elpatal, M. A., Hota, S., and Bhushan, P. (2019). Evaluation of different pretreatment efficacy with fluoride-releasing material on shear bond strength of orthodontic bracket: an *in vitro* study. *J. Contemp. Dent. Pract* 20 (12), 1442–1446. doi:10.5005/jp-journals-10024-2697

Kumasaka, T., Ohno, A., Hori, N., Hoshi, N., Maruo, K., and Kuwabara, A. (2018). Influence of ultraviolet irradiation treatment on porcelain bond strength of titanium surfaces. *Dent. Mater. J* 37 (3), 422–428. doi:10.4012/dmj.2016-417

Markovic, D. L., Petrovic, B. B., Peric, T. O., Trisic, D., Kojic, S., and Kuljic, B. L. (2019). Evaluation of sealant penetration in relation to fissure morphology, enamel surface preparation protocol and sealing material. *Oral Health Prev. Dent* 17 (4), 349–355. doi:10.3290/j.ohpd.a42689

Nguyen, T. M. T., Wang, P. W., Hsu, H. M., Cheng, F. Y., Shieh, D. B., Wong, T. Y., Chang, H. J., et al. (2019). Dental cement's biological and mechanical properties improved by ZnO nanospheres. *Mater. Sci. Eng. C Mater. Biol. Appl* 97, 116–123. doi:10.1016/j.msec.2018.12.007

Paing, S. Y., Tichy, A., Hosaka, K., Nagano, D., Nakajima, M., and Tagami, J. (2020). Effect of smear layer deproteinization with HOCl solution on the dentin bonding of conventional and resin-modified glass-ionomer cements. *Eur. J. Oral Sci* 128 (3), 255–262. doi:10.1111/eos.12694

Qiu, X. H., Xu, S., Hao, Y., Peterson, B., Li, B., Yang, K., et al. (2020). Biological effects on tooth root surface topographies induced by various mechanical treatments. *Colloids Surf. B Biointerfaces* 188, 110748. doi:10.1016/j.colsurfb.2019.110748

Ramakrishnaiah, R., Alkheraif, A. A., Divakar, D. D., Matinlinna, J. P., and Vallittu, P. K. (2016). The effect of hydrofluoric acid etching duration on the surface micromorphology, roughness, and wettability of dental ceramics. *Int. J. Mol. Sci* 17 (6), 17. doi:10.3390/ijms17060822

Ruse, N. D., and Feduik, D. (1996). Notchless triangular prism (NTP) fracture toughness testing of dental luting cements. *J. Dent. Res* 75, 23.

Sai, K., Takamizawa, T., Imai, A., Tsujimoto, A., Ishii, R., and Barkmeier, W. W. (2018). Influence of application time and etching mode of universal adhesives on enamel adhesion. *J. Adhes. Dent* 20 (1), 65–77. doi:10.3290/j.jad.a39913

Sang, T., Ye, Z., Fischer, N. G., Skoe, E. P., Echeverría, C., Wu, J., et al. (2020). Physical-chemical interactions between dental materials surface, salivary pellicle and *Streptococcus gordonii*. *Colloids Surf. B Biointerfaces* 190, 10. doi:10.1016/j.colsurfb.2020.110938

Sato, T., Takagaki, T., Ikeda, M., Nikaido, T., Burrow, M. F., and Tagami, J. (2018). Effects of selective phosphoric acid etching on enamel using "no-wait" self-etching adhesives. *J. Adhes. Dent* 20 (5), 407–415. doi:10.3290/j.jad.a41359

Shahid, S., Billington, R. W., Hill, R. G., and Pearson, G. J. (2010). The effect of ultrasound on the setting reaction of zinc polycarboxylate cements. *J. Mater. Sci. Mater. Med* 21 (11), 2901–2905. doi:10.1007/s10856-010-4146-x

Shimizu, H., Inokoshi, M., Takagaki, T., Uo, M., and Minakuchi, S. (2018). Bonding efficacy of 4-META/MMA-TBB resin to surface-treated highly translucent dental zirconia. *J. Adhes. Dent* 20 (5), 453–459. doi:10.3290/j.jad.a41330

Sofan, E., Sofan, A., Palaia, G., Tenore, G., Romeo, U., and Migliau, G. (2017). Classification review of dental adhesive systems: from the IV generation to the universal type. *Ann. Stomatol* 8 (1), 1–17. doi:10.11138/ads/2017.8.1.001

Souza, A. C. D., Gonçalves, F. C. P., Anami, L. C., de Melo, R. M., Bottino, M. A., and Valandro, L. P. (2015). Influence of insertion techniques for resin cement and mechanical cycling on the bond strength between fiber posts and root dentin. *J. Adhes. Dent* 17 (2), 175–180. doi:10.3290/j.jad.a33993

Thoppul, S. D., Finegan, J., and Gibson, R. F. (2009). Mechanics of mechanically fastened joints in polymer-matrix composite structures–a review. *Compos. Sci. Technol* 69 (3–4), 301–329. doi:10.1016/j.compscitech.2008.09.037

van der Spoel, D., van Maaren, P. J., Larsson, P., and Tîmneanu, N. (2006). Thermodynamics of hydrogen bonding in hydrophilic and hydrophobic media. *J. Phys. Chem. B* 110 (9), 4393–4398. doi:10.1021/jp0572535

Wang, R., Liu, H., and Wang, Y. (2019). Different depth-related polymerization kinetics of dual-cure, bulk-fill composites. *Dent. Mater* 35 (8), 1095–1103. doi:10.1016/j.dental.2019.05.001

Wetzel, R., Eckardt, O., Biehl, P., Brauer, D. S., and Schacher, F. H. (2020). Effect of poly(acrylic acid) architecture on setting and mechanical properties of glass ionomer cements. *Dent. Mater* 36 (3), 377–386. doi:10.1016/j.dental.2020.01.001

Yoshihara, K., Nagaoka, N., Sonoda, A., Maruo, Y., Makita, Y., Okihara, T., et al. (2016). Effectiveness and stability of silane coupling agent incorporated in 'universal' adhesives. *Dent. Mater* 32 (10), 1218–1225. doi:10.1016/j.dental.2016.07.002

Conflict of Interest: The authors declare that the research was conducted in the absence of any commercial or financial relationships that could be construed as a potential conflict of interest.

frontiers
in Bioengineering and Biotechnology

ORIGINAL RESEARCH
published: 12 January 2021
doi: 10.3389/fbioe.2020.621788

Graphene-Modified Titanium Surface Enhances Local Growth Factor Adsorption and Promotes Osteogenic Differentiation of Bone Marrow Stromal Cells

Jiayu Lu[1†], Jiayue Sun[1†], Derong Zou[1], Jinlin Song[2,3,4*] and Sheng Yang[2,3,4*]

[1] Department of Stomatology, Shanghai Jiao Tong University Affiliated Sixth People's Hospital, Shanghai, China, [2] College of Stomatology, Chongqing Medical University, Chongqing, China, [3] Chongqing Key Laboratory of Oral Diseases and Biomedical Sciences, Chongqing Medical University, Chongqing, China, [4] Chongqing Municipal Key Laboratory of Oral Biomedical Engineering of Higher Education, Chongqing Medical University, Chongqing, China

OPEN ACCESS

Edited by:
Junchao Wei,
Nanchang University, China

Reviewed by:
Buer Sen,
University of North Carolina at Chapel Hill, United States
Lei Sui,
Tianjin Medical University, China

Correspondence:
Sheng Yang
ysdentist@hospital.cqmu.edu.cn
Jinlin Song
songjinlin@hospital.cqmu.edu.cn

† These authors have contributed equally to this work

Specialty section:
This article was submitted to Biomaterials, a section of the journal Frontiers in Bioengineering and Biotechnology

Received: *27 October 2020*
Accepted: *14 December 2020*
Published: *12 January 2021*

Citation:
Lu J, Sun J, Zou D, Song J and Yang S (2021) Graphene-Modified Titanium Surface Enhances Local Growth Factor Adsorption and Promotes Osteogenic Differentiation of Bone Marrow Stromal Cells. Front. Bioeng. Biotechnol. 8:621788. doi: 10.3389/fbioe.2020.621788

Graphene coating exhibits excellent abilities of protein adsorption and cell adhesion, which might expand the osteogenic activity of titanium implant surface to adapt to the environment of low bone mass and poor bone quality. In this paper, we designed and explored the graphene-coated titanium sheet, through the surface modification of oxygen-containing functional groups, to optimize the adsorption capacity of material by improving the electrostatic interactions, and successfully adsorbed and sustained-released a variety of osteogenic related growth factors in the autologous concentrated growth factors. Compared with the pure titanium, we observed that the bone marrow stromal cells (BMSCs) on the graphene-coated titanium with concentrated growth factors showed a flat shape and expressed osteogenic related genes and proteins, while the coating surfaces promoted and accelerated the osteogenic differentiation ability of BMSCs. The results suggested that it might be a feasible alternative to improve the osteogenesis of dental implant in the early stage.

Keywords: graphene, graphene coating, concentrated growth factors, osteogenic differentiation, bone marrow stromal cells

INTRODUCTION

With the rapid development of surface nano-modification technology, metal implants have become the main orthopedic biomaterials (Chrcanovic et al., 2014). SLA (**S**andblasting, **L**arge grid, **A**cid-etched) treated surface metal implants prepared by acid etching and roughening can increase the implant-bone interface contact area by more than 60% due to the preparation of a porous titanium implant surface topography, and significantly enhance the torque resistance of the implant and greatly increase the success rate (Li et al., 2002). However, improving the osseointegration ability of metal materials, enhancing local cytokine enrichment, and improving the osteogenic microenvironment around the implant are very important to further improve the osteogenesis ability of the implants.

Growth factors or cytokines can be used as biological signal initiating factors in a specific microenvironment to promote the mobilization of endogenous stem cells in the body, regulate tissue cells to quickly adapt to implants, and promote osseointegration and bone defect repair (Varkey et al., 2004; Tayalia and Mooney, 2009). The use of safe and reliable concentrated growth factors excludes the possibility of immune rejection and cross-infection with exogenous growth factors (Chen et al., 2010). Due to the lack of anticoagulants, the coherent fibrin scaffolds in current platelet-rich products including platelet-rich fibrin (PRF), advanced platelet-rich fibrin (A-PRF), and concentrated growth factors (CGF) prevent binding to the bone grafts. Liquid concentrated growth factor preparations such as injectable PRF (i-PRF) and liquid CGF, the sparse fibrin networks of which contain high concentrations of multiple growth factors, can be used alone or as a supplement to other biomaterials in regenerative medicine to promote tissue regeneration (Simonpieri et al., 2012; Mourao et al., 2015; Murray, 2018).

Building materials with adsorption capacity on the surface of the implant is an effective way to enrich the above-mentioned various cytokines and proteins. Graphene coating has become an excellent candidate material for its high strength, large specific surface area, and porosity (Yan et al., 2017; Stephens-Fripp et al., 2018; Wu et al., 2019; Xing et al., 2019). It has also generated great expectations in the biomedical field due to its extraordinary mechanical properties, biocompatibility, electrical conductivity and so on (Liao et al., 2018; Ryan et al., 2018). In particular, graphene has broad application prospects in the field of biomaterials. Graphene is reported to have osteoinductivity, which promotes osteogenesis and osseointegration and further repairs bone defects (Lu et al., 2016; Holt et al., 2017). The cells on the surface exhibit enhanced proteins adsorption and osteogenic activity owing to the large surface area and oxygen-containing functional groups of graphene (Dubey et al., 2015).

Our research uses graphene coating technology to increase the electrostatic and chemical functional groups on the surface of the titanium plate to optimize the adsorption capacity. After interacting with autologous concentrated growth factors, the graphene-coated titanium can successfully adsorb and sustained release several osteogenic related growth factors. The results revealed that BMSCs on the graphene- coated titanium sheets exhibited flattened shapes and expressed more obvious osteogenic related genes and proteins compared to the pure titanium. The RhoA/ROCK1/ERK1/2 signaling pathway related to cytoskeleton deformation was also up-regulated. In addition, the adsorption of various growth factors on the surface of graphene-coated titanium sheet could further promote and accelerate the osteogenic differentiation of BMSCs. The results suggested that the graphene-coated titanium with concentrated growth factors may enhance the osteogenic ability as bone tissue engineering scaffold, bone repair, dental implant and bone graft materials.

MATERIALS AND METHODS

Preparation of Graphene-Coated Titanium Sheets

The surface of titanium sheet was treated by SLA, and immersed in 3% ethanol solution of 3-aminopropyltriethoxysilane (3-APTES, 3% ethanol solution of APTES) for 30 min to improve the adhesion between graphene and titanium. Then reduced graphene oxide (rGO) nanosheets were loaded on the titanium sheets by immersing the functionalized samples into the rGO solution (0.4, 0.04, and 0.004 mg/ml) for 1 h, which were synthesized by chemical reduction of a GO solution acquired by chemical oxidation and exfoliation of natural graphite using our previously reporte d method and characterized by atomic force microscopy (AFM) (Lu et al., 2016). The synthesized graphene-coated titanium sheets were then cleaned under ultrasonic for 30 min to remove the uncoated rGO nanosheets.

Characterization of Graphene-Coated Titanium Sheets

Raman spectroscopy (Bruker Optic SENTERRA, R-200L) was used to identify the surface characteristics of graphene-coated titanium sheets at room temperature with a laser wavelength of 633 nm. The chemical compositions of the samples were analyzed by X-ray photoelectron spectroscopy (XPS, AXIS Ultra DLD, Kratos). Fourier transform infrared radiation (FTIR) was conducted by a Perkin Elmer Spectrum 100 analyzer. The conductivity of the samples was measured by using a four-probe technique (Jandel Model RM3000). A field emission scanning electron microscope (SEM, Nova NanoSEM, NPE218) was used to observe the morphology of the samples.

Biocompatibility of Graphene-Coated Titanium Sheets

In order to isolate bone marrow stromal cells (BMSCs), 5 ml bone marrow was collected from rabbit iliac crest of 12-month-old rabbits (average weight 2.5 kg) and cultured in Dulbecco modified Eagle medium (DMEM) (Gibco, USA) containing 10% FBS (Gibco, USA) in 5% CO_2 incubator. The medium was changed every 2 days. When the cells reached 80% confluence, the cells are passaged. Animal experiments were approved by the Animal Welfare Ethics Committee of Shanghai Sixth People's Hospital affiliated to Shanghai Jiao Tong University, School of Medicine (No: DWLL2020-0577).

All samples were sterilized by autoclaving (125°C/0.14 MPa, 30 min) before use. The BMSCs were cultured on the graphene-coated titanium sheets for 2 days. The potential cytotoxic effects of the samples were assessed using the Live/Dead Staining Kit (ScienCell, USA) according to the manufacturer's instructions. Live cells were stained with the fluoresces green polyanionic dye calcein, while dead cells with damaged membranes allowed EthDIII to enter and bind to nucleic acids fluoresced red under the fluorescence microscope (DMI6000B; Leica, Germany).

Adsorption and Sustained Release of Concentrated Growth Factors by Graphene-Coated Titanium Sheets

After intravenous anesthesia with pentobarbital sodium (30 mg/kg), chest hair of 12-month-old rabbits (average weight 2.5 kg) was taken and skin was disinfected. Then, 10 ml of whole blood was extracted from the heart and transferred to a centrifuge tube containing an anticoagulant (heparin lithium). At centrifuging at 3,000 rpm for 10 min (TR-18, Trausiam, China), 1 mL of liquid containing concentrated growth factors was collected from 3 mm above the red blood cell aggregation on the bottom. 800,000U of penicillin was injected to prevent infection for 3 days.

The graphene-coated titanium sheets were immersed in the concentrated growth factors at 37°C for 2 days for adsorption. Then the remaining liquid was collected. The growth factors of original and remaining concentrated growth factors including PDGF, VEGF, TGF-β, IGF, FGF, and BMP-2 were quantified by ELISA assay according to the manufacturer's protocol. In short, 40 µL of test dilutions and 10 µL of the sample were co-cultured in 96 well antibody precoated plates at 37°C for 30 min. Wells then were washed five times. After incubation with enzyme solution in the dark for 15 min, 50 µL stop solution was added to stop the enzyme reaction. The absorbance was measured at 450 nm with a microplate reader (iMark, Bio-Rad, USA). All samples were measured in triplicate.

The graphene-coated titanium sheets with concentrated growth factors were placed in 2 mL PBS to allow the growth factors to release. At each time point (1, 2, 7, and 14 days), the supernatant was collected. Sustained release of PDGF, VEGF, TGF-β, IGF, FGF, and BMP-2 were quantified by ELISA assay according to the manufacturer's protocol above.

Morphological Changes of the BMSCs on Graphene-Coated Titanium Sheets With Concentrated Growth Factors

The BMSCs were cultured on samples with concentrated growth factors (2 days' adsorption) for 3 days, then fixed overnight with 2.5% glutaraldehyde at 4°C and freeze-dried (Alpha 1-2; Christ, Germany). Finally, the adhesion and growth of the BMSCs on the sheets were observed by field emission scanning electron microscope (SEM, Nova NanoSEM, NPE218).

The morphology of the BMSCs was observed by labeling the actin cytoskeleton with Phalloidia-TRITC (Sigma, USA). In short, the BMSCs were cultured on the samples with concentrated growth factors for 24 h, and then fixed in 4% paraformaldehyde at room temperature for 30 min. After 0.1% Triton X-100 for 20 min, the actin cytoskeleton was labeled by incubating with Phalloidia-iFluor 488 (Abcam, USA) for 30 min and visualized with a fluorescence microscope (DMI6000B; Leica, Germany).

Osteogenic Differentiation of the BMSCs on Graphene-Coated Titanium Sheets

The BMSCs were seeded on the samples with concentrated growth factors and culture dishes in a growth medium or osteogenic medium (growth medium containing 50 µg/mL L-ascorbic acid, 10 mM glycerophosphate and 100 nM dexamethasone) (Su et al., 2020). ALP activity was evaluated as previously described on days 1, 4, and 7 after cell seeding. Briefly, the cells were isolated from the plate with trypsin/EDTA and resuspended in 0.2% NP-40 lysis buffer. Each sample was mixed with 1 mg/mL p-nitrophenyl phosphate (pNPP, sigma, USA) in 1 M diethanolamine as a substrate and incubated at 37°C for 15 min. The reaction was stopped by adding 3N NaOH. ALP activity was quantified by absorbance at 405 nm (ELX808; Bio-tek, USA). The total protein content of the same sample was determined by Bradford method with Bio-Rad protein analysis kit (Bio-Rad, USA), read at 630 nm and calculated according to a series of BSA (Sigma, USA) standards. ALP activity was calculated as the absorbance of 405 nm (OD value) per mg of total cell protein. All experiments were conducted in three times.

The BMSCs were seeded on the samples with concentrated growth factors and culture dishes in a growth medium or osteogenic medium for 21 days. The mineral deposits in the extracellular matrix were analyzed by staining with 10 mg/L Alizarin Red S for 5–7 days, and then visualized using a fluorescence microscopy (DMI6000 B, Leica, Germany).

The BMSCs were seeded on the samples with concentrated growth factors and culture dishes in a growth medium or osteogenic medium for 15 days. The cells on substrates were fixed by 4% paraformaldehyde for 30 min. The anti-BMP-2 and anti-RUNX-2 primary antibody (Abcam, USA) was added onto the samples at 4°C overnight. After rinsing, fluorescein isothiocyanate (FITC) goat anti-mouse second antibody (Abcam, USA) was added onto each chip and incubated at room temperature for 1 h. The chips were inverted onto glass slides mounted with Fluoroshield with DAPI (Sigma, USA) and visualized under a fluorescence microscope (DMI6000B, Leica, Germany).

The BMSCs were seeded on the samples with concentrated growth factors and culture dishes in a growth medium or

TABLE 1 | Primer sequences of osteogenic genes expressed by BMSCs.

Gene Target	Primers sequence (5′-3′)
ALP	Forward primer: 5′ CGTGGCAACTCCATCTT 3′ Reverse primer: 5′ AGGGTTTCTTGTCCGTGT 3′
BMP-2	Forward primer: 5′ TGAGGATTAGCAGGTCTTT 3′ Reverse primer: 5′ TGGATTTGAGGCGTTT 3′
ERK1/2	Forward primer: 5′ GCGTGGTGTTCAAGGT 3′ Reverse primer: 5′ TCTCGCCATCGCTGTA 3′
OCN	Forward primer: 5′ ACTCTTGTCGCCCTGCTG 3′ Reverse primer: 5′ TCGCTGCCCTCCCTCT 3′
OPN	Forward primer: 5′ TACCTTCTGATTGGGACA 3′ Reverse primer: 5′ CGAAATTCACGGCTCT 3′
RohA	Forward primer: 5′ CAAGATGAAGCAGGAGC 3′ Reverse primer: 5′ ACAAGACAAGGCACCC3 3′
ROCK	Forward primer: 5′ GTGAAGCCTGACAACA 3′ Reverse primer: 5′ CTCGTCCATAATAACCAT 3′
RUNX-2	Forward primer: 5′ GACCACCCAGCCGAACT 3′ Reverse primer: 5′ CAGCACCGAGCACAGGA 3′

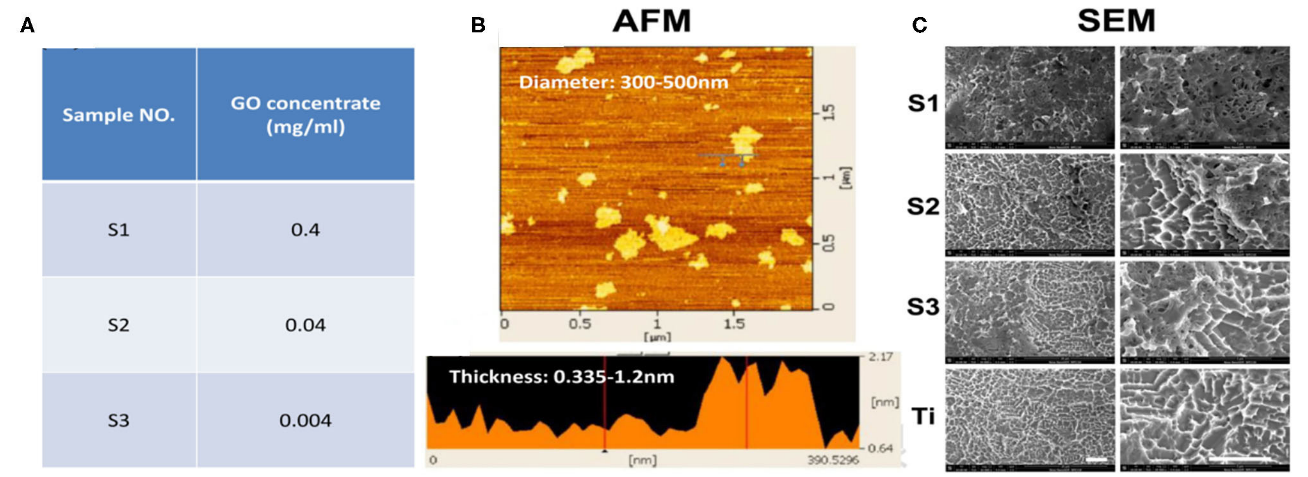

Sample NO.	GO concentrate (mg/ml)
S1	0.4
S2	0.04
S3	0.004

FIGURE 1 | Preparation and SEM images of the graphene-coated titanium sheets. **(A)** Sample No. of **S1**, **S2**, and **S3** indicates the 0.4, 0.04, and 0.004 mg/ml of the rGO solution. **(B)** The thickness and the diameter of the loaded rGO nanosheets were characterized by AFM. **(C)** SEM images of graphene coating on SLA treated titanium sheets and pure SLA treated titanium (**Ti**). Scale bars: 5 µm.

osteogenic medium for 1, 7, and 15 days. Whole RNA was extracted from the cells according to the vendor's protocol (Invitrogen, USA). PrimeScript reagent kit of reverse reaction (Thermo Fisher Scientific, USA) was used to carry out reverse transcription reaction on RNA following the protocols of the manufacturer. Quantitative analysis on the change of expression level of ALP, BMP-2, ERK1/2, OCN, OPN, RhoA, ROCK, RUNX-2 genes (**Table 1**) was conducted by Maxima SYBR Green Master Mix (Thermo Fisher Scientific, USA) in ABI PRISM 9700 PCR (ABI, USA). Realtime RCR reaction was performed at 94°C for 10 min and 40 cycles of amplification, which consisted of denaturation step at 94°C for 15 s, annealing step at 65°C for 30 s, and extension step at 72°C for 30 s. The primer sequences were shown subsequently in **Table 1**. The relative expressions of these genes were normalized to the β-Actin gene expression. The change in the expression of mRNA was assessed by the 2-ΔΔCt approach.

Statistical Analysis

All sample values were expressed as the Mean values ± standard deviation and analyzed by Prism software (GraphPad Prism 8). Statistically significant values were defined as $*p < 0.05$, $^{**}p < 0.01$, $^{***}p < 0.001$, and $^{****}p < 0.0001$ based on one-way analysis of variance (ANOVA).

RESULTS

Preparation and Characterization of Graphene-Coated Titanium Sheets

The thickness of the loaded rGO nanosheets (0.4, 0.04, and 0.004 mg/ml) was about 0.335–1.2 nm and the diameter was about 300–500 nm (**Figures 1A,B**). SEM images (**Figure 1C**) clearly showed that the surface of titanium treated by SLA formed a porous structural morphology with a diameter of about 2 µm. It is reported that the biological activity of the implant surface and the bond strength of the implant-bone interface can be improved by roughening the surface. SEM also showed the graphene-coated titanium sheets with graphene coating attached on the porous surface (**Figure 1C**). On the S1, rGO coated the entire surface and stacked up. As the concentration decreased, the graphene distributed more evenly. On the S3, graphene concentration was too low and the surface of titanium exposed.

The Raman spectra (**Figure 2A**) of S1–S3 samples showed the characteristic peaks of graphene at about 1,580 and 1,350 cm-1, revealing that their surfaces are all coated with graphene, while these two peaks are not seen on the surface of titanium sheet. As shown in **Figure 2B**, XPS measurement spectra of graphene-coated titanium sheets showed that the relative intensity of C1s/O1s peak decreased significantly with the decrease of loading concentration, indicating the weakening of oxygen functional groups. The high resolution XPS C1s core level spectra (**Figure 2C**) showed three peaks with centers at 284.7, 285.7 and 288.2 eV, corresponding to C-C/C=C, C-O and C=O (carbon-carbon bond, hydroxyl group and carbonyl group, respectively). With the decrease of the load concentration, the three peaks gradually weaken. FTIR spectra (**Figure 2D**) showed the characteristic peaks of rGO (C-OH at 3,315 cm-1, C=O of 1,608 cm-1 and epoxy resin of 1,075 cm-1), which means that functional rGO nanosheets have been successfully introduced into the surface of porous titanium sheets. With the increase of loading concentration, the conductivity of the sheets also increased (**Figure 2E**), which indicated that rGO nanosheets has been successfully introduced into the surface of porous titanium sheets and increased the conductivity of the sheets.

Biocompatibility of Graphene-Coated Titanium Sheets

After growing 2 days on the graphene-coated titanium sheets, the BMSCs in all groups showed green living cells, with only a few red dead cells, revealing that the graphene-coated titanium

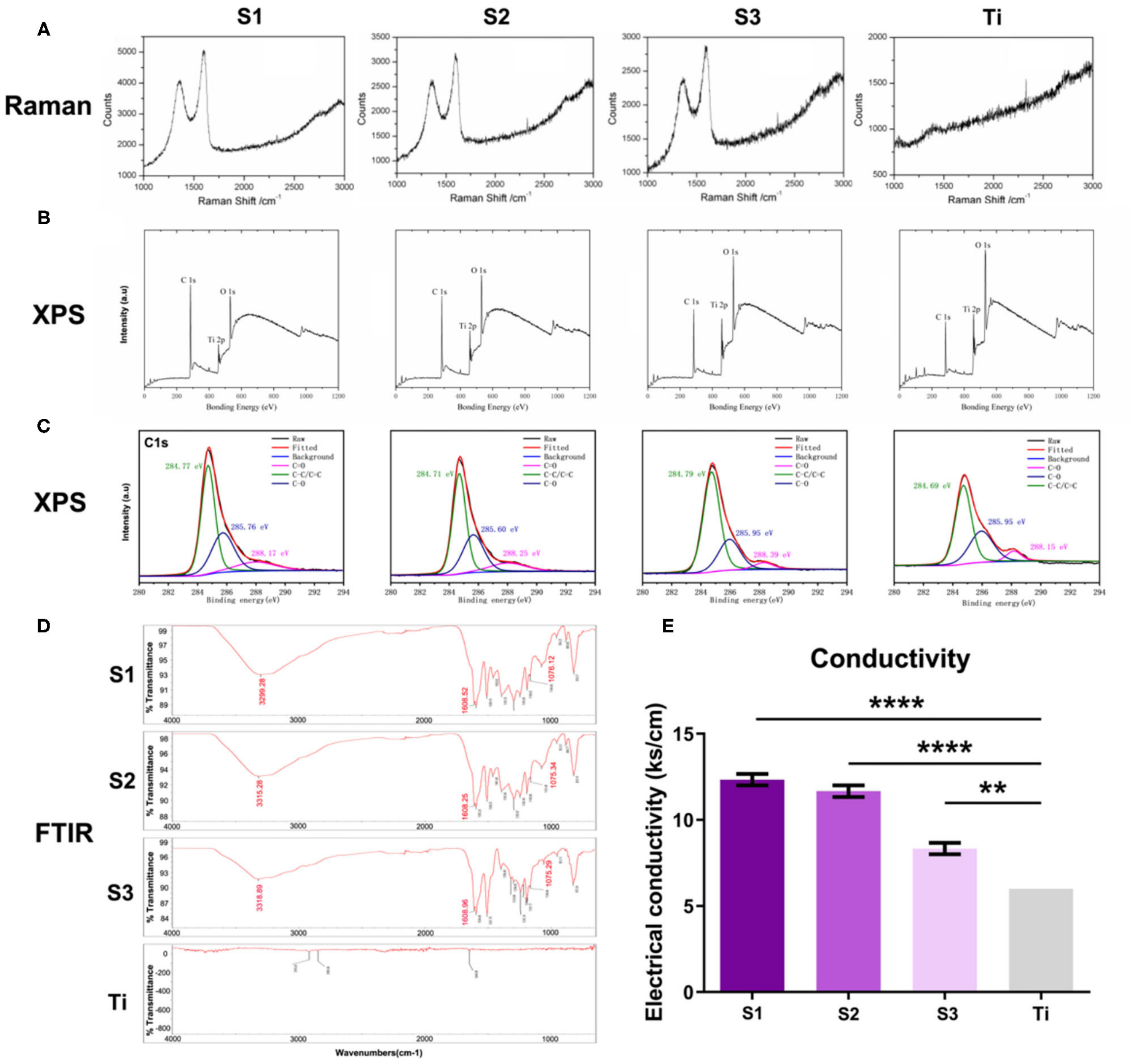

FIGURE 2 | The characterization of the graphene-coated titanium sheets. **(A)** The Raman spectra, **(B)** XPS measurement spectra, **(C)** the high resolution XPS C1s core level spectra, **(D)** FTIR spectra and **(E)** the conductivity of graphene-coated titanium sheets (**S1, S2, and S3**) and titanium sheet (**Ti**). (**$p < 0.01$ and ****$p < 0.0001$).

sheets had good biocompatibility and were suitable as implants for bone regeneration (**Figure 3A**). Cell viability, expressed as the ratio of live to dead cells, was 96.98 ± 0.22%, 98.09 ± 0.61%, 97.97 ± 1.35%, 97.72 ± 1.52%, and 99.40 ± 0.17% on samples S1–S3, titanium sheet and cell slide, respectively (**Figure 3B**), further confirmed the non-toxic to cells. After growing 3 days on the samples, SEM observation (**Figure 3C**) showed that the cells on each sample were spread out and appeared confluent, indicating that the cells grew well on the materials. Changes in cell morphology may be the result of a combination of rGO coating surface morphology, mechanical properties, and electrical conductivity. In general, the adhesion, adaptation and proliferation of BMSCs on the surface of graphene-coated titanium plates were similar to that of the titanium plate, which indicated that the graphene-coated titanium plates had good biocompatibility.

Adsorption and Sustained Release of Osteogenic Growth Factors

After centrifugation, concentrated growth factors can be easily obtained on the erythrocyte deposition layer. Immersed in the concentrated growth factors for 2 days for adsorption, the

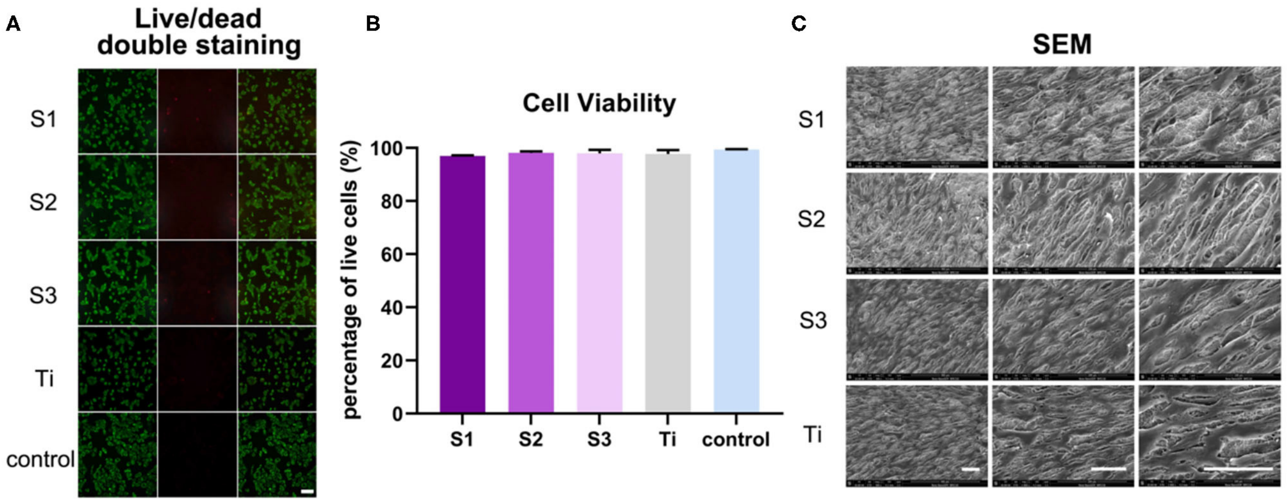

FIGURE 3 | BMSCs viability and growth on graphene-coated titanium sheets and titanium sheet. **(A)** Live/dead double staining of BMSCs on different samples (live cells were stained florescent green, and dead cells appeared red). **(B)** Cell viability of BMSCs on graphene-coated titanium sheets and titanium sheet. **(C)** SEM images of adhesion of BMSCs onto graphene-coated titanium sheets and titanium sheet at 3 days after seeding. Scale bars: 100 μm.

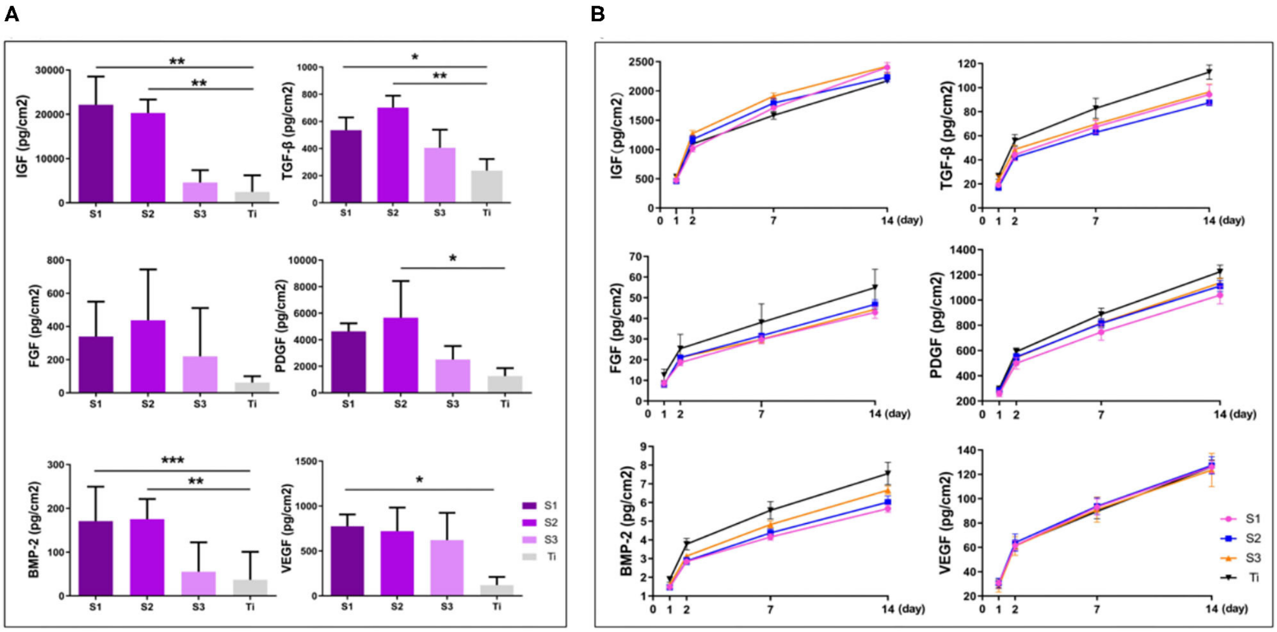

FIGURE 4 | Adsorption **(A)** and cumulative sustained release **(B)** of osteogenic growth factors of graphene-coated titanium sheets and titanium sheet (*$p < 0.05$, **$p < 0.01$, and ***$p < 0.001$).

graphene-coated titanium sheets can adsorb more growth factors than the titanium sheet, especially TGF-β, IGF and BMP-2 (**Figure 4A**). We calculated the cumulative release of growth factors at day 1, 2, 7, and 14. The results showed that the sustained release of PDGF, VEGF, TGF-β, IGF, FGF, and BMP-2 in all groups over the 14-day observation period (**Figure 4B**). Since graphene absorbs growth factors through chemisorption such as electrostatic force and hydrogen bond. While the titanium plates lack these adsorption mechanisms and growth factors can only be physically adsorbed, the binding forces of which are much smaller than chemisorption (Pan et al., 2019). When releasing, the growth factors physically absorbed on the titanium sheet and graphene release easily. After 14 days, the growth factors on the titanium plates were almost released, while still a lot of growth factors remained on the surface of the graphene-coated titanium plates, especially **S1** and **S2.**

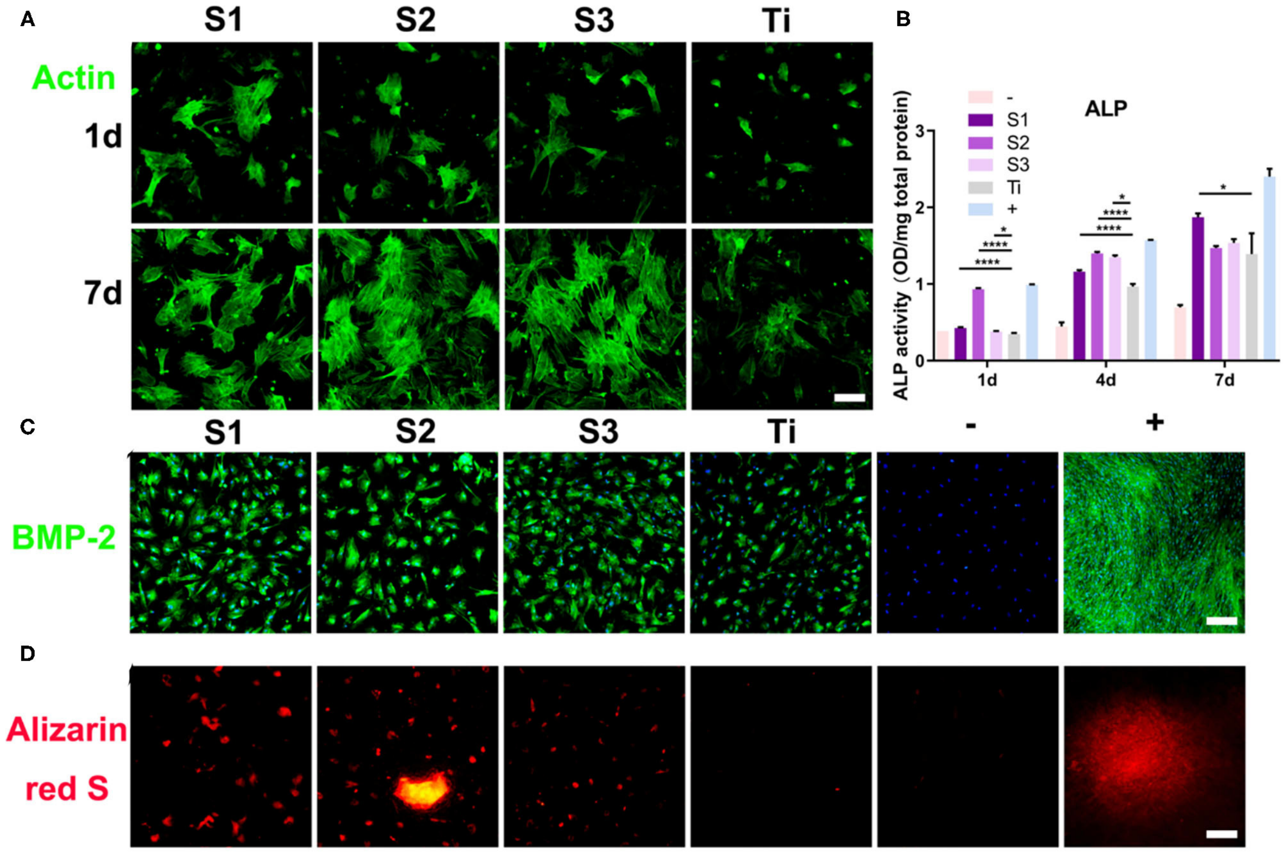

FIGURE 5 | Morphological changes and osteogenic differentiation of BMSCs on the graphene-coated titanium sheets. **(A)** Actin filament network of cell morphologies on graphene-coated titanium sheets and titanium sheet, 24 h and 7d after seeding. **(B)** ALP activity of BMSCs at 1, 4, and 7 days on different samples. **(C)** Immunofluorescence staining for BMP-2 in differentiated BMSCs at 15 days and **(D)** alizarin red S (ARS) staining for mineralized nodules at 21 days. –: BMSCs on glass slides with growth medium. Graphene-coated titanium sheets (**S1–S3**) and titanium sheet (**Ti**) were treated with growth medium. +: BMSCs on glass slides with osteogenic medium (*$p < 0.05$ and ****$p < 0.0001$).

Morphological Changes and Osteogenic Differentiation of BMSCs on Graphene-Coated Titanium Sheets

On the surface of graphene-coated titanium sheets, there were more cellular micro extensions and larger extension areas, and actin filaments had regular directions (**Figure 5A**). This indicates that BMSCs have better adaptability, proliferation and differentiation ability on the surface of the material, which may be due to the higher specific surface area, wrinkled surface morphology, mechanical property, electrical conductivity, reasonable number of functional groups, and more growth factors adsorbed on the graphene-coated titanium sheets.

Alkaline phosphatase (ALP) regulates the metabolism of organic or inorganic phosphates through the hydrolysis of phosphate esters. As a plasma membrane transporter of inorganic phosphates, ALP can be used as an early marker of osteoblast differentiation. In this study, the ALP activity of the cells cultured on graphene-coated titanium sheets increased significantly on the first day after incubation, which was close to that of the osteogenic medium group (**Figure 5B**). At 4 and 7 days after incubation, ALP level of cells on graphene-coated titanium sheets was also higher than that of control titanium sheet group.

Immunofluorescence staining of BMP-2 also confirmed the enhancement of osteogenic differentiation. **Figure 5C** shows that the immunofluorescence expression of the proteins increased significantly on the 15th day after incubation on the graphene-coated titanium sheets. The cells on the control glass slide showed weak fluorescence, while the expression on the titanium plate was also relatively weak. These results indicate that the adsorption of concentrated growth factors on graphene-coated titanium sheets is enough to induce the osteogenic differentiation of BMSCs. The positive Alizarin Red S staining strongly supports our findings that graphene-coated titanium sheets can effectively promote the osteogenic differentiation and calcium deposition of stem cells (**Figure 5D**), and enhance the early osteoblast differentiation.

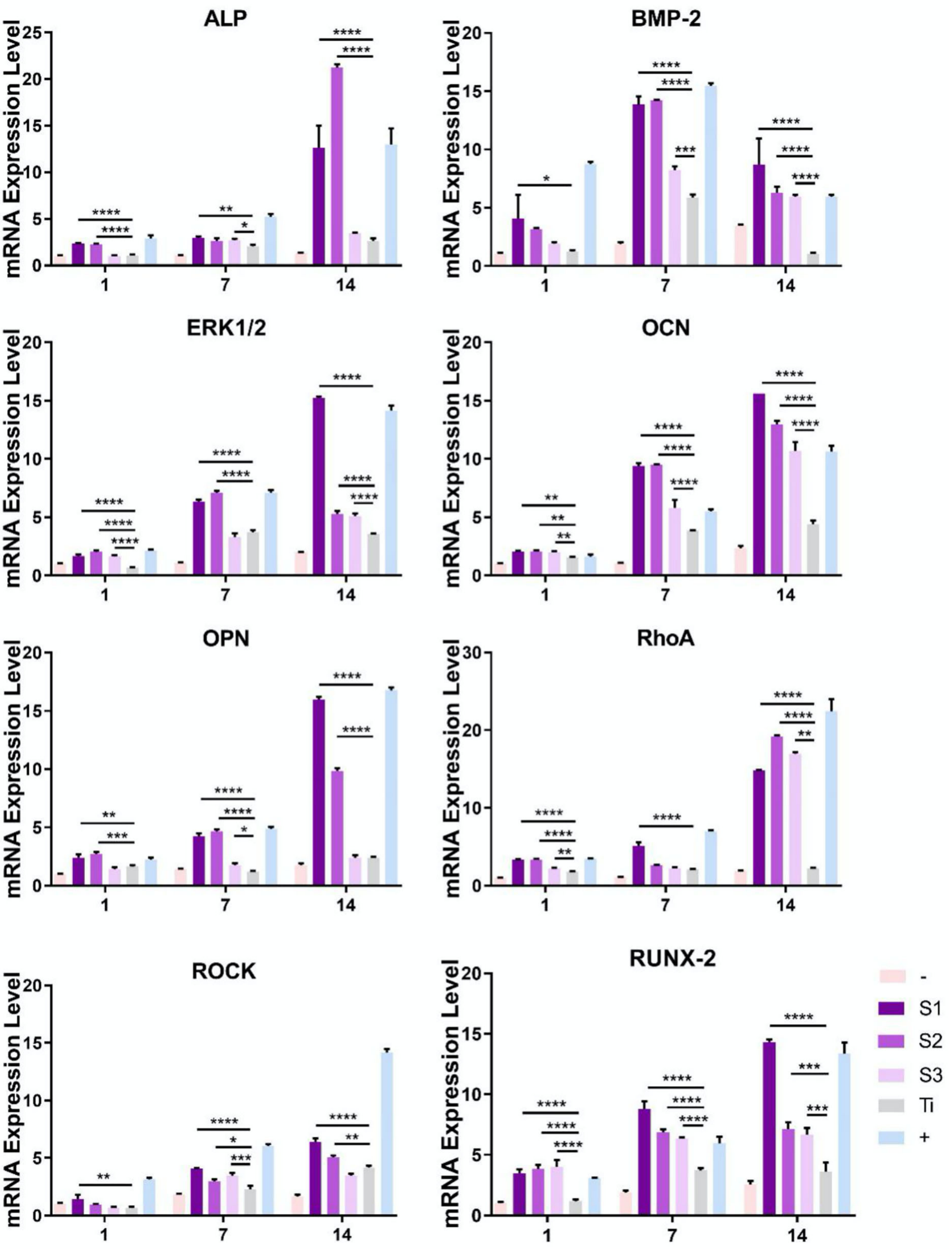

FIGURE 6 | Quantitative RT-PCR analyses for the expression of genes mediating osteogenesis and differentiation processes. −: BMSCs on glass slide with growth medium. Graphene-coated titanium sheets (**S1–S3**) and titanium sheet (**Ti**) were treated with growth medium. +: BMSCs on glass slide with osteogenic medium. Scale bars: 50 μm ($^*p < 0.05$, $^{**}p < 0.01$, $^{***}p < 0.001$, and $^{****}p < 0.0001$).

Gene Expression During Differentiation of BMSCs on Graphene-Coated Titanium Sheets

Specific osteoblast mRNA expression was used to evaluate the differentiation of BMSCs into osteoblast lineage (**Figure 6**). The negative control of each experiment was cells cultured on glass slides (control group), and no osteogenic specific genes were detected. In addition, osteogenic medium was used as positive control to induce osteogenic differentiation on glass slides, resulting in significantly higher osteogenic specific gene expression. We first detected the expression of ALP, a marker of early osteoblast differentiation. From the first day, ALP expression level of BMSCs on the graphene-coated titanium sheets (**S1** and **S2**) was much higher than that of titanium sheet group, and the expression was similar on day 7 and 14. BMP-2 is an early marker of osteogenic differentiation. We found that the expression of BMP-2 in the cells seeded on graphene-coated titanium sheets was significantly higher than that on titanium sheet on day 7 and 14. The expression of ERK1/2, OCN, OPN, RhoA, ROCK, and RUNX-2 showed the same trend.

DISCUSSION

We used SLA coarsening to form a porous structure of about 2 μm on the titanium sheet. After modified by APTES solution, rGO sheets with diameter of 300–500 nm were loaded on the titanium surface, covalent bonds were formed between rGO and APTES, which could promote the rGO sheet to adhere to the porous structure as much as possible, and ultrasonic vibration could not peel them off. On the three concentrations of graphene-coated titanium sheets (0.4, 0.04, and 0.004 mg/ml), the cells showed spreading and confluence phenomenon, which indicated that the materials had good biocompatibility.

Graphene has good osteogenic ability, which is largely attributed to its surface morphology and mechanical properties (Borghi et al., 2018). Surface morphology of materials is the decisive factor of osteogenic differentiation. It has been reported that rough and disordered surfaces can induce osteogenic differentiation (Wall et al., 2009; Sun et al., 2018). The corrugated and porous surface of graphene can also provide anchor points for cytoskeleton, and affect the cytoskeleton tension, thus changing the cell morphology. It has been reported that cell morphology regulates the transition of lineage commitment by regulating endogenous RhoA, which is an important small G protein involved in cell signal transduction and cytoskeleton (McBeath et al., 2004). The results showed that the RhoA/ROCK1/ERK1/2 signaling pathway related to cytoskeleton deformation was also up-regulated. The cells with flat and well-diffused shape will undergo osteogenesis, and BMSCs on graphene-coated titanium sheets will also osteogenic differentiate.

With the increase of rGO coating concentration, the oxygen-containing groups such as hydroxyl groups, epoxy compound and carbonyl groups, as well as the conductivity increase. Graphene coating can optimize the adsorption capacity of materials by improving static electricity and van der Waals force, interact with autologous concentrated growth factors, and successfully adsorb and continuously release a variety of growth factors related to osteogenesis. There are more growth factors remaining on the surface of the materials, which can significantly promote the expression of ALP, BMP-2, RUNX-2, OCN, and OPN of the stem cells on the surface of the materials, suggesting that the materials can promote bone formation earlier and more strongly. Optimum graphene concentration ensures the appropriate amount of growth factors will be adsorbed and release to cooperate with the surface morphology to promote osteogenic. For cell morphology, ALP activity, expression of genes and the amount of growth factors adsorbed and released, we considered the concentration of S2 (0.04 mg/ml) to be the appropriate option.

In summary, rGO was successfully coated on SLA treated titanium surfaces, and graphene-coated titanium sheet surfaces showed good biocompatibility and distinguished capability of adsorbing and sustained releasing several osteogenic related growth factors. BMSCs on the graphene-coated titanium sheet were flattened and expressed more obvious osteogenic related genes and proteins compared to pure titanium, owing to the fact that graphene coating mediated cytoskeletal deformation through the RhoA/ROCK1/ERK1/2 signaling pathway to accelerate the osteogenic differentiation of BMSCs. In addition, the adsorption of various growth factors on the surface of graphene-coated titanium sheet could further promote the osteogenic differentiation ability of BMSCs. The rGO coating with concentrated growth factors was shown to facilitate osteogenic differentiation of implants and to be a potential substance for the modification of dental implants and a scaffold for bone regeneration.

DATA AVAILABILITY STATEMENT

The raw data supporting the conclusions of this article will be made available by the authors, without undue reservation.

ETHICS STATEMENT

The animal study was reviewed and approved by Animal Welfare Ethics Committee of Shanghai Sixth People's Hospital.

AUTHOR CONTRIBUTIONS

SY and JL conceived the original idea and led the project. JL, JS, and DZ performed most of the assays. JL, JS, and SY performed data analysis and wrote the manuscript. All the authors have approved it for publication.

FUNDING

This work was funded by the Natural Science Foundation of China (82071160, 81870806, 81974152, and 81500894), Youth top-notch talent development plan of Shanghai, Special Fund for Scientific and Technological Innovation of Shanghai

Jiao Tong University (ZH2018ZDB09), Double hundred Project of Medical School of Shanghai Jiao Tong University (20191832), Innovative research team of high-level local universities in Shanghai (Oral and maxillofacial regeneration and functional restoration, SSMU-ZDCX20180900), the Basic Research and Frontier Exploration Grant of Chongqing Science and Technology Commission (General Project, Grant No. cstc2019jcyj-msxmX0366).

REFERENCES

Borghi, F. F., Bean, P. A., Evans, M. D. M., van der Laan, T., Kumar, S., and Ostrikov, K. (2018). Nanostructured graphene surfaces promote different stages of bone cell differentiation. *Nanomicro. Lett.* 10:47. doi: 10.1007/s40820-018-0198-0

Chen, F. M., Zhang, M., and Wu, Z. F. (2010). Toward delivery of multiple growth factors in tissue engineering. *Biomaterials* 31, 6279–6308. doi: 10.1016/j.biomaterials.2010.04.053

Chrcanovic, B. R., Albrektsson, T., and Wennerberg, A. (2014). Reasons for failures of oral implants. *J. Oral Rehabil.* 41, 443–476. doi: 10.1111/joor.12157

Dubey, N., Bentini, R., Islam, I., Cao, T., Castro Neto, A. H., et al. (2015). Graphene: a versatile carbon-based material for bone tissue engineering. *Stem Cells Int.* 2015:804213. doi: 10.1155/2015/804213

Holt, B. D., Wright, Z. M., Arnold, A. M., and Sydlik, S. A. (2017). Graphene oxide as a scaffold for bone regeneration. *Wiley Interdiscip. Rev. Nanomed. Nanobiotechnol.* 9:e1437. doi: 10.1002/wnan.1437

Li, D., Ferguson, S. J., Beutler, T., Cochran, D. L., Sittig, C., and Hirt, H. P. (2002). Biomechanical comparison of the sandblasted and acid-etched and the machined and acid-etched titanium surface for dental implants. *J. Biomed. Mater. Res.* 60, 325–332. doi: 10.1002/jbm.10063

Liao, C., Li, Y., and Tjong, S. C. (2018). Graphene nanomaterials: synthesis, biocompatibility, and cytotoxicity. *Int. J. Mol. Sci.* 19:3564. doi: 10.3390/ijms19113564

Lu, J., Cheng, C., He, Y. S., Lyu, C., Wang, Y., Yu, J., et al. (2016). Multilayered graphene hydrogel membranes for guided bone regeneration. *Adv. Mater* 28, 4025–4031. doi: 10.1002/adma.201505375

McBeath, R., Pirone, D. M., Nelson, C. M., Bhadriraju, K., and Chen, C. S. (2004). Cell shape, cytoskeletal tension, and RhoA regulate stem cell lineage commitment. *Dev. Cell* 6, 483–495. doi: 10.1016/S1534-5807(04)00075-9

Mourao, C. F., Valiense, H., Melo, E. R., Mourao, N. B., and Maia, M. D. (2015). Obtention of injectable platelets rich-fibrin (i-PRF) and its polymerization with bone graft: technical note. *Rev. Col. Bras. Cir.* 42, 421–423. doi: 10.1590/0100-69912015006013

Murray, P. E. (2018). Platelet-rich plasma and platelet-rich fibrin can induce apical closure more frequently than blood-clot revascularization for the regeneration of immature permanent teeth: a meta-analysis of clinical efficacy. *Front. Bioeng. Biotech.* 6:139. doi: 10.3389/fbioe.2018.00139

Pan, S., Qi, Z., Li, Q., Ma, Y., Fu, C., Zheng, S., et al. (2019). Graphene oxide-PLGA hybrid nanofibres for the local delivery of IGF-1 and BDNF in spinal cord repair. *Artif. Cell Nanomed. Biotechnol.* 47, 651–664. doi: 10.1080/21691401.2019.1575843

Ryan, A. J., Kearney, C. J., Shen, N., Khan, U., Kelly, A. G., Probst, C., et al. (2018). Electroconductive biohybrid collagen/pristine graphene composite biomaterials with enhanced biological activity. *Adv. Mater* 30:e1706442. doi: 10.1002/adma.201706442

Simonpieri, A., Del Corso, M., Vervelle, A., Jimbo, R., Inchingolo, F., Sammartino, G., et al. (2012). Current knowledge and perspectives for the use of Platelet-Rich Plasma (PRP) and Platelet-Rich Fibrin (PRF) in oral and maxillofacial surgery part 2: bone graft, implant and reconstructive surgery. *Curr. Pharm. Biotechnol.* 13, 1231–1256. doi: 10.2174/138920112800624472

Stephens-Fripp, B., Sencadas, V., Mutlu, R., and Alici, G. (2018). Reusable flexible concentric electrodes coated with a conductive graphene ink for electrotactile stimulation. *Front. Bioeng. Biotech.* 6:179. doi: 10.3389/fbioe.2018.00179

Su, J., Du, Z., Xiao, L., Wei, F., Yang, Y., Li, M., et al. (2020). Graphene oxide coated titanium surfaces with osteoimmunomodulatory role to enhance osteogenesis. *Mater. Sci. Eng. C Mater. Biol. Appl.* 113:110983. doi: 10.1016/j.msec.2020.110983

Sun, M., Chi, G., Li, P., Lv, S., Xu, J., Xu, Z., et al. (2018). Effects of matrix stiffness on the morphology, adhesion, proliferation and osteogenic differentiation of mesenchymal stem cells. *Int. J. Med. Sci.* 15, 257–268. doi: 10.7150/ijms.21620

Tayalia, P., and Mooney, D. J. (2009). Controlled growth factor delivery for tissue engineering. *Adv. Mater.* 21, 3269–3285. doi: 10.1002/adma.200900241

Varkey, M., Gittens, S. A., and Uludag, H. (2004). Growth factor delivery for bone tissue repair: an update. *Expert. Opin. Drug Deliv.* 1, 19–36. doi: 10.1517/17425247.1.1.19

Wall, I., Donos, N., Carlqvist, K., Jones, F., and Brett, P. (2009). Modified titanium surfaces promote accelerated osteogenic differentiation of mesenchymal stromal cells *in vitro*. *Bone* 45, 17–26. doi: 10.1016/j.bone.2009.03.662

Wu, Z., Wang, Y., Liu, X., Lv, C., Li, Y., Wei, D., et al. (2019). Carbon-nanomaterial-based flexible batteries for wearable electronics. *Adv. Mater.* 31:e1800716. doi: 10.1002/adma.201800716

Xing, J., Tao, P., Wu, Z., Xing, C., Liao, X., and Nie, S. (2019). Nanocellulose-graphene composites: a promising nanomaterial for flexible supercapacitors. *Carbohyd. Polym.* 207, 447–459. doi: 10.1016/j.carbpol.2018.12.010

Yan, S., Zhu, X., Frandsen, L. H., Xiao, S., Mortensen, N. A., Dong, J., et al. (2017). Slow-light-enhanced energy efficiency for graphene microheaters on silicon photonic crystal waveguides. *Nat. Commun.* 8:14411. doi: 10.1038/ncomms14411

Conflict of Interest: The authors declare that the research was conducted in the absence of any commercial or financial relationships that could be construed as a potential conflict of interest.

frontiers
in Bioengineering and Biotechnology

REVIEW
published: 12 January 2021
doi: 10.3389/fbioe.2020.631616

Bioinspired Modifications of PEEK Implants for Bone Tissue Engineering

*Xinming Gu, Xiaolin Sun, Yue Sun, Jia Wang, Yiping Liu, Kaixuan Yu, Yao Wang and Yanmin Zhou**

Department of Oral Implantology, Hospital of Stomatology, Jilin University, Changchun, China

In recent years, polyetheretherketone (PEEK) has been increasingly employed as an implant material in clinical applications. Although PEEK is biocompatible, chemically stable, and radiolucent and has an elastic modulus similar to that of natural bone, it suffers from poor integration with surrounding bone tissue after implantation. To improve the bioactivity of PEEK, numerous strategies for functionalizing the PEEK surface and changing the PEEK structure have been proposed. Inspired by the components, structure, and function of bone tissue, this review discusses strategies to enhance the biocompatibility of PEEK implants and provides direction for fabricating multifunctional implants in the future.

Keywords: polyetheretherketone, surface modification, implants, bioactivity, osseointegration

Edited by:
Jianxun Ding,
Chinese Academy of Sciences, China

Reviewed by:
Yunhe Zhang,
Jilin University, China
Weizhong Yang,
Sichuan University, China
Qu Minjie,
Dalian Polytechnic University, China

***Correspondence:**
Yanmin Zhou
zhouym@jlu.edu.cn

Specialty section:
This article was submitted to Biomaterials, a section of the journal Frontiers in Bioengineering and Biotechnology

Received: *20 November 2020*
Accepted: *10 December 2020*
Published: *12 January 2021*

Citation:
Gu X, Sun X, Sun Y, Wang J, Liu Y, Yu K, Wang Y and Zhou Y (2021) Bioinspired Modifications of PEEK Implants for Bone Tissue Engineering. Front. Bioeng. Biotechnol. 8:631616. doi: 10.3389/fbioe.2020.631616

INTRODUCTION

Bone defects caused by aging, trauma, disease, congenital abnormalities, and surgical resections are widespread all over the world. It's reported that the number of fractures is estimated to rise from 2.1 million to over 3 million during 2005–2025 in the United States (Quarto and Giannoni, 2016). In the past decades, numerous biomaterials have been employed to repair bone defects. Conventional implants used in bone tissue engineering are commonly made of titanium (Ti) or its alloys due to their good biocompatibility, chemical stability, and mechanical properties. However, these materials suffer from limitations such as the release of harmful metal ions, osteolysis, allergenic effects, and radiopaqueness (Niki et al., 2001; Fage et al., 2016). In particular, Ti possesses an elastic modulus of more than 100 GPa, which contributes to stress shielding and the resorption of surrounding bone (Huiskes et al., 1992). To overcome these drawbacks and reduce negative post-implantation biological reactions, polyetheretherketone (PEEK) and PEEK-based compounds have emerged as viable alternatives to Ti and its alloys.

PEEK, which is a dominant member of the polyaryletherketone (PAEK) family, was first synthesized by British scientists via nucleophilic displacement in 1972 (Eschbach, 2000). In the late 1990s, PEEK was approved by the U.S. Food and Drug Administration as an implantable biomaterial (Kurtz and Devine, 2007). Since then, PEEK has been extensively employed in the fields of orthopedics, trauma, spinal and dental implants. Another important member of PAEK named polyetherketoneketone (PEKK), has also been extensively studied as a promising orthopedic implant recently (Wang et al., 2017; Yuan et al., 2018). PAEK has numerous beneficial characteristics such as non-toxicity, excellent mechanical properties, natural radiolucency, and good chemical and sterilization resistance (Wenz et al., 1990; Katzer et al., 2002; Godara et al., 2007). However, smooth PEEK implants can lead to poor osseointegration characterized by fibrous encapsulation, potentially leading to clinical failure (Walsh et al., 2015). This phenomenon can be explained by the hydrophobic and chemically inert properties of PEEK. Consequently, considerable efforts should focus on modifying the surfaces of PEEK implants. It is expected that the reinforced PEEK implants can result in enhanced ingrowth of osteoblasts (osteoconduction), direct contact with surrounding bone (osseointegration) and stimulation of immature cells into osteogenic cells (osteoinduction).

This review presents an overview of the properties of PEEK and multiple strategies for the modification of PEEK implants inspired by the constituents, structure, and function of human bone (**Figure 1**). Subsequently, we discuss several aspects in need of further exploration and highlight future directions in the field of multifunctional implants.

PROPERTIES OF PEEK

Bulk Properties

Bulk properties are determined by the atomic composition and structure of a material (Binyamin et al., 2006), including the mechanical, chemical, thermal, and radiation characteristics, which are fundamental to the performance of an implant. PEEK is a semi-crystalline linear polycyclic aromatic thermoplastic that has an aromatic molecular backbone interconnected by ketone and ether functional groups between the aryl rings (Kurtz and Devine, 2007). Regarding its mechanical behavior, the tensile modulus, bending modulus, and compressive modulus of PEEK are ∼3.8, 3.6, and 2.8 GPa, respectively (Han et al., 2019b). At room temperature, PEEK is chemically stable in all conventional solvents except for 98% sulfuric acid (Ha et al., 1997). At high temperatures, PEEK maintains stability and displays resistance to damage from chemical components and radiation. The glass transition temperature of PEEK is ∼143°C, whereas the crystalline melt transition occurs at around 343°C (Kurtz and Devine, 2007). In addition, gamma irradiation can be used to sterilize PEEK in air at doses of 25–40 kGy in clinical practice (Kurtz and Devine, 2007).

Surface Properties

The interactions that occur at the interface of a material define its surface properties (Binyamin et al., 2006). For PEEK implants, one of the key surface properties is biocompatibility. A previous study showed that PEEK has no cytotoxic or mutagenic effects (Katzer et al., 2002). Moreover, human gingival fibroblasts (HGFs) and osteoblasts adhered on the surface of PEEK displayed increased proliferation and viability compared to those on Ti, indicating that PEEK exhibits desirable performance with both soft and hard tissues (da Cruz et al., 2019). Other surface properties, including surface topography, chemistry, energy, and wettability, should also be considered. Surface topography and chemistry can influence the tissue response to an implant by altering protein adsorption and subsequent cell adhesion and differentiation. The surface energy has been confirmed to affect cell maturation, differentiation, and osseointegration (Kilpadi and Lemons, 1994; Zhao et al., 2005). Surfaces with higher surface energy exhibit more rapid cell activation and differentiation than those with lower surface energy. Unmodified PEEK with a water contact angle of 80–90° is inherently hydrophobic and bioinert. When the surface of an implant becomes hydrophilic, plasma proteins and cells are more likely to adhere to it (Jimbo et al., 2010). Surface wettability is related to surface roughness, Elawadly et al. proposed that the water contact angle of PEEK-based materials was below 90° when the surface average roughness (Ra) value was either <1.0 or >1.7 μm (Elawadly et al., 2017).

MODIFICATIONS INSPIRED BY THE COMPONENTS OF BONE

Addition of Inorganic Phases

Human bone is mainly composed of inorganic and organic phases. Calcium phosphate (CaP), which is the primary inorganic constituent of human bone, has been extensively studied in bone tissue engineering owing to its superb biocompatibility, osseointegration, osteoconduction, and osteoinductivity (Eliaz and Metoki, 2017). CaP can enhance the local concentrations of calcium and phosphate ions and form apatite on the surface of the substrate. Meanwhile, CaP can adsorb extracellular matrix (ECM) proteins and activate osteoblastic differentiation via cell–ECM interactions (Eliaz and Metoki, 2017). CaP coatings have been shown to remarkably enhance the proliferation of MC3T3-E1 cells and apatite-forming ability in simulated body fluid (SBF) (Jabbari et al., 2018). In another study, surface functionalization with a combination of phosphate and calcium remarkably promoted the osteogenic activity of rabbit bone marrow-derived mesenchymal stem cells *in vitro* and the osseointegration ability *in vivo* (Sunarso et al., 2019). It is worth noting that amorphous calcium phosphate can be fabricated on the PEEK surface within 1 day, and strong adhesion with PEEK can be obtained using a novel PrA treatment (involving three steps: H_2SO_4 treatment, O_2 plasma treatment, and alkaline SBF treatment) (Yabutsuka et al., 2017, 2018). Further study revealed that the PrA treatment resulted in zero cytotoxicity and produced excellent bone-bonding properties (Masamoto et al., 2019). However, the use of CaP-based materials in high-load-bearing areas is limited due to the poor mechanical properties of CaP (Ambard and Mueninghoff, 2006).

Hydroxyapatite (HA) is widely used in bone regeneration since its composition is close to that of natural bone (Yoshikawa and Myoui, 2005). HA is the most stable and least soluble CaP ceramic and has the molecular formula $Ca_{10}(PO_4)^6\ (OH)_2$, in which the Ca/P ratio is approximately 1.67 (Klein et al., 1990; He et al., 2003). HA is considered to be osteoconductive but not osteoinductive (Samavedi et al., 2013). HA can be used as either a coating or a reinforcement component to produce bioactive PEEK composites. Coating PEEK with HA can impart PEEK with a rough and hydrophilic surface, which is beneficial for cell growth (**Figure 2A**; Lee et al., 2013). Numerous treatments including cold spraying, plasma spraying, ion beam-assisted deposition, and electrophoretic co-deposition have been adopted to deposit HA coatings (Lee et al., 2013; Suska et al., 2014; Durham et al., 2016; Baştan et al., 2018). Unfortunately, plasma-sprayed HA coatings suffer from insufficient adhesion strength to PEEK and tend to delaminate, resulting in the infiltration of multinucleated giant cells (Reigstad et al., 2011).

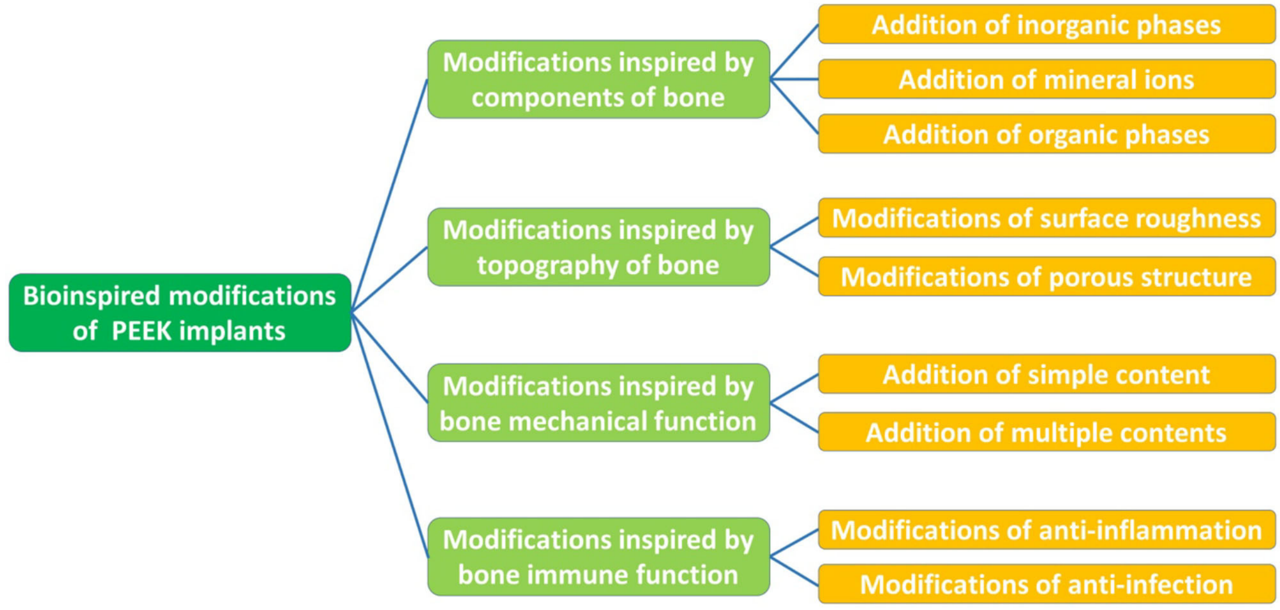

FIGURE 1 | Summary of bioinspired modifications of PEEK implants.

In addition, the detachment of thick, layered apatite coatings was found to cause severe inflammatory response and bone resorption (Røkkum et al., 2003). To suppress such negative responses, a thin nanosized HA (nHA) layer was applied to the PEEK surface. *In vivo* studies indicated that this nHA coating significantly improved the removal torque, early bone integration, and osteoconductive properties of PEEK implants (Barkarmo et al., 2013; Johansson et al., 2014, 2015, 2016, 2018). Chemical modifications such as the grafting of phosphonate groups have also performed positive effects on the adhesion strength between HA and PEEK implants (Mahjoubi et al., 2017).

Subsequent studies attempted to develop bioactive PEEK composites by adding HA, nHA, or ion-substituted HA to PEEK (Wong et al., 2009; Deng et al., 2015b; Liu et al., 2016; Ma and Guo, 2019; Bastan, 2020; Dong et al., 2020). For instance, the addition of strontium-containing HA not only improved the bending modulus of PEEK, it also enhanced apatite formation in SBF and cell-mediated mineralization *in vitro* (Wong et al., 2009). Moreover, increasing the HA content can improve the elastic modulus, compressive strength, and hardness of the composite but not the tensile strength. A HA/PEEK composite containing 30 wt% HA exhibited a higher elastic modulus and slightly lower tensile strength than that of pure PEEK (Ma and Guo, 2019). To optimize the mechanical properties of HA/PEEK hybrid materials, researchers have focused on incorporating reinforcement components [e.g., carbon fiber (CF) and carbon nanotubes (CNTs)] and identifying the optimal content of HA (Deng et al., 2015b; Liu et al., 2016).

Addition of Mineral Ions

To evaluate the biological properties of PEEK implants, it is crucial to choose biomaterials with good osteogenesis ability for bone repair. Metal ions are strong candidates as coating materials for PEEK implants. Han et al. proposed that electron beam deposition could be used to deposit a Ti layer on the surface of PEEK with strong adhesion and enhanced wettability. Compared to PEEK alone, the Ti-coated PEEK implants exhibited two times greater proliferation and differentiation of MC3T3-E1 cells along with better osseointegration ability (Han et al., 2010). Ti plasma spraying, another coating process, increased the microscale surface area by 40% and accelerated cement line formation in human osteoprogenitor cells (hFOB 1.19) while also increasing the shear strength and bone integration at the implant surface (Walsh et al., 2015; Hickey et al., 2019). Moreover, the addition of Ti increased the compressive strength and stiffness of PEEK (Jung et al., 2016).

Titanium dioxide (TiO_2) can also be deposited onto the surface of PEEK using several coating methods. Before sol-gel coating, pretreatment with UV, O_2 plasma, or sandblasting can enhance the bonding strength of the coating layer, while post-treatment with HCl can induce apatite formation, which is related to the bone-bonding ability *in vivo* (Kizuki et al., 2015; Shimizu et al., 2016). Different TiO_2 nanostructures such as nanoparticles, nanotubes, and nanofibers can also be employed to improve the cytocompatibility, soft tissue integration, and osseointegration of PEEK implants due to their favorable bioactivity and surface morphology (**Figures 2B,C**; Wu et al., 2012; Lu et al., 2014; Wang X. et al., 2016; Liu et al., 2018).

Other coating materials such as tantalum, tantalum pentoxide, and niobium pentoxide can not only elevate the surface energy, surface roughness, hydrophilicity, protein absorption, and mechanical properties of PEEK implants, they can also induce positive cellular responses and osteointegration (Lu et al., 2015; Mei et al., 2019; Ge et al., 2020). Silicon-based compounds

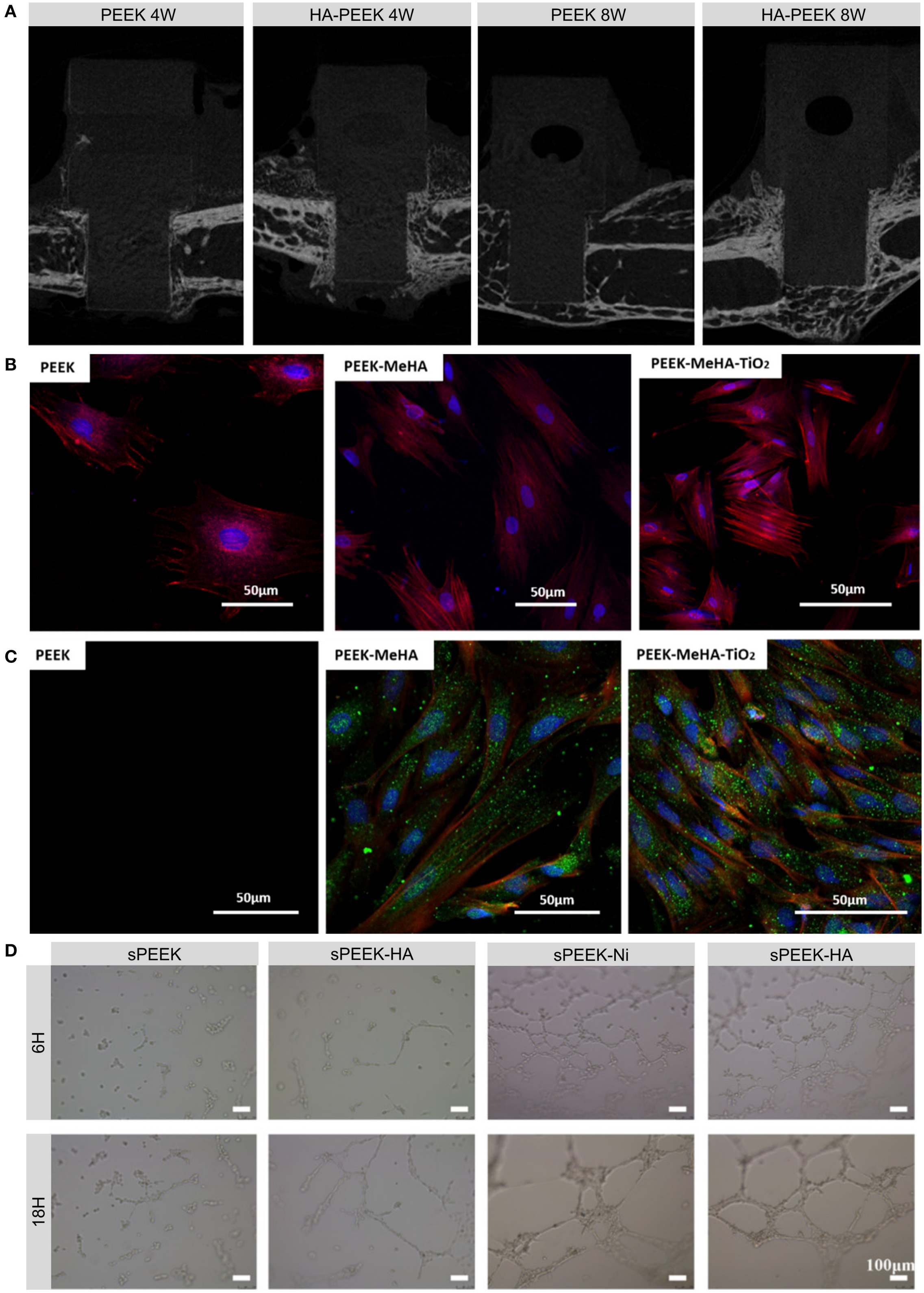

FIGURE 2 | Examples and biological effects of modifications inspired by the components of bone. **(A)** Micro-CT images of new bone formed on HA-coated PEEK and on uncoated PEEK at 4 and 8 weeks after implantation. **(B)** Fluorescence micrographs of actin (red) and nucleus (blue) in rBMSCs grown on PEEK, PEEK-MeHA, and *(Continued)*

FIGURE 2 | PEEK-MeHA-TiO$_2$ for 24 h. **(C)** Immunofluorescence analysis of actin (red), collagen I (green), and nucleus (blue) in rBMSCs grown on PEEK-MeHA and PEEK-MeHA-TiO$_2$ for 7 days. **(D)** HUVEC tube formation ability in extracts of sulfonated PEEK (sPEEK), sPEEK-HA, sPEEK-Ni, and sPEEK-Ni-HA at 6 and 18 h. Reproduced with permission from Dong et al. (2020). Copyright (2020) American Chemical Society.

have been found to reinforce the mechanical properties, surface hydrophilicity, apatite mineralization, and cell and bone tissue responses (Ma et al., 2014; Wen et al., 2016; Monich et al., 2017; Zhang et al., 2018a). Other additives such as phosphonate, amorphous magnesium phosphate, graphene, and diamond-like carbon were found to exert similar effects (Wang et al., 2010; Mahjoubi et al., 2017; Ren et al., 2018; Yan J. H. et al., 2018; Sikder et al., 2020).

Addition of Organic Phases

The organic phase of bone tissue includes a plethora of growth factors and proteins that play a prominent role in osteogenesis and angiogenesis. Bone morphogenetic protein-2 (BMP-2), which is one of the strongest osteoinductive factors, can initiate the differentiation of mesenchymal stem cells (MSCs) into osteoblasts and promote osteogenesis (Ryoo et al., 2006). Therefore, to improve the biological behavior of PEEK, researchers have attempted to immobilize BMP-2 on PEEK through several methods, including the deposition of nanoporous TiO$_2$ layers, polyelectrolyte multilayer films, and phosphorylated gelatin coatings along with sulfonation treatment (Han et al., 2014; Guillot et al., 2016; Sun et al., 2018; Wu et al., 2018). It was reported that BMP-2-coated PEEK with a dose of 9.3 μg could lead to localized and temporary bone impairment (Guillot et al., 2016). Thereby, further studies should focus on determining the optimal dose of BMP-2 to maximize osteogenic activity. Functionalizing cell-interfacing surfaces with cell-modulatory proteins can also improve the biological properties of the implant. For example, the ECM protein tropoelastin has been shown to promote the biological behavior of human osteoblast-like osteosarcoma cells (SAOS-2) on PEEK via plasma immersion ion implantation (PIII) treatment (Wakelin et al., 2018). Adiponectin (APN), which is adipocyte-secreted adipokine, has been confirmed to increase the osteogenic ability *in vitro* and osseointegration *in vivo* of sPEEK implants (Wang et al., 2019; Deng et al., 2020). Out of these proteins, bone forming peptide (BFP) can also be utilized to improve the osteogenic differentiation and maturation of MG-63 cells (Wang et al., 2018).

In addition to the aforementioned osteoinductive agents, angiogenic growth factors such as vascular endothelial growth factor (VEGF), transforming growth factor-β, placental growth factor, and fibroblast growth factor can regulate angiogenesis, which involves endothelial cell proliferation, migration, and tube formation (Stegen et al., 2015). However, the short half-lives and complicated structures of these growth factors make them easy to degrade and deactivate. Alternatively, nickel hydroxide nanoparticles immobilized on the micro-/nanostructured surfaces of PEEK implants can facilitate the migration, tube formation, and angiogenic gene expression of human umbilical vein endothelial cells (HUVECs; **Figure 2D**; Dong et al., 2020). Apart from applying these osteogenic and angiogenic organic constituents, a recent study provided a novel direction for future research on genes such as human bone morphogenetic protein-4 (hBMP-4) to enhance bone regeneration (Cui et al., 2020).

MODIFICATIONS INSPIRED BY THE TOPOGRAPHY OF BONE

Modifications of Surface Roughness

Bone is an inhomogeneous 3D structure with complicated topography. Surface roughness plays a pivotal role in topographical modification due to its effect on bone formation and implant fixation. Proper surface roughness can promote the absorption extra-cellular matrix (ECM) proteins (e.g., vitronectin, fibronectin and collagen I) and benefit the adhesion of osteoblasts (Pashkuleva et al., 2010). Subsequently, the ECM proteins provide a RGD sequence which performs as a receptor for osteoblast membrane proteins (mainly Integrins) and then initiate cell spreading, proliferation and differentiation (Mavropoulos et al., 2013). For instance, untreated PEEK with high surface roughness formed via fused filament fabrication displayed remarkably higher osteoblast proliferation and metabolic activity compared to grit-blasted PEEK with a smooth surface (**Figure 3A**; Han et al., 2019a). However, when the surface roughness exceeded 2.19 μm, osteoblast adhesion was inhibited because it is difficult to form osteoblastic pseudopodia between the larger crests and grooves (Anselme et al., 2000).

Microscale to nanoscale surface topography has been shown to affect osteoblastic cell adhesion. Micrometer-scale surface modifications (e.g., sandblasting) of PEEK implants have been used to enhance MG-63 cell behavior and bone-bonding ability (Deng et al., 2015a). Spraying PEEK surfaces with Ti plasma generated hierarchical roughness and increased the surface area (by 40% at the microscale), resulting in enhanced cell proliferation and accelerated cement line formation in hFOB 1.19 cells (Hickey et al., 2019). Compared to micro-roughness surfaces, nano-roughness surfaces showed greater initial protein (e.g., vitronectin and fibronectin) absorption, which subsequently mediates cell adhesion (Khang et al., 2007).

To date, several processes have been used to make nanoscale modifications to the surfaces of PEEK implants. The incorporation of nanosized particles like nHA via spin-coating can enhance the wettability, removal torque, and biocompatibility of PEEK (Johansson et al., 2014). The addition of nanoscale TiO$_2$ (nTiO$_2$) to PEEK via powder mixing and compression molding demonstrated that the enhanced surface roughness effectively promoted cell attachment and new bone regeneration (Wu et al., 2012). Other modifications including treatment with nitrogen, water, and ammonia PIII also displayed similar biological effects on PEEK (Lu et al., 2015;

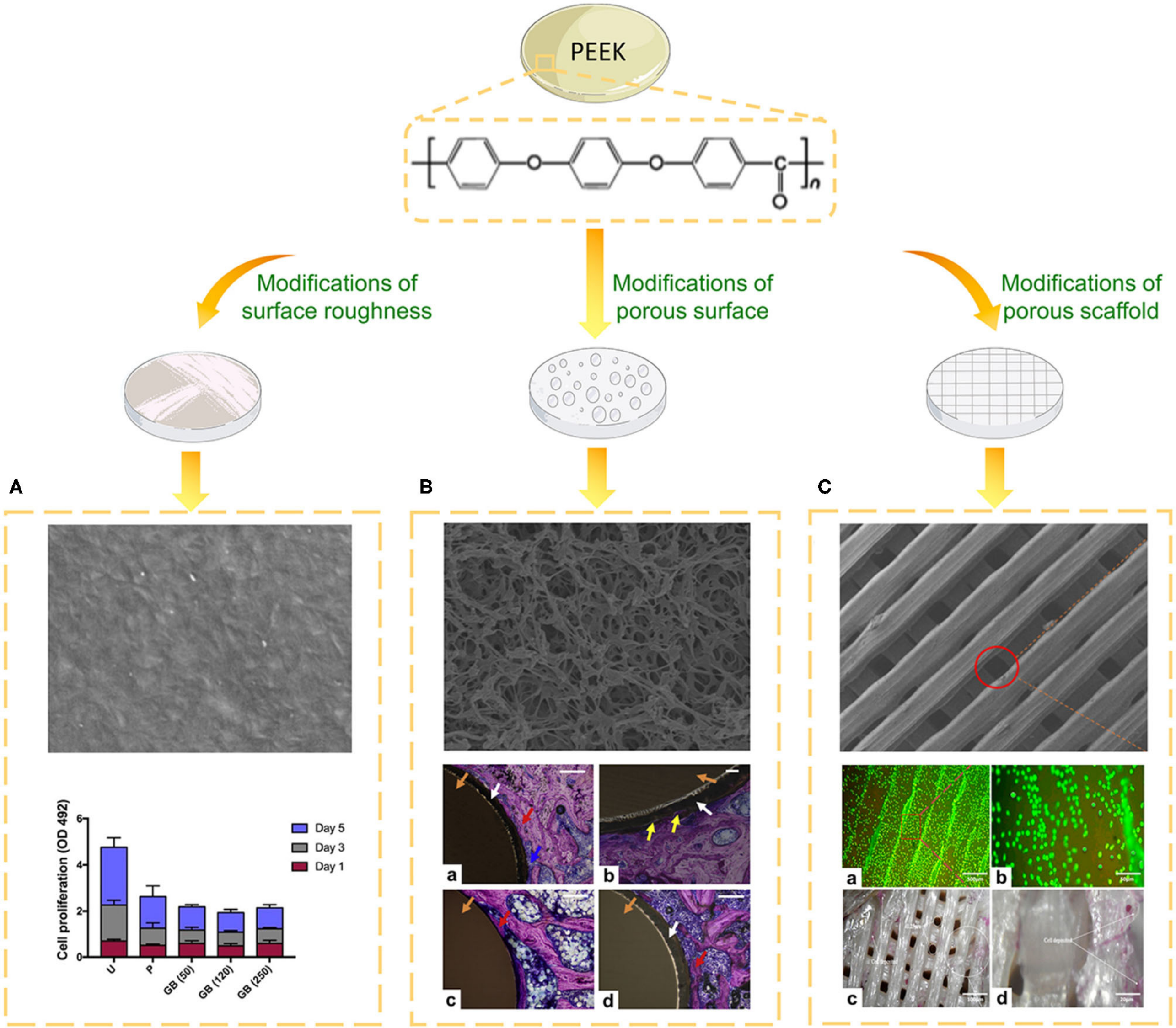

FIGURE 3 | Biological evaluation of PEEK implants with different topographies. **(A)** SEM image of the surface of PEEK formed via fused filament fabrication and the cell proliferation of different groups on days one, three, and five. U, untreated; P, polished, GB (50), 50 μm grit-blasted; GB (120), 120 μm grit-blasted; and GB (250), 250 μm grit-blasted (Han et al., 2019a). **(B)** SEM image of the surface of sPEEK-WA and Giemsa-stained hard tissue around the implant at 8 weeks after implantation. Red arrows represent the newly formed bone, yellow arrows represent bone ingrowth, blue arrows represent osteoblasts, white arrows represent the sPEEK layer, and orange arrows represent the PEEK implant. (a) PEEK, (b) sPEEK-W, (c) sPEEK-A (low magnification), and (d) sPEEK-WA (high magnification). Scale bar is 200 μm. Reproduced from Zhao et al. (2013). Copyright (2013), with permission from Elsevier. **(C)** SEM image, cell spreading (a,b) and ALP activity (c,d) of the PEEK/cHAp scaffold after cultivation for 14 days: (a) magnification of 300 μm, (b) magnification of 50 μm, (c) magnification of 100 μm, and (d) magnification of 20 μm. Reproduced from Oladapo et al. (2020). Copyright (2020), with permission from Elsevier.

Zhao et al., 2016). Furthermore, the combination of oxygen plasma treatment and sandblasting imparted the PEEK surface with a micro/nano-topographical structure, which triggered the osteogenic differentiation of MG-63 cells and new bone formation (Xu et al., 2015).

Modifications of the Porous Structure

Mimicking the morphology of trabecular bone is a crucial concept in the development of porous implant surfaces. Compared to rough surfaces, porous PEEK surfaces exhibit increased osteoblastic differentiation and bonding strength with bone (Torstrick et al., 2018, 2020). Numerous techniques have been applied to develop porous structures on the PEEK surface, including sulfonation, melt extrusion, porogen templating, and PIII technique (Zhao et al., 2013; Lu et al., 2014; Evans et al., 2015; Torstrick et al., 2016; Hieda et al., 2017; Yabutsuka et al., 2017; Deng L.-J. et al., 2018; Wu et al., 2018; Yuan et al., 2018; Conrad and Roeder, 2020; Swaminathan et al., 2020; Wan et al., 2020). Cell viability evaluations revealed that the optimal sulfonation treatment time was 5 min (Ma R. et al., 2020). Sulfonation can generate a 3D porous structure along with -SO$_3$H groups, which are beneficial for pre-osteoblast functions, apatite formation, and bone growth (**Figure 3B**; Zhao et al., 2013). It's worth noting that sulfonation treatment can introduce more micropores and -SO$_3$H groups on PEKK than PEEK for the reason that PEKK prossesses more ketone groups (Yuan et al., 2018). To further reinforce the bioactivity of porous PEEK, promising drug loading platforms were created by adding gelatin, hydrogel, chitosan, or polydopamine on the surface of PEEK (Deng L.-J. et al., 2018; Ouyang et al., 2018; Wu et al., 2018; Wang et al., 2019). For instance, poly(L-lactic acid)/simvastatin-loaded PEEK coated with a hyaluronic acid hydrogel enhanced the osteogenic differentiation of MC3T3-E1 and the expression of VEGF mRNA compared to uncoated PEEK (Deng L.-J. et al., 2018).

In recent years, clinical interest in 3D printing has grown rapidly. Techniques such as selective laser sintering (SLS) and fused filament fabrication have been adopted to construct PEEK scaffolds with controlled pore size (Roskies et al., 2016; Shuai et al., 2016; Deng et al., 2017; Peng et al., 2017; Oladapo et al., 2020; Spece et al., 2020). Up to now, there has been little consensus on the optimal pore size of scaffolds. Results revealed that porous PEEK with pore sizes ranged 200 to 508 μm exhibited higher proliferation and mineralization compared with smooth PEEK and Ti6Al4V (Torstrick et al., 2016). Another study presented that PEEK scaffold with 450 μm pore size displayed improved ingrowth of new bone and vascular perfusion (Feng et al., 2020). Although developed pore formation processes provide the ability to control the pore structures of PEEK implants, a deeper understanding of how pore size affects cell and tissue responses is needed. To further strengthen the biological properties of scaffolds for bone tissue engineering applications, HA and calcium HA were introduced into the PEEK matrix (**Figure 3C**; Vaezi et al., 2016; Oladapo et al., 2020). To reinforce the interfacial bonding between HA and PEEK, graphene oxide (GO) can be employed as an interfacial phase (Peng et al., 2017). Furthermore, the addition of graphene nanosheets, CNTs, or CF can boost the mechanical properties of PEEK/HA scaffolds (Shuai et al., 2016; Uddin et al., 2019; Swaminathan et al., 2020).

MODIFICATIONS INSPIRED BY BONE MECHANICAL FUNCTION

Bone mainly consists of outer cortical bone and inner cancellous bone. The high modulus (16–23 GPa) of cortical bone endows it with stability and allows it to support the inner porous structure (Augat and Schorlemmer, 2006). The elastic modulus of PEEK (3–4 GPa) is close to that of human cortical bone, reducing the risk of high stress peaks and stress shielding effects during load transfer at the implant–bone interface. The stress shielding is a phenomenon which depicts stiff implants (e.g., titanium) cannot strain the surrounding bone adequately and then lead to bone resorption (Huiskes et al., 2000).

TABLE 1 | Mechanical and biological properties of carbon-based PEEK compounds.

Composite	Content	Technique	Mechanical properties	Biological properties	References
HA/CF/PEEK	Not reported	Plasma spray coating	Not reported	Enhanced the bone response to PEEK implants *in vivo*	Suska et al., 2014
HA/GNS+CNT/PEEK	10 wt% HA; 1 wt% GNS+CNT (weight ratio = 2:8)	SLS	Compressive strength = 78.65 MPa; compressive modulus = 4.79 GPa	Improved apatite-forming ability; enhanced cell adhesion, spreading, and proliferation	Shuai et al., 2016
nHA/CF/PEEK	25 wt% nHA; 20 wt% CF	Compounding and injection molding	Elastic modulus = 16.5±0.7 GPa	Promoted MG63 cell attachment, proliferation, and osteogenic differentiation; enhanced calcium nodule formation and osseointegration	Deng et al., 2015b
nHA/multiwalled CNTs/PEEK	15 vol % nHA; 1.88 vol % CNTs	Melt-compounding and injection molding	Elastic modulus = 7.13 GPa; tensile strength = 64.48 MPa; elongation at break = 1.74%	Enhanced attachment, proliferation, differentiation, and mineralization of MC3T3-E1 cells	Liu et al., 2016
nTiO$_2$/CF/PEEK	30 vol% CF	PIII	Improved elastic recovery and acceptable stability	Improved adhesion, proliferation, and osteoblastic differentiation of rBMSCs; imparted partial antibacterial activity against *S. aureus* and *E. coli*	Lu et al., 2014
GO/CF/PEEK	25 wt% and 40 wt% CF	Immersed in GO aqueous solution	Not reported	Enhanced adhesion, proliferation, ALP activity and mineralization of rBMSCs; promoted new bone formation *in vivo*	Qin et al., 2020
Amino groups/CF/PEEK	30 vol% CF	Plasma-enhanced chemical vapor deposition (PECVD)	Not reported	Promoted adhesion, proliferation, and osteogenic differentiation of MG-63 cells	Yu et al., 2020

In consideration of the above, the mechanical properties of PEEK implants need to be elevated under specific clinical conditions. It's reported that CFs, CNTs, glass fibers (GFs), and graphene nanosheets (GNS) can be introduced into the PEEK matrix to satisfy the requirements and broaden its applications in load-bearing areas (Ji et al., 2015; Shuai et al., 2016; Yang et al., 2018; Han et al., 2019b). For instance, the stress distribution of a PEEK implant with 60% endless carbon fibers was similar to that of a titanium implant in dental application (Schwitalla et al., 2015). Mechanical property evaluations suggested that the elastic modulus of CF/PEEK and GF/PEEK could reach to 18 and 12 GPa, respectively (Lee et al., 2012). Furthermore, the mechanical properties of PEEK can be controlled by adding different amounts or lengths of fibers to the composite. For example, the bending strengths of CF/PEEK containing 25, 30, 35, and 40 wt% CF were 230.1–264.6 MPa, and the compressive strengths were 191.2–215.8 MPa (Qin et al., 2019). Meanwhile, the mechanical strengths of CF/PEEK composites containing CFs with lengths of 2–3 mm were more than two times those of the composites containing CFs with lengths of 150–200 µm (Li et al., 2019b). While fiber-reinforced PEEK has been manufactured through the traditional injection molding process, a novel technique called fused deposition modeling (FDM) has been applied currently. CF/PEEK formed via FDM was found to possess similar strength and toughness as the injection-molded samples along with better tensile and bending strengths compared to pure PEEK (Han et al., 2019b; Li et al., 2019a).

Although reinforced PEEK performs excellent mechanical properties, further investigations are needed to increase the bioactivity of hybrid PEEK materials. Researchers have proposed

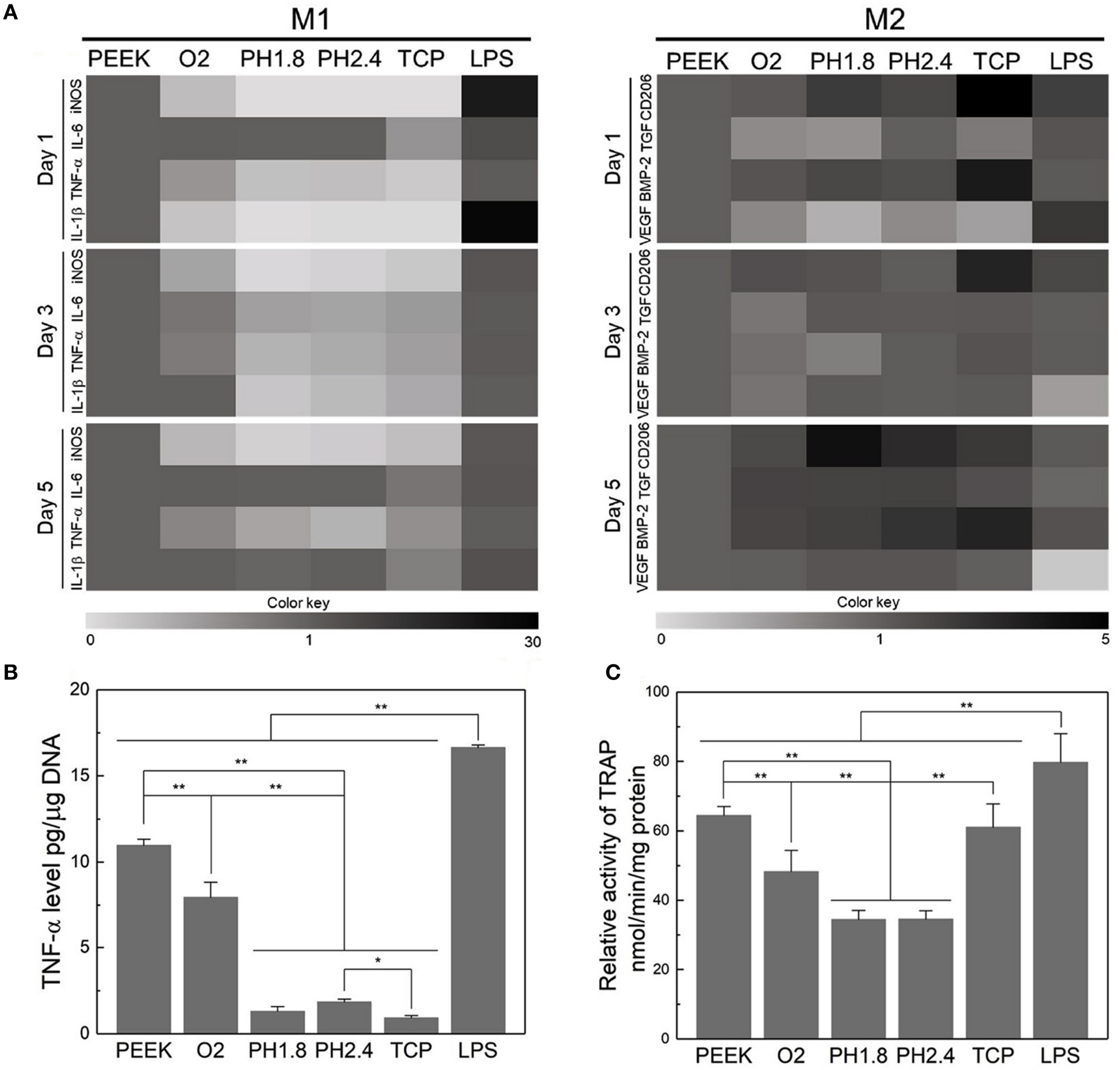

FIGURE 4 | Evaluation of the acute inflammatory responses of RAW264.7 cells on different samples. **(A)** Heat map of the RT-PCR results of M1- and M2-related genes after incubation for 1, 3, and 5 days. **(B)** Level of TNF-α released by RAW264.7 cells after culturing for three days. **(C)** TRAP activity after culturing for 8 days to evaluate the osteoclastic differentiation of RAW264.7 cells. *$p < 0.05$, **$p < 0.01$. Reproduced from Gao et al. (2020). Copyright (2020), with permission from Elsevier.

numerous hybrid materials containing different bioactive components, their mechanical and biological properties are summarized in **Table 1**. Moreover, the modification of CF-reinforced PEEK surfaces via chemical treatment, graphene functionalization, and PrA treatment has resulted in similar biological properties (Miyazaki et al., 2017; Yabutsuka et al., 2018; Yan J. H. et al., 2018; Ma J. et al., 2020).

MODIFICATIONS INSPIRED BY BONE IMMUNE FUNCTION

Upon implantation, the innate immune response of bone tissue is mainly initiated by macrophages, which release a series of cytokines and growth factors. Macrophages can be divided into the pro-inflammatory M1 phenotype and anti-inflammatory M2 phenotype (Mosser and Edwards, 2008). To modulate the inflammatory response to PEEK implants, Gao et al. proposed a layer-by-layer self-assembly technique that facilitates the polarization of macrophages into the M2 phenotype and contributes to the upregulation of osteogenesis and the downregulation of osteoclastogenesis (**Figure 4**; Gao et al., 2020). Fukuda et al. found that the plasma treatment and subsequent phosphorylation on the PEEK surface attenuated the phenotypic polarization of RAW264.7 macrophages to an inflammatory phenotype (Fukuda et al., 2019). A recent study revealed that PEEK modified with hydrofluoric acid and nitric acid could promote the polarization of macrophages (M2 phenotype) and inhibit the expression of proinflammatory factors via the NF-κB pathway (Huo et al., 2020).

Researchers have also focused on surface modifications that target microbial infections. To the best of our knowledge, there are two ways to fabricate an anti-biofilm surface: depositing antibacterial coatings that release antimicrobial constituents or depositing antiadhesive coatings that restrict the adhesion of bacteria. Various antibiotics (e.g., lawsone, dexamethasone, minocycline, hinokitiol, tobramycin, gentamicin sulfate, and antimicrobial peptides) have been adopted to treat infections caused by implants (Ur Rehman et al., 2018; Zhang et al., 2018b; Deng et al., 2019; Xu et al., 2019; Yuan et al., 2019; Xue

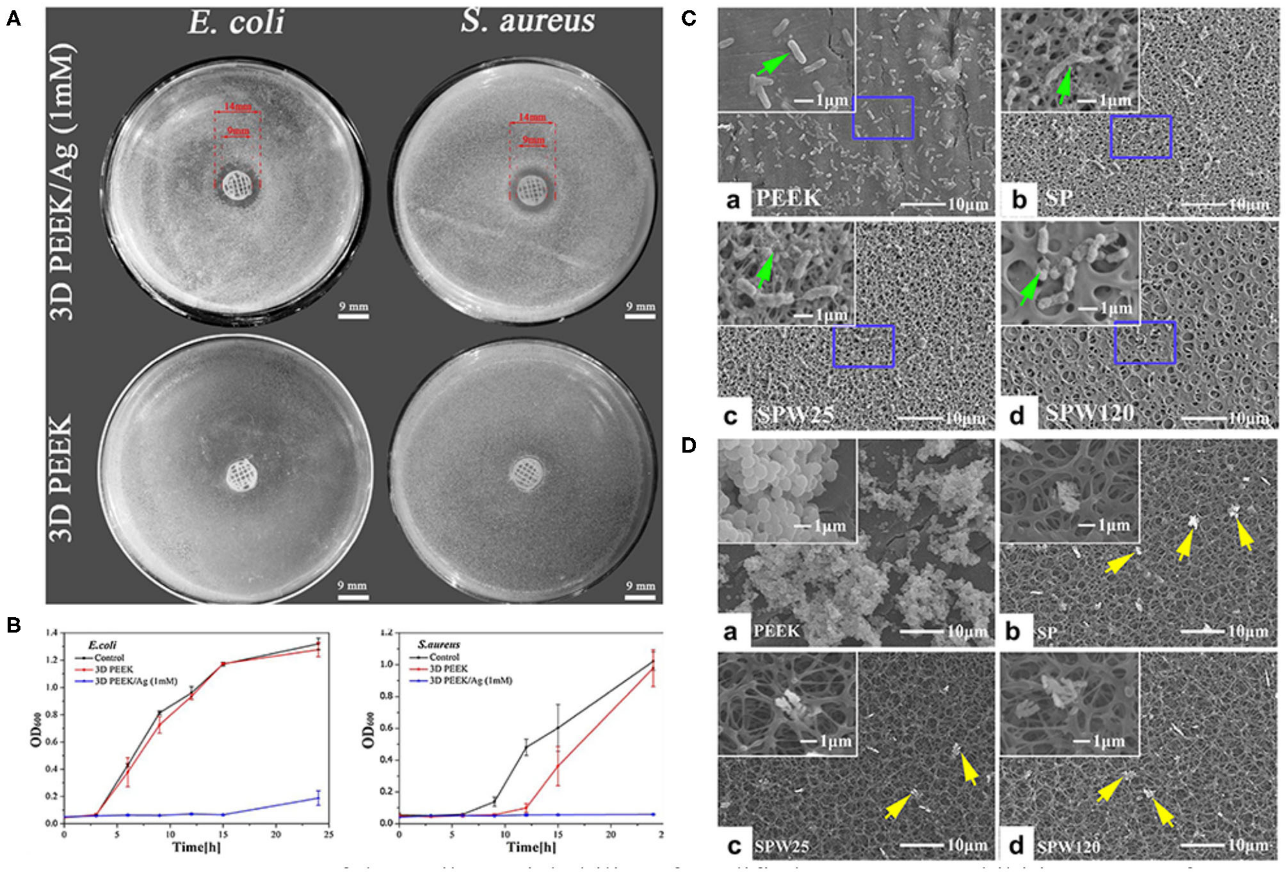

FIGURE 5 | Assessment of the antibacterial ability of modified PEEK. **(A)** Inhibition zones of 3D PEEK and 3D PEEK/Ag against *E. coli* and *S. aureus*. **(B)** Bacterial dynamic curves of *E. coli* and *S. aureus* on 3D PEEK and 3D PEEK/Ag at OD600. Reproduced from Deng et al. (2017). Copyright (2017), with permission from Elsevier. **(C)** *E. coli* and **(D)** *S. aureus* seeded on the PEEK, SP (sulfonated only), SPW25 (sulfonated and hydrothermal treated at 25°C), and SPW120 (sulfonated and hydrothermal treated at 120°C) at a bacteria concentration of 10^7 cfu/ml. The green arrows indicate the morphology of *E. coli* (high magnification), while the yellow arrows show the morphology of *S. aureus* (low magnification). Reproduced from Ouyang et al. (2016). Copyright (2016), with permission from Elsevier.

TABLE 2 | Summary of studies on antibacterial ions and their biological effects.

Ions	Type	Technique	Biological effects	References
Sulfur	Concentrated sulfuric acid (95–98%)	Sulfonation followed by hydrothermal treatment	Enhanced proliferation and osteogenic differentiation of rBMSCs; improved osseointegration; generated antibacterial properties against *E. coli* and *S. aureus*	Ouyang et al., 2016
Fluorine	Hydrofluoric acid	PIII followed by hydrofluoric acid treatment	Enhanced rBMSCs adhesion, spreading, proliferation, ALP activity, and osseointegration; resulted in a good bacteriostatic effect against *Porphyromonas gingivalis*	Chen et al., 2017
Nitrogen	N_2	PIII	Enhanced biological activity and antibacterial activity against *S. aureus*	Gan et al., 2016
Selenium	Red selenium nanoparticles and gray selenium nanorods	Quick precipitation	Inhibited the growth of *Pseudomonas aeruginosa*	Wang Q. et al., 2016
Silver	Silver nitrite	Soft-solution process	Generated strong antibacterial activity against *S. aureus* and *E. coli*	Kakinuma et al., 2015
	Nanoparticles	Catecholamine chemistry	Resulted in a significant antibacterial effect against *S. aureus* and *E. coli*; enhanced MG63 cell proliferation and ALP activity	Deng et al., 2017
	Nano-silver	Magnetron sputtering technology	Significantly increased surface roughness and water contact angle; improved antibacterial activity against *S. mutans* and *S. aureus*; improved the bacterial adhesion ability of PEEK	Liu et al., 2017
	Nanoclusters	Radio frequency co-sputtering	Generated antibacterial effects against *E. coli* and *S. carnosus*	Ur Rehman et al., 2017
Copper	Nanoparticles	Magnetron sputtering	Produced a bactericidal effect against methicillin-resistant *S. aureus* (MRSA); activated macrophage polarization to a pro-inflammatory phenotype with improved phagocytosis for MRSA	Liu et al., 2019
ZnO	Nanopowder	Melt-blending	Improved the mechanical and tribological properties; resulted in superior antibacterial activity against *S. aureus* and *E. coli*	Díez-Pascual and Díez-Vicente, 2014
Ag/ZnO	Nanoparticles	Sulfonation and layer-by-layer self-assembly	Inhibit the reproduction of *E. coli* and *S. aureus*; enhanced the adhesion, proliferation, and spreading of MG-63 cells; increased ALP activity and the levels of osteogenesis-related genes	Deng Y. et al., 2018
Titanium	Titanium ions	PIII	Promoted the adhesion, proliferation, and osteoblastic differentiation of bMSCs; generated partial resistance to *S. aureus* and *E. coli*	Lu et al., 2014
	TiO_2 nanoparticles	PIII	improved the adhesion, migration, proliferation, and collagen secretion ability of HGFs; produced antibacterial properties against *Streptococcus mutans*, *Fusobacterium nucleatum*, and *P. gingivalis*	Wang X. et al., 2016
Magnesium	Particles	Vapor deposition method	Strongly killed *S. aureus* with anti- bacterial rate reaching to 99%	Yu et al., 2018
Si_3N_4	Powder	Melt blending	Significantly improved osteoconduction in SAOS-2 cells; improved the bacteriostatic properties against *Staphylococcus epidermidis*	Pezzotti et al., 2018
Zinc-magnesium silicate	Nanopowder	Melt blending	Improved the mechanical properties, surface roughness, hydrophilicity, and apatite mineralization ability; enhanced the attachment, proliferation, and differentiation of MC3T3-E1 cells; inhibited the growth of *E. coli*	Tang et al., 2019

et al., 2020; Yin et al., 2020). Since the abuse of antibiotics has contributed to the emergence of bacterial resistance, several ions and their nanoparticles have emerged as promising alternatives to antibiotics (**Figures 5A,B**). The details of the techniques involved and the biological effects of these ions are summarized in **Table 2**. It is worth noting that the uncontrolled release of bactericides will exacerbate bacterial resistance. To avoid this phenomenon, silk fibroin, which was reported to cause the pH-responsive controlled release of bactericides, has been introduced into PEEK implants (Yan J. et al., 2018).

Surface roughness and hydrophobicity are the dominant factors affecting bacterial adhesion and biofilm formation. Bollen et al. suggested that enhancing the surface roughness can improve the attachment of bacteria when Ra $>0.2\,\mu m$ (Bollen et al., 1996). In addition, it has been reported that bacteria tend to adhere on implants with hydrophilic surfaces (Das et al., 2010). To prepare porous surfaces, sulfonation followed by hydrothermal treatment which can remove residues are applied (Ouyang et al., 2016; Yuan et al., 2019). Moreover, a porous surface can limit the adhesion of bacteria with different shapes and sizes. For instance, porous structures are considered to be more easily to trap spherical *S. aureus* compared to elongated *E. coli* (**Figures 5C,D**; Ouyang et al., 2016).

Except for microbial infections, bone tumor like osteosarcoma should also be taken into consideration. In order to reduce the risk of tumor recurrence after a bone removal surgery, applying an implant with anti-cancer agents is an effective method. Studies confirmed that the anti-cancer drugs (e.g., methotrexate, and 5-fluorouracil) loaded in ceramic cements could inhibit the growth of osteosarcoma cell line (Prasad et al., 2018; Wu et al., 2020). Currently, light-assisted photothermal therapy (PTT) based on photothermal conversion agent (e.g., MXenes) was introduced to PEEK implants to defect osteosarcoma cells (Yin et al., 2020).

CONCLUSION

After decades of research, PEEK implants in bone tissue engineering have experienced three stages of development: (1) first-generation implants possessing outstanding mechanical properties; (2) second-generation implants with prominent cytocompatibility and osteogenic activity; and (3) third-generation implants equipped with outstanding osseointegration and anti-inflammation/-infection ability. According to previous studies, we have grouped PEEK modifications into four categories based on their inspiration: the constituents (inorganic phase, mineral ions, and organic phase), structure (surface roughness and porosity), mechanical function, and immune function of human bone.

Although the techniques for modifying PEEK have matured, numerous remaining obstacles must be overcome before modified PEEK implants can be applied in clinical practice: (1) the ratio of different constituents must be optimized to maximize bone regeneration and the mechanical properties; (2) methods must be developed to control the release of biomolecules and achieve the desired long-term effects; and (3) experiments are needed to identify the ideal pore structure to optimize biological performance. Thus, extensive studies are still needed to observe the long-term implantation of PEEK *in vivo* and elucidate which strategies are appropriate to modify PEEK in clinical settings. In this respect, the complexity, reproducibility, stability and cost-effectiveness of the manufacturing process should also be considered. In the future, researchers will focus on PEEK implants possessing the optimal combination of osteointegration, vascularization, anti-inflammation/-infection, and mechanical properties. It is worth noting that modifications that mimic the components, structure, and function of human bone are expected to be the key to fabricating multifunctional implants. Also, it can provide inspirations for researchers to modify other PAEK materials and expand their applications in the field of orthopedic, spinal and dental impalnts.

AUTHOR CONTRIBUTIONS

XG conceptualized and designed the manuscript. XG and XS drafted the manuscript. YS and JW designed the table. YL, KY, and YW designed the figure. YZ revised the manuscript. All authors approved the final version.

FUNDING

This work was supported by Department of Finance of Jilin Province (jcsz2020304-1) and the Department of Science and Technology of Jilin Province (20200201302JC).

REFERENCES

Ambard, A. J., and Mueninghoff, L. (2006). Calcium phosphate cement: review of mechanical and biological properties. *J. Prosthodont.* 15, 321–328. doi: 10.1111/j.1532-849X.2006.00129.x

Anselme, K., Bigerelle, M., Noel, B., Dufresne, E., Judas, D., Iost, A., et al. (2000). Qualitative and quantitative study of human osteoblast adhesion on materials with various surface roughnesses. *J. Biomed. Mater. Res.* 49, 155–166. doi: 10.1002/(SICI)1097-4636(200002)49:2<155::AID-JBM2>3.0.CO;2-J

Augat, P., and Schorlemmer, S. (2006). The role of cortical bone and its microstructure in bone strength. *Age Ageing* 35 (Suppl. 2):ii27–ii31. doi: 10.1093/ageing/afl081

Barkarmo, S., Wennerberg, A., Hoffman, M., Kjellin, P., Breding, K., Handa, P., et al. (2013). Nano-hydroxyapatite-coated PEEK implants: a pilot study in rabbit bone. *J. Biomed. Mater. Res. Part A* 101A, 465–471. doi: 10.1002/jbm.a.34358

Bastan, F. E. (2020). Fabrication and characterization of an electrostatically bonded PEEK- hydroxyapatite composites for biomedical applications. *J. Biomed. Mater. Res. Part B Appl. Biomater*. 108, 2513–2527. doi: 10.1002/jbm.b.34583

Baştan, F. E., Atiq Ur Rehman, M., Avcu, Y. Y., Avcu, E., Üstel, F., and Boccaccini, A.R. (2018). Electrophoretic co-deposition of PEEK-hydroxyapatite composite coatings for biomedical applications. *Colloids Surf. B Biointerfaces* 169, 176–182. doi: 10.1016/j.colsurfb.2018.05.005

Binyamin, G., Shafi, B. M., and Mery, C. M. (2006). Biomaterials: a primer for surgeons. *Semin. Pediatr. Surg.* 15, 276–283. doi: 10.1053/j.sempedsurg.2006.07.007

Bollen, C. M., Papaioanno, W., Van Eldere, J., Schepers, E., Quirynen, M., and van Steenberghe, D. (1996). The influence of abutment surface roughness on plaque accumulation and peri-implant mucositis. *Clin. Oral Implants Res.* 7, 201–211. doi: 10.1034/j.1600-0501.1996.070302.x

Chen, M., Ouyang, L., Lu, T., Wang, H., Meng, F., Yang, Y., et al. (2017). Enhanced bioactivity and bacteriostasis of surface fluorinated polyetheretherketone. *ACS Appl. Mater. Interf.* 9, 16824–16833. doi: 10.1021/acsami.7b02521

Conrad, T. L., and Roeder, R. K. (2020). Effects of porogen morphology on the architecture, permeability, and mechanical properties of hydroxyapatite whisker reinforced polyetheretherketone scaffolds. *J. Mech. Behav. Biomed. Mater*. 106:103730. doi: 10.1016/j.jmbbm.2020.103730

Cui, L., Zhang, J., Zou, J., Yang, X., Guo, H., Tian, H., et al. (2020). Electroactive composite scaffold with locally expressed osteoinductive factor for synergistic bone repair upon electrical stimulation. *Biomaterials* 230:119617. doi: 10.1016/j.biomaterials.2019.119617

da Cruz, M. B., Marques, J. F., Penarrieta-Juanito, G. M., Costa, M., Souza, J. C., Magini, R. S., et al. (2019). Hard and soft tissue cell behavior on polyetheretherketone, zirconia, and titanium implant materials. *Int. J. Oral Maxillofac. Implants* 34, 39–46. doi: 10.11607/jomi.6926

Das, T., Sharma, P. K., Busscher, H. J., van der Mei, H. C., and Krom, B. P. (2010). Role of extracellular DNA in initial bacterial adhesion and surface aggregation. *Appl. Environ. Microbiol.* 76, 3405–3408. doi: 10.1128/AEM.03119-09

Deng, L., Deng, Y., and Xie, K. (2017). AgNPs-decorated 3D printed PEEK implant for infection control and bone repair. *Colloids Surf B Biointerf.* 160, 483–492. doi: 10.1016/j.colsurfb.2017.09.061

Deng, L., He, X., Xie, K., Xie, L., and Deng, Y. (2019). Dual therapy coating on micro/nanoscale porous polyetheretherketone to eradicate biofilms and accelerate bone tissue repair. *Macromol. Biosci.* 19:e1800376. doi: 10.1002/mabi.201800376

Deng, L.-J., Wu, Y.-L., He, X.-H., Xie, K.-N., Xie, L., and Deng, Y. (2018). Simvastatin delivery on PEEK for bioactivity and osteogenesis enhancements. *J. Biomater. Sci. Polym. Ed.* 29, 2237–2251. doi: 10.1080/09205063.2018.1534668

Deng, Y., Gao, X., Shi, X.-L., Lu, S., Yang, W., Duan, C., et al. (2020). Graphene oxide and adiponectin-functionalized sulfonated poly(etheretherketone) with effective osteogenicity and remotely repeatable photodisinfection. *Chem. Mater.* 32, 2180–2193. doi: 10.1021/acs.chemmater.0c00290

Deng, Y., Liu, X., Xu, A., Wang, L., Luo, Z., Zheng, Y., et al. (2015a). Effect of surface roughness on osteogenesis *in vitro* and osseointegration *in vivo* of carbon fiber-reinforced polyetheretherketone-nanohydroxyapatite composite. *Int. J. Nanomedicine* 10, 1425–1447. doi: 10.2147/IJN.S75557

Deng, Y., Yang, L., Huang, X., Chen, J., Shi, X., Yang, W., et al. (2018). Dual Ag/ZnO-decorated micro-/nanoporous sulfonated polyetheretherketone with superior antibacterial capability and biocompatibility via layer-by-layer self-assembly strategy. *Macromol. Biosci.* 18:e1800028. doi: 10.1002/mabi.201800028

Deng, Y., Zhou, P., Liu, X., Wang, L., Xiong, X., Tang, Z., et al. (2015b). Preparation, characterization, cellular response and *in vivo* osseointegration of polyetheretherketone/nano-hydroxyapatite/carbon fiber ternary biocomposite. *Colloids Surf. B Biointerfaces* 136, 64–73. doi: 10.1016/j.colsurfb.2015.09.001

Díez-Pascual, A. M., and Díez-Vicente, A. L. (2014). Development of nanocomposites reinforced with carboxylated poly(ether ether ketone) grafted to zinc oxide with superior antibacterial properties. *ACS Appl. Mater. Interfaces* 6, 3729–3741. doi: 10.1021/am500171x

Dong, T., Duan, C., Wang, S., Gao, X., Yang, Q., Yang, W., et al. (2020). Multifunctional surface with enhanced angiogenesis for improving long-term osteogenic fixation of poly(ether ether ketone) implants. *ACS Appl. Mater. Interfaces* 12, 14971–14982. doi: 10.1021/acsami.0c02304

Durham, J. W., Montelongo, S. A., Ong, J. L., Guda, T., Allen, M. J., and Rabiei, A. (2016). Hydroxyapatite coating on PEEK implants: biomechanical and histological study in a rabbit model. *Mater. Sci. Eng. C* 68, 723–731. doi: 10.1016/j.msec.2016.06.049

Elawadly, T., Radi, I. A. W., El Khadem, A., and Osman, R. B. (2017). Can PEEK be an implant material? Evaluation of surface topography and wettability of filled versus unfilled peek with different surface roughness. *J. Oral. Implantol.* 43, 456–461. doi: 10.1563/aaid-joi-D-17-00144

Eliaz, N., and Metoki, N. (2017). Calcium phosphate bioceramics: a review of their history, structure, properties, coating technologies and biomedical applications. *Materials* 10:334. doi: 10.3390/ma10040334

Eschbach, L. (2000). Nonresorbable polymers in bone surgery. *Injury* 31 (Suppl. 4): 22–27. doi: 10.1016/S0020-1383(00)80019-4

Evans, N. T., Torstrick, F. B., Lee, C. S., Dupont, K. M., Safranski, D. L., Chang, W. A., et al. (2015). High-strength, surface-porous polyether-ether-ketone for load-bearing orthopedic implants. *Acta Biomater.* 13, 159–167. doi: 10.1016/j.actbio.2014.11.030

Fage, S. W., Muris, J., Jakobsen, S. S., and Thyssen, J. P. (2016). Titanium: a review on exposure, release, penetration, allergy, epidemiology, and clinical reactivity. *Contact Derm.* 74, 323–345. doi: 10.1111/cod.12565

Feng, X., Ma, L., Liang, H., Liu, X., Lei, J., Li, W., et al. (2020). Osteointegration of 3D-printed fully porous polyetheretherketone scaffolds with different pore sizes. *ACS Omega* 5, 26655–26666. doi: 10.1021/acsomega.0c03489

Fukuda, N., Tsuchiya, A., Sunarso, Toita, R., Tsuru, K., Mori, Y., et al. (2019). Surface plasma treatment and phosphorylation enhance the biological performance of poly(ether ether ketone). *Colloids Surf. B Biointerfaces* 173, 36–42. doi: 10.1016/j.colsurfb.2018.09.032

Gan, K., Liu, H., Jiang, L., Liu, X., Song, X., Niu, D., et al. (2016). Bioactivity and antibacterial effect of nitrogen plasma immersion ion implantation on polyetheretherketone. *Dent. Mater.* 32, e263–e274. doi: 10.1016/j.dental.2016.08.215

Gao, A., Liao, Q., Xie, L., Wang, G., Zhang, W., Wu, Y., et al. (2020). Tuning the surface immunomodulatory functions of polyetheretherketone for enhanced osseointegration. *Biomaterials* 230:119642. doi: 10.1016/j.biomaterials.2019.119642

Ge, J., Wang, F., Xu, Z., Shen, X., Gao, C., Wang, D., et al. (2020). Influences of niobium pentoxide on roughness, hydrophilicity, surface energy and protein absorption, and cellular responses to PEEK based composites for orthopedic applications. *J. Mater. Chem. B* 8, 2618–2626. doi: 10.1039/C9TB02456E

Godara, A., Raabe, D., and Green, S. (2007). The influence of sterilization processes on the micromechanical properties of carbon fiber-reinforced PEEK composites for bone implant applications. *Acta Biomater.* 3, 209–220. doi: 10.1016/j.actbio.2006.11.005

Guillot, R., Pignot-Paintrand, I., Lavaud, J., Decambron, A., Bourgeois, E., Josserand, V., et al. (2016). Assessment of a polyelectrolyte multilayer film coating loaded with BMP-2 on titanium and PEEK implants in the rabbit femoral condyle. *Acta Biomater.* 36, 310–322. doi: 10.1016/j.actbio.2016.03.010

Ha, S. W., Kirch, M., Birchler, F., Eckert, K. L., Mayer, J., Wintermantel, E., et al. (1997). Surface activation of polyetheretherketone (PEEK) and formation of calcium phosphate coatings by precipitation. *J. Mater. Sci. Mater. Med.* 8, 683–690. doi: 10.1023/A:1018535923173

Han, C. M., Jang, T. S., Kim, H. E., and Koh, Y. H. (2014). Creation of nanoporous TiO2 surface onto polyetheretherketone for effective immobilization and delivery of bone morphogenetic protein. *J. Biomed. Mater. Res. A* 102, 793–800. doi: 10.1002/jbm.a.34748

Han, C. M., Lee, E. J., Kim, H. E., Koh, Y. H., Kim, K. N., Ha, Y., et al. (2010). The electron beam deposition of titanium on polyetheretherketone (PEEK) and the resulting enhanced biological properties. *Biomaterials* 31, 3465–3470. doi: 10.1016/j.biomaterials.2009.12.030

Han, X., Sharma, N., Xu, Z., Scheideler, L., Geis-Gerstorfer, J., Rupp, F., et al. (2019a). An *in vitro* study of osteoblast response on fused-filament fabrication 3D printed PEEK for dental and cranio-maxillofacial implants. *J. Clin. Med.* 8:771. doi: 10.3390/jcm8060771

Han, X., Yang, D., Yang, C., Spintzyk, S., Scheideler, L., Li, P., et al. (2019b). Carbon fiber reinforced PEEK composites based on 3D-printing technology for orthopedic and dental applications. *J. Clin. Med.* 8:240. doi: 10.3390/jcm8020240

He, G., Dahl, T., Veis, A., and George, A. (2003). Nucleation of apatite crystals *in vitro* by self-assembled dentin matrix protein 1. *Nat. Mater.* 2, 552–558. doi: 10.1038/nmat945

Hickey, D. J., Lorman, B., and Fedder, I. L. (2019). Improved response of osteoprogenitor cells to titanium plasma-sprayed PEEK surfaces. *Colloids Surf. B Biointerfaces* 175, 509–516. doi: 10.1016/j.colsurfb.2018.12.037

Hieda, A., Uemura, N., Hashimoto, Y., Toda, I., and Baba, S. (2017). *In vivo* bioactivity of porous polyetheretherketone with a foamed surface. *Dent. Mater. J.* 36, 222–229. doi: 10.4012/dmj.2016-277

Huiskes, R., Ruimerman, R., van Lenthe, G. H., and Janssen, J. D. (2000). Effects of mechanical forces on maintenance and adaptation of form in trabecular bone. *Nature* 405, 704–706. doi: 10.1038/35015116

Huiskes, R., Weinans, H., and van Rietbergen, B. (1992). The relationship between stress shielding and bone resorption around total hip stems and the effects of flexible materials. *Clin. Orthop. Relat. Res.* 274, 124–134. doi: 10.1097/00003086-199201000-00014

Huo, S., Meng, X., Zhang, S., Yue, B., Zhao, Y., Long, T., et al. (2020). Hydrofluoric acid and nitric acid cotreatment for biofunctionalization of polyetheretherketone in M2 macrophage polarization and osteogenesis. *J. Biomed. Mater. Res. Part A.* 108, 2473–2483. doi: 10.1002/jbm.a.37079

Jabbari, E., Oyane, A., Nakamura, M., Sakamaki, I., Shimizu, Y., Miyata, S., et al. (2018). Laser-assisted wet coating of calcium phosphate for surface-functionalization of PEEK. *PLoS ONE* 13:e0206524. doi: 10.1371/journal.pone.0206524

Ji, S., Sun, C., Zhao, J., and Liang, F. (2015). Comparison and analysis on mechanical property and machinability about polyetheretherketone and carbon-fibers reinforced polyetheretherketone. *Materials* 8, 4118–4130. doi: 10.3390/ma8074118

Jimbo, R., Ivarsson, M., Koskela, A., Sul, Y. T., and Johansson, C. B. (2010). Protein adsorption to surface chemistry and crystal structure modification of titanium surfaces. *J. Oral Maxillofac. Res.* 1:e3. doi: 10.5037/jomr.2010.1303

Johansson, P., Barkarmo, S., Hawthan, M., Peruzzi, N., Kjellin, P., and Wennerberg, A. (2018). Biomechanical, histological, and computed X-ray tomographic analyses of hydroxyapatite coated PEEK implants in an extended healing model in rabbit. *J. Biomed. Mater. Res. A* 106, 1440–1447. doi: 10.1002/jbm.a.36345

Johansson, P., Jimbo, R., Kjellin, P., Currie, F., Chrcanovic, B. R., and Wennerberg, A. (2014). Biomechanical evaluation and surface characterization of a nano-modified surface on PEEK implants: a study in the rabbit tibia. *Int. J. Nanomedicine* 9, 3903–3911. doi: 10.2147/IJN.S60387

Johansson, P., Jimbo, R., Kozai, Y., Sakurai, T., Kjellin, P., Currie, F., et al. (2015). Nanosized hydroxyapatite coating on PEEK implants enhances early bone formation: a histological and three-dimensional investigation in rabbit bone. *Materials* 8, 3815–3830. doi: 10.3390/ma8073815

Johansson, P., Jimbo, R., Naito, Y., Kjellin, P., Currie, F., and Wennerberg, A. (2016). Polyether ether ketone implants achieve increased bone fusion when coated with nano-sized hydroxyapatite: a histomorphometric study in rabbit bone. *Int. J. Nanomedicine* 11, 1435–1442. doi: 10.2147/IJN.S100424

Jung, H. D., Park, H. S., Kang, M. H., Li, Y., Kim, H. E., Koh, Y. H., et al. (2016). Reinforcement of polyetheretherketone polymer with titanium for improved mechanical properties and *in vitro* biocompatibility. *J. Biomed. Mater. Res. Part B Appl. Biomater.* 104, 141–148. doi: 10.1002/jbm.b.33361

Kakinuma, H., Ishii, K., Ishihama, H., Honda, M., Toyama, Y., Matsumoto, M., et al. (2015). Antibacterial polyetheretherketone implants immobilized with silver ions based on chelate-bonding ability of inositol phosphate: processing, material characterization, cytotoxicity, and antibacterial properties. *J. Biomed. Mater. Res. Part A* 103, 57–64. doi: 10.1002/jbm.a.35157

Katzer, A., Marquardt, H., Westendorf, J., Wening, J. V., and von Foerster, G. (2002). Polyetheretherketone–cytotoxicity and mutagenicity *in vitro*. *Biomaterials* 23, 1749–1759. doi: 10.1016/S0142-9612(01)00300-3

Khang, D., Kim, S. Y., Liu-Snyder, P., Palmore, G. T., Durbin, S. M., and Webster, T. J. (2007). Enhanced fibronectin adsorption on carbon nanotube/poly(carbonate) urethane: independent role of surface nano-roughness and associated surface energy. *Biomaterials* 28, 4756–4768. doi: 10.1016/j.biomaterials.2007.07.018

Kilpadi, D. V., and Lemons, J. E. (1994). Surface energy characterization of unalloyed titanium implants. *J. Biomed. Mater. Res.* 28, 1419–1425. doi: 10.1002/jbm.820281206

Kizuki, T., Matsushita, T., and Kokubo, T. (2015). Apatite-forming PEEK with TiO_2 surface layer coating. *J. Mater. Sci. Mater. Med.* 26:5359. doi: 10.1007/s10856-014-5359-1

Klein, C. P., de Blieck-Hogervorst, J. M., Wolke, J. G., and de Groot, K. (1990). Studies of the solubility of different calcium phosphate ceramic particles *in vitro*. *Biomaterials* 11, 509–512. doi: 10.1016/0142-9612(90)90067-Z

Kurtz, S. M., and Devine, J. N. (2007). PEEK biomaterials in trauma, orthopedic, and spinal implants. *Biomaterials* 28, 4845–4869. doi: 10.1016/j.biomaterials.2007.07.013

Lee, J. H., Jang, H. L., Lee, K. M., Baek, H. R., Jin, K., Hong, K. S., et al. (2013). *In vitro* and *in vivo* evaluation of the bioactivity of hydroxyapatite-coated polyetheretherketone biocomposites created by cold spray technology. *Acta Biomater.* 9, 6177–6187. doi: 10.1016/j.actbio.2012.11.030

Lee, W.-T., Koak, J.-Y., Lim, Y.-J., Kim, S.-K., Kwon, H.-B., and Kim, M.-J. (2012). Stress shielding and fatigue limits of poly-ether-ether-ketone dental implants. *J. Biomed. Mater. Res. Part B Appl. Biomater.* 100, 1044–1052. doi: 10.1002/jbm.b.32669

Li, Q., Zhao, W., Li, Y., Yang, W., and Wang, G. (2019a). Flexural properties and fracture behavior of CF/PEEK in orthogonal building orientation by FDM: microstructure and mechanism. *Polymers* 11:656. doi: 10.3390/polym11040656

Li, Y., Wang, D., Qin, W., Jia, H., Wu, Y., Ma, J., et al. (2019b). Mechanical properties, hemocompatibility, cytotoxicity and systemic toxicity of carbon fibers/poly(ether-ether-ketone) composites with different fiber lengths as orthopedic implants. *J. Biomater. Sci. Polym. Ed* 30, 1709–1724. doi: 10.1080/09205063.2019.1659711

Liu, C., Chan, K., Shen, J., Liao, C., Yeung, K., and Tjong, S. (2016). Polyetheretherketone hybrid composites with bioactive nanohydroxyapatite and multiwalled carbon nanotube fillers. *Polymers* 8:425. doi: 10.3390/polym8120425

Liu, S., Zhu, Y., Gao, H., Ge, P., Ren, K., Gao, J., et al. (2018). One-step fabrication of functionalized poly(etheretherketone) surfaces with enhanced biocompatibility and osteogenic activity. *Mater. Sci. Eng. C Mater. Biol. Appl.* 88, 70–78. doi: 10.1016/j.msec.2018.03.003

Liu, W., Li, J., Cheng, M., Wang, Q., Qian, Y., Yeung, K. W. K., et al. (2019). A surface-engineered polyetheretherketone biomaterial implant with direct and immunoregulatory antibacterial activity against methicillin-resistant staphylococcus aureus. *Biomaterials* 208, 8–20. doi: 10.1016/j.biomaterials.2019.04.008

Liu, X., Gan, K., Liu, H., Song, X., Chen, T., and Liu, C. (2017). Antibacterial properties of nano-silver coated PEEK prepared through magnetron sputtering. *Dental Mater.* 33, e348–e360. doi: 10.1016/j.dental.2017.06.014

Lu, T., Liu, X., Qian, S., Cao, H., Qiao, Y., Mei, Y., et al. (2014). Multilevel surface engineering of nanostructured TiO_2 on carbon-fiber-reinforced polyetheretherketone. *Biomaterials* 35, 5731–5740. doi: 10.1016/j.biomaterials.2014.04.003

Lu, T., Wen, J., Qian, S., Cao, H., Ning, C., Pan, X., et al. (2015). Enhanced osteointegration on tantalum-implanted polyetheretherketone surface with bone-like elastic modulus. *Biomaterials* 51, 173–183. doi: 10.1016/j.biomaterials.2015.02.018

Ma, J., Liang, Q., Qin, W., Lartey, P. O., Li, Y., and Feng, X. (2020). Bioactivity of nitric acid and calcium chloride treated carbon-fibers reinforced polyetheretherketone for dental implant. *J. Mech. Behav. Biomed. Mater.* 102:103497. doi: 10.1016/j.jmbbm.2019.103497

Ma, R., and Guo, D. (2019). Evaluating the bioactivity of a hydroxyapatite-incorporated polyetheretherketone biocomposite. *J. Orthop. Surg. Res.* 14:32. doi: 10.1186/s13018-019-1069-1

Ma, R., Tang, S., Tan, H., Qian, J., Lin, W., Wang, Y., et al. (2014). Preparation, characterization, *in vitro* bioactivity, and cellular responses to a polyetheretherketone bioactive composite containing nanocalcium silicate for bone repair. *ACS Appl. Mater. Interfaces* 6, 12214–12225. doi: 10.1021/am504409q

Ma, R., Wang, J., Li, C., Ma, K., Wei, J., Yang, P., et al. (2020). Effects of different sulfonation times and post-treatment methods on the characterization and cytocompatibility of sulfonated PEEK. *J. Biomater. Appl.* 35, 342–352. doi: 10.1177/0885328220935008

Mahjoubi, H., Buck, E., Manimunda, P., Farivar, R., Chromik, R., Murshed, M., et al. (2017). Surface phosphonation enhances hydroxyapatite coating adhesion on polyetheretherketone and its osseointegration potential. *Acta Biomater.* 47, 149–158. doi: 10.1016/j.actbio.2016.10.004

Masamoto, K., Fujibayashi, S., Yabutsuka, T., Hiruta, T., Otsuki, B., Okuzu, Y., et al. (2019). *In vivo* and *in vitro* bioactivity of a "precursor of apatite" treatment on polyetheretherketone. *Acta Biomater.* 91, 48–59. doi: 10.1016/j.actbio.2019.04.041

Mavropoulos, E., Hausen, M., Costa, A. M., Alves, G., Mello, A., Ospina, C. A., et al. (2013). The impact of the RGD peptide on osteoblast adhesion and spreading on zinc-substituted hydroxyapatite surface. *J. Mater. Sci. Mater. Med.* 24, 1271–1283. doi: 10.1007/s10856-013-4851-3

Mei, S., Yang, L., Pan, Y., Wang, D., Wang, X., Tang, T., et al. (2019). Influences of tantalum pentoxide and surface coarsening on surface roughness, hydrophilicity, surface energy, protein adsorption and cell responses to PEEK based biocomposite. *Colloids Surf. B Biointerfaces* 174, 207–215. doi: 10.1016/j.colsurfb.2018.10.081

Miyazaki, T., Matsunami, C., and Shirosaki, Y. (2017). Bioactive carbon-PEEK composites prepared by chemical surface treatment. *Mater. Sci. Eng. C Mater. Biol. Appl. 70*, 71–75. doi: 10.1016/j.msec.2016.08.058

Monich, P. R., Berti, F. V., Porto, L. M., Henriques, B., Novaes de Oliveira, A. P., Fredel, M. C., et al. (2017). Physicochemical and biological assessment of PEEK composites embedding natural amorphous silica fibers for biomedical applications. *Mater. Sci. Eng. C* 79, 354–362. doi: 10.1016/j.msec.2017.05.031

Mosser, D. M., and Edwards, J. P. (2008). Exploring the full spectrum of macrophage activation. *Nat. Rev. Immunol.* 8, 958–969. doi: 10.1038/nri2448

Niki, Y., Matsumoto, H., Otani, T., Suda, Y., and Toyama, Y. (2001). Metal ion concentrations in the joint fluid immediately after total knee arthroplasty. *Mod. Rheumatol.* 11, 192–196. doi: 10.3109/s101650170003

Oladapo, B. I., Ismail, S. O., Bowoto, O. K., Omigbodun, F. T., Olawumi, M. A., and Muhammad, M. A. (2020). Lattice design and 3D-printing of PEEK with Ca10(OH)(PO4)3 and in-vitro bio-composite for bone implant. *Int. J. Biol. Macromol.* 165, 50–62. doi: 10.1016/j.ijbiomac.2020.09.175

Ouyang, L., Sun, Z., Wang, D., Qiao, Y., Zhu, H., Ma, X., et al. (2018). Smart release of doxorubicin loaded on polyetheretherketone (PEEK) surface with 3D porous structure. *Colloids Surf. B Biointerfaces* 163, 175–183. doi: 10.1016/j.colsurfb.2017.12.045

Ouyang, L., Zhao, Y., Jin, G., Lu, T., Li, J., Qiao, Y., et al. (2016). Influence of sulfur content on bone formation and antibacterial ability of sulfonated PEEK. *Biomaterials* 83, 115–126. doi: 10.1016/j.biomaterials.2016.01.017

Pashkuleva, I., Marques, A. P., Vaz, F., and Reis, R. L. (2010). Surface modification of starch based biomaterials by oxygen plasma or UV-irradiation. *J. Mater. Sci. Mater. Med.* 21, 21–32. doi: 10.1007/s10856-009-3831-0

Peng, S., Feng, P., Wu, P., Huang, W., Yang, Y., Guo, W., et al. (2017). Graphene oxide as an interface phase between polyetheretherketone and hydroxyapatite for tissue engineering scaffolds. *Sci. Rep.* 7:46604. doi: 10.1038/srep46604

Pezzotti, G., Marin, E., Adachi, T., Lerussi, F., Rondinella, A., Boschetto, F., et al. (2018). Incorporating Si_3N_4 into PEEK to produce antibacterial, osteocondutive, and radiolucent spinal implants. *Macromol. Biosci.* 18:1800033. doi: 10.1002/mabi.201800033

Prasad, S. R., Kumar, T. S. S., and Jayakrishnan, A. (2018). Ceramic core with polymer corona hybrid nanocarrier for the treatment of osteosarcoma with co-delivery of protein and anti-cancer drug. *Nanotechnology* 29:015101. doi: 10.1088/1361-6528/aa9a21

Qin, W., Li, Y., Ma, J., Liang, Q., Cui, X., Jia, H., et al. (2020). Osseointegration and biosafety of graphene oxide wrapped porous CF/PEEK composites as implantable materials: the role of surface structure and chemistry. *Dental Mater.* 36, 1289–1302. doi: 10.1016/j.dental.2020.06.004

Qin, W., Li, Y., Ma, J., Liang, Q., and Tang, B. (2019). Mechanical properties and cytotoxicity of hierarchical carbon fiber-reinforced poly (ether-ether-ketone) composites used as implant materials. *J. Mech. Behav. Biomed. Mater.* 89, 227–233. doi: 10.1016/j.jmbbm.2018.09.040

Quarto, R., and Giannoni, P. (2016). "Bone tissue engineering: past-present-future," in *Mesenchymal Stem Cells: Methods and Protocols,* ed. *M. Gnecchi (New York, NY: Springer New York),* 21–33. doi: 10.1007/978-1-4939-3584-0_2

Reigstad, O., Johansson, C., Stenport, V., Wennerberg, A., Reigstad, A., and Røkkum, M. (2011). Different patterns of bone fixation with hydroxyapatite and resorbable CaP coatings in the rabbit tibia at 6, 12, and 52 weeks. *J. Biomed. Mater. Res. Part B Appl. Biomater.* 99, 14–20. doi: 10.1002/jbm.b.31866

Ren, Y., Sikder, P., Lin, B., and Bhaduri, S. B. (2018). Microwave assisted coating of bioactive amorphous magnesium phosphate (AMP) on polyetheretherketone (PEEK). *Mater. Sci. Eng. C* 85, 107–113. doi: 10.1016/j.msec.2017.12.025

Røkkum, M., Reigstad, A., Johansson, C. B., and Albrektsson, T. (2003). Tissue reactions adjacent to well-fixed hydroxyapatite-coated acetabular cups. Histopathology of ten specimens retrieved at reoperation after 0.3 to 5.8 years. *J. Bone Joint Surg. Br.* 85, 440–447. doi: 10.1302/0301-620X.85B3.12834

Roskies, M., Jordan, J. O., Fang, D., Abdallah, M. N., Hier, M. P., Mlynarek, A., et al. (2016). Improving PEEK bioactivity for craniofacial reconstruction using a 3D printed scaffold embedded with mesenchymal stem cells. *J. Biomater. Appl.* 31, 132–139. doi: 10.1177/0885328216638636

Ryoo, H. M., Lee, M. H., and Kim, Y. J. (2006). Critical molecular switches involved in BMP-2-induced osteogenic differentiation of mesenchymal cells. *Gene* 366, 51–57. doi: 10.1016/j.gene.2005.10.011

Samavedi, S., Whittington, A. R., and Goldstein, A. S. (2013). Calcium phosphate ceramics in bone tissue engineering: a review of properties and their influence on cell behavior. *Acta Biomater.* 9, 8037–8045. doi: 10.1016/j.actbio.2013.06.014

Schwitalla, A. D., Abou-Emara, M., Spintig, T., Lackmann, J., and Muller, W. D. (2015). Finite element analysis of the biomechanical effects of PEEK dental implants on the peri-implant bone. *J. Biomech.* 48, 1–7. doi: 10.1016/j.jbiomech.2014.11.017

Shimizu, T., Fujibayashi, S., Yamaguchi, S., Yamamoto, K., Otsuki, B., Takemoto, M., et al. (2016). Bioactivity of sol-gel-derived TiO_2 coating on polyetheretherketone: *in vitro* and *in vivo* studies. *Acta Biomater.* 35, 305–317. doi: 10.1016/j.actbio.2016.02.007

Shuai, C., Peng, S., Wu, P., Gao, C., Huang, W., Deng, Y., et al. (2016). A nano-sandwich construct built with graphene nanosheets and carbon nanotubes enhances mechanical properties of hydroxyapatiteandndash;polyetheretherketone scaffolds. *Int. J. Nanomedicine* 11, 3487–3500. doi: 10.2147/IJN.S110920

Sikder, P., Ferreira, J. A., Fakhrabadi, E. A., Kantorski, K. Z., Liberatore, M. W., Bottino, M. C., et al. (2020). Bioactive amorphous magnesium phosphate-polyetheretherketone composite filaments for 3D printing. *Dent. Mater.* 36, 865–883. doi: 10.1016/j.dental.2020.04.008

Spece, H., Yu, T., Law, A. W., Marcolongo, M., and Kurtz, S. M. (2020). 3D printed porous PEEK created via fused filament fabrication for osteoconductive orthopaedic surfaces. *J. Mech. Behav. Biomed. Mater.* 109:103850. doi: 10.1016/j.jmbbm.2020.103850

Stegen, S., van Gastel, N., and Carmeliet, G. (2015). Bringing new life to damaged bone: the importance of angiogenesis in bone repair and regeneration. *Bone* 70, 19–27. doi: 10.1016/j.bone.2014.09.017

Sun, Z., Ouyang, L., Ma, X., Qiao, Y., and Liu, X. (2018). Controllable and durable release of BMP-2-loaded 3D porous sulfonated polyetheretherketone (PEEK) for osteogenic activity enhancement. *Colloids Surf. B Biointerfaces* 171, 668–674. doi: 10.1016/j.colsurfb.2018.08.012

Sunarso, T. A., Toita, R., Tsuru, K., and Ishikawa, K. (2019). Enhanced osseointegration capability of poly(ether ether ketone) via combined phosphate and calcium surface-functionalization. *Int. J. Mol. Sci.* 21:198. doi: 10.3390/ijms21010198

Suska, F., Omar, O., Emanuelsson, L., Taylor, M., Gruner, P., Kinbrum, A., et al. (2014). Enhancement of CRF-PEEK osseointegration by plasma-sprayed hydroxyapatite: a rabbit model. *J. Biomater. Appl.* 29, 234–242. doi: 10.1177/0885328214521669

Swaminathan, P. D., Uddin, M. N., Wooley, P., and Asmatulu, R. (2020). Fabrication and biological analysis of highly porous PEEK bionanocomposites incorporated with carbon and hydroxyapatite nanoparticles for biological applications. *Molecules* 25:3572. doi: 10.3390/molecules25163572

Tang, X., Dai, J., Sun, H., Nabanita, S., Petr, S., Wang, D., et al. (2019). Mechanical strength, surface properties, cytocompatibility and antibacterial activity of nano zinc-magnesium silicate/polyetheretherketone biocomposites. *J. Nanosci. Nanotechnol.* 19, 7615–7623. doi: 10.1166/jnn.2019.16727

Torstrick, F. B., Evans, N. T., Stevens, H. Y., Gall, K., and Guldberg, R. E. (2016). Do surface porosity and pore size influence mechanical properties and cellular response to PEEK? *Clin. Orthop. Relat. Res.* 474, 2373–2383. doi: 10.1007/s11999-016-4833-0

Torstrick, F. B., Lin, A. S. P., Potter, D., Safranski, D. L., Sulchek, T. A., Gall, K., et al. (2018). Porous PEEK improves the bone-implant interface compared to plasma-sprayed titanium coating on PEEK. *Biomaterials* 185, 106–116. doi: 10.1016/j.biomaterials.2018.09.009

Torstrick, F. B., Lin, A. S. P., Safranski, D. L., Potter, D., Sulchek, T., Lee, C. S. D., et al. (2020). Effects of surface topography and chemistry on polyether-ether-ketone (PEEK) and titanium osseointegration. *Spine* 45, E417–E424. doi: 10.1097/BRS.0000000000003303

Uddin, M. N., Dhanasekaran, P. S., and Asmatulu, R. (2019). Mechanical properties of highly porous PEEK bionanocomposites incorporated with carbon and hydroxyapatite nanoparticles for scaffold applications. *Progress Biomater.* 8, 211–221. doi: 10.1007/s40204-019-00123-1

Ur Rehman, M. A., Bastan, F. E., Nawaz, Q., Goldmann, W. H., Maqbool, M., Virtanen, S., et al. (2018). Electrophoretic deposition of lawsone loaded bioactive glass (BG)/chitosan composite on polyetheretherketone (PEEK)/BG layers as antibacterial and bioactive coating. *J. Biomed. Mater. Res. Part A* 106, 3111–3122. doi: 10.1002/jbm.a.36506

Ur Rehman, M. A., Ferraris, S., Goldmann, W. H., Perero, S., Bastan, F. E., Nawaz, Q., et al. (2017). Antibacterial and bioactive coatings based on radio frequency co-sputtering of silver nanocluster-silica coatings on PEEK/bioactive glass layers obtained by electrophoretic deposition. *ACS Appl. Mater. Interf.* 9, 32489–32497. doi: 10.1021/acsami.7b08646

Vaezi, M., Black, C., Gibbs, D. M., Oreffo, R. O., Brady, M., Moshrefi-Torbati, M., et al. (2016). Characterization of new PEEK/HA composites with 3D HA network fabricated by extrusion freeforming. *Molecules* 21:687. doi: 10.3390/molecules21060687

Wakelin, E. A., Yeo, G. C., McKenzie, D. R., Bilek, M. M. M., and Weiss, A. S. (2018). Plasma ion implantation enabled bio-functionalization of PEEK improves osteoblastic activity. *APL Bioeng* 2:026109. doi: 10.1063/1.5010346

Walsh, W. R., Bertollo, N., Christou, C., Schaffner, D., and Mobbs, R. J. (2015). Plasma-sprayed titanium coating to polyetheretherketone improves the bone-implant interface. *Spine J.* 15, 1041–1049. doi: 10.1016/j.spinee.2014.12.018

Wan, T., Jiao, Z., Guo, M., Wang, Z., Wan, Y., Lin, K., et al. (2020). Gaseous sulfur trioxide induced controllable sulfonation promoting biomineralization and osseointegration of polyetheretherketone implants. *Bioact. Mater.* 5, 1004–1017. doi: 10.1016/j.bioactmat.2020.06.011

Wang, C., Wang, S., Yang, Y., Jiang, Z., Deng, Y., Song, S., et al. (2018). Bioinspired, biocompatible and peptide-decorated silk fibroin coatings for enhanced osteogenesis of bioinert implant. *J. Biomater. Sci. Polym. Ed.* 29, 1595–1611. doi: 10.1080/09205063.2018.1477316

Wang, H., Xu, M., Zhang, W., Kwok, D. T., Jiang, J., Wu, Z., et al. (2010). Mechanical and biological characteristics of diamond-like carbon coated poly aryl-ether-ether-ketone. *Biomaterials* 31, 8181–8187. doi: 10.1016/j.biomaterials.2010.07.054

Wang, M., Bhardwaj, G., and Webster, T. J. (2017). Antibacterial properties of PEKK for orthopedic applications. *Int. J. Nanomedicine* 12, 6471–6476. doi: 10.2147/IJN.S134983

Wang, Q., Mejía Jaramillo, A., Pavon, J. J., and Webster, T. J. (2016). Red selenium nanoparticles and gray selenium nanorods as antibacterial coatings for PEEK medical devices. *J. Biomed. Mater. Res. Part B Appl. Biomater.* 104, 1352–1358. doi: 10.1002/jbm.b.33479

Wang, S., Yang, Y., Li, Y., Shi, J., Zhou, J., Zhang, L., et al. (2019). Strontium/adiponectin co-decoration modulates the osteogenic activity of nano-morphologic polyetheretherketone implant. *Colloids Surf. B Biointerfaces* 176, 38–46. doi: 10.1016/j.colsurfb.2018.12.056

Wang, X., Lu, T., Wen, J., Xu, L., Zeng, D., Wu, Q., et al. (2016). Selective responses of human gingival fibroblasts and bacteria on carbon fiber reinforced polyetheretherketone with multilevel nanostructured TiO_2. *Biomaterials* 83, 207–218. doi: 10.1016/j.biomaterials.2016.01.001

Wen, J., Lu, T., Wang, X., Xu, L., Wu, Q., Pan, H., et al. (2016). *In vitro* and *in vivo* evaluation of silicate-coated polyetheretherketone fabricated by electron beam evaporation. *ACS Appl. Mater. Interfaces* 8, 13197–13206. doi: 10.1021/acsami.5b10229

Wenz, L. M., Merritt, K., Brown, S. A., Moet, A., and Steffee, A. D. (1990). *In vitro* biocompatibility of polyetheretherketone and polysulfone composites. *J. Biomed. Mater. Res.* 24, 207–215. doi: 10.1002/jbm.820240207

Wong, K. L., Wong, C. T., Liu, W. C., Pan, H. B., Fong, M. K., Lam, W. M., et al. (2009). Mechanical properties and *in vitro* response of strontium-containing hydroxyapatite/polyetheretherketone composites. *Biomaterials* 30, 3810–3817. doi: 10.1016/j.biomaterials.2009.04.016

Wu, J., Li, L., Fu, C., Yang, F., Jiao, Z., Shi, X., et al. (2018). Micro-porous polyetheretherketone implants decorated with BMP-2 via phosphorylated gelatin coating for enhancing cell adhesion and osteogenic differentiation. *Colloids Surf. B Biointerfaces* 169, 233–241. doi: 10.1016/j.colsurfb.2018.05.027

Wu, X., Liu, X., Wei, J., Ma, J., Deng, F., and Wei, S. (2012). Nano-TiO2/PEEK bioactive composite as a bone substitute material: *in vitro* and *in vivo* studies. *Int. J. Nanomedicine* 7, 1215–1225. doi: 10.2147/IJN.S28101

Wu, Y., Woodbine, L., Carr, A. M., Pillai, A. R., Nokhodchi, A., and Maniruzzaman, M. (2020). 3D printed calcium phosphate cement (CPC) scaffolds for anti-cancer drug delivery. *Pharmaceutics* 12:1077. doi: 10.3390/pharmaceutics12111077

Xu, A., Liu, X., Gao, X., Deng, F., Deng, Y., and Wei, S. (2015). Enhancement of osteogenesis on micro/nano-topographical carbon fiber-reinforced polyetheretherketone-nanohydroxyapatite biocomposite. *Mater. Sci. Eng. C Mater. Biol. Appl.* 48, 592–598. doi: 10.1016/j.msec.2014.12.061

Xu, X., Li, Y., Wang, L., Li, Y., Pan, J., Fu, X., et al. (2019). Triple-functional polyetheretherketone surface with enhanced bacteriostasis and anti-inflammatory and osseointegrative properties for implant application. *Biomaterials* 212, 98–114. doi: 10.1016/j.biomaterials.2019.05.014

Xue, Z., Wang, Z., Sun, A., Huang, J., Wu, W., Chen, M., et al. (2020). Rapid construction of polyetheretherketone (PEEK) biological implants incorporated with brushite (CaHPO4.2H2O) and antibiotics for anti-infection and enhanced osseointegration. *Mater. Sci. Eng. C Mater. Biol. Appl.* 111:110782. doi: 10.1016/j.msec.2020.110782

Yabutsuka, T., Fukushima, K., Hiruta, T., Takai, S., and Yao, T. (2017). Effect of pores formation process and oxygen plasma treatment to hydroxyapatite formation on bioactive PEEK prepared by incorporation of precursor of apatite. *Mater. Sci. Eng. C* 81, 349–358. doi: 10.1016/j.msec.2017.07.017

Yabutsuka, T., Fukushima, K., Hiruta, T., Takai, S., and Yao, T. (2018). Fabrication of Bioactive Fiber-reinforced PEEK and MXD6 by Incorporation of Precursor of Apatite. *J. Biomed. Mater. Res. Part B Appl. Biomater.* 106, 2254–2265. doi: 10.1002/jbm.b.34025

Yan, J., Zhou, W., Jia, Z., Xiong, P., Li, Y., Wang, P., et al. (2018). Endowing polyetheretherketone with synergistic bactericidal effects and improved osteogenic ability. *Acta Biomater.* 79, 216–229. doi: 10.1016/j.actbio.2018.08.037

Yan, J. H., Wang, C. H., Li, K. W., Zhang, Q., Yang, M., Di-Wu, W. L., et al. (2018). Enhancement of surface bioactivity on carbon fiber-reinforced polyether ether ketone via graphene modification. *Int. J. Nanomedicine* 13, 3425–3440. doi: 10.2147/IJN.S160030

Yang, X., Wu, Y., Wei, K., Fang, W., and Sun, H. (2018). Non-isothermal crystallization kinetics of short glass fiber reinforced poly (Ether Ether Ketone) composites. *Materials* 11:2094. doi: 10.3390/ma11112094

Yin, J., Han, Q., Zhang, J., Liu, Y., Gan, X., Xie, K., et al. (2020). MXene-based hydrogels endow polyetheretherketone with effective osteogenicity and combined treatment of osteosarcoma and bacterial infection. *ACS Appl. Mater. Interfaces* 12, 45891–45903. doi: 10.1021/acsami.0c14752

Yoshikawa, H., and Myoui, A. (2005). Bone tissue engineering with porous hydroxyapatite ceramics. *J. Artif. Organs* 8, 131–136. doi: 10.1007/s10047-005-0292-1

Yu, W., Zhang, H., A, L., Yang, S., Zhang, J., Wang, H., et al. (2020). Enhanced bioactivity and osteogenic property of carbon fiber reinforced polyetheretherketone composites modified with amino groups. *Colloids Surf. B Biointerfaces* 193:111098. doi: 10.1016/j.colsurfb.2020.111098

Yu, X., Ibrahim, M., Liu, Z., Yang, H., Tan, L., and Yang, K. (2018). Biofunctional Mg coating on PEEK for improving bioactivity. *Bioact. Mater.* 3, 139–143. doi: 10.1016/j.bioactmat.2018.01.007

Yuan, B., Cheng, Q., Zhao, R., Zhu, X., Yang, X., Yang, X., et al. (2018). Comparison of osteointegration property between PEKK and PEEK: Effects of surface structure and chemistry. *Biomaterials* 170, 116–126. doi: 10.1016/j.biomaterials.2018.04.014

Yuan, X., Ouyang, L., Luo, Y., Sun, Z., Yang, C., Wang, J., et al. (2019). Multifunctional sulfonated polyetheretherketone coating with beta-defensin-14 for yielding durable and broad-spectrum antibacterial activity and osseointegration. *Acta Biomater.* 86, 323–337. doi: 10.1016/j.actbio.2019.01.016

Zhang, J., Cai, L., Wang, T., Tang, S., Li, Q., Tang, T., et al. (2018a). Lithium doped silica nanospheres/poly(dopamine) composite coating on polyetheretherketone to stimulate cell responses, improve bone formation and osseointegration. *Nanomedicine* 14, 965–976. doi: 10.1016/j.nano.2018.01.017

Zhang, J., Wei, W., Yang, L., Pan, Y., Wang, X., Wang, T., et al. (2018b). Stimulation of cell responses and bone ingrowth into macro-microporous implants of nano-bioglass/polyetheretherketone composite and enhanced antibacterial activity by release of hinokitiol. *Colloids Surf. B Biointerfaces* 164, 347–357. doi: 10.1016/j.colsurfb.2018.01.058

Zhao, G., Schwartz, Z., Wieland, M., Rupp, F., Geis-Gerstorfer, J., Cochran, D. L., et al. (2005). High surface energy enhances cell response to titanium substrate microstructure. *J. Biomed. Mater. Res. A* 74, 49–58. doi: 10.1002/jbm.a.30320

Zhao, Y., Wong, H. M., Lui, S. C., Chong, E. Y., Wu, G., Zhao, X., et al. (2016). Plasma surface functionalized polyetheretherketone for enhanced osseo-integration at bone-implant interface. *ACS Appl. Mater. Interfaces* 8, 3901–3911. doi: 10.1021/acsami.5b10881

Zhao, Y., Wong, H. M., Wang, W., Li, P., Xu, Z., Chong, E. Y. W., et al. (2013). Cytocompatibility, osseointegration, and bioactivity of three-dimensional porous and nanostructured network on polyetheretherketone. *Biomaterials* 34, 9264–9277. doi: 10.1016/j.biomaterials.2013.08.071

Conflict of Interest: The authors declare that the research was conducted in the absence of any commercial or financial relationships that could be construed as a potential conflict of interest.

The reviewer YZ declared a shared affiliation, with no collaboration, with the authors to the handling Editor at the time of the review.

frontiers
in Bioengineering and Biotechnology

ORIGINAL RESEARCH
published: 20 January 2021
doi: 10.3389/fbioe.2020.611684

Nanostructured Zirconia Surfaces Regulate Human Gingival Fibroblasts Behavior Through Differential Modulation of Macrophage Polarization

*Jincheng Wu, Pei Yu, Huling Lv, Shuang Yang and Zhe Wu**

Guangzhou Key Laboratory of Basic and Applied Research of Oral Regenerative Medicine, Department of Prosthodontics, Affiliated Stomatology Hospital of Guangzhou Medical University, Guangzhou, China

Zirconia exhibits excellent biocompatibility and is widely used as dental implant materials in prosthodontics. Over the past years, research and development of dental implant biomaterials has focused on osseointegration, but few reports exist regarding the role of the immune environment on cellular responses to these materials. The present study investigates the effect of different nanostructured zirconia surface topographies on macrophage phenotypes and their influence on gingival fibroblast behavior. Three different nanostructured zirconia surfaces are characterized using scanning electron microscopy, atomic force microscopy, and water contact angle. Blank-machined zirconia (BMZ) surfaces were superior to RAW264.7 cell proliferation and adhesion. RAW264.7 seeded on all nanostructured zirconia surfaces polarized toward both inflammatory M1 and anti-inflammatory M2 macrophages with more M2 macrophage phenotype on BMZ surfaces. Meanwhile, conditioned media (CM) from RAW264.7 culture on three nanostructured zirconia surfaces inhibited cell apoptosis to human gingival fibroblasts (HGFs) but promoted HGF proliferation and secretion. Under modulation of RAW264.7 culture, HGFs cultured on BMZ surfaces significantly secreted more extracellular matrix with a higher expression of collagen-I (COL-I), vinculin (VCL), and fibronectin (FN) than those coated on self-glazed zirconia (CSGZ) and self-glazed zirconia (SGZ) surfaces. After being coated with a nano zirconia film, CSGZ surfaces showed certain changes in cell proliferation, adhesion, and protein production compared with SGZ surfaces. These findings will provide an overview of manipulating surface topography to modulate macrophage phenotypes in order to create an effective macrophage immune response and reinforce soft tissue integration.

Keywords: zirconia, macrophages, human gingival fibroblasts, cell adhesion, cell proliferation

Edited by:
Junchao Wei,
Nanchang University, China

Reviewed by:
Marta Miola,
Politecnico di Torino, Italy
Xianghong Luan,
Texas A&M University, United States

***Correspondence:**
Zhe Wu
zhewudentist@gzhmu.edu.cn

Specialty section:
This article was submitted to Biomaterials, a section of the journal Frontiers in Bioengineering and Biotechnology

Received: *29 September 2020*
Accepted: *16 December 2020*
Published: *20 January 2021*

Citation:
Wu J, Yu P, Lv H, Yang S and Wu Z (2021) Nanostructured Zirconia Surfaces Regulate Human Gingival Fibroblasts Behavior Through Differential Modulation of Macrophage Polarization. Front. Bioeng. Biotechnol. 8:611684. doi: 10.3389/fbioe.2020.611684

INTRODUCTION

Zirconia has gained outstanding popularity in recent years and is recommended as a dental material for implant because of its good biocompatibility (Zhang and Lawn, 2018), superior mechanical properties (Turon-Vinas and Anglada, 2018), low plaque affinity (Roehling et al., 2017), and excellent esthetic outcomes (Tabatabaian, 2019). Over the past years, research and development of dental implant biomaterials has focused on osseointegration. However, published studies addressing the effect of immune reaction on soft tissue integration are scarce. The biological seal in the transmucosal part of an implant acts as a biological barrier, prevents bacterial penetration, and protects the alveolar bone (Baltriukiene et al., 2014). The incidence of peri-implantitis was diagnosed in 31.2% of patients, and an undesirable clinical complication, such as soft tissue recession and marginal bone resorption, most often occurs as a result of inflammation, which threatens the long-term success of dental implants (Han et al., 2014; Bosshardt et al., 2017). Oftentimes, adverse immune reactions against foreign materials can lead to dramatic, immediate outcomes, such as intense pain, excessive inflammation, or rejection of the implanted material (Kzhyshkowska et al., 2015). Thus, sufficient soft tissue integration is essential to support the peri-implant tissues, improve esthetics, ensure a soft tissue seal against microorganisms, and preserve crestal bone level, ultimately increasing the longevity of the restoration (Atsuta et al., 2016).

A series of host responses can be elicited once surgical materials are implanted into living tissues (Anderson et al., 2008). Macrophages and fibroblasts are two regulatory cells participating in the host immune reaction to biomaterials (Glaros et al., 2009). Macrophages play a more prominent role in the immune responses, whereas fibroblasts are more significant during tissue remodeling (Witherel et al., 2019).

When the implant is inserted, macrophages derived from monocytes will first infiltrate rapidly to the implant site and attack foreign objects by producing various cytokines to regulate the immune microenvironment around the implant site (Zhou et al., 2015). Macrophages show phenotypic plasticity based on the topological structure of foreign materials and are classified into pro-inflammatory M1 and anti-inflammatory M2 types, with a vital role in disease, tissue healing following surgical injury, and biomaterial performance (Mosser and Edwards, 2008; Brown et al., 2012; Murray et al., 2014). M1 macrophages support inflammation by releasing pro-inflammatory cytokines, such as tumor necrosis factor-α (TNF-α) and inducible nitric oxide synthase (iNOS), while M2 macrophages promote tissue repair through producing tissue remodeling cytokines including IL-10, CD206, and transforming growth factor-β (TGF-β) that mediate cell migration, proliferation, and matrix remodeling (Galli et al., 2011; Wynn et al., 2013). Researches have claimed that shifting the macrophage phenotype from M1 to M2 was conducive to implant integration (Ma et al., 2014). In contrast, the presence of a great proportion of M1 relative to M2 is highly related to implant failure (Rao et al., 2012). The cytokines and growth factors secreted by M2 macrophages can support the migration, adhesion, and differentiation of human gingival fibroblasts (Wynn and Vannella, 2016).

Following modulation of macrophage phenotype polarization, gingival fibroblasts migrate to the wound site for the production of a new matrix and act as the major cell type responsible for creating a functional seal from the outside mucosa (Wang et al., 2016). It is well-known that surface properties may change macrophage functions such as cell survival, cell adhesion, and cytokine secretion and further regulate the adhesion and function of progenitor cells (Tan et al., 2006; Kearns et al., 2013). Modification of the processing methods may lead to different surface properties, subsequently influencing cell behavior (Rohr et al., 2020). Nanostructured surfaces have been considered to affect cell function in a different way in contrast to microscale surfaces (Xu et al., 2018). Reports discovered that an oriented alignment of human gingival fibroblasts can be induced on nanonet structuration of titanium surfaces, with more deposition of collagen (Llopis-Grimalt et al., 2019). Another report revealed that titanium surfaces coated with nanoscale silver possess antimicrobial efficacy and human gingival fibroblast cytocompatibility (Kheur et al., 2017). In addition, it is reported that TiO_2 with nanotubes at diameters of 30 nm was conductive to induce macrophages to the M2 phenotype, leading to higher osteogenesis and better osseointegration in an *in vivo* study (Wang et al., 2018). Currently, the widely used zirconia is a representative of a technique based on a dry-pressing method, which is made by milling the partially interbred blanks followed by cold incrustation pressing, while self-glazed zirconia is formed by local plastic deformation introduced during a precision wet-chemistry process (Liu et al., 2016). At present, knowledge of how the nanostructured zirconia surfaces influence immune response and their interplay with fibroblast behavior is currently limited.

Thus, the aim of this study is 2-fold: first, the effect of nanostructured zirconia surface topography was investigated on macrophage polarization toward either an M1 or M2 macrophage phenotype. Thereafter, conditioned media (CM) collected from RAW264.7 culture on these nanostructured zirconia surfaces was harvested and cultured with gingival fibroblasts on their respective surfaces. Herein, we aim to investigate the macrophage phenotypes on nanostructured surfaces and to determine which implant surface tends to more favorably generate an optimal microenvironment from host macrophages for soft tissue cell integration.

MATERIALS AND METHODS

Preparation of Nanostructured Zirconia Discs

All discs used in the experiment were provided by ErRan (Hanzhou, China) with a 20-mm diameter and a thickness of 1 mm. These tested discs fit directly to the bottom of 24-well culture plates. All discs were divided into three groups for the experiments: blank-machined zirconia (BMZ), self-glazed zirconia (SGZ), and coated self-glazed zirconia (CSGZ). The tissue culture plate (TCP) is used as a control group. Briefly, the BMZ surfaces were fabricated by a technique depending on a dry-pressing method. The SGZ surfaces were formed by the precision additive 3D gel deposition approach. The CSGZ surfaces were formed by self-glazed zirconia coated with a nano zirconia film. Prior to use, all discs were cleaned ultrasonically in acetone, anhydrous ethanol, and distilled water sequentially.

Surface Characterization

SEM Measurements

The surface nanostructure of the blank-machined zirconia, self-glazed zirconia, and coated zirconia surfaces was characterized by using a scanning electron microscope (SEM, Gemini Sigma 300/VP, Zeiss, Oberkochen, Germany). The samples were washed with distilled water and acetone in an ultrasonic bath and dried at room temperature. The SEM observation was carried out on the surfaces. Accelerating voltages of 1 and 2 kV were applied in order to reduce the charging up of the samples.

AFM Measurements

The surface topography of the samples was characterized in a 2-cm × 2-cm area by an atomic force microscope (AFM, Dimension Icon, Finland and Sweden) in DC-EFM mode with scan rate of 0.8 Hz. The surface roughness was also characterized by a white light interferometer. Average roughness (Ra) and mean square roughness (Rq) were measured by the NanoScope Analysis software v1.8 (Bruker, Germany). The sample was washed with water in an ultrasonic bath and dried at room temperature before the observation.

Water Contact Angle Measurements

Water contact angle (WCA) measurements were carried out using the sessile-drop method on an optical contact angle measuring device (Biolin Theta Flex, Sweden). Five droplets of 2 μl ultrapure water were dropped onto each surface and the obtained values were used to calculate means and standard deviations. The experiments were conducted in triplicate and the mean ± standard deviations of two independent experiments were calculated.

Cell Culture

The murine-derived macrophage cell line RAW264.7 (China Center for Type Culture Collection, Shanghai, China) and human gingival fibroblasts (HGFs) (iCell Bioscience, Shanghai, China) were utilized in this study. For the macrophage experiments, RAW264.7 cells were seeded on 1) BMZ, 2) SGZ, and 3) CSGZ surfaces in 24-well plates containing Dulbecco's modified Eagle's medium (DMEM) supplemented with 10% fetal bovine serum (FBS) and 1% penicillin/streptomycin (HyClone, Thermo Fisher Scientific Inc.) at 37°C in a humidified 5% CO_2 atmosphere. HGFs were cultured in conditioned media in a humidified atmosphere of 95% air and 5% CO_2.

Collection of Conditioned Media

The collection of conditioned media is used to mimic the *in vivo* microenvironment in which the macrophage on nanostructured zirconia surfaces secretes pro- and anti-inflammatory cytokines to influence the behavior of gingival fibroblasts. Briefly, RAW264.7 cells were cultured on BMZ, SGZ, and CSGZ surfaces in 24-well plates at a density of 10^5 cells per well. After 3 days, the culture medium was collected and centrifuged at 1,500 rpm for 20 min at 4°C to remove the cell debris, and frozen at −80°C until experimental seeding. The conditioned medium is the mixture of culture medium from macrophage and DMEM at a ratio of 1:1.

Behavior of Macrophage on Nanostructured Zirconia Surfaces

Adhesion and Proliferation Assay

RAW264.7 cells were seeded on TCP, BMZ, SGZ, and CSGZ surfaces in 24-well plates at a density of 2×10^4 cells per well. At time points 2, 4, and 8 h after seeding, cells were rinsed with PBS to remove the unattached cells and fixed in 4% formaldehyde for 10 min followed by counterstaining with DAPI. Images were taken on a confocal laser scanning microscope (Leica TCS SP8, Germany). Ten fields of view were taken per sample at random, and nuclei were counted using the ImageJ software (Maryland, USA). The Cell Counting Kit-8 assay (CCK8, Dojindo, Kyushu, Japan) was selected to detect the proliferation of RAW264.7 at preset time points (1 and 3 days). In brief, at each time point, the medium was discarded, and the cells were rinsed with PBS. Each well was filled with 100 μl medium and 10 μl of CCK8 solution. After incubation at 37°C for 1 h, the culture medium was transferred to a 96-well plate, and the absorbance was measured using a microplate reader (Multiskan FC, Thermo Fisher) at 450 nm.

The Polarization Gene Expression

Total RNA from RAW264.7 was isolated using TRIzol (Invitrogen) according to the manufacturer's instructions at day 3. The concentrations of RNA were quantified using NanoDrop 2000 (Thermo Fisher Scientific), then 1 μg RNA from each sample was used for reverse transcription to cDNA using OligodT and AMV reverse transcriptase (TaKaRa, Japan). Real-time RT-PCR was performed using QuantiFast SYBRGreen PCR Kit (QIAGEN, Venlo, Holland) and quantified on a CFX Connect Real-Time PCR Detection System (Bio-Rad). All samples were assayed in triplicate with three independent experiments performed. The sequences of primers for M1 macrophage polarization markers (TNF-α, iNOS, IL-1β, and CCR7), M2 macrophage polarization markers (IL-10, TGF-β, and CD206) and GAPDH used as a housekeeping gene are listed in **Table 1**.

Releasing Profile of Cytokines

The concentrations of TNF-α and IL-10 in the supernatants of the culture medium were determined by ELISA kits (ab100747, ab100697, Abcam, USA) following the manufacturer's instructions. The culture medium was collected at day 3 and centrifuged at 1,500 rpm for 20 min at 4°C to remove cell debris, and the supernatant was used for protein quantification.

Behavior of HGFs Under the Conditioned Media From Macrophage Culture on Nanostructured Zirconia Surfaces

Morphology Observation and Proliferation Assay

HGFs were seeded at a density of 10^4 cells per well on TCP, BMZ, SGZ, and CSGZ surfaces in 24-well plates with or without CM and cultured for 4, 8, and 24 h for morphology observation as well as for 1, 3, and 5 days for the proliferation assays. At time points 4, 8, and 24 h for cell morphology observation, cells were gently washed with PBS three times to remove the unbound gingival

TABLE 1 | Primer sequences used in the qRT-PCR.

Genes	Forward Primer sequences (5′-3′)	Reverse Primer sequences (5′-3′)
GAPDH (M)	TGACCACAGTCCATGCCATC	GACGGACACATTGGGGGTAG
TNF-α (M)	CTGAACTTCGGGGTGATCGG	GGCTTGTCACTCGAATTTTGAGA
iNOS (M)	CAGAAGTGCAAAGTCTCAGACAT	GTCATCTTGTATTGTTGGGCT
IL-1β (M)	TGGAGAGTGTGGATCCCAAG	GGTGCTGATGTACCAGTTGG
CCR7 (M)	ATGACGTCACCTACAGCCTG	CAGCCCAAGTCCTTGAAGAG
IL-10 (M)	GAGAAGCATGGCCCAGAAATC	GAGAAATCGATGACAGCGCC
TGF-β (M)	GTGGAAATCAACGGGATCAGC	CAGCAGTTCTTCTCTGTGGAGC
CD206 (M)	AGACGAAATCCCTGCTACTG	CACCCATTCGAAGGCATTC
GAPDH (H)	CGCTGAGTACGTCGTGGAGTC	GCTGATGATCTTGAGGCTGTTGTC
COL-I (H)	GTGAACCTGGTCAAACTGGTCCTG	CCTGTGGTCCAACAACTCCTCTCT
VCL (H)	TCAGATGAGGTGACTCGGTTGG	TTATGGTTGGGATTCGCTCACA
FN (H)	AAGCCCATAGCTGAGAAGTGTTTTG	GGATGTCCTTGTGTCCTGATCGT

M, murine; H, human.

fibroblasts. The attached cells were fixed in 4% PFA for 15 min, treated with 0.5% Triton X-100 in PBS for 5 min, and incubated with fluorescein isothiocyanate-phalloidin (Solarbio) for 30 min. The nuclei were subsequently stained with DAPI for 10 min at room temperature. Finally, images were taken on a confocal laser scanning microscope (Leica TCS SP8, Germany). The CCK8 assay (Dojindo, Kyushu, Japan) was selected to characterize the proliferation of HGFs at preset time points (1, 3, and 5 days). In brief, at each time point, the medium was discarded, and the cells were washed with PBS. Each well was filled with 100 μl medium and 10 μl of CCK8 solution. After incubation at 37°C for 2 h, the culture medium was transferred to a 96-well plate, and the absorbance was measured using a microplate reader (Multiskan FC, Thermo Fisher) at 450 nm.

Apoptosis Assay

HGFs were seeded onto each sample at a concentration of 5×10^4 cells per well with or without CM. After 3 days of incubation, the cells on each sample were harvested, washed twice with ice-cold PBS, resuspended in binding buffer, and stained with Annexin V-APC for 15 min in darkness and with PI for 5 min on ice. The cells were then analyzed by flow cytometry (BD Biosciences, San Jose, CA, USA). Both Annexin V+/PI– (early apoptotic) and Annexin V+/PI+ (late apoptotic) cells were included in apoptotic death determinations. The flow cytometry data were analyzed using FlowJo 10.0.7 software (USA).

Adhesion-Related Gene Expression

HGFs were cultured onto each sample in 24-well plates at a density of 5×10^4 cells per well with or without CM for real-time PCR experiments. After 3 days of culture, total RNA was isolated from HGFs for the detection of the expression of collagen-I (COL-I), fibronectin (FN), and vinculin (VCL) genes using qRT-PCR. GAPDH used as a housekeeping gene is listed in **Table 1**. Experiments were performed in triplicate with three independent experiments.

Immunofluorescence Staining Assay

The secretion and deposition of COL-I, VCL, and FN by HGFs cultured with CM or without were visualized on zirconia surface using immunofluorescence staining. All samples were fixed with 4% PFA for 15 min, permeabilized with 0.5% Triton X-100 for 5 min, and subsequently blocked with 5% bovine serum albumin (BSA) in PBS for 30 min. After blocking, the samples were incubated overnight in a primary antibody solution diluted with 5% BSA in PBS with rabbit anti-COL-I (ab34710, Abcam, USA), rabbit anti-VCL (ab129002, Abcam, USA), and rabbit anti-FN (ab2413, Abcam, USA) at 4°C. After washing twice with PBS, the samples were incubated in the dark for 1 h with the secondary antibody solution (1:200 Alexa Fluor 488/594 goat anti-rabbit IgG [H + L], Bioss). Finally, cells were reacted with DAPI for 10 min. After each step, the cells were washed with PBS three times. Ten images were taken on a confocal laser scanning microscope (Leica TCS SP8, Germany).

Western Blot Analysis

HGFs were cultured onto each sample in 24-well plates at a density of 5×10^4 cells per well with or without CM for Western blot experiments. After 7 days of culture, HGFs were lysed in RIPA buffer and proteins were separated on 8% SDS-PAGE gels. Proteins were transferred onto polyvinylidene difluoride (PVDF) membranes which were blocked for 1 h by QuickBlock buffer (Beyotime, Jiangsu, China) at room temperature. Membranes were washed in TBST and probed overnight at 4°C with one of the following primary antibodies: collagen-I (ab34710, 1:2,000; Abcam, USA), vinculin (ab129002, 1:10,000; Abcam, USA), fibronectin (ab2413, 1:1,000; Abcam, USA), and β-actin (1:1,000, ab8227; Abcam, USA). Membranes were washed in TBST and incubated for 1 h with HRP-conjugated secondary antibodies at room temperature. Proteins were visualized using the ECL system (Beyotime, Jiangsu, China).

Statistical Analysis

All statistical calculations were performed with GraphPad software v.6 (GraphPad Software, La Jolla, CA, USA). All data are expressed as mean ± standard deviation (SD). Differences between groups were analyzed using analysis of variance (ANOVA) followed by Bonferroni test. A $p < 0.05$ was considered statistically significant.

RESULTS

Surface Characteristics

Surface morphology of nanostructured zirconia surfaces was observed by using SEM (**Figures 1A–C**). Blank-machined zirconia surfaces showed flat surfaces with regular nanogrooves, while self-glazed zirconia and coated self-glazed zirconia surfaces revealed a shaggy and irregular structure with random distribution of coarse zirconia crystalline owing to a 3D local plastic deformation process. CSGZ surfaces appeared to display an ultrafine grain and become smoother than SGZ after the coating procedure. The atomic force microscopy (AFM) data shown in **Figures 1D–F** were in good agreement with the Ra values. BMZ presented the lowest surface roughness among the samples tested (Ra: 7.6 ± 0.3 nm; Rq: 10.6 ± 1.1 nm), which was statistically significantly different ($p < 0.01$) compared with CSGZ surfaces (Ra: 22.0 ± 1.1 nm; Rq: 26.7 ± 3.4 nm), as well as with SGZ (Ra: 49.3 ± 3.5 nm; Rq: 62.7 ± 3.3 nm). Moreover, SGZ surfaces presented statistically significantly higher roughness compared with CSGZ surfaces ($p < 0.05$ for parameters Ra and Rq) (**Figures 1G,H**). The wettability of nanostructured zirconia surfaces was determined by water contact angle measurements. The mean angles of BMZ and CSZG surfaces were 85.55 and 68.67°, respectively, while SZG surfaces showed favorable hydrophilicity with a relatively lower water contact angle of ∼61.19° after coating (**Figure 1I**).

Macrophage Adhesion and Proliferation

The effect of nanostructured zirconia surface was investigated on macrophage adhesion and proliferation (**Figure 2**). It was observed that all surface topographies demonstrated high attachment, and no significant differences were observed among all groups at 2 or 4 h post-seeding. At time point 8 h, cell attachment on BMZ surfaces showed significant differences from CSGZ and SGZ surfaces (**Figures 2A,B**). Analysis of cell proliferation demonstrated that no differences were observed among all the groups at day 1 post-seeding. At 3 days, however, macrophages seeded on BMZ and CSGZ surfaces showed significantly higher cell proliferation when compared with SGZ surfaces ($p < 0.001$; **Figure 2C**). TCP demonstrated significantly the highest cell proliferation at 3 days when compared with all the other groups ($p < 0.001$; **Figure 2C**).

Macrophage Polarization Gene Expression

The expression levels of polarization genes produced by macrophage cells are believed to modulate soft tissue healing. The expression of IL-1β, iNOS, and CCR7 was markedly higher in the macrophage cultured on the SGZ surfaces compared with the TCP, BMZ, and CSGZ surfaces at 3 days post-seeding ($p < 0.05$; **Figures 3B–D**). The expression of TNF-α was higher on SGZ surfaces compared with BMZ surfaces ($p < 0.05$; **Figure 3A**). The expression levels of M2 macrophage polarization genes (IL-10, TGF-β, and CD206) are shown in **Figures 3E–G**. There was a significant difference in the TGF-β expression level on SGZ surfaces compared with BMZ and CSGZ surfaces. The expression level of CD206 on SGZ surfaces showed statistical difference compared with CSGZ surfaces ($p < 0.05$; **Figure 3G**). Conversely, the cells showed the strongest expression of IL-10 on the BMZ surfaces with statistical differences among samples at 3 days of culture ($p < 0.05$; **Figure 3E**).

Pro- and Anti-inflammatory Cytokine Production

RAW264.7 cells grown on the SGZ surfaces secreted significantly greater TNF-α into cell culture media at 3 days than the BMZ and CGGZ surfaces ($p < 0.05$; **Figure 3H**). There were no differences in the production of anti-inflammatory (IL-10) cytokines on the nanostructured zirconia surfaces (TCP, CSGZ, and SGZ) at 3 days. Interestingly, BMZ surfaces markedly increased IL-10 production level in RAW264.7 cells compared with CSGZ and SGZ with rough nanostructure surfaces ($p < 0.05$; **Figure 3I**).

Morphology Observation and Proliferation Assay of HGFs

Thereafter, a series of experiments investigating the nanostructured surfaces with or without CM from RAW264.7 culture on HGFs behavior were performed. **Figure 4** shows the morphology of HGFs cultured with or without CM at 4, 8, and 24 h. It was found that after 4 and 8 h, cells had spread on all surfaces except the SGZ surfaces with a round appearance, whereas by 24 h, cell spreading on all three zirconia surfaces became apparent. Interestingly, the addition of CM tended to promote the spreading of HGFs, especially on TCP and BMZ surfaces (**Figure 4**). There were no significant differences observed in cell proliferation among the samples at 1 day, while it was found that HGFs cultured with CM on CSGZ and SGZ surfaces demonstrated significantly lower cell proliferation in comparison with BMZ surfaces at both 3 and 5 days ($p < 0.05$; **Figure 5**). However, when CM was added to the culture media, significantly higher cell proliferation was observed at 5 days on all three zirconia surfaces compared with their respective controls ($p < 0.05$; **Figure 5**).

Apoptosis Assay of HGFs

The apoptotic behavior of HGFs after culturing on each sample with or without CM for 3 days was determined through a flow cytometric analysis. As shown in **Figure 6**, the apoptotic rates of HGFs cultured without CM on TCP, BMZ, CSGZ, and SGZ surfaces were 3.85, 5.88, 8.50, and 5.98%, respectively, while the apoptotic rates of HGFs cultured with CM were 2.01, 2.21, 3.28, and 2.56% (**Figure 6**), which indicate that CM reduced cell apoptosis of HGFs cultured on all sample surfaces.

The Adhesion Gene Expression in HGFs

After incubation of the HGFs with or without CM for 3 days, it was observed that CM significantly upregulated the expression levels of COL-I, VCL, and FN on all sample surfaces when compared with their respective controls ($p <$

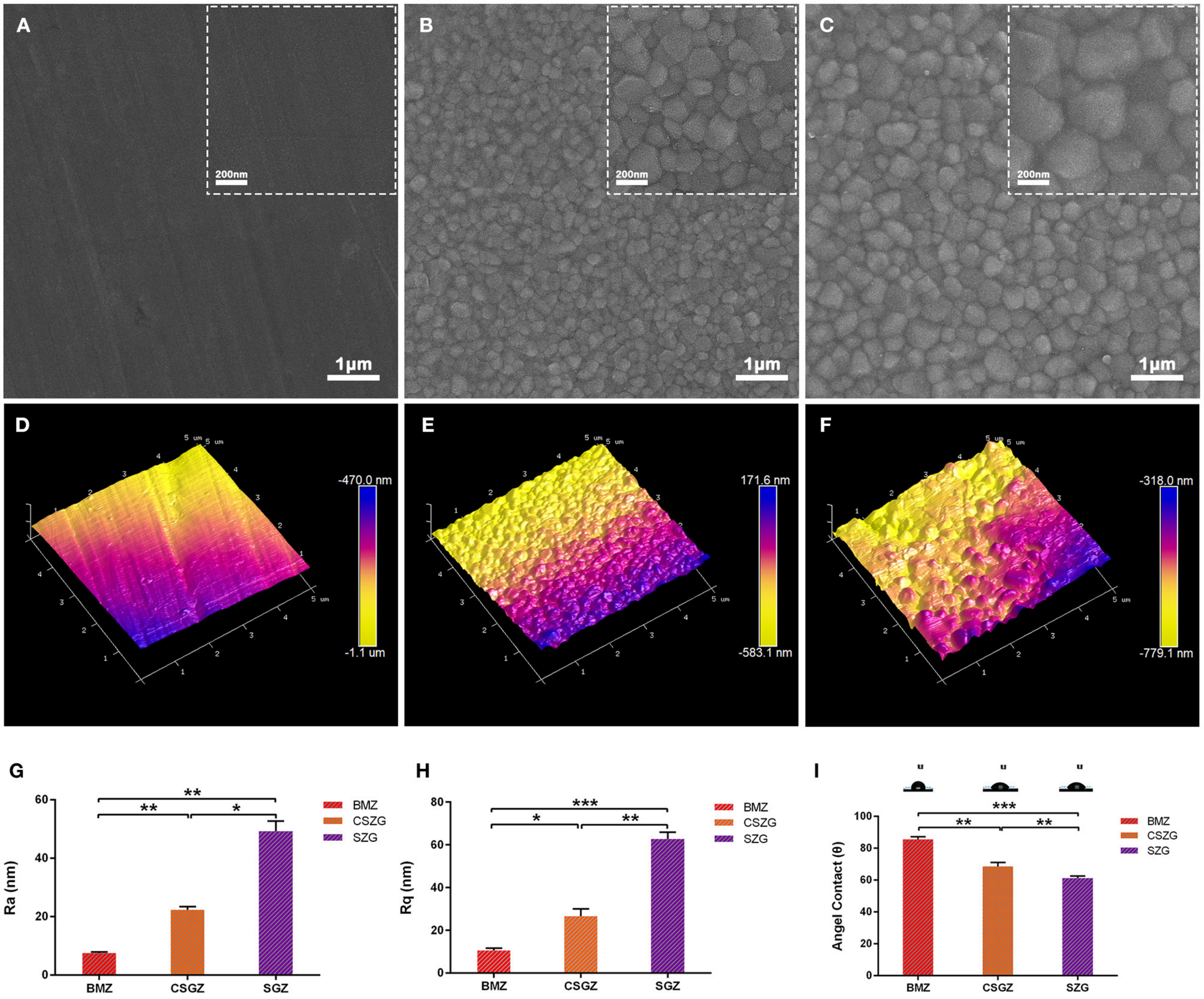

FIGURE 1 | Surface measurements and analysis of nanostructured zirconia surfaces. **(A–C)** Representative SEM images show the morphology of nanostructured surfaces (original magnifications are ×50,000 for larger- and ×20,000 for smaller-scale bar images). **(D–F)** Representative AFM images show the topography of nanostructured surfaces. **(G,H)** Roughness of nanostructured zirconia surfaces measured by AFM. **(I)** Hydrophilicity of nanostructured zirconia surfaces analyzed by water contact angle. Data are means ± SE. *$p < 0.05$, **$p < 0.01$, ***$p < 0.001$.

0.05; **Figures 7A–C**). Once again, the relative expression levels of COL-I, VCL, and FN on CSGZ and SGZ surfaces were similar and showed no significance, while BMZ surfaces had the most pronounced and detrimental effect, whereby the addition of CM significantly increased COL-I, VCL, and FN expression compared with CSGZ and SGZ surfaces ($p < 0.05$; **Figures 7A–C**).

Immunofluorescence Staining Assay for the Protein Expression of HGFs

The secretion of target proteins by HGFs was confirmed semi-quantitatively by immunofluorescence staining after culturing for 7 days. The immunofluorescence staining images of COL-I, VCL, and FN were then utilized to visualize the extracellular matrix deposition of human gingival fibroblasts onto nanostructured zirconia surfaces (**Figures 7D–F**). The results of the semi-quantitative analysis are shown in **Figures 7G–I**. No differences could be observed between CSGZ and SGZ surfaces with respect to the staining intensity of COL-I, VCL, and FN. In addition, the protein distributions of COL-I, VCL, and FN on BMZ surfaces with CM appeared to be significantly higher when compared with those on CSGZ and SGZ surfaces. Furthermore, it was found that CM significantly upregulated the expression levels of COL-I, VCL, and FN on BMZ, CSGZ, and SGZ surfaces when compared with their respective controls ($p < 0.05$; **Figures 7G–I**).

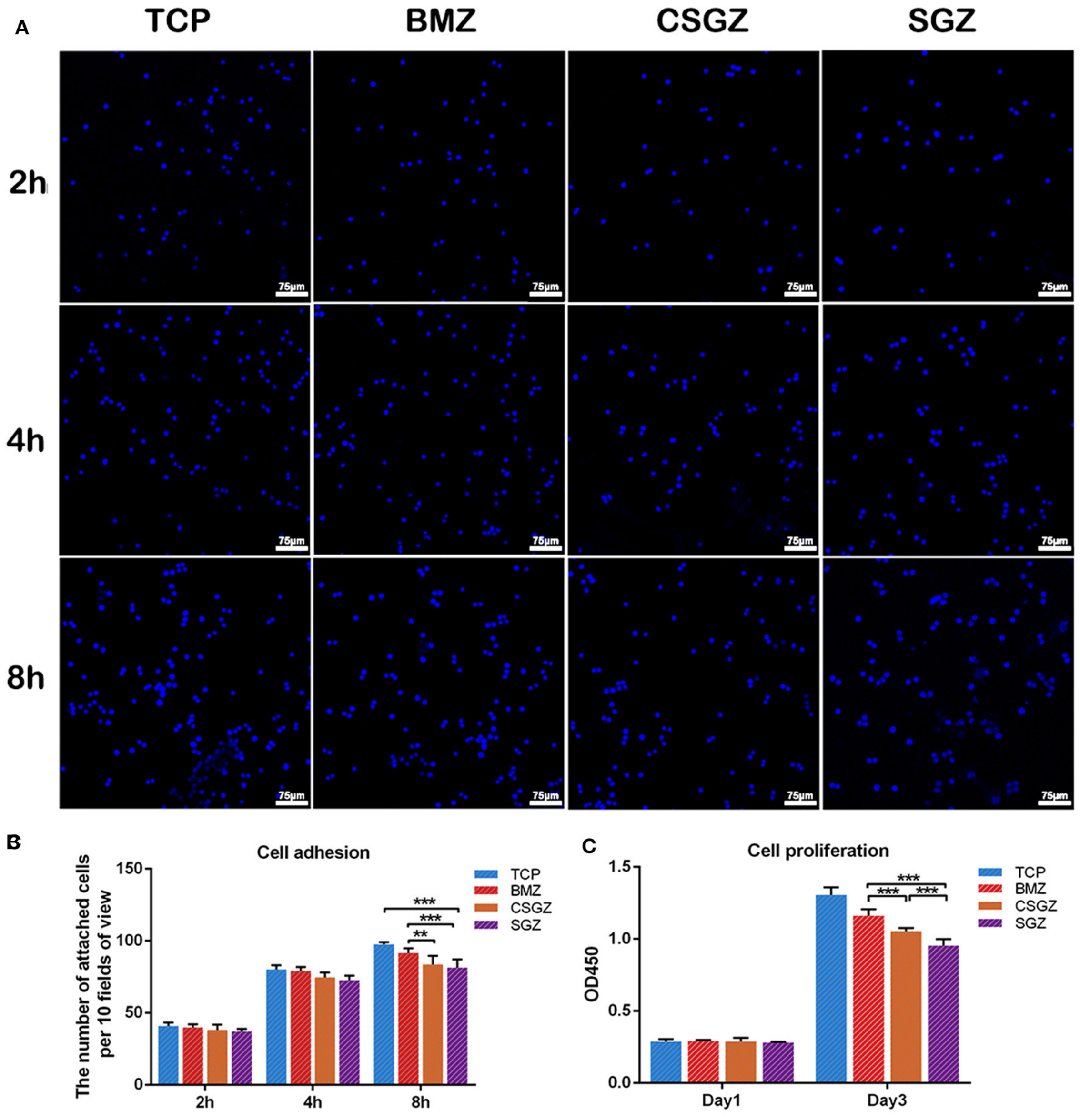

FIGURE 2 | Effect of nanostructured zirconia surfaces on RAW264.7 cell adhesion and proliferation for (1) tissue culture plastic (TCP), (2) BMZ, (3) CSGZ, and (4) SGZ samples. **(A,B)** Cell adhesion images and the number of attached cells at 2, 4, and 8 h. **(C)** Cell proliferation at 1 and 3 days. Data are means ± SE. $^{**}p < 0.01$, $^{***}p < 0.001$.

Western Blot Analysis for the Expression of COL-I, VCL, and FN in HGFs

The Western blotting results also demonstrated that CM notably upregulated the protein expression levels of COL-I, VCL, and FN on BMZ, CSGZ, and SGZ surfaces when compared with their respective controls, which was in accordance with immunofluorescence staining observations. Meanwhile, compared with CSGZ and SGZ surfaces, HGFs cultured with CM on BMZ surfaces expressed higher COL-I, VCL, and FN ($p < 0.05$; **Figures 8A–D**). There were no statistically significant differences in the VCL and FN expression between the CSGZ and SGZ surfaces (**Figures 8C,D**). However, the protein of COL-I on CSGZ surfaces with CM appeared to be significantly higher when compared with SGZ surfaces ($p < 0.05$; **Figure 8B**).

DISCUSSION

There is an increasing interest in the biomaterials community about the effect of macrophages on the integration around the peri-implant tissue in recent years (Brown et al., 2012). While early studies on dental implants have emphasized the necessity for the integration of soft tissues, it is of great importance to demonstrate that macrophages, one

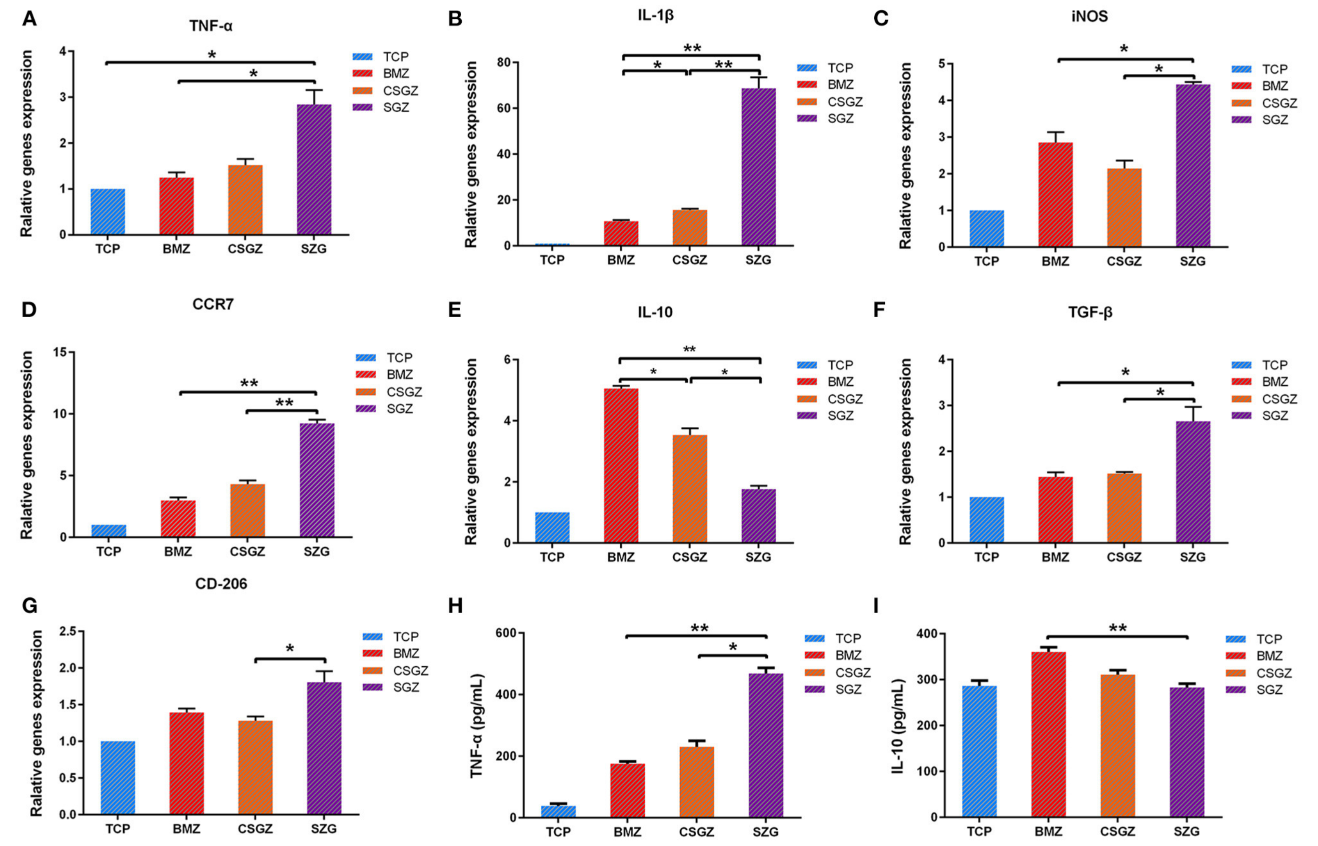

FIGURE 3 | RAW264.7 cell polarization gene expression. **(A–G)** The expression of related polarization genes: TNF-α, IL-1β, iNOS, CCR7, IL-10, TGF-β, and CD206 in RAW264.7 cultured on nanostructured zirconia surfaces at 3 days. GAPDH was used as housekeeping genes. **(H,I)** Quantified TNF-α and IL-10 secretion from macrophages cultured on different nanostructured zirconia surfaces at 3 days using ELISA assay. Data are means ± SE. $^*p < 0.05$, $^{**}p < 0.01$.

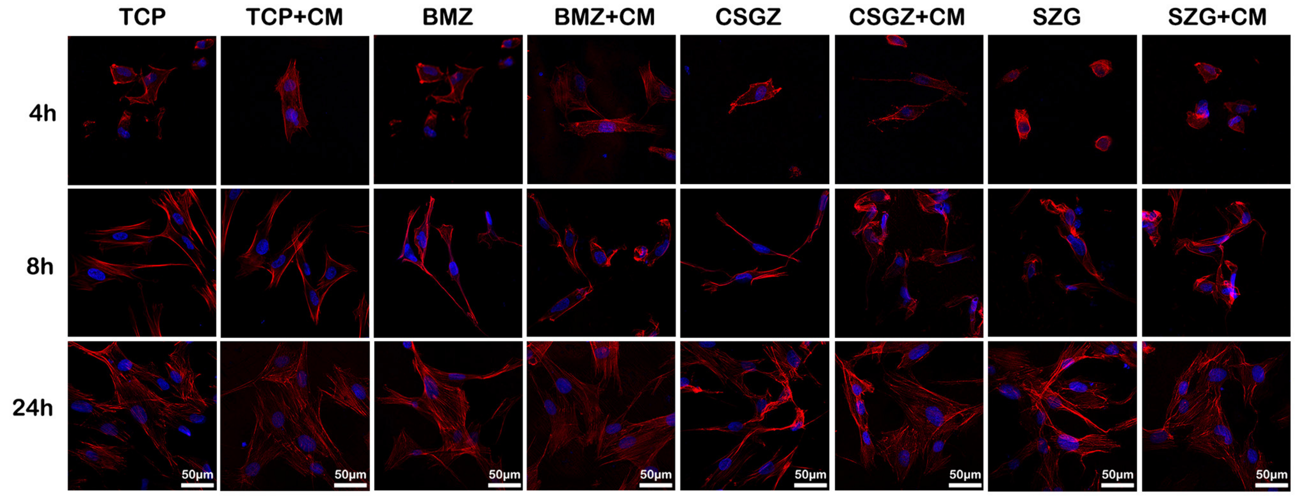

FIGURE 4 | Spreading of human gingival fibroblasts cultured with or without CM on nanostructured zirconia surfaces after 4, 8, and 24 h of seeding. Cells were stained with phalloidin (red) and DAPI (blue).

of the main immune cell types that interact with foreign implanted biomaterials, are responsible for regulating tissue remodeling including tissue integration of various biomaterials (Miron and Bosshardt, 2016). Notably, despite the many studies examining the interaction between macrophage and biomaterials in the medical field (Jia et al., 2019),

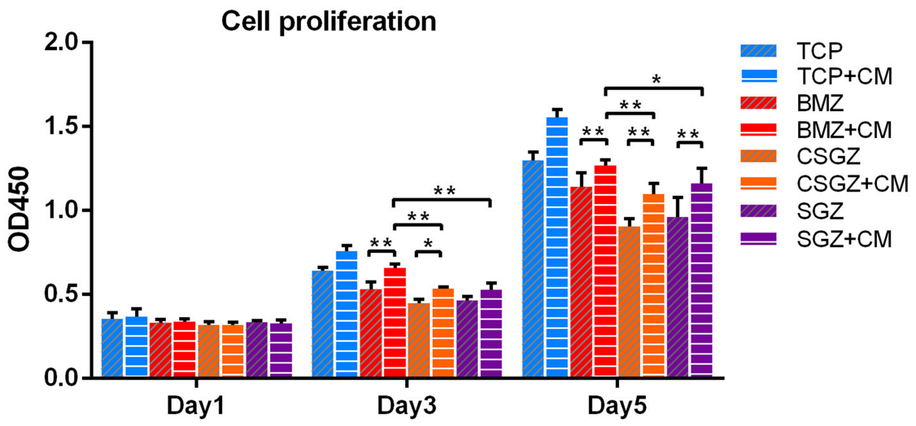

FIGURE 5 | Effects of nanostructured zirconia surfaces on human gingival fibroblast proliferation cultured with or without CM at 1, 3, and 5 days. Data are means ± SE. *$p < 0.05$, **$p < 0.01$.

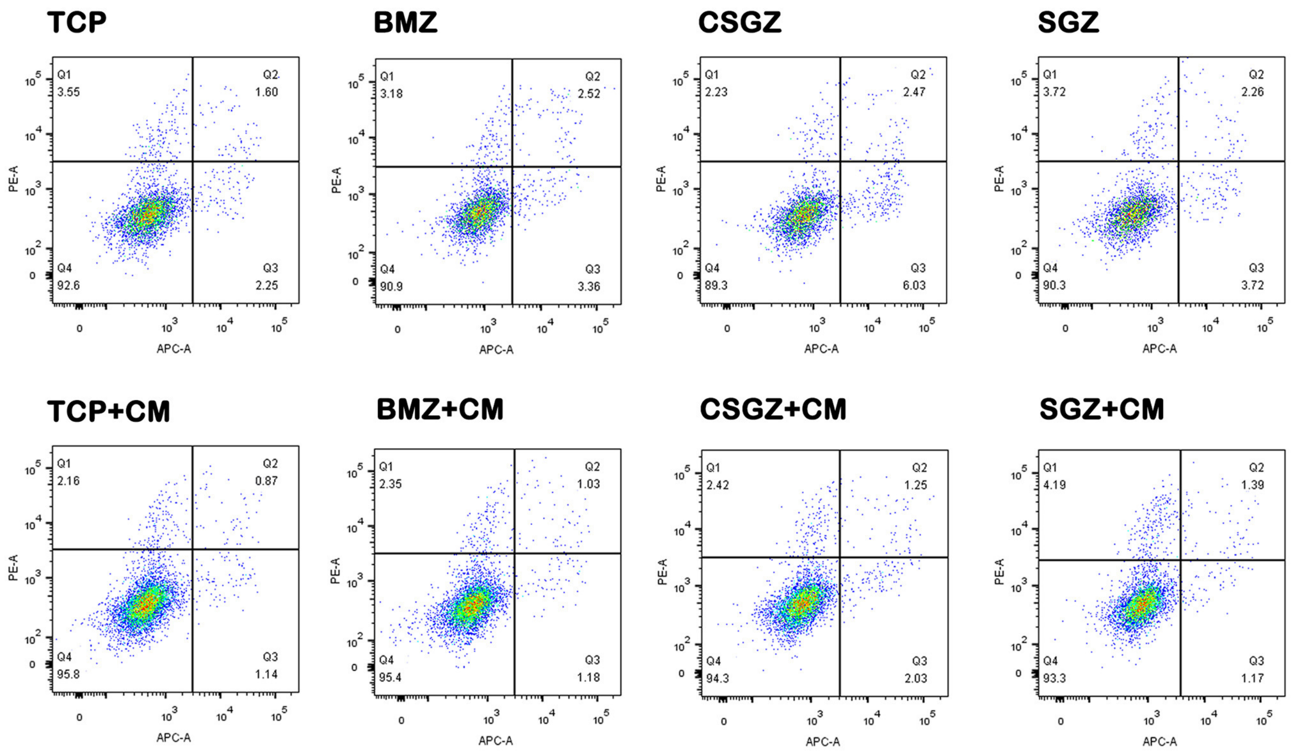

FIGURE 6 | Effects of nanostructured zirconia surfaces on the apoptosis of human gingival fibroblasts cultured with or without CM. Flow cytometric analysis of human gingival fibroblast cell apoptosis after 3 days of culture with or without conditioned media on nanostructured zirconia surfaces.

their function in implant dentistry has not been completely understood. A recent systematic review investigating relevant cellular researches regarding implant surfaces discovered that there are about 90% of all published literature paying attention to mesenchymal cell behavior on implant surfaces and approximately 10% concentrated on immune cells including monocytes, macrophages, osteoclasts, leukocytes, and multinucleated giant cells (Thalji and Cooper, 2014). This finding indicates the lack of study with immune modulation of implant surfaces despite the fact that tissue integration is routinely found preceded by macrophage accumulation (Chehroudi et al., 2009).

Since macrophages arrive at the implant surfaces earlier than HGFs and can affect the HGFs' behavior, studies have been done to modify the implant surfaces by regulating macrophages to achieve better implant integration. Previous

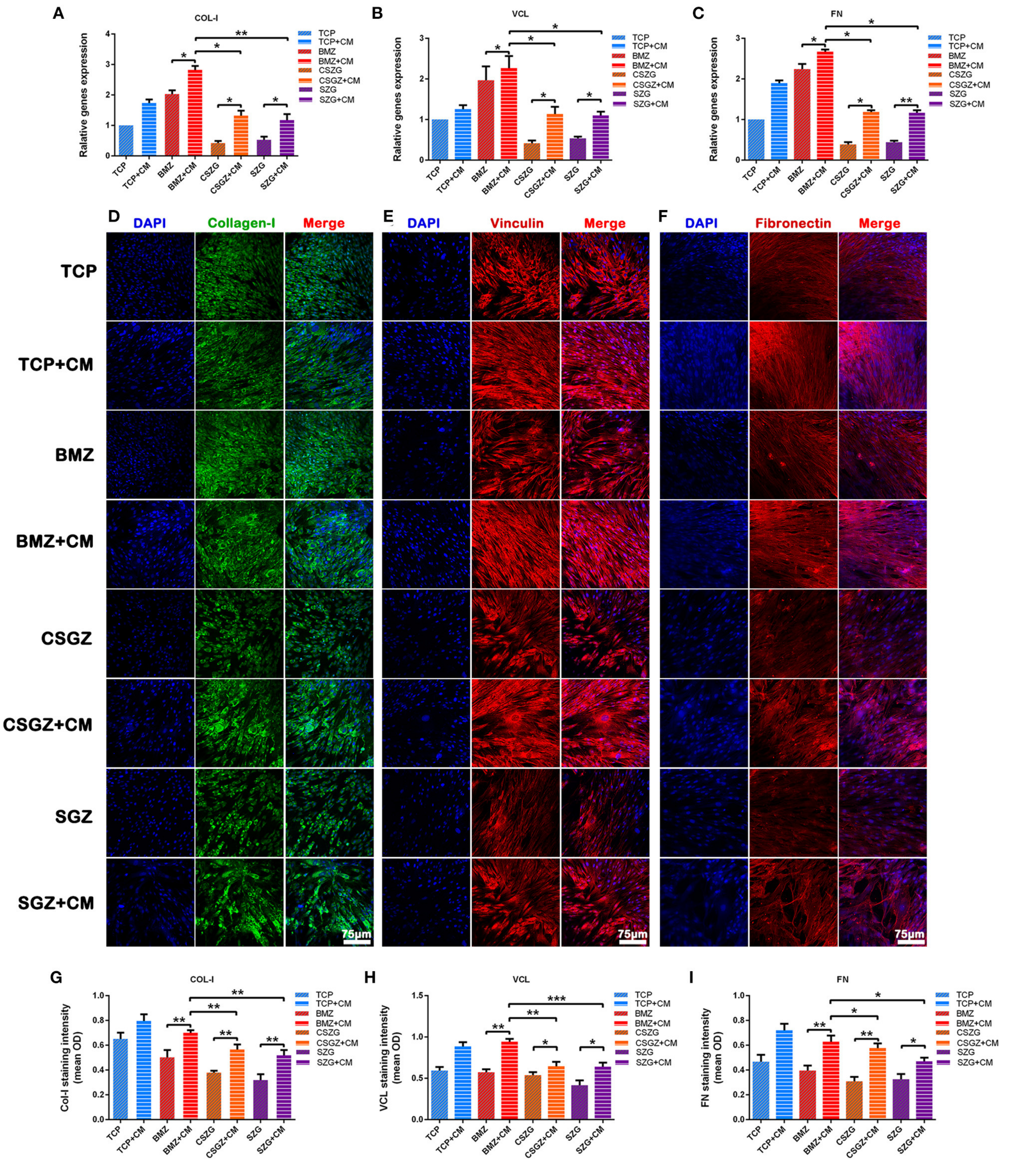

FIGURE 7 | Relative gene expression and immunofluorescence staining of collagen-I, vinculin, and fibronectin. **(A–C)** The expression of adhesion-related genes: COL-I, VCL, and FN in HGFs cultured on nanostructured zirconia surfaces at 3 days. **(D–F)** Representative immunofluorescence staining images of COL-I, VCL, and FN in HGFs cultured with or without CM on nanostructured zirconia surfaces at 7 days. **(G–I)** The protein expression of COL-I, VCL, and FN by semi-quantitative analysis. Data are means ± SE. COL-I, collagen type I; VCL, vinculin; FN, fibronectin; HGFs, human gingival fibroblasts. Data are means ± SE. $^*p < 0.05$, $^{**}p < 0.01$, $^{***}p < 0.001$.

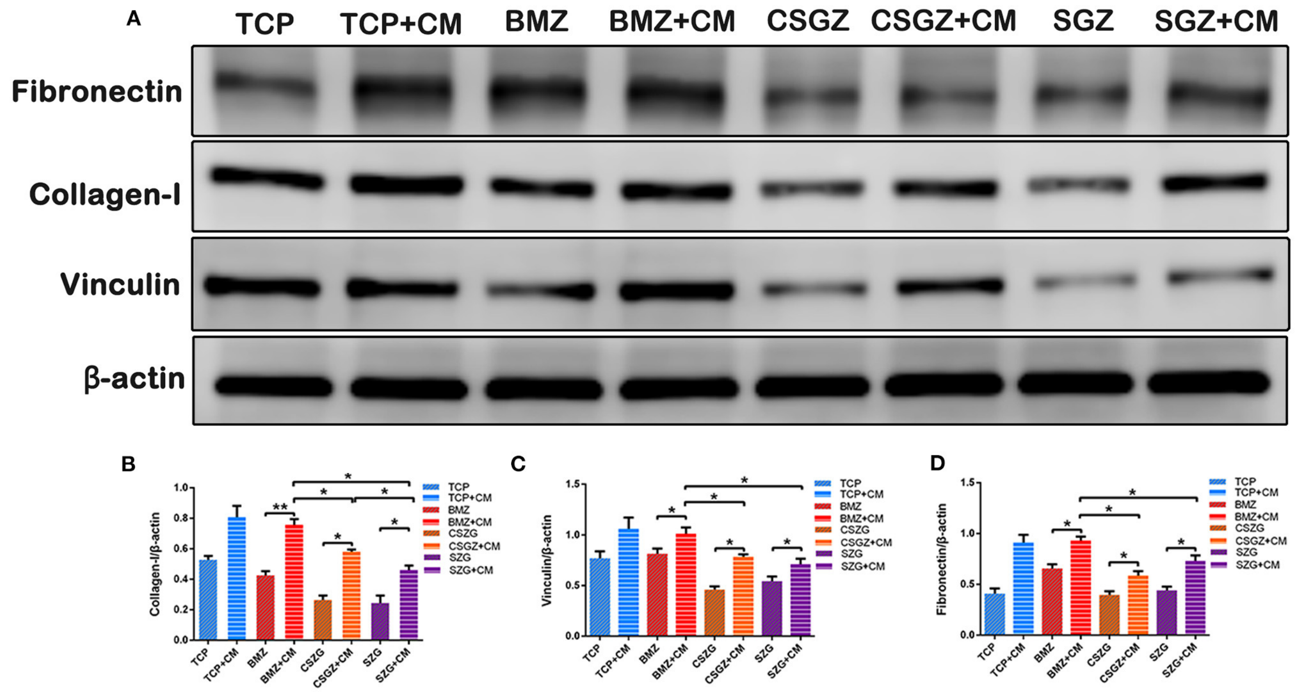

FIGURE 8 | Expression of adhesion-related proteins detected by Western blot. **(A)** Representative images of COL-I, VCL, and FN expression. **(B–D)** Quantitative analysis of COL-I, VCL, and FN expression in HGFs with or without CM on nanostructured zirconia surfaces at 7 days. β-Actin was used to normalize the data. COL-I, collagen type I; VCL, vinculin; FN, fibronectin; HGFs, human gingival fibroblasts. Data are means ± SE. *$p < 0.05$, **$p < 0.01$.

studies have revealed that alteration of the implants' surface roughness and topography can modulate macrophage functions including cell adhesion and cytokine secretion (Yim and Leong, 2005; Ainslie et al., 2009). In this study, macrophages were prone to favor adhesion on BMZ and CSGZ surfaces. It was also noteworthy that SGZ surfaces displayed less macrophage cell attachment, which is consistent with the result at later time points following macrophage proliferation (**Figures 2A–C**). These results are in accordance with the recent investigations which have found that a smooth surface allows macrophages to attach and spread more than on a rough surface (Hotchkiss et al., 2016). In addition, a rough surface would induce more M1 macrophages compared with a smooth surface, and the inflammatory cytokines secreted later might hinder the tissue healing process (Alfarsi et al., 2014; Hotchkiss et al., 2016). Generally, the polarization of macrophages could be induced by the addition of specific cytokines and the stimuli of the local microenvironment (Yao et al., 2019). However, there were no foreign cytokines and stimuli introduced in this study, indicating that the nanostructured surface topography could directly modulate macrophage polarization. Our results prove that macrophages on SGZ surfaces tended to induce higher M1 polarization and a lower M2 polarization was observed with a low expression of IL-10 (**Figures 3A–E**). By contrast, on the BMZ and CSGZ surfaces, M2 polarization was significantly higher and M1 polarization was lower than that on the SGZ surfaces on day 3. Consistently, ELISA test for TNF-α and IL-10 expressions showed that nanostructured surfaces can modulate macrophage polarization *in vitro*. At 3 days after culture, the BMZ surfaces induced both IL-10 production and TNF-α synthesis. In contrast, more TNF-α expression and less IL-10 expression cells were detected in the supernatant from the SGZ surfaces compared with those on BMZ surfaces (**Figures 3H,I**), which may reflect the progression of more serious inflammation on rough surfaces. In fact, the large ratio of M1 macrophages to M2 macrophages is highly related to the failure of artificial joints (Rao et al., 2012).

Interestingly, although surface roughness tends to promote a pro-inflammatory response, its effect on HGF cell behavior is controversial. Whereas fibroblasts initially are inclined to adhere better on a smooth surface, they showed rapid cell proliferation on a rough surface (Rompen et al., 2006). However, reports have shown that an implant surface with grooves can promote cell stretching and guide the cells to be aligned in parallel within the surface grooves (Mustafa et al., 2005; Pae et al., 2009). In fact, cells on a smoother surface have to stretch themselves and form a strong cytoskeletal structure so as to stabilize themselves mechanically on the topography of the surface, when compared with a rough surface (Kunzler et al., 2007). Hence, a smoother surface may facilitate more cell proliferation to the topographical "limit" of the surface. It is acknowledged that immunologic response is another factor, which could be regulated by both macrophage and surface topography (De Marco et al., 2017).

Surface topography generates an impact on macrophage polarization as well as on fibroblast behavior. Herein, we further investigated that macrophage phenotypes modulated by nanostructured zirconia surfaces could affect the interaction between the zirconia surfaces and the HGFs in a co-culture system. Our results illustrated that CM from RAW264.7 culture on BMZ, CSGZ, and SGZ surfaces more strongly enhanced the proliferation of HGFs as compared with their respective controls at 5 days (**Figure 5**). Additionally, CM from RAW264.7 culture on BMZ, CSGZ, and SGZ surfaces upregulated adhesion gene expression and secretion of COL-I, VCL, and FN compared with their respective controls (**Figures 7A–I**). Meanwhile, HGFs cultured under collected CM on BMZ surfaces tend to display a higher expression and secretion of COL-I, VCL, and FN than those on CSGZ and SGZ surfaces (**Figures 7A–I**). These results could explain the favorable modulation effects of macrophages cultured on BMZ surfaces on tissue integration. In response to different implantable biomaterials, macrophages with different phenotypes vary the production of cytokines, chemokines, growth factors, and other molecules that contribute to the local milieu and further modulate tissue activities to regulate the function of target cells (Jia et al., 2019). Once activated, macrophages secrete various bioactive components, including growth factors, cytokines, and exosomes, according to their specific phenotypes (Das et al., 2015). After taking the conditioned medium into consideration, the apoptotic rate of fibroblasts on TCP, BMZ, CSGZ, and SGZ surfaces reduced by 1.84, 3.67, 5.22, and 3.42%, respectively, compared with their respective controls (**Figure 6**), which indicated that CM collected from RAW264.7 culture in all samples slightly inhibited the apoptotic effect on fibroblasts. The conditioned medium from M2 macrophages has been shown to affect fibroblast behavior which secrete extracellular matrix (ECM), specifically collagen that can enhance efficacious implant integration (Fujioka-Kobayashi et al., 2020). Our Western blotting results showed that fibroblasts cultured with CM on BMZ surfaces produce more ECM with a higher expression of COL-I, VCL, and FN as compared with those on CSGZ and SGZ surfaces (**Figures 8A–D**). In addition, the CM upregulated the gene expression levels of COL-I, VCL, and FN on BMZ, CSGZ, and SGZ surfaces (**Figures 7A–C**), when compared with their respective controls, which was in accordance with the immunofluorescence staining results (**Figures 7D–I**). Therefore, macrophages may play a prominent role in tissue integration. The strategies adopted to better regulate macrophage immune response through altering the surface topography of biomaterials are essential and necessary.

Surface wettability is another vital factor that influences cell adhesion on the biomaterials' surface (Rupp et al., 2004). Indeed, a more hydrophilic surface is usually accompanied by a favorable wettability on the basis of the Wenzel law, but it has been demonstrated that wettability did not increase in accordance with roughness in some situations (MacDonald et al., 2002). In our case as shown in **Figure 1I**, the initial contact angle value of SGZ was 61.19, and after decreasing the grain size, a more hydrophobic surface was observed with an angle of 68.67° in CSGZ. The result of this study is in accordance with that of previous studies, which found that wettability decreased with the decrease in grain particle size (Karunakaran et al., 2015; Youshia et al., 2017). According to the literature, the wettability of the material surface will control the proteins' ability to adsorb onto the surface and there will be a formation of blood clot and fibrin network (Kopf et al., 2015). A related research shows that an increase in anti-inflammatory cell response has been shown to occur with increased wettability of the surface (Zhou et al., 2015). In particular, it was found that a switch of macrophage phenotype from M1 toward M2 at the implant–tissue interface by means of surface modifications is instrumental for wound healing and tissue integration (Ma et al., 2014). Therefore, changing surface wettability may act as an applicable approach to control macrophage phenotype and further improve tissue healing.

During implantation, an early-stage immunological response begins with protein adsorption on the extraneous implant surface, which can subsequently modulate macrophage recognition and activation and, eventually, evoke an adverse foreign body reaction (FBR) (Mariani et al., 2019). Macrophages fuse to form foreign body giant cells (FBGC), which is a crucial feature of FBR in case that they fail to internalize foreign biomaterial through phagocytosis (Trindade et al., 2016). Since a dense fibrous capsule forming during the process of FBR could obstruct the oxygen and nutrient exchange between the host and the biomaterial, causing the biomaterial to be non-functional, effective strategies to modify or optimize FBR are of fundamental importance for the advancement of implant materials (Zhou et al., 2015). The results obtained in the present study further emphasize that macrophages have a crucial regulator effect on cell function and behavior. To this end, future researches should be performed to elucidate the pivotal interaction between the host immune response and the biomaterial.

CONCLUSIONS

In this study, we discovered that BMZ surfaces were superior to macrophage proliferation and adhesion. All nanostructured zirconia surfaces induced macrophage polarization toward both inflammatory M1 and anti-inflammatory M2 phenotype with more M2 macrophage phenotype on BMZ surfaces. Meanwhile, our studies confirmed that CM from RAW264.7 culture on three nanostructured zirconia surfaces upregulated HGFs' functions including cell proliferation and ECM formation, suggesting enhanced soft tissue integration abilities of immunoregulation. Collectively, the synergistic regulation of surface topography and CM could enhance HGFs' behavior with higher expression of COL-I, VCL, and FN on BMZ surfaces. After coated with a nano zirconia film, CSGZ surfaces showed some difference in cell proliferation, adhesion, and protein production compared with SGZ surfaces. Our present study suggests that a favorable immune microenvironment can be developed by macrophage modulation through the functional surface design of biomaterials and, subsequently, regulate the behavior and function of progenitor cells.

DATA AVAILABILITY STATEMENT

The original contributions presented in the study are included in the article/supplementary materials, further inquiries can be directed to the corresponding author/s.

AUTHOR CONTRIBUTIONS

ZW contributed to the conception and design of the study. JW performed the experiments. PY and HL carried out the data analysis. All authors participated in the drafting of the manuscript and critical revision of the draft. All authors have read and approved the final version of the manuscript.

FUNDING

We gratefully acknowledge the financial support from Guangzhou Science and Technology Program key projects (Grant Number: 201804010407) and High-Level University Clinical Research Cultivation Project of Guangzhou Medical University (Grant Number: 2017160019).

ACKNOWLEDGMENTS

The authors acknowledge Prof. Zhijian Shen (Stockholm University, Sweden) for the experimental support and Hangzhou Eran Technology Co. Ltd (Hangzhou, China) for sample processing.

REFERENCES

Ainslie, K. M., Tao, S. L., Popat, K. C., Daniels, H., Hardev, V., Grimes, C. A., et al. (2009). *In vitro* inflammatory response of nanostructured titania, silicon oxide, and polycaprolactone. *J. Biomed. Mater. Res. A* 91, 647–655. doi: 10.1002/jbm.a.32262

Alfarsi, M. A., Hamlet, S. M., and Ivanovski, S. (2014). Titanium surface hydrophilicity modulates the human macrophage inflammatory cytokine response. *J. Biomed. Mater. Res. A* 102, 60–67. doi: 10.1002/jbm.a.34666

Anderson, J. M., Rodriguez, A., and Chang, D. T. (2008). Foreign body reaction to biomaterials. *Semin. Immunol.* 20, 86–100. doi: 10.1016/j.smim.2007.11.004

Atsuta, I., Ayukawa, Y., Kondo, R., Oshiro, W., Matsuura, Y., Furuhashi, A., et al. (2016). Soft tissue sealing around dental implants based on histological interpretation. *J. Prosthodont. Res.* 60, 3–11. doi: 10.1016/j.jpor.2015.07.001

Baltriukiene, D., Sabaliauskas, V., Balčiunas, E., Melninkaitis, A., Liutkevičius, E., Bukelskiene, V., et al. (2014). The effect of laser-treated titanium surface on human gingival fibroblast behavior. *J. Biomed. Mater. Res. A* 102, 713–720. doi: 10.1002/jbm.a.34739

Bosshardt, D., Chappuis, V., and Buser, D. (2017). Osseointegration of titanium, titanium alloy and zirconia dental implants: current knowledge and open questions. *Periodontol. 2000* 73, 22–40. doi: 10.1111/prd.12179

Brown, B. N., Ratner, B. D., Goodman, S. B., Amar, S., and Badylak, S. F. (2012). Macrophage polarization: an opportunity for improved outcomes in biomaterials and regenerative medicine. *Biomaterials* 33, 3792–3802. doi: 10.1016/j.biomaterials.2012.02.034

Chehroudi, B., Ghrebi, S., Murakami, H., Waterfield, J. D., Owen, G., and Brunette, D. M. (2009). Bone formation on rough, but not polished, subcutaneously implanted Ti surfaces is preceded by macrophage accumulation. *J. Biomed. Mater. Res. A* 93, 724–737. doi: 10.1002/jbm.a.32587

Das, A., Sinha, M., Datta, S., Abas, M., Chaffee, S., Sen, C. K., et al. (2015). Monocyte and macrophage plasticity in tissue repair and regeneration. *Am. J. Pathol.* 185, 2596–2606. doi: 10.1016/j.ajpath.2015.06.001

De Marco, P., Zara, S., De Colli, M., Radunovic, M., Lazović, V., Ettorre, V., et al. (2017). Graphene oxide improves the biocompatibility of collagen membranes in an in vitro model of human primary gingival fibroblasts. *Biomed. Mater.* 12:055005. doi: 10.1088/1748-605X/aa7907

Fujioka-Kobayashi, M., Ülgür, I., Katagiri, H., Vuignier, S., and Schaller, B. (2020). *In vitro* observation of macrophage polarization and gingival fibroblast behavior on three-dimensional xenogeneic collagen matrixes. *J. Biomed. Mater. Res. A* 108, 1408–1418. doi: 10.1002/jbm.a.36911

Galli, S. J., Borregaard, N., and Wynn, T. A. (2011). Phenotypic and functional plasticity of cells of innate immunity: macrophages, mast cells and neutrophils. *Nat. Immunol.* 12, 1035–1044. doi: 10.1038/ni.2109

Glaros, T., Larsen, M., and Li, L. (2009). Macrophages and fibroblasts during inflammation, tissue damage and organ injury. *Front. Biosci.* 14, 3988–3993. doi: 10.2741/3506

Han, H. J., Kim, S., and Han, D. H. (2014). Multifactorial evaluation of implant failure: a 19-year retrospective study. *Int. J. Oral Maxillofac. Implants* 29, 303–310. doi: 10.11607/jomi.2869

Hotchkiss, K. M., Reddy, G. B., Hyzy, S. L., Schwartz, Z., Boyan, B. D., and Olivares-Navarrete, R. (2016). Titanium surface characteristics, including topography and wettability, alter macrophage activation. *Acta Biomater.* 31, 425–434. doi: 10.1016/j.actbio.2015.12.003

Jia, Y., Yang, W., Zhang, K., Qiu, S., Xu, J., Wang, C., et al. (2019). Nanofiber arrangement regulates peripheral nerve regeneration through differential modulation of macrophage phenotypes. *Acta Biomater.* 83, 291–301. doi: 10.1016/j.actbio.2018.10.040

Karunakaran, G., Suriyaprabha, R., Rajendran, V., and Kannan, N. (2015). Effect of contact angle, zeta potential and particles size on the *in vitro* studies of Al2O3 and SiO2 nanoparticles. *IET Nanobiotech.* 9, 27–34. doi: 10.1049/iet-nbt.2013.0067

Kearns, V. R., Williams, R. L., Mirvakily, F., Doherty, P. J., and Martin, N. (2013). Guided gingival fibroblast attachment to titanium surfaces: an *in vitro* study. *J. Clin. Periodontol.* 40, 99–108. doi: 10.1111/jcpe.12025

Kheur, S., Singh, N., Bodas, D., Rauch, J., Jambhekar, S., Kheur, M., et al. (2017). Nanoscale silver depositions inhibit microbial colonization and improve biocompatibility of titanium abutments. *Colloids Surf. B Biointerfaces* 159, 151–158. doi: 10.1016/j.colsurfb.2017.07.079

Kopf, B., Ruch, S., Berner, S., Spencer, N., and Maniura-Weber, K. (2015). The role of nanostructures and hydrophilicity in osseointegration: *in-vitro* protein-adsorption and blood-interaction studies. *J. Biomed. Mater. Res. A* 103, 2661–2672. doi: 10.1002/jbm.a.35401

Kunzler, T. P., Drobek, T., Schuler, M., and Spencer, N. D. (2007). Systematic study of osteoblast and fibroblast response to roughness by means of surface-morphology gradients. *Biomaterials* 28, 2175–2182. doi: 10.1016/j.biomaterials.2007.01.019

Kzhyshkowska, J., Gudima, A., Riabov, V., Dollinger, C., Lavalle, P., and Vrana, N. E. (2015). Macrophage responses to implants: prospects for personalized medicine. *J. Leukoc. Biol.* 98, 953–962. doi: 10.1189/jlb.5VMR0415-166R

Liu, Y., Wang, Y., Wang, D., Ma, J., Liu, L., and Shen, Z. (2016). Self-glazed zirconia reducing the wear to tooth enamel. *J. Eur. Ceram. Soc.* 36, 2889–2894. doi: 10.1016/j.jeurceramsoc.2015.11.029

Llopis-Grimalt, M., Amengual-Tugores, A., Monjo, M., and Ramis, J. (2019). Oriented cell alignment induced by a nanostructured titanium surface enhances expression of cell differentiation markers. *Nanomaterials* 9:1661. doi: 10.3390/nano9121661

Ma, Q. L., Zhao, L. Z., Liu, R. R., Jin, B. Q., Song, W., Wang, Y., et al. (2014). Improved implant osseointegration of a nanostructured titanium surface via mediation of macrophage polarization. *Biomaterials* 35, 9853–9867. doi: 10.1016/j.biomaterials.2014.08.025

MacDonald, D., Deo, N., Markovic, B., Stranick, M., and Somasundaran, P. (2002). Adsorption and dissolution behavior of human plasma fibronectin on thermally and chemically modified titanium dioxide particles. *Biomaterials* 23, 1269–1279. doi: 10.1016/s0142-9612(01)00317-9

Mariani, E., Lisignoli, G., Borzì, R., and Pulsatelli, L. (2019). Biomaterials: foreign bodies or tuners for the immune response? *Int. J. Mol. Sci.* 20:636. doi: 10.3390/ijms20030636

Miron, R. J., and Bosshardt, D. D. (2016). OsteoMacs: key players around bone biomaterials. *Biomaterials* 82, 1–19. doi: 10.1016/j.biomaterials.2015.12.017

Mosser, D. M., and Edwards, J. P. (2008). Exploring the full spectrum of macrophage activation. *Nat. Rev. Immunol.* 8, 958–969. doi: 10.1038/nri2448

Murray, P. J., Allen, J. E., Biswas, S. K., Fisher, E. A., Gilroy, D. W., Goerdt, S., et al. (2014). Macrophage activation and polarization: nomenclature and experimental guidelines. *Immunity* 41, 14–20. doi: 10.1016/j.immuni.2014.06.008

Mustafa, K., Oden, A., Wennerberg, A., Hultenby, K., and Arvidson, K. (2005). The influence of surface topography of ceramic abutments on the attachment and proliferation of human oral fibroblasts. *Biomaterials* 26, 373–381. doi: 10.1016/j.biomaterials.2004.02.037

Pae, A., Lee, H., Kim, H. S., Kwon, Y. D., and Woo, Y. H. (2009). Attachment and growth behaviour of human gingival fibroblasts on titanium and zirconia ceramic surfaces. *Biomed. Mater.* 4:025005. doi: 10.1088/1748-6041/4/2/025005

Rao, A. J., Gibon, E., Ma, T., Yao, Z., Smith, R. L., and Goodman, S. B. (2012). Revision joint replacement, wear particles, and macrophage polarization. *Acta Biomater.* 8, 2815–2823. doi: 10.1016/j.actbio.2012.03.042

Roehling, S., Astasov-Frauenhoffer, M., Hauser-Gerspach, I., Braissant, O., Woelfler, H., Waltimo, T., et al. (2017). *In vitro* biofilm formation on titanium and zirconia implant surfaces. *J. Periodontol.* 88, 298–307. doi: 10.1902/jop.2016.160245

Rohr, N., Zeller, B., Matthisson, L., and Fischer, J. (2020). Surface structuring of zirconia to increase fibroblast viability. *Dent. Mater.* 36, 779–786. doi: 10.1016/j.dental.2020.03.024

Rompen, E., Domken, O., Degidi, M., Pontes, A., and Piattelli, A. (2006). The effect of material characteristics, of surface topography and of implant components and connections on soft tissue integration: a literature review. *Clin. Oral Implants Res.* 17(Suppl. 2), 55–67. doi: 10.1111/j.1600-0501.2006.01367.x

Rupp, F., Scheideler, L., Rehbein, D., Axmann, D., and Geis-Gerstorfer, J. (2004). Roughness induced dynamic changes of wettability of acid etched titanium implant modifications. *Biomaterials* 25, 1429–1438. doi: 10.1016/j.biomaterials.2003.08.015

Tabatabaian, F. (2019). Color aspect of monolithic zirconia restorations: a review of the literature. *J. Prosthodont.* 28, 276–287. doi: 10.1111/jopr.12906

Tan, K. S., Qian, L., Rosado, R., Flood, P. M., and Cooper, L. F. (2006). The role of titanium surface topography on J774A.1 macrophage inflammatory cytokines and nitric oxide production. *Biomaterials* 27, 5170–5177. doi: 10.1016/j.biomaterials.2006.05.002

Thalji, G., and Cooper, L. (2014). Molecular assessment of osseointegration *in vitro*: a review of current literature. *Int. J. Oral Maxillofac. Implants* 29, e171–e199. doi: 10.11607/jomi.te55

Trindade, R., Albrektsson, T., Tengvall, P., and Wennerberg, A. (2016). Foreign body reaction to biomaterials: on mechanisms for buildup and breakdown of osseointegration. *Clin. Implant Dent. Relat. Res* 18, 192–203. doi: 10.1111/cid.12274

Turon-Vinas, M., and Anglada, M. (2018). Strength and fracture toughness of zirconia dental ceramics. *Dent. Mater.* 34, 365–375. doi: 10.1016/j.dental.2017.12.007

Wang, J., Meng, F., Song, W., Jin, J., Ma, Q., Fei, D., et al. (2018). Nanostructured titanium regulates osseointegration via influencing macrophage polarization in the osteogenic environment. *Int. J. Nanomed.* 13, 4029–4043. doi: 10.2147/ijn.s163956

Wang, Y., Zhang, Y., and Miron, R. J. (2016). Health, maintenance, and recovery of soft tissues around implants. *Clin. Implant Dent. Relat. Res.* 18, 618–634. doi: 10.1111/cid.12343

Witherel, C., Abebayehu, D., Barker, T., and Spiller, K. (2019). Macrophage and fibroblast interactions in biomaterial-mediated fibrosis. *Adv. Healthc. Mater.* 8:e1801451. doi: 10.1002/adhm.201801451

Wynn, T. A., Chawla, A., and Pollard, J. W. (2013). Macrophage biology in development, homeostasis and disease. *Nature* 496, 445–455. doi: 10.1038/nature12034

Wynn, T. A., and Vannella, K. M. (2016). Macrophages in tissue repair, regeneration, and fibrosis. *Immunity* 44, 450–462. doi: 10.1016/j.immuni.2016.02.015

Xu, R., Hu, X., Yu, X., Wan, S., Wu, F., Ouyang, J., et al. (2018). Micro-/nano-topography of selective laser melting titanium enhances adhesion and proliferation and regulates adhesion-related gene expressions of human gingival fibroblasts and human gingival epithelial cells. *Int. J. Nanomed.* 13, 5045–5057. doi: 10.2147/ijn.s166661

Yao, Y., Xu, X., and Jin, L. (2019). Macrophage polarization in physiological and pathological pregnancy. *Front. Immunol.* 10:792. doi: 10.3389/fimmu.2019.00792

Yim, E. K., and Leong, K. W. (2005). Significance of synthetic nanostructures in dictating cellular response. *Nanomedicine* 1, 10–21. doi: 10.1016/j.nano.2004.11.008

Youshia, J., Ali, M., and Lamprecht, A. (2017). Artificial neural network based particle size prediction of polymeric nanoparticles. *Eur. J. Pharm. Biopharm.* 119, 333–342. doi: 10.1016/j.ejpb.2017.06.030

Zhang, Y., and Lawn, B. (2018). Novel zirconia materials in dentistry. *J. Dent. Res.* 97, 140–147. doi: 10.1177/0022034517737483

Zhou, G., Loppnow, H., and Groth, T. (2015). A macrophage/fibroblast co-culture system using a cell migration chamber to study inflammatory effects of biomaterials. *Acta Biomater.* 26, 54–63. doi: 10.1016/j.actbio.2015.08.020

Conflict of Interest: The authors declare that the research was conducted in the absence of any commercial or financial relationships that could be construed as a potential conflict of interest.

frontiers
in Bioengineering and Biotechnology

ORIGINAL RESEARCH
published: 29 January 2021
doi: 10.3389/fbioe.2020.630094

Combination of Polydopamine Coating and Plasma Pretreatment to Improve Bond Ability Between PEEK and Primary Teeth

Rui Teng[1†], Yuchen Meng[1†], Xiaodan Zhao[1], Jie Liu[1], Rui Ding[1], Yilong Cheng[2], Yunhe Zhang[3], Yanfeng Zhang[2], Dandan Pei[1] and Ang Li[1,4]*

[1] Key Laboratory of Shaanxi Province for Craniofacial Precision Medicine Research, College of Stomatology, Xi'an Jiaotong University, Xi'an, China, [2] School of Chemistry, Xi'an Jiaotong University, Xi'an, China, [3] Engineering Research Center of Super Engineering Plastics, Ministry of Education, College of Chemistry, Jilin University, Changchun, China, [4] Department of Periodontology, College of Stomatology, Xi'an Jiaotong University, Xi'an, China

OPEN ACCESS

Edited by:
Jianxun Ding,
Chinese Academy of Sciences, China

Reviewed by:
Xueqing Huang,
Sun Yat-sen University, China
Jian Yu,
Wuhan University, China
Fucong Tian,
Augusta University, United States

****Correspondence:***
Ang Li
drliang@mail.xjtu.edu.cn

† These authors have contributed equally to this work

Specialty section:
This article was submitted to Biomaterials, a section of the journal Frontiers in Bioengineering and Biotechnology

Received: *16 November 2020*
Accepted: *21 December 2020*
Published: *29 January 2021*

Citation:
Teng R, Meng Y, Zhao X, Liu J, Ding R, Cheng Y, Zhang Y, Zhang Y, Pei D and Li A (2021) Combination of Polydopamine Coating and Plasma Pretreatment to Improve Bond Ability Between PEEK and Primary Teeth. Front. Bioeng. Biotechnol. 8:630094. doi: 10.3389/fbioe.2020.630094

Preformed crowns are preferred to reduce the failure risk of restoration of primary teeth, but some drawback of conventional material is still a main barrier for their clinical use. Polyether etherketone (PEEK), a tooth colored, high-performance thermoplastic polymer, has been recognized as a promising alternative to manufacture the restoration of primary teeth. However, the hydrophobic surface and low surface energy of PEEK make it hard to establish a strong and durable adhesion. In this study, we have evaluated a modification method of polydopamine (PDA) coating with plasma pretreatment for the PEEK films by physical and chemical characterization, bonding properties, and biocompatibility. The surface properties of PEEK were well-characterized by scanning electron microscope (SEM) and X-ray photoelectron spectroscopy (XPS). The adhesive strength of the PEEK films was greatly improved without significant reduction of the proliferation rate of human gingival fibroblast cells in MTT and Live/Dead assays. Therefore, PDA coating with plasma pretreatment may give a new solution for effective clinical application of PEEK in primary performed crowns.

Keywords: polyetheretherketone, polydopamine, plasma, bonding properties, biocompatibility

INTRODUCTION

Dental caries in the primary teeth is a highly prevalent public health problem (Ludwig et al., 2014; Innes et al., 2015; Smaïl-Faugeron et al., 2018). The untreated primary dental caries develop rapidly and frequently, leading to discomfort, pain, and further infection (Ortiz et al., 2014; Monte-Santo et al., 2018; Schwendicke et al., 2018; Zeng et al., 2018; Vollu et al., 2019). When dissolution of primary molars progresses into cavitation, placing preformed crowns is a preferred restorative treatment to reduce the failure risk of restoration in the long term, particularly with multi-surface cavities in the clinic (Santamaria et al., 2014; Santamaría et al., 2018; Seale and Randall, 2015; Boyd et al., 2018; Korolenkova and Arzumanyan, 2019; Santamar et al., 2020). Despite recommendations for preformed metal crowns, silver-colored appearance is still a main barrier for their clinical use (Santamaria et al., 2014, 2018; Maciel et al., 2017; Lopez-Cazaux et al., 2019). Moreover, possible metal sensitization is also a contraindication. Recently, zirconia preformed crowns have been developed and used for primary molars (Donly et al., 2018; Mathew et al., 2020; Santamar et al., 2020). However, zirconia preformed crowns may require more tooth tissue removal to create sufficient space for crown placing as well as gingival bleeding on account of the rigid and unbending materials (Innes et al., 2015; Aiem et al., 2017). Besides, the cost of zirconia primary molar crowns is high. All of these limit its clinical use in daily practice (Santamar et al., 2020).

Polyether etherketone (PEEK), as a tooth colored, high-performance thermoplastic polymer, has been considered to be a promising alternative to ceramic materials in crown restoration (Tsuka et al., 2019; Attia and Shokry, 2020; Papathanasiou et al., 2020). PEEK features attractive mechanical properties (similar to dentin and enamel), wear and chemical resistance, dimensional stability, high polishing qualities, good aesthetics, and excellent biocompatibility (Najeeb et al., 2016; Skirbutis et al., 2018; Bathala et al., 2019; Caglar et al., 2019; Tsuka et al., 2019; Papathanasiou et al., 2020). Recently, PEEK has also been applied in clinical dentistry for fixed dental prostheses, implants, abutment, temporary prostheses, and removable prosthodontics (Najeeb et al., 2016; Zoidis et al., 2016; Skirbutis et al., 2018; Papathanasiou et al., 2020). Thus, PEEK should be an ideal and reliable material with the potential to manufacture the restoration of primary molar teeth (Najeeb et al., 2016; Klur et al., 2019).

Effective bonding to PEEK is a prerequisite for its use as a preformed crown material (Tsuka et al., 2019). However, its inert hydrophobic surface and low surface energy make it hard to establish a strong and durable adhesion with dental material (Chaijareenont et al., 2018; Skirbutis et al., 2018). In order to address this issue, several studies have employed different surface-modified methods, such as sand-blasting, silica coating, etching the surface with sulfuric acid, piranha solution, or hydrofluoric acid, to increase the roughness of the PEEK surface for micromechanical interlocking (Zhou et al., 2014; Silthampitag et al., 2016; Caglar et al., 2019; Tsuka et al., 2019). The reactive groups generated by modification may enhance the adhesive strength between PEEK and dental materials through chemical or physical interactions (Schwitalla et al., 2017; Bötel et al., 2018). For example, it has been reported that 98% sulfuric acid etching increased shear bond strength (SBS) more greatly [from 1.75 (0.66) to 27.36 (3.95) MPa] than the aforementioned modifying methods (Chaijareenont et al., 2018). However, the application of the aggressive acidic solutions is not clinically feasible due to the extremely hazardous nature. Hence, exploiting a green and efficient way for the surface modification of PEEK to improve the adhesive property is on demand for the clinical applications in performed crowns.

Dopamine (DA) and its derivatives are attracting materials that have been widely used to functionalize various surfaces for different applications (Lee et al., 2007; Lynge et al., 2011; Liu et al., 2014; Ryu et al., 2018). Immerging materials into the DA solution under alkaline conditions can form a tightly adherent polydopamine (PDA) layer through oxidative polymerization, which can firmly stick to the surfaces of the materials through multiple interaction, including hydrogen bonding, electrostatic interaction, and π-π interaction. In this work, we hypothesize that the deposition of PDA on the surface of PEEK may improve the affinity between PEEK and glass ionomer cement (GIC). In order to further improve the surface modification efficiency, PEEK was processed for plasma treatment, followed by PDA modification. Plasma treatment is a useful technique that can prime any surface for better secondary surface modification, by which carbonyl, hydroxyl, and other groups can be generated to enhance the adhesiveness of surfaces (Zanini et al., 2007; Safinia et al., 2008; Chen and Su, 2011). Through the combination of plasma treatment and PDA deposition (**Scheme 1**), the adhesive strength between PDA and GIC should be further improved. We carefully studied the surface morphologies of PEEK with different treatments and investigated the adhesive strength of the PEEK films by lap-shear tensile experiments. Furthermore, the SBS of PEEK was also evaluated with dentin of primary molar teeth. MTT and Live/Dead assays were used to test the biocompatibility of the modified PEEK films. Our work may give a new solution to the potential clinical application of PEEK in performed crowns for primary molar teeth.

MATERIALS AND METHODS

Materials

The PEEK films were purchased from Changchun Jilin University Super Engineering Plastics Research Co., Ltd., and the model was 021Film-15. 3-Hydroxytyramine hydrochloride and Tris–HCl were obtained from damas-beta. GIC (Ketac^{TM} CemEasymix) was bought from 3M ESPE (St. Paul, MN, USA). Cell culture materials and chemicals related to evaluating cell viability were purchased from Sigma-Aldrich (St. Louis, MO, USA). The other chemical agents were obtained from Aladdin without further purification.

Preparation of the PEEK Films

The PEEK films were cut into 5 × 5 cm pieces and washed in an ultrasonic bath for 20 min in ethanol and then in ultrapure water. After drying at 60°C, the PEEK films were kept for further use. The plasma-treated PEEK films were prepared by a plasma surface treatment machine (ZLD-2; Hangzhou Shangqiang Intelligent Technology Co., Ltd., China) for 30 s, which was operated at a frequency of 3×10^4 Hz and a maximum power of about 2 kW. 3-Hydroxytyramine hydrochloride (2 mg/ml) was dissolved into 10 mM Tris–HCl buffer at pH = 8.5. The PEEK films with or without plasma treatment (30 s) were subsequently immersed in the solution for 2, 6, 12, 24, and 48 h, respectively. Continuous stirring was adopted to avoid non-specific deposition. During the process, the color of the solution turned from yellow to dark brown owing to the pH-induced oxidation. After the coating process, the films were washed by ultrapure water to remove the un-conglutinated PDA and dried in the air. The uncoating particles on the surface were wiped off gently.

Physical and Chemical Characterization

Microstructures Observation

Before scanning electron microscope (SEM) analysis, the surfaces of neat PEEK and plasma-treated PEEK with 0, 2, 6, 12, 24, and 48 h PDA coating were mounted on metal stubs

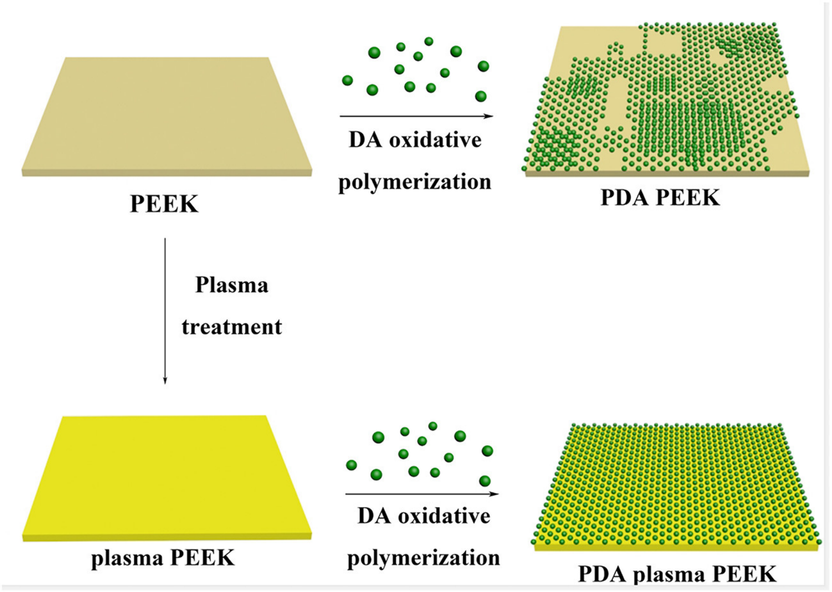

SCHEME 1 | Illustration of the process of PDA deposition on the surfaces of normal PEEK and plasma-treated PEEK.

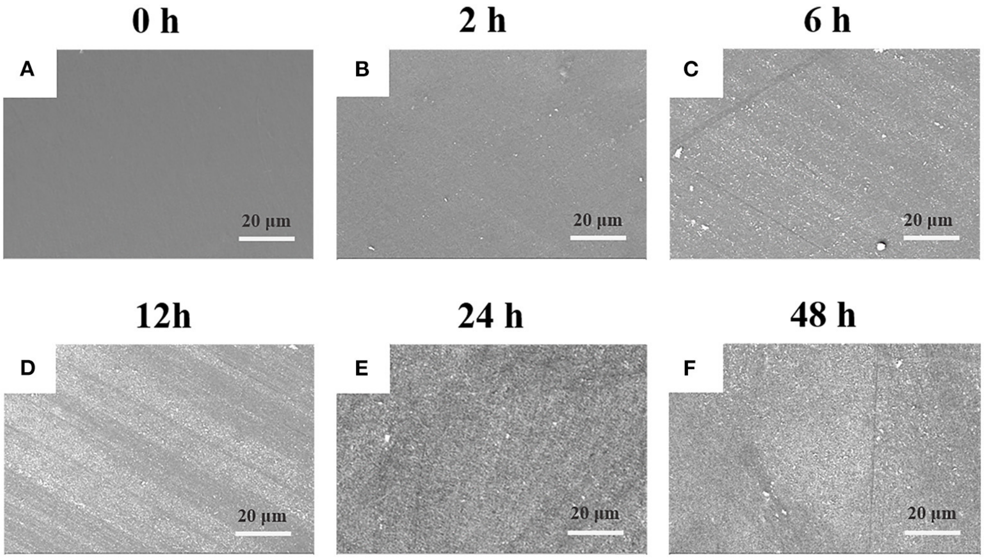

FIGURE 1 | SEM images of plasma-treated PEEK coating with PDA film for **(A)** 0, **(B)** 2, **(C)** 6, **(D)** 12, **(E)** 24, and **(F)** 48 h.

using a double-sided conductive tape and vacuum-coated with the gold sputtering layer. The surface morphologies were visually characterized by SEM (Gemini SEM 500; Carl Zeiss, Germany) at ×500 magnification under 20 kV accelerating voltage. All measurements were completed by the same investigator.

Elemental Analysis

X-ray photoelectron spectroscopy (XPS) studies were carried out by an AXIS ULTRA photoelectron spectrometer (Kratos Analytical Ltd., Manchester, UK) on the surface of the neat PEEK, plasma-treated PEEK, PDA-coated PEEK (24 h), plasma-pretreated PEEK, and PDA-coated PEEK (24 h). The X-ray source of monochromatized Al Kα (hν = 1,486.7 eV) was operated at 50 W and 15 kV. Elemental compositions (C, O, and N) were determined on the PEEK surfaces. The component peak in the C 1 s spectrum was used as a reference with a binding energy of 284.8 eV. Data analysis was performed using the Kratos spectra deconvolution software (version 2.2.9; Kratos Analytical Ltd., Manchester, UK).

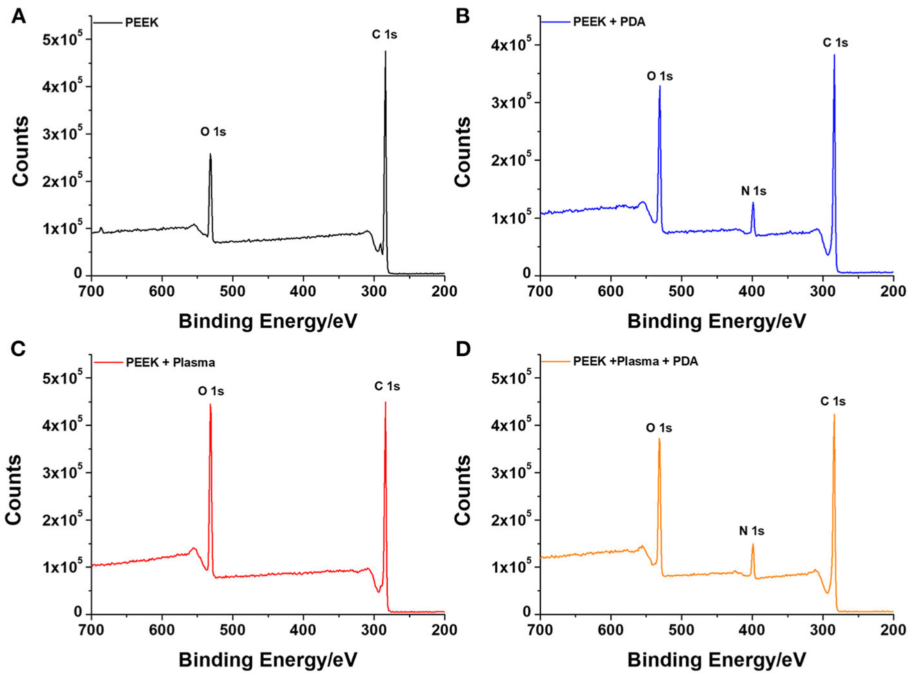

FIGURE 2 | XPS analysis of the various surfaces with or without different treatments for **(A)** neat PEEK, **(B)** PDA-coated PEEK (24 h), **(C)** plasma-treated PEEK, and **(D)** plasma-treated PEEK coating with PDA (24 h).

Bonding Properties

Bond Strength Between PEEK Films and Dental Adhesive

Bond strength of PEEK with dental adhesive was tested using lap-shear test. The neat PEEK films and plasma-treated PEEK films with 0, 2, 6, 12, and 24 h PDA coating were cut into rectangular sheets with a dimension of 30 × 10 mm. GIC was adopted as a conventional dental adhesive. The cement agent was mixed strictly following the manufacturer's instructions and evenly applied on the surface of the PEEK films with a bonding area of 10 × 10 mm by the same operator. The test was carried out using a CMT1503 tensile testing machine (Zhuhai SUST Electrical Equipment Co., Ltd, China) at a constant loading rate of 1 mm/min at ambient temperature. Five replicate tests were conducted in each case, and the bond strength was expressed in kPa. The calculation formula is derived by dividing the loading force (N) at the time of fracture by the bonding area (mm^2).

Bond Strength Between PEEK Films and Dentin

Sound primary molar teeth with complete crowns were extracted after informed consent of the donors and their parents from the Department of Pediatric Dentistry, College & Hospital of Stomatology, Xi'an Jiaotong University. The teeth were stored in 0.02% NaN_3 at 4°C for no longer than 3 months. Mid-coronal dentin disks of 1 mm thick were performed by parallel cuts using a low speed water-cooled diamond saw (Isomet; Buehler, Evanston, IL, USA). The surface of dentin disks was polished with wet 600-grit silicon carbide papers for 1 min to create a standard smear layer. The dimension of each disk was measured with a digital caliper to calculate the bonding area.

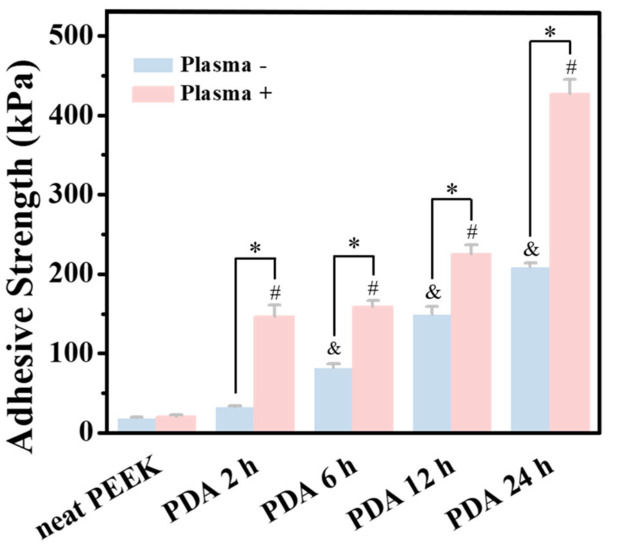

FIGURE 3 | Bonding strength tests of PEEK and plasma-treated PEEK coating with PDA in lap-shear test. *A statistically significant difference was observed at the same PDA-coating time ($P < 0.05$). $^{\&}$A statistically significant difference was observed compared with the neat PEEK (0 h) in the group without plasma pretreatment ($P < 0.05$). $^{\#}$A statistically significant difference was observed compared with the plasma-treated PEEK (0 h) in the plasma-pretreated group ($P < 0.05$).

The adhesive procedure was performed with the GIC following the instructions and applied on the dentin surface evenly. The neat PEEK films, plasma-treated PEEK films, PDA-coated PEEK films (24 h), plasma-pretreated PEEK films, and PDA-coated PEEK films (24 h) were placed carefully to ensure complete contact with each dentin disk. The SBS tests were performed on a universal test machine at a speed of 1 mm/min. The bonding strength value (kPa) was determined by dividing the loading force (N) at the time of fracture by the bonding area (mm^2). Five replicate tests were conducted for each group.

In vitro Biocompatibility

Cell Culture

Primary human gingival fibroblast cells (HGF-1; ATCC, VA, USA) were used to assay the biocompatibility of the PEEK films. Cells were cultured in dishes with growth medium at 37°C in air with 95% humidity plus 5% CO_2, and the medium was changed every 2–3 days. The growth medium consisted of 89% α-minimum essential medium, 10% fetal bovine serum, and 1% antibiotic (100 U/ml streptomycin and 100 U/ml penicillin). The cells were passaged after reaching 80–90% of confluence. The passages 3–5 of the cells were used in the present study.

Preparation of Extracts From the PEEK Films

In order to simulate the physiological environment of the oral cavity, the extracts of the PEEK films were adopted to demonstrate biocompatibility. All the samples were prepared according to the ISO-10993-12:2012. The neat PEEK films, plasma-treated PEEK films, PDA-coated PEEK films (24 h), plasma-pretreated PEEK films, and PDA-coated PEEK films (24 h) were cut into square sheets with a dimension of 10 × 10 mm under completely aseptic conditions and then exposed to UV light for 1 h for sterilization. For each group, every three samples were transferred to a sterile cell-culture 24-well plate, and 1 ml of the growth medium was added to each well, and then were cultured at 37°C in air with 95% humidity plus 5% CO_2. Finally, the extracts were collected at 3 days.

MTT Assay

The cells were seeded into sterile 96-well plates at 2×10^3 per well in the growth medium as described above and followed to attach for 24 h at 37°C under 5% CO_2. After treated with a series of the extracts for 24, 48, or 72 h, the cells were added at a final concentration of 0.5 mg/ml MTT and incubated for 4 h. After removing the medium, 150 μl of DMSO was added. The absorbance was determined at 490 nm, and the cell viabilities were expressed as a percentage of the control. All samples were performed in triplicate.

Live/Dead Staining

The viability of the cells was evaluated using a Live/Dead kit according to the manufacturer's protocol. The cells were planted into 24-well plate with a density of 2×10^4 per well and cultured in the growth medium for 24 h. After replacing the growth medium with fresh extract from the PEEK films, the cells were further cultured for 24 h. Then, the cells were stained with 500 μl of calcein-AM/propidium iodide dye for 15 min and observed under a fluorescent microscope (DMi8; Leica, Germany) for the green (492 nm) and red (545 nm) fluorescence. All experiments were performed in triplicate.

Statistical Analysis

SPSS software (v18; IBM, Chicago, IL, USA) was used to analyze data. Data of bonding properties analysis were presented as mean ± standard deviation. For comparing the bond strength of neat PEEK and plasma-pretreated PEEK with 0, 2, 6, 12, and 24 h PDA coating, two-way analysis of variance (ANOVA) followed by Tukey's *post-hoc* test was conducted to evaluate the significant differences among groups. Statistically significant differences (P) of cell viabilities among groups were measured using one-way ANOVA followed by Tukey's multiple-comparison analysis. The level of significant differences was set in advance at $P < 0.05$.

RESULTS AND DISCUSSION

The PEEK film was immersed into DA solution at room temperature under basic condition to initiate the self-oxidative polymerization for surface modification (Lee et al., 2007). As shown in **Supplementary Figure 1**, it was found that there was a small amount of PDA particles deposited on the surface of PEEK with the treatment for 2 h compared with the neat PEEK film, and that the surface tended to be rough. With the increase of incubation time, the deposited PDA particles gradually increased, and there was no obvious difference observed between 24 and 48 h (**Supplementary Figure 1**), which was consistent with the previous work for the modification of polyvinylidene fluoride (PVDF) film (Jiang et al., 2011). Moreover, we found that the PDA particles aggregated into large clusters for 24 h incubation, which made the PEEK film surface rougher and more non-uniform and may be beneficial for the improvement of the adhesive behaviors of PEEK. Comparatively, with the prior treatment by plasma, the deposition of PDA on the surface was significantly enhanced (**Figure 1**). It is worthy to note that there was no difference on the surface morphology observed after plasma treatment compared with the neat PEEK film. Since there were polar groups generated after plasma treatment, the non-covalent interactions between PDA and modified PEEK, such as electrostatic interaction and hydrogen bonding, should be enhanced, which may lead to more PDA deposition (Thakur et al., 2014). We found that a uniform deposition of PDA particles was observed, and that the PEEK surface was almost fully covered after incubation for 24 h, indicating the efficient coating of PDA on the plasma-treated PEEK surface (**Figure 1**). Representative photographs of neat PEEK, plasma-treated PEEK, PDA-coated PEEK (24 h), plasma-pretreated PEEK, and PDA-coated PEEK (24 h) were listed in **Supplementary Figure 2**. Macroscopically, there was no difference in appearance for the neat and plasma-treated PEEK films, and both showed uniform light-yellow surfaces. The surface of the PEEK film coated by PDA with/without plasma pretreatment turned from yellow to dark brown as the modifying time increases, and it is related to the self-oxidative polymerization of DA similar to the formation of melanin (Lee et al., 2007).

To further confirm the successful deposition of PDA on the surface of PEEK, XPS analysis was employed to characterize

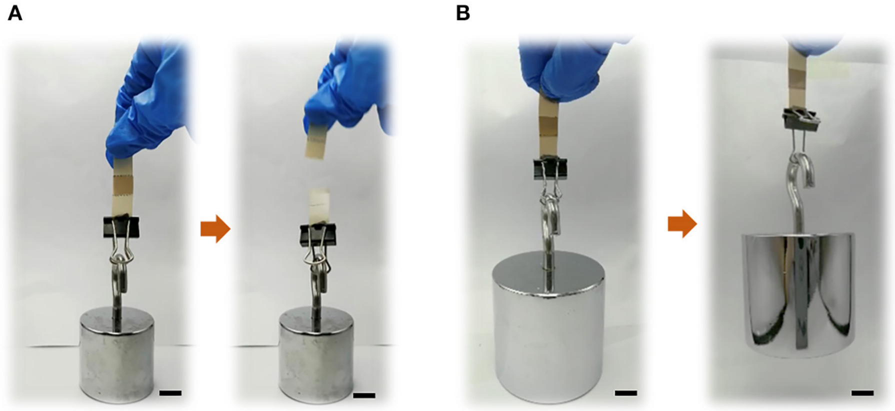

FIGURE 4 | Bond strength exhibitions of **(A)** neat PEEK (loading 200 g) and **(B)** plasma-treated PEEK coating with PDA for 24 h (loading 2 kg). Scale bar = 10 mm.

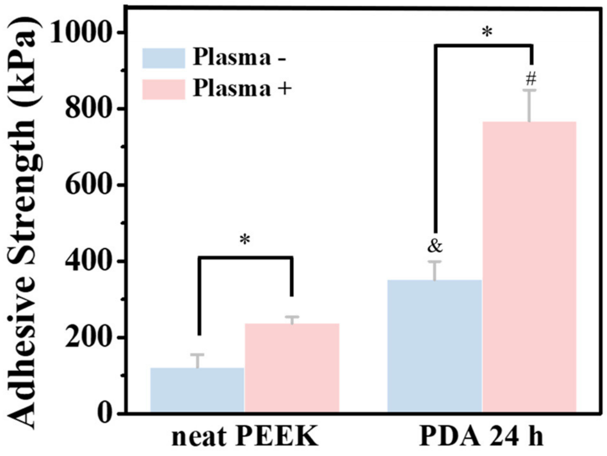

FIGURE 5 | Bonding strength of normal PEEK and plasma-treated PEEK coating with PDA with dentin disk of primary molar teeth. *A statistically significant difference was observed at the same PDA-coating time ($P < 0.05$). $^{\&}$A statistically significant difference was observed compared with the neat PEEK (0 h) in the group without plasma pretreatment ($P < 0.05$). $^{\#}$A statistically significant difference was observed compared with the plasma-treated PEEK (0 h) in the plasma-pretreated group ($P < 0.05$).

the surface chemical compositions. **Figure 2** shows the survey scan spectra of neat PEEK, PDA-coated PEEK, plasma-treated PEEK, and PDA-coated PEEK after plasma treatment. It was found that two separated peaks that correspond to C 1s (285 eV) and O 1s (532 eV) were detected in all the surfaces of the PEEK films, and that there was no new peak observed when the film was treated with plasma. However, after PDA deposition, a distinct peak at 400 eV attributed to N 1s appeared, indicating the successful coating of PDA. This is consistent with the results by SEM observation. Furthermore, the deconvolution of the narrow scan C1s peak shown in **Supplementary Figures 3A,B** indicated that the saturated hydrocarbon C–C/C–H peak decreased from 73.25 to 61.44% as well as the increase of C–O (from 17.15 to 23.35%) and C=O (from 3.00 to 10.38%) peaks after plasma treatment, suggesting the introduction of oxygen functionalities and the increase in carboxyl groups on the surface. Plasma-assisted modification results in the formation of reactive functional groups on the surface, thus facilitating the effective surface functionalization of PEEK by PDA (Thakur et al., 2014). Hence, there was more PDA deposited on the PEEK film surface owing to the application of plasma.

Based on the surface modification results, we speculate that the resulted rough surface may be beneficial to the improvement of the bond strength between PEEK and primary teeth. GIC is the material of choice for treatment of primary teeth in several countries due to the properties of fluoride release and good biocompatibility, which may reduce secondary caries progression, as well as the simple clinical application. It has been confirmed that there is a stable chemical bond formed between GIC and teeth surfaces (Bonifácio et al., 2012; Alves et al., 2013). Therefore, GIC was applied in the evaluation of the bond strength between PEEK films and primary teeth.

First, lap-shear experiments were employed to qualify the bond strength of GIC and PEEK films with different treatments. Because of the inertness of the neat PEEK film, poor adhesiveness to dental adhesive (with 18.4 ± 0.9 kPa bond strength) was detected (**Figure 3**). During the test, the two PEEK films bonded by dental luting cement were very easy to disconnect. In addition, we did not find obvious improvement in the bond strength for the plasma-pretreated PEEK films (20.46 ± 1.7 kPa) and 2 h of PDA coating (32.4 ± 1.8 kPa) compared with the neat PEEK group. However, after PDA treatment for 6, 12, and 24 h, the bond strength was significantly increased to 82.2 ± 4.2, 149.2 ± 9.5, and 209.4 ± 4.4 kPa, respectively. The PDA deposition significantly enhanced the PEEK films' adhesive effect with dental luting cement. Furthermore, the combination of plasma pretreatment and further PDA coating greatly boosted the bond strength. The bond strength corresponding to 2, 6, 12, and 24 h PDA polymerization after plasma treatment was

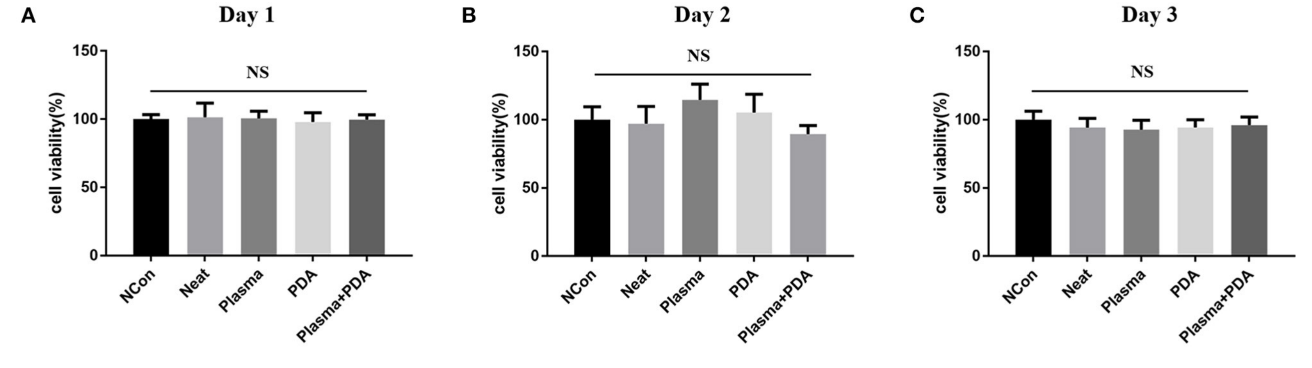

FIGURE 6 | Cell proliferation was determined using MTT assay for **(A)** 24, **(B)** 48, or **(C)** 72 h. NS ($P > 0.05$).

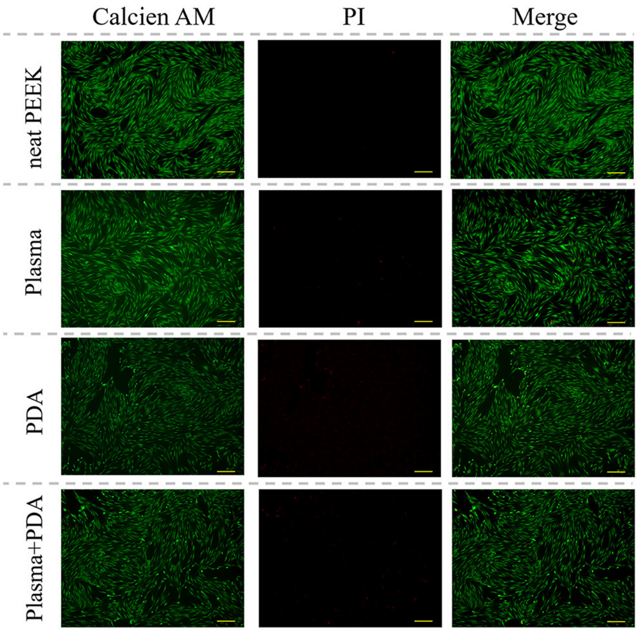

FIGURE 7 | Representative microscopic fluorescence images of live/dead staining specimens for 24 h. Scale bar = 163 μm.

further significantly increased to 146.3 ± 14.5, 158.6 ± 7.9, 225.1 ± 11.5, and 427.0 ± 18.3 kPa, respectively. Surface topography affected the bond strength between the dental luting cement and the PEEK films due to the micromechanical locking force (Silthampitag et al., 2016). The improvement for bond strength may be attributed to more PDA deposition on the PEEK films, leading to the rougher surfaces. It is worthy to mention that the bond strength obtained by the PEEK films with PDA coating for 24 h was 11 times higher than that by the neat PEEK films, which was elevated to 14 times by the intervention of plasma treatments. A significant similar increase in bond strength between PEEK and resin composites was previously observed by 90 or 98% sulfuric acid etching (Chaijareenont et al., 2018). The high concentration of sulfuric acid etching was still considered to be the most recommended treatment to modify the surface of PEEK to improve bonding (Zhou et al., 2014; Silthampitag et al., 2016). The result of the lap-shear experiments demonstrated that the PDA coating with plasma pretreatment may give a good solution to the bonding of PEEK.

Furthermore, to verify our hypothesis, the two PEEK films bonded using GIC (adhesive area: 10 × 10 mm) were processed to lift different weights to observe the bonding stability. As shown in **Figure 4A** and **Supplementary Movie 1**, it was found that the bonded neat PEEK films were too fragile to withstand the weight of 200 g. Comparatively, the plasma-pretreated and PDA-coated PEEK films can constantly lift 2 kg weight (**Figure 4B** and **Supplementary Movie 2**), demonstrating the significant increase of the adhesiveness between dental luting cement and PEEK films.

To mimic the practical applications, the bond strength of the PEEK films with or without surface modification to dentin disk of primary molar teeth was also tested (**Figure 5** and **Supplementary Figure 4**). The bond strengths of the neat PEEK films with or without plasma treatment to dentin disks were 122.3 ± 32.7 and 237.3 ± 16.9 kPa, respectively. Since there were various polar groups generated on the surface of the PEEK film with plasma treatment, it is predictable that the bond strength can be significantly enhanced by plasma treatment. Moreover, after PDA coating for 24 h on the PEEK film, the bond strength was significantly increased to 351.9 ± 47.5 kPa. As expected, the PEEK film with both plasma treatment and PDA coating for 24 h exhibited the strongest bonding (767.8 ± 81.5 kPa). These results suggested that our methods for the PEEK film modification may be useful for the clinical applications. Moreover, a previous result confirmed that the PDA-coating process was performed after plasma pretreatment for the reinforcement of the adhesive force and the stability of the PDA-coating layer on the polytetrafluoroethylene (PTFE) substrates (Cheng et al., 2019). Therefore, the modification of PDA coating with plasma pretreatment on the PEEK surface may have great potential to provide an effective and durable bond with primary molar teeth.

The cell biocompatibility of the PEEK films was evaluated by MTT assay and live/dead staining. As shown in **Figure 6**, there was no obvious difference found among the neat PEEK group, PDA-coated PEEK (24 h), plasma-treated PEEK, and PDA-coated PEEK (24 h) after the plasma treatment groups in the MTT assay at 1, 2, and 3 days. Afterward, the live/dead staining was used to visually observe the cell biocompatibility. The live and dead cells were stained with green and red fluorescence, respectively. It was found that the majority of the cells presented normal morphology in all the PEEK groups (**Figure 7**). Therefore, these results showed that the modified PEEK films own good cell biocompatibility and should be safe for further *in vivo* application.

CONCLUSION

Modified PEEK by PDA coating for different times with/without plasma pretreatment was fabricated and well-characterized using SEM and XPS. The modification treatments had a significant impact on the bonding properties of the PEEK surfaces without causing a significantly decreased proliferation rate of human gingival fibroblast cells. Among those treatments, PDA coating for 24 h with plasma pretreatment seems to be most effective with obvious improvement of adhesive strength between modified films and dentin disk of primary molar teeth. Our work provides a green, safe, and effective way for the modification of the PEEK surface and may give a new solution for the employment of PEEK primary performed crowns in potential clinical applications.

DATA AVAILABILITY STATEMENT

The original contributions presented in the study are included in the article/**Supplementary Material**, further inquiries can be directed to the corresponding author/s.

AUTHOR CONTRIBUTIONS

DP and AL supervised the study. RT, YM, XZ, JL, and RD performed the experiments and discussed the results. YM and XZ conducted the evaluation of bonding properties and SEM and XPS analyses. JL and RD participated in biocompatibility experiments. RT wrote the first draft of the manuscript. YC, YuZ, YaZ, DP, and AL coordinated the work, designed the experiments, and performed its final revision. All authors contributed to the article and approved the submitted version.

FUNDING

The authors appreciated the support by the National Natural Science Foundation of the People's Republic of China (81870798) and the Fundamental Research Funds for the Central Universities (xtr012019007).

SUPPLEMENTARY MATERIAL

The Supplementary Material for this article can be found online at: https://www.frontiersin.org/articles/10.3389/fbioe.2020.630094/full#supplementary-material

REFERENCES

Aiem, E., Smail-Faugeron, V., and Muller-Bolla, M. (2017). Aesthetic preformed paediatric crowns: systematic review. *Int. J. Paediatr. Dent*. 27, 273–282. doi: 10.1111/ipd.12260

Alves, F. B., Hesse, D., Lenzi, T. L., Guglielmi Cde, A., Reis, A., Loguercio, A. D., et al. (2013). The bonding of glass ionomer cements to caries-affected primary tooth dentin. *Pediatr. Dent*. 35, 320–324.

Attia, M. A., and Shokry, T. E. (2020). Effect of different fabrication techniques on the marginal precision of polyetheretherketone single-crown copings. *J. Prosthet. Dent*. 124, 565.e1–7. doi: 10.1016/j.prosdent.2020.04.003

Bathala, L., Majeti, V., Rachuri, N., Singh, N., and Gedela, S. (2019). The role of polyether ether ketone (Peek) in dentistry - a review. *J. Med. Life*. 12, 5–9. doi: 10.25122/jml-2019-0003

Bonifácio, C. C., Shimaoka, A. M., de Andrade, A. P., Raggio, D. P., van Amerongen, W. E., and de Carvalho, R. C. (2012). Micro-mechanical bond strength tests for the assessment of the adhesion of GIC to dentine. *Acta. Odontol. Scand*. 70, 555–563. doi: 10.3109/00016357.2011.640280

Bötel, F., Zimmermann, T., Sütel, M., Müller, W. D., and Schwitalla, A. D. (2018). Influence of different low-pressure plasma process parameters on shear bond strength between veneering composites and PEEK materials. *Dent. Mater*. 34, e246–e54. doi: 10.1016/j.dental.2018.06.004

Boyd, D. H., Page, L. F., and Thomson, W. M. (2018). The Hall Technique and conventional restorative treatment in New Zealand children's primary oral health care - clinical outcomes at two years. *Int. J. Paediatr. Dent*. 28, 180–188. doi: 10.1111/ipd.12324

Caglar, I., Ates, S. M., and Yesil Duymus, Z. (2019). An *in vitro* evaluation of the effect of various adhesives and surface treatments on bond strength of resin cement to polyetheretherketone. *J Prosthodont*. 28, e342–e49. doi: 10.1111/jopr.12791

Chaijareenont, P., Prakhamsai, S., Silthampitag, P., Takahashi, H., and Arksornnukit, M. (2018). Effects of different sulfuric acid etching concentrations on PEEK surface bonding to resin composite. *Dent. Mater. J*. 37, 385–392. doi: 10.4012/dmj.2017-141

Chen, J. P., and Su, C. H. (2011). Surface modification of electrospun PLLA nanofibers by plasma treatment and cationized gelatin immobilization for cartilage tissue engineering. *Acta. Biomater*. 7, 234–243. doi: 10.1016/j.actbio.2010.08.015

Cheng, B., Inoue, Y., and Ishihara, K. (2019). Surface functionalization of polytetrafluoroethylene substrate with hybrid processes comprising plasma treatment and chemical reactions. *Colloids Surf. B Biointerfaces*. 173, 77–84. doi: 10.1016/j.colsurfb.2018.09.051

Donly, K. J., Sasa, I., Contreras, C. I., and Mendez, M. J. C. (2018). Prospective randomized clinical trial of primary molar crowns: 24-month results. *Pediatr. Dent*. 40, 253–258.

Innes, N. P., Ricketts, D., Chong, L. Y., Keightley, A. J., Lamont, T., and Santamaria, R. M. (2015). Preformed crowns for decayed primary molar teeth. *Cochrane Database Syst. Rev*. 2015:*CD*005512. doi: 10.1002/14651858.CD005512.pub3

Jiang, J., Zhu, L., Zhu, L., Zhu, B., and Xu, Y. (2011). Surface characteristics of a self-polymerized dopamine coating deposited on hydrophobic polymer films. *Langmuir* 27, 14180–14187. doi: 10.1021/la202877k

Klur, T., Hasan, I., Ottersbach, K., Stark, H., Fichte, M., Dirk, C., et al. (2019). PEKK-made indirect temporary crowns and bridges: a clinical pilot study. *Clin. Oral Investig*. 23, 771–777. doi: 10.1007/s00784-018-2493-z

Korolenkova, M. V., and Arzumanyan, A. P. (2019). Effectiveness of fillings and stainless-steel pediatric crowns for primary molars restoration: the results of prospective randomized split mouth study. *Stomatologiia* 98, 83–86. doi: 10.17116/stomat20199803183

Lee, H., Dellatore, S. M., Miller, W. M., and Messersmith, P. B. (2007). Mussel-inspired surface chemistry for multifunctional coatings. *Science* 318, 426–430. doi: 10.1126/science.1147241

Liu, Y., Ai, K., and Lu, L. (2014). Polydopamine and its derivative materials: synthesis and promising applications in energy, environmental, and biomedical fields. *Chem. Rev*. 114, 5057–5115. doi: 10.1021/cr400407a

Lopez-Cazaux, S., Aiem, E., Velly, A. M., and Muller-Bolla, M. (2019). Preformed pediatric zirconia crown versus preformed pediatric metal crown: study protocol for a randomized clinical trial. *Trials* 20:530. doi: 10.1186/s13063-019-3559-1

Ludwig, K. H., Fontana, M., Vinson, L. A., Platt, J. A., and Dean, J. A. (2014). The success of stainless steel crowns placed with the Hall technique: a retrospective study. *J. Am. Dent. Assoc*. 145, 1248–1253. doi: 10.14219/jada.2014.89

Lynge, M. E., van der Westen, R., Postma, A., and Städler, B. (2011). Polydopamine–a nature-inspired polymer coating for biomedical science. *Nanoscale* 3, 4916–4928. doi: 10.1039/c1nr10969c

Maciel, R., Salvador, D., Azoubel, K., Redivivo, R., Maciel, C., da Franca, C., et al. (2017). The opinion of children and their parents about four different types of dental restorations in a public health service in Brazil. *Eur. Arch. Paediatr. Dent*. 18, 25–29. doi: 10.1007/s40368-016-0262-8

Mathew, M. G., Samuel, S. R., Soni, A. J., and Roopa, K. B. (2020). Evaluation of adhesion of Streptococcus mutans, plaque accumulation on zirconia and stainless steel crowns, and surrounding gingival inflammation in primary molars: randomized controlled trial. *Clin. Oral Investig*. 24, 3275–3280. doi: 10.1007/s00784-020-03204-9

Monte-Santo, A. S., Viana, S. V. C., Moreira, K. M. S., Imparato, J. C. P., Mendes, F. M., and Bonini, G. (2018). Prevalence of early loss of primary molar and its impact in schoolchildren's quality of life. *Int. J. Paediatr. Dent*. 28, 595–601. doi: 10.1111/ipd.12416

Najeeb, S., Zafar, M. S., Khurshid, Z., and Siddiqui, F. (2016). Applications of polyetheretherketone (PEEK) in oral implantology and prosthodontics. *J. Prosthodont. Res*. 60, 12–19. doi: 10.1016/j.jpor.2015.10.001

Ortiz, F. R., Tomazoni, F., Oliveira, M. D., Piovesan, C., Mendes, F., and Ardenghi, T. M. (2014). Toothache, associated factors, and its impact on oral health-related quality of life (OHRQoL) in preschool children. *Braz. Dent. J*. 25, 546–553. doi: 10.1590/0103-6440201302439

Papathanasiou, I., Kamposiora, P., Papavasiliou, G., and Ferrari, M. (2020). The use of PEEK in digital prosthodontics: a narrative review. *BMC Oral Health* 20:217. doi: 10.1186/s12903-020-01202-7

Ryu, J. H., Messersmith, P. B., and Lee, H. (2018). Polydopamine surface chemistry: a decade of discovery. *ACS Appl. Mater Interfaces* 10, 7523–7540. doi: 10.1021/acsami.7b19865

Safinia, L., Wilson, K., Mantalaris, A., and Bismarck, A. (2008). Through-thickness plasma modification of biodegradable and nonbiodegradable porous polymer constructs. *J. Biomed Mater Res. A* 87, 632–642. doi: 10.1002/jbm.a.31731

Santamar, R. M., Abudrya, M. H., Gul, G., Mourad, M. S., Gomez, G. F., and Zandona, A. G. F. (2020). How to intervene in the caries process: dentin caries in primary teeth. *Caries Res*. 54:306–323. doi: 10.1159/000508899

Santamaria, R. M., Innes, N. P., Machiulskiene, V., Evans, D. J., and Splieth, C. H. (2014). Caries management strategies for primary molars: 1-yr randomized control trial results. *J. Dent. Res*. 93, 1062–1069. doi: 10.1177/0022034514550717

Santamaría, R. M., Innes, N. P. T., Machiulskiene, V., Schmoeckel, J., Alkilzy, M., and Splieth, C. H. (2018). Alternative caries management options for primary molars: 2.5-year outcomes of a randomised clinical trial. *Caries Res*. 51, 605–614. doi: 10.1159/000477855

Santamaria, R. M., Pawlowitz, L., Schmoeckel, J., Alkilzy, M., and Splieth, C. H. (2018). Use of stainless steel crowns to restore primary molars in Germany: questionnaire-based cross-sectional analysis. *Int. J. Paediatr. Dent*. 28, 587–594. doi: 10.1111/ipd.12415

Schwendicke, F., Krois, J., Splieth, C. H., Innes, N., Robertson, M., Schmoeckel, J., et al. (2018). Cost-effectiveness of managing cavitated primary molar caries lesions: a randomized trial in Germany. *J. Dent*. 78, 40–45. doi: 10.1016/j.jdent.2018.05.022

Schwitalla, A. D., Bötel, F., Zimmermann, T., Sütel, M., and Müller, W. D. (2017). The impact of argon/oxygen low-pressure plasma on shear bond strength between a veneering composite and different PEEK materials. *Dent. Mater*. 33, 990–994. doi: 10.1016/j.dental.2017.06.003

Seale, N. S., and Randall, R. (2015). The use of stainless steel crowns: a systematic literature review. *Pediatr. Dent*. 37, 145–160.

Silthampitag, P., Chaijareenont, P., Tattakorn, K., Banjongprasert, C., Takahashi, H., and Arksornnukit, M. (2016). Effect of surface pretreatments on resin composite bonding to PEEK. *Dent. Mater J*. 35, 668–674. doi: 10.4012/dmj.2015-349

Skirbutis, G., Dzingute, A., Masiliunaite, V., Šulcaite, G., and Žilinskas, J. (2018). PEEK polymer's properties and its use in prosthodontics. A review. *Stomatologija* 20, 54–58.

Smaïl-Faugeron, V., Glenny, A.-M., Courson, F., Durieux, P., Muller-Bolla, M., and Fron Chabouis, H. (2018). Pulp treatment for extensive decay in primary teeth. *Cochrane Database Syst. Rev*. 5:CD003220. doi: 10.1002/14651858.CD003220.pub3

Thakur, V. K., Vennerberg, D., and Kessler, M. R. (2014). Green aqueous surface modification of polypropylene for novel polymer nanocomposites. *ACS Appl. Mater. Interfaces*. 6, 9349–9356. doi: 10.1021/am501726d

Tsuka, H., Morita, K., Kato, K., Kimura, H., Abekura, H., Hirata, I., et al. (2019). Effect of laser groove treatment on shear bond strength of resin-based luting agent to polyetheretherketone (PEEK). *J. Prosthodont. Res*. 63, 52–57. doi: 10.1016/j.jpor.2018.08.001

Vollu, A. L., Rodrigues, G. F., Rougemount Teixeira, R. V., Cruz, L. R., Dos Santos Massa, G., de Lima Moreira, J. P., et al. (2019). Efficacy of 30% silver diamine fluoride compared to atraumatic restorative treatment on dentine caries arrestment in primary molars of preschool children: a 12-months parallel randomized controlled clinical trial. *J. Dent*. 88:103165. doi: 10.1016/j.jdent.2019.07.003

Zanini, S., Müller, M., Riccardi, C., and Orlandi, M. (2007). Polyethylene glycol grafting on polypropylene membranes for anti-fouling properties. *Plasma Chem. Plasma Process*. 27, 446–457. doi: 10.1007/s11090-007-9094-y

Zeng, L., Zeng, Y., Zhou, Y., Wen, J., Wan, L., Ou, X., et al. (2018). Diet and lifestyle habits associated with caries in deciduous teeth among 3- to 5-year-old preschool children in Jiangxi province, China. *BMC Oral Health*. 18:224. doi: 10.1186/s12903-018-0686-0

Zhou, L., Qian, Y., Zhu, Y., Liu, H., Gan, K., and Guo, J. (2014). The effect of different surface treatments on the bond strength of PEEK composite materials. *Dent. Mater*. 30, e209–e215. doi: 10.1016/j.dental.2014.03.011

Zoidis, P., Papathanasiou, I., and Polyzois, G. (2016). The use of a modified poly-ether-ether-ketone (PEEK) as an alternative framework material for removable dental prostheses. *Clin. Rep. J. Prosthodont*. 25, 580–584. doi: 10.1111/jopr.12325

Conflict of Interest: The authors declare that the research was conducted in the absence of any commercial or financial relationships that could be construed as a potential conflict of interest.

frontiers in Materials

ORIGINAL RESEARCH
published: 12 March 2021
doi: 10.3389/fmats.2021.621416

Composite System of 3D-Printed Polymer and Acellular Matrix Hydrogel to Repair Temporomandibular Joint Disc

*Ping Yi[1†], Jiadi Liang[2†], Futing Huang[1], Zuodong Zhao[1], Xiaohui Zhou[1], Qianya Gao[1], Min Huang[1], Baoyi Chen[1], Zhenzhao Guo[3] and Chang Liu[1]**

[1]Guangzhou Key Laboratory of Basic and Applied Research of Oral Regenerative Medicine, Department of Orthodontics, Affiliated Stomatology Hospital of Guangzhou Medical University, Guangzhou, China, [2]Center of Stomatology, Shunde Hospital of Southern Medical University, Foshan, China, [3]Guangzhou Key Laboratory of Basic and Applied Research of Oral Regenerative Medicine, Affiliated Stomatology Hospital of Guangzhou Medical University, Guangzhou, China

Tissue engineering is a promising approach to restore or replace a damaged temporomandibular joint (TMJ) disc. However, constructing a scaffold that can mimic biomechanical and biological properties of the natural TMJ disc remains a challenge. In this study, three-dimensional (3D) printing technology was used to fabricate polycaprolactone (PCL)/polyurethane (PU) scaffolds and PU scaffolds to imitate the region-specific biomechanical properties of the TMJ disc. The scaffolds were coated with polydopamine (PDA) and combined with a decellularized matrix (dECM). Then, rat costal chondrocytes and mouse L929 fibroblasts, respectively, were suspended on the composite scaffolds and the biological functions of the cells were studied. The properties of the scaffolds were characterized by scanning electron microscopy (SEM), X-ray photoelectron spectroscopy (XPS), contact angle analysis, and biomechanical testing. To verify the biocompatibility of the scaffolds, the viability, proliferation, and extracellular matrix (ECM) production of the cells seeded on the scaffolds were assessed by LIVE/DEAD staining, Cell Counting Kit-8 assay, biochemical content analysis, immunofluorescence staining, and qRT-PCR. The functionalized hybrid scaffolds were then implanted into the subcutaneous space of nude mice for 6 weeks, and the regenerated tissue was evaluated by histological staining. The biomechanical properties of PCL/PU and PU scaffolds were comparable to that of the central and peripheral zones, respectively, of a native human TMJ disc. The PDA-coated scaffolds displayed superior biomechanical, structural, and functional properties, creating a favorable microenvironment for cell survival, proliferation, ECM production, and tissue regeneration. In conclusion, 3D-printed polymer scaffolds coated with PDA and combined with dECM hydrogel were found to be a promising substitute for TMJ disc tissue engineering.

Keywords: temporomandibular joint disc, tissue engineering, decellularized extracellular matrix, three-dimensional (3D), polydopamine

Edited by:
Jianxun Ding,
Chinese Academy of Sciences, China

Reviewed by:
Xianghong Luan,
Texas A&M University, United States
He Liu,
Jilin University, China
Jinlin Song,
Chongqing Medical University, China

***Correspondence:**
Chang Liu
changliudentist@gzhmu.edu.cn

[†]These authors have contributed equally to this work and share first authorship

Specialty section:
This article was submitted to Biomaterials, a section of the journal Frontiers in Materials

***Received:** 09 November 2020*
***Accepted:** 15 January 2021*
***Published:** 12 March 2021*

Citation:
Yi P, Liang J, Huang F, Zhao Z, Zhou X, Gao Q, Huang M, Chen B, Guo Z and Liu C (2021) Composite System of 3D-Printed Polymer and Acellular Matrix Hydrogel to Repair Temporomandibular Joint Disc. Front. Mater. 8:621416. doi: 10.3389/fmats.2021.621416

INTRODUCTION

Temporomandibular disorder (TMD) has been reported to affect 10%–15% of the population, and only 5% of patients seek treatment (Lim and Sbhalang, 2010; Gonçalves et al., 2011). As a major component of the temporomandibular joint (TMJ), the disc usually undergoes degenerative changes, such as displacement without reduction and perforation in patients with severe TMD, and these pathological changes greatly compromise normal jaw movement and functions, including the ability to eat and speak (Eiji and Theo, 2003). The TMJ disc has poor regeneration capability due to the limited vascularization. At the advanced stage of TMD, the only option for the treatment of the damaged disc is surgical resection (Miloro and Henriksen, 2010; Renapurkar, 2018). Though discectomy can partially relieve symptoms, permanent recovery will not occur due to the development of condylar remodeling (Eriksson and Westesson, 1992; Abdala-Junior et al., 2018). To avoid progressive degenerative changes of the affected TMJ, placement of an interpositional material is highly recommended. However, replacement of the damaged disc with alloplastic or autogenous graft leads to a range of complications, which considerably limit the clinical application (Dolwick, 2007; Dimitroulis, 2011).

Tissue engineering is emerging as a promising approach to attenuate symptoms of TMD, even repair or potentially replace the injured discs. Scaffolding materials play a crucial role in providing mechanical support and biochemical signals for tissue regeneration. Until now, numerous natural materials and synthetic polymers have been used to engineer the disc (Wu et al., 2014; Kobayashi et al., 2015; Bousnaki et al., 2018; Wang et al., 2018; Moura et al., 2020). Natural scaffolds, especially the tissue-specific decellularized extracellular matrix (dECM), generally possess high biocompatibility and recognition domains to facilitate cell adhesion, proliferation, and differentiation through inherent biochemical cues within native tissues, while the poor mechanical strength impedes its application in regenerating load-bearing tissues (Brown et al., 2012; Liang et al., 2020). On the other hand, the lack of mechanical properties of these biomaterials can be overcome by combining them with synthetic polymers to form composite structures with superior mechanical strength, biocompatibility, and biodegradability (Pina et al., 2019).

At present, the main methods used to prepare scaffolds are electrospinning, freeze-drying, three-dimensional (3D) printing, and so on (Acri et al., 2019). 3D printing technology is an ideal way to fabricate biomimetic scaffolds with a desired shape, suitable mechanical properties, and a well-controlled microstructure to facilitate cell infiltration and distribution (Legemate et al., 2016; Tamay et al., 2019). Various synthetic polymers, including poly(lactic-co-glycolic acid) (PLGA), polylactic acid (PLA), polycaprolactone (PCL), and polyurethane (PU), have been used for printing soft and hard tissues due to their fine-tunable properties (Daly et al., 2017). Recently, PCL and PU have been widely investigated for regeneration of cartilaginous tissue because they possess excellent biocompatibility and adequate mechanical properties, which can be maintained for a long time (Bahcecioglu et al., 2019; Theodoridis et al., 2019; Wen et al., 2019). However, scaffolds made of these materials have smooth surfaces, are hydrophobic, and lack cell recognition sites; thus, their ability to promote cell adhesion, proliferation, and differentiation is poor (Zhu et al., 2002). To address this challenge, various surface modification techniques have been developed to mediate cell adhesion and subsequent cell responses (Richbourg et al., 2019). Recently, functionalizing biomaterials with different biomacromolecules, such as proteins, peptides, or growth factors, has attracted much attention since this approach may evoke cell- and tissue-specific reactions (Lee et al., 2014; Tarafder et al., 2016; Capellato et al., 2020). Compared to other chemical conjugation methods, the polydopamine (PDA) coating tends to be nontoxic, solvent-free, and time-saving (Qiu et al., 2018). This innovative surface modification method has therefore been extensively explored for applications in engineering various hard and soft tissues, such as bone, cartilage, blood vessels, nerves, and muscle (Qian et al., 2018; Bock et al., 2020; Godoy-Gallardo et al., 2020; Wei et al., 2020).

In the present study, we aimed to develop a biomimetic composite scaffold of 3D printed synthetic polymers and tissue-specific dECM hydrogel to repair the TMJ disc. The composite scaffold developed can provide an ideal physical and biochemical microenvironment to promote cell attachment, proliferation, differentiation, and tissue regeneration by combining PDA-coated PCL/PU and PU scaffolds with tissue-specific decellularized ECM hydrogel derived from porcine TMJ discs. Therefore, this biomimetic composite scaffold holds potential to be a promising approach for TMJ disc tissue engineering.

MATERIALS AND METHODS

Fabrication of the 3D Printed Scaffolds

Based on the region-specific mechanical properties of TMJ disc, 3D printed scaffolds were fabricated using a mixture of PCL (Sigma, USA) and PU (Tecoflex, EG-100A, United States) at a ratio of 1:1, according to the results of our pilot study. PCL and PU particles were heated at 100°C for 30 min in the miniature twin screw extruder (MiniJet, HAAKE MiniJet, Germany), then the mixture was extruded at a speed of 100 r/min at a temperature of 140°C. PCL/PU and PU scaffolds with a pore size of about 350 μm were fabricated using a 3D printer (Regenovo, China). The materials were melted at 170°C in printing chamber, printed through a 22 gauge metal needle at pressure 0.45 Mpa and deposition speed of 0.5 mm/s. Printed scaffolds were immersed in a dopamine solution (2 mg/ml, pH 8.5) at room temperature for 16 h under continuous stirring (Jo et al., 2013) and then rinsed several times with deionized water. Samples were used after vacuum drying for 24 h. Scaffolds coated with PDA were classified as "modified" groups and were referred to as PDA-PCL/PU and PDA-PU scaffolds, respectively. The scaffolds without PDA coating were classified as "original" groups.

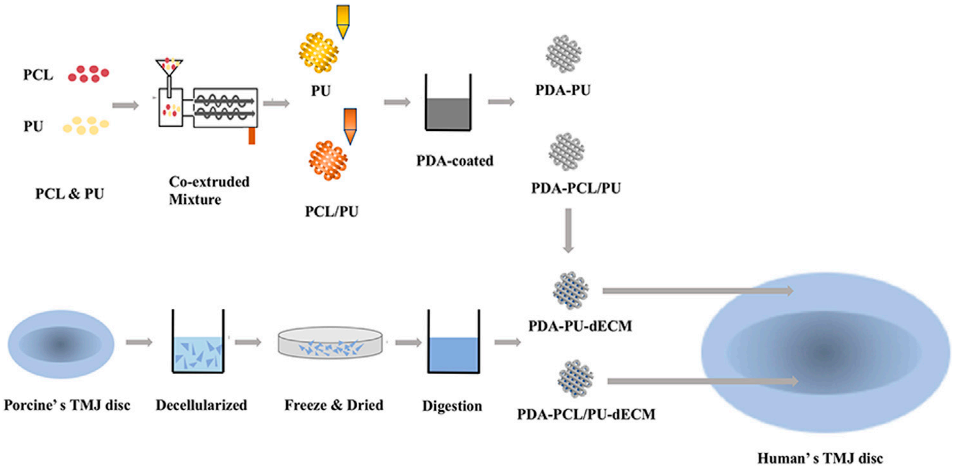

FIGURE 1 | Schematic illustration of the construction process of the composite scaffolds of the experimental design.

Characterization of 3D Printed Scaffolds

The morphology of the scaffolds was visualized by scanning electron microscopy (SEM, Thermo Fisher Scientific, United States). Samples were sputter-coated with gold at 20 mA for 60 s, mounted on aluminum stubs, fixed with carbon tape, and observed under a SEM at an accelerating voltage of 10 kV. The chemical composition of the scaffolds was analyzed by X-ray photoelectron spectroscopy (XPS, Thermo Fisher K-Aloha, United States). The containment C1s hydrocarbon peak at 284.7 eV was applied to calibrate the binding energies, and the sensitivity factors of C1s, N1s, and O1s were quantitatively calculated. The water contact angle of the scaffolds was used to evaluate the hydrophobicity of the scaffolds. Briefly, the same amount of water was dropped onto the surface of each scaffold at room temperature, and the image was captured using a contact angle analyzer (JY-PH, JINHE, China).

Preparation of the Composite Scaffolds

Preparation of the Hydrogel

The decellularization process of TMJ disc was carried out as described in prior study (Liang et al., 2020). Briefly, the minced tissue pieces were placed into a hypotonic Tris-HCl buffer followed by four cycles of freezing and thawing. These samples were treated with 0.5% trypsin solution for 24 h and then with nuclease solution (50 U/ml DNase and 1 U/ml RNase, pH 7.5) at room temperature for 4 h. Afterward, these samples were treated with 1% Triton X-100 for 48 h and washed with deionized water for at least 3 days. The dECM powder was digested with 0.1% pepsin in 0.01 M HCl at room temperature for 48 h. The flowable solution was neutralized by adding 0.1 M NaOH, followed by adding 10 × PBS to adjust the physiological acidity and salinity. The pregel solution was diluted to the predetermined concentration (8 mg/ml) using 1 × PBS for subsequent study, since this concentration has been proven to be the most cells-friendly concentration in a preceding study (Liang et al., 2020).

Fabrication of the Composite Scaffolds

The dECM solution (8 mg/ml) was infused into the 3D printed scaffolds using a dropper and then incubated in a 37°C incubator for 30 min to complete the gelation of the hydrogel. The size of the scaffolds used in the subsequent cell experiments corresponded to the size of the well plates, e.g., when a cell experiment was performed with 48-well plates, the scaffold size was matched to that of the 48-well plate size. A schematic illustration of the preparation procedure of scaffolds is presented in **Figure 1**.

Mechanical Tests of the Composite Scaffolds

Mechanical tests were performed as described previously (Legemate et al., 2016), using Instron mechanical testing instrument (Instron 3,342, Instron, Norwood, MA, United States). Cylinders with 5 mm diameter and 3 mm height were prepared for compression test. Bone-shaped scaffolds with 1 mm thickness and 25 mm length were printed for tensile test. All scaffolds tested were combined with dECM hydrogel. Compression and tensile mechanical tests were performed at 0.25 mm/min after samples had been preconditioned with 15 cycles with strain ranging from 0 to 10% strain.

Cell Culture Experiments

Cells Culture

L929 cells (i-CELL, China) were cultured in Dulbecco's Modified Eagle's Medium (DMEM) (Hyclone, China) supplemented with 10% FBS and 1% penicillin-streptomycin in an atmosphere containing 5% CO_2 at 37°C. Primary rat chondrocytes isolated from 4-week-old specific pathogen free rat (SPF), according to an established method (Barbero et al., 2004). Briefly, costal cartilage fragments were digested with 0.2% collagenase at 37°C overnight. Cells were collected from the digested solution and cultured using DMEM/F-12 (Hyclone, China) supplemented with 10% FBS and 1% penicillin-streptomycin in a humidified incubator with 5%

TABLE 1 | Primer of qPCR.

Target gene	Primer sequences
Col I (mouse)	Forward: 5′-ATGCCGCGACCTCAAGATG-3′ Reverse: 5′-TGAGGCACAGACGGCTGATA-3′
GAPDH (mouse)	Forward: 5′-TGTGTCCGTCGTGGATCTC-3′ Reverse: 5′-TTGCTGTTGAAGTCGCAGGA-3′
Col II (rat)	Forward: 5′-AATTTGGRGRGGACATAGGG-3′ Reverse: 5′-AAGTATTTGGGTCCTTTGGG-3′
Sox 9 (rat)	Forward: 5′-AGGAAGCTGGCAGACCAGTA-3′ Reverse: 5′-ACGAAGGGTCTCTTCTCGCT-3′
GAPDH (rat)	Forward: 5′-TATGACTCTACCCACGGCAAGT-3′ Reverse: 5′-ATACTCAGCACCAGCATCACC-3′

CO_2 at 37°C. Cells at passage 2 were used for all experiments. All animal experiments were approved by Guangzhou Medical University (No. GY2020-044) and conducted according to standard guidelines for the use and care of laboratory animals.

Cell Seeding onto Scaffolds and Viability Assay

The sterilized composite scaffolds were placed in 48-well plates. L929 and chondrocytes, respectively, were implanted at a density of 1.0×10^4 cells/scaffold to construct cell-laden composite scaffolds and cultured with the growth medium suitable for growth of each type of cells. The viability of the cells on the composite scaffolds was evaluated using a LIVE/DEAD staining kit (BestBio, China) at 1 and 7 days of culture following the manufacturer protocol. The stained cells were observed by confocal laser scanning microscope (Leica TCS SP8, Germany). Cell proliferation was quantified by the Cell Counting Kit-8 assay (CCK8, Dojindo, Japan) at 1, 4, and 7 days of culture and measured at 450 nm wavelength in a microplate reader (Thermo Scientific, Shanghai, China).

Differentiation and Maturation of Cells

Gene Expression Analysis

Cell-loaded composite scaffolds were cultured in 6-well plates for 14 days, then total RNA was extracted using a TaKaRa MiniBEST Universal RNA Extraction Kit (TaKaRa Biotechnology, Japan). The content and purity of RNA were measured using NanoDrop 2000 (Thermo Fisher, United States). Total RNA (1 μg) was reverse-transcribed into cDNA using a PrimeScript TM RT reagent Kit (TaKaRa Biotechnology, Japan). Reverse-transcribed cDNA was subjected to quantitative real-time PCR (SYBR Premix Ex Taq, TaKaRa, Japan) using specific primers targeting *Sox 9*, collagen type II (*ColII*), collagen type I (*ColI*), and *GAPDH* according to the manufacturer's instructions. GAPDH was used as a housekeeping gene. The primer sequences of the target genes are shown in **Table 1**.

Immunofluorescence Staining and Analysis

Cell-loaded composite scaffolds were cultured in 24-well plates for 14 days, then immunofluorescence staining was used to visualize the deposition of Col I and Col II, respectively. Briefly, the samples were gently washed 3 times with PBS, fixed in 4% paraformaldehyde (PFA) for 15 min, and immersed in 0.1% Triton X-100 for 20 min. Then the samples were blocked with 5% bovine serum albumin (BSA) for 30 min and incubated overnight in a primary antibody solution diluted with 1% BSA in PBS with rabbit anti-Col I and rabbit anti-Col II (1:100, Abcam, USA) at 4°C. After washing 3 times with PBS, the scaffolds were incubated in the dark with the secondary antibody (1:200, Goat anti-rabbit IgG (H + L), Affinity, China) for 30 min. Finally, samples were stained with 4′,6-diamidino-2-phenylindole (Dapi, Beyotime, China) for 15 min in the dark. The images were taken using a confocal laser scanning microscope (Leica TCS SP8, Germany).

Biochemical Content Analysis

Cell-laden composite scaffolds were cultured in 24-well plates for 14 days, and the biochemical content of sulfated glycosaminoglycans (GAG) and collagen was assessed as described in a previous study (Romanazzo et al., 2018). Briefly, the scaffolds were digested in 1 ml of papain mixture (125 μg/ml papain in 0.1 M sodium acetate, 5 mM L-cysteine HCL, and 0.05 M EDTA) at 65°C for 18 h and then were centrifuged at 10,000 rpm for 10 min to collect supernatant for quantification tests. Using a chondroitin sulphate standard, the dimethylmethylene blue dye binding assay was utilized to quantify sulfated GAG. Total collagen was determined by measuring the hydroxyproline content. Samples were hydrolyzed at 110°C for 18 h in 38% HCl diluted in H_2O and then examined using a chloramine-T assay with a hydroxyproline:collagen ratio of 1:7.69.

Scaffolds Implantation and *In Vivo* Analysis

Cell-loaded composite scaffolds were implanted into subcutaneous pockets in the dorsal surface of 4-week-old female nude mice to compare the ability of chondrogenesis and fibrogenesis between modified groups and original groups. Briefly, cylindrical composite scaffolds with 5 mm in diameter and 1 mm in height were prepared as described above, and 2×10^6 cells were seeded on each scaffold to construct cell-laden composite scaffold. At 6 weeks after implantation, the mice were sacrificed and all implants were retrieved. Prior to sectioning, the implants were embedded in optimal cutting temperature (OCT) compound (Tissue-Tek®, Sakura, Japan) and then sectioned transversely at a thickness of 10 μm. Tissue sections were stained with Alcian blue (AB) and Picrosirius red (PR) to evaluate chondrogenesis and fibrogenesis of the scaffolds, respectively.

Statistical Analysis

All values were reported as mean ± standard deviation (mean ± SD). At least three samples per group were selected for statistical analysis. Statistical analysis was performed with GraphPad Prism 7 (GraphPad Software, Inc., La Jolla, CA). Statistical significance was analyzed using Student's t-test. The significant difference for all statistical analyses was defined as $p < 0.05$.

RESULTS

Characterization of the Scaffolds

A color change to dark brown in the modified groups indicated the successful surface modification with PDA coating. Microscopically, SEM analysis showed that surface morphology of the original scaffolds was remarkably altered

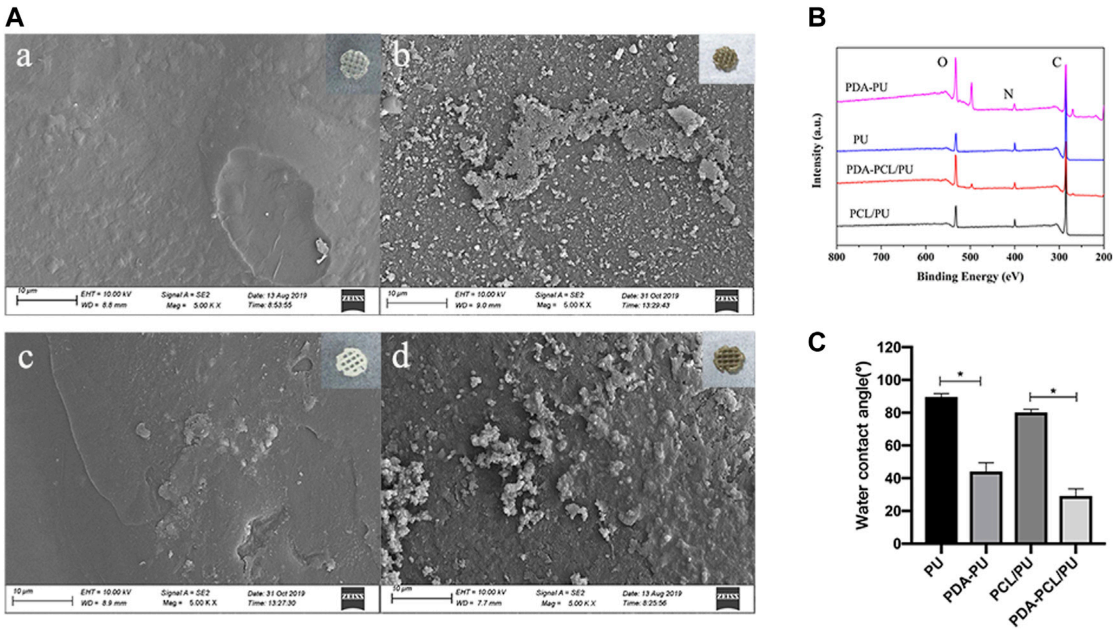

FIGURE 2 | Characterization of the 3D printed scaffolds. **(A)** SEM micrographs and gross images of the scaffolds: **(A)** PU; **(B)** PDA-PU; **(C)** PCL/PU; **(D)** PDA-PCL/PU. The gross images at the upper right corner. **(B)** XPS spectra of scaffolds. **(C)** Water contact angle of scaffolds (n = 3, **p* < 0.05).

TABLE 2 | Surface chemical composition of scaffolds.

Sample	C (%)	O (%)	N (%)	N/C
PU	83.26	11.37	5.36	0.06
PDA-PU	70.20	23.91	5.89	0.08
PCL/PU	80.63	14.40	4.97	0.06
PDA-PCL/PU	70.00	23.35	6.65	0.10

after PDA coating (**Figure 2A**). Compared with the smooth surfaces of original groups, spherical aggregates were observed on the surfaces in the modified groups.

The surface chemical compositions of the scaffolds were analyzed by XPS. The spectra showed the existence of carbon (C1s, 284.5 eV), oxygen (O1s, 531.0 eV), and nitrogen (N1s, 399.6 eV) atoms in all scaffolds (**Figure 2B**). The nitrogen/carbon (N/C) ratio in the modified groups was higher than that in the original groups, mainly because PDA contains a large number of nitrogen atoms (**Table 2**).

The water contact angle was measured to evaluate the efficiency of PDA attachment on original scaffolds. The surfaces of PCL/PU and PU scaffolds became relatively hydrophilic as shown with the significant decrease in water contact angle from 80.20° to 29.13° and 89.67° to 44.70°, after PDA coating (**Figure 2C**).

The tensile modulus and compressive modulus of the modified groups were significantly higher than those of the original groups ($p < 0.05$). The compression modulus of PDA-PCL/PU (15.970 Mpa) and PDA-PU (6.617 Mpa) scaffolds was similar to that of the middle region (about 15 Mpa) and the surrounding area (about 5 Mpa) of human TMJ disc, respectively (**Figure 3**).

Biocompatibility of the Scaffolds

The results of cell viability examined by LIVE/DEAD staining are shown in **Figure 4A**. The living cells, colored green, were the dominant population of seeded cells and primarily resided in the hydrogel at day 1 and day 7. As determined by the amount of green fluorescence, the cell density in the modified groups remarkably increased after 7 days of culture. The proliferation of costal chondrocytes and L929 cells in the scaffolds was evaluated by the CCK-8 assay (**Figures 4B,C**). The optical density (OD) values increased from day 1 to 7 in all groups, suggesting the composite scaffolds were suitable for cell growth and nutrient transmission. Significantly higher OD values can be found in modified groups compared to original groups at 4 and 7 days ($p < 0.05$), indicating that cell proliferation was enhanced by the PDA coating.

Cell Differentiation and Maturation

The expression level of chondrocyte and fibroblast marker genes was evaluated with qPCR after 14 days of culture. The modified groups exhibited significant upregulation of the chondrogenic-specific markers (*Sox 9 and Col II*) and fibrous-specific marker (*Col I*) compared with the original groups ($p < 0.05$) (**Figure 5**). These results indicated that the cell differentiation and maturation were promoted in the modified groups.

Immunofluorescence Staining and Biochemical Study

The presence of collagens in the cell-laden composite scaffolds after 14 days of culture was visualized by immunofluorescence staining. (**Figure 6**: Col-I [green] and Col-II [red]). The number

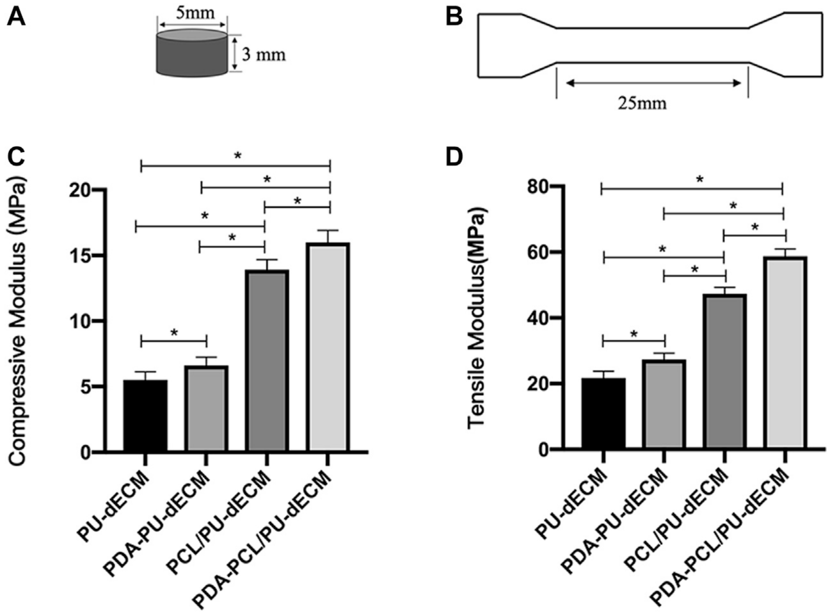

FIGURE 3 | Compressive and tensile modulus of the scaffolds. **(A)** Graphical representation of the compressive test specimen. **(B)** Graphical representation of the tensile test specimen. **(C)** Compressive modulus of the scaffolds. **(D)** Tensile modulus of the scaffolds. (* Comparison between groups, n = 5, $^*p < 0.05$).

of cells positive for Col I and Col II in the modified groups was remarkably higher than that in the original groups, suggesting larger amounts of collagens were synthesized in the modified groups. Quantification of collagen and GAG content was carried out using biochemical analysis and the result was shown in **Figure 7**. There were significantly greater amounts of collagen and GAG deposition in the modified groups than the original groups ($p < 0.05$). These results indicated that the surface modification with PDA was beneficial to the secretion of these two major components of the extracellular matrix.

In Vivo Cartilage and Fibrous Tissue Regeneration

Sirius red and Alcian blue are common methods for staining the extracellular matrix to identity fibroblasts and cartilage. Significant histological differences were observed between the modified and original groups at 6 weeks after implantation (**Figure 8**). The areas of hydrogel were filled with loose reticular red-stained fibroblast tissue or blue-stained cartilage tissue in the original groups. While the same areas in the modified groups were filled with regular dense fibrous or cartilage tissues, suggesting the PDA coating improved both chondrogenesis and fibrogenesis *in vivo*.

DISCUSSION

The goal of tissue engineering is to construct ideal scaffolds which can provide a microenvironment that facilitates the proliferation and differentiation of implanted cells by mimicking the natural ECM and that can provide suitable mechanical strength to meet the requirements of various tissues (Acri et al., 2019). The TMJ disc is a load-bearing tissue and subjected to complex mechanical forces during function, thus, the ability of an engineered disc to withstand anisotropic physiological forces is essential to successful regeneration. In this study, we fabricated a biomimetic composite system of 3D-printed synthetic polymers and dECM hydrogel for the reconstruction of TMJ disc. The compressive modulus of the PCL/PU and PU scaffolds was comparable to that of the central and peripheral zone of a native human TMJ disc, respectively. The PDA-coated composite constructs promoted chondrocyte and fibroblast attachment, proliferation, differentiation, and tissue regeneration. Therefore, the biomimetic composite system developed has the potential to be a promising substitute for damaged TMJ disc.

It has been reported that a tissue-specific ECM environment plays a critical role in regulating the cellular behaviors of cells, such as cell attachment, proliferation, and differentiation (Acri et al., 2019). In our prior study, porcine TMJ disc was processed into tissue-specific hydrogel that possessed outstanding biological properties and biocompatibility; however, weak mechanical strength prevented it from withstanding compression when implanted into a TMJ disc defect (Liang et al., 2020). Synthetic polymers are typically associated with improved mechanical properties and usually used as scaffolds to regenerate hard tissues (Aljohani et al., 2018). Recently, hybridization of natural and synthetic polymer materials is proven to be a promising approach to construct tissue-engineered scaffolds which combines the advantages of both materials and meets diverse requirements (Setayeshmehr et al., 2019). This strategy has been applied to fabricate a variety of hybrid scaffolds to regenerate various hard tissues (Haaparanta et al., 2014; Chen et al., 2019a; Chen et al., 2019b). Therefore, in

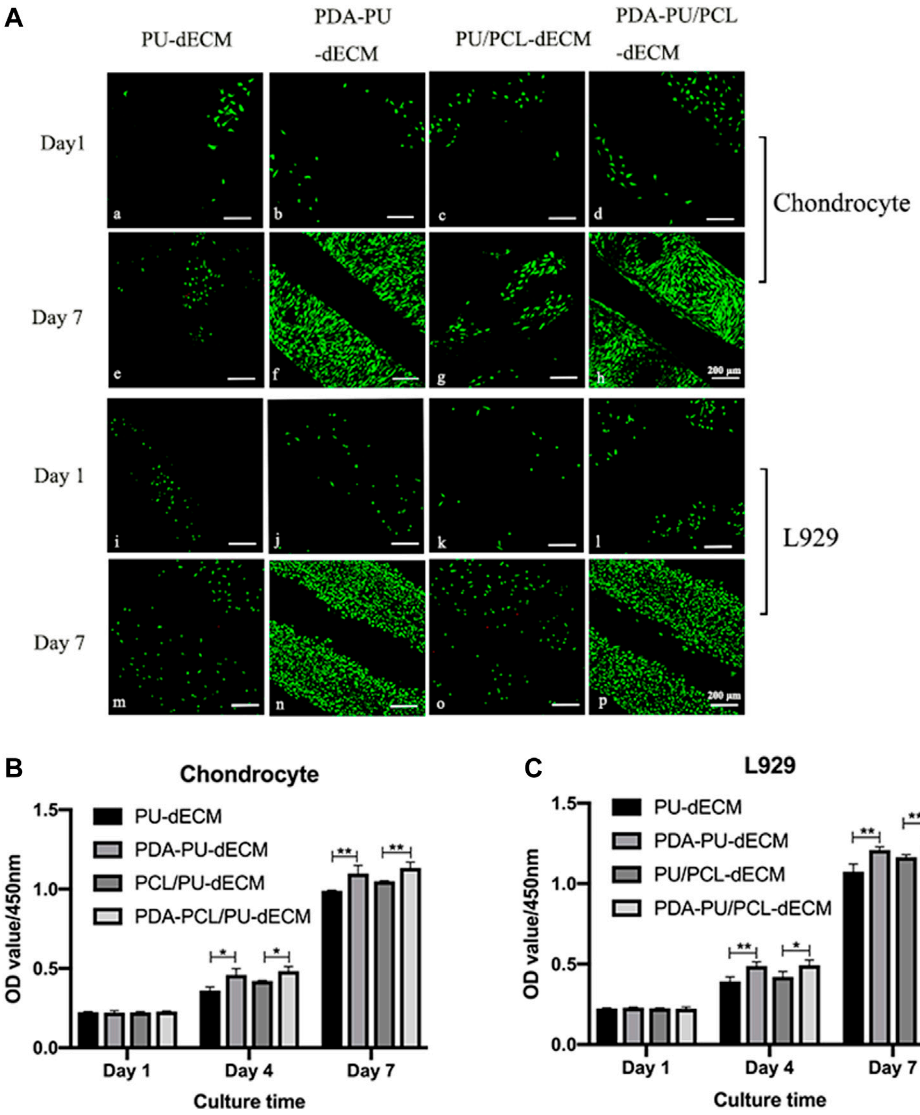

FIGURE 4 | Cell viability of the scaffolds. **(A)** LIVE/DEAD staining of the scaffolds: (a)-(h) chondrocyte, (i)-(p) L929. **(B,C)** Cell proliferation of the scaffolds. (*Comparison between original groups and modified groups, n = 3, $*p < 0.05$, $**p < 0.01$).

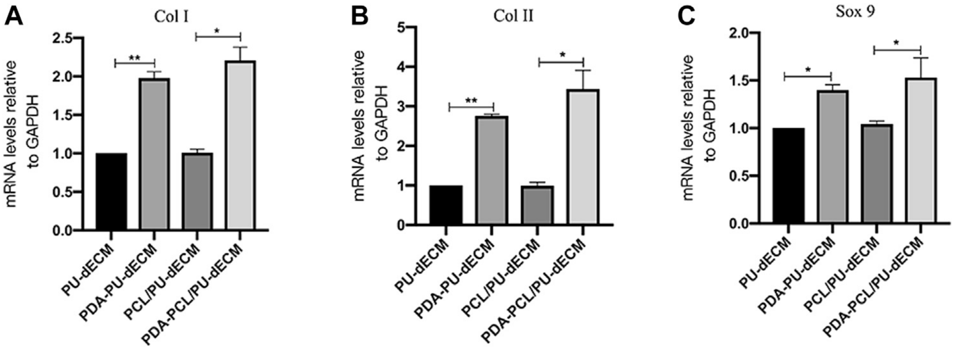

FIGURE 5 | Genes expression of the scaffolds. **(A)** *COL I*, **(B)** *COL II,* and **(C)** *SOX 9*. (*Comparison between original groups and modified groups, n = 3, $*p < 0.05$, $**p < 0.01$).

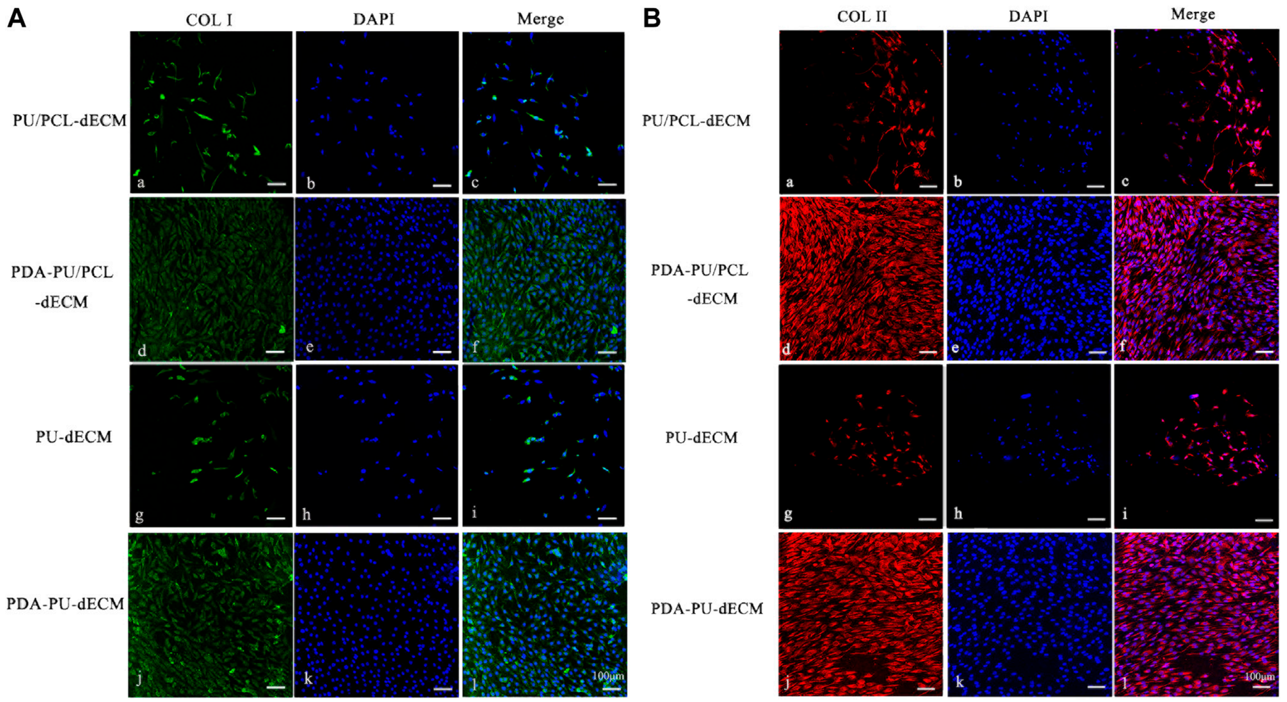

FIGURE 6 | Immunofluorescence staining images of the scaffolds. **(A)** COL I and **(B)** COL II.

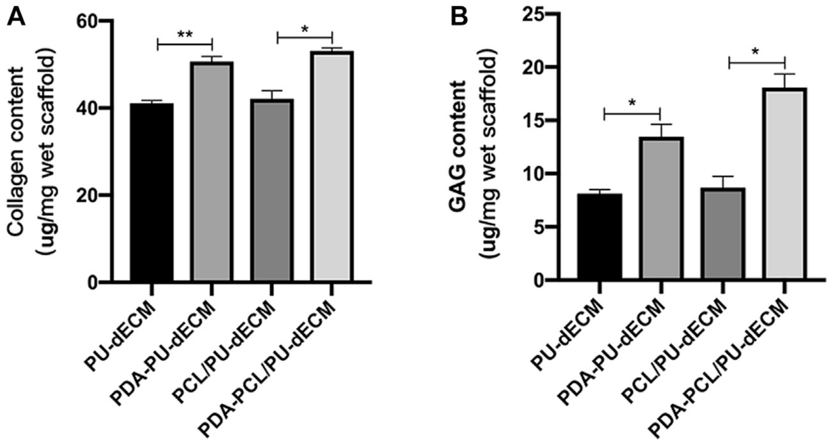

FIGURE 7 | Biochemical analysis for collagen and GAG quantification. **(A)** Collagen content of the scaffolds; **(B)** GAG content of the scaffolds. (*Comparison between original groups and modified groups, n = 3, *$p < 0.05$, **$p < 0.01$).

this study we chose polymer materials as the backbone of the composite scaffolds due to their excellent physical properties and TMJ disc-derived dECM hydrogel as a cell delivery system because of its superior biological properties, to engineer TMJ discs.

Compared with conventional approaches, 3D printing can produce specific implantable devices with architectural complexity that mimics that of the target tissue (Kumar et al., 2013). Although parameters vary according to the target tissue, pore sizes ranging from 200 to 350 μm are necessary to promote cellular activities such as cell proliferation, migration, and differentiation (Kim et al., 2018; Li et al., 2019). Thus, we constructed 3D printed scaffolds with a pore size of about 350 μm. 3D printed PU and PCL scaffolds have been widely used in hard tissue engineering because of their excellent biological performance and desirable physical properties which can be tailored for specific applications (Wen et al., 2019; Han et al., 2020). However, PCL and PU exhibit poor cell attachment

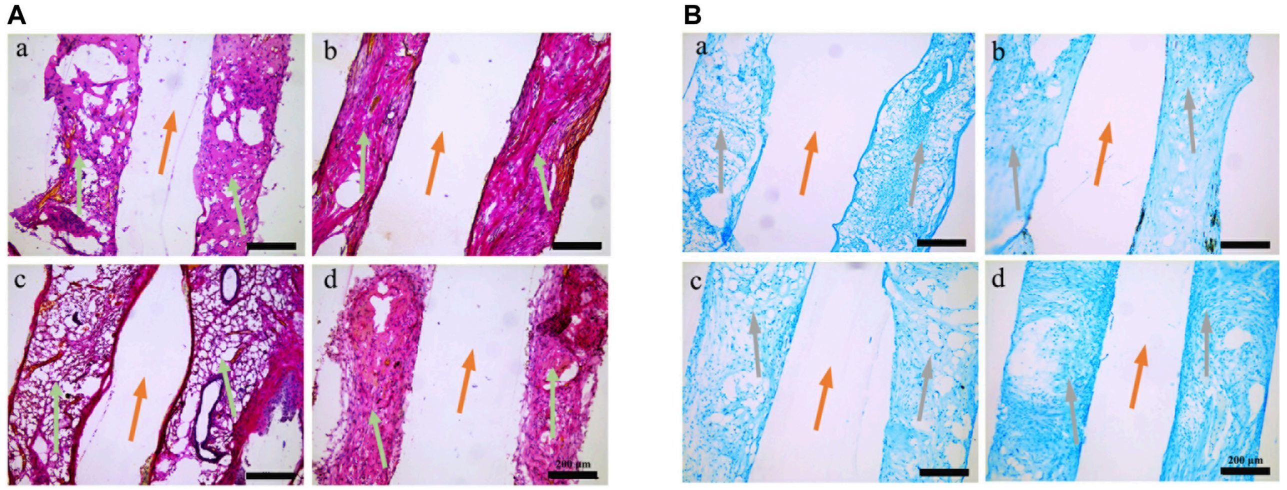

FIGURE 8 | Histological analysis of the scaffolds retrieved from nude mice. **(A)** Picrosirius red staining. **(B)** Alcian blue staining. **(a)** PU-dECM; **(b)** PDA-PU- dECM; **(c)** PCL/PU-dECM; **(d)** PDA-PCL/PU- dECM. Orange arrows, 3D printed scaffolds framework lines; green arrows, collagen positively stained red with Picrosirius red; grey arrows, GAG positively stained blue with Alcian blue.

due to their hydrophobic properties and lack of biological cell recognition. Recently, it has been suggested that PDA coating can improve the hydrophobicity of PCL and PU and also significantly facilitate cell adhesion (Ghorbani et al., 2020). In this study, we modified the surface of the scaffolds with PDA coating to provide a more cell-friendly polymeric surface, and success of surface modification was confirmed by SEM and XPS. Previous studies indicated that increased surface roughness can be ascribed to the thorough distribution of submicron-sized particulates following PDA coating by atomic force microscopic analysis (Ju et al., 2011; Shin et al., 2011). The increased nitrogen/carbon ratio in modified groups was also confirmed by a previous study which revealed the presence of nitrogen peaks corresponding to primary amine groups present in the polydopamine structure (Shin et al., 2011). The decreased static contact angle in modified groups manifested that PDA coating led to improved hydrophilicity of the materials. Actually, the hydrophilicity can be increased independent of the underlying substrate's surface chemistry (Madhurakkat Perikamana et al., 2015). The enhanced mechanical properties in modified groups can be explained by the fact that DOPA contributes to cohesive strength through self-polymerization, which improves the overall mechanical strength of the composite scaffold (Zhao et al., 2018). In addition, a 600 nm PDA layer formed on scaffold surface maintained the optimal pore size of scaffold to facilitate cell infiltration and nutrition supply (Ma et al., 2016). Therefore, PDA coating is a promising approach to functionalize biomaterials by changing their physiochemical properties.

Chondrocytes, fibroblasts, and a combination of both have been widely used to evaluate the suitability of scaffolds for fibrocartilage tissue repair and regeneration (Vanderploeg et al., 2004; Singh et al., 2011). Thus, in this study rat costal chondrocytes and L929 fibroblasts were used to evaluate the biofunctions and biocompatibility of the composite scaffolds *in vitro* and *in vivo*. The LIVE/DEAD test and CCK-8 assay showed that surface modification significantly enhanced cell adhesion and proliferation in modified groups. Previous studies have confirmed that the adhesion and proliferation of chondroblasts and fibroblasts can be improved by topological changes of the material surface (den Braber et al., 1995; Boyan et al., 1996). It was suggested that amine groups contained in PDA confer hydrophilicity and positive charge to substrates (Madhurakkat Perikamana et al., 2015). Furthermore, highly reactive amine groups can undergo secondary conjugation with various biomacromolecules in the culture medium and TMJ disc dECM hydrogel, which further facilitate cell adhesion and other biofunctions. Therefore, the deposition of polydopamine on the scaffold surface provided a favorable biomimetic ECM microenvironment, improving a range of cell metabolic functions.

The TMJ disc contains a heterogeneous collection of morphologically variable cells with characteristics of fibroblasts and chondrocytes. Selection of cell sources is of paramount importance for TMJ disc tissue engineering (Donahue et al., 2019). Besides various stem cells used to engineer the TMJ disc, the combination of costal cartilage and fibroblast was advocated to be a promising cell source due to relative tissue abundance and surgical accessibility (Huwe et al., 2018; Vapniarsky et al., 2018). In our study, the enhanced gene expression and protein deposition of collagens in modified groups were verified by qPCR and immunofluorescence staining. Collagen I and II are considered as the phenotypic markers of fibroblasts and chondrocytes, and the expression levels can be used to represent the differentiation and maturation of these two cells. As a pivotal transcription factor that plays a dominant role in chondrogenesis and chondrocyte differentiation pathways, *Sox9* is required to enhance chondrocyte survival, maintain expression of cartilage-specific markers already active, such as Col II, and activate markers of overtly differentiated chondrocytes (Lefebvre and Dvir-Ginzberg, 2017). The elevated expression of these tissue-specific markers in modified groups indicated the increased fibrogenesis and chondrogenesis following PDA coating. Collagen and GAG are the primary biochemical constituents that impart tensile and compressive strength to the TMJ disc (Lowe and Almarza, 2017). Thus, the higher level of collagen and GAG deposition can be associated to reinforced mechanical properties of the cell-laden composite scaffolds in the modified groups. Increased fibrogenesis and chondrogenesis *in vivo* can also be observed in the modified groups with Sirius red and Alcian blue staining. These histological results were consistent with our previous results which revealed enhanced cell adhesion, proliferation, differentiation, and maturation following PDA coating.

Although we have constructed a biomimetic cell-laden composite scaffold for engineering of TMJ disc, there are still some hurdles that need to be overcome to achieve ideal TMJ disc regeneration. First, polymeric scaffolds mimicking the complex geometric shape and region-specific mechanical properties of TMJ disc should be tailored by multiple-tool biofabrication strategies based on the image of MRI (Barbieri et al., 2020). Second, we have confirmed the fibrogenesis and chondrogenesis of the cell-laden composite scaffolds in nude mice; however, the successful regeneration of TMJ disc should be evaluated in physiologically mechanical environment by orthotopic implantation of these scaffolds in big animal model, such as mini pig (Helgeland et al., 2018). Third, the degradation velocity and mechanical strength of the polymeric scaffolds and hydrogel did not match each other perfectly, and these discrepancies probably compromised the biological and mechanical performance of the composite scaffolds in functional environment *in vivo*. Therefore, further study should focus on improving physical properties of these biomaterials to construct an ideal biomimetic substitute for TMJ disc tissue engineering (Kundu et al., 2015; Rothrauff et al., 2018).

CONCLUSION

In this study, a biomimetic composite scaffold was developed by combining 3D printed polymeric scaffolds and TMJ disc dECM hydrogel, and the biological and biomechanical properties of this scaffold were characterized. PDA-coated composite scaffolds possessed superior biomechanical properties and created a favorable microenvironment for cell adhesion, proliferation, differentiation, and maturation. The increased fibrogenesis and chondrogenesis of the cell-laden composite scaffolds *in vitro* and *in vivo* provided evidence of a promising strategy for TMJ disc regeneration. Overall, these results demonstrated that the biomimetic composite scaffold has therapeutic potential for TMJ disc engineering and regeneration.

DATA AVAILABILITY STATEMENT

The raw data supporting the conclusions of this article will be made available by the authors, without undue reservation.

ETHICS STATEMENT

The animal study was reviewed and approved by Guangzhou Medical University.

AUTHOR CONTRIBUTIONS

CL contributed to conception and design of the study; PY performed most of the experiments; JL carried out data analysis. All authors participated in drafting of the manuscript and critical revision of the draft. All authors have read and approved the final version of the manuscript.

FUNDING

This work was supported by the National Natural Science Foundation of China (31900946).

ACKNOWLEDGMENTS

The authors thank the Laboratory of Stomatology Hospital of Guangzhou Medical University for technical support.

REFERENCES

Abdala-Junior, R., Cortes, A. R. G., Aoki, E. M., Ferreira, S., Luz, J. G. C., Arita, E. S., et al. (2018). Impact of temporomandibular joint discectomy on condyle morphology: an animal study. *J. Oral Maxillofac. Surg.* 76 (5), 955 e951–955 e955. doi:10.1016/j.joms.2017.12.019

Acri, T. M., Shin, K., Seol, D., Laird, N. Z., Song, I., Geary, S. M., et al. (2019). Tissue engineering for the temporomandibular joint. *Adv Healthc Mater.* 8 (2), e1801236. doi:10.1002/adhm.201801236

Aljohani, W., Ullah, M. W., Zhang, X., and Yang, G. (2018). Bioprinting and its applications in tissue engineering and regenerative medicine. *Int. J. Biol. Macromol.* 107 (Part A), 261–275. doi:10.1016/j.ijbiomac.2017.08.171

Bahcecioglu, G., Hasirci, N., Bilgen, B., and Hasirci, V. (2019). A 3D printed PCL/hydrogel construct with zone-specific biochemical composition mimicking that of the meniscus. *Biofabrication* 11 (2), 025002. doi:10.1088/1758-5090/aaf707

Barbero, A., Grogan, S., Schafer, D., Heberer, M., Mainil-Varlet, P., and Martin, I. (2004). Age related changes in human articular chondrocyte yield, proliferation and post-expansion chondrogenic capacity. *Osteoarthritis Cartilage* 12 (6), 476–484. doi:10.1016/j.joca.2004.02.010

Barbieri, A. A., Costa, A. L. F., Perez Gomes, J. P., Ricardo, A. L. F., Braz-Silva, P. H., and Lopes, S. (2020). Association of volume and voxel intensity of the articular disc and lateral pterygoid muscle in migraine patients: a study with magnetic resonance imaging. *Acta Odontol. Scand.* 78 (3), 189–195. doi:10.1080/00016357.2019.1676917

Bock, N., Pham, T. L., Nguyen, T. B., Nguyen, T. B., Tran, H. A., and Tran, P. A. (2020). Polydopamine coating of uncrosslinked chitosan as an acellular scaffold for full thickness skin grafts. *Carbohydr. Polym.* 245, 116524. doi:10.1016/j.carbpol.2020.116524

Bousnaki, M., Bakopoulou, A., Papadogianni, D., Barkoula, N. M., Alpantaki, K., Kritis, A., et al. (2018). Fibro/chondrogenic differentiation of dental stem cells into chitosan/alginate scaffolds towards temporomandibular joint disc regeneration. *J. Mater. Sci. Mater. Med.* 29 (7), 97. doi:10.1007/s10856-018-6109-6

Boyan, B. D., Hummert, T. W., Dean, D. D., and Schwartz, Z. (1996). Role of material surfaces in regulating bone and cartilage cell response. *Biomaterials.* 17 (2), 137–146. doi:10.1016/0142-9612(96)85758-9

Brown, B. N., Chung, W. L., Almarza, A. J., Pavlick, M. D., Reppas, S. N., Ochs, M. W., et al. (2012). Inductive, scaffold-based, regenerative medicine approach to reconstruction of the temporomandibular joint disk. *J. Oral Maxillofac. Surg.* 70 (11), 2656–2668. doi:10.1016/j.joms.2011.12.030

Capellato, P., Camargo, S. E. A., and Sachs, D. (2020). Biological response to nanosurface modification on metallic biomaterials. *Curr. Osteoporos. Rep.* 18 (6), 790–795. doi:10.1007/s11914-020-00635-x

Chen, M., Feng, Z., Guo, W., Yang, D., Gao, S., Li, Y., et al. (2019a). PCL-MECM-based hydrogel hybrid scaffolds and meniscal fibrochondrocytes promote whole meniscus regeneration in a rabbit meniscectomy model. *ACS Appl. Mater. Interfaces* 11 (44), 41626–41639. doi:10.1021/acsami.9b13611

Chen, Y., Lee, K., Kawazoe, N., Yang, Y., and Chen, G. (2019b). PLGA-collagen-ECM hybrid scaffolds functionalized with biomimetic extracellular matrices secreted by mesenchymal stem cells during stepwise osteogenesis-co-adipogenesis. *J. Mater. Chem. B.* 7 (45), 7195–7206. doi:10.1039/c9tb01959f

Daly, A. C., Freeman, F. E., Gonzalez-Fernandez, T., Critchley, S. E., Nulty, J., and Kelly, D. J. (2017). 3D bioprinting for cartilage and osteochondral tissue engineering. *Adv Healthc Mater.* 6 (22), 1700298. doi:10.1002/adhm.201700298

den Braber, E. T., de Ruijter, J. E., Smits, H. T., Ginsel, L. A., von Recum, A. F., and Jansen, J. A. (1995). Effect of parallel surface microgrooves and surface energy on cell growth. *J. Biomed. Mater. Res.* 29 (4), 511–518. doi:10.1002/jbm.820290411

Dimitroulis, G. (2011). A critical review of interpositional grafts following temporomandibular joint discectomy with an overview of the dermis-fat graft. *Int. J. Oral Maxillofac. Surg.* 40 (6), 561–568. doi:10.1016/j.ijom.2010.11.020

Dolwick, M. F. (2007). Temporomandibular joint surgery for internal derangement. *Dent. Clin.* 51 (1), 195–208. doi:10.1016/j.cden.2006.10.003

Donahue, R. P., Hu, J. C., and Athanasiou, K. A. (2019). Remaining hurdles for tissue-engineering the temporomandibular joint disc. *Trends Mol. Med.* 25 (3), 241–256. doi:10.1016/j.molmed.2018.12.007

Eiji, T., and Theo, V. E. (2003). Biomechanical behavior of the temporomandibular joint disc. *Crit. Rev. Oral Biol. Med.* 14 (2), 138–150.

Eriksson, L., and Westesson, P. L. (1992). Temporomandibular joint diskectomy. No positive effect of temporary silicone implant in a 5-year follow-up. *Oral Surg. Oral Med. Oral Pathol.* 74 (3), 259–272. doi:10.1016/0030-4220(92)90056-v

Ghorbani, F., Ghalandari, B., Khan, A. L., Li, D., Zamanian, A., and Yu, B. (2020). Decoration of electrical conductive polyurethane-polyaniline/polyvinyl alcohol matrixes with mussel-inspired polydopamine for bone tissue engineering. *Biotechnol. Prog.* 36 (6), e3043. doi:10.1002/btpr.3043

Godoy-Gallardo, M., Portoles-Gil, N., Lopez-Periago, A. M., Domingo, C., and Hosta-Rigau, L. (2020). Multi-layered polydopamine coatings for the immobilization of growth factors onto highly-interconnected and bimodal PCL/HA-based scaffolds. *Mater Sci. Eng. C Mater Biol. Appl.* 117, 111245. doi:10.1016/j.msec.2020.111245

Gonçalves, D., Camparis, C., Speciali, J., Franco, A., Castanharo, S., and Bigal, M. (2011). Temporomandibular disorders are differentially associated with headache diagnoses: a controlled study. *Clin. J. Pain* 27 (7), 611–615. doi:10.1097/AJP.0b013e31820e12f5

Haaparanta, A. M., Jarvinen, E., Cengiz, I. F., Ella, V., Kokkonen, H. T., Kiviranta, I., et al. (2014). Preparation and characterization of collagen/PLA, chitosan/PLA, and collagen/chitosan/PLA hybrid scaffolds for cartilage tissue engineering. *J. Mater. Sci. Mater. Med.* 25 (4), 1129–1136. doi:10.1007/s10856-013-5129-5

Han, Y., Lian, M., Sun, B., Jia, B., Wu, Q., Qiao, Z., et al. (2020). Preparation of high precision multilayer scaffolds based on Melt Electro-Writing to repair cartilage injury. *Theranostics* 10 (22), 10214–10230. doi:10.7150/thno.47909

Helgeland, E., Shanbhag, S., Pedersen, T. O., Mustafa, K., and Rosen, A. (2018). Scaffold-based temporomandibular joint tissue regeneration in experimental animal models: a systematic review. *Tissue Eng. B Rev.* 24 (4), 300–316. doi:10.1089/ten.TEB.2017.0429

Huwe, L. W., Brown, W. E., Hu, J. C., and Athanasiou, K. A. (2018). Characterization of costal cartilage and its suitability as a cell source for articular cartilage tissue engineering. *J Tissue Eng Regen Med.* 12 (5), 1163–1176. doi:10.1002/term.2630

Jo, S., Kang, S. M., Park, S. A., Kim, W. D., Kwak, J., and Lee, H. (2013). Enhanced adhesion of preosteoblasts inside 3D PCL scaffolds by polydopamine coating and mineralization. *Macromol. Biosci.* 13 (10), 1389–1395. doi:10.1002/mabi.201300203

Ju, K. Y., Lee, Y., Lee, S., Park, S. B., and Lee, J. K. (2011). Bioinspired polymerization of dopamine to generate melanin-like nanoparticles having an excellent free-radical-scavenging property. *Biomacromolecules* 12 (3), 625–632. doi:10.1021/bm101281b

Kim, J. Y., Ahn, G., Kim, C., Lee, J. S., Lee, I. G., An, S. H., et al. (2018). Synergistic effects of beta tri-calcium phosphate and porcine-derived decellularized bone extracellular matrix in 3D-printed polycaprolactone scaffold on bone regeneration. *Macromol. Biosci.* 18 (6), e1800025. doi:10.1002/mabi.201800025

Kobayashi, E., Nakahara, T., Inoue, M., Shigeno, K., and Nakamura, T. (2015). Experimental study on *in situ* tissue engineering of the temporomandibular joint disc using autologous bone marrow and collagen sponge scaffold. *J. Hard Tissue Biol.* 24 (2), 211–218. doi:10.2485/jhtb.24.211

Kumar, A., Webster, T. J., Biswas, K., and Basu, B. (2013). Flow cytometry analysis of human fetal osteoblast fate processes on spark plasma sintered hydroxyapatite-titanium biocomposites. *J. Biomed. Mater. Res.* 101 (10), 2925–2938. doi:10.1002/jbm.a.34603

Kundu, J., Shim, J. H., Jang, J., Kim, S. W., and Cho, D. W. (2015). An additive manufacturing-based PCL-alginate-chondrocyte bioprinted scaffold for cartilage tissue engineering. *J Tissue Eng Regen Med.* 9 (11), 1286–1297. doi:10.1002/term.1682

Lee, C. H., Rodeo, S. A., Fortier, L. A., Lu, C., Erisken, C., and Mao, J. J. (2014). Protein-releasing polymeric scaffolds induce fibrochondrocytic differentiation of endogenous cells for knee meniscus regeneration in sheep. *Sci. Transl. Med.* 6 (266), 266ra171. doi:10.1126/scitranslmed.3009696

Lefebvre, V., and Dvir-Ginzberg, M. (2017). SOX9 and the many facets of its regulation in the chondrocyte lineage. *Connect. Tissue Res.* 58 (1), 2–14. doi:10.1080/03008207.2016.1183667

Legemate, K., Tarafder, S., Jun, Y., and Lee, C. (2016). Engineering human TMJ discs with protein-releasing 3D-printed scaffolds. *J. Dent. Res.* 95 (7), 800–807. doi:10.1177/0022034516642404

Li, J., Yao, Q., Xu, Y., Zhang, H., Li, L. L., and Wang, L. (2019). Lithium chloride-releasing 3D printed scaffold for enhanced cartilage regeneration. *Med. Sci. Monit.* 25, 4041–4050. doi:10.12659/MSM.916918

Liang, J., Yi, P., Wang, X., Huang, F., Luan, X., Zhao, Z., et al. (2020). Acellular matrix hydrogel for repair of the temporomandibular joint disc. *J. Biomed. Mater. Res. B Appl. Biomater.* 108 (7), 2995–3007. doi:10.1002/jbm.b.34629

Lim, P. F., and Sbhalang, S. (2010). Development of temporomandibular disorders is associated with greater bodily pain experience. *Clin. J. Pain* 26 (2), 116–120. doi:10.1097/AJP.0b013e3181c507ef

Lowe, J., and Almarza, A. J. (2017). A review of *in-vitro* fibrocartilage tissue engineered therapies with a focus on the temporomandibular joint. *Arch. Oral Biol.* 83, 193–201. doi:10.1016/j.archoralbio.2017.07.013

Ma, H., Luo, J., Sun, Z., Xia, L., Shi, M., Liu, M., et al. (2016). 3D printing of biomaterials with mussel-inspired nanostructures for tumor therapy and tissue regeneration. *Biomaterials* 111, 138–148. doi:10.1016/j.biomaterials.2016.10.005

Madhurakkat Perikamana, S. K., Lee, J., Lee, Y. B., Shin, Y. M., Lee, E. J., Mikos, A. G., et al. (2015). Materials from mussel-inspired chemistry for cell and tissue engineering applications. *Biomacromolecules* 16 (9), 2541–2555. doi:10.1021/acs.biomac.5b00852

Miloro, M., and Henriksen, B. (2010). Discectomy as the primary surgical option for internal derangement of the temporomandibular joint. *J. Oral Maxillofac. Surg.* 68 (4), 782–789. doi:10.1016/j.joms.2009.09.091

Moura, C., Trindade, D., Vieira, M., Francisco, L., Angelo, D. F., and Alves, N. (2020). Multi-material implants for temporomandibular joint disc repair:

tailored additive manufacturing production. *Front Bioeng Biotechnol.* 8, 342. doi:10.3389/fbioe.2020.00342

Pina, S., Ribeiro, V. P., Marques, C. F., Maia, F. R., Silva, T. H., Reis, R. L., et al. (2019). Scaffolding strategies for tissue engineering and regenerative medicine applications. *Materials* 12 (11). doi:10.3390/ma12111824

Qian, Y., Zhao, X., Han, Q., Chen, W., Li, H., and Yuan, W. (2018). An integrated multi-layer 3D-fabrication of PDA/RGD coated graphene loaded PCL nanoscaffold for peripheral nerve restoration. *Nat. Commun.* 9 (1), 323. doi:10.1038/s41467-017-02598-7

Qiu, W. Z., Yang, H. C., and Xu, Z. K. (2018). Dopamine-assisted co-deposition: an emerging and promising strategy for surface modification. *Adv. Colloid Interface Sci.* 256, 111–125. doi:10.1016/j.cis.2018.04.011

Renapurkar, S. K. (2018). Discectomy versus disc preservation for internal derangement of the temporomandibular joint. *Oral Maxillofac. Surg. Clin.* 30 (3), 329–333. doi:10.1016/j.coms.2018.05.002

Richbourg, N. R., Peppas, N. A., and Sikavitsas, V. I. (2019). Tuning the biomimetic behavior of scaffolds for regenerative medicine through surface modifications. *J. Tissue Eng Regen Med.* 13 (8), 1275–1293. doi:10.1002/term.2859

Romanazzo, S., Vedicherla, S., Moran, C., and Kelly, D. J. (2018). Meniscus ECM-functionalised hydrogels containing infrapatellar fat pad-derived stem cells for bioprinting of regionally defined meniscal tissue. *J. Tissue Eng Regen Med.* 12 (3), e1826–e1835. doi:10.1002/term.2602

Rothrauff, B. B., Coluccino, L., Gottardi, R., Ceseracciu, L., Scaglione, S., Goldoni, L., et al. (2018). Efficacy of thermoresponsive, photocrosslinkable hydrogels derived from decellularized tendon and cartilage extracellular matrix for cartilage tissue engineering. *J. Tissue Eng. Regen. Med.* 12 (1), e159–e170. doi:10.1002/term.2465

Setayeshmehr, M., Esfandiari, E., Rafieinia, M., Hashemibeni, B., Taheri-Kafrani, A., Samadikuchaksaraei, A., et al. (2019). Hybrid and composite scaffolds based on extracellular matrices for cartilage tissue engineering. *Tissue Eng. B Rev.* 25 (3), 202–224. doi:10.1089/ten.TEB.2018.0245

Shin, Y. M., Lee, Y. B., and Shin, H. (2011). Time-dependent mussel-inspired functionalization of poly(L-lactide-co-varepsilon-caprolactone) substrates for tunable cell behaviors. *Colloids Surf. B Biointerfaces* 87 (1), 79–87. doi:10.1016/j.colsurfb.2011.05.004

Singh, M., Pierpoint, M., Mikos, A. G., and Kasper, F. K. (2011). Chondrogenic differentiation of neonatal human dermal fibroblasts encapsulated in alginate beads with hydrostatic compression under hypoxic conditions in the presence of bone morphogenetic protein-2. *J. Biomed. Mater. Res.* 98 (3), 412–424. doi:10.1002/jbm.a.33129

Tamay, D. G., Dursun Usal, T., Alagoz, A. S., Yucel, D., Hasirci, N., and Hasirci, V. (2019). 3D and 4D printing of polymers for tissue engineering applications. *Front. Bioeng. Biotechnol.* 7, 164. doi:10.3389/fbioe.2019.00164

Tarafder, S., Koch, A., Jun, Y., Chou, C., Awadallah, M. R., and Lee, C. H. (2016). Micro-precise spatiotemporal delivery system embedded in 3D printing for complex tissue regeneration. *Biofabrication* 8 (2), 025003. doi:10.1088/1758-5090/8/2/025003

Theodoridis, K., Aggelidou, E., Manthou, M., Demiri, E., Bakopoulou, A., and Kritis, A. (2019). Assessment of cartilage regeneration on 3D collagen-polycaprolactone scaffolds: evaluation of growth media in static and in perfusion bioreactor dynamic culture. *Colloids Surf. B Biointerfaces* 183, 110403. doi:10.1016/j.colsurfb.2019.110403

Vanderploeg, E. J., Imler, S. M., Brodkin, K. R., Garcia, A. J., and Levenston, M. E. (2004). Oscillatory tension differentially modulates matrix metabolism and cytoskeletal organization in chondrocytes and fibrochondrocytes. *J. Biomech.* 37 (12), 1941–1952. doi:10.1016/j.jbiomech.2004.02.048

Vapniarsky, N., Huwe, L. W., Arzi, B., Houghton, M. K., Wong, M. E., Wilson, J. W., et al. (2018). Tissue engineering toward temporomandibular joint disc regeneration. *Sci. Transl. Med.* 10 (446). doi:10.1126/scitranslmed.aaq1802

Wang, C., Wang, S., Zhang, B., Zhang, X., Tong, X., Peng, H., et al. (2018). Layering Poly (lactic-co-glycolic acid)-based electrospun membranes and co-culture cell sheets for engineering temporomandibular joint disc. *J. Biol. Regul. Homeost. Agents.* 32 (1), 55–61.

Wei, P., Xu, Y., Gu, Y., Yao, Q., Li, J., and Wang, L. (2020). IGF-1-releasing PLGA nanoparticles modified 3D printed PCL scaffolds for cartilage tissue engineering. *Drug Deliv.* 27 (1), 1106–1114. doi:10.1080/10717544.2020.1797239

Wen, Y. T., Dai, N. T., and Hsu, S. H. (2019). Biodegradable water-based polyurethane scaffolds with a sequential release function for cell-free cartilage tissue engineering. *Acta. Biomater.* 88, 301–313. doi:10.1016/j.actbio.2019.02.044

Wu, Y., Gong, Z., Li, J., Meng, Q., Fang, W., and Long, X. (2014). The pilot study of fibrin with temporomandibular joint derived synovial stem cells in repairing TMJ disc perforation. *BioMed Res. Int.* 2014, 454021. doi:10.1155/2014/454021

Zhao, X. G., Hwang, K.-J., Lee, D., Kim, T., and Kim, N. (2018). Enhanced mechanical properties of self-polymerized polydopamine-coated recycled PLA filament used in 3D printing. *Appl. Surf. Sci.* 441, 381–387. doi:10.1016/j.apsusc.2018.01.257

Zhu, Y., Gao, C., and Shen, J. (2002). Surface modification of polycaprolactone with poly(methacrylic acid) and gelatin covalent immobilization for promoting its cytocompatibility. *Biomaterials* 23 (24), 4889–4895. doi:10.1016/s0142-9612(02)00247-8

Conflict of Interest: The authors declare that the research was conducted in the absence of any commercial or financial relationships that could be construed as a potential conflict of interest.

frontiers in Materials

ORIGINAL RESEARCH
published: 21 June 2021
doi: 10.3389/fmats.2021.642135

The Optimization of Ti Gradient Porous Structure Involves the Finite Element Simulation Analysis

Bowen Liu[1], Wei Xu[1,2], Xin Lu[1]*, Maryam Tamaddon[2], Mingying Chen[1], Jiaqi Dong[1], Yitong Liu[3], Lijia Guo[3], Jiazhen Zhang[1], Xuanhui Qu[1], Xinbo He[1] and Chaozong Liu[2]*

[1]Beijing Advanced Innovation Center for Materials Genome Engineering, Institute for Advanced Materials and Technology, State Key Laboratory for Advanced Metals and Materials, University of Science and Technology Beijing, Beijing, China, [2]Division of Surgery and Interventional Science, University College London, Royal National Orthopaedic Hospital, Stanmore, United Kingdom, [3]Capital Medical University School of Basic Medical Sciences, Beijing, China

Titanium (Ti) and its alloys are attracting special attention in the field of dentistry and orthopedic bioengineering because of their mechanical adaptability and biological compatibility with the natural bone. The dental implant is subjected to masticatory forces in the oral environment and transfers these forces to the surrounding bone tissue. Therefore, by simulating the mechanical behavior of implants and surrounding bone tissue we can assess the effects of implants on bone growth quite accurately. In this study, dental implants with different gradient pore structures that consisted of simple cubic (structure a), body centered cubic (structure b) and side centered cubic (structure c) were designed, respectively. The strength of the designed gradient porous implant in the oral environment was simulated by three-dimensional finite element simulation technique to assess the mechanical adaptation by the stress-strain distribution within the surrounding bone tissue and by examining the fretting of the implant-bone interface. The results show that the maximum equivalent stress and strain in the surrounding bone tissue increase with the increase of porosity. The stress distribution of the gradient implant with a smaller difference between outer and inner pore structure is more uniform. So, a-b type porous implant exhibited less stress concentration. For a-b structure, when the porosity is between 40 and 47%, the stress and strain of bone tissue are in the range of normal growth. When subject to lingual and buccal stresses, an implant with higher porosity can achieve more uniform stress distribution in the surrounding cancellous bone than that of low porosity implant. Based on the simulated results, to achieve an improved mechanical fixation of the implant, the optimum gradient porous structure parameters should be: average porosity 46% with an inner porosity of 13% (b structure) and outer porosity of 59% (a structure), and outer pore sized 500 μm. With this optimized structure, the bone can achieve optimal ingrowth into the gradient porous structure, thus provide stable mechanical fixation of the implant. The maximum equivalent stress achieved 99 MPa, which is far below the simulation yield strength of 299 MPa.

Keywords: titanium, gradient porosity, oral implants, three-dimensional finite element simulation, bone stress

OPEN ACCESS

Edited by:
Bing Han,
Peking University School and Hospital of Stomatology, China

Reviewed by:
Qiang Chen,
Southeast University, China
Sarabjeet Singh Sidhu,
Beant College of Engineering and Technology, India

***Correspondence:**
Xin Lu
luxin@ustb.edu.cn
Chaozong Liu
chaozong.liu@ucl.ac.uk

Specialty section:
This article was submitted to Biomaterials,
a section of the journal Frontiers in Materials

Received: *15 December 2020*
Accepted: *08 June 2021*
Published: *21 June 2021*

Citation:
Liu B, Xu W, Lu X, Tamaddon M, Chen M, Dong J, Liu Y, Guo L, Zhang J, Qu X, He X and Liu C (2021) The Optimization of Ti Gradient Porous Structure Involves the Finite Element Simulation Analysis.
Front. Mater. 8:642135.
doi: 10.3389/fmats.2021.642135

INTRODUCTION

Titanium and its alloy materials have been extensively researched and applied in the field of medical materials due to their good mechanical properties, as well as good biocompatibility and corrosion resistance (He et al., 2012; Yavari et al., 2013; Wally et al., 2019)' compared with other traditional medical metallic materials. Since they have high specific strength and low elastic modulus they can be used as the preferred material for human hard tissue substitutes (Lewis, 2013; Chia and Wu, 2015; Tane et al., 2016). However, most of the medical titanium implants currently used on the market are solid structures; Compared to bone tissue, the dense titanium still has a higher elastic modulus, which produces a larger stress shield and leads to bone tissue resorption. Therefore, the development of porous titanium implants has effectively addresses this shortcoming (Taniguchi et al., 2016). In addition, the interconnecting pores are also conducive to the adhesion and growth of osteoblasts and the transportation of body fluids and nutrients. According to statistics, the optimal pore size range for osteoblast growth is 400–800 μm and the optimal porosity range is 55–85%. The porous titanium implant with large pore size and high porosity can provide space for cell growth and facilitate cell attachment, which can promote bone ingrowth and improve osseointegration. However, the strength of porous titanium that meets this condition is significantly reduced, and it cannot meet the needs of implants. So there has been a lot of emphasis on designing the structure of gradient porous implants and related research (Weissmann et al., 2016; Chen et al., 2017; Liu et al., 2018; Roy et al., 2018).

However, the current evaluations of gradient porous implants are mostly focused on the mechanical properties, and fewer researchers have looked at the biological adaptation of gradient porous implants in specific biological environments. The implant is affected by the chewing force in the oral environment and transfers the force to the surrounding bone tissue. Some scholars have studied the numerical simulation of osteoblast growth under mechanical stress stimulation in combination with osteoblast culture experiments, and revealed the laws of mechanical stress stimulation and implant structure on cell growth and proliferation (Carpenter et al., 2018; San et al., 2018; Liu et al., 2019; Liu et al., 2020). The results show that the outer layer with high porosity and large pore size has biological advantages. The overall compressive strength of double-layer gradient structure is higher than that of single-layer outer structure (Lee et al., 2019). At the same time, the inner layer improves the higher strength, and the outer layer improves the good bone conductivity (Jiang et al., 2015). In this paper, the effect of the intrinsic properties of the material on the biomechanical adaptation is considered. The fretting value of the implanted bone should be less than 50 μm (Brunski et al., 2000; Trisi et al., 2009). According to Frost's minimum effective strain theory (Forst, 2004); there are four thresholds for the influence of stress and strain on bone tissue. Specifically, if the stress on the bone tissue is less than 1–2 MPa (strain less than 50–100 με), the bone resorption rate is greater than the reconstruction rate, and the bone tissue is resorbed; when the stress is in the range of 2–20 MPa (strain is in the range of 100–1,500 με), the bone formation rate and the absorption rate are roughly the same, maintaining normal bone quality, and increasing appropriately; when the stress is in the range of 20–60 MPa (strain is in the range of 1,500–3,000 με) we are in the active state of bone plastic construction, and bone stress can promote the growth of bone tissue; when the stress is in the range of 60–120 MPa (strain is in the range of 3,000–25,000 με), micro-damage is accumulated in the bone tissue.

In order to make oral implants with better mechanical properties under the condition of bone ingrowth, this experiment designed gradient porous structure implants with different pore structures. Using ANSYS Workbench numerical simulation software, the implants with different gradient structures were placed in a simulated oral environment. The compression strength of the implant, the stress and strain distribution of the bone tissue around the implant and the micro-motion of the bone tissue interface are evaluated, and the influence of the gradient structure on the performance of the implant is obtained, and the best gradient porous structure to meet the requirements of the implant is identified.

MATERIALS AND METHODOLOGY

Model Construction

In this study, lattice structural units were used to construct a gradient porous implant model. Taking into account the strength requirements of the gradient structure, the suitable aperture range for bone ingrowth, and the uniform connection between the inner and outer layers, the selected lattice structure units are cubic units (a), cubic-centered units (b), and cubic-centered units (c), as shown in **Figure 1**. The side length of the cube is 1 mm, and the change of porosity can be controlled by changing the radius of its pillars.

The gradient porous implants are designed with a-b gradient structure with b as the core and a-c gradient structure with c as the core. The size of the gradient porous structure is 4 mm × 4 mm × 10 mm, of which the core structure is 2 mm × 2 mm × 10 mm. The overall cut is a gradient porous structure with a bottom diameter of 4 mm and a height of 10 mm. By adjusting the pillar radius of a, b, c lattice structure, the porosity and pore diameter of the implant can be adjusted. **Figure 2** shows the model of a-b and a-c gradient porous structure cylinders. The inner and outer layer porosity, outer layer pore size and average porosity calculated by the gradient porous structure of the two combinations are shown in **Table 1**. The compressive performance test of the a-b structure gradient porous cylinder is performed, and the stress-strain curve is shown in **Figure 3**. The compressive specimens were manufactuer by the SLM-125 HL machine (Solutions Gmbh, Germany) under a Ar atmosphere contain below 0.02% oxygen. The laser power, laser scanning speed, layer thickness, and hatching distance were 200 W, 900 mm/s, 30 μm, and 0.14 mm. The compressive yield strength and elastic modulus values of each gradient porous structure column are calculated from the stress-strain curve, the results are shown in **Figures 3A,B**.

Using Solidworks modeling software, the gradient porous implant model and the mandible model of the implant environment were constructed. Since the actual model of the human mandible is relatively complicated, the implant has a certain effect on the surrounding strong bone tissue when the implant is loaded. For the convenience of calculation, the constructed mandible model is a simple cuboid shape. 1) The implant body has a gradient porous structure with the length of

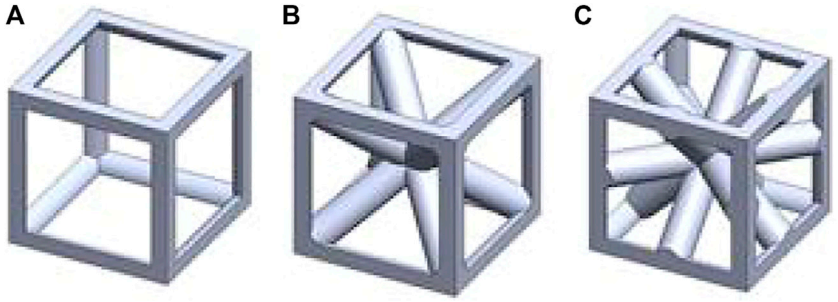

FIGURE 1 | Geometrical sketch of designed unit structures. **(A)** cubic structure **(B)** cubic center **(C)** cubic edge center

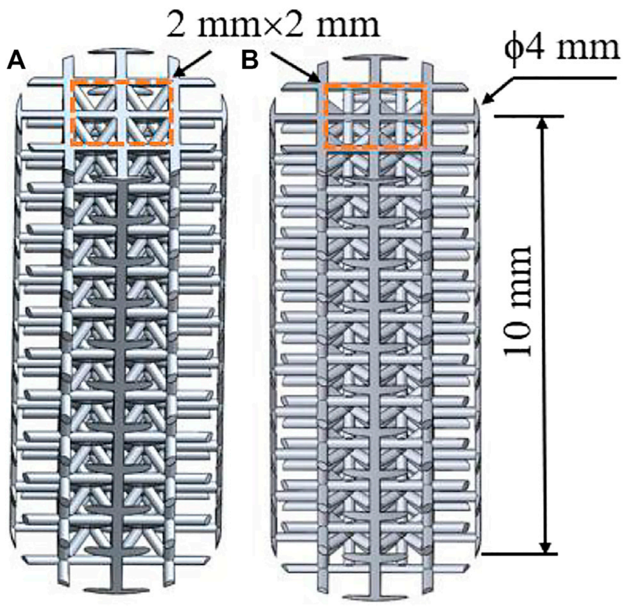

FIGURE 2 | Model diagram of gradient porous structure column **(A)** a-b type structure **(B)** a-c type structure.

10 mm and the diameter of 4 mm; the neck height is 1.8 mm, the upper diameter is 4.8 mm, and the lower bottom diameter is 4 mm. A 5 mm high abutment is designed on the upper part of the implant. The top diameter of the abutment is 3 mm and the bottom diameter is 4 mm, which is simplified as a whole with the implant. 2) The simplified mandibular bone model has a total height of 28.6 mm, a mesiodistal length of 25.4 mm, a buccal-lingual length of 10 mm, and an outer cortical bone thickness of 1.3 mm, The thickness of the constructed cortical bone is close to that of the biological bone, and the total depth of the entire implant inserted into the mandible is 11.3 mm. The model is shown in **Figures 3C,D**.

Implant Static Analysis

The finite element analysis software used in this experiment is ANSYS Workbench 18.0. The basic parameters of the Ti material used are the characteristics obtained by the research team in the previous study: density 4.46 g⋅cm^{-3}, elastic modulus 110 GPa, compressive yield strength 607 MPa, tensile strength 894 MPa. Because the porous structure of this experiment is irregular, the method of freely dividing the grid is adopted by manually adjusting the grid accuracy, using a hexahedral grid with a size set to 0.5 mm. For the convenience of calculation, the lower surface is added as a fixed constraint, the bite force is 120 N, and

TABLE 1 | Structural parameters of gradient porous structure model.

Structure	Pillar radius/mm	Porosity (%)	Core porosity (%)	Outer porosity (%)	Outer diameter/μm
a-b	0.1	87.32	75.72	91.71	800
	0.15	74.50	53.16	82.61	700
	0.175	67.30	42.00	77.00	650
	0.2	60.00	30.56	71.35	600
	0.225	52.86	21.00	65.00	550
	0.25	46.08	13.12	58.77	500
	0.275	39.83	0.80	52.00	450
	0.3	34.08	0.40	46.00	400
a-c	0.1	86.23	72.30	91.71	800
	0.15	72.57	47.12	82.61	700
	0.2	57.52	22.78	71.35	600
	0.25	43.67	5.55	58.77	500

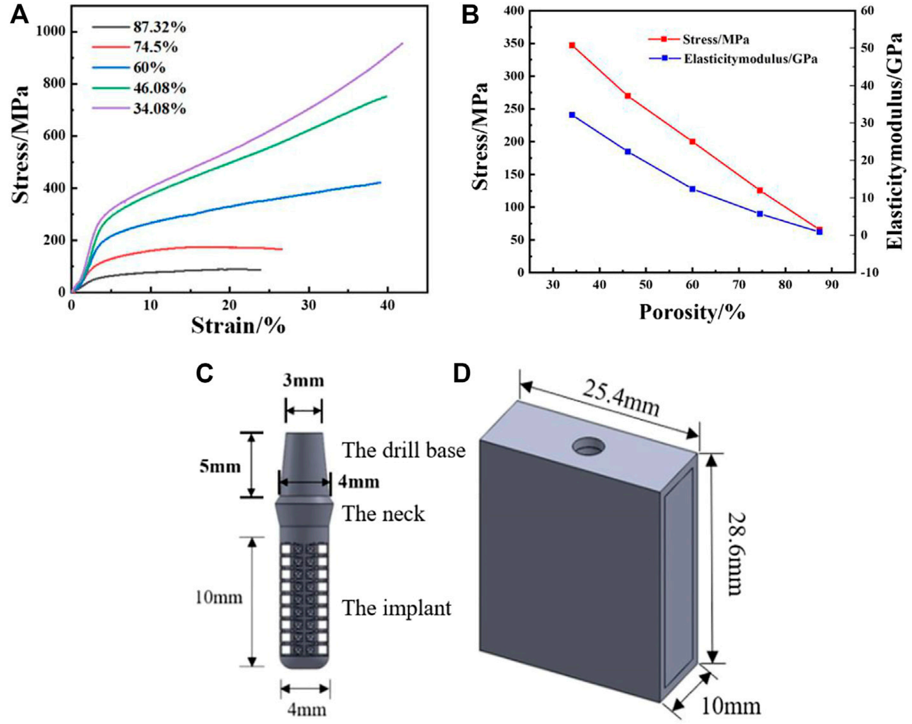

FIGURE 3 | Actual measured value of SLM samples: **(A)** Compression yield strength, **(B)** Elasticity modulus; **(C)** Gradient porous dental implant mode, **(D)** Simplified mandible model.

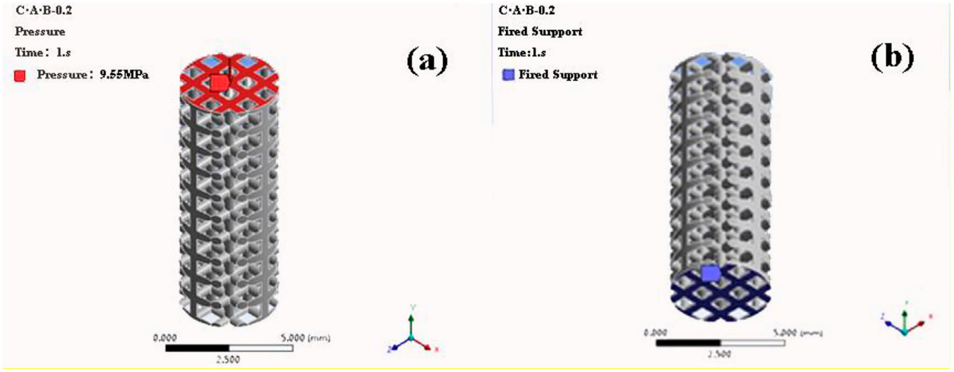

FIGURE 4 | Compression simulation parameter settings **(A)** Load mode **(B)** Constraint conditions (a-b structure with porosity of 46.08% as an example).

the upper surface is applied vertically. The restraint and loading methods are shown in **Figure 4**. Each model contains 160 units.

Analysis of Biological Fit of Implants in Oral Environment

Material Parameter Setting

The use of three-dimensional finite element analysis for biomechanical analysis requires simplified processing of complex human tissues and materials. The implant material is titanium. The mandibular model is composed of cancellous bone and cortical bone. The relevant parameters of bone tissue and implant materials are shown in **Table 2** (Santos et al., 2015).

TABLE 2 | Elastic modulus and Poisson's ratio of bone tissue and implant material.

Material	Elastic modulus/GPa	Poisson's ratio
Titanium	110	0.35
Cortical bone	13.7	0.3
Cancellous bone	1.37	0.3

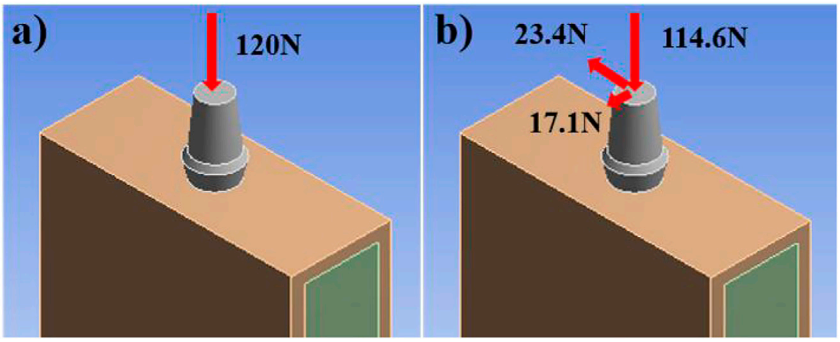

FIGURE 5 | Load regime. **(A)** vertical loading (120 N) and **(B)** oblique loading (118.2 N).

Contact Conditions and Constraints

The implant body and neck, implant neck and abutment, and cortical bone and cancellous bone are all set to be in binding contact. When analyzing the maximum equivalent stress and maximum equivalent strain of the bone tissue, it is assumed that complete osseointegration occurs between the implant and the surrounding bone, That is to simulate the changes in stress and strain at the end of planting. Therefore, the binding contact between the implant and the surrounding bone is set as a binding contact without sliding friction. When measuring the micro-movement of the implant-bone tissue interface, it is assumed that a fter the implant is stressed, there will be a pressing effect between the implant and the bone interface, and there will be a slight sliding along the interface, the friction coefficient is set to 0.3, That is, it simulates the micro-movement of the interface between the implant and the surrounding bone tissue at the early stage of implantation. In the simulation process, the buccal-lingual surface, mesiodistal surface, and bottom surface of the bone block model are set as rigid constraints, that is, it is assumed that the mandible does not move and does not shift. The setting of the above situation may have a certain error with the actual planting situation, but it has a certain guiding effect for the exploration of general rules. This is also to more conveniently and quickly find the best implant structure parameters.

Meshing

The implants in the oral environment are divided into tetrahedral meshes. The size of the grid will have a certain impact on the accuracy of the calculation result. The tighter the grid, the more accurate the result, but the larger the calculation amount. Therefore, dense grids are used for the implants and surrounding tissues. The rest uses a relatively loose grid. The 0.6 mm thickness of the implant-bone tissue interface adopts a dense grid, the grid size of this part is set to 0.3 mm, and the grid size of other parts is set to 0.5 mm, and the models of each group are consistent.

Loading Method

In this experiment, an average bite force of 120 N was used as the vertical load. At the same time, the combined force is set to simulate the limit bite force, which are 114.6 N in the axial direction, 17.1 N in the buccal and tongue direction, and 23.4 N in the proximal and distal directions. The combined force of the three directions is 15% with the long axis of the implant, and the size is 118.2 N. The two loading methods are shown in **Figure 5**.

Calculation Analysis and Observation Index

We usedse ANSYS Workbench software to perform static analysis on the model, obtain the stress and strain distribution cloud diagram of the implant and the bone tissue around the implant, calculate the stress dispersion of the implant and the cancellous bone, and analyze the distribution of the equivalent strain interval of the cancellous bone. The stress dispersion is defined as the ratio of the width of the stress distribution to the average stress. The smaller the dispersion, the more uniform the stress distribution. The definition formula of dispersion is shown in **Eq. 1**.

$$D = (S_{Max} - S_{Min})/S_{Savr} \tag{1}$$

Where D represents the degree of dispersion, S_{Max} is the maximum value of the stress or strain data, S_{Min} is the minimum value of the data, and S_{Savr} is the average value of the data.

The calculation of fretting is to define a node on the surface of the implant and determine the node at the corresponding position of the bone interface. After the loading force is applied, the relative displacement between the two nodes on the *x*-axis, *y*-axis and *z*-axis of the three-dimensional coordinate system is calculated. Therefore, when measuring implant micromotion, we took a reference point on the neck, body, and end of the implant, and measured the buccal-lingual (*x*-axis), vertical (y), and near-distal (*z*-axis) directions. The directional displacements are dx_1, dy_1, dz_1, and the displacements of the corresponding points on the bone tissue interface are measured at the same time as dx_2, dy_2, dz_2. According to **Eq. 2**, the comprehensive relative displacement, that is, the fretting value, is calculated:

$$S = \sqrt{(dx1 - dx2)^2 + (dy1 - dy2)^2 + (dz1 - dz2)^2} \tag{2}$$

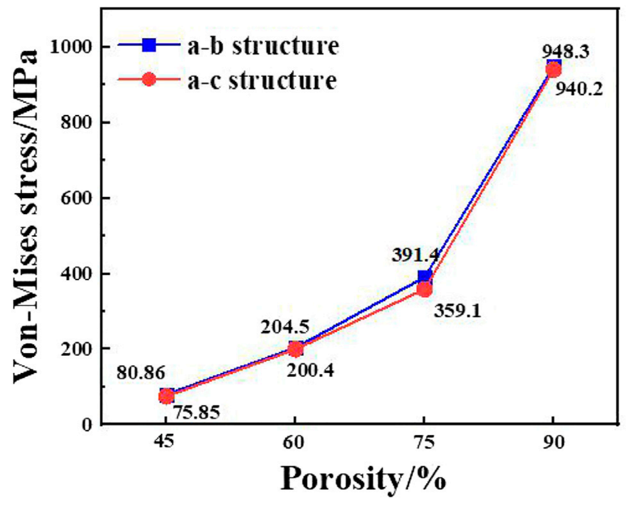

FIGURE 6 | Maximum equivalent stress of two structures with different porosity.

RESULTS AND DISCUSSION

The Effect of Structural Elements on the Mechanical Properties of Implants

The maximum equivalent stresses of the a-b structure and the a-c structure obtained by the axial force loading and compression simulation of the implant are shown in **Figure 6**. When the pillar radius of the two structures is 0.1˚mm, the porosity is 87.32 and 86.23%, and the maximum equivalent stress is 948.3 and 940.2˚MPa, respectively. The compressive yield strength of titanium is 607 MPa, therefore, yield occurs during use. When the pillar radius is the same, the overall porosity of the a-c structure is lower than that of the a-b structure, and the supporting area of the porous structure is larger, and the equivalent stress is smaller. But when the pillar radius is the same, the maximum equivalent stress of the a-b structure and the a-c structure is not much different, so the compressive performance of the two structures is basically the same.

The experiment further carried out simulation analysis for the a-b type structure with a small difference between the inner and outer layer structures. According to the principle of finite element analysis, the whole object is decomposed into finite structural elements, and the stress of each element is calculated, and the overall stress is obtained. The stress data of each cell in the model is derived, analogous to the calculation principle of the dispersion of particle size distribution, and the stress value of each element is analogous to the particle size, and the equivalent stress distribution is calculated. The result is shown in **Figure 7**. Overall, according to the obtained uniform stress distribution, under the action of axial force, as the porosity decreases, the effective bearing area of the force increases, and the stress distribution of the implant becomes more uniform; under the action of lateral force, the porosity is respectively 60.00, 52.86, 46.08% of the gradient structure and implants have good stress uniformity.

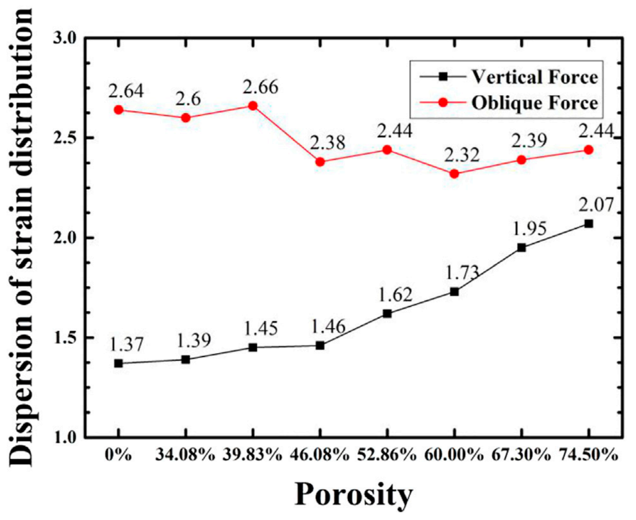

FIGURE 7 | Variation of stress distribution of implant with porosity for implant with a-b gradient structure and compact structure.

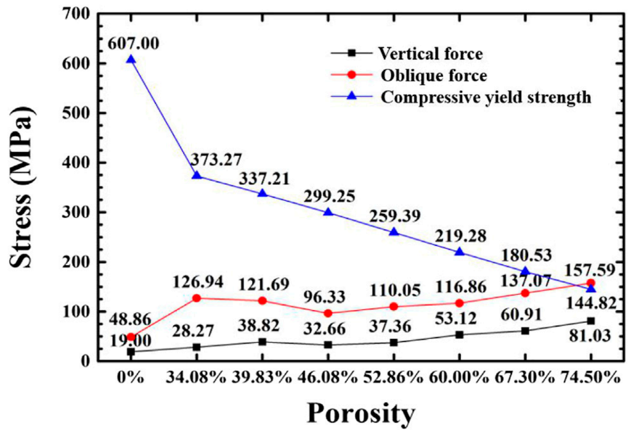

FIGURE 8 | Variation of maximum equivalent stress and compressive yield strength of the implant with porosity under two loading regimes.

The Effect of Porosity on the Mechanical Properties of Implants

Figure 8 shows the simulated maximum equivalent stress and theoretical yield strength of implants with different porosity gradient structures under two loads. The Compressive yield strength of the solid implant model is 607 MPa, and the finite element simulation results of the maximum equivalent stress under axial force and lateral force are 19.00 and 48.86 MPa, respectively, which are far lower than the yield strength of the material, and the compressive performance is optimum. In each group of gradient porous structure implants: under the action of axial force, as the porosity increases, the peak equivalent stress of the implant increases and the theoretical yield strength and compressive performance decrease. When the porosity is 74.50%, it cannot meet the mechanical performance

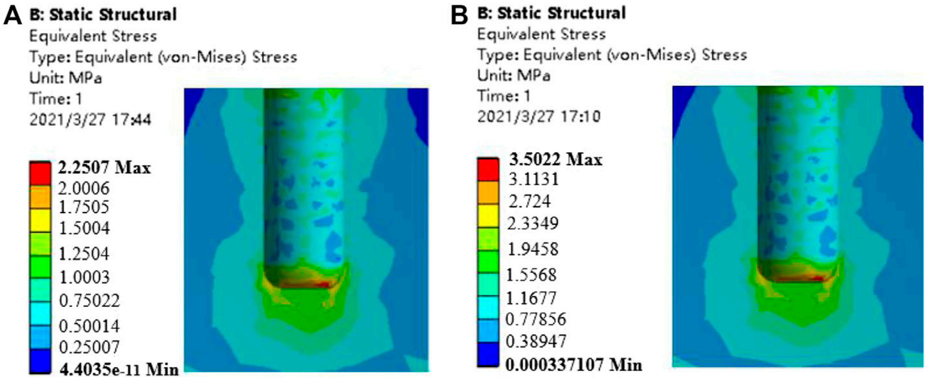

FIGURE 9 | Stress nephrogram of cancellous bone under 120 N vertical loading. **(A)** porosity of 46.08% **(B)** porosity of 74.50%.

requirements; when the porosity is less than 60.00% under lateral force, the maximum equivalent stress of the implant should be less than 50% of the yield strength to meet the requirements of stomatology for the mechanical performance of the implant. The minimum equivalent stress peak value of 46.08% implants is 96.33 MPa. Therefore, it is believed that the implants with 46.08% porosity have higher compressive strength and show better mechanical properties under lateral force.

The Effect of Porosity on the Biological Fit of the Implant

According to the theory of bone mechanics, if the stress of bone tissue is less than 2 MPa (strain is less than 100 με), bone tissue will resorb; when the stress is in the range of 2–20 MPa (strain is in the range of 100–1,500 με), the bone tissue maintains normal bone quality and grows appropriately; when the stress is in the range of 20–60 MPa (strain is in the range of 1,500–3,000 με), it is in an active state of bone plastic construction; when the stress exceeds 60 MPa (strain exceeds 3,000 με), the bone tissue is in a pathologically over-loaded state, and a small load can cause a fracture. In addition, the micro-motion value of the implant-bone tissue should not exceed 50–100 μm in order to achieve the bone tissue surrounding the implant and good osseointegration. In the experiment, the critical value of bone tissue stress and the proportion within the interval were used as the analysis basis to evaluate the biocompatibility of implants with gradient structures with different porosities.

The bone tissue mainly in contact with the gradient structure of the implant is cancellous bone, and the bone tissue within 4.2 mm from the surface of the implant (Liu et al., 2019) is the main stress-affected area. Therefore, this part of the cancellous bone block was cut and observed. Under the action of axial force and oblique force, the implants with the porosity of 46.08 and 74.50%, and the surrounding bone tissue stress cloud diagrams are shown in **Figures 9**, **10**, respectively. It can be seen from the stress cloud diagram that when the axial force is applied, the stress concentration of high-porosity implants is in the neck, and the stress concentration of low-porosity implants is around the body pores, which can reduce the tooth damage caused by excessive stress. When the lateral force is applied, the stress concentration of the implants of all structures appears in the neck.

Figure 11 shows the comparison of the maximum equivalent stress and maximum equivalent strain of each group of gradient structure implant models and compact implant models. For compact implants, due to the stress shielding effect, the equivalent stress of the cancellous bone is lower than the normal growth value regardless of the axial force or the oblique force. When the porosity is lower than 39.83%, the maximum equivalent stress is lower than 2 MPa, which is the inactive mode threshold of bone tissue, and osteoblasts do not receive sufficient mechanical stimulation, resulting in disuse resorption of bone tissue. When the porosity is higher than 46.08%, and the maximum equivalent strain exceeds 3000 με of the bone repair micro-fatigue damage strain value, it results in pathological overload. The micro-fatigue damage accumulated in the bone in these areas can easily cause pathological fractures. The porosity of the gradient structure implant is in the range of 39.83–46.08%, which can meet the normal growth of bone tissue.

When the strain of the bone tissue is 100–1,500 με, the existing surrounding bone tissue can be maintained to prevent bone loss, and when the strain is high, it is conducive to the formation of bone (Liu et al., 2019). For the cancellous bone within 100–1,500 με, we plotted the frequency histogram of the strain data and calculated the average equivalent strain, the porosity of the gradient structure implants with 46.08 and 74.50%, and the strain distribution of cancellous bone around the dense structure implant. As shown in **Figures 12**, **13**, as the porosity decreases, the strain distribution width decreases, the peak value increases, and the strain distribution in the bone tissue become more uniform. The comparison of the average equivalent strain results of each group of gradient structure implants is shown in **Figure 14**. According to the statistical results, under the action of axial force, the larger average equivalent strain is the implant with porosity 39.83 and 46.08%; under the action of lateral force, the larger average equivalent strain is the porosity 39.83 and 46.08% and 52.86% of implants. The larger the average equivalent strain, the greater the strain on the whole cancellous bone, which is considered to be closer to the range of active reconstruction of bone tissue and beneficial to bone formation. In the two loading

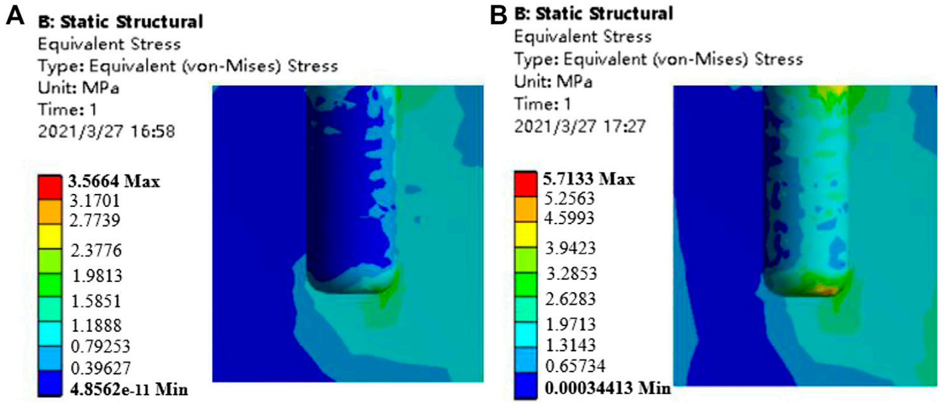

FIGURE 10 | Stress nephrogram of cancellous bone under 118.2 N oblique loading (a) porosity of 46.08% b) porosity of 74.50%.

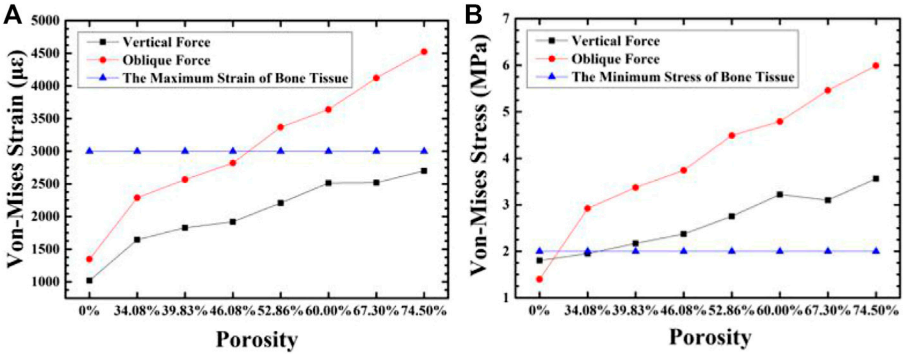

FIGURE 11 | The variation of maximum equivalent strain **(A)** and stress **(B)** in the cancellous bone around the implant with the porosity of the implant.

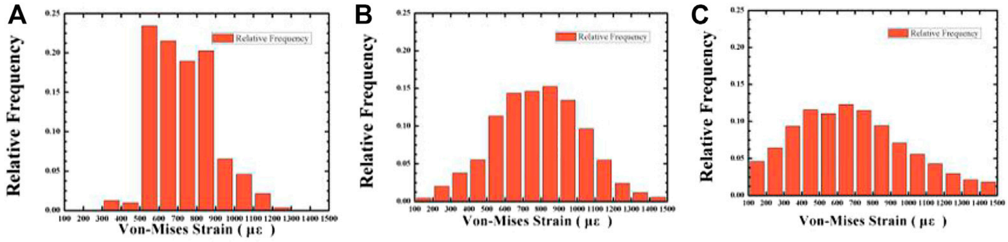

FIGURE 12 | The variation of the relative frequency with Von-mizes strain in the cancellous bone under 120 N vertical loading. Average porosity: **(A)** 0% (compact structure); **(B)** 46.08%; **(C)** 74.50%.

modes, the average equivalent strain of the implants with the porosity of 39.83 and 46.08% is larger, which is more conducive to bone formation.

When the strain of bone tissue is in the range of 1,500–3,000 με, the rate of bone formation is faster than that of bone resorption, and lamellar bone formed on the bone surface. The proportion of unit cells that have an equivalent strain in the range of 1,500–3,000 με in the cancellous bone around the implant under two loading regimes are calculated, and are shown in **Figure 15**. It can be seen that with the porosity increase, the proportion of cells with an equivalent strain in the range of 1,500–3,000 με increases, that is, there are more bone tissues in an active bone-forming state, and the quantitative binding capacity increases. Compared with the porosity of 39.83%, when the porosity is 46.08%, there are more unit cells in the surrounding cancellous bone for active bone formation.

The optimal gradient structure implant in this experiment was compared with the gradient structure implant [23] that has been

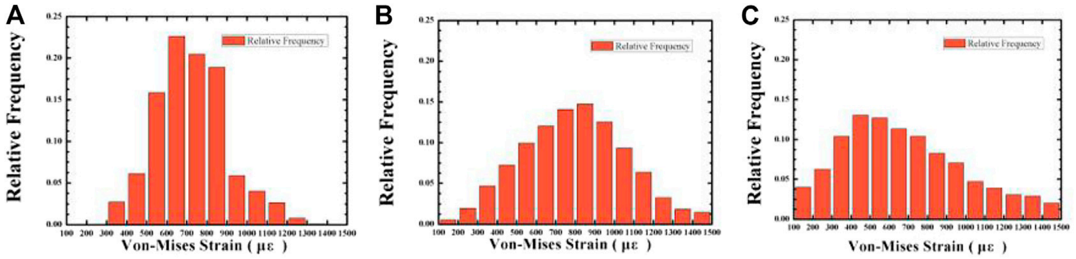

FIGURE 13 | The variation of the relative frequency with Von-mizes strain in the cancellous bone under 118.2 N oblique loading. Average porosity: **(A)** 0% (compact structure); **(B)** 46.08%; **(C)** 74.50%.

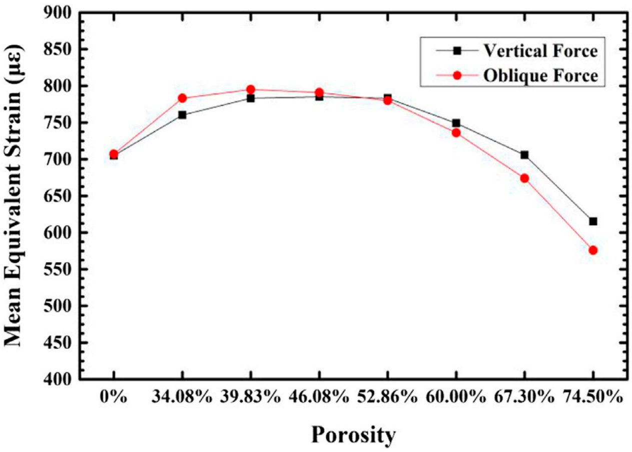

FIGURE 14 | The variation of equivalent strain in the cancellous bone around implants with porosity.

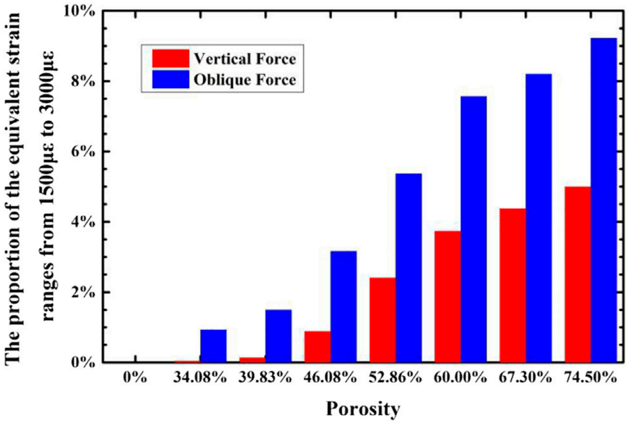

FIGURE 15 | The variation of the proportion of cancellous bone around the implant that have strain in the range of 1,500–3,000°με with the porosity of the implant.

studied. The comparison results are shown in **Table 3**. It can be seen that the pore parameters of the two structures are basically the same. *In vivo*, animal experiments were carried out in the research of Wang Yaling[23], and it was concluded that the designed gradient structure implant has good osseointegration performance. The maximum equivalent stress of the bone tissue in this experiment is similar to the results[23]. It can be seen that the best gradient structure implant obtained in this experiment also has considerable osseointegration capacity. This experiment adopts a gradient lattice structure, compared with the gradient structure obtained by directly opening the holes in the reference, it is also a side load stress. The maximum equivalent stress of the optimal gradient structure implant obtained in this experiment is 96.33 MPa. The proposity of structure in this study is lower than the design of the Wang Yaling, and it is not easy to break. In addition, the compression strength of the implant in the work of Wang Yaling (Wang, 2017) is 259.39 MPa, while the compression strength of the implant in this experiment is 299.25 MPa.

Gradient Structure Implant-Bone Tissue Section Micro-movement

The initial stability of the implant means that in the initial stage of implantation into the bone tissue, the implant will not have a large relative displacement between the interface and the bone tissue due to external force. The small mobility between the implant and the bone interface in the early stage of implantation is not conducive to the adhesion of osteoblasts around the implant. It will also repeatedly interfere with the normal bone reconstruction process, reduce the osseointegration effect, and affect the area that has reached healing and causes damage. The calculation of fretting is to define a node on the surface of the implant and determine the node at the corresponding position of the bone interface. After the loading force is applied, the relative displacement between the two nodes on the x-axis, y-axis and z-axis of the three-dimensional coordinate system is calculated. This experiment calculated the micro-movements of the implant-cortical bone interface, the implant-cancellous bone (top) interface, and the implant-cancellous bone (bottom) interface in each group of implant models. For the implant-bone tissue in each group, the fretting value of the interface is between 6.63 and 22.53 μm. It is generally believed that the fretting value of the implant-bone tissue should not exceed 50–100 μm to achieve the bone tissue surrounding the implant instead of fibrous tissue surrounding the implant. Therefore, the micro-movement of the implant-bone tissue interface of each gradient structure does not exceed 50 μm, and it has the ability to complete osseointegration.

TABLE 3 | The optimal gradient structure implant in this study and in other's study.

	Core porosity (%)	Maximum equivalent stress of implant/MPa	Maximum equivalent stress of bone tissure/MPa	Compressive strength/MPa
References (Trisi et al., 2009)	19.6	134.7	49.04	259.39
This study	13.12	96.33	44.42	299.25

CONCLUSION

1) As the porosity decreases, the compressive strength of the gradient porous implant increases. For the a-b structure with a porosity of 46.08%, the maximum equivalent stress is the lowest under the lateral force environment, and the stress distribution is uniform.
2) With the increase of porosity, the maximum equivalent stress and maximum equivalent strain in the bone tissue increase. When the porosity of the implant is 39.83–46.08%, the stress and strain of the bone tissue are in the range that satisfies normal growth. As the porosity decreases, the average equivalent strain of cancellous bone first increases and then decreases, and the proportion of strain decreases in the range of 1,500–3,000 με. Under the action of axial force, the stress distribution in the cancellous bone becomes more uniform as the porosity decreases; under the action of lateral force, the stress distribution in the cancellous bone becomes more even when the porosity is higher.
3) The best gradient porous structure parameters were: average porosity 46.08%, inner porosity 13.12%, outer porosity 58.77%, outer pore size 500 um. Under this structure, the equivalent strain is in a suitable range for the active bone growth and integration. The maximum equivalent stress under the oral ultimate stress is 99.33 MPa, much lower than the yield strength of 269.72 MPa.

DATA AVAILABILITY STATEMENT

The original contributions presented in the study are included in the article/supplementary material, further inquiries can be directed to the corresponding authors.

AUTHOR CONTRIBUTIONS

Paper Write: BL; Funding Administration: XL, CL; Paper Revised: WX, MT, JD; Experiment: BL, MC, YL; Thesis guidance: XQ, XH, JZ, LG.

FUNDING

This research work is supported by the National Natural Science Foundation of China (51922004, 51874037), State Key Lab of Advanced Metals and Materials, University of Science and Technology Beijing (2019-Z14,2020Z-04), Fundamental Research Funds for the Central Universities (FRF-TP-19005C1Z), European Union via H2020-MSCA-RISE program (BAMOS project, grant no: 734156) and Royal Society via International Exchange Programme (grant no: IEC\NSFC\191253). WX acknowledges the support from the China Scholarship Council (CSC) for a CSC Ph.D. scholarship (201906460106). Engineering and Physical Science Research Council (EPSRC) via DTP CASE programme (Grant No: EP/T517793/1).

REFERENCES

Brunski, J. B., Puleo, D. A., and Nanci, A. (2000). Biomaterials and Biomechanics of Oral and Maxillofacial Implants: Current Status and Future Developments. *Int. J. Oral Maxillofac. Implants* 15 (1), 15–46. doi:10.1046/j.1365-2591.2000.00269.x

Carpenter, R. D., Klosterhoff, B. S., Torstrick, F. B., Foley, K. T., Burkus, J. K., Lee, C. S. D., et al. (2018). Effect of Porous Orthopaedic Implant Material and Structure on Load Sharing with Simulated Bone Ingrowth: A Finite Element Analysis Comparing Titanium and PEEK. *J. Mech. Behav. Biomed. Mater.* 80, 68–76. doi:10.1016/j.jmbbm.2018.01.017

Chen, S. Y., Huang, J. C., Pan, C. T., Lin, C. H., Yang, T. L., Huang, Y. S., et al. (2017). Microstructure and Mechanical Properties of Open-Cell Porous Ti-6Al-4V Fabricated by Selective Laser Melting. *J. Alloys Compounds* 713 (8), 248–254. doi:10.1016/j.jallcom.2017.04.190

Chia, H. N., and Wu, B. M. (2015). Recent Advances in 3D Printing of Biomaterials. *J. Biol. Eng.* 9 (1), 1–14. doi:10.1186/s13036-015-0001-4

Forst, H. M. (2004). A 2003 Update of Bone Physiology and Wolff's Law for Clinicians. *Angle Orthodontist* 74 (1), 3–15. doi:10.1043/0003-3219(2004)0742.0.CO;2

He, G., Liu, P., and Tan, Q. (2012). Porous Titanium Materials with Entangled Wire Structure for Load-Bearing Biomedical Applications. *J. Mech. Behav. Biomed. Mater.* 5 (1), 16–31. doi:10.1016/j.jmbbm.2011.09.016

Jiang, G., Li, Q., Wang, C., Dong, J., and He, G. (2015). Fabrication of Graded Porous Titanium-Magnesium Composite for Load-Bearing Biomedicalapplications. *Mater. Des.* 67 (2), 354–359. doi:10.1016/j.matdes.2014.12.001

Lee, H., Park, S., and Noh, G. (2019). Biomechanical Analysis of 4 Types of Short Dental Implants in a Resorbed Mandible. *The J. Prosthetic Dentistry* 121 (4), 659–670. doi:10.1016/j.prosdent.2018.07.013

Lewis, G. (2013). Properties of Open-Cell Porous Metals and Alloys for Orthopaedic Applications. *J. Mater. Sci. Mater. Med.* 24 (10), 2293–2325. doi:10.1007/s10856-013-4998-y

Liu, F., Zhang, D., Zhang, P., Zhao, M., and Jafar, S. (2018). Mechanical Properties of Optimized Diamond Lattice Structure for Bone Scaffolds Fabricated via Selective Laser Melting. *Materials* 11 (3), 374–391. doi:10.3390/ma11030374

Liu, L., Duan, J., Shi, Q., Chen, Q., Yao, Q., and Li, Z. (2020). Mechanical Effect on the Evolution of Bone Formation during Bone Ingrowth into a 3D-Printed Ti-alloy Scaffold. *Mater. Lett.* 273, 127921. doi:10.1016/j.matlet.2020.127921

Liu, L., Shi, Q., Chen, Q., and Li, Z. (2019). Mathematical Modeling of Bone In-Growth into Undegradable Porous Periodic Scaffolds under Mechanical Stimulus. *J. Tissue Eng.* 10, 204173141982716. doi:10.1177/2041731419827167

Roy, S., Dey, S., Khutia, N., Roy Chowdhury, A., and Datta, S. (2018). Design of Patient Specific Dental Implant Using FE Analysis and Computational Intelligence Techniques. *Appl. Soft Comput.* 65 (1), 272–279. doi:10.1016/j.asoc.2018.01.025

San, C. V., Paul, F., Aadil, M., Melanie, J. C., and Gordon, W. B. (2018). Novel Adaptive Finite Element Algorithms to Predict Bone Ingrowth in Additive Manufactured Porous Implants. *J. Mech. Behav. Biomed. Mater.* 87, 230–239. doi:10.1016/j.jmbbm.2018.07.019

Santos, L. S. d. M., Rossi, A. C., Freire, A. R., Matoso, R. I., Caria, P. H. F., and Prado, F. B. (2015). Finite-Element Analysis of 3 Situations of Trauma in the Human Edentulous Mandible. *J. Oral Maxillofacial Surg.* 73 (4), 683–691. doi:10.1016/j.joms.2014.10.014

Tane, M., Hagihara, K., Ueda, M., Nakano, T., and Okuda, Y. (2016). Elastic-modulus Enhancement during Room-Temperature Aging and its Suppression in Metastable Ti-Nb-Based Alloys with Low Body-Centered Cubic Phase Stability. *Acta Materialia* 102 (1), 373–384. doi:10.1016/j.actamat.2015.09.030

Taniguchi, N., Fujibayashi, S., Takemoto, M., Sasaki, K., Otsuki, B., Nakamura, T., et al. (2016). Effect of Pore Size on Bone Ingrowth into Porous Titanium Implants Fabricated by Additive Manufacturing: An *In Vivo* experiment. *Mater. Sci. Eng. C* 59 (2), 690–701. doi:10.1016/j.msec.2015.10.069

Trisi, P., Perfetti, G., Baldoni, E., Berardi, D., Colagiovanni, M., and Scogna, G. (2009). Implant Micromotion Is Related to Peak Insertion Torque and Bone Density. *Clin. Oral Implants Res.* 20 (5), 467–471. doi:10.1111/j.1600-0501.2008.01679.x

Wally, Z. J., Haque, A. M., Feteira, A., Claeyssens, F., Goodall, R., and Reilly, G. C. (2019). Selective Laser Melting Processed Ti6Al4V Lattices with Graded Porosities for Dental Applications. *J. Mech. Behav. Biomed. Mater.* 90 (8), 20–29. doi:10.1016/j.jmbbm.2018.08.047

Wang, Yaling. (2017). *Research on the Performance of Porous Structure Implants Based on Laser Selective Melting technology[D]*. PhD Thesis. Chongqing, China. Chongqing University.

Weissmann, V., Bader, R., Hansmann, H., and Laufer, N. (2016). Influence of the Structural Orientation on the Mechanical Properties of Selective Laser Melted Ti6Al4V Open-Porous Scaffolds. *Mater. Des.* 95 (4), 188–197. doi:10.1016/j.matdes.2016.01.095

Yavari, S. A., Wauthle, R., van der Stok, J., Riemslag, A. C., Janssen, M., Mulier, M., et al. (2013). Fatigue Behavior of Porous Biomaterials Manufactured Using Selective Laser Melting. *Mater. Sci. Eng. C Mater. Biol. Appl.* 33 (8), 4849–4858. doi:10.1016/j.msec.2013.08.006

Conflict of Interest: The authors declare that the research was conducted in the absence of any commercial or financial relationships that could be construed as a potential conflict of interest.

Advantages of publishing in Frontiers

OPEN ACCESS
Articles are free to read
for greatest visibility
and readership

FAST PUBLICATION
Around 90 days
from submission
to decision

HIGH QUALITY PEER-REVIEW
Rigorous, collaborative,
and constructive
peer-review

TRANSPARENT PEER-REVIEW
Editors and reviewers
acknowledged by name
on published articles

Frontiers
Avenue du Tribunal-Fédéral 34
1005 Lausanne | Switzerland

Visit us: www.frontiersin.org
Contact us: frontiersin.org/about/contact

REPRODUCIBILITY OF RESEARCH
Support open data
and methods to enhance
research reproducibility

DIGITAL PUBLISHING
Articles designed
for optimal readership
across devices

FOLLOW US
@frontiersin

IMPACT METRICS
Advanced article metrics
track visibility across
digital media

EXTENSIVE PROMOTION
Marketing
and promotion
of impactful research

LOOP RESEARCH NETWORK
Our network
increases your
article's readership